A kinetic and spectroscopic study of chemistry relating to the atmospheric role of iodine species

Thomas John Gravestock

Submitted in accordance with the requirements for the degree of Doctor of Philosophy

The University of Leeds

School of Chemistry

September 2006

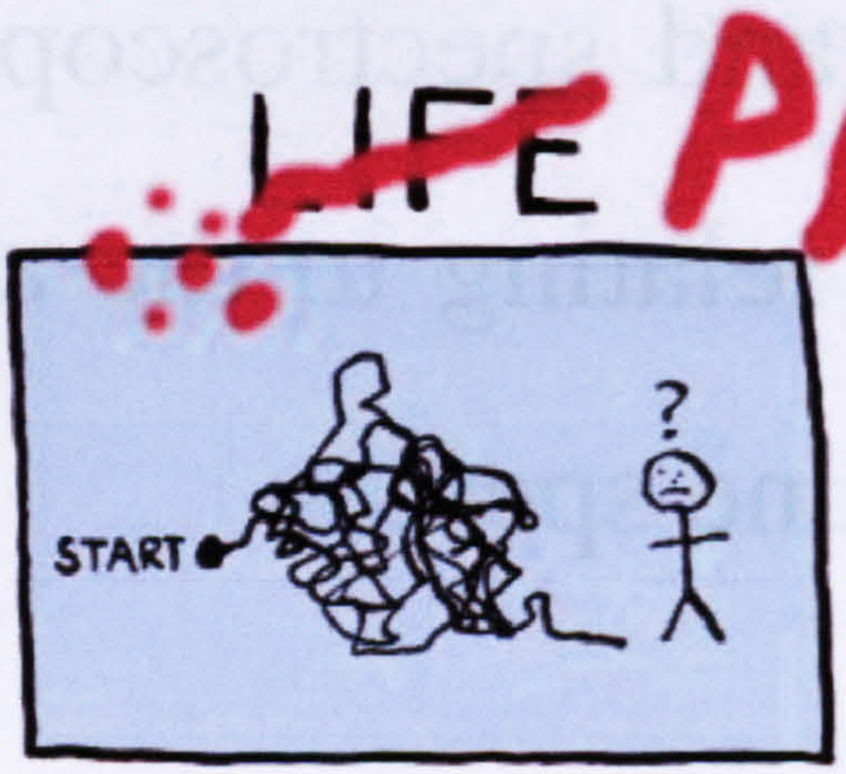

the
INTERESTING
thoughts of
EDWARD
MONKTON

"Life" by Edward Monkton
(http://www.edwardmonkton.com)

Drawing reproduced and modified with the kind permission of Edward Monkton.

"not when the truth is dirty, but when it is shallow, does the enlightened man dislike to wade into its waters"[1]

1. http://www.brainyquote.com/quotes/authors/f/friedrich-nietzsche.html

This work is dedicated to the memory of James Casey McGinley; a provoker of tradition and seeker of truth, and to Louie, for whom the following lines have been written:

The Journey of Life

From the tributaries to the meandering river
The water is removed from its source
Cast in perpetual motion
Its history in constant flux
Its origins diluted and lost
A cycle of chaos
Over infinite boundaries
Leads to an unknown place.

To a Sea of conflicting souls
Your fate is bequeathed
Forces beyond understanding
Have no tolerance of individuality
And crowd your freedom
Against the shoulders of strangers
You travel downstream.

A period of calm precedes turbulence
All will befall you as nature intended
Yield to the currents
And reflect and rejoice with the turn of the tides
With your creator
And together we come of age

Preface

To justify spending the past four years of my life (excluding any sporadic bursts of introverted melancholy and distemper) studying towards my PhD, I feel it is necessary to explain to myself, and to those who have not received as much of my attention as they were due, the intrinsic value of academic research.

Presumably, as long as human beings have existed in what may be thought of as a vaguely intelligible state, the peculiarity of existence has been a profound preoccupation of thought, and an unsettling concept. The Greek philosopher, Socrates (470 – 399 BC) is accredited with the quote, "I know nothing except the fact of my ignorance"[1]. Although there may be some level of absolute truth in this statement, it merely reflects the (internally felt) insignificance of human life to the totality of the Universe, much in the same way that a musical note may be seen as insignificant to the beauty and grandeur of an opera, and a point of view that is not particularly useful to the every day life of most human beings. For example, if I decided that I wanted to eat baked beans on toast for my tea, my state-of-being is naturally concerned with the task of purchasing what I recognise to be a tin of beans, and not with whether the baked bean actually exists, what its absolute nature is, or what my metaphysical relationship to the bean, which I am going to devour, might be. Once the bean is consumed, however, my human curiosity may once again be evoked, as I ponder the profound release of gas from such a small, apparently solid object.

Despite our common requirement for the fundamentals of life, it would appear that a thirst for knowledge is one property that separates human beings from the general animal population – it is difficult to imagine a moth wondering how IKEA managed to sell a light bulb, which singed its eyeballs, for such a cheap price (although this statement may also be applicable to many humans). Indeed, Socrates is also believed to have said that, "The unexamined life is not worth living for a human being"[1]. How then, is it best to examine life? The arts are perhaps considered the most human of academic disciplines. One definition of art is, "human skill and agency (opp. to nature): application of skill to production of beauty (esp. visible beauty) and works of creative imagination"[2]. The arts allow an expression of the world around us in terms of our experience, enhancing identity and a sense of emotional security, thereby aiding the development of society and culture.

Science is generally regarded as "knowledge ascertained by observation and experiment"[2] or "accounts of the world which depend on no particular perspective on the world and no particular type of observer"[3]. These, rather inhumane, definitions of science puzzle me – how is it that a discipline created by human beings can be independent of perspective or observer? Far from being the mundane interpretation of observation, it would seem to me that

science requires, perhaps, the greatest "creative imagination" of all and could be regarded as the truest of arts. One of the greatest scientists of the modern era, Albert Einstein (1880 – 1976), appeared to have intrinsic "artistic" qualities: "Imagination is more important than knowledge"[4]; "The only real valuable thing is intuition"[4]. The fact that a scientist as great as Einstein seemingly centred his beliefs from such an artistic (or human) perception would tend to suggest that science, while undoubtedly a faculty centred around observation and experiment, is directed, and partially evolves through the artistic nature of human beings. In essence, therefore, science is a human interpretation of the world around us, derived by the application of thought to observation, providing a means to satisfy our peculiar disposition for knowledge and gain some sort of rationalisation to what it means to be alive. In the absence of humans, science (as is also the case for any academic enquiry) is absolutely redundant and non-existent: a void within a void; an end before a beginning.

Although the findings of science may often be disconcerting and do not offer the same emotional comforts as the conventional arts, far from being an untenable academic subject, or simply a means by which human beings can satisfy their ego, science is the material foundation of human civilisation *via* its application through technology. Practically all that we see around us (of human creation) is, at least partially, the direct result of the application of scientific research. It is no coincidence that periods of human history are often defined by their technological skill: the Bronze Age; the medieval agricultural age; the industrial age; the .com age. Naturally, science can be exploited to the detriment of human civilisation (as can art, philosophy or religion), for example through its application to the manufacture of weapons of war. However, knowledge acquired through scientific research can also be used for the greater good of humanity, vividly illustrated by the example of the Antarctic ozone hole.

In the early 1970's it was observed that the atmospheric concentration of CFC's (ChloroFluoroCarbons, used chiefly as aerosol propellants and refrigerants) was approximately equal to the total amount ever produced [5]. An important study considering the potential implications of these observations soon followed [6], predicting that the presence of CFC's in the atmosphere could have severe consequences for stratospheric ozone concentrations (the ozone layer). The ozone layer is essential to life on Earth as it prevents harmful ultraviolet radiation reaching the Earth's surface and thermally stabilises the atmosphere. Measurements of stratospheric ozone levels in Antarctica by scientists from the British Antarctic Survey (BAS) in the late 1970's found that dramatic reductions in ozone were occurring in the lower stratosphere, and in 1985 the observed reduction was so dramatic that the BAS scientists thought their instruments were broken. Replacing their instruments, the scientists discovered that their initial measurements were correct – the Antarctic ozone hole was unambiguously identified [7].

By proving that CFC's in the atmosphere were directly responsible for the decrease in stratospheric ozone, the scientific community forced the world's governments to introduce suitable legislation and the Montreal protocol of 1987, with subsequent amendments, saw the (almost) complete ban of CFC production and emission by 1995. To date, only six states (the most well known being Iraq) are not ratified to the Montreal Protocol, all of which do not emit significant amounts of ozone depleting substances. Hence, within two decades, the application of the research of atmospheric scientists had led to the hypothesis, observation, and (partial) solution to the depletion of stratospheric ozone. Since the implementation of the Montreal protocol, stratospheric levels of ozone are no longer decreasing and it is thought that a complete recovery may be realised within several decades [8]. Three scientists were awarded the 1995 Nobel Prize for chemistry for their contribution towards our understanding of stratospheric ozone depletion. Hence the ozone hole is an example of scientific research that has led to the satisfaction of the human ego, and unarguable benefit to the health of life on Earth.

In the current age of global climate change, atmospheric research has never been more relevant to the benefits of human civilisation. The British Prime Minister, Tony Blair (1946 – present) said in September 2005 that climate change was, "the world's greatest environmental challenge", and, "so far reaching in its impact and irreversibility in its destructive power, that it alters radically human existence"[9]. Sadly, however, the problem of global warming is an entirely different beast to that of the ozone hole. The restriction of CFC's had no major impact on the economies of the world's super powers, whereas the restricted use of fossil fuels clearly does. The policies of governments (which largely reflect the desires, and ignorance, of their inhabitants) can only change by the provision of research-driven political pressure resulting from incontrovertible evidence of the devastating effects of climate change, coupled with a greater public awareness.

Although my research is a tiny piece of the atmospheric jigsaw (like the note of an opera) I, therefore, feel justified in the essence of my perseverance, and am proud that by the application of my thought and will, may help to create a better future for our children.

I would like to end this preface with a quote from the Dutch Philosopher, Arthur Schopenhauer (1788 – 1860)

"Without books the development of civilisation would have been impossible. They are the engines of change, windows on the world, "lighthouses" as the poet said "erected in the sea of time". They are companions, teachers, magicians, banker of the treasures of the mind. Books are humanity in print."[10]

References

1. http://en.wikiquote.org/wiki/Socrates
2. *The Wordsworth Concise English Dictionary*, Eds. G. W. Davidson, M. A. Seaton and J. Simpson, Wordsworth Editions Ltd., Hertfordshire, 1994.
3. *The Oxford Companion to Philosophy*, Ed, T. Honderich, Oxford University Press, Oxford, 1995.
4. http://rescomp.stanford.edu/~chesire/EinsteinQuotes.html
5. J. E. Lovelock, R. J. Maggs and R. J. Wade, "Halogenated Hydrocarbons in and over the Atlantic", *Nature*, **241**, 194, 1973.
6. M. J. Molina and F. S. Rowland, "Stratospheric sink for chlorofluoromethanes. Chlorine atom-catalysed destruction of ozone", *Nature*, **249**, 810 – 812, 1974.
7. J. C. Farman, B. G. Gardiner and J. D. Shanklin, "Large losses of total ozone in Antarctica reveal seasonal ClO_x/NO_x interaction", *Nature*, **315**, 207 – 210, 1985.
8. S. Solomon, "The hole truth: What's news and what's not about the ozone hole", *Nature*, **427**, 289 – 291, 2004.
9. http://www.foe.co.uk/resource/press_releases/election_campaign_ignores_21042005.html
10. http:// www.brainyquote.com/quotes/authors/a/arthur_schopenhauer.html

Acknowledgements

As Ian Dury once said, "There Ain't Half Been Some Clever Bastards", and I have been looking forward to this opportunity for expressing my thanks to some of them for their help during the course of my PhD.

In keeping with tradition, I must first thank my Supervisor, Professor Dwayne Ellis Heard. Dwayne's disposition for exploring novel and applicable aspects of atmospheric science has been a guiding example to me over the past four years. On a personal note, I would like to express my sincere appreciation to Dwayne for his great qualities of patience, understanding, acceptance, and faith – all of which he has required as my Supervisor.

Then there is the peculiar character of Dr. Mark Blitz. Mark has always been open with his scientific knowledge and experience, his criticism, and his praise. The Dainton laboratory, which I have immensely enjoyed being a part of, owes much of its unique research environment to Mark – and whatever my future, I will look back fondly on my time there. From Dainton I also thank Kenny, Tracy, Namil, Maite, Andy, Liming, Patti, Ramesh, Sally, Ben, Kelly and Scott (not to mention the crazy Hungarian, Tomaz Kovacs – Bazd Meg!). I particularly thank Maite for help with kinetic analyses, and Sally and Kelly for allowing me precious laboratory time for the completion of experiments.

Among the other folk at Leeds I would like to thank Drs Trevor Ingham and William Bloss for their interest, enthusiasm, knowledge, and input into my research. Professor Mike Pilling remains the connecting service when my academic enquiries have reached their terminus. For their technical assistance and expertise I would like to thank John Dixon, Peter Halford-Maw and John Spence for creating the scientific apparatus, without which the ramblings of my mental efforts would be redundant. Special thanks are due to John Dixon, who somehow managed to accurately recreate the visions of my mind (and my technical drawings of a five year olds standard) into a fluorescence cell, which is currently making the first point measurements of atmospheric IO.

I must also express my appreciation to Professor Andrew Orr-Ewing from the University of Bristol for invaluable discussions regarding the spectroscopy of IO, and his rapid, coherent and informative email correspondence. The knowledge of Dr. Terry Dillon from the Max-Planck-Institut für Chemie (Mainz) has also been a helpful addition to my research.

In the transition from my University life to that of the wider world, I thank my comrades-in-arms and the fools that are Rachel M^{c}ilWaine and David Cryer. I'm sure I would have enjoyed living with both of you more under different circumstances. Although are relationships have not always been constructive they have invariably been entertaining, and I wish you an interesting, fulfilling, and happy future.

From the Leeds community, I have been privileged to have Craig, Karen, Muttley and Mini as neighbours for the past few years. Craig has "done me proud" countless times: whether wall-papering my ceiling, changing my starter motor, installing radiators in my house (all free of charge) and just being there as a mate, a confident, and a drinking companion.

Thanks to Jill and Kas for our continued friendship and their genuine care, from our undergraduate days, and to Maria for her cheerful and comical emails.

Now, I must briefly turn to my home town, Brighton. Thanks to Bob for being a true friend since school, and for fitting me a new bathroom and kitchen. Despite being entombed for eternity, the bath plumbing is showing no signs of leaks thus far. Thanks to Daz for just being Daz, an alternative chemist one might say, and a memorable couple of weeks in Leeds at a difficult time for us both – hope you get back up soon (to Leeds). Thanks also to Mike and Miz for countless good times over the past years.

The support from my family has always been unconditional and entire. Thanks to my sister Ab, for her ever wise and compassionate ear, and my Auntie Janet for her good chat. I cannot express in words my appreciation for the support of my mum and dad. I have probably not always deserved it but where would I be without it? Their tolerance and allowance for me to pursue my own path in life has enabled me to explore many aspects of life that have greatly enhanced my appreciation of the wider world.

I cannot write an Acknowledgements section without mentioning Cait. I do not fully understand our relationship or your influence in my life, but both are undoubtedly substantial. I love you! Hopefully the future will hold better times.

Abstract

The impact of halogen chemistry on important atmospheric processes such as ozone depletion and (potentially) climate regulation is becoming increasingly apparent. Yet only the most fundamental atmospheric chemistry of halogen species is included in global tropospheric models. Spectroscopic measurements of the concentration of halogen species within the Earth's atmosphere, and the accurate determination of kinetic information regarding the rates and mechanisms of chemical processes in the laboratory, greatly facilitate the evolution of our quantitative understanding of the atmospheric role of halogen species, ultimately leading to their inclusion in atmospheric chemistry models.

The research presented in this thesis addresses previously un-investigated areas (or areas requiring further elucidation) of iodine chemistry. Specifically, Chapter Three uses new spectroscopic data to reassess the viability of a laser-induced fluorescence (LIF) instrument for the detection of ambient iodine monoxide radicals (IO), a key species in the atmospheric chemistry of iodine, which may help to enhance our understanding of important atmospheric processes *via* its spatially resolved detection. Chapter Four presents a kinetic and spectroscopic investigation into the mechanism and products of the reaction of CH_2I radicals with O_2, which has potential implications for particle formation in the marine boundary layer (MBL). The reaction of Cl atoms with alkyl iodides, CH_3I and CH_2I_2, has been studied in detail by the detection of adducts formed in these reactions, which have been observed by LIF for the first time, and is the subject of Chapter Five. As part of the course of this PhD, the reaction kinetics of the reaction of IO with dimethyl sulphide (DMS) was investigated. The results obtained have led to a re-evaluation of the atmospheric significance of this reaction.

The data obtained assist the development of our knowledge of the atmospheric chemistry of iodine species and, at a more fundamental level, the electronic structure and physical processes of gas phase species.

Contents

List of Tables

List of Figures

Glossary of Terms

λ_{pr}	Probe laser wavelength
λ_{ex}	Excimer laser wavelength
λ_{i}	Photoionisation laser wavelength
λ_{m}	Monochromator wavelength
P_{pr}	Probe laser power
P_{ex}	Excimer laser power
F	Photolysis laser fluence
PRF	Pulsed repetition frequency
M_r	Monochromator resolution
M_g	Monochromator diffraction grating
M_{ss}	Monochromator scan speed
Δt	Delay time (usually between probe and excimer lasers)
sccm	Standard cubic centimetre per minute
slm	Standard litre per minute
sccs	Standard cubic centimetre per second
LIF	Laser-induced fluorescence
LOD	Limit of detection
MBL	Marine boundary layer
DOAS	Differential optical absorption spectroscopy
CRDS	Cavity ring-down spectroscopy
RET	Rotational energy transfer
VET	Vibrational energy transfer

Chapter One: An introduction to the chemical role of halogen species in the Earth's atmosphere

The atmospheric role of iodine species is often coupled, and analogous, to that of chlorine and bromine compounds, thus a generic review of atmospheric halogen chemistry is required in order to appreciate its significance. Further, as the impact of halogen chemistry in the Earth's atmosphere largely resides through the interaction of these species with more fundamental chemical processes, a basic introduction to the chemistry of the troposphere and stratosphere is also necessary in order to understand the atmospheric importance of iodine species. For a more complete description of the composition, chemical behaviour and climatic processes of the atmosphere the reader is directed to several accessible and comprehensive texts[1-5].

1.1 Fundamental Chemical Processes of the Troposphere

The lower region of the Earth's atmosphere, the troposphere, which extends from the Earth's surface to an altitude of approximately 10 km at middle and high latitudes, and around 17 km at the tropics, is a well-mixed, convective region in which the most complex atmospheric chemistry occurs. The convective nature of the troposphere arises from its negative temperature gradient, changing from ~ 300 K (~ 27 °C) at ground level to ~ 220 K (~ -53 °C) at the tropopause – the region separating the troposphere and stratosphere – as a result of its heating being predominantly controlled by the absorption of ultra-violet (UV) radiation by the Earth's surface. Although the concentrations of the bulk constituents of the atmosphere (N_2, O_2, Ar and H_2O), comprising more than 99.9 % of its volume, are determined by natural processes that have been occurring for hundreds of millions of years, the concentration of trace constituents, such as CO, CO_2, CH_4, NO_x ($NO + NO_2$) and O_3, can be altered by anthropogenic (human) activity and result in dramatic climatic and chemical change of the troposphere. The trace chemical constituents of the atmosphere are generally emitted from the Earth's surface by a variety of biogenic and anthropogenic sources. Man's contribution to the accelerated greenhouse effect (global warming), mainly by the emission of CO_2 from the burning of fossil fuels, is an inescapable issue of the modern age, but less well illuminated are the effects of anthropogenic and biogenic emissions on the chemical nature of the atmosphere.

The chemistry of the troposphere is largely defined by its oxidising capacity, or the rate of production of ozone (O_3). Despite being harmful to plant and animal life, and acting as a greenhouse gas, tropospheric ozone is the precursor to the hydroxyl radical (OH), which acts as the "detergent" of the atmosphere by initiating the removal of most trace constituents emitted from the Earth's surface by oxidation. Paradoxically, therefore, the presence of O_3 in the

troposphere is of both benefit and detriment to life on Earth. In the troposphere, O_3 is photolysed by solar radiation, producing electronically excited oxygen atoms, O (^{1}D), and molecular oxygen (O_2). The O (^{1}D) atoms can then react with water vapour (H_2O), producing two OH radicals, or be quenched to the groundstate configuration, O (^{3}P), resulting in the regeneration of O_3

$$O_3 + h\nu\ (\lambda < 340\ nm) \rightarrow O\ (^1D) + O_2 \qquad (P1)$$
$$O\ (^1D) + N_2\ (or\ O_2) \rightarrow O\ (^3P) + N_2\ (or\ O_2) \qquad (R1)$$
$$O\ (^1D) + H_2O \rightarrow 2\ OH \qquad (R2)$$
$$O\ (^3P) + O_2 + M \rightarrow O_3 + M \qquad (R3)$$

In the background troposphere (*i.e.* regions of insignificant anthropogenic emissions), OH radicals react with carbon monoxide (CO) and methane (CH_4), resulting in the destruction of O_3 (and the reduction of the oxidising capacity of the troposphere) in the absence of NO_x

$$OH + CO \rightarrow H + CO_2 \qquad (R4)$$
$$H + O_2 + M \rightarrow HO_2 + M \qquad (R5)$$
$$HO_2 + O_3 \rightarrow OH + 2\ O_2 \qquad (R6)$$
$$\textbf{Net: } CO + O_3 \rightarrow CO_2 + O_2$$

$$OH + CH_4 \rightarrow CH_3 + H_2O \qquad (R7)$$
$$CH_3 + O_2 + M \rightarrow CH_3O_2 + M \qquad (R8)$$
$$CH_3O_2 + HO_2 \rightarrow CH_3O_2H + O_2 \qquad (R9)$$
$$CH_3O_2H + OH \rightarrow CH_2O + H_2O + OH \qquad (R10)$$
$$\textbf{Net: } CH_4 + OH + HO_2 \rightarrow CH_2O + 2\ H_2O$$

Or the net production of O_3 (and increase in the oxidising capacity of the atmosphere) in the presence of NO_x

$$OH + CO \rightarrow H + CO_2 \qquad (R4)$$
$$H + O_2 + M \rightarrow HO_2 + M \qquad (R5)$$
$$NO + HO_2 \rightarrow NO_2 + OH \qquad (R11)$$
$$NO_2 + h\nu\ (\lambda < 420\ nm) \rightarrow NO + O\ (^3P) \qquad (P2)$$
$$O\ (^3P) + O_2 + M \rightarrow O_3 + M \qquad (R3)$$
$$\textbf{Net: } CO + 2\ O_2 \rightarrow CO_2 + O_3$$

$$OH + CH_4 \rightarrow H_2O + CH_3 \quad \text{(R7)}$$

$$CH_3 + O_2 + M \rightarrow CH_3O_2 + M \quad \text{(R8)}$$

$$CH_3O_2 + NO \rightarrow NO_2 + CH_3O \quad \text{(R12)}$$

$$CH_3O + O_2 \rightarrow CH_2O + HO_2 \quad \text{(R13)}$$

$$HO_2 + NO \rightarrow NO_2 + OH \quad \text{(R11)}$$

$$2\,(NO_2 + h\nu) \rightarrow 2\,(NO + O\,^3P) \quad \text{(P2)}$$

$$2\,(O\,^3P + O_2 + M) \rightarrow 2\,(O_3 + M) \quad \text{(R3)}$$

$$\textbf{Net: } CH_4 + 4\,O_2 \rightarrow CH_2O + H_2O + 2\,O_3$$

The photolysis of NO_2, P2, is the predominant (and sole anthropogenic) source of O_3 in the troposphere. In the background troposphere, ~ 80 % of the OH radicals react with CO, and it is found that an NO mixing ratio of ~ 3 – 8 pptv is required for a net balance of tropospheric O_3[6].

Thus, it is clear that by altering the concentrations of NO_x, and organic compounds emitted into the atmosphere, man can have a complex influence on the oxidising capacity of the troposphere.

1.2 Fundamental Chemical Processes of the Stratosphere

The stratosphere is the region of the Earth's atmosphere directly above the troposphere, and extends to an altitude of ~ 50 km. The temperature profile of the stratosphere is opposite to that of the troposphere, increasing with altitude, due to the absorption of UV and infra-red (IR) radiation by O_2 and O_3. The increase in temperature with altitude in the stratosphere hinders vertical mixing, and results in the accumulation of O_3 (the ozone layer). Ozone has a very different role in the stratosphere, than the troposphere, as it absorbs harmful UV-C (λ = 200 – 280 nm) and UV-B (λ = 280 – 315 nm) radiation. UV-B radiation is known to have a wide range of detrimental effects on plant and animal health[7], and the presence of stratospheric ozone – the sunscreen of the lower atmosphere – is thus critical to the well-being of life on Earth. Stratospheric ozone is formed by the photolysis of molecular oxygen

$$O_2 + h\nu \rightarrow 2\,O \quad \text{(P3)}$$

$$2\,(O + O_2 + M) \rightarrow 2\,(O_3 + M) \quad \text{(R3)}$$

$$\textbf{Net: } 3\,O_2 + h\nu \rightarrow 2\,O_3$$

However, in the absence of other trace constituents, the stratospheric concentration of O_3 is limited by two further processes: the photolysis of O_3, and the reaction of O atoms with O_3

$$O_3 + h\nu \rightarrow O + O_2 \qquad \text{(P4)}$$
$$O + O_3 \rightarrow 2\,O_2 \qquad \text{(R14)}$$

Processes P3, R3, P4 and R14 are collectively known as the odd-oxygen cycle, or the Chapman mechanism, and result in the establishment of a steady-state O_3 concentration, which can be expressed by E. 1.1[8]

$$[O_3] = \sqrt{\frac{J_3[O_2]}{k_{14}}}\sqrt{\frac{k_3[O_2][M]}{J_4}} \qquad \text{E. 1.1}$$

Where J_3 and J_4 are the photolysis rates of O_2 and O_3 respectively, and k_3 and k_{14} are the rate coefficients for reactions R3 and R14.

The Chapman mechanism is found to significantly overestimate the concentration of stratospheric O_3, however, as in the presence of other trace constituents catalytic O_3 destruction can occur. For example, nitrous oxide (N_2O), emitted at the Earth's surface and inert in the troposphere, is transported to the stratosphere where it reacts with O (^1D), generating NO

$$N_2O + O\,{}^1D \rightarrow 2\,NO \qquad \text{(R15)}$$

Nitric oxide (NO) interferes in the odd-oxygen cycle, resulting in a net depletion of stratospheric O_3

$$NO + O_3 \rightarrow NO_2 + O_2 \qquad \text{(R16)}$$
$$O_3 + h\nu \rightarrow O + O_2 \qquad \text{(P4)}$$
$$NO_2 + O \rightarrow NO + O_2 \qquad \text{(R17)}$$
$$\textbf{Net: } 2\,O_3 + h\nu \rightarrow 3\,O_2$$

Other species that can result in the catalytic destruction of stratospheric O_3 are, OH (derived from the photolysis of H_2O vapour, which is predominantly produced by the oxidation of stratospheric CH_4), and chlorine and bromine atoms (produced by the photolysis of halogenated organic species persisting into the stratosphere).

Clearly, therefore, the emission of stable molecules from the Earth's surface can have significant effects on the levels of stratospheric ozone, and serious implications for the Earth's climate and life-systems.

1.3 Atmospheric Chemistry of Halogen Species

As highlighted by the example of the Antarctic ozone hole, the accurate prediction of atmospheric change is inextricably linked to all facets of atmospheric science. Successful modeling requires the precise and accurate measurement of the concentration of trace constituents of the atmosphere, the accurate estimation of source strengths, and a quantitative understanding of the rates and mechanisms of chemical processes in the atmosphere. Although a topic of enthusiastic and ever-extending research, tropospheric halogen chemistry is in its relative infancy, and only understood at a semi-quantitative level. For that reason, halogen chemistry is almost entirely omitted from global tropospheric models. As the atmospheric significance of halogen chemistry becomes more evident, therefore, so does the need for the accurate quantification of its role. The aim of this central section of the introduction is to detail the known and hypothesised roles of halogen species in the atmosphere (with particular emphasis on the troposphere), highlighting the most topical areas of research at the time of writing.

1.3.1 Sources of Halogen Species in the Atmosphere

Halogen species enter the atmosphere in both inorganic and organic form. By weight, chlorine, bromine and iodine contribute ~ 58.2, 0.2 and 0.0002 % respectively[5] to the total composition of sea salt, and substantial amounts of chlorine (and bromine) therefore enter the atmosphere in the form of sea-salt aerosol particles, generated by wave action. As much as 6000 Tg Cl yr^{-1} (1 Tg = 10^{12} g) may enter the atmosphere in the form of sea-salt aerosol, although ~ 90 % of this probably returns to the Earth's surface *via* precipitation and dry deposition[2]. However, it is now known that several reactions, involving heterogeneous chemistry, can result in the liberation of gas phase inorganic halogen species from aerosols to the atmosphere. For example, the reaction of acids with NaCl[9-11]

$$HNO_{3(g)} + NaCl_{(s)} \rightarrow NaNO_{3(s)} + HCl_{(g)} \quad \text{(R18)}$$

$$H_2SO_{4(g)} + 2\,NaCl_{(s)} \rightarrow Na_2SO_{4(s)} + 2\,HCl_{(g)} \quad \text{(R19)}$$

and the reaction of nitrogen oxide (N_xO_y) species with NaX (X = Cl or Br)[11-15]

$$2\,NO_{2(g)} + NaX_{(s)} \rightarrow NaNO_{3(s)} + XNO_{(g)} \quad \text{(R20)}$$

$$N_2O_{5(g)} + NaX_{(s)} \rightarrow NaNO_{3(s)} + XNO_{2(g)} \quad \text{(R21)}$$

$$NO_{3(g)} + NaX_{(s)} \rightarrow NaNO_{3(s)} + X \quad \text{(R22)}$$

Inorganic halogen species are also released by reaction of O_3[16], OH[17], and HO_2[18] with NaCl, and from the reactions of O_3[19,20] and OH[20,21] with halide ions (Cl^- and Br^-) at the air-water interface of aerosol particles. Heterogeneous halogen activation is discussed in greater detail in section 1.3.3.2.i.

Hydrochloric acid, HCl, is also emitted into the atmosphere from volcanic eruptions[4] and from anthropogenic sources, such as emissions from solid rocket motors[3], and molecular chlorine, Cl_2, is thought to have substantial industrial sources[27], such as emissions from biocides in cooling towers. However, natural oceanic sources are by far the predominant source of inorganic halogen species in the atmosphere.

Sources of inorganic iodine species are not well established. Garland and Curtis[22] proposed that I_2 can be liberated by the uptake of O_3 to the surface of the oceans, and could provide a significant flux to the total atmospheric loading of iodine species

$$2\,I^-_{(aq)} + O_{3(g)} + 2H^+_{(aq)} \rightarrow I_{2(g)} + O_2 + H_2O \qquad \text{(R23)}$$

and Miyake and Tsunogai[23] predicted that I_2 can be liberated from the ocean by the photochemical oxidation of iodide in sea water

$$2\,I^-_{(aq)} + 0.5\,O_2 + H_2O + h\nu \rightarrow I_{2(g)} + 2\,OH^-_{(aq)} \qquad \text{(R24)}$$

Recently, it has been found that biogenic sources of inorganic I_2 exist[24-26]. McFiggans *et. al.*[24] observed that *Laminaria* macroalgae (seaweed) generate I_2, under conditions of oxidative stress, that can be emitted to the atmosphere when the seaweed is exposed at low tide[24,25]. Further, Amachi *et. al.*[26] have found that iodide-oxidising bacteria found in natural gas brine waters and seawater emit I_2 in large quantities, and could contribute significantly to the atmospheric iodine cycle.

With respect to the emission of organic halogen species, natural sources are also predominant. Nearly 4000 organohalogen compounds are known to be produced naturally by a diversity of sources: ranging from volcanoes to humans[28], although only the lighter, more volatile, of these compounds can be emitted into the atmosphere.

Over the past few decades, significant anthropogenic sources of organic chlorine compounds have included CFC's, *e.g.* CFC-11 ($CFCl_3$) and CFC-12 (CF_2Cl_2), HCFC's (hydrochlorofluorocarbons – initial CFC replacements), and CCl_4 and CH_3CCl_3, which have been used as non-toxic, non-flammable refrigerants and solvents. Under the Montreal Protocol[29], however, the production and emission of these compounds has been phased out in the developed world, although emissions of the current inventories are still allowed in developing countries. Methyl chloride (CH_3Cl) is also emitted in industrial processes but the

major source of atmospheric CH_3Cl is from biomass burning (*i.e.* the anthropogenic and natural burning of organic matter) and other biogenic sources[3].

Anthropogenic bromine emissions are predominantly in the form of Halons – the bromine analogues of the CFC's, *e.g.* H-1211 ($CBrClF_2$), which are used as fire extinguishing gases, and methyl bromide (CH_3Br). The production and emission of Halons has also been phased out in the developed countries under the Montreal Protocol, although the developing world still emits large quantities. The Peoples Republic of China, for example, is responsible for ~ 90 % of the global emission of H-1211[30]. In addition to emissions associated with biomass burning, soil fumigation and automobile emissions[3] from the developing world, anthropogenic emissions of CH_3Br continue to be released from some developed countries[31], despite the passing of the Montreal Protocol's phase-out target last year. However, biogenic and natural emissions of CH_3Br: from macroalgae[32,33], marine diatoms (phytoplankton)[34], fungi[35], rice paddies[36], the photolysis of surface snow[37], and volcanoes[38], account for the majority of atmospheric methyl bromide[3].

Although there are no known major industrial sources of iodine to the atmosphere, very high methyl iodide concentrations (up to 3800 ppt, 1 ppt $\approx 2.5 \times 10^7$ molecule cm^{-3} at ground-level) have been observed in industrial locations, possibly originating from the combustion of coal and petroleum[39].

Biogenic emissions of the mono-substituted methyl halides are predominantly attributed to biological processes involving marine macroalgae[32,33]. Wuosmaa and Hager[32] found that methyl transferase enzymes, present in samples of certain fungi, algae and plant, efficiently catalyse the methylation of halide ions. A large variety of di- and tri-substituted organic halogen species (*e.g.* CH_2I_2, CH_2Br_2, CH_2IBr, CH_2ICl, $CHBr_2Cl$, $CHBr_3$) have now been observed in the atmosphere[40-48], however, and these compounds are thought to be produced by a different mechanism in macroalgae, involving peroxidase enzymes, acting under cell defence in conditions of oxidative stress[49,50]. The peroxidase enzymes catalyse the reaction of halide ions with hydrogen peroxide (H_2O_2), resulting in the production of hypohalous acids, HOX (X = Cl, Br, I). The HOX can then react with organic matter, producing a wide range of substituted halocarbons, although it is not known whether these halocarbons are predominantly produced inside the algal cell or in the surrounding seawater[51,52]. When the macroalgae are exposed to the sun-lit atmosphere, at low-tide, the halogen compounds can be emitted directly into the atmosphere. Recent studies[53-55] show that CH_2I_2 is not emitted directly into the atmosphere from the open-oceans, as its photolysis lifetime in the surface water is too short, but may be converted to CH_2ICl, which has a sufficiently long photolysis lifetime for emission to the atmosphere.

There is growing evidence to suggest that phytoplankton and diatoms[34,41,56] may also be responsible for significant production of various organoiodides and bromides, and as these

species cover ~ 99.5 % of the Earth's oceans, may provide a prolific liberation of these compounds into the marine atmosphere. A recent study[57] found evidence for emissions of $CHCl_3$ and $CHBr_3$ from a peatland source in the West coast of Ireland.

Finally, it is thought that organic halogen species can be released into the atmosphere from the photolysis of compounds within surface snow[37], and from volcanic emissions[38]. Anthropogenic emissions of organic halogen species (other than those discussed above) are thought to be small, although some industrial processes, such as the desalination of sea-water, are known to release di-and tri-substituted halogen compounds into the atmosphere[58].

Once emitted into the atmosphere, halogen species are removed by photolysis, and reaction with OH and Cl atoms, initiating complex chemical mechanisms. As most chlorine containing compounds have strong bonds, they are relatively inert to photolysis in the troposphere (with the notable exception of Cl_2) and may be transported to the stratosphere, initiating catalytic ozone destruction (see next section), whereas the majority of brominated compounds (with the exception of Halons and CH_3Br) are removed in the troposphere. Due to their weak, photolabile C-I bonds, all iodocarbons are essentially removed by photolysis in the troposphere. There is some speculation as to the possible role of iodine species in stratospheric O_3 depletion, however[59].

As a result of their short atmospheric lifetimes and most prolific sources being found in marine environments, the tropospheric chemistry of halogen species has predominantly been associated with the marine boundary layer (MBL). However, as halogen species have now been detected all over the Earth's marine environments[40-48] (*e.g.* the Arctic, Antarctic, Atlantic, Pacific, tropical and coastal regions) and their sources (both anthropogenic and biogenic) are still not well identified or quantified, it may well be that halogens are ubiquitous species in the Earth's lower atmosphere, and are important for the natural regulation of climate, for example[7,60].

Table 1.1-1 lists the chemical formula, typical MBL concentration range, estimated source strength and atmospheric lifetime for a number of halogen species emitted into the atmosphere.

Atmospheric Species	MBL Conc. range / ppt	Emission Rate / G (10^9) g yr^{-1}	Atmospheric lifetime
$CFCl_3$ (CFC-11)	~ 262 [61 a]	~ 76.4 [61 a]	52 yrs [61]
CF_2Cl_2 (CFC-12)	543 [62 b]	~ 134 [62 b]	~ 100 yrs [62]
CHF_2Cl (HCFC-22)	140 – 145 [63 b]	275 [63 b]	12 yrs [63]
$CBrClF_2$ (H-1211)	4.0 [30 c]	12.4 [30 c]	17 yrs [30]
CH_3Cl	585 [43]	2800 – 4600 [67]	~ 1.5 yrs [3]
C_2H_5Cl	3.3 [43]		~ 40 days [64]
CH_3Br	9.3 – 875 [42,48]	110 [10]	~ 292 days [69]
C_2H_5Br	0.09 – 865 [42,48]		
CH_3I	0.12 – 1830 [42,48]	1000 – 2000 [39]	3 – 5 days [42]
C_2H_5I	< 0.02 – 96.9 [42,48]		3 – 5 days [42]
CH_2Cl_2	9 – 39 [64]	700 [68]	73 – 146 days [70]
CH_2ICl	< 0.004 – 12.4 [42,48]		Several hrs. [42]
CH_2Br_2	0.28 – 262 [44,48]	104 [10]	53 – 183 days [71]
CH_2IBr	< 0.02 – 9.9 [42,48]		< 1 hr. [42]
CH_2I_2	< 0.02 – 19.8 [42,48]		~ 5 mins. [42]
$CHCl_3$	18.5 – 40 [65]	350 – 600 [65]	~ 183 days [65]
$CHBrCl_2$	0.1 – 246 [48]	7.9 [10]	~ 40 days [72]
$CHBr_2Cl$	0.3 – 128.2 [42,48]	18 [10]	~ 35 days [72]
$CHBr_3$	1.9 – 393 [42,48]	379 [10]	~ 22 days [71]
I_2	< 3 – 93 [66]	~ 1000 [d]	~ 8 s [73]

Table 1.1-1 – Reported MBL concentration range, source strength, and atmospheric lifetime of various organohalogen compounds. The values given in [a, b] and [c] are for the years of 1999, 2000 and 1997 respectively. The source strength given for I_2, [d], is the combined estimate from references 22, 23 and 66.

It should be noted that the wide range (and omission) of some values for the atmospheric source strength and lifetime of individual species listed in Table 1.1, largely reflects the current lack of information with respect to atmospheric halogen chemistry. Further, the wide concentration ranges presented are indicative of the complex nature of the sources and sinks of atmospheric halogen species, and their regional dependence. Improving the accuracy and precision of these data is of integral importance to our quantitative understanding of the role of halogen species within the troposphere.

1.3.2 Stratospheric Chemistry of the Halogens

Due to their lack of sinks in the troposphere, long lived organochlorine and organobromine compounds are transported to the stratosphere where they are photolysed, releasing reactive halogen atoms. For example, the photolytically initiated destruction of CFC-11 [2]

$$CFCl_3 + h\nu \rightarrow\rightarrow CO_2 + HF + 3\,Cl\ (\text{or } 3\,ClO) \qquad (P5)$$

Chlorine atoms and chlorine monoxide radicals (ClO) can catalytically destroy stratospheric O_3 *via* the following cycles

$$Cl + O_3 \rightarrow ClO + O_2 \qquad (R25)$$
$$O_3 + h\nu \rightarrow O + O_2 \qquad (P4)$$
$$ClO + O \rightarrow Cl + O_2 \qquad (R26)$$
$$\textbf{Net: } 2\,O_3 + h\nu \rightarrow 3\,O_2$$

$$ClO + ClO + M \rightarrow Cl_2O_2 + M \qquad (R27)$$
$$Cl_2O_2 + h\nu \rightarrow\rightarrow 2\,Cl + O_2 \qquad (P6)$$
$$2\,(Cl + O_3) \rightarrow 2\,(ClO + O_2) \qquad (R25)$$
$$\textbf{Net: } 2\,O_3 + h\nu \rightarrow 3\,O_2$$

Although analogous cycles exist for Br and BrO, the concentration of bromine species within the stratosphere is relatively small [64], and catalytic O_3 destruction by bromine-only chemistry is inefficient. The chlorine and bromine cycles may be coupled, however, *via* the reaction of ClO and BrO

$$ClO + BrO \rightarrow Br + OClO \qquad (R28a)$$
$$\rightarrow Br + ClOO \qquad (R28b)$$
$$\rightarrow BrCl + O_2 \qquad (R28c)$$
$$OClO + h\nu \rightarrow O + ClO \qquad (P7)$$
$$ClOO + M \rightarrow Cl + O_2 + M \qquad (R29)$$
$$BrCl + h\nu \rightarrow Br + Cl \qquad (P8)$$

The halogen monoxides result in further O_3 loss by coupling to the HO_x (OH + HO_2) cycle

$$XO + HO_2 \rightarrow HOX + O_2 \qquad (R30)$$
$$HOX + h\nu \rightarrow OH + X \qquad (P10)$$
$$OH + O_3 \rightarrow HO_2 + O_2 \qquad (R31)$$
$$X + O_3 \rightarrow XO + O_2 \qquad (R32)$$
$$\textbf{Net: } 2\,O_3 + h\nu \rightarrow 3\,O_2$$

where, X = Cl or Br.

The reaction of halogen monoxides with CH_3O_2 may also be important[74]. As the concentration of atomic oxygen is relatively small in the lower stratosphere (~ 15 – 25 km), O_3 destruction is primarily driven by the cross-reactions of ClO, BrO and HO_2 [75], whereas the contribution from halogen atoms (R25, P4, R26) becomes more significant at higher altitudes[76].

The extent of halogen-catalysed stratospheric O_3 depletion is restricted by reactions that lock up the active chlorine and bromine in "reservoir" species. For example

$$Cl + CH_4 \rightarrow HCl + CH_3 \qquad (R33)$$
$$Br + HO_2 \rightarrow HBr + O_2 \qquad (R34)$$
$$XO + NO_2 \rightarrow XONO_2 \qquad (R35)$$

It should be noted, however, that HCl, HBr and the halogen nitrates, $XONO_2$, are only temporary reservoirs, as the halogens can be released in their active forms by photolysis or reaction. For example

$$ClONO_2 + h\nu \rightarrow Cl + NO_3 \qquad (P10)$$
$$HCl + OH \rightarrow Cl + H_2O \qquad (R36)$$

Atom-for-atom, bromine is much more effective than chlorine in O_3 destruction as its reservoir species are relatively unstable, thus bromine spends more time in its catalytically active forms. As no stratospheric iodine reservoirs are known to exist, a total concentration of stratospheric iodine species as low as 1 ppt could make a major contribution to stratospheric O_3 depletion, at altitudes below ~ 20 km, through the cross reactions of IO with BrO and ClO [59].

In addition to photolysis, the halogen nitrates can undergo rapid heterogeneous reactions, releasing catalytically active halogen species. These processes can be very important in the stratosphere and result in dramatic O_3 loss, such as the Antarctic ozone hole, by effectively removing all halogen reservoir species. In the Antarctic winter (June – August) the temperature of the upper stratosphere drops rapidly due to the lack of sunlight. The cool air descends creating a column of cold air with temperatures as low as ~ 185 K. The temperature

gradient between the Antarctic and mid-latitude air masses results in the generation of a vortex[77] at the edge of the Antarctic atmosphere, where wind speeds of more than 200 mph isolate the air within the vortex, prohibiting latitudinal mixing of Antarctic air. The low temperatures result in the dehydration and denitrification of the Antarctic air as water and nitric acid condense on sulphate particles forming PSC's (polar stratospheric clouds), which comprise of both solid and liquid particles. Hydrochloric acid is then adsorbed onto the surface of the PSC particles, where it may react with gas phase halogen nitrates[78-80], generating molecular halogen species in the gas phase and nitric acid, which is retained in the PSC due to its low vapour pressure at stratospheric temperatures.

$$XONO_{2(g)} + HCl_{(PSC)} \rightarrow XCl_{(g)} + HNO_{3(PSC)} \qquad (R37)$$

These reactions are very important for two reasons. First, that halogens are released in a catalytically active form (Cl_2 and BrCl are rapidly photolysed to halogen atoms), and secondly that the retention of HNO_3 on the PSC results in the denitrification of the Antarctic stratosphere, inhibiting the reformation of reservoir species.

Additional reactions[80-84] also occur on the surface of PSC's, generating catalytically active halogen species and denitrifying the atmosphere

$$N_2O_{5(g)} + H_2O_{(PSC)} \rightarrow 2\,HNO_{3(PSC)} \qquad (R38)$$

$$XONO_{2(g)} + H_2O_{(PSC)} \rightarrow HOX_{(g)} + HNO_{3(PSC)} \qquad (R39)$$

$$HOX_{(g)} + HCl_{(PSC)} \rightarrow XCl_{(g)} + H_2O_{(PSC)} \qquad (R40)$$

Hence, the concentration of XCl (X = Cl, Br) builds up in the Antarctic vortex over winter, and results in the almost complete annihilation of ozone upon the turn of spring (mid – late September) when the returning sunlight generates high concentrations of halogen atoms, initiating an extreme O_3 depletion event through the cycles outlined above. The formation of the Antarctic ozone hole is thought to be predominantly due to the self-reaction of ClO (R27), accounting for approximately 75 % of the observed O_3 depletion[85]. Lesser contributions are attributed to the reactions of ClO + BrO (~ 15 %), ClO + O (~ 5 %) and ClO + HO_2 (~ 5 %) [85].

As spring progresses, the vortex collapses and the Antarctic stratosphere begins to warm, resulting in the evaporation of PSC's and the re-nitrification of the atmosphere. Thus the equilibrium between halogens in their catalytically active and reservoir forms is re-established, leading to repair of the Antarctic ozone. From measuring the concentration of CFC's in the atmosphere, the Montreal Protocol can be seen to have taken effect [64,86], although due to the long atmospheric lifetime of some of the CFC's (50 – 100) years, the stratospheric

concentration of chlorine compounds will not be low enough to prevent the formation of the Antarctic ozone hole in the austral spring for several decades[64,87].

Although halogen-catalysed stratospheric ozone destruction also occurs in the Arctic polar vortex [88,89], an analogous Arctic ozone hole is not formed to the same extent. This is primarily due to the higher temperatures of the Arctic stratosphere (~ 10 K warmer than the Antarctic stratosphere), which inhibit PSC formation and results in a less stable polar vortex, allowing a greater extent of latitudinal mixing of stratospheric air masses [90-92].

1.3.3 Tropospheric Chemistry of the Halogens

Fig. 1.3-1 outlines the chemical role of halogen species within the MBL. As can be seen, the chemistry is complex, interlinked, and involves both homogeneous (gas phase) and heterogeneous (aerosol) processes. The following sub-sections discuss the most important of these processes.

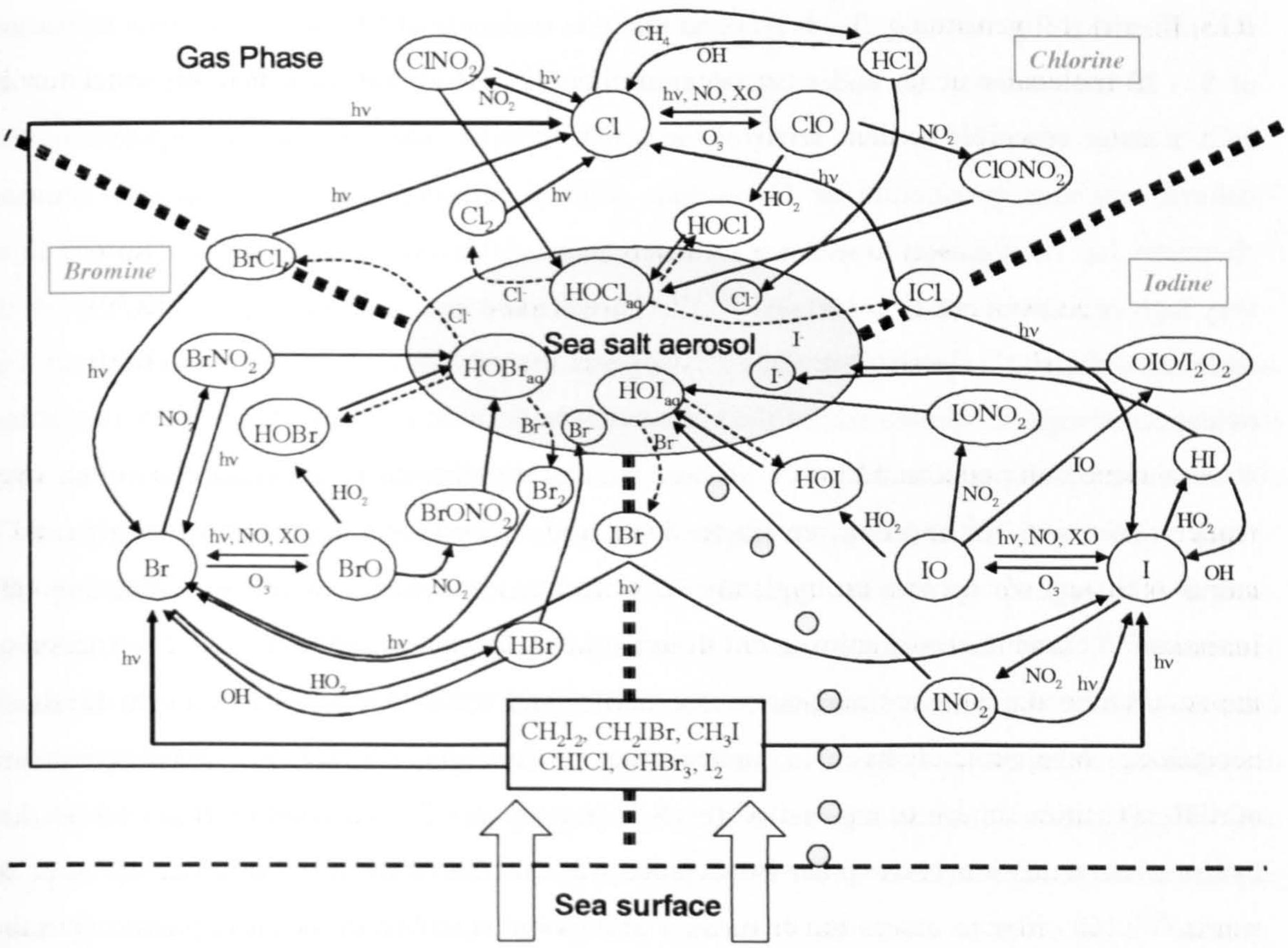

Fig. 1.3-1 – Schematic diagram of halogen chemistry within the MBL. The figure was kindly provided by Prof. J. M. C. Plane from the University of Leeds.

1.3.3.1 Gas Phase Chemistry

1.3.3.1.i Halogens and Ozone

Similarly to in the stratosphere, the tropospheric gas phase chemistry of the halogens is foremost associated with O_3. Paradoxically, however, chlorine chemistry is generally associated with O_3 formation in the troposphere. Chlorine atoms, once generated by the photolysis of the shorter-lived halogen species (notably, Cl_2, BrCl and ICl), have one of two fates in the troposphere: i) reaction with O_3 (R25), generating ClO; or ii) reaction with organic species, such as CH_4, generating alkyl radicals and HCl

$$Cl + CH_4 \rightarrow CH_3 + HCl \qquad (R41)$$

The organic radicals formed in R41, and analogous reactions, will be consumed by O_2 producing peroxy species (RO_2), which in the presence of NO_x will partake in reactions R11 – R13, P2 and R3, generating O_3. It is found that one molecule of Cl_2 can result in the formation of 5 – 10 molecules of O_3 under certain conditions[93,94]. However, note that the formation of HCl, a stable reservoir species, removes the active form of chlorine from the troposphere: the chlorine initiated production of O_3 is thus a local phenomenon. Nevertheless, chlorine chemistry has been shown to increase O_3 levels in urban environments by more than 100 % to very high concentrations of > 100 ppb [12,93,94]. Furthermore, recent observations of high levels of molecular chlorine in coastal regions[95,96], suggest that chlorine chemistry can dominate the oxidation of organic species within the early sunlit hours, and increase O_3 levels in the marine atmosphere by as much as 12 ppb [12]. These studies suggest that Cl atom concentrations may reach in excess of 10^5 molecule cm^{-3} in the MBL and, as the rate coefficients for reaction of Cl atoms with organic species are typically 10 – 100 times higher than the corresponding OH reactions[97-104] (and the concentration of OH in the MBL is typically 10^6 molecule cm^{-3}), chlorine atoms may be the primary oxidant in the MBL (and urban environments) under localised conditions. A recent study has also predicted that Cl atoms could be responsible for up to 50 % of CH_4 oxidation in some regions of the free troposphere[105], and another study found that hydrocarbon oxidation in the polar troposphere was dominated by chlorine chemistry at polar sunrise[106]. In order to assess the frequency and global significance of such chemistry, more complete and accurate measurements of Cl atoms, and/or their precursors, are necessary. The reactions of bromine and iodine atoms with most organic compounds are too slow to compete with their oxidation by OH and Cl, although Br atoms may be important for the oxidation of some unsaturated hydrocarbons, such as ethyne[106].

Although the photolysis of organoiodine species is rapid in the troposphere, it has been proposed that their reaction with Cl atoms can be a competitive removal process[107]. An investigation into the reaction kinetics, products, and mechanism of the reaction of Cl atoms with CH_3I and CH_2I_2 is the focus of Chapter Five of this thesis.

As previously stated, Cl atoms may also react with O_3 in the troposphere, generating ClO. However, the self-reaction of ClO, R27, is of little atmospheric significance in the troposphere. This is because, under tropospheric conditions, the ClO dimer, Cl_2O_2, predominantly undergoes thermal decomposition to 2 ClO[108], rather than photolysis to 2 Cl + O_2 as in the stratosphere[109]. Thus, the reformation of ClO means that catalytic O_3 destruction does not occur. Further, the rate coefficient of the ClO self-reaction is relatively small under tropospheric conditions, as is the concentration of Cl atoms in the MBL. However, ClO concentrations of up to 25.3 ppb have been measured in volcanic plumes[110] and, under these conditions, localised O_3 depletion is observed. Chlorine-catalysed O_3 destruction can occur from the reaction of ClO with HO_2[111], BrO[112,113] or IO[114,115] as these reactions can result in the release of active forms of the halogens, and have higher rate coefficients than the ClO self-reaction. For example

ClO + IO	→	I + OClO	(R42a)
	→	I + Cl + O_2	(R42b)
	→	ICl + O_2	(R42c)

Under tropospheric conditions the rate coefficient for R42 is ~ 20 times greater than that of the ClO self-reaction. However, it should be noted that I + OClO is the major reaction channel of R42 (accounting for 55 % of the products)[115], which does not lead to a net O_3 depletion as OClO is photolysed to O + ClO[116], thus regenerating O_3 *via* R3.

Bromine and iodine atoms, generated by the photolysis of molecular halogens, organobromines and organoiodines in the troposphere, principally react with O_3 to produce halogen monoxide radicals, XO. (It has also been proposed that the reaction of CH_2I, produced from the photolysis of CH_2I_2, with O_2 directly generates IO radicals[117]. A detailed investigation into the products of this reaction is the subject of Chapter Four of this thesis). The halogen monoxides may be photolysed, reforming X + O_3, or lead to catalytic O_3 depletion in the presence of other trace species[39,118], such as HO_2

XO + HO_2	→	HOX + O_2	(R30)
HOX + hν	→	OH + X	(P10)
OH + O_3	→	HO_2 + O_2	(R31)

$$X + O_3 \rightarrow XO + O_2 \qquad \text{(R32)}$$

$$\text{Net: } 2\,O_3 + h\nu \rightarrow 3\,O_2$$

other halogen monoxide radicals

$$XO + YO \rightarrow OXO + Y \qquad \text{(R43a)}$$

$$\rightarrow XOYO \qquad \text{(R43b)}$$

$$\rightarrow XY + O_2 \qquad \text{(R43c)}$$

$$\rightarrow X + Y + O_2 \qquad \text{(R43d)}$$

and NO_2

$$XO + NO_2 + M \rightarrow XONO_2 + M \qquad \text{(R35)}$$

$$XONO_2 + h\nu \rightarrow X + NO_3 \qquad \text{(P11)}$$

$$NO_3 + h\nu \rightarrow NO + O_2 \qquad \text{(P12)}$$

$$X + O_3 \rightarrow XO + O_2 \qquad \text{(R32)}$$

$$NO + O_3 \rightarrow NO_2 + O_2 \qquad \text{(R16)}$$

$$\text{Net: } 2\,(O_3 + h\nu) \rightarrow 3\,O_2$$

The reaction of the halogen monoxides with NO_2 leads to less efficient catalytic O_3 destruction, than indicated by the above cycle, for several reasons. First, IO can react with NO, forming I and NO_2, which leads to no net O_3 destruction, and secondly that NO_3 can also be photolysed to $NO_2 + O$ [119] (resulting in no net destruction of O_3). Finally, $XONO_2$ may: i) be photolysed to $XO + NO_2$ (for $BrONO_2$)[119]; ii) undergo heterogeneous uptake to aerosol particles; and iii) be hydrolysed on cloud and aerosol particles, forming HOX and HNO_3. As these heterogeneous processes result in the denitrification of the troposphere (*via* the formation of nitric acid, which can be removed by precipitation) and the liberation of reactive halogen species from aerosol (see section 1.3.3.2.i), however, tropospheric O_3 concentrations are indirectly suppressed by the alternative $XONO_2$ loss processes. At a recent field campaign in the dead sea[120], NO_2 concentrations were observed to decrease below the detection limit in the presence of high halogen monoxide concentrations. Model studies have shown that the hydrolysis of $BrONO_2$ on cloud particles can be responsible for more than 40 % of bromine-driven O_3 destruction in the troposphere[121], and account for up to 35 % of nitric acid formation[105].

At relatively low XO (and NO_x) concentrations, the majority of halogen-catalysed O_3 destruction occurs through reaction with HO_2 [122]. The reaction of IO with HO_2 is most

important, due to the relative instability of HOI; and can result in a significant reduction of the HO_2/OH ratio in the MBL[123,124], thus partially counteracting the reduction in the oxidising capacity of the troposphere arising from the destruction of O_3. It has also been proposed that the reaction of IO + CH_3O_2 (and other RO_2 species) could be of atmospheric significance[122]. However, there is some uncertainty over the rate coefficient and products of this reaction[125-127].

At higher concentrations (typically greater than 2 ppt)[128,129], the self- and cross-reactions of BrO and IO become the dominant halogen-catalysed O_3 destruction cycles in the troposphere. The efficiencies of these cycles depend on: i) the concentrations of BrO and IO; and ii) the rate coefficients and products of reaction. For example, the BrO self-reaction progresses through channels R43c (~ 20 %) and R43d (~80 %) [130] resulting in a net O_3 depleting efficiency of 2 O_3 → 3 O_2 (note that Br_2 is readily photolysed to two Br atoms). However, the rate coefficient for this reaction is relatively slow, and in the presence of IO, bromine-driven destruction of O_3 will progress predominantly through the IO + BrO reaction, which has a rate coefficient ~ 30 times higher than the BrO self-reaction under tropospheric conditions, and a major product channel of Br + OIO (65 – 93 %)[131,132]. The efficiency of catalytic O_3 destruction *via* the IO + BrO reaction is less clear due to uncertainties in the atmospheric fate of OIO (see below).

The IO self-reaction is rapid and would appear to predominantly progress through channels R43a (~ 35 %) and R43b (65 %) at tropospheric temperature and pressure[10,133,134]. A major uncertainty in modeling the atmospheric chemistry of iodine species arises from the lack of information regarding the atmospheric fate of OIO and I_2O_2. Laboratory studies have shown that OIO does not photolyse to O + IO (in contrast to OClO) but a small fraction may undergo photodissociation to I + O_2 [134-136]. If this is the case then the BrO + IO and IO self-reactions could result in efficient O_3 destruction. However, it is thought that reaction with NO and OH may also be important for the atmospheric chemistry of OIO[137,138], particularly in polluted environments, and evidence is emerging for rapid reactions for the self- and cross-reactions of the iodine oxides [10,134,139], such as IO + OIO, and OIO + OIO, which may result in the formation of new particles in the MBL (see section 1.3.3.2.ii) and be the major sink of OIO in the marine atmosphere [138,140]. The existence of such loss mechanisms for OIO in the atmosphere are reinforced by the detection of only small day-time concentrations of OIO (< 3 ppt) in the atmosphere [66,141]. In a recent study[142], however, OIO was observed at concentrations in excess of 10 ppt at night. As I_2, NO_3 and IO were also observed at night, it is thought that the reaction of I_2 with NO_3 [143], followed by self-reaction of IO, is responsible for the night-time production of OIO

$$I_2 + NO_3 \rightarrow I + INO_3 \qquad \text{(R44)}$$

$$I + O_3 \rightarrow IO + O_2 \qquad \text{(R32, X = I)}$$

However, the night-time ratio of IO/OIO was observed to be much smaller than the known chemistry should predict, and the authors hypothesise that there must be an unknown reaction that converts IO to OIO: most probably the reaction of IO with NO_3

$$IO + NO_3 \rightarrow OIO + NO_2 \qquad \text{(R45)}$$

There have been no experimental investigations of R45, which clearly requires future efforts, and R44 has only been the subject of one experimental investigation[143].

The IO dimer, I_2O_2, has tentatively been detected spectroscopically in the laboratory [133,144], although little is known about its structure, gas phase / heterogeneous chemistry or photochemistry. Clearly the iodine oxides require future theoretical and experimental research.

Bromine oxide concentrations are observed to rapidly increase episodically in the Arctic and Antarctic troposphere at polar sunrise, resulting in the almost complete destruction of O_3 for periods of several days [145]. The origins of the high BrO concentrations (> 30 ppt)[146] are thought to be heterogeneous processes (which are described in the section 1.3.3.2.i). At the observed concentrations the O_3 destruction is thought to progress primarily through the BrO self-reaction (and the ClO + BrO cross-reaction), although it has recently been shown that small amounts of iodine species could significantly enhance the O_3 depletion [147]. Further, the currently unpublished observation of very high concentrations of IO in the Antarctic boundary layer[148] suggests that iodine chemistry may be the most important contributor to the depletion of O_3 in the polar boundary layer.

Bromine oxide has been detected at high concentrations in other parts of the MBL, also suggesting the involvement of heterogeneous chemistry [120,149]. It is now widely believed that BrO may be a ubiquitous species in the free troposphere [150] and could account for up to 40 % of the total O_3 destruction [151].

Iodine species are thought to be responsible for up to ~ 50 % of the total O_3 destruction in the MBL [118,122], and may significantly alter the ratios of NO_2/NO [152] and HO_2/OH [123,124]. However, there are major uncertainties with regard to the distribution of IO in the MBL, and atmosphere in general. As the precursors of reactive iodine species are generally short lived and emitted from localised sources, the coastal *versus* open-ocean concentrations of IO are not known, for example. The development of an *in situ* detection method, whereby point measurements of IO could be made at terrestrial, oceanic and airborne locations, is thus highly desirable, and is the motivation for the work discussed in Chapter Three of this thesis. The atmospheric concentration of IO is discussed in greater detail in section 1.4.

1.3.3.1.ii Halogens and Dimethylsulfide (DMS)

Constituting approximately half of the biogenic emission of sulphur compounds into the atmosphere [153], Dimethylsulfide (DMS) is an important species in the troposphere. The gas phase oxidation of DMS by species such as OH and NO_3 ultimately leads to the formation of SO_2 and hence H_2SO_4 [60,154]. Sulphuric acid forms aerosol particles in the marine atmosphere, contributing to the formation of cloud condensation nuclei (CCN). Cloud formation plays an important role in the hydrological cycle and in the Earth's albedo – the fraction of solar radiation reflected back to space. Thus DMS has been proposed to be a natural regulator of the Earth's climate [155]. Under tropospheric conditions, the reactions of OH and NO_3 with DMS predominantly proceed *via* hydrogen abstraction mechanisms

$$X + CH_3SCH_3 \rightarrow HX + CH_3SCH_2 \qquad \text{(R46a)}$$

The reactions can also proceed *via* addition mechanisms, forming adducts (CH_3SXCH_3)

$$X + CH_3SCH_3 + M \rightarrow CH_3SXCH_3 + M \qquad \text{(R46b)}$$

Generally, the abstraction mechanism eventually leads to SO_2 and H_2SO_4 formation [60,154], and the addition mechanism leads to the formation of DMSO (CH_3SOCH_3)[60,154]. DMSO, and its derivatives, does not form new particles in the atmosphere but undergo rapid uptake to existing aerosols and CCN, increasing their size and mass. The formation of DMSO thus leads to increased precipitation and decreases cloud formation in the atmosphere, reducing the Earth's albedo [60,154].

Chlorine and bromine atoms are known to react rapidly with DMS [156,157]. The reaction of DMS with atomic chlorine predominantly proceeds through the addition mechanism (80 %)[158], possibly leading to the formation of DMSO under atmospheric conditions (depending on the extent of reaction of the CH_3SClCH_3 adduct with O_2)[154]. Bromine atoms also react with DMS through the addition channel[157], although under atmospheric conditions the principal fate of the adduct is decomposition back to reactants. A small fraction of the CH_3SBrCH_3 adduct is thought to undergo dissociation to $CH_3SBr + CH_3$ [159]. However, the tropospheric concentration of Cl and Br atoms are too low for their reaction with DMS to be of atmospheric significance – the reactions do not compete with the oxidation of DMS by OH (or NO_3). Their have been no experimental investigations of the reaction of iodine atoms with DMS. Although the rates of reactions involving halogen atoms generally decrease in the order Cl > Br > I, as the concentration of iodine atoms is relatively high in regions of the MBL, this reaction could

potentially be of significance (ultimately depending on the stability of the CH_3SICH_3 adduct) and should be a focus of future research.

The halogen monoxides are also known to react with DMS [158-160]. It would appear that these reactions produce DMSO and halogen atoms *via* the formation of weakly bound adducts[154]

$$XO + CH_3SCH_3 \leftrightarrow CH_3S(OX)CH_3 \rightarrow CH_3SOCH_3 + X \qquad (R47)$$

These reactions could be of climatic significance, therefore, due to the direct formation of DMSO (as opposed to SO_2 and H_2SO_4), if their atmospheric rates are competitive with the oxidation of DMS by OH (and NO_3). Note also that, as the reactions regenerate halogen atoms, they can participate in catalytic O_3 destruction

$$XO + DMS \rightarrow DMSO + X \qquad (R47)$$
$$X + O_3 \rightarrow XO + O_2 \qquad (R32)$$
$$\textbf{Net: DMS} + O_3 \rightarrow \textbf{DMSO} + O_2$$

Due to the small rate coefficient for the reaction between ClO and DMS, and the low concentration of ClO in the MBL, R47 (X = Cl) is not important in the atmosphere. However, the rate coefficient for the reaction of BrO with DMS is sufficiently large for bromine monoxide to be the dominant sink for DMS in the MBL, accounting for up to ~ 80 % of its total gas phase oxidation[60]. Although the rate coefficient for the reaction of IO with DMS was previously considered too small to be of atmospheric significance [160], a recent investigation [161] reported the rate coefficient to be more than an order of magnitude greater than previously assumed. A higher value for the rate coefficient of the reaction of IO and DMS was also supported by theoretical calculations[162]. As part of the course of this PhD, the reaction kinetics of the IO + DMS reaction was investigated. It was found that the initial evaluation of the rate coefficient was correct, and that the reaction probably proceeds *via* a direct, oxygen atom transfer mechanism – in disagreement with the findings of the recent experimental[161] and theoretical[162] studies. As the work has been published[163], the findings are not presented in the bulk of this thesis, but the published article is attached as an appendix. The results of our study have largely been confirmed by a further recent experimental investigation[164]. The primary implication of this result is that IO is not a predominant oxidant of DMS in the MBL. However, as IO concentrations may be much higher than previously assumed[140], the IO + DMS reaction may still be of atmospheric significance under localised conditions. Another interesting inference of the work is the apparent reactivity trend of the halogen monoxides with DMS (BrO > IO ≈ ClO, as opposed to the expected IO > BrO > ClO). This observed reactivity trend is probably due to the XO + DMS reactions proceeding through different reaction mechanisms – the formation of a

weakly bound adduct in the BrO + DMS reaction, but bimolecular mechanisms in the ClO and IO reactions with DMS. It is unclear, however, as to why a BrO-DMS adduct is apparently formed, but an IO-DMS adduct is not.

1.3.3.1.iii Halogens and Mercury

Atomic mercury (Hg^0) is emitted into the atmosphere from a variety of anthropogenic sources such as coal fired power stations and mining operations[165]. Natural sources, such as volcanic emissions, also exist[165]. As Hg^0 is relatively insoluble in aqueous solution and inert, it is persistent in the atmosphere and distributed relatively uniformly[165]. However, at polar sunrise, mercury depletion events (MDE's) are known to occur in both hemispheres[166,167], in which elemental mercury is removed from the gas phase and deposited in the surface snow in more soluble forms. The accumulation of these soluble forms of mercury has serious environmental implications: the contamination of food chains at times of high biological activity, for example.

As polar MDE's coincide with ozone depletion events (and the concentration of Hg^0 is correlated with O_3 and anti-correlated with BrO), it is now known that the MDE's are a result of bromine chemistry. Atomic mercury reacts rapidly with Br atoms[168] (and BrO)[169]

$$Hg + Br + M \rightarrow HgBr + M \qquad (R48)$$

$$Hg + BrO + M \rightarrow OHgBr + M \qquad (R49)$$

The HgBr can then react further to generate a variety of species, in which mercury is in the +2 oxidation state[170], which are relatively soluble and can be deposited by dry deposition to the surface snow.

$$HgBr + X + M \rightarrow XHgBr + M \qquad (R50)$$

Here, the most likely candidates for X are Br and BrO, and the final products of mercury oxidation are considered to be HOHgBr (derived from reaction of OHgBr with HO_2) and $HgBr_2$[169].

A recent study[169] has shown that iodine chemistry could significantly contribute to polar MDE's, if relatively low concentrations of iodine species are present. The enhanced mercury depletion is attributed to an increased Br atom production, from the reaction of IO with BrO. Iodine chemistry is not considered to directly contribute to the MDE's because HgI, formed from the reaction of mercury and iodine atoms, is assumed to undergo rapid dissociation before its reaction with other trace species can occur. This assumption is based on the results of one

theoretical study[171], however, and should receive experimental verification. The reaction of Hg with IO (and the reactions of HgBr with I and IO) would also appear to be a notable candidate for future research, in order to investigate any links between iodine chemistry and MDE's.

1.3.3.2 Heterogeneous Chemistry

1.3.3.2.i Halogen Activation

Inorganic, gas phase products of halogen chemistry, such as HOX and $XONO_2$ (X = Cl, Br, I), are relatively soluble and may undergo uptake to aerosol particles. Although particulate scavenging of these species removes gas phase halogens from the atmosphere, heterogeneous processes occurring in the bulk, or on the surface, of aerosols can result in halogen activation – the liberation of more photolabile, and therefore more reactive, halogen species (e.g. Br_2, BrCl, Cl_2). For example, the aqueous reaction of hypohalous acids with halide ions result in the release of molecular halogens into the gas phase[172]

$$HOX + Y^- + H^+ \rightarrow H_2O + XY \qquad (R51)$$

Note that, whereas, X can be Cl, Br or I, Y^- is most likely to be chloride or bromide, as iodide is a relatively insignificant component of sea-salt. Further, as R51 is acid-catalysed, the aerosol particle must be of sufficiently low pH for this reaction to be important. The reaction of Caro's acid (HSO_5^-, formed by aqueous phase chemistry of sulphur species) with halide ions may also provide a halogen activation mechanism[172]

$$HSO_5^- + X^- \rightarrow HOX + SO_4^{2-} \qquad (R52)$$

where the generated hypohalous acid will undergo additional aqueous phase chemistry to liberate gas phase halogen species.

Other reactions, which may contribute to the release of particulate halogen species, involve the halogen nitrates ($XONO_2$)[11]

$$XONO_2 + Y^- \rightarrow XY + NO_3^- \qquad (R53)$$

$$XONO_2 + H_2O \rightarrow HOX + HNO_3 \qquad (R54)$$

These processes have enhanced atmospheric significance as they result in the denoxification of the atmosphere[173].

Heterogeneous reactions preferentially liberate bromine species from aerosol particles (due to the higher rates of reactions involving bromine species), although the degassing of chlorine species become more important as the particles are depleted of bromide[174]. Measurements of the Cl/Br ratio in marine aerosol particles support this argument, where the ratio is found to increase with particulate age[175].

Reactions of OH and O_3 with halide ions at the air-water interface of aerosol particles may be of atmospheric significance[11,20]

$$OH + X^- \rightarrow \tfrac{1}{2} Cl_2 + OH^- \quad \text{(R55)}$$

$$O_3 + X^- \rightarrow \tfrac{1}{2} X_2 + O_3^- \quad \text{(R56)}$$

Halide ions have a preference for residing at the surface of aerosol particles, as opposed to the bulk aqueous solution, because the asymmetric arrangement of water molecules surrounding the halide at the interface results in the creation of a dipole that leads to attractive forces, which overcome the partial loss of solvation energy (compared to the bulk solution)[11]. Thus the polarizability of the halide ion influences its preference for the interface, and bromide ions are more strongly bound at the interface than chloride ions. However, it has recently been shown that interface reactions are more important for chloride ions because of their enhanced rate of reactions as compared to the bulk solution (which is not the case for the analogous bromide reactions)[20]. The fact that the surface reactions are not acid-catalysed could have important implications for particulate sulphur chemistry. The particulate uptake of SO_2, and its oxidation by O_3, is pH dependent – being most efficient in alkaline conditions. As SO_2 is oxidised to H_2SO_4, the particle pH becomes more acidic, and the uptake of SO_2 is inhibited – the uptake and oxidation of SO_2 is self-regulating. However, the oxidation of halide ions by OH results in the formation of hydroxide ions, which increases the alkalinity of the particles, and thus partially neutralises this effect[11].

Heterogeneous chemistry is thought to be responsible for the polar ozone depletion events that are witnessed in the Arctic and Antarctic troposphere at polar sunrise[176,177]. It is thought that a "seed", such as the heterogeneous reaction of O_3 and Br^- (or possibly iodine chemistry)[148] initiates the release of Br_2 (and BrCl) from aerosol particles[11,20]. When sunlight returns at polar spring, the molecular bromine is rapidly photolysed producing two Br atoms, which react with O_3 forming two molecules of BrO. The bromine monoxide radicals can then react with HO_2 radicals producing two HOBr molecules. The hydrobromous acid is then adsorbed on the surface of particles where it results in the heterogeneous production of two more molecules of Br_2 *via* R51. The photolysis of two molecules of Br_2 now leads to the production of four bromine atoms, BrO radicals, and HOBr molecules, and so on – an

exponential growth in BrO concentrations results: a phenomenon known as the bromine explosion. The overall process can be written as[178]

$$BrO + O_3 + Br^- + H^+ \xrightarrow{surface,HOx} 2\,BrO + products \qquad (R57)$$

It is thought that aerosol particles deposited on sea ice form the surface on which the heterogeneous reactions occur[179,180]. Here bromide ion concentrations can be enhanced by a factor of three relative to the surrounding sea water[11], and the formation of frost flowers – crystalline structures that grow out of the concentrated brines on newly forming sea ice – are thought to play an important role, although there is some uncertainty over this issue[180,181].

Heterogeneous chemistry is probably the most dominant source of reactive chlorine and bromine compounds (and molecular halogens at night-time) at low altitudes in the MBL – the photolysis of organochlorines and organobromines becoming more important at higher altitudes[121,182]. Although the major source of reactive iodine species in the MBL has hitherto been assumed to be the photolysis of organoiodines and I_2, recent observations[120] of high IO concentration in the Dead Sea – a region of low biological activity – suggests that significant heterogeneous sources of iodine species must also exist (such as the photochemical liberation of I_2 from the surface water, as suggested by Miyake and Tsunogai[23]). The authors of this study[120] suggest a new mechanism for the heterogeneous production of I_2

$$HOI + HOX \rightarrow IO_2^- + X^- + 2\,H^+ \qquad (R58)$$
$$HOI + IO_2^- \rightarrow IO_3^- + I^- + H^+ \qquad (R59)$$
$$IO_3^- + 5\,I^- + 6\,H^+ \rightarrow 3\,I_2 + 3\,H_2O \qquad (R60)$$
$$3\,I_{2(aq)} \rightarrow 3\,I_{2(g)} \qquad (R61)$$

where all reactions occur in the aqueous phase.

Recent observations of particulate organic iodine suggest that HOI may undergo competitive aqueous phase reactions with organic molecules in aerosol particles, rather than reaction with halide ions[183]. Further, recent measurements of much higher I^-/IO_3^- ratios in aerosol particles suggest that the previous assumption that particulate iodine is predominantly in the form of iodate[118], IO_3^-, is incorrect[183,184]. It was also previously assumed that iodate was relatively inert[185] – in contrast to the heterogeneous iodate chemistry proposed by Zingler and Platt[120] (R58 – R59).

The heterogeneous chemistry of halogen (and in particular iodine) species is only partially understood and a more complete knowledge of these processes in integral to our understanding of the atmospheric significance of halogen species. For example, a recent study

has found that cloud particles (in which the halide content is significantly less than sea salt aerosols) could provide an important flux of halogen atoms into the atmosphere[182] – emphasising the potential importance of halogen species on a global basis.

1.3.3.2.ii New Particle Formation

A recent study in the North-east Atlantic, PARFORCE (new PARticle FORmation and fate in the Coastal Environment)[186] reported massive aerosol formation events under conditions where the sampled air had passed over exposed coastal areas at low tide in daylight. Analysis of the size distribution of the new particles indicated that their size was less than 10 nm, characteristic of the particles being in the nucleation mode (several – tens of molecules). Observations of CH_2I_2[42] and IO[187] at Mace Head, Ireland (the site of the PARFORCE campaign) with peak concentrations at low tide, suggested that the new particle formation may be attributable to photolysis of CH_2I_2 and subsequent gas-phase chemistry of the iodine oxides.

Initial laboratory investigations[188-190] showed that particle formation could indeed result from the photolysis of CH_2I_2 in the presence of O_3, but it was concluded that the known concentrations of CH_2I_2 in the MBL were insufficient to explain the observed particle production, with required IO / OIO concentrations of ~ 50 – 100 / 10 ppt[190]: around an order of magnitude higher than measured. A subsequent study[24] found that new particle formation also results from the irradiation of *Laminaria* macroalgae (collected from Mace Head), or the photolysis of I_2, in the presence of O_3, and that the particles were of similar composition to the earlier studies[189]. Further, the establishment of a direct link between seaweed biomass, and molecular iodine and particle concentration[25,191], and the observations of high I_2 concentrations[66], have now confirmed I_2 as the most important precursor to particle formation at Mace Head (and possibly most coastal sites, therefore). It is worth mentioning, however, that high CH_2I_2 concentrations have recently been measured at a coastal site, where I_2 was not detected above the instrumental detection limit[48]

The gas-phase mechanism to particle formation is unclear. Hoffmann *et. al.*[188], initially proposed the self-reaction of OIO as the nucleating step to particle formation

$I + O_3$	$\rightarrow$	$IO + O_2$	(R32, X = I)
$IO + IO$	$\rightarrow$	$OIO + I$	(R43a, X = Y = I)
$OIO + OIO$	$\rightarrow$	I_2O_4	(R62)
$I_2O_4 + nOIO$	$\rightarrow$	$[\text{-I-O-IO}_2\text{-}]_{1+n/2}$	(R63)

However, the reaction of IO with OIO has also been proposed as a nucleation step[139]

$$IO + OIO \rightarrow I_2O_3 \qquad \text{(R64)}$$

Transmission electron microscopy (TEM) indicates that the iodine particles are probably composed of I_2O_5[24,139], which Saunders and Plane[139] propose to be formed by the oxidation of iodine oxides by O_3 (R65), in competition with iodine oxide coagulation (R66)

$$I_2O_2 (+ O_3) \rightarrow I_2O_3 (+ O_3) \rightarrow I_2O_4 (+ O_3) \rightarrow I_2O_{5(g\rightarrow s)} \qquad \text{(R65)}$$

$$I_2O_x + I_yO_z \rightarrow I_{2+y}O_{x+z(g\rightarrow s)} \qquad \text{(R66)}$$

Modeling studies[138,140,192] generally reproduce experimental and field data more satisfactorily when R64 is considered as an additional nucleation process to the self-reaction of OIO. Further experimental and theoretical work is required to deduce the gas-phase chemistry responsible for the formation of the iodine particles.

Other outstanding issues surrounding the formation of new particles are whether iodine species form new particles over the open-oceans[193], and whether the iodine particles contribute to CCN formation (either directly or indirectly) in the marine atmosphere[140,193,194].

1.4 Atmospheric Measurements of IO

As this thesis is concerned with the atmospheric role of iodine species, and in particular IO, this section provides a generic review of atmospheric observations of iodine monoxide to date. Hitherto, IO has exclusively been detected in the atmosphere by long-path differential absorption spectroscopy (DOAS)[195]. DOAS operates on the principle of the Beer-Lambert law, E. 1.4-1

$$I_t = I_0 \exp(-\sigma c \ell) \qquad \text{E. 1.4-1}$$

where, I_t and I_0 are the intensities of transmitted and incident radiation respectively, of a light source passing through a sample of path length, ℓ, of an absorbing species of concentration, c. The absorption cross-section, σ, of the absorbing species is a fundamental molecular property and is dependent on the wavelength of the light source, and the temperature of the sample.

In a DOAS experiment, the light source can be artificial (*e.g.* a broadband Xe arc-lamp) or natural (*e.g.* the sun). The basic procedure of a typical DOAS experiment in the MBL is as follows. The broadband emission from a Xe lamp is passed through a region of the atmosphere to a suitable detector, such as a diode array. The detector resolves the light into its composite

wavelengths, yielding a spectrum, whose structure is dependent on several factors: the natural spectrum of the Xe lamp; the absorption of light by atmospheric species; and the scatter of light by air molecules (Rayleigh and Raman scattering) and aerosol particles (Mie scattering). To obtain information with regards to any one absorbing species, therefore, relies on that species possessing a unique spectral fingerprint (an absorption structure) in the wavelength range of the recorded spectrum. For IO, the relevant absorption structure corresponds to several vibrational transitions in the $A^2\Pi_{3/2} \leftarrow X^2\Pi_{3/2}$ electronic transition, over an approximate wavelength range of 415 – 450 nm (see Chapter Three for a detailed discussion of the spectroscopy of IO). To process the recorded spectrum, background spectra of the Xe lamp and scattered light are recorded and deconvoluted from the total signal, yielding a spectrum that is attributable to any atmospheric absorbers over the investigated wavelength range. To determine the atmospheric concentration of IO, the deconvoluted spectrum must then be corrected for absorption by any known atmospheric absorbers (NO_2 and H_2O in the case of DOAS detection of IO) using reference spectra. The resultant differential absorption spectrum of IO can then be converted into an absolute IO concentration by prior knowledge of its absorption-cross section. Thus two disadvantages of the DOAS technique are immediately apparent. First, that converting the IO absorption signal into an absolute concentration relies on the accurate knowledge of the absorption cross-section of IO (determined in the laboratory), and secondly that the spectral deconvolution procedure is complex and subject to interference from unknown absorbers and fluctuation of experimental variables.

Further, as the absorption signal of a species is directly proportional to the path length over which it absorbs, long path lengths are required in DOAS experiments (typically 8 – 11 km) to achieve sufficient instrumental sensitivity. This results in the determined concentration being the average value over the experimental path length, which may be erroneous for species with localised sources and sinks. This is especially true for coastal IO, where its production may be predominantly governed by local emissions of iodine containing compounds from seaweed. To reduce the required path length, DOAS experiments often utilise reflectors that are situated at a suitable location away from the light source, resulting in halving the effective path length over which the absorbing species is averaged. The typical detection limit for IO in boundary layer DOAS experiments is 0.2 – 0.9 ppt [196].

Stratospheric measurements of IO can also be performed using DOAS. In these experiments, light from a natural source (typically the sun) is collected by a ground-based[197] (or balloon-based[198-201]) detector. The absorption spectrum is measured as a function of solar zenith angle, resulting in a varying path length through the Earth's atmosphere. Similarly to boundary layer experiments, the spectral deconvolution procedure is complex[197,201], and the concentration of IO can be obtained by applying various radiative transfer and photochemical models,

although the vertical distribution of IO can only be estimated (particularly for ground-based measurements).

Table 1.4-1 lists the maximum ambient IO concentrations that have been reported from DOAS observations at a variety of locations.

Region	Location, (Year)	$[IO]_{max}$ / ppt	Reference
MBL	Mace Head, Ireland (1997)	6.6 ± 0.5	187
MBL	Mace Head, Ireland (1997)	3.0 ± 0.4	196
MBL	Mace Head, Ireland (1998)	7.2 ± 0.3	205
MBL	Mace Head, Ireland (2002)	7 ± 0.5 (day)	66, 142
		3 ± 0.5 (night)	66, 142
MBL	Tasmania (1999)	2.3 ± 0.4	196
MBL	Tenerife (1997)	3.5 ± 0.4	196
MBL	Antarctica (1999)	10	202
MBL	Antarctica (2004)	20.5 ± 1.2	148
MBL	Kerguelen Islands, Indian Ocean	9.8	203
MBL	Kerguelen Islands, Indian Ocean	<1.4	204
MBL	Mediterranean Sea, Crete	<0.8	203
MBL	Arctic	0.73 ± 0.23	203
MBL	Dead Sea (Israel) (2001)	10.2 ± 2.4	120
MBL	North Sea (Germany) (2002)	2.1 ± 0.5	48
MBL	Brittany (2003)	7.7 ± 0.5	48
UTLS	Kitt Peak, Arizona (1995)	0.20 ± 0.01	198
UTLS	Sweden, Norway, France (1995)	0.2 (+0.3, -0.2)	199
UTLS	Arctic (1997)	0.8 ± 0.2	197
UTLS	Arctic (1999, 2000)	1.1 ± 1.2	200
UTLS	Arctic (1997)	0.1 ± 0.02	201

Table 1.4-1 – Concentrations and locations of atmospheric measurements of IO (MBL = Marine Boundary Layer, UTLS = Upper Troposphere – Lower Stratosphere).

The data presented in Table 1.4-1 highlights the wide range of concentrations and locations that IO has been detected at in the atmosphere. Alicke *et. al.*[187] suggested that a mixing ratio of 6 ppt IO can enhance the destruction of O_3 by as much as 70 % over the ocean and 10 % over the land, and significantly alter the $[HO_2]/[OH]$ and $[NO_2]/[NO]$ ratios, illustrating the impact of

relatively low concentrations of IO in the MBL. However, it is considered that ambient IO concentrations may be underestimated by DOAS observations. For example, a recent modeling study[140] of the experimental observations of Saiz-Lopez and Plane[66,142], showed that the DOAS measured $[IO]/[I_2]$ ratio could not be reproduced unless the iodine species were located over approximately 8 % of the 4.2 km path length, and that the average IO concentration could have been as high as 47 ppt in this inter-tidal zone, under conditions where particle bursts were observed (low tide and solar irradiance). Clearly, ambient IO concentrations of this magnitude have serious implications for particle formation, CCN production, and the oxidising capacity of the MBL, albeit under very localised and temporary conditions. Conversely, another recent study[48] found that the observed IO concentrations in a coastal region of Brittany could adequately be reproduced by the measured iodocarbon concentrations (and were predominantly governed by CH_2I_2). Although molecular iodine was not detected in that study, adding a small, estimated I_2 concentration (< 0.5 ppt) to the model, significantly enhanced the modelled IO concentration, indicating that either I_2 was not a significant source of atmospheric iodine at that location, or that (by omitting particle formation) an important IO sink was missing from the model. The authors recommend that future research should focus on point measurements of IO and OIO, and particle production at such locations. An IO LIF instrument, designed and constructed as part of the course of this PhD, is making preliminary measurements of IO at a coastal site in Brittany at the time of writing – representing the first point measurement of this species in the atmosphere. The initial results suggest that IO concentrations have reached in excess of 20 ppt.

The ambient concentrations of IO hitherto measured (or not measured) in the UTLS indicate that iodine chemistry makes no significant contribution to stratospheric ozone depletion. For example, Bosch *et. al.*[201] have shown that their measured concentration of stratospheric IO contributes less than 1 % to the total ozone destruction. However, Solomon *et. al.*[59] have suggested that iodine concentrations of 1 ppt in the stratosphere could enhance O_3 destruction by as much as 30 %. The measurements of Wittrock *et. al.*[197] therefore suggests that iodine chemistry could be significant in the stratosphere, although there is no apparent reason why their measured IO concentrations are greater than those from the other UTLS studies[201]. It would appear that significant iodine concentrations in the stratosphere are generally the exception rather than the rule. However, the poor spatial resolution of DOAS measurements may mean that the observed stratospheric concentrations of IO are underestimated, and that iodine chemistry has a much greater impact, occurring under localised conditions, than previously thought. Trifluoromethyl iodide (CF_3I), a potential halon replacement, has recently been found to have a substantially greater potential for stratospheric O_3 depletion than previously thought[206].

Clearly, the development of a point measurement detection method for IO in coastal, open ocean and UTLS regions would greatly enhance our understanding of iodine chemistry in the atmosphere and is the focus of the work reported in Chapter Three of this thesis.

1.5 Summary

In this introduction to halogen chemistry, it has been shown that major uncertainties exist with regards to the sources, gas-phase chemistry, heterogeneous chemistry, and concentration of halogen (and in particular iodine) species within the Earth's atmosphere. The work reported in the remainder of this thesis is motivated by the need to improve our quantitative understanding of atmospheric iodine chemistry, with the long-term goal of the inclusion of halogen chemistry within global atmospheric chemistry models.

References

1. T. E. Graedel and P. J. Crutzen, "*Atmosphere, Climate, and Change*", Scientific American Library, New York, 1995.
2. T. E. Graedel and P. J. Crutzen, "*Atmospheric Change: An Earth System Perspective*", W. H. Freeman and Company, New York, 1993.
3. R. P. Wayne, "*Chemistry of Atmospheres*", Third Edition, Oxford University Press, Oxford, 2000.
4. G. P. Brasseur, J. J. Orlando and G. S. Tyndall, "*Atmospheric Chemistry and Global Change*", Oxford University Press, Oxford, 1999.
5. B. J. Finlayson-Pitts and J. N. Pitts, Jr., "*Chemistry of the Upper and Lower Atmosphere: Theory, Experiments, and Applications*", Academic Press, San Diego, 2000.
6. P. J. Crutzen, "*An overview of atmospheric chemistry*", in Chapter IV, European Research Course on Atmospheres, Volume 1: *Topics in Atmospheric and Interstellar Physics and Chemistry*, Ed. C. F. Boutron, EDP Sciences, Les Ulis, 1994.
7. United Nations Environment Programme, Environmental Effects Assessment Panel, "Environmental effects of ozone depletion and its interactions with climate change: Progress report, 2005", *Photochem. Photobiol. Sci.*, **5**, 13 – 24, 2006.
8. M. J. Pilling and P. W. Seakins, "*Reaction Kinetics*", Oxford University Press, Oxford, 1999.
9. R. P. Wayne, G. Poulet, P. Biggs, J. P. Burrows, R. A. Cox, P. J. Crutzen, G. D. Hayman, M. E. Jenkin, G. Lebras, G. K. Moorgat, U. Platt and R. N. Schindler, "Halogen oxides: radicals, sources and reservoirs in the laboratory and in the atmosphere", *Atmos. Environ.*, **29**, 2677 – 2881, 1995.
10. R. A. Cox, "*THalOz: Tropospheric Halogens – Effect on Ozone*", Project: EVK2-CT-2001-00104, Final Report: 1st Feb 2002 – 30th April 2005.
11. B. J. Finlayson-Pitts, "The Tropospheric Chemistry of Seal-Salt: A Molecular-Level View of the Chemistry of NaCl and NaBr", *Chem. Rev.*, **103**, 4801 – 4822, 2003.
12. E. M. Knipping and D. Dabdub, "Impact of Chlorine Emissions from Sea-Salt Aerosol on Coastal Urban Ozone", *Environ. Sci. Technol.*, **37**, 275 – 284, 2003.
13. B. J. Finlayson-Pitts and S. N. Johnson, "The Reaction of NO_2 with NaBr: Possible Source of BrNO in Polluted Marine Atmospheres", *Atmos. Environ.*, **22**, 1107 – 1112, 1988.

14. M. Y. Gershenzon, S, Il'in, N. G. Fedotov, Y. M. Gershenzon, E. V. Aparina and V. V. Zelenov, "The mechanism of reactive NO_3 uptake on dry NaX (X = Cl, Br)", *J. Atmos. Chem.*, **34**, 119 – 135, 1999.
15. R. C. Hoffmann, M. E. Gebel, B. S. Fox and B. J. Finlayson-Pitts, "Knudsen cell studies of the reactions of N_2O_5 and $ClONO_2$ with NaCl: development and application of a model for estimating available surface areas and corrected uptake coefficients", *Phys. Chem. Chem. Phys.*, **5**, 1780 – 1789, 2003.
16. A. Alebic-Juretic, T. Cvitas and L. Klasinc, "Ozone destruction on powders", *Ber. Bunsen-Ges. Phys. Chem.*, **96**, 493 – 495, 1992.
17. A. V. Ivanov, Y. M. Gershenson, F. Gratpanche, P. Devolder and J. P. Sawersyn, "Heterogeneous loss of OH on NaCl and NH_4NO_3 at tropospheric temperatures", *Ann. Geophys.*, **14**, 659 – 664, 1996.
18. R. G. Remorov, Y. M. Gershenzon, L. T. Molina and M. J. Molina, "Kinetics and Mechanism of HO_2 Uptake on Solid NaCl", *J. Phys. Chem. A.*, **106**, 4558 – 4565, 2002.
19. S. W. Hunt, M. Roeselova, W. Wang, L. M. Wingen, E. M. Knipping, D. J. Tobias, D. Dabdub abd B. J. Finlayson-Pitts, "Formation of Molecular Bromine from the Reaction of Ozone with Deliquesced NaBr Aerosol: Evidence for Interface Chemistry", *J. Phys. Chem. A*, **108**, 11559 – 11572, 2004.
20. J. L. Thomas, A. Jimenez-Aranda, B. J. Finlayson-Pitts and D. Dabdub, "Gas-Phase Molecular Halogen Formation from NaCl and NaBr Aerosols: When Are Interface Reactions Important?", *J. Phys. Chem. A.*, **110**, 1859 – 1867, 2006.
21. E. M. Knipping, M. J. Lakin, K. L. Foster, P. Jungwirth, D. J. Tobias, R. B. Gerber, D Dabdub and B. J. Finlayson-Pitts, "Experiments and Simulations of Ion-Enhanced Interfacial Chemistry on Aqueous NaCl Aerosols", *Science*, **288**, 301 – 306, 2000.
22. J. A. Garland and H. Curtis, "Emission of Iodine From the Sea Surface in the Presence of Ozone", *J. Geophys. Res.*, **86**, 3183 – 3186, 1981.
23. Y. Miyake and S. Tsunogai, "Evaporation of Iodine from the Ocean", *J. Geophys. Res.*, **68**, 3989 - 3993, 1963.
24. G. McFiggans, H. Coe, R. Burgess, J. Allen, M. Cubison, M. R. Alfarra, R. Saunders, A. Saiz-Lopez, J. M. C. Plane, D. J. Wevill, L. J. Carpenter, A. R. Rickard and P. S. Monks, "Direct evidence for coastal iodine particles from Laminaria macroalgae – linkage to emissions of molecular iodine", *Atmos. Chem. Phys.*, **4**, 701 – 713, 2004.
25. C. J. Palmer, T. L. Anders, L. J. Carpenter, F. C. Kupper and G. B. McFiggans, "Iodine and Halocarbon Response of *Laminaria digitata* to Oxidative Stress and Links to Atmospheric New Particle Production", *Environ. Chem.*, **2**, 282 – 290, 2005.
26. S. Amachi, Y. Muramatsu, Y. Akiyama, K. Miyazaki, S. Yoshiki, S. Hanada, Y. Kamagat, T. Ban-nai, H. Shinoyama and T. Fujii, "Isolation of Iodide-Oxidising Bacteria from Iodide-Rich Natural Gas Brines and Seawaters", *Microb. Ecol.*, **49**, 547 – 557, 2005.
27. S. Chang, E. McDonald-Buller, Y. Kimura, G. Yarwood, J. Neece, M. Russell, P. Tanaka and D. Allen, "Sensitivity of urban ozone formation to chlorine emission estimates", *Atmos. Env.*, **36**, 4991 – 5003, 2002.
28. G. W. Gribble, "The diversity of naturally produced organohalogens", *Chemosphere*, **52**, 289 – 297, 2003.
29. http://ozone.unep.org/pdfs/Montreal-Protocol2000.pdf
30. P. J. Fraser, D. E. Oram, C. E. Reeves, S. A. Penkett and A. McCulloch, "Southern Hemisphere halon trends (1978 – 1998) and global halon emissions", *J. Geophys. Res.*, **104**, D13, 15985 – 15999, 1999.
31. P. Patel-Predd, "Removing methyl bromide from shipping operations", *Environ. Sci. Technol.*, **40**, 4540, 2006.
32. A. M. Wuosmaa and L. P. Hager, "Methyl Chloride Transferase: A Carbocation Route for Biosynthesis of Halometabolites", *Science*, **249**, 160 – 162, 1990.
33. J. M. Baker, W. T. Sturges, J. Sugier, G. Sunnenberg, A. A. Lovett, C. E. Reeves, P. D. Nightingale and S. A. Penkett, "Emissions of CH_3Br, organochlorines, and organoiodines from temperate macroalgae", *Chemosphere*, **3**, 93 – 106, 2001.

34. R. M. Moore, M. Webb, R. Tokarczyk and R. Wever, "Bromoperoxidase and iodoperoxidase enzymes and production of halogenated methanes in marine diatom cultures", *J. Geophys. Res.*, **101**, 20899 – 20908, 1996.
35. K. R. Redeker, K. K. Treseder and M. F. Allen, "Ectomycorrhizal fungi: A new source of atmospheric methyl halides?", *Glob. Change Biol.*, 10, 1009 – 1016, 2004.
36. J. Lee-Taylor and K. R. Redeker, "Reevaluation of global emissions from rice paddies of methyl iodide and other species", *Geophys. Res. Lett.*, **32**, L15801, 2005.
37. A. L. Swanson, N. J. Blake, J. E. Dibb, M. R. Albert, D. R. Blake and F. S. Rowland, "Photochemically induced production of CH_3Br, CH_3I, C_2H_5I, ethane, and propene within surface snow at Summit", Greenland, *Atmos. Environ.*, **36**, 2671 – 2682, 2002.
38. F. M. Schwandner, T. M. Seward, A. P. Gize, P. A. Hall and V. J. Dietrich, "Diffuse emission of organic trace gases from the flank and crater of a quiescent active volcano (Vulcano, Aeolian Islands, Italy)", *J. Geophys. Res.*, **109**, D04301, 2004.
39. W. L. Chameides and D. D. Davis, "Iodine: Its Possible Role in Tropospheric Photochemistry", *J. Geophys. Res.*, **85**, 7383 – 7398, 1980.
40. W. Reifenhauser and K. Heumann, "Bromo- and Bromochloromethanes in the Antarctic Atmosphere and South Polar Sea", *Chemosphere*, **24**, 1293 – 1300, 1992.
41. C. Schall and K. G. Heumann, "GC determination of volatile organoiodine and organobromine compounds in Arctic seawater and air samples", *Fresenius J. Anal. Chem.*, **346**, 717 – 722, 1993.
42. L. J. Carpenter, W. T. Sturges, S. A. Penkett, P. S. Liss, B. Alicke, K. Hebestreit and U. Platt, "Short-lived alkyl iodides and bromides at Mace Head, Ireland: Links to biogenic sources and halogen oxide production", *J. Geophys. Res.*, **104**, 1679 – 1689, 1999.
43. J. C. Low, N. Y. Wang, J. Williams and R. J. Cicerone, "Measurements of ambient atmospheric C_2H_5Cl and other ethyl and methyl halides at coastal California sites and over the Pacific Ocean", *J. Geophys. Res.*, **108**, D19, 4608, 2003.
44. L. J. Carpenter, P. S. Liss and S. A. Penkett, "Marine organohalogens in the atmosphere over the Atlantic and Southern Oceans", *J. Geophys. Res.*, **108**, D9, 4256, 2003.
45. Y. Zhou, R. K. Varner, R. S. Russo, O. W. Wingenter, K. B. Haase, R. Talbot and B. C. Sive, "Coastal water source of short-lived halocarbons in New England", *J. Geophys. Res.*, **110**, D21302, 2005.
46. L. J. Carpenter, J. R. Hopkins, C. E. Jones, A. C. Lewis, R. Parthipan, D. J. Wevill, L. Poissant, M. Pilote and P. Constant, "Abiotic Source of Reactive Organic Halogens in the Sub-Arctic Atmosphere?", *Environ. Sci. Technol.*, **39**, 8812 – 8816, 2005.
47. Y. Yokouchi, F. Haseby, M. Fujiwara, H. Takashima, M. Shiotani, N. Nishi, Y. Kanaya, S. Hashimoto, P. Fraser, D. Toom-Sauntry, H. Mukai, and Y. Nojiri, "Correlations and emission ratios among bromoform, dibromochloromethane, and dibromomethane in the atmosphere", *J. Geophys. Res.*, **110**, D23309, 2005.
48. C. Peters, S. Pechtl, J. Stutz, K. Hebestreit, G. Honninger, K. G. Heumann, A. Schwarz, J. Winterlik and U. Platt, "Reactive and organic halogen species in three different European coastal environments", *Atmos. Chem. Phys.*, **5**, 3357 – 3375, 2005.
49. M. Pedersen, J. Collen, K. Abrahamsson and A. Ekdahl, "Production of halocarbons from seaweeds: an oxidative stress reaction", *Scientia Marina*, **60**, 257 – 263, 1996.
50. K. van Pee and S. Unversucht, "Biological dehalogenation and halogenation reactions", *Chemosphere*, **52**, 299 – 312, 2003.
51. P. M. Gschwend, J. K. MacFarlane and K. A. Newman, "Volatile Halogenated Organic Compounds Released to Seawater from Temperate Marine Macroalgae", *Science*, **227**, 1033 – 1035, 1985.
52. R. Wever, M. G. M. Tromp, B. E. Krenn, A. Marjani and M. Van Tol, "Brominating Activity of the Seaweed Ascophyllum nodosum: Impact on the Biosphere", *Environ. Sci. Technol.*, **25**, 446 – 449, 1991.
53. C. E. Jones and L. J. Carpenter, "Solar Photolysis of CH_2I_2, CH_2ICl, and CH_2IBr in Water, Saltwater, and Seawater", *Environ. Sci. Technol.*, **39**, 6130 – 6137, 2005.
54. M. Martino, P. S. Liss and J. M. C. Plane, "The Photolysis of Dihalomethanes in Surface Seawater", *Environ. Sci. Technol.*, **39**, 7097 – 7101, 2005.

55. M. Martino, P. S. Liss and J. M. C. Plane, "Wavelength-dependence of the photolysis of diiodomethane in seawater", *Geophys. Res. Lett.*, **33**, L06606, 2006.
56. W. T. Sturges, G. F. Cota and P. T. Buckley, "Bromoform emission from Arctic ice Algae", *Nature*, **358**, 660 – 662, 1992.
57. L. J. Carpenter, D. J. Wevill, S. O'Doherty, G. Spain and P. G. Simmonds, "Atmospheric bromoform at Mace Head, Ireland: seasonality and evidence for a peatland source", *Atmos. Chem. Phys.*, **5**, 2927 – 2934, 2005.
58. M. Y. Ali and J. P. Riley, "The Production of Brominated Methanes in Desalination Plants in Kuwait", *Wat. Res.*, **23**, 1099 – 1106, 1989.
59. S. Solomon, R. R. Garcia and A. R. Ravishankara, "On the role of iodine in ozone depletion", *J. Geophys. Res.*, **99**, 20491 – 20499, 1994.
60. R. von Glasow and P. J. Crutzen, "Model study of multiphase DMS oxidation with a focus on halogens", *Atmos. Chem. Phys.*, **4**, 589 – 608, 2004.
61. A. McCulloch, P. Ashford and P. M. Midgley, "Historic emissions of fluorotrichloromethane (CFC-11) based on a market survey", *Atmos. Environ.*, **35**, 4387 – 4397, 2001.
62. A. McCulloch, P. M. Midgley and P. Ashford, "Releases of refrigerant gases (CFC-12, HCFC-22 and HFC-134a) to the atmosphere", *Atmos. Environ.*, **37**, 889 – 902, 2003.
63. A. McCulloch, P. M. Midgley and A. A. Lindley, "Recent changes in the production and global emissions of chlorodifluoromethane (HCFC-22)", *Atmos. Environ.*, **40**, 936 – 942, 2006.
64. World Meteorological Organisation (WMO), *"Scientific Assessment of Ozone Depletion: 2002"*, Global Ozone Research and Monitoring Project, Report No. 47, published February 2003.
65. M. A. K. Khalil and R. A. Rasmussen, "Atmospheric Chloroform", *Atmos. Environ.*, **33**, 1151 – 1158, 1999.
66. A. Saiz-Lopez and J. M. C. Plane, "Novel iodine chemistry in the marine boundary layer", *Geophys. Res. Lett.*, **31**, L04112, 2004.
67. M. A. K. Khalil and R. A. Rasmussen, "Atmospheric methyl chloride", *Atmos. Environ.*, **33**, 1305 – 1321, 1999.
68. W. C. Keene, M. A. K. Khalil, D. J. Erickson III, A. McCulloch, T. E. Graedel, J. M. Lobert, M. L. Aucott, S. L. Gong, D. B. Harper, G. Kleiman, P. Midgley, R. M. Moore, C. Seuzaret, W. T. Sturges, C. M. Benkovitz, V. Koropalov, L. A. Barrie and Y. F. Li, "Composite global emissions of reactive chlorine from anthropogenic and natural sources: Reactive Chlorine Emissions Inventory", *J. Geophys. Res.*, **104**, 8429 – 8440, 1999.
69. S. A. Yvon and J. H. Butler, "An improved estimate of the oceanic lifetime of atmospheric CH_3Br", *Geophys. Res. Lett.*, **23**, 53 – 56, 1996.
70. M. A. K. Khalil, R. M. Moore, D. B. Harper, J. M. Lobert, D. J. Erikson, V. Koropalov, W. T. Sturges and W. C. Keene, "Natural emissions of chlorine-containing gases: Reactive Chlorine Emissions Inventory", *J. Geophys. Res.*, **104**, 8333 – 8346, 1999.
71. L. J. Carpenter and P. S. Liss, "On temperate sources of bromoform and other reactive organic bromine gases", *J. Geophys. Res.*, **105**, 20539 – 20547, 2000.
72. M. Bilde, T. J. Wallington, C. Ferronato, J. J. Orlando, G. S. Tyndall, E. Estupinan and S. Haberkorn, "Atmospheric Chemistry of CH_2BrCl, $CHBrCl_2$, $CHBr_2Cl$, $CF_3CHBrCl$, and CBr_2Cl_2", *J. Phys. Chem. A*, **102**, 1976 – 1986, 1998.
73. A. Saiz-Lopez, R. W. Saunders, D. M. Joseph, S. H. Ashworth and J. M. C. Plane, "Absolute absorption cross-section and photolysis rate of I_2", *Atmos. Chem. Phys.*, **4**, 1443 – 1450, 2004.
74. P. J. Crutzen, R. Muller, C. Bruhl, and T. Peter, "On the Potential Importance of the Gas Phase Reaction $CH_3O_2 + ClO \rightarrow ClOO + CH_3O$ and the Heterogeneous Reaction $HOCl + HCl \rightarrow H_2O + Cl_2$ in 'Ozone Hole' Chemistry", *Geophys. Res. Lett.*, **19**, 1113 – 1116, 1992.
75. P. O. Wennberg, R. C. Cohen, R. M. Stimpfle, J. P. Koplow, J. G. Anderson, R. J. Salawitch, D. W. Fahey, E. L. Woodbridge, E. R. Keim, R. S. Gao, C. R. Webster, R.

D. May, D. W. Toohey, L. M. Avallone, M. H. Proffitt, M. Loewenstein, J. R. Podolske, K. R. Chan and S. C. Wofsy, "Removal of Stratospheric O_3 by Radicals: *In Situ* Measurements of OH, HO_2, NO, NO_2, ClO, and BrO", *Science*, **266**, 398 – 404, 1994.

76. R. R. Garcia and S. Solomon, "A New Numerical Model of the Middle Atmosphere. 2. Ozone and Related Species", *J. Geophys. Res.*, **99**, 12937 – 12951, 1994.
77. M. R. Schoeberl and D. L. Hartmann, "The Dynamics of the Stratospheric Polar Vortex and its Relation to Springtime Ozone Depletions", *Science*, **251**, 46 – 52, 1991.
78. M. J. Molina, A. J. Colussi, L. T. Molina and F. C. Wang, "Antarctic Stratospheric Chemistry of Chlorine Nitrate, Hydrogen Chloride, and Ice: Release of Active Chlorine", *Science*, **238**, 1253 – 1257, 1987.
79. D. R. Hanson and A. R. Ravishankara, "Reactions of Halogen Species on Ice Surfaces", in *The Tropospheric Chemistry of Ozone in the Polar Regions*, Eds. H. Niki and K. H. Becker, NATO ASI Series, Vol. 17, Springer-Verlag, Berlin, 1993.
80. M. A. Tolbert, M. J. Rossi, R. Malhotra and D. M. Golden, "Reaction of Chlorine Nitrate with Hydrogen Chloride and Water at Antarctic Stratospheric Temperatures", *Science*, **238**, 1258 – 1260, 1987.
81. M. A. Tolbert, M. J. Rossi and D. M. Golden, "Antarctic Ozone Depletion Chemistry: Reactions of N_2O_5 with H_2O and HCl on Ice Surfaces", *Science*, **240**, 1018 – 1021, 1988.
82. D. R. Hanson, A. R. Ravishankara and E. R. Lovejoy, "Reaction of $BrONO_2$ with H_2O on Submicron Sulfuric Acid Aerosol and the Implications for the Lower Stratosphere", *J. Geophys. Res.*, **101**, 9063 – 9069, 1996.
83. M. J. Prather, "More Rapid Polar Ozone Depletion through the Reaction of HOCl with HCl on Polar Stratospheric Clouds", *Nature*, **355**, 534 – 537, 1992.
84. J. P. D. Abbatt, "Heterogeneous Reaction of HOBr with HBr and HCl on Ice Surfaces at 228 K", *Geophys. Res. Lett.*, **21**, 665 – 668, 1994.
85. J. G. Anderson, D. W. Toohey and W. H. Brune, "Free Radicals within the Antarctic Vortex: The Role of CFC's in Antarctic Ozone Loss", *Science*, **251**, 39 – 46, 1991.
86. S. Solomon, "How can we tell if the Montreal Protocol is working?", *Nature*, **427**, 291, 2004.
87. S. Solomon, "The hole truth: What's news (and what's not) about the ozone hole", *Nature*, **427**, 289 – 291, 2004.
88. N. Larsen, B. M. Knudsen, I. S. Mikkelsen, T. S. Jorgensen, and P. Eriksen, "Ozone Depletion in the Arctic Stratosphere in Early 1993", *Geophys. Res. Lett.*, **21**, 1611 – 1614, 1994.
89. R. Muller, P. J. Crutzen, J. Groob, C. Bruhl, J. M. Russell III and A. F. Tuck, "Chlorine Activation and Ozone Depletion in the Arctic Vortex: Observations by the Halogen Occultation Experiment on the Upper Atmospheric Research Satellite", *J. Geophys. Res.*, **101**, 12531 – 12554, 1996.
90. M. R. Schoeberl, L. R. Lait, P. A. Newman and J. E. Rosenfield, "The Structure of the Polar Vortex", *J. Geophys. Res.*, **97**, 7859 – 7882, 1992.
91. G. L. Manney and R. W. Zurek, "Interhemispheric Comparison of the Development of the Stratospheric Polar Vortex during Fall: A 3-Dimensional Perspective for 1991-1992", *Geophys. Res. Lett.*, **20**, 1275 – 1278, 1993.
92. G. L. Manney, M. L. Santee, L. Froidevaux, J. W. Waters and R. W. Zurek, "Polar Vortex Conditions during the 1995 – 96 Arctic Winter: Meteorology and MLS Ozone", *Geophys. Res. Lett.*, **23**, 3202 – 3206, 1996.
93. P. L. Tanaka, S. Oldfield, J. D. Neece, C. B. Mullins and D. T. Allen, "Anthropogenic Sources of Chlorine and Ozone Formation in Urban Atmospheres", *Environ. Sci. Technol.*, **34**, 4470 – 4473, 2000.
94. S. Chang and D. T. Allen, "Atmospheric Chlorine Chemistry in Southeast Texas: Impacts on Ozone Formation and Control", *Environ. Sci. Technol.*, **40**, 251 – 262, 2006.

95. W. C. Keene, J. R. Maben, A. A. P. Pszenny and J. N. Galloway, "Measurement technique for inorganic chlorine gases in the marine boundary layer", *Environ. Sci. Technol.*, **27**, 866 – 874, 1993.
96. C. W. Spicer, E. G. Chapman, B. J. Finlayson-Pitts, R. A. Plasteridge, J. M. Hubbe, J. D. Fast and C. M. Berkowitz, "Unexpectedly high concentrations of molecular chlorine in coastal air", *Nature*, **394**, 353 – 356, 1998.
97. A. Notario, G. Le Bras and A. Mellouki, "Absolute Rate Constants for the Reactions of Cl Atoms with a Series of Esters", *J. Phys. Chem. A.*, **102**, 3112 – 3117, 1998.
98. C. E. Canosa-Mas, E. S. N. Cotter, J. Duffy, K. C. Thompson and R. P. Wayne, "The reactions of atomic chlorine with acrolein, methacrolein and methyl vinyl ketone", *Phys. Chem. Chem. Phys.*, **3**, 3075 – 3084, 2001.
99. W. Wang, M. J. Ezell, A. A. Ezell, G. Soskin and B. J. Finlayson-Pitts, "Rate constants for the reactions of chlorine atoms with a series of unsaturated aldehydes and ketones at 298 K: structure and reactivity", *Phys. Chem. Chem. Phys.*, **4**, 1824 – 1831, 2002.
100. G. Thiault, A. Mellouki and G. Le Bras, "Kinetics of gas phase reactions of OH and Cl with aromatic aldehydes", *Phys. Chem. Chem. Phys.*, **4**, 2194 – 2199, 2002.
101. M. J. Ezell, W. Wang, A. A. Ezell, G. Soskin and B. J. Finlayson-Pitts, "Kinetics of reactions of chlorine atoms with a series of alkenes at 1 atm and 298 K: structure and reactivity", *Phys. Chem. Chem. Phys.*, **4**, 5813 – 5820, 2002.
102. J. Albaladejo, A. Notario, C. A. Cuevas, E. Jimenez, B. Cabanas and E. Martinez, "Gas-phase chemistry of atmospheric Cl atoms: a PLP-RF kinetic study with a series of ketones", *Atmos. Environ.*, **37**, 455 – 463, 2003.
103. C. A. Cuevas, A. Notario, E. Martinez and J. Albaladejo, "A kinetic study of the reaction of Cl with a series of linear and ramified ketones as a function of temperature", *Phys. Chem. Chem. Phys.*, **6**, 2230 – 2236, 2004.
104. C. A. Cuevas, A. Notario, E. Martinez and J. Albaladejo, "Influence of temperature in the kinetics of the gas-phase reactions of a series of acetates with Cl atoms", *Atmos. Environ.*, **39**, 5091 – 5099, 2005.
105. D. J. Lary, "Halogens and the chemistry of the free troposphere", *Atmos. Chem. Phys.*, **5**, 227 – 237, 2005.
106. P. A. Ariya, H. Niki, G. W. Harris, K. G. Anlauf and D. E. Worthy, "Polar sunrise experiment 1995: hydrocarbon measurements and tropospheric Cl and Br-atoms chemistry", *Atmos. Environ.*, **33**, 931 – 938, 1999.
107. E. S. N. Cotter, N. J. Booth, C. E. Canosa-Mas, D. J. Gray, D. E. Shallcross and R. P. Wayne, "Reactions of Cl atoms with CH_3I, C_2H_5I, 1-C_3H_7I, 2-C_3H_7I and CF_3I: kinetics and atmospheric relevance", *Phys. Chem. Chem. Phys.*, **3**, 402 – 408, 2001.
108. S. L. Nickolaisen, R. R. Friedl and S. P. Sander, "Kinetics and Mechanism of the ClO + ClO Reaction: Pressure and Temperature Dependences of the Bimolecular and Termolecular Channels and Thermal Decomposition of Chlorine Peroxide", *J. Phys. Chem.*, **98**, 155 – 169, 1994.
109. L. T. Molina and M. J. Molina, "Production of Cl_2O_2 from the Self-reaction of the ClO Radical", *J. Phys. Chem.*, **91**, 433 – 436, 1987.
110. C. Lee, Y. J. Kim, H. Tanimoto, N. Bobrowski, U. Platt, T. Mori, K. Yamamoto and C. S. Hong, "High ClO and ozone depletion observed in the plume of Sakurajima volcano, Japan", *Geophys. Res. Lett.*, **32**, L21809, 2005.
111. M. Finkbeiner, J. N. Crowley, O. Horie, R. Muller, G. K. Moortgat and P. J. Crutzen, "Reaction between HO_2 and ClO: Product Formation between 210 and 300 K", *J. Phys. Chem. A.*, **99**, 1624 – 16275, 1995.
112. S. P. Sander and R. R. Friedl, "Kinetics and product studies of the bromine oxide (BrO) + chlorine oxide (ClO) reaction: Implications for Antarctic chemistry", *Geophys. Res. Lett.*, **15**, 887 – 890, 1988.
113. G. Poulet, I. T. Lancar, G. Laverdet and G. Le Bras, "Kinetics and products of the bromine monoxide + chlorine monoxide reaction", *J. Phys. Chem.*, **94**, 278 – 284, 1990.

114. A. A. Turnipseed, M. K. Gilles, J. B. Burkholder and A. R. Ravishankara, "Kinetics of the IO Radical. 1. Reaction of IO with ClO", *J. Phys. Chem. A.*, **101**, 5517 – 5525, 1997.
115. Y. Bedjanian, G. Le Bras and G. Poulet, "Kinetics and Mechanism of the IO + ClO Reaction", *J. Phys. Chem. A*, **101**, 4088 – 4096, 1997.
116. W. G. Lawrence, K. C. Clemitshaw and V. A. Apkarian, "On the Relevance of OClO Photodissociation to the Destruction of Stratospheric Ozone", *J. Geophys. Res.*, **95**, 18591 – 18595, 1990.
117. S. Enami, "Formation of Iodine Monoxide Radical from the Reaction of CH_2I with O_2", *J. Phys. Chem. A.*, **108**, 6347-6350, 2004.
118. G. McFiggans, J. M. C. Plane, B. J. Allan and L. J. Carpenter, "A modeling study of iodine chemistry in the marine boundary layer", *J. Geophys. Res.*, **105**, 14371 – 14385, 2000.
119. S. P. Sander, R. R. Friedl, A. R. Ravishankara, D. M. Golden, C. E. Kolb, M. J. Kurylo, R. E. Huie, V. L. Orkin, M. J. Molina, G. K. Moortgat and B.J. Finlayson-Pitts, *"Chemical Kinetics and Photochemical Data for Use in Atmospheric Studies: Evaluation Number 14"*, JPL Publication 02-25, February 1, 2003.
120. J. Zingler and U. Platt, "Iodine oxide in the Dead Sea Valley: Evidence for inorganic sources of boundary layer IO", *J. Geophys. Res.*, **110**, D07307, 2005.
121. X. Yang, R. A. Cox, N. J. Warwick, J. A. Pyle, G. D. Carver, F. M. O'Connor and N. H. Savage, "Tropospheric bromine chemistry and its impacts on ozone: A model study", *J. Geophys. Res.*, **110**, D23311, 2005.
122. J. Stutz, K. Hebestreit, B. Alicke and U. Platt, "Chemistry of Halogen Oxides in the Troposphere: Comparison of Model Calculations with Recent Field Data", *J. Atmos. Chem.*, **34**, 65 – 85, 1999
123. W. J. Bloss, J. D. Lee, G. P. Johnson, R. Sommariva, D. E. Heard, A. Saiz-Lopez, J. M. C. Plane, G. McFiggans, H. Coe, M. Flynn, P. Williams, A. R. Rickard and Z. L. Fleming, "Impact of halogen monoxide chemistry upon boundary layer OH and HO_2 concentrations at a coastal site", *Geophys. Res. Lett.*, **32**, L06814, 2005.
124. R. Sommariva, W. J. Bloss, N. Brough, N. Carslaw, M. Flynn, A.-L. Haggerstone, D. E. Heard, J. R. Hopkins, J. D. Lee, A. C. Lewis, G. McFiggans, P. S. Monks, S. A. Penkett, M. J. Pilling, J. M. C. Plane, K. A. Read, A. Saiz-Lopez, A. R. Rickard and P. I. Williams, "OH and HO_2 chemistry during NAMBLEX: roles of oxygenates, halogen oxides and heterogeneous uptake", *Atmos. Chem. Phys.*, **6**, 1135 – 1153, 2006.
125. C. S. E. Bale, C. E. Canosa-Mas, D. E. Shallcross and R. P. Wayne, "A discharge-flow study of the kinetics of the reactions of IO with CH_3O_2 and CF_3O_2, *Phys. Chem. Chem. Phys.*, **7**, 2164 – 2172, 2005.
126. S. Enami, T. Yamanaka, S. Hashimoto, M. Kawasaki, Y. Nakano and T. Ishiwata, "Kinetic Study of IO Radical with RO_2 (R = CH_3, C_2H_5, and CF_3) Using Cavity Ring-Down Spectroscopy", *J. Phys. Chem. A.*, **110**, 9861 – 9866, 2006.
127. T. J. Dillon, M. E. Tucceri and J. N. Crowley, "Laser Induced Fluorescence Studies of Iodine Oxide Chemistry, Part 2. The Reactions of IO with CH_3O_2, CF_3O_2 and O_3", Submitted to *Phys. Chem. Chem. Phys.*, 2006.
128. A. Saiz-Lopez, J. M. C. Plane and J. A. Shhillito, "Bromine oxide in the mid-latitude marine boundary layer", *Geophys. Res. Lett.*, **31**, L03111, 2004.
129. A. Vipond, C. E. Canosa-Mas, M. L. Flugge, D. J. Gray, D. E. Shallcross, D. Shah and R. P. Wayne, "A discharge-flow study of the self-reaction of IO", *Phys. Chem. Chem. Phys.*, **4**, 3648 – 3658, 2002.
130. M. H. Harwood, D. M. Rowley, R. A. Cox and R. L. Jones, Kinetics and Mechanism of he BrO Self-Reaction: Temperature- and Pressure-Dependent Studies", *J. Phys. Chem. A.*, **102**, 1790 – 1802, 1998.
131. Y. Bedjanian, G. Le Bras and G. Poulet, "Kinetics and Mechanism of the IO + BrO Reaction", *J. Phys. Chem. A.*, **102**, 10501 – 10511, 1998.

132. D. M. Rowley, W. J. Bloss, R. A. Cox and R. L. Jones, "Kinetics and Products of the IO + BrO Reaction", *J. Phys. Chem. A.*, **105**, 7855 – 7864, 2001.
133. W. J. Bloss, D. M. Rowley, R. A. Cox and R. L. Jones, "Kinetics and Products of the IO Self-Reaction", *J. Phys. Chem. A.*, **105**, 7840 – 7854, 2001.
134. D. M. Joseph, S. H. Ashworth and J. M. C. Plane, "The absorption cross-section and photochemistry of OIO", *J. Photochem. Photobiol. A.*, **176**, 68 – 77, 2005.
135. T. Ingham, M. Cameron and J. N. Crowley, "Photodissociation of IO (355 nm) and OIO (532 nm): Quantum Yields for O (^3P) and I (^2P_J) Production", *J. Phys. Chem. A.*, **104**, 8001 – 8010, 2000.
136. M. E. Tucceri, D. Holscher, A. Rodriguez, T. J. Dillon and J. N. Crowley, "Absorption cross section and photolysis of OIO", *Phys. Chem. Chem. Phys.*, **8**, 834 – 846, 2006.
137. J. M. C. Plane, D. M. Joseph, B. J. Allan, S. H. Ashworth and J. S. Francisco, "An Experimental and Theoretical Study of the Reactions OIO + NO and OIO + OH", *J. Phys. Chem. A.*, **110**, 93 – 100, 2006.
138. S. Pechtl, E. R. Lovejoy, J. B. Burkholder and R. von Glasow, "Modeling the possible role of iodine oxides in atmospheric new particle formation", *Atmos. Chem. Phys.*, **6**, 505 – 523, 2006.
139. R. W. Saunders and J. M. C. Plane, "Formation Pathways and Composition of Iodine Oxide Ultra-Fine Particles", *Environ. Chem.*, **2**, 299 – 303, 2005.
140. A. Saiz-Lopez, J. M. C. Plane, G. McFiggans, P. I. Williams, S. M. Ball, M. Bitter, R. L. Jones, C. Hongwei and T. Hoffman, "Modelling molecular iodine emissions in a coastal marine environment: the link to new particle formation", *Atmos. Chem. Phys.*, **6**, 883 – 895, 2006.
141. B. J. Allan, J. M. C. Plane and G. McFiggans, "Observations of OIO in the remote marine boundary layer", *Geophys. Res. Lett.*, **28**, 1945 – 1948, 2001.
142. A. Saiz-Lopez, J. A. Shillito, H. Coe and J. M. C. Plane, "Measurements and modelling of I_2, IO, OIO, BrO and NO_3 in the mid-latitude marine boundary layer" *Atmos. Chem. Phys.*, **6**, 1513 – 1528, 2006.
143. R. M. Chambers, A. C. Heard and R. P. Wayne, "Inorganic gas-phase reactions of the nitrate radical – I_2 + NO_3 and I + NO_3", *J. Phys. Chem.*, **96**, 3321 – 3331, 1992.
144. P. Spietz, J. Carlos Gomez Martin and J. P. Burrows, "Spectroscopic studies of the I_2/O_3 photochemistry Part 2. Improved spectra of iodine oxides and analysis of the IO absorption spectrum", *J. Photochem. Photobiol. A.*, **176**, 50 – 67, 2005.
145. L. A. Barrie, J. W. Bottenheim, R. C. Schnell, P. J. Crutzen and R. A. Rasmussen, "Ozone destruction and photochemical reactions at polar sunrise in the lower Arctic atmosphere", *Nature*, **334**, 138 – 141, 1988.
146. M. Hausmann and U. Platt, "Spectroscopic measurements of bromine oxide and ozone in the high Arctic during Polar Sunrise Experiment 1992", *J. Geophys. Res.*, **99**, 25399 – 25414, 1994.
147. J. G. Calvert and S. E. Lindberg, "Potential influence of iodine-containing compounds on the chemistry of the troposphere in the polar spring. I. Ozone depletion", *Atmos. Environ.*, **38**, 5087 – 5104, 2004.
148. A. Saiz-Lopez, A. S. Mahajan, R. A. Salmon, S. J. Bauguitte, A. E. Jones, H. K. Roscoe and J. M. C. Plane, "Boundary layer halogens and ozone depletion in Antarctica", submitted to *Nature*, 2006.
149. G. Honninger, N. Bobrowski, E. R. Palengue, R. Torrez and U. Platt, "Reactive bromine and sulphur emissions at Salar de Uyuni, Bolivia", *Geophys. Res. Lett.*, **31**, L04101, 2004.
150. P. Wennberg, "Bromine explosion", *Nature*, **397**, 299 – 300, 1999.
151. R. von Glasow, R. von Kuhlmann, M G. Lawrence, U. Platt and P. J. Crutzen, "Impact of reactive bromine chemistry in the troposphere", *Atmos. Chem. Phys.*, **4**, 2481 – 2497, 2004.
152. U. Platt and G. Honninger, "The role of halogen species in the troposphere", *Chemosphere*, **52**, 325 – 338, 2003.

153. M. O. Andreae, "Ocean-atmosphere interactions in the global biogeochemical cycle", Mar. Chem., **30**, 1 – 29, 1990.
154. I. Barnes, J. Hjorth and N. Mihalopoulos, "Diemtly Sulfide and Dimethyl Sulfoxide and Their Oxidation in the Atmosphere", *Chem. Rev.*, **106**, 940 – 975, 2006.
155. R. J. Charlson, J. E. Lovelock, M. O.Andreae and S. G. Warren, "Oceanic phytoplankton, atmospheric sulphur, cloud albedo and climate", *Nature*, **326**, 655 – 661, 1987.
156. O. J. Nielsen, H. W. Sidebottom, L. Nelson, O. Rattigan, J. J. Treacy and D. J. O'Farrell, "Rate constants for the reactions of OH radicals and chlorine atoms with diethyl sulphide, dipropyl sulphide, and dibutyl sulphide", Int. J. Chem. Kinet., **22**, 603 – 612, 1990.
157. T. Ingham, D. Bauer, R. Sander, P. J. Crutzen and J. N. Crowley, "Kinetics and products of the reactions BrO + DMS and Br + DMS at 298 K", *J. Phys. Chem. A.*, **103**, 7199 – 7209, 1999.
158. Y. Diaz-de-Mera, A. Aranda, D. Rodriguez, R. Lopez, B. Cabaoas and E. Martinez, "Gas-Phase Reactions of Chlorine Atoms and ClO Radicals with Dimethyl Sulfide. Rate Coefficients and Temperature Dependencies", *J. Phys. Chem. A.*, **106**, 8627 – 8633, 2002.
159. T. Maurer, I. Barnes and K. H. Becker, "FT-IR kinetic and product study of the Br-initiated oxidation of dimethyl sulfide", *Int. J. Chem. Kinet.*, **31**, 883 – 893, 1999.
160. E. P. Daykin and P. H. Wine, "Rate of reaction of IO radicals with dimethylsulfide", *J. Geophys. Res.*, **95**, 18547 – 18553, 1990.
161. Y. Nakano, S. Enami, S. Nakamichi, S. Aloisio, S. Hashimoto and M. Kawasaki, "Temperature and Pressure Dependence Study of the Reaction of IO Radicals with Dimethyl Sulfide by Cavity Ring-Down Laser Spectroscopy", *J. Phys. Chem. A*, **107**, 6381 – 6387, 2003.
162. H. Sayin and M. L. McKee, "Computational Study of the Reactions between XO (X = Cl, Br, I) and Dimethyl Sulfide", *J. Phys. Chem. A.*, **108**, 7613 – 7620, 2004.
163. T. Gravestock, M. A. Blitz and D. E. Heard, "Kinetics study of the reaction of iodine monoxide radicals with dimethyl sulphide", *Phys. Chem. Chem. Phys.*, **7**, 2173 – 2181, 2005.
164. T. J. Dillon, R. Karunandan and J. N. Crowley, "The reaction of IO with CH_3SCH_3: products and temperature dependent rate coefficients by laser induced fluorescence", *Phys. Chem. Chem. Phys.*, **8**, 847 – 855, 2006.
165. L. D. Hylander and M. E. Goodsite, "Environmental costs of mercury pollution", *Sci. Tot. Env.*, **368**, 352 – 370, 2006.
166. W. H. Schroeder, K. G. Anlauf, L. A. Barrie, J. Y. Lu, A. Steffen, D. R. Schneeberger and T. Berg, "Arctic springtime depletion of mercury", *Nature*, **394**, 331 – 332, 1998.
167. R. Ebinghaus, H. K. Koch, C. Temme, J. W. Einax, A. G. Lowe, A. Richter, J. P. Burrows and W. H. Scroeder, "Antarctic Springtime Depletion of Atmospheric Mercury", *Environ. Sci. Technol.*, **36**, 1238 – 1244, 2002.
168. P. A. Ariya, A. Khalizov and A. Gidas, "Reactions of Gaseous Mercury with Atomic and Molecular Halogens: Kinetics, Product Studies, and Atmospheric Implications" *J. Phys. Chem. A.*, **106**, 7310 – 7320, 2002.
169. J. G. Calvert and S. E. Lindberg, "The potential influence of iodine-containing compounds on the chemistry of the troposphere in the polar spring. II. Mercury depletion", *Atmos. Environ.*; **38**, 5105 – 5116, 2004.
170. S. E. Lindberg, S. Brooks, C. Lin, K. Scott, T. Meyers, L. Chambers, M. Landis and R. Stevens, "Formation of Reactive Gaseous Mercury in the Arctic: Evidence of Oxidation of Hg0 to Gas-Phase Hg-II Compounds After Arctic Sunrise", *Water, Air, Soil, Pollut.*, **1**, 295 – 302, 2001.
171. M. E. Goodsite, J. M. C. Plane and H. Skov, "A theoretical study of the oxidation of Hg^0 to $HgBr_2$ in the troposphere", *Environ. Sci. Technol.*, **38**, 1772 – 1776, 2004.

172. R. Vogt, P. J. Crutzen and R. Sander, "A mechanism for halogen release from sea-salt aerosol in the remote marine boundary layer", *Nature*, **383**, 327 – 330, 1996.
173. R. Sander, Y. Rudich, R. von Glasow and P. J. Crutzen, "The role of $BrNO_3$ in marine tropospheric chemistry: A model study", *Geophys. Res. Lett.*, **26**, 2857 – 2860, 1999.
174. S. Fickert, J. W. Adams and J. N. Crowley, "Activation of Br_2 and BrCl via uptake of HOBr onto aqueous salt solutions", *J. Geophys. Res.*, **104**, 23719 – 23727, 1999.
175. K. Hara, K. Osada, K. Matsunaga, Y. Iwasaka and T. Shibata, "Atmospheric inorganic chlorine and bromine species in Arctic boundary layer of the winter/spring", *J. Geophys. Res.*, **107** (D 18), AAC4/1 – AAC4/15, 2002.
176. S. Fan and D. J. Jacob, "Surface ozone depletion in Arctic spring sustained by bromine reactions on aerosols", *Nature*, **359**, 522 – 524, 1992.
177. T. Tang and J. C. McConnell, "Autocatalytic release of bromine from Arctic snow pack during polar sunrise", *Geophys. Res. Lett.*, **23**, 2633 – 2636, 1996.
178. P. S. Monks, "Gas-phase radical chemistry in the troposphere", *Chem. Soc. Rev.*, **34**, 376 – 395, 2005.
179. U. Frieb, J. Hollwedel, G. Konig-Langlo, T. Wagner and U. Platt, "Dynamics and chemistry of tropospheric bromine explosion events in the Antarctic coastal region", *J. Geophys. Res.*, **109**, D06305, 2004.
180. A. E. Jones, P. S. Anderson, E. W. Wolff, J. Turner, A. M. Rankin and S. R. Colwell, "A role for newly forming sea ice in springtime polar tropospheric ozone loss? Observational evidence from Halley station, Antarctica", *J. Geophys. Res.*, **111**, D08306, 2006.
181. L. E. Kalnajs and L. M. Avallone, "Frost flower influence on springtime boundary0layer ozone depletion events and atmospheric bromine levels", *Geophys. Res. Lett.*, **33**, L10810, 2006.
182. H. Herrmann, Z. Majdik, B. Revens and D. Weise, "Halogen production from aqueous tropospheric particles", *Chemosphere*, **52**, 485 – 502, 2003.
183. A. R. Baker, "Marine Aerosol Iodine Chemistry: The Importance of Soluble Organic Iodine", *Environ. Chem.*, **2**, 295 – 298, 2005.
184. A. R. Baker, "Inorganic iodine speciation in tropical Atlantic aerosol", *Geophys. Res. Lett.*, **31**, L23S02, 2004.
185. R. Vogt, R. Sander, R. von Glasow and P. J. Crutzen, "Iodine Chemistry and its Role in Halogen Activation and Ozone Loss in the Marine Boundary Layer: A Model Study", *J. Atmos. Chem.*, **32**, 375 – 395, 1999.
186. C. D. O'Dowd, K. Haemeri, J. M. Maekelae, L. Pirjola, M. Kulmala, S. G. Jennings, H. Berresheim, H. Hansson, G. de Leeuw, G. J. Kunz, A. G. Allen, C. N. Hewitt, A. Jackson, Y. Viisanen and T. Hoffmann, "A dedicated study of new particle formation and fate in the coastal environment (PARFORCE): overview of objectives and achievements", *J. Geophys. Res.*, **107** (D19), PAR1/1 – PAR1/16, 2002.
187. B. Alicke, K. Hebestreit, J. Stutz and U. Platt, "Iodine oxide in the marine boundary layer", *Nature*, **397**, 572 – 573, 1999.
188. T. Hoffmann, C. D. O'Dowd and J. H. Seinfeld, "Iodine oxide homogeneous nucleation: An explanation for coastal new particle production", *Geophys. Res. Lett.*, **28**, 1949 – 1952, 2001.
189. J. L. Jimenez, R. Bahreini, D. R. Cocker III, H. Zhuang, V. Varutbangkul, R. C. Flagan, J. H. Seinfeld, C. D. O'Dowd and T. Hoffmann, "New particle formation from photooxidation of diiodomethane", *J. Geophys. Res.*, **108** (D23), AAC5/1 – AAC5/25, 2003.
190. J. B. Burkholder, J. Curtius, A. R. Ravishankara and E. R. Lovejoy, "Laboratory studies of the homogeneous nucleation of iodine oxides", *Atmos. Chem. Phys.*, **4**, 19 – 34, 2004.
191. K. Sellegri, Y. J. Yoon, S. G. Jennings, C. D. O'Dowd, L. Pirjola, S. Cautenet, H. Chen and T. Hoffmann, "Quantification of coastal new ultra-fine particles formation

from in situ and chamber measurements during the BIOFLUX campaign", *Environ. Chem.*, **2**, 260 – 270, 2005.
192. L. Pirjola, C. D. O'Dowd, Y. J. Yoon and K. Sellegri, "Modelling Iodine Particle Formation and Growth from Seaweed in a Chamber", *Environ. Chem.*, **2**, 271 – 281, 2005.
193. C. D. O'Dowd, "Marine aerosol formation from biogenic iodine emissions", *Nature*, **417**, 632 – 636, 2002.
194. G. McFiggans, "Marine aerosols and iodine emissions", *Nature*, **433**, E13 – E14, 2005.
195. J. M. C. Plane and N. Smith, "Atmospheric monitoring by differential optical absorption spectroscopy", in "*Advances in Spectroscopy*", *Volume 24: Spectroscopy in Environmental Science*, (Eds. R. J. H. Clark and R. E. Hester), John Wiley and Sons Ltd., Chichester, 1995, 223 – 262.
196. B. J. Allen, G. McFiggans and J. M. C. Plane, "Observations of iodine monoxide in the remote marine boundary layer", *J. Geophys. Res.*, **105**, 14363 – 14369, 2000.
197. F. Wittrock, R. Muller, A. Richter, H. Bovensmann and J. P. Burrows, "Measurements of Iodine monoxide (IO) above Spitsbergen", *Geophys. Res. Lett.*, **27**, 1471 – 1474, 2000.
198. P. O. Wennberg, J. W. Brault, T. F. Hanisco, R. J. Salawitch and G. H. Mount, "The atmospheric column abundance of IO: Implications for stratospheric ozone", *J. Geophys. Res.*, **102**, 8887 – 8898, 1997.
199. I. Pundt, J. Pommereau, C. Phillips and E. Lateltin, "Upper Limit of Iodine Oxide in the Lower Stratosphere", *J. Atmos. Chem.*, **30**, 173 – 185, 1998.
200. G. Berthet, J. B. Renard, M. Chartier, M. Pirre and C. Robert, "Analysis of OBrO, IO, and OIO absorption signature in UV-visible spectra measured at night and at sunrise by stratospheric balloon-borne instruments", *J. Geophys. Res.*, **108**, D5, 4161, 2003.
201. H. Bosch, C. Camy-Peyret, M. P. Chipperfield, R. Fitzenberger, H. Harder, U. Platt and K. Pfeilsticker, "Upper limits of stratospheric IO and OIO inferred from centre-to-limb-darkening-corrected balloon-borne solar occultation visible spectra: Implications for total gaseous iodine and stratospheric ozone", *J. Geophys. Res.*, **108**, D5, 4455, 2003.
202. U. Frieb, T. Wagner, I. Pundt, K. Pfeilsticker and U. Platt, "Spectroscopic Measurements of Tropospheric Iodine Oxide at Neumayer Station, Antarctica", *Geophys. Res. Lett.*, **28**, 1941 – 1944, 2001.
203. G. Hönninger, *PhD Thesis*, 2002. As cited in reference 48.
204. O. Sebastián, *PhD Thesis*, 2004. As cited in reference 48.
205. K. Hebestreit, *PhD Thesis*, 2001. As cited in reference 48.
206. World Meteorological Organisation (WMO), *Executive Summary*, "*Scientific Assessment of Ozone Depletion: 2006*", 18th August 2006.

Chapter Two: Experimental Procedures for Determining the Physico-Chemical Properties of Atmospheric Species

2.1 Introduction

This chapter will provide an outline of the experimental techniques employed in this thesis for the determination of physico-chemical properties of atmospherically relevant species. The work reported in this study specifically focuses on the spectroscopy and reaction kinetics of gas-phase systems. Spectroscopy is a generic term for the study of spectra: "a display of different frequencies over a certain range"[1]. In the context of this study, spectroscopy refers to the way in which specific chemical species interact with electromagnetic radiation in the ultra-violet (UV) and visible regions (*i.e.* light). Every molecule reacts with light in a unique way as a result of its physical and chemical structure: the mass and number of electrons associated with the individual components (atoms) of the molecule; and the nature of the chemical bonds. The spectrum of a molecule can therefore be regarded as its "fingerprint", which can be exploited by experimental methods to gain information of atmospheric relevance. For example, knowing the precise spectroscopic properties of a molecule may allow the detection, and determination of the absolute concentration, of that species in the atmosphere. From this information we can assess the atmospheric importance of such a species and test our current understanding of the complex workings of the chemical atmosphere.

Reaction kinetics is "the study of the rates at which chemical reactions proceed, and the influence of such factors as temperature, pressure and concentrations of reactants upon the rates of reaction"[1]. Knowing the reaction kinetics of a chemical reaction is paramount in order to assess its potential influence in the atmosphere. Studying the reaction kinetics of potentially important reactions in the laboratory can be achieved by following the temporal profile of one, or more, of the chemical species involved, in a simplified system designed to simulate the physical properties of the atmosphere.

2.2 Reaction Kinetics of Gas-Phase Systems

This section will briefly discuss two important classes of gas-phase reactions – bimolecular and association (also known as termolecular) reactions – and how their reaction kinetics can be determined in the laboratory.

A bimolecular reaction involves the interaction of two species that leads to an overall chemical change of the system, such as the reaction between hydroxyl radicals and methane

$$OH + CH_4 \rightarrow H_2O + CH_3 \qquad \text{(R2-1)}$$

By definition, a bimolecular reaction is independent of pressure and proceeds *via* the formation of a short-lived reactive intermediate (transition state) that undergoes rearrangement to reaction products. A bimolecular reaction can proceed solely to one set of reaction products or yield a number of product channels depending on the nature of the transition state and the thermodynamic accessibility of the possible reaction products. Bimolecular reactions are usually temperature dependent, and most commonly display a positive dependence on temperature (their rate increases with increasing temperature). The temperature dependence of a bimolecular reaction is commonly expressed by an empirical relationship given by the Arrhenius equation

$$k(T) = Ae^{(-E_a/RT)} \qquad \text{E. 2.2-1}$$

where: k is the bimolecular rate coefficient at temperature, T; A is known as the pre-exponential factor; E_a is the activation energy; and R is the molar gas constant (R = 8.314 J $K^{-1}mol^{-1}$) and allows the evaluation of the average translational energy (or kinetic energy) of a gas at temperature, T.

If every collision between two ideal gas molecules resulted in reaction then the theoretical gas-kinetic rate coefficient is given by the product of the collision cross-section, σ and the relative mean speed of the gas molecules, $\bar{c}_{rel}$. If we suppose that N_2 and O_2 undergo reactive collisions, at 300 K, the gas-kinetic rate coefficient can be calculated to be ~ 2.7×10^{-10} $cm^3molecule^{-1}s^{-1}$ (σ = 0.42 nm^2, $\bar{c}_{rel}$ = 650 ms^{-1}). In reality, however, bimolecular reactions do not proceed at the gas-kinetic limit. This is because most rates of reaction depend on the relative orientation of colliding species and hence the probability (or loss of entropy) of forming a reactive transition state. Further, not all collisions will occur with sufficient energy to overcome the energetic barrier (the activation energy) that may be associated with the initial rearrangement of electrons in a reactant molecule, which is required for reaction. In the Arrhenius equation therefore, the pre-exponential factor, A, can be regarded as the limit of the bimolecular rate coefficient for a particular reaction (*i.e.* the upper limit if the reaction has a positive temperature dependence, or the lower limit for the converse), and the exponential term, $\exp(-E_a/RT)$, can be regarded as the fraction of molecules which possess sufficient energy to undergo reactive collisions. Fig. 2.2-1 displays the potential energy of a chemical system for a typical bimolecular reaction.

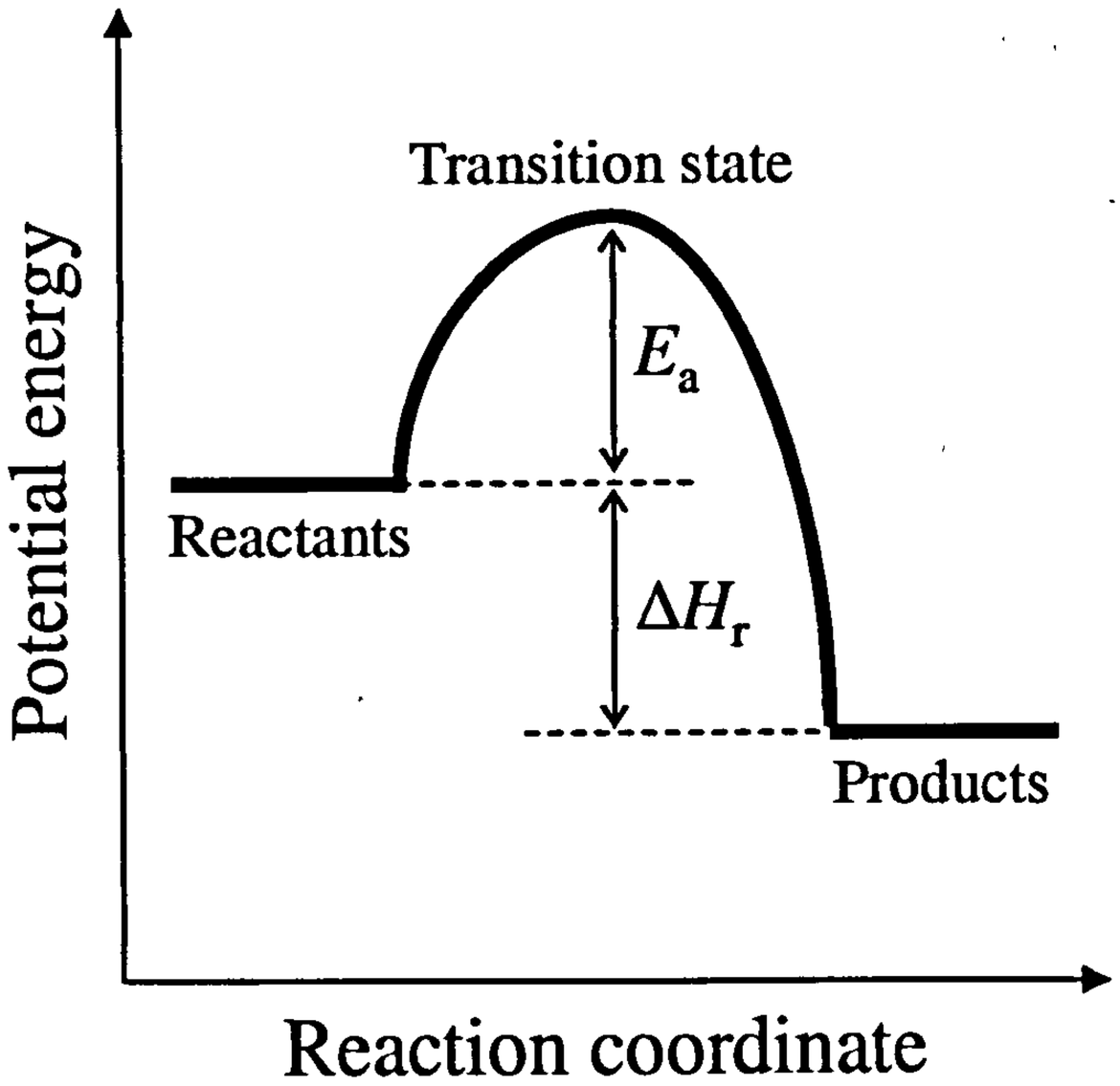

Fig. 2.2-1 – Potential energy diagram for a chemical system moving from reactants to products. The activation energy, E_a, is the difference in energy between reactants and transition state. ΔH_r is the enthalpy of reaction: the difference in energy between products and reactants.

The definition of a bimolecular reaction is somewhat open to personal interpretation. For, example, the reaction of OH with acetone (CH_3COCH_3) proceeds *via* the formation of a weakly bound intermediate involving hydrogen bonding, but as this intermediate does not contribute to the overall bimolecular rate coefficient, the reaction can still be described as a bimolecular process[2]. This is even true when a reaction intermediate does contribute to the overall bimolecular rate coefficient, such as for the reaction of OH with methanethiol (CH_3SH)[2]. Examples of bimolecular reactions that may proceed *via* weakly bound intermediates, and are relevant to this thesis, are the IO self-reaction[3,4]

$IO + IO$	$\rightarrow$	$OIO + I$	(30 – 46 %)
	$\rightarrow$	I_2O_2	(42 – 55 %)
	$\rightarrow$	$2\,I + O_2$	(7 – 15 %)
	$\rightarrow$	$I_2 + O_2$	(0 – 5 %)

and the reaction of IO with dimethylsulfide (DMS)[5,6]

$IO + DMS$	$\rightarrow$	$DMSO + I$	(100 %)

If the concentration of reactants is equal, or comparable, in a bimolecular reaction then the reaction kinetics will obey second-order kinetics: the rate of reaction will depend on the product of the concentration of reactants. For example, let us consider the IO self-reaction. The rate of removal of IO is given by

$$\frac{d[IO]}{dt} = -2k[IO]^2 \qquad \text{E. 2.2-2}$$

where, k is a constant of proportionality, *i.e.* the bimolecular rate coefficient. If we state that the concentration of IO at the initiation of reaction is $[IO]_0$, and $[IO]_t$ at a later time, t, we can rearrange and integrate E. 2.2-2

$$-\frac{d[IO]}{[IO]^2} = 2kdt$$

$$-\int_{[IO]_0}^{[IO]_t} d\frac{[IO]}{[IO]^2} = 2k\int_0^t dt$$

and as the integral of $1/x^2$ is $-1/x$ we obtain E. 2.2-3

$$\frac{1}{[IO]_t} - \frac{1}{[IO]_0} = 2kt \qquad \text{E. 2.2-3}$$

Thus, a plot of $1/[IO]_t$ against time should yield a straight line with slope, $2k$, and intercept, $1/[IO]_0$. Note, therefore, that in order to obtain the rate coefficient of a second-order reaction it is necessary to know the absolute concentration of reactants as a function of reaction time.

Now let us suppose that we are monitoring the decay of IO in the presence of dimethylsulfide (DMS). The rate of IO removal is given by E. 2.2-4

$$\frac{d[IO]}{dt} = -k[IO][DMS] \qquad \text{E. 2.2-4}$$

Again, the reaction is second order. However, if we arrange the reaction conditions such that the concentration of DMS is in great excess to that of IO (pseudo-first-order reaction conditions), [DMS] effectively becomes a constant and we can rewrite E. 2.2-4 as

$$\frac{d[IO]}{dt} = -k'[IO] \qquad \text{E. 2.2-5}$$

where,

$$k' = k[DMS] \qquad \text{E. 2.2-6}$$

Rearrangement and integration of E. 2.2-5 for the reaction limits yields E. 2.2-7

$$[IO]_t = [IO]_0 e^{(-k' \cdot t)} \qquad \text{E. 2.2-7}$$

Thus the IO decay will be observed to follow exponential behaviour. This is a useful result as the pseudo-first-order rate coefficient, *k'*, can be extracted by fitting the temporal behaviour of IO to an exponential function, in which the units of concentration are irrelevant as long as we have some experimental signal which is directly proportional to [IO]. Hence, to determine the rate coefficient, knowledge of the absolute concentration of IO is not required, increasing the range of experimental techniques that can be used to investigate the reaction kinetics. If the pseudo-first-order rate coefficient, *k'*, is determined as a function of [DMS] then the bimolecular rate coefficient, *k*, can be determined from the gradient of a plot of *k'* against [DMS] (see E. 2.2-6). The rate coefficient of any bimolecular reaction can be determined by this procedure.

To determine the Arrhenius parameters of a bimolecular reaction, A and E_a, the bimolecular rate coefficient is measured as a function of temperature. A plot of $\ln(k)$ against the reciprocal temperature thus yields a straight line with slope, $-E_a/R$ and intercept, $\ln(A)$ (see E. 2.2-1).

An association, or termolecular reaction, is a third-order process whose rate depends upon the concentration of three species. An example of an association reaction is that of IO with NO_2[7,8].

$$IO + NO_2 + M \rightarrow IONO_2 + M \qquad \text{(R35, X = I)}$$

Initially the reaction proceeds *via* a bimolecular encounter of the two reactant molecules resulting in the formation of an energetically excited reaction intermediate (also known as an association complex or adduct), $IONO_2$*. The excited association complex can have one of three fates: i) unimolecular decomposition back to reactants; ii) unimolecular decomposition to reaction products, or; iii) pressure stabilisation by collisional encounters with a third body, M. The rate of reaction is therefore dependent on pressure, [M], and also the nature of M, as different third bodies have different efficiencies of collisional stabilisation due to their internal degrees of freedom that can except excess energy from the excited adduct. The complexity of

the adduct will also affect the pressure dependence of the association reaction as large association complexes will have a high density of states, and more modes of internal motion, in which excess energy from the reaction can be dissipated. The yield of the various products from an association reaction will often display a pressure dependence, as different product channels become more accessible or favourable. Association reactions most commonly have a negative temperature dependence, as the increased thermal energy at higher temperatures favours dissociation of the association complex, and results in less efficient collisional stabilisation. Fig. 2.2-2 displays a typical potential energy surface for an association reaction.

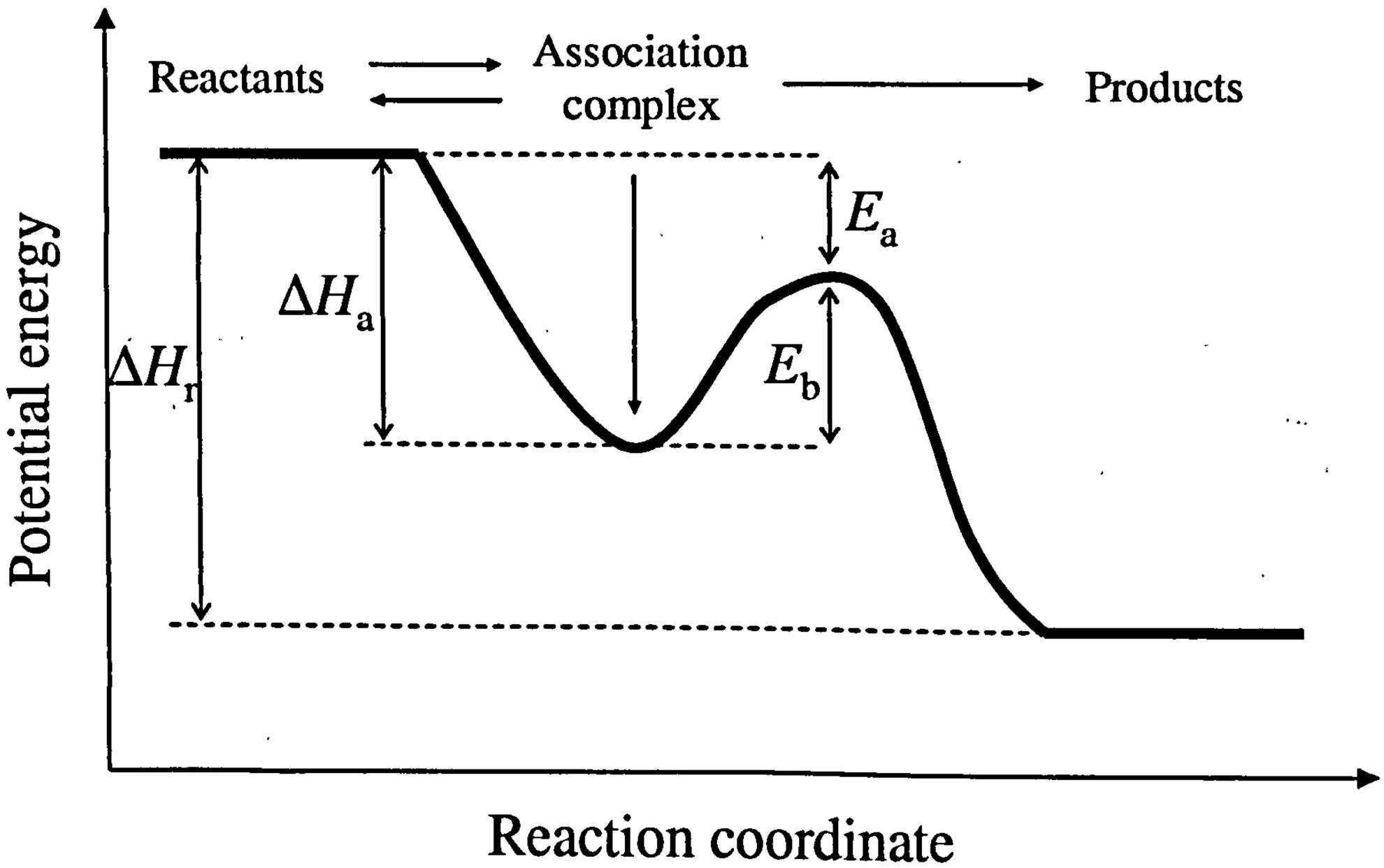

Fig. 2.2-2 – Typical potential energy profile for an association reaction in moving from reactants to association complex to products. The enthalpy of association reaction is given by ΔH_a, and the binding energy of the adduct by, E_b. Note that the reaction has a negative activation energy, E_a.

The pressure dependence of an association reaction can be investigated by determining the effective bimolecular rate coefficient as a function of pressure. The bimolecular rate coefficient at any given pressure is determined as previously described and for a specific third body and temperature. Fig. 2.2-3 displays how the effective bimolecular rate coefficient of an association reaction may typically vary with pressure of the third body.

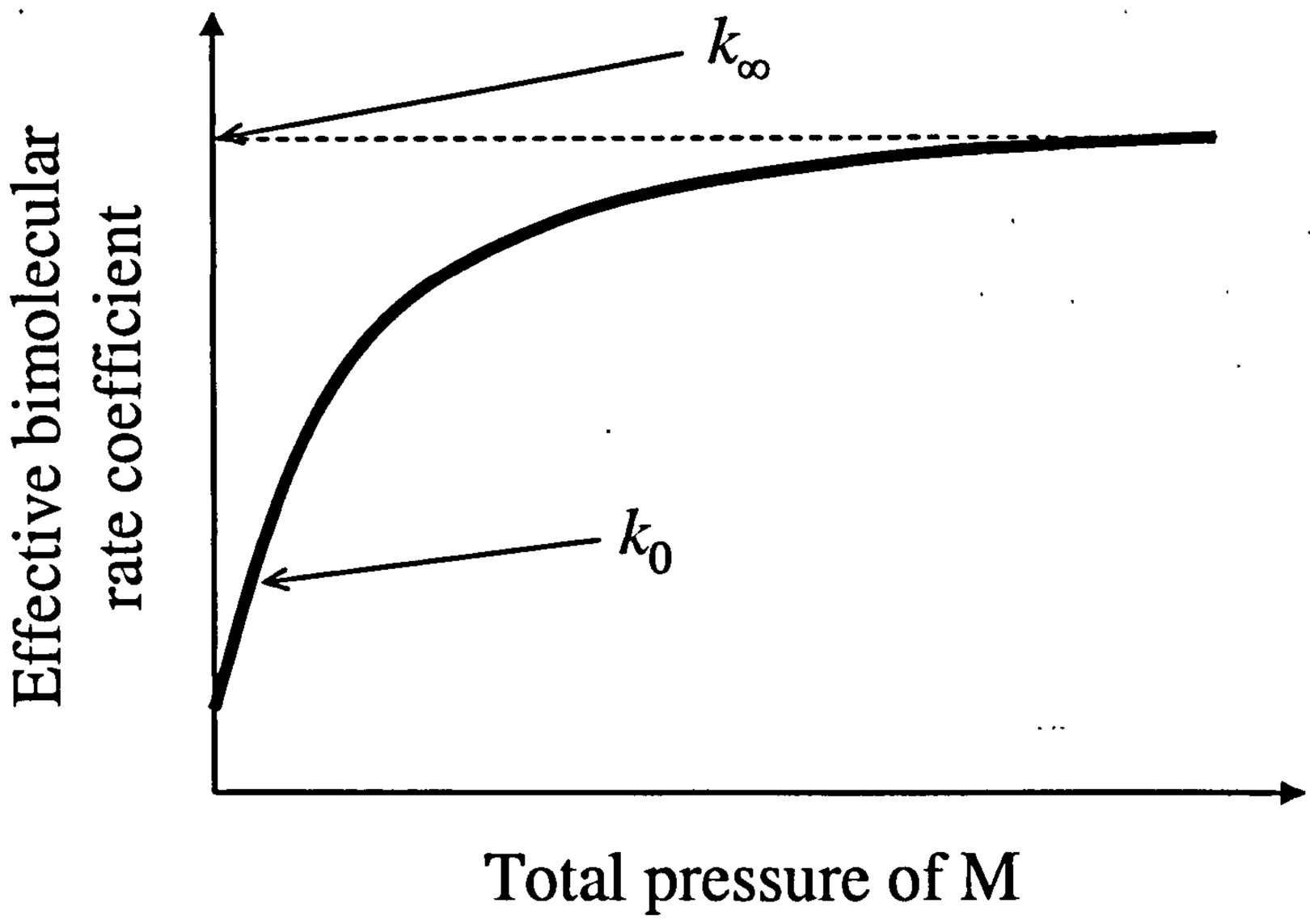

Fig. 2.2-3 – Typical dependence of the effective bimolecular rate coefficient on concentration of M for an association reaction. The low – and high – pressure rate coefficients are represented by k_0 and k_∞ respectively. Note that k_0 is equal to the slope in the low pressure region.

The high pressure limit, k_∞, of an association reaction is the effective bimolecular rate coefficient at infinite pressure, where the rate of adduct stabilisation is infinitely greater than the rate of adduct dissociation, and the reaction proceeds as if a bimolecular process. The high pressure limit is independent (or weakly dependent) of temperature and third body, although the total pressure at which it is reached will depend on both of these variables. The low pressure limit, k_0, is the rate coefficient of the third order process, and is dependent on both temperature and third body. The high and low pressure limits of an association reaction can be determined by Troe fittings of the experimental data[9]

$$k_{([M],T)} = \frac{k_0 k_\infty [M] F_c^{\ X}}{(k_\infty + k_0 [M])} \qquad \text{E. 2.2-8}$$

where, $X = \left\{1 + [\log(k_0[M]/k_\infty)]^2\right\}^{-1}$, and F_c is known as the broadening factor and is typically 0.6.

2.3 Pulsed Laser Photolysis

In order to investigate the reaction kinetics of a chemical system (or the spectroscopy of an unstable species), a method is required in which to initiate the chemical reaction (or generate the required radicals). Pulsed laser photolysis (PLP) was exclusively employed for this purpose in the course of this work. PLP involves the irradiation of a suitable precursor mixture with UV laser radiation prior to detection of the species of interest by another experimental technique (described subsequently).

For example, in order to generate the IO radical, ground state oxygen atoms ($O\ ^3P$) are commonly reacted with trifluoromethyliodide (CF_3I). O atoms are highly reactive radical species, requiring *in situ* generation, and a common O atom source is the 193 nm photolysis of N_2O. The O atoms are initially produced in an electronically excited state ($O\ ^1D$) but are quickly quenched to the ground state in a sufficient pressure of bath gas, such as N_2. The reaction sequence is thus

$$N_2O + 193\ nm \rightarrow N_2 + O(^1D) \qquad (R2\text{-}2)$$

$$O(^1D) + N_2 \rightarrow O(^3P) + N_2 \qquad (R2\text{-}3)$$

$$O(^3P) + CF_3I \rightarrow IO + CF_3 \qquad (R2\text{-}4)$$

The amount of O atoms (and hence IO) generated will depend on the photon density (fluence) of the laser radiation, and the concentration and absorption cross-section of N_2O. Absorption cross-sections are strongly wavelength dependent and usually weakly dependent on temperature. Equation 2.3-1 gives the relationship between the concentration of species, X, generated from the photolysis of precursor, Y.

$$[X] = [Y] F \sigma_{Y(\lambda,T)} \Phi_{Y(\lambda,T)} \qquad \text{E. 2.3-1}$$

where, [] is the concentration of X or Y (molecule cm^{-3}), F is the laser fluence (photons cm^{-2}), $\sigma_{Y(\lambda,T)}$ is the absorption cross-section of species Y at wavelength, λ, and temperature, T, (cm^2 $molecule^{-1}$), and Φ is the photolysis quantum yield of species Y at wavelength, λ, and temperature, T. The photolysis quantum yield of a molecule is the fraction of molecules which dissociate per photon absorbed. Thus if every 193 nm photon absorbed by N_2O at 298 K results in dissociation to $O\ (^1D) + N_2$ (which it does[10]), the photolysis quantum yield is unity. The photolysis quantum yield of a molecule can be greater than one: for example, the photolysis quantum yield for OH production from the 248 nm photolysis of H_2O_2 is two[10]. Thus, for a N_2O concentration of 1×10^{15} molecule cm^{-3} and a laser fluence of 50 mJ cm^{-2} (4.86×10^{16} photons

cm^{-2} at 193 nm), the concentration of O atoms generated at 298 K will be 4.35×10^{12} molecule cm^{-3} ($\sigma_{N_2O(193nm,298K)} = 8.95 \times 10^{-20} cm^2$ molecule^{-1})[10].

The wavelength of laser radiation chosen for the generation of radical species in a PLP experiment requires careful consideration of the reagent mixture, and the nature of the experiment. For example, if we were intending on measuring the rate coefficient for the reaction of IO with DMS, the method outlined above would be unsuitable for the generation of IO. As discussed in section 2.2 the reaction would be studied under pseudo-first-order conditions so that the IO decay rate would be measured as a function of [DMS] (which would always remain in great excess to [IO]). Although the absorption cross-section of CF_3I is relatively small at 193 nm ($\sigma = 2 \times 10^{-21} cm^2$ molecule^{-1})[10] the absorption cross-section of DMS is large ($\sigma = 1 \times 10^{-17} cm^2$molecule^{-1})[11] and, therefore, a significant amount of radicals will be produced by its photolysis, which will vary with the concentration of DMS. If these unwanted photolysis products were to react with IO, then the determined reaction kinetics of the reaction of IO with DMS could be subject to interference and therefore uncertainty. A better method for IO generation would involve a longer (lower energy) photolysis wavelength that would not result in significant photolysis of the reagent precursors (with the exception of the O atom precursor). For example, at 351 nm, NO_2 can be dissociated with unit efficiency to yield NO + O (^3P)[10]. The absorption cross-sections of CF_3I and DMS are negligibly small at 351 nm ($< 2 \times 10^{-22} cm^2$molecule^{-1})[10,11], thus the reaction of IO with DMS can be studied under photolytically clean conditions (providing that the concentration of NO_2, and hence NO, is unchanged throughout the experiment).

For spectroscopic experiments, where we are only concerned with the interaction of molecules with light, these considerations are not as important as we only require the target species to be present at sufficient concentration to be detectable, and at an approximately constant concentration for any given time between its generation and detection.

In all experiments reported in this work, an Excimer laser was employed as the source of PLP radiation. An Excimer laser operates *via* the electrical discharge of a mixture containing both inert (*e.g.* Kr/Xe/Ne) and halogen containing (*e.g.* F_2/HCl) gases in a He buffer. Upon electrical discharge a high energy complex (an exciplex) is formed between ions generated in the gas mixture (such as Kr^+F^- for example), which spontaneously emits a photon of UV radiation as it returns to the groundstate. As the groundstate is dissociative, a population inversion – a prerequisite of a laser – is maintained between the ground and excited states of the exciplex. The emitted radiation is focused and collimated into a well defined beam of high energy laser radiation and emitted from the laser cavity. The wavelength of the laser radiation depends on the nature of the exciplex and, therefore, the gas mixture. The most frequently employed Excimer wavelengths are 193 nm (Ar, F_2, He), 248 nm (Kr, F_2, He), 308 nm (Xe,

HCl, He) and 351 nm (Xe, F_2, He). At 193 nm, the photon energy (~ 620 kJ mol^{-1}) is more than sufficient for the dissociation of most covalent chemical bonds of gas phase molecules. Due to the short fluorescence lifetime of the exciplex, the pulse width of an Excimer laser is typically 10 – 20 ns, meaning that the radical species are produced over a narrow and well-defined temporal span. The variable pulsed repetition frequency (PRF) and high laser powers (< 500 mJ $pulse^{-1}$) at which Excimer lasers can be operated makes them particularly useful tools in laboratory PLP experiments, and capable of generating high radical concentrations from relatively low amounts of precursor concentrations.

2.4 Laser Induced Fluorescence

Laser induced fluorescence (LIF) is an extremely useful and adaptable technique for studying the spectroscopy and reaction kinetics of systems relevant to atmospheric (and general physical) chemistry. LIF is a spectroscopic technique, which utilises laser radiation to transit a population of molecules from one state of energy to another. At temperatures relevant to atmospheric chemistry, the majority of diatomic (and many small polyatomic) molecules will exist in their ground electronic and vibrational states – the states of lowest energy – as the available thermal energy is much less than the spacing between successive states. The laser frequency is tuned to the exact energy required to excite a population of molecules from a specific rotational level in the ground state to a specific ro-vibrational level in a bound, electronically excited state. The terminal state will be selected on consideration of a number of factors. It is fundamental that the excited electronic state is bound (*i.e.* not significantly dissociative), exhibits fluorescence and is accessible from the ground state on the basis of the electronic selection rules. An excited bound electronic state may have a number of possible fates. These include: i) fluorescence – the spontaneous emission of radiation as the molecule relaxes to a lower energy state; ii) energy transfer – the redistribution of the excited state population from the initially populated ro-vibrational level; iii) phosphorescence – inter system crossing (ISC) of the molecule to another electronic state (of different spin), and subsequent emission of radiation; iv) quenching – deactivation of the electronically exited state by collision with other molecules (in either reactive or unreactive collisions); or v) predissociation – the transfer of excited state population to an unbound state, resulting in dissociation. The fluorescence lifetime of a molecule will depend on all of the above factors and is typically in the region of tens to hundreds of nanoseconds. Thus in an LIF experiment, an excited electronic state will be selected in which fluorescence is the predominant fate – or at least where the magnitude of the fluorescence quantum yield (the fraction of photons emitted per photon absorbed) allows sensitive detection of the target species.

Fig. 2.4-1 displays a schematic diagram of the possible fates of an electronically excited state and the basis of a typical LIF experiment.

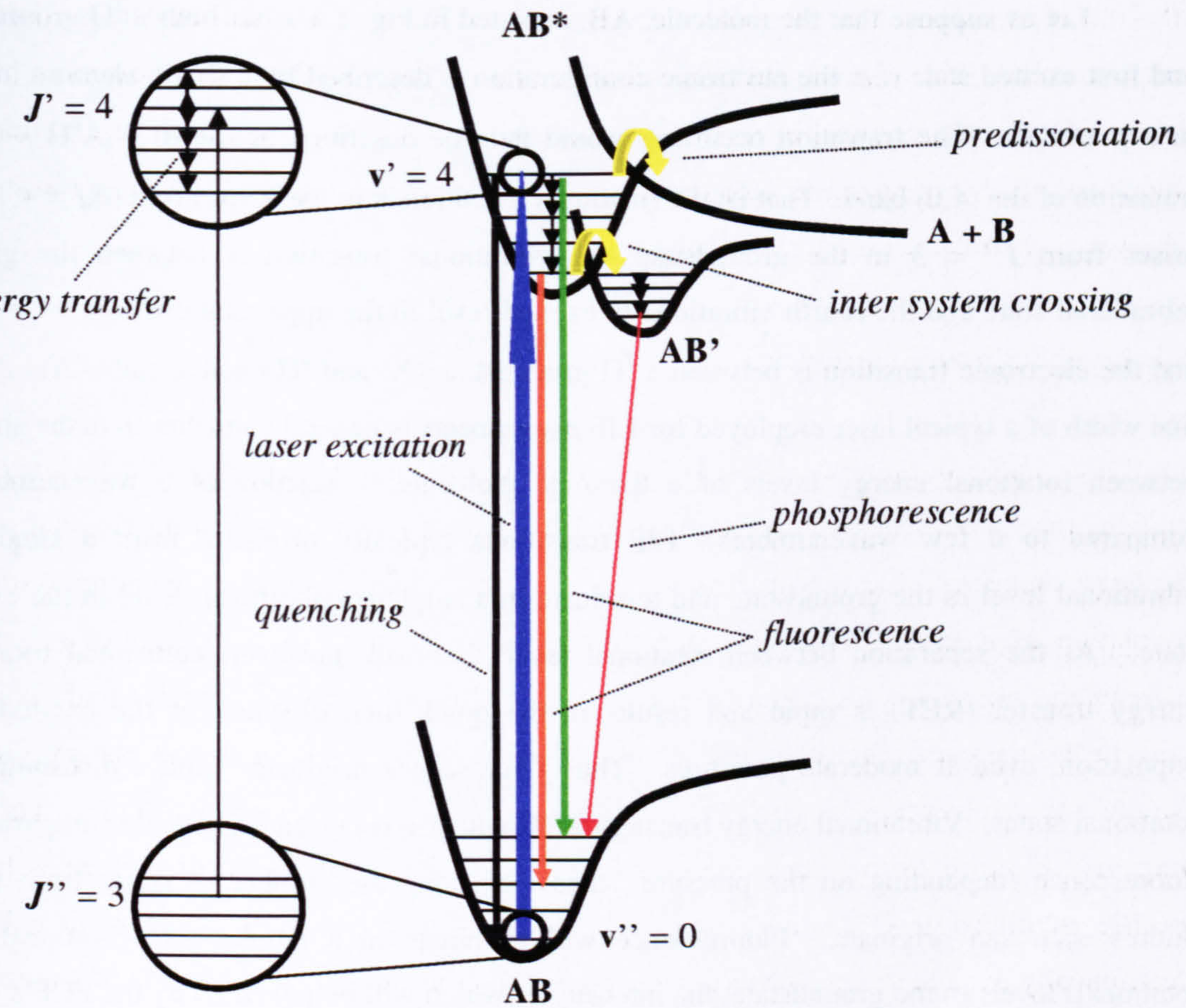

Fig. 2.4-1 – Schematical representation of the typical processes involved in LIF. The molecule is excited from the groundstate, AB, to an excited state, AB*, by laser radiation. The excited state ro-vibrational level, initially populated, undergoes energy transfer to other rotational and vibrational levels, and the total excited state population is depopulated by fluorescence, predissociation, collisional quenching and phosphorescence.

Essentially no spectroscopic selection rules are applicable to changes in vibrational level for a concomitant electronic transition. Thus the terminal vibrational level of an excited state will be selected predominantly by the magnitude of the Franck Condon factor (FCF) for the transition between ground and excited states: the probability of a transition between the two states, or more specifically the square of the overlap of the excited and ground state wavefunctions. The fluorescence lifetime of the excited state may be dependent on vibrational level (as for IO)[12], which may also have to be taken into consideration.

Generally, rotational transitions between ground and excited states are limited to those in which the rotational quantum number does not change by more than one, $\Delta J = 0, \pm 1$. As the absorption intensity of a spectroscopic transition is directly proportional to the groundstate

population (see Chapter Three), the groundstate rotational level excited in an LIF experiment will typically be that of maximum population, as governed by the Boltzmann (thermal) distribution.

Let us suppose that the molecule, AB, depicted in Fig. 2.4-1 has both a $^2\Pi$ groundstate and first excited state (*i.e.* the electronic configuration is described by a single electron located in a p-orbital). The transition occurring would thus be described as the R(3) $A^2\Pi \leftarrow X^2\Pi$ transition of the (4,0) band. That is: the rotational transition is in the R manifold ($\Delta J = +1$) and arises from $J'' = 3$ in the groundstate; the vibrational transition is between the ground vibrational state and the fourth vibrationally excited level in the upper state: $v' = 4 \leftarrow v'' = 0$; and the electronic transition is between a $^2\Pi$ groundstate (X) and $^2\Pi$ excited state (A). As the line width of a typical laser employed for LIF experiments is generally smaller than the spacing between rotational energy levels of a diatomic molecule (a fraction of a wavenumber as compared to a few wavenumbers), LIF transitions typically originate from a single ro-vibrational level in the groundstate and terminate in a single ro-vibrational level in the excited state. As the separation between rotational levels is small, however, collisional rotational energy transfer (RET) is rapid and results in the quick thermalisation of the excited state population, even at moderate pressures. Thus fluorescence originates from a distribution of rotational states. Vibrational energy transfer (VET) can also occur on a timescale comparable to fluorescence (depending on the pressure), thus increasing the number of states from which fluorescence can originate. Fluorescence will terminate in a number of vibrational (and rotational) levels in the groundstate, the intensity of which will be governed by the FCF's of the individual vibrational transitions (and the appropriate selection rules). In LIF experiments, therefore, fluorescence is usually significantly red-shifted (*i.e.* occurs at longer wavelengths) to the excitation wavelength.

Fluorescence is detected by a light-sensitive device, usually a photomultiplier tube (PMT) that converts photons of the visible region into an amplified flow of electrons, or current. LIF is therefore a direct but relative technique – the fluorescence signal is directly proportional to the absolute concentration of the fluorescing species, but provides no quantitative information as to its magnitude, in the absence of an accurate calibration (the observed fluorescence signal from an accurately known concentration of substance). A successful LIF experiment requires the efficient separation of fluorescence from laser light as a PMT is indiscriminate to the origin of the photons it detects, and the laser radiation will be of much greater intensity than that of the fluorescence. The fact that fluorescence is often red-shifted to the excitation wavelength aids this process, as a suitable interference filter can be introduced to the experimental system that provides an impervious shield to the PMT from laser radiation but allows the transmission of fluorescence at longer wavelengths over a limited range. Very favourable instrumental signal-

to-noise (S/N) is thus obtainable in LIF experiments, where the fluorescence signal can effectively be monitored on a zero background, enabling the detection of very low concentrations of reactive species. In reality, interference filters are imperfect and the S/N of an LIF instrument is usually the limiting factor to the detection limit of the apparatus. As the temporal profile of a laser pulse (10 – 20 ns) is shorter than the fluorescence lifetime of many species, fluorescence can be distinguished from laser radiation by monitoring the PMT signal at times where no laser radiation remains – gated fluorescence collection. Fig. 2.4-2 illustrates a gated fluorescence experiment.

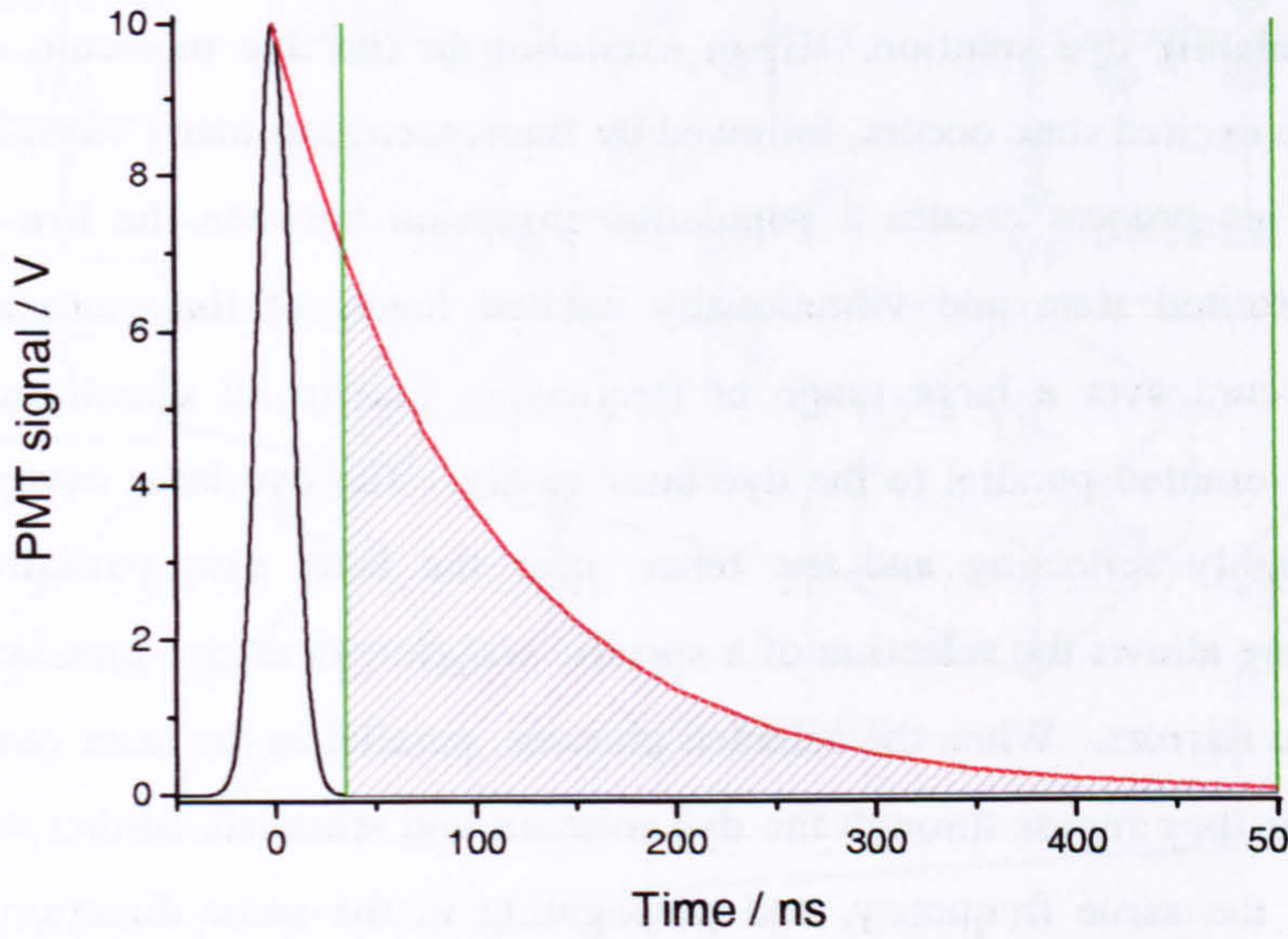

Fig. 2.4-2 – Illustration of gated fluorescence collection. The solid red line represents the fluorescence intensity from a species with a 100 ns fluorescence lifetime, excited at time zero by a laser pulse (solid black line) of Gaussian form with a 20 ns FWHM. The solid green line represents the fluorescence collection gate: the period of time over which the fluorescence signal is integrated. The shaded area indicates the fraction of fluorescence detected.

In the example given in Fig. 2.4-2 the fluorescence collection gate is set to integrate the fluorescence signal over the temporal range of 35 – 500 ns after the laser pulse. Thus a large fraction of the total fluorescence (~ 70 %) can be detected in the complete absence of laser radiation. Note that fluorescence can be detected in the absence of an interference filter *via* gated collection, which is particularly important if the molecule only fluoresces resonantly, *i.e.* at the same wavelength as excitation (as is predominantly the case for the (0,0) band of the $A^2\Sigma^+ \leftarrow X^2\Pi_{3/2}$ system of OH)[13]. However, in this situation, electronic gating of the PMT is required in order to reduce the effects of its electronic saturation, which can have a significant recovery time. This can be achieved with the incorporation of an electronic switching device (or "gating box") which effectively turns off the voltage supply to the PMT over the duration of the laser

pulse. This method is successfully employed for the LIF detection of the OH radical in the atmosphere by the FAGE technique[14-17] enabling an extremely low detection limit of ~ 1×10^5 molecule cm^{-3}. If the fluorescence lifetime of a species is shorter, or comparable, to the duration of the laser pulse (as is the case for the (2,0) band of the $A^2\Pi_{3/2} \leftarrow X^2\Pi_{3/2}$ system of IO)[12] gated fluorescence detection cannot be employed as all fluorescence occurs within the laser pulse. In this scenario, fluorescence must be detected off-resonantly, at longer wavelengths than the excitation, with the incorporation of interference filters.

For all LIF experiments reported in this thesis, a Dye laser was used for generation of the excitation wavelength. A Dye laser operates on the stimulated emission of an organic dye molecule. Laser radiation from an Nd:YAG or Excimer laser is focused into a dye cuvette that contains a circulating dye solution. Upon excitation of the dye molecule, rapid vibrational relaxation in the excited state occurs, followed by fluorescence to many vibrational levels in the groundstate. This process creates a population inversion between the low-lying vibrational levels of the excited state and vibrationally excited levels of the groundstate. Although fluorescence occurs over a large range of frequencies and in all directions in space, some photons will be emitted parallel to the dye laser cavity. The dye laser cavity consists of two mirrors, one highly reflecting and the other, near the laser exit, partially reflecting. A diffraction grating allows the selection of a specific wavelength of dye emission to be reflected between the two mirrors. When the selected photons, parallel to the laser cavity, are reflected through the laser they repass through the dye solution and stimulate further emission from the excited state at the same frequency, and propagating in the same direction, to the incident radiation. This additional radiation then traverses the dye laser cavity generating yet more stimulated emission. The increasing extent of stimulated emission soon begins to predominate over other processes occurring in the excited state, such as fluorescence and intersystem crossing, and lasing results. A well defined laser beam of narrow frequency range is thus established and exits from the laser through the partially reflecting laser mirror. Due to the range of excitation wavelengths with which a dye can be pumped, the range of frequencies that can be selected with a diffraction grating, the incorporation of frequency doubling and mixing crystals, and the wide range of organic dyes available, Dye lasers are extremely versatile and can be used to generate an extensive range of wavelengths to which perform LIF experiments.

In summary, LIF is an extremely sensitive and selective technique for the investigation of the spectroscopy and reaction kinetics of chemical systems in the laboratory. Selectivity is enhanced relative to other techniques, such as absorption spectroscopy, as any species which may pose as a potential interference must absorb and fluoresce at the same wavelength as the investigated species (and possess a similar spectral structure), and over a similar timescale. In effect, both the absorption structure and excited state dynamics of a fluorescing molecule can be exploited to enhance the selectivity of an LIF experiment, and the possibility of detecting

fluorescence in noise-free conditions yields LIF superior sensitivity with respect to other experimental techniques.

Fig. 2.4-3 shows the schematic arrangement of apparatus for a PLP-LIF experiment, as used in this study.

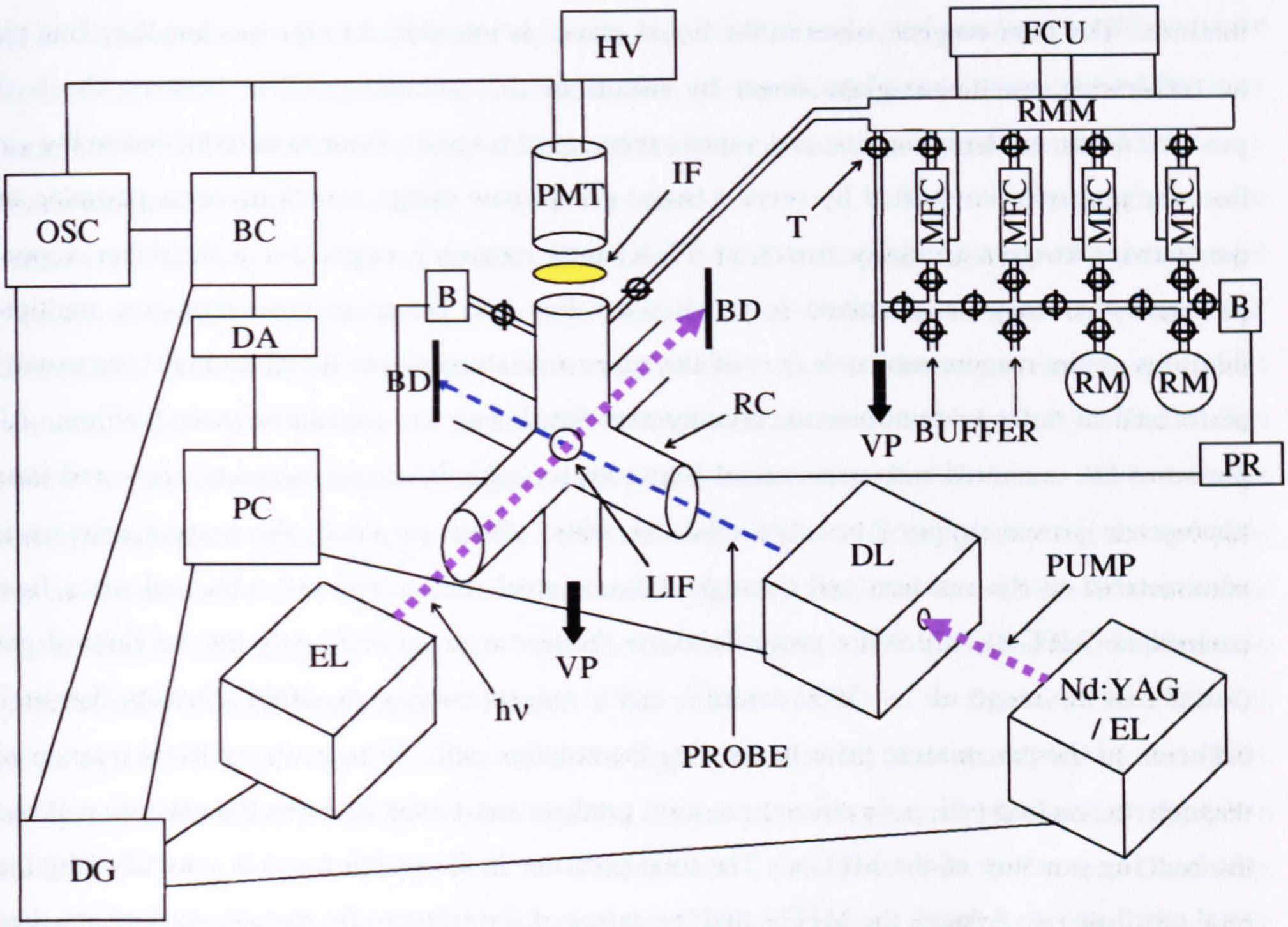

Fig. 2.4-3 – Schematic arrangement of apparatus for an LIF experiment. B = Baratron; BC = gated integrator and boxcar averager; BD = beam dump; BUFFER = buffer gas supply; DA = digital-to-analogue converter; DG = delay generator; DL = Dye laser; EL = Excimer laser; FCU = mass flow control unit; hν = photolysis laser beam; HV = high voltage supply; IF = interference filter; LIF = LIF excitation region; MFC = mass flow controller; OSC = oscilloscope; PC = control personal computer; PMT = photomultiplier tube; PR = pressure read out unit; PROBE = excitation laser beam; PUMP = pump laser beam; RC = reaction cell; RM = reagent mixture; RMM = reagent mixing manifold; T = two-way tap; VP = vacuum pumping system.

A suitable reagent mixture is prepared and administered to the reaction cell *via* a gas handling line. The gas handling line is constructed of stainless steel tubing linked together by a series of two-way taps and connected to a vacuum pumping system. The vacuum system consists of an oil diffusion pump and a rotary-vane pump. The rotary pump evacuates the gas handling line to a base pressure of ~ 10 mTorr, which is further reduced to ~ 10^{-2} mTorr by the diffusion pump. The diffusion pump is important for the removal of reagents from the walls of the system between experiments, and the efficient evacuation of the glass bulbs in which

reagent mixtures are prepared. Reagent mixtures are prepared in 5 litre glass bulbs by diluting the required precursor in a suitable buffer gas (usually He or N_2). The total pressure of the glass bulb is made up to ~ 2 atm and the mole fraction of reagent is adjusted according to the concentration of precursor required in the experiment, which may vary greatly. The precursor molecule may typically represent 0.001 – 10 % of the total concentration of gas in the precursor mixture. The pure reagent, often in the liquid phase, is introduced to the gas handling line *via* an (otherwise evacuated) glass finger by means of the pressure gradient between the base pressure of the gas handling line and vapour pressure of reagent. Prior to introduction to the gas line, the precursor is purified by several freeze-pump-thaw cycles, which involves pumping on the thawing reagent (initially frozen at 77 K) thus removing impurities with higher vapour pressures that may be dissolved in the liquid. For low precursor concentrations, multiple dilutions of the reagent molecule (*i.e.* of the reagent mixture within the glass bulb) are usually performed in order to minimise uncertainty associated with the calculated mole fraction. All pressures are measured with commercial Baratrons (or capacitance manometers), powered from appropriate power supply / pressure read-out units. Once prepared, the reagent mixture is administered to the reaction cell through stainless steel tubing and *via* calibrated mass flow controllers (MFC's), which are preset to allow the transit of an accurately known flow of gas (usually in the range of 1 – 5000 sccm)[18], and a reagent mixing manifold allowing thorough diffusion of the gas mixture prior to entering the reaction cell. In order for efficient transfer of reagents to reaction cell, a significant pressure gradient must exist between the reaction cell and the backing pressure of the MFC's. The total pressure in the reaction cell is controlled by the total gas flow rate through the MFC's and the extent of throttling to the vacuum system attached to the reaction cell. The total gas flow rate is maintained at a value that ensures the LIF excitation region is replenished with a fresh gas mixture many times between laser pulses. In some circumstances, where the build-up of unreactive, long-lived fluorescing species may pose a potential interference to the LIF measurements, the flow rate may be sufficiently high that the entire reaction cell is replenished with fresh gas between laser shots.

Two main types of reaction cell can be employed in the LIF experiments, which are specifically designed for measurements conducted above or below room temperature. For high temperature experiments, the reaction cell is constructed of cast iron and has several cartridge heaters embedded into the body of the cell, which can be electrically heated. The cell temperature is measured and regulated by a feedback loop between the electrical supply to the cartridge heaters and a type K thermocouple, situated near to the centre of the reaction cell. For low temperature experiments, a jacketed stainless steel reaction cell is employed. The surrounding jacket can be filled with a cooling agent, such as a water/ice slurry or solvent/cardice slurry. Similarly, the temperature of the reaction cell is determined by means of a thermocouple. Both types of reaction cell usually consist of a six-way cross of cylindrical

arms. Four arms are arranged on the horizontal axis, and two on the vertical axis of the reaction cell. All reaction cell ports (with the exception of the pumping axis) are covered with 50 mm diameter fused silica windows and sealed with o-rings. The internal volume of a reaction cell is typically 500 cm^3.

To generate the species to be monitored by LIF, the reagent mixture is irradiated with a pulse of Excimer (or photolysis) laser radiation, which initiates a set of reactions resulting in the formation of the target species. At some time later, Δt, the pump laser (either a second Excimer laser or Nd:YAG laser) is fired, stimulating the emission of radiation of a preselected frequency from the probe laser (Dye laser). The two laser beams are arranged orthogonally on the horizontal cell axis and intersect at the cell centre (the LIF excitation region). When the target species is irradiated with probe laser light (of frequency corresponding to a specific LIF transition), fluorescence is emitted with an intensity that is directly proportional to its concentration. The fluorescence is detected on the vertical reaction cell axis, by a PMT. The PMT is shielded from the photolysis and probe laser radiation by means of a suitable interference filter, situated between the PMT and cell window, allowing only the transmission of fluorescence. The analogue fluorescence signal recorded by the PMT is sent to an oscilloscope and a gated integrator and boxcar averager. The oscilloscope displays the unprocessed fluorescence signal from the PMT and is interlinked to the boxcar so that the fluorescence collection gate can be set at the appropriate width and sensitivity to record the integrated fluorescence signal. An analogue-to-digital converter transfers the boxcar signal to a control PC for storage and analysis at a later date. The photolysis and pump lasers are externally triggered by a delay generator that operates under control of the PC. The oscilloscope and boxcar are also triggered by the delay generator, at the same time as the pump laser, to observe signal from the PMT during fluorescence only. The frequency of the dye laser is controlled by the PC and is tuned to the correct frequency of an LIF transition by means of a wavemeter.

For reaction kinetics experiments, the probe laser frequency is maintained at a constant value and the delay time between photolysis and pump lasers, Δt, is varied over a suitable range to observe the growth or decay of the species of interest. Fig. 2.4-4 displays a typical kinetic trace for the formation of the CH_3I-Cl adduct in a reagent mixture of $Cl_2SO/CH_3I/N_2$ after photolysis at 248 nm.

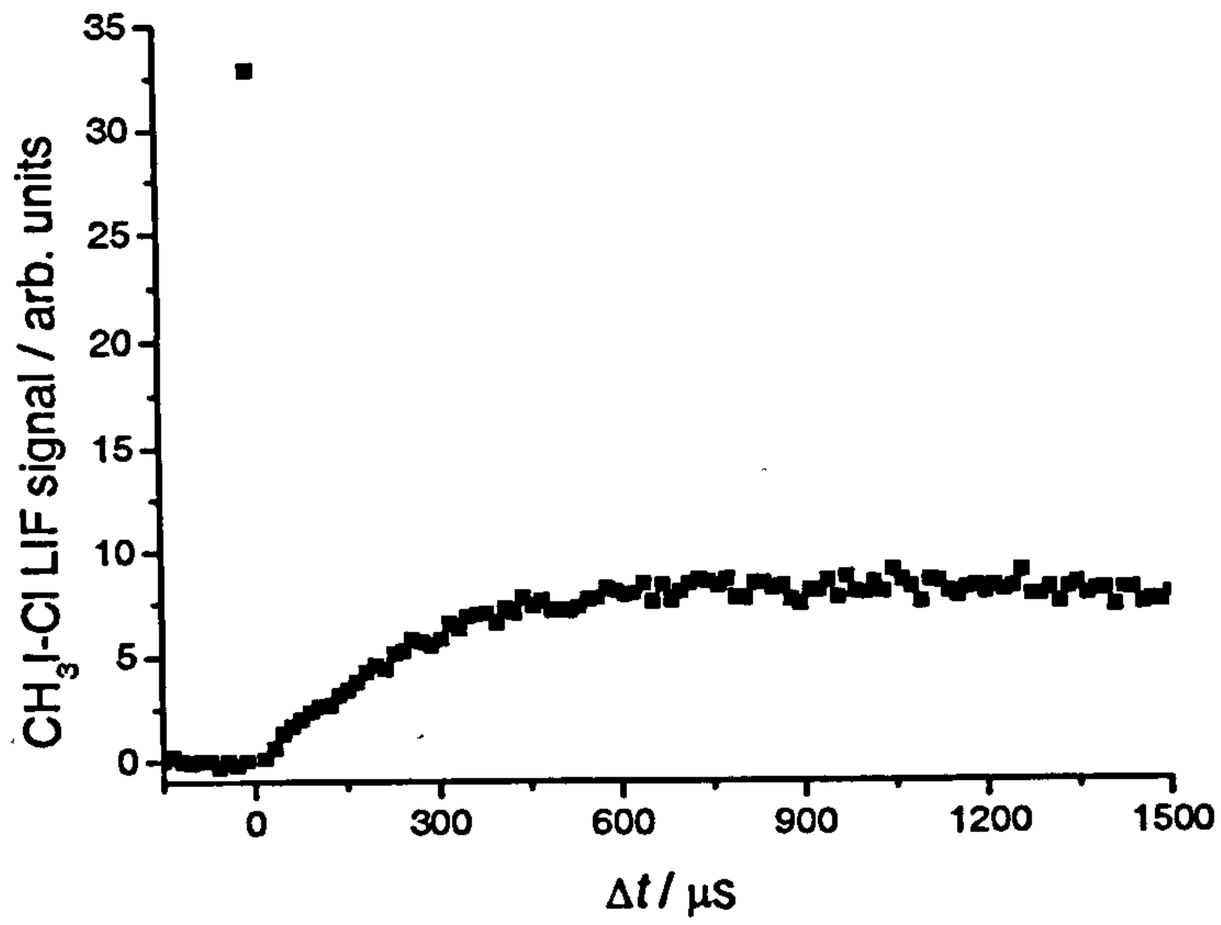

Fig. 2.4-4 – Kinetic formation of CH_3I-Cl in a precursor mixture of $Cl_2SO/CH_3I/N_2$ post photolysis at 248 nm. Experimental conditions: T = 296 K; P = 102 Torr; $[Cl_2SO] = 6.06 \times 10^{13}$ molecule cm^{-3}; $[CH_3I] = 7.1 \times 10^{12}$ molecule cm^{-3}; $[N_2]$ = balance; $\lambda_{pr} = 360.57$ nm; $P_{pr} = 1.4$ mJ pulse^{-1}; $\lambda_{ex} = 248$ nm; $P_{ex} = 3$ mJ pulse^{-1}. Note that all non-standard abbreviations used in figure captions throughout this thesis are defined in the Glossary of Terms (p. xxvii).

The LIF signal of CH_3I-Cl increases as the extent of reaction between Cl and CH_3I progresses. When all Cl atoms are consumed the LIF signal increases no more, and at larger values of Δt, the LIF signal will be seen to decrease as CH_3I-Cl diffuses out of the LIF excitation region and reacts with other species within the reaction cell. The reaction kinetics of Cl + CH_3I, and the spectroscopy of CH_3I-Cl are discussed in length in Chapter Five. A spuriously high signal at Δt = 0 is apparent in the kinetic trace displayed in Fig. 2.4-4. This is due to incomplete discrimination of excimer laser radiation by the interference filter (and/or red-shifted scatter from the reaction cell walls, and fluorescence from the substrate of the interference filter, induced by scattered excimer laser radiation). However, the excimer laser pulse is so short (< 20 ns) on the timescale of the kinetic experiment that it poses no interference to the LIF signal at any other delay time as all excimer laser radiation has long expired before the probe laser and boxcar are triggered by the delay generator.

For PLP-LIF experiments designed to probe the spectroscopic properties of molecules, the delay time between photolysis and probe lasers may typically be held constant and some other parameter varied, such as the probe laser frequency thus obtaining an LIF spectrum. Fig. 2.4-5 displays a LIF spectrum of the (2,0) band of the $A^2\Pi_{3/2} \leftarrow X^2\Pi_{3/2}$ electronic transition of IO.

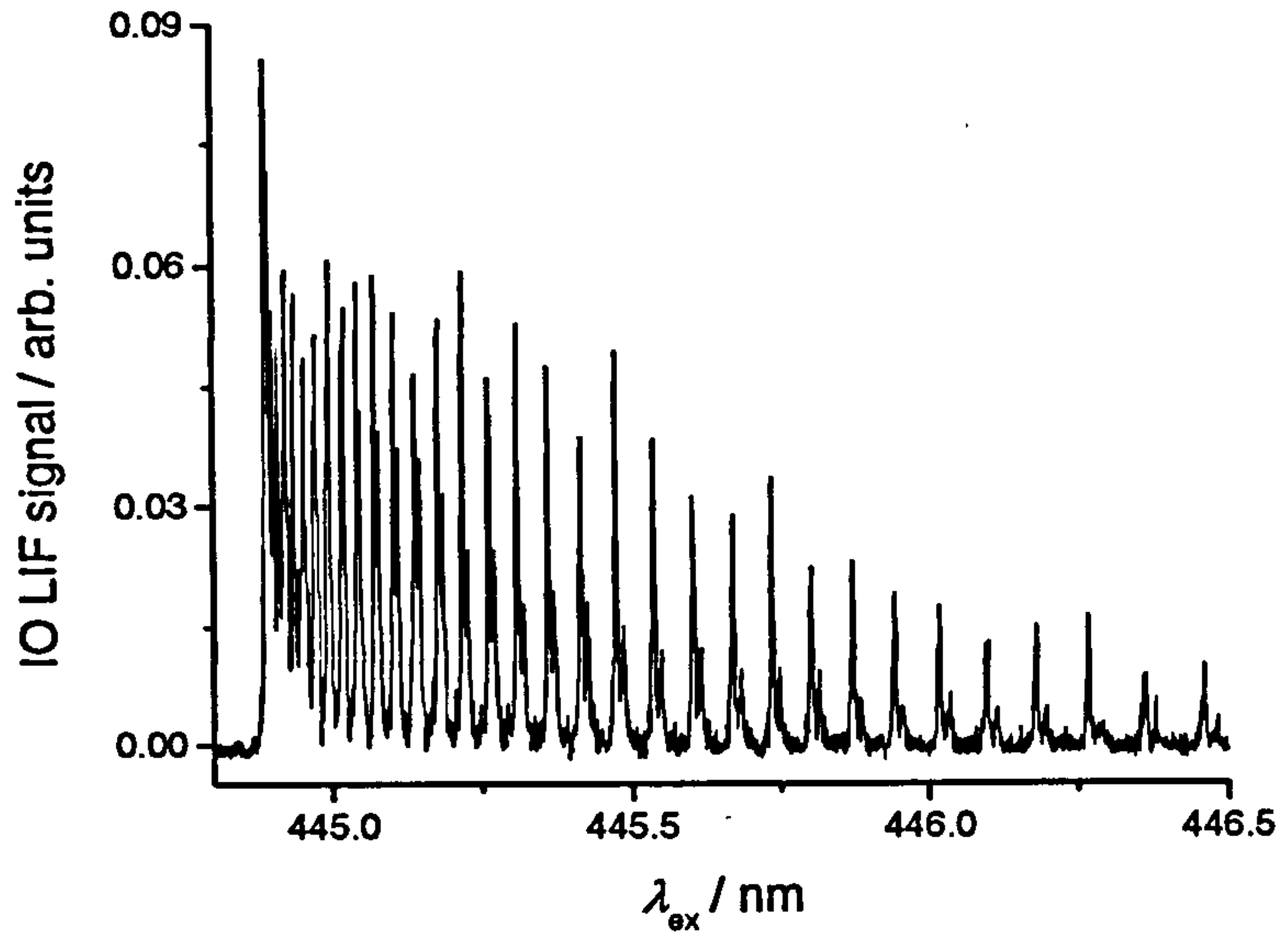

Fig. 2.4-5 – LIF spectrum of the IO (2,0) $A^2\Pi_{3/2} \leftarrow X^2\Pi_{3/2}$ band. Experimental conditions: T = 296 K; P = 150 Torr; $[N_2O] = 1 \times 10^{15}$ molecule cm^{-3}; $[CF_3I] = 2 \times 10^{14}$ molecule cm^{-3}; $[N_2]$ = balance; λ_{ex} = 193 nm; P_{ex} = 15 mJ $pulse^{-1}$; P_{pr} = 100 μJ $pulse^{-1}$; Δt = 3000 μs.

A detailed discussion of the spectroscopy of the $A^2\Pi \leftarrow X^2\Pi$ system of IO is given in Chapter Three.

2.5 Absorption Spectroscopy

As all molecules absorb to some extent in the UV and visible regions of the electromagnetic spectrum, absorption spectroscopy is, in principle, a universal technique. As the method depends only on the absorption of light, it is more applicable than other techniques, such as LIF, where the fate of an excited state may also be relevant. The amount of light absorbed by an absorbing species is related to its concentration by the Beer-Lambert law, E. 2.5-1

$$I = I_0 e^{(-\sigma c l)} \qquad \text{E. 2.5-1}$$

where, I is the intensity of transmitted radiation of a particular wavelength of light (with initial intensity, I_0) after passing through a sample of absorbing species of concentration, c, in path length, l, with absorption cross-section, σ, at the wavelength of incident radiation. The Beer-Lambert law only strictly applies for relatively low levels of absorption, as it relies on a population gradient between ground and excited states. If the excited state of a molecule is long-lived then strong absorption will result in significant population of that state and stimulated

emission will compete with absorption (*i.e.* the excited state will absorb radiation, stimulating emission that will propagate in the same direction and be of the same frequency as the incident radiation, thus competing with absorption). As a result, absorption spectroscopy can be an extremely useful technique for studying molecules with short-lived excited states such as BrO[19] (and IO)[12] where LIF cannot always be employed due to the extremely short fluorescence lifetime, and hence negligible fluorescence quantum yield.

A wide variety of light sources can be used for the incident radiation in absorption spectroscopy. A particularly useful and common source of UV-vis radiation is a Xe arc lamp due to the wide range of wavelengths generated. An electrical discharge promotes groundstate Xe atoms to electronically excited states. As the Xe atoms are present at high pressure, they emit radiation over a large frequency range as they relax to the groundstate. The emitted radiation is reflected and focused inside the lamp housing and emitted in a beam of broadband UV-vis radiation. A general disadvantage of absorption spectroscopy is that many species will tend to absorb over a particular wavelength range of the electromagnetic spectrum and a broadband light source will provide no discrimination between them, or speciation. The deconvolution of the individual components of an absorption signal for a particular excitation wavelength can therefore be a complex process. To partially resolve this issue, lasers are sometimes employed in absorption experiments, where the frequency range of the laser radiation is sufficiently narrow to allow the specific absorption of individual rovibrational transitions of an electronic transition. However, these experiments are still not as selective as LIF experiments, where the properties of the excited state provide an additional discriminatory asset. Cavity ring down spectroscopy (CRDS) is a relatively recent and successful application of narrow-band lasers in absorption spectroscopy[20]. In CRDS, a laser pulse traverses a reaction cell with two highly reflective mirrors at each end. As the laser pulse reflects off the surface of each mirror, a small amount of radiation leaks through the mirror and is detected by a PMT. The intensity of the detected radiation decays exponentially as the laser pulse traverses the cavity. The observed decay constant is characteristic of the apparatus and is known as the ring-down time. When an absorbing species is introduced to the reaction cell, additional losses of the laser radiation occur, and the ring-down time decreases (the decay rate of the laser radiation increases). The measured change in ring-down time, in the presence and absence of absorbing species, allows the determination of the absolute concentration of the absorbing species providing that the path length of the apparatus (the length of the cavity multiplied by the number of passes made by the laser pulse) and the absorption cross-section of the species are known.

Another general disadvantage of absorption spectroscopy is its sensitivity. The detection of a molecule requires a measurable change in the intensity of light before and after passing through a sample of absorbing species, which is hindered by the large background

signal of the incident radiation. It can be seen from E. 2.5-1 that this relies on either a substantial concentration of the absorbing species or a sufficiently long path length. For the atmospheric detection of IO by DOAS[21,22], a path length of > 8 km is required in order to gain sufficient sensitivity for its measurement, resulting in a poor spatial resolution and hence the assumption that the IO is equally partitioned along the path length of absorption. CRDS has the advantage that, as the laser pulse can traverse the reaction cell thousands of times, an effective km pathlength can be achieved for a point measurement instrument.

For the absorption experiments reported in this thesis, a pulsed laser photolysis single-pass absorption (PLP-SPA) system was used. Fig. 2.5-1 shows a schematic diagram of the apparatus involved.

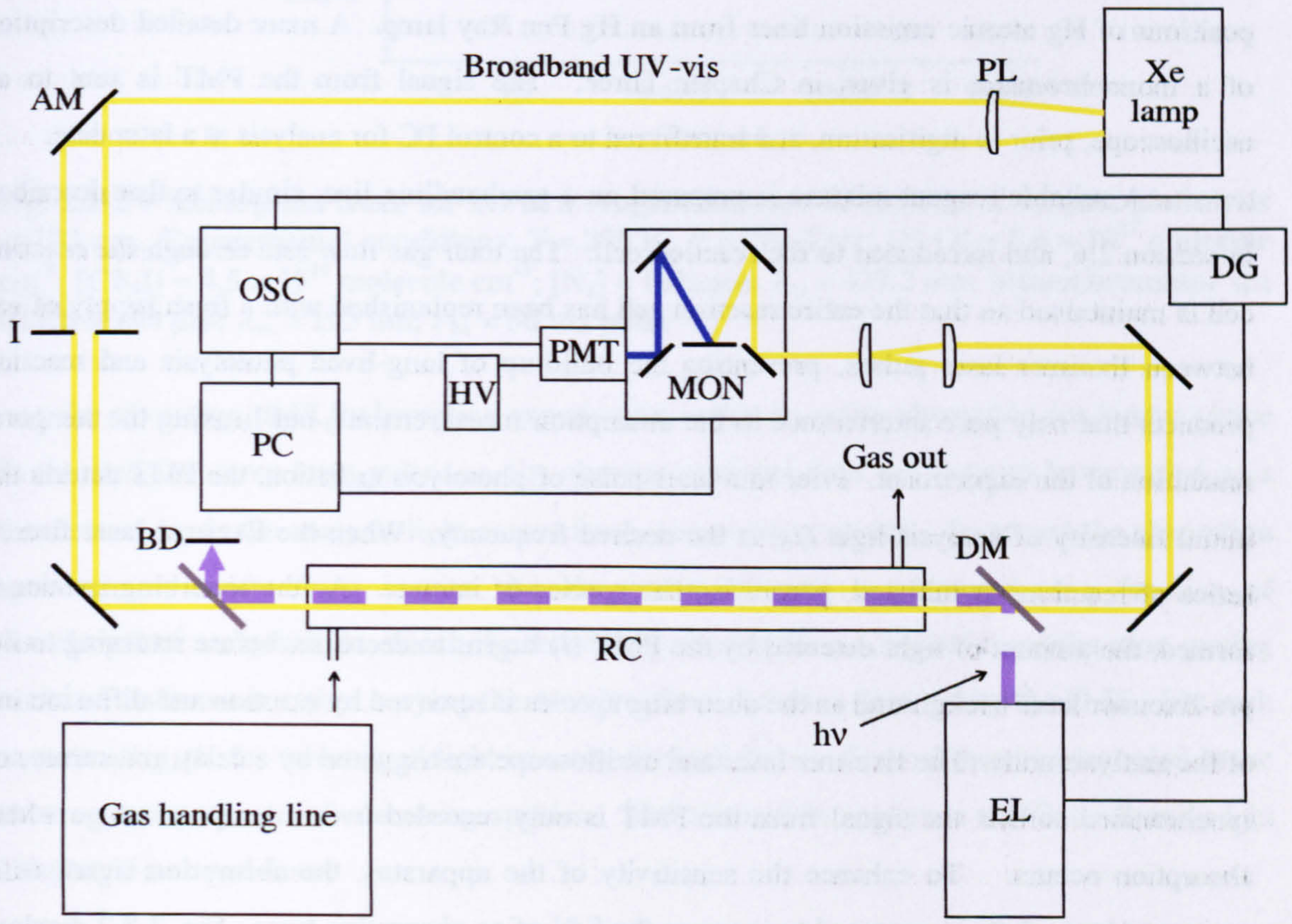

Fig. 2.5-1 – Schematic arrangement of apparatus for a PLP-SPA experiment. AM = aluminium coated mirror; Broadband UV-vis = analysis beam; DM = dichroic mirror; Gas out = reaction cell exhaust; I = iris; MON = monochromator; PL = plano-convex lens and collimating and focusing optics; Xe lamp = Xe arc lamp. All other apparatus are as previously assigned in Fig. 2.4-3.

The expanding, broadband emission of a Xe arc lamp is collimated and directed through a reaction cell (typically of one metre length) *via* a series of plano-convex lenses and aluminium coated mirrors. A pulsed beam of Excimer laser radiation is directed through the reaction cell, parallel to the incident UV-vis radiation, using suitable dichroic mirrors and terminated at a beam dump. The dichroic mirrors reflect the Excimer laser radiation but allow the transmission of radiation of all other wavelengths (*i.e.* the analysis light). The analysis light is trimmed by

means of an iris prior to entering the reaction cell so that there is a complete overlap between analysis and photolysis light beams. After exiting the reaction cell, the analysis light is directed into a monochromator *via* a series of mirrors and focusing and collimating optics, ensuring maximum collection of light. A diffraction grating inside the monochromator reflects the analysis light so that only a specified frequency of radiation, corresponding to a vibrational-electronic transition of the species of interest, is detected by the PMT. The resolution of the monochromator, or wavelength range detected by the PMT, is governed by the number of grooves on the diffraction grating and the entrance and exit slit widths of the monochromator. The diffraction grating of the monochromator is electronically controlled by the PC and the wavelength and resolution of the monochromator are calibrated by comparison to the known positions of Hg atomic emission lines from an Hg Pen Ray lamp. A more detailed description of a monochromator is given in Chapter Three. The signal from the PMT is sent to an oscilloscope, prior to digitisation, and transferred to a control PC for analysis at a later date.

A suitable reagent mixture is prepared on a gas handling line, similar to that described in section 2.4, and introduced to the reaction cell. The total gas flow rate through the reaction cell is maintained so that the entire reaction cell has been replenished with a fresh supply of gas between Excimer laser pulses, preventing the build-up of long-lived photolysis and reaction products that may pose interference to the absorption measurements, but limiting the temporal resolution of the experiment. Prior to a laser pulse of photolysis radiation, the PMT detects the initial intensity of analysis light (I_0) at the desired frequency. When the Excimer laser fires, a series of reactions is initiated, generating the species of interest. As the absorbing species is formed, the amount of light detected by the PMT (I) begins to decrease, before returning to the pre-Excimer laser background as the absorbing species is removed by reaction and diffusion out of the analysis zone. The Excimer laser and oscilloscope are triggered by a delay generator, and synchronised so that the signal from the PMT is only recorded over a temporal range where absorption occurs. To enhance the sensitivity of the apparatus, the absorption signal from numerous laser shots is averaged to increase the S/N of an absorption trace. Fig. 2.5-2 displays a typical absorption trace for IO (detected at 427.2 nm – the peak of the (4,0) $A^2\Pi_{3/2} \leftarrow X^2\Pi_{3/2}$ transition) in a mixture of $N_2O/CF_3I/N_2$, post photolysis at 193 nm. As can be seen from the absorption trace in Fig. 2.5-2, before time zero (*i.e.* when the Excimer laser fires) the PMT observes the initial intensity of the Xe arc lamp emission at 427.2 nm. After the Excimer laser fires, the signal from the PMT begins to decrease as IO is formed from the reaction of $O + CF_3I$, and absorbs some of the 427.2 nm analysis light. As IO begins to react with itself, its concentration diminishes and the light intensity returns to the pre-Excimer laser value as the absorption due to IO becomes weaker.

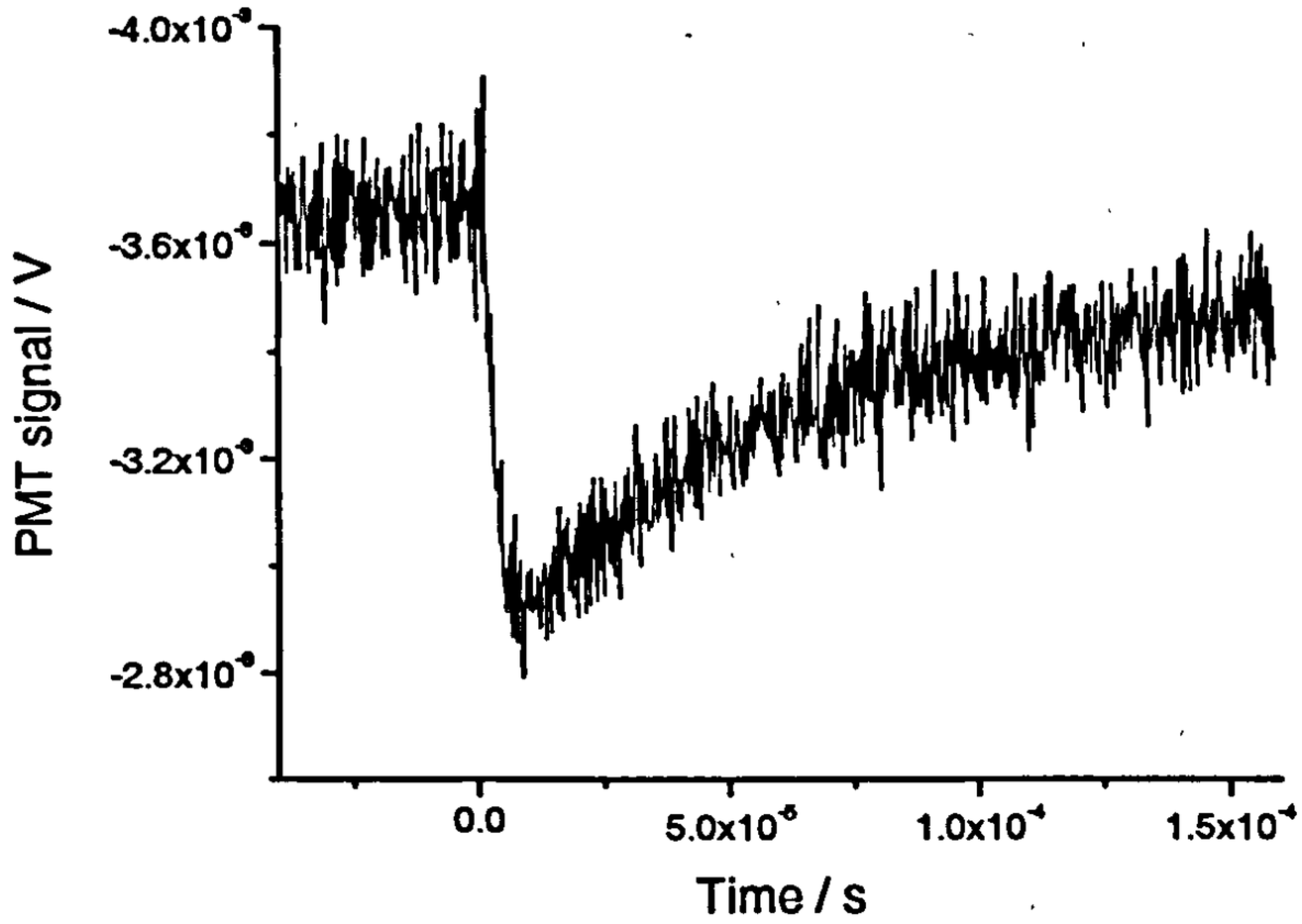

Fig. 2.5-2 – Absorption trace for IO in a reagent mixture of $N_2O/CF_3I/N_2$, post photolysis at 193 nm. Experimental conditions: $T = 296$ K; $P = 760$ Torr; $[N_2O] = 5.6 \times 10^{17}$ molecule cm^{-3}; $[CF_3I] = 4.5 \times 10^{16}$ molecule cm^{-3}; $[N_2]$ = balance; $\lambda_m = 427.2$ nm; Monochromator slit width = 100 μm; $\lambda_{ex} = 193$ nm; $P_{ex} = 50$ mJ $pulse^{-1}$.

An advantage of PLP-absorption experiments is that an entire absorption (or kinetic) trace is obtained for every laser pulse, *i.e.* the absorption signal does not have to be recorded as a function of Δt, as the analysis light comes from a continuous source. To record the absorption spectrum of an absorbing species, the absorption intensity is measured as a function of wavelength of analysis light, which is achieved by altering the position of the diffraction grating in the monochromator, thus varying the wavelength of radiation detected by the PMT. For each new wavelength, the transmitted light intensity through the reaction cell must be recorded in the absence and presence of absorbing species. The absorption spectrum of IO is discussed in Chapters Three and Four.

2.6 Mass Spectrometry

Not involving the use of light, and due to the fact that all matter possesses mass, mass spectrometry (MS) is effectively a universal detection method. In MS experiments, the gas sample is ionised by photoionisation or electron impact and the resulting ions are detected according to their mass, usually by one of two types of spectrometer: i) a quadrupole mass spectrometer; or ii) a time-of-flight (TOF) mass spectrometer. A quadrupole mass spectrometer operates by deflecting the flight path of ions in an oscillating electric field. The extent of deflection of the ions is dependent on their charge and mass ratio, and the strength and oscillatory frequency of the electric field. Thus species of different mass can be discriminated

by scanning the position of an ion detector in a constant electric field, or varying the strength of the electric field for a fixed ion detector location. A TOF-MS operates on the principle of detecting ions according to their flight time between formation and detection, which is inversely proportional to their kinetic energy and, therefore, an indicator of their mass. The ionised gas sample is collimated into an ion beam by a series of electric fields and directed on to an ion detector. The time taken for an ion to reach the detector is proportional to the square root of its mass.

The universal nature of MS means that it can be an ideal technique for studying the reaction kinetics of chemical systems as the temporal profile of reactants, products and reaction intermediates can be monitored simultaneously, potentially yielding a complete description of the reaction mechanism and the determination of product branching ratios. Disadvantages of the technique are that not all species will be ionised by the ionisation source and/or some reagent molecules may undergo photofragmentation to generate ions of the same mass as the reactants or products of the reaction being studied, thus posing an interference to their detection. Further, as MS is a non-spectroscopic technique, speciation between molecules of the same (or very similar mass) cannot be achieved.

For the MS study described in Chapter Four of this thesis, a laser photoionisation TOF-MS experiment was employed[23]. The apparatus is schematically represented in Fig. 2.6-1. A typical experiment is performed by the following procedure. A reagent mixture, prepared on a gas handling line, is introduced into the reaction cell (a quartz flow tube of ~ 50 cm length and 10 mm diameter) and irradiated with a beam of Excimer laser radiation, which overlaps the entire length of the reaction cell. The reaction cell is maintained at a total pressure of ~ 1 Torr, and a small amount of the reagent mixture is allowed to diffuse through a pinhole (of ~ 1 mm diameter in the reaction cell wall) into a low pressure vacuum chamber, which is pumped independently to a pressure of ~ 10^{-5} Torr. The gas exiting the pinhole is photoionised in the vacuum chamber by an intersecting laser pulse of VUV (vacuum ultra-violet) radiation, which is triggered at a specific delay time, Δt, after the Excimer laser pulse. The photoionisation radiation is generated from an Nd:YAG-pumped dye laser. The second harmonic of the Nd:YAG laser at 532 nm excites a pyridine dye in the Dye laser, generating radiation in the 680 – 720 nm range. The red light is frequency doubled by a SHG crystal inside the Dye laser before being passed through a tripling cell, containing Xe gas at ~ 80 Torr total pressure, to generate the VUV photoionisation radiation. Depending on the frequency of the red radiation selected by the diffraction grating of the Dye laser, a tuneable photoionisation wavelength range of ~ 113 – 120 nm is accessible, thus allowing some degree of specificity to ionisation, which can be of use in experiments where ionisation of the precursor could be problematic.

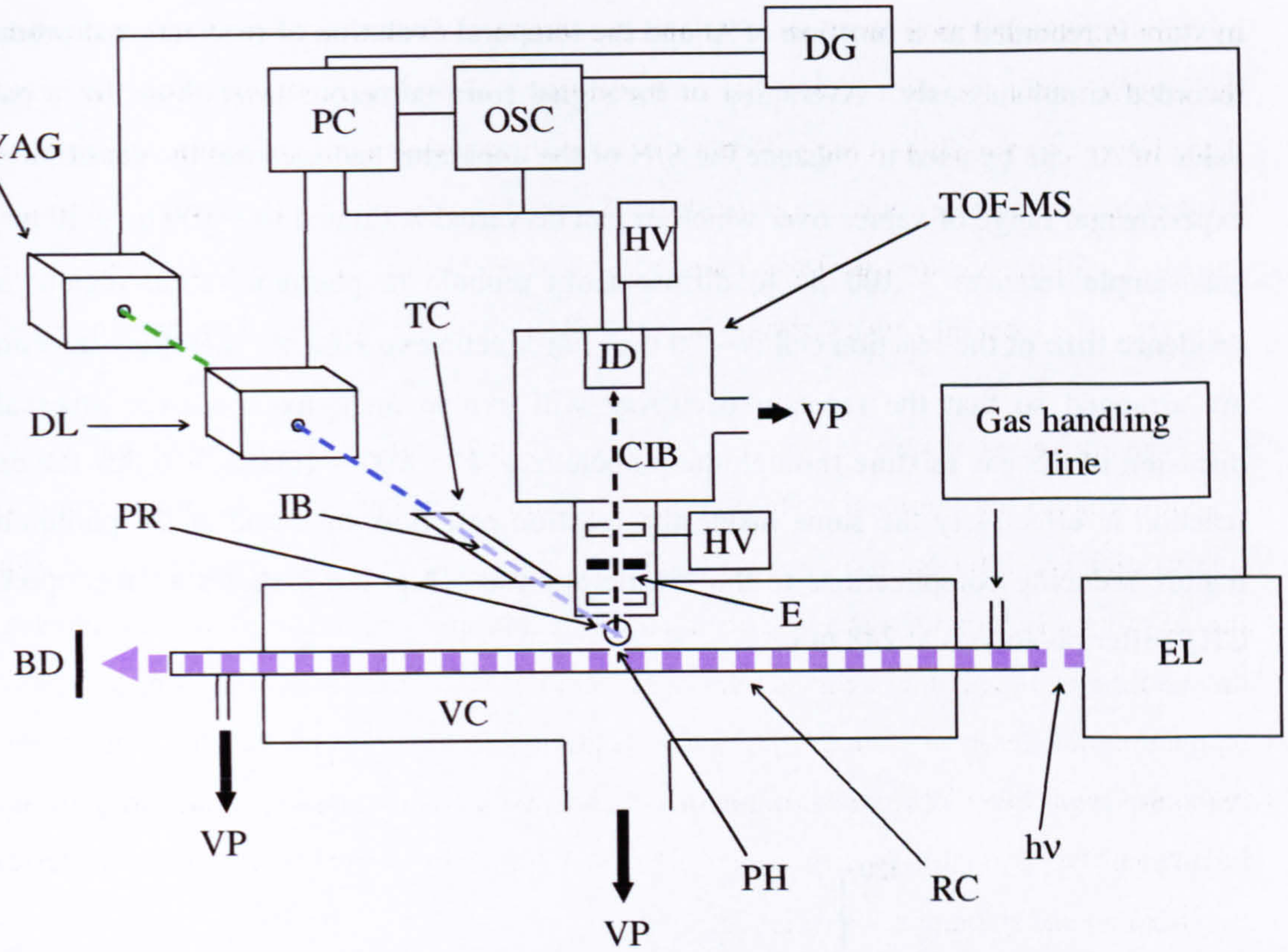

Fig. 2.6-1 – Schematic diagram of TOF-MS apparatus used in this study. CIB = collimated ion beam; E = electrodes; IB = photoionisation beam; ID = ion detector; PH = pinhole; PR = photoionisation region; TC = tripling cell; TOF-MS = time-of-flight mass spectrometer; VC = vacuum chamber. All other apparatus are as previously assigned in Fig. 2.4-3.

Once ionised, the gas sample is drawn into the mass spectrometer by a negatively charged electric field, which is generated by a series of electrodes inside the mass spectrometer. The ion stream entering the mass spectrometer is collimated and accelerated by a series of electric fields, and directed through the flight chamber to an electron multiplier detector (ion detector). The flight chamber of the mass spectrometer is independently pumped to a base pressure of ~ 10^{-6} Torr. The signal from the electron multiplier is sent to an oscilloscope and to an ion-counting card on the control PC. The Excimer laser, Nd:YAG laser, oscilloscope and ion-counting card are triggered by a delay generator operating under computer control. As the flight time of ions within the mass spectrometer is of the order of microseconds, the ion-counting card has a nanosecond resolution in order to sufficiently resolve the mass of the ions reaching the detector. The resolution of the mass spectrometer is such that 1 mass in 200 can be detected, *i.e.* discrimination between species of mass 200 and 201 can be achieved. The ion-counting card is triggered at the same time delay as the photoionisation laser and bins the ion signal at regular intervals (of a few nanoseconds) over a suitable time period. To record a kinetic trace, Δt, is varied over a suitable range to observe the kinetic growth and decay of the various species present in the reaction mixture (and mass spectrum). Thus the mass spectrum of the reaction

mixture is recorded as a function of Δt and the temporal evolution of reactants and products are recorded simultaneously. Averaging of the signal from numerous laser shots, for a particular value of Δt, can be used to enhance the S/N of the apparatus and increase the sensitivity. The experimental range of values over which Δt can be varied is limited to ~ 100 μs – 20 ms, as the gas sample requires ~ 100 μs to diffuse from pinhole to photoionisation region, and the residence time of the reaction cell is ~ 20 ms. For kinetic experiments, therefore, the conditions are arranged so that the reaction occurring will evolve on a much slower timescale than diffusion of the gas mixture through the pinhole (*e.g.* $k' = 100 - 1000\ s^{-1}$) so that the extent of reaction is effectively the same inside the reaction cell flow tube and at the photoionisation region, reducing complications to the kinetic analysis. Fig. 2.6-2 shows a mass spectrum of CH_2I_2 after photolysis at 248 nm.

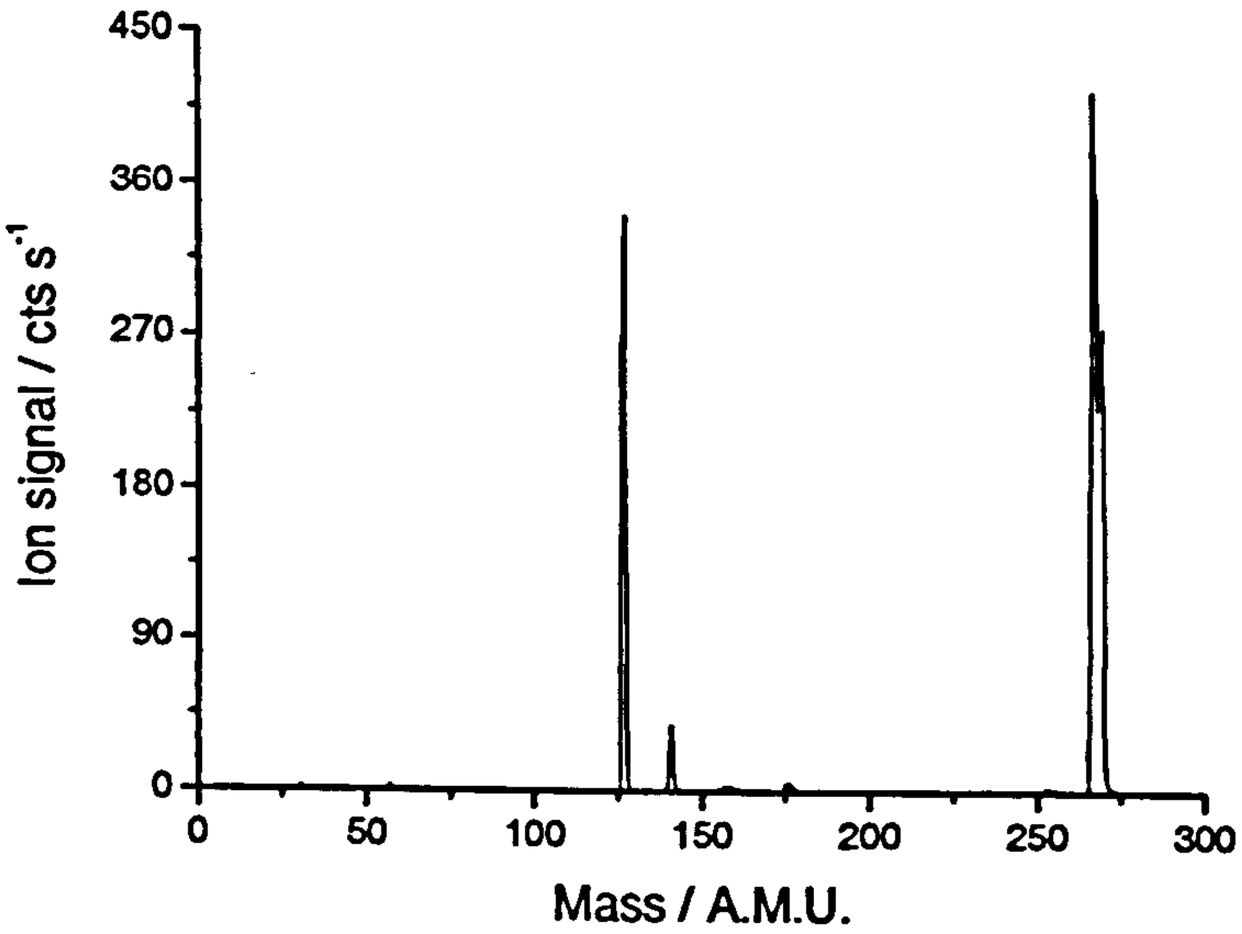

Fig. 2.6-2 – Mass spectrum of CH_2I_2 post photolysis at 248 nm. Experimental conditions: $T = 296$ K; $P = 1.1$ Torr; $[CH_2I_2] = 1 \times 10^{12}$ molecule cm^{-3}; $[O_2] = 1 \times 10^{14}$ molecule cm^{-3}; [He] = balance; $\lambda_i = 118$ nm; $P_i = 3$ mJ pulse^{-1}; $P_{ex} = 100$ mJ pulse^{-1}; $\Delta t = 500$ μs.

The predominant peaks in the mass spectrum displayed in Fig. 2.6-2 are attributable to I^+, CH_2I^+ and $CH_2I_2^+$ at 127, 141 and 268 atomic mass units respectively. The mass spectrum of CH_2I_2, and the reaction kinetics of the reaction of $CH_2I + O_2$ are explored in Chapter Four.

References

1. A. Godman and R. Denney, *"Cambridge Illustrated Thesaurus of Chemistry"*, Consultant: Roger Norton, Cambridge University Press, Cambridge, 1985.
2. À. González-Lafont and J. M. Lluch, "Rate constants of gas-phase hydrogen abstraction reactions: a balance between the association and the abstraction dynamical bottlenecks", *Theochem.*, **709**, 35 – 43, 2004.
3. W. J. Bloss, D. M. Rowley, R. A. Cox and R. L. Jones, "Kinetics and Products of the IO Self-Reaction", *J. Phys. Chem. A.*, **105**, 7840 – 7854, 2001.
4. R. A. Cox, "*THalOz: Tropospheric Halogens – Effect on Ozone*", Project: EVK2-CT-2001-00104, Final Report: 1st Feb 2002 – 30th April 2005.
5. T. Gravestock, M. A. Blitz and D. E. Heard, "Kinetics study of the reaction of iodine monoxide radicals with dimethyl sulphide", *Phys. Chem. Chem. Phys.*, **7**, 2173 – 2181, 2005.
6. T. J. Dillon, R. Karunandan and J. N. Crowley, "The reaction of IO with CH_3SCH_3: products and temperature dependent rate coefficients by laser induced fluorescence", *Phys. Chem. Chem. Phys.*, **8**, 847 – 855, 2006.
7. E. P. Daykin and P. H. Wine, "Kinetics of the reactions of iodine monoxide radicals with nitric oxide and nitrogen dioxide", *J. Phys. Chem.*, **94**, 4528 – 4535, 1990.
8. D. Hoelscher and R. Zellner, "LIF study of the reactions of the IO radical with NO and NO2 over an extended range of temperature and pressure", *Phys. Chem. Chem. Phys.*, **4**, 1839 – 1845, 2002.
9. J. Troe, "Analysis of the temperature and pressure dependence of the reaction HO + NO_2 + M ↔ $HONO_2$ + M", *Int. J. Chem. Kinet.*, **33**, 868 – 877, 2001.
10. Sander S.P., Friedl R.R., Ravishankara A.R., Golden D.M., Kolb C.E., Kurylo M.J., Huie R.E., Orkin V.L., Molina M.J., Moortgat G.K. and B.J. Finlayson-Pitts, *"Chemical Kinetics and Photochemical Data for Use in Atmospheric Studies: Evaluation Number 14"*, JPL Publication 02-25, February 1, 2003.
11. C. H. Hearn, E. Turcu and J. A. Joens, "The near UV absorption spectra of dimethyl sulphide, diethyl sulphide and dimethyl disulfide at T = 300 K", *Atmos. Env.*, **24**, 1939 – 1944, 1990.
12. S. M. Newman, W. H. Howie, I. C. Lane, M. R. Upson and A. J. Orr-Ewing, "Predissociation of the $A^2\Pi_{3/2}$ state of IO studied by cavity ring-down spectroscopy", *J. Chem. Soc. Faraday Trans.*", **94**, 2681 – 2688, 1998.
13. J. Luque and D.R. Crosley, "LIFBASE: database and spectral simulation program (version 1.5)", *SRI* International, Report MP 99-009, 1999.
14. P. S. Stevens, J. H. Mather and W. H. Brune, "Measurement of tropospheric OH and HO_2 by laser-induced fluorescence at low pressure", *J. Geophys. Res.*, **99**, 3542-3557, 1994.
15. A. Hofzumahaus, U. Aschmutat, M. Hessling, F. Holland and D. H. Ehhalt, "The measurement of tropospheric OH radicals by laser-induced fluorescence spectroscopy during the POPCORN field campaign", *Geophys. Res. Lett*, **23**, 2541-2544, 1996.
16. D. J. Creasey, P. A. Halford-Maw, D. E. Heard, M. J. Pilling and B. J. Whitaker, "Implementation and initial deployment of a field instrument for measurement of OH and HO_2 in the troposphere by laser-induced fluorescence", *J. Chem. Soc., Faraday Trans.*, **93**, 2907-2913, 1997.
17. Y. Kanaya, Y. Sadanaga, J. Hirokawa, Y. Kajii and H. Akimoto, "Development of a ground-based LIF instrument for measuring HO_x radicals: Instrumentation and calibrations", *J. Atmos. Chem.*, **38**, 73-110, 2001.
18. sccm = standard cubic centimetre per minute (at 0 °C and 1 bar).
19. M. D. Wheeler, S. M. Newman, T. Ishiwata, M. Kawasaki and A. J. Orr-Ewing, "Cavity ring-down spectroscopy of the $A^2\Pi_{3/2} – X^2\Pi_{3/2}$ transition of BrO", *Chem. Phys. Lett.*, **285**, 346 – 351, 1998.

20. A. O'Keefe and D. A. G. Deacon, "Cavity ring-down optical spectrometer for absorption measurements using pulsed laser sources", *Rev. Sci. Instrum.*, 59, 2544 – 2551, 1988.
21. B. Alicke, K. Hebestreit, J. Stutz and U. Platt, "Iodine oxide in the marine boundary layer", *Nature*, 397, 572 – 573, 1999
22. B. J. Allen, G. McFiggans and J. M. C. Plane, "Observations of iodine monoxide in the remote marine boundary layer", *J. Geophys. Res.*, 105, 14363 – 14369, 2000.
23. M. A. Blitz, A. Goddard, T. Ingham and M. J. Pilling, "Time-of-Flight Mass Spectrometry for time-resolved measurements", submitted to *Rev. Sci. Instrum.* 2006.

Chapter Three: A Spectroscopic Investigation of the IO Radical Relating to the Development of an LIF Instrument for its Detection in the Atmosphere

3.1 Introduction

As discussed in Chapter One, the IO radical plays an important role in the tropospheric chemistry of the marine atmosphere. However, a major deficiency in our quantitative understanding of its importance arises from the lack of an *in situ* detection method for determining the ambient concentration of IO. Local IO concentrations, particularly in coastal regions, may be significantly underestimated by differential optical absorption spectroscopy (DOAS) measurements due to local sources of iodine compounds emitted during periodic "bursts" of chemical activity. As important processes in the marine boundary layer (MBL), such as new particle formation and the oxidation of dimethylsulfide (DMS), are likely to be sensitive to localised concentrations of IO, the development of a point measurement detection method for IO is particularly desirable. In addition, the implementation of an *in situ* instrument would allow atmospheric measurements of IO to be extended into largely unexplored regions, such as over the open ocean and in the upper troposphere – lower stratosphere (UTLS), by deployment of the instrument on boat or aeroplane.

In a previous paper[1], we assessed the feasibility of an LIF instrument for the ambient detection of IO and estimated a theoretical limit of detection (LOD) of < 0.004 ppt (< 10^5 molecule cm^{-3}), more than sufficient for the detection of IO in the atmosphere. However, in that work, various assumptions had to be made with regards to certain physical properties of IO (and the physical conditions of the experiment), specifically: the wavelength dependence of the fluorescence intensity; and the rate of excited state fluorescence quenching. The aim of the work reported in this chapter was to investigate, and quantify, these previously unreported parameters and to reassess the theoretical sensitivity of an IO LIF field instrument, which has ultimately led to its construction and implementation in a field campaign (RHaMBLE – Reactive Halogens in the Marine Boundary Layer Experiment) in the late summer of 2006.

3.2 The Atmospheric Detection of Ambient Species by LIF

Laser induced fluorescence (LIF) is a suitable *in situ* detection method for atmospheric species due to its high sensitivity and selectivity, and has been extensively employed for the measurement of OH and HO_2 in the atmosphere[2-5]. In addition to the fundamental molecular properties discussed in Chapter Two, the viability of an atmospheric LIF instrument often relies on the molecule of interest exhibiting extensive rotational structure, so that a correction for the

background contribution to the fluorescence signal from other absorbing species can be applied by taking "on-line" and "off-line" measurements. In a typical atmospheric LIF experiment the fluorescence signal, observed when the laser is tuned to the peak of a specific LIF transition of the species of interest, is averaged over a specified time period. This type of data point is known as an on-line measurement, and the averaging time, t, defines the temporal resolution of the instrument. To obtain an off-line data point, the laser wavelength is tuned to a nearby frequency where no absorption by the species of interest occurs, and the background fluorescence signal is averaged (usually over the same time period). The difference between the on-line and off-line measurements yields the LIF signal due to the species of interest, which is related to its atmospheric concentration by a calibration factor, C_x. The LOD of an atmospheric LIF instrument is given by E. 3.2-1

$$[LOD] = \frac{S/N}{(C_X/P)P}\sqrt{\left(\frac{1}{m}+\frac{1}{n}\right)}\sqrt{\frac{1}{t}(S_{lb}+S_{sb}+S_{ds})} \qquad \text{E. 3.2-1}$$

where, S/N is the signal-to-noise ratio of the instrument; P is the laser power; m is the number of on-line measurement points; n is the number of off-line measurement points; S_{lb} is the laser background; S_{sb} is the solar background; and S_{db} is the dark-count background of the PMT. The calibration factor, C_x is given by E. 3.2-2

$$C_x = \frac{S_x}{[X]} \qquad \text{E. 3.2-2}$$

where, S_x is the LIF signal observed for a known concentration of the species of interest, [X]. C_x can therefore be determined experimentally, providing a quantifiable source of X is available, or theoretically by E. 3.2-3[4]

$$C_X = \left(\frac{B_{if}}{c^2}\right)\left(\frac{4\ln(2)}{\pi}\right)^{1/2} P\frac{1}{\sqrt{\Delta\nu_D{}^2+\Delta\nu_L{}^2}}\frac{N_{(v'',J'')}}{N}\ell\varepsilon\eta Tf_{gate}\phi\left(\frac{\rho_{in}}{\rho_{out}}\right)\gamma_{sampling} \qquad \text{E. 3.2-3}$$

Notable parameters in E. 3.2-3 (all parameters in E. 3.2-3 are discussed in greater detail in section 3.6.1) are: B_{if} – the Einstein coefficient for absorption of the LIF transition; $\left(\sqrt{\Delta\nu_D{}^2+\Delta\nu_L{}^2}\right)^{-1}$ – a term relating to the overlap of the laser spectral linewidth and the natural linewidth of the species of interest; $\frac{N_{(v'',J'')}}{N}$ – the fractional population of the electronic

groundstate rotational level(s) excited by the laser; ηT – essentially the fraction of fluorescence detected by the PMT; and ϕ – the fraction of excited state population undergoing fluorescence (or the fluorescence quantum yield).

In the work of Bloss *et. al.*[1], assumptions had to be made with regards to the parameters, ηT and ϕ, and the aim of the work reported in this chapter is to quantify the processes relating to these terms *via* a spectroscopic study of IO. The information obtained is used for a re-evaluation of the theoretical sensitivity of an IO LIF field instrument, its optimum operating conditions, and its construction, calibration and deployment.

3.3 Spectroscopy Relating to the LIF Detection of IO

As LIF is a spectroscopic technique, and the interpretation of the results presented in this chapter requires some spectroscopic knowledge, a relatively brief discussion of the spectroscopy of IO (relating to its detection by LIF) is pertinent here.

As discussed in Chapter Two, a molecular electronic transition relies on the groundstate absorption of radiation resulting in the population of a bound electronically excited state. The electronic groundstate of IO is described by the term symbol, $X^2\Pi$. A term symbol is a short hand description of the spin and orbital angular momentum of the uppermost occupied molecular orbital, which is most descriptive of the chemical properties of a species. In the term symbol, $X^2\Pi$, the X denotes that the electronic state is the groundstate; the ^{2} denotes the component of the spin angular momentum along the internuclear axis, which is given by the multiplicity $2S+1$, and indicates that the uppermost occupied molecular orbital contains an unpaired electron (the spin of an electron, S, is $^1/_2$); and the Π denotes the axial component of the electronic orbital angular momentum, which is 1 for a Π state. In a diatomic molecule, the axial components of the spin, Σ, and orbital, Λ, angular momentum couple to give the total angular momentum along the internuclear axis, Ω, and as the there are $2S+1$ components of Σ, there are also $2S+1$ components to Ω. Thus a $^2\Pi$ state is split into two multiplets with total angular momentum along the internuclear axis of $^1/_2$ and $^3/_2$. The difference in energy between multiplets depends on the strength of interaction between the axial components of the orbital and spin angular momentum, and is known as the spin-orbit coupling constant, A, which increases rapidly with an increasing number of electrons. In IO, the axial components of the spin and orbital angular momentum are strongly coupled, resulting in a relatively large spin-orbit coupling constant of 2091 cm^{-1} [6]. At room temperature, states separated in energy by 2091 cm^{-1} have a population ratio of $\sim 4 \times 10^{-5}$, thus the $X^2\Pi_{3/2}$ multiplet can be regarded as the "true" groundstate of IO (note that IO has an inverted groundstate as the $^2\Pi_{3/2}$ multiplet is the lower in energy). It should also be noted that all electronic states possessing orbital angular momentum

are doubly degenerate, and can be separated in energy by interaction of molecular rotations with the orbital angular momentum – a process known as Λ-type doubling. However, the splitting of states by Λ-type doubling is very small (fractions of a wavenumber), and is negligible for the $X^2\Pi_{3/2}$ state of IO in comparison to the spectral linewidth of most lasers[7,8].

The selection rules governing the allowed electronic transitions of a diatomic molecule are principally determined by the various ways in which the different types of angular momentum couple together to form the total angular momentum, $\boldsymbol{J}$. For IO, or any diatomic molecule possessing non-zero orbital angular momentum and more than a few electrons, the coupling of the different types of angular momentum is best described by Hund's case *a* [9], which is depicted in Fig. 3.3-1. In Hund's case *a*, the spin, $\boldsymbol{S}$, and orbital, $\boldsymbol{L}$, angular momentum are strongly coupled to the internuclear axis (and only very weakly coupled to the nuclear rotation), and the total axial angular momentum, Ω, couples with the nuclear angular momentum, $\boldsymbol{N}$, to form the total angular momentum vector, $\boldsymbol{J}$. As, for IO (or any $^2\Pi$ state), Ω is half-integral and a component of $\boldsymbol{J}$, $\boldsymbol{J}$ also takes half-integer values of, $\boldsymbol{J} = \Omega, \Omega+1, \Omega+2, \ldots$ Hence, $\boldsymbol{J}$ cannot be less than Ω and the lowest rotational state of a $^2\Pi_{3/2}$ state is $\boldsymbol{J} = 3/2$.

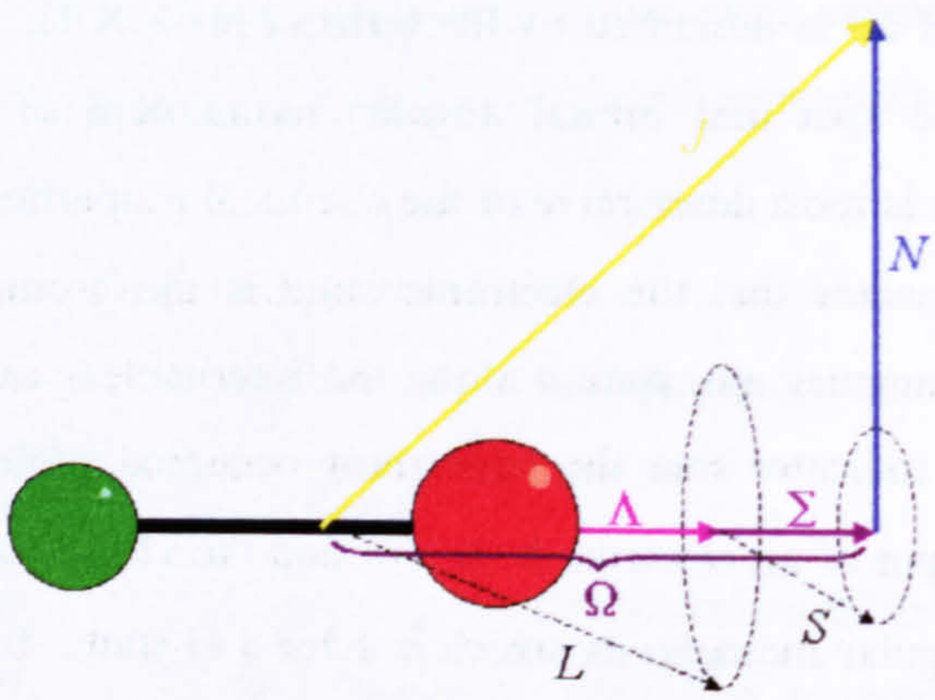

Fig. 3.3-1 – Vector diagram for Hund's case *a* (adapted from *Herzberg*[9]), displaying the coupling of the various angular momentum vectors for the $X^2\Pi$ state of IO. Note that the total spin, S, and orbital, L, angular momentum vectors are strongly coupled to the internuclear axis. The axial components of the spin, Σ, and orbital, Λ, angular momentum couple to form the total axial component of angular momentum, Ω, which couples with the nuclear rotation, N, to form the total angular momentum, J.

Hund's case *a* leads to the following selection rules with respect to an electronic transition:

i) $\Delta J = 0, \pm 1$ (with the restriction of $J = 0 \nrightarrow J = 0$)

ii) $\Delta\Lambda = 0, \pm 1$

iii) $\Delta\Sigma = 0$ (if both states are case *a*)

iv) $\Delta\Omega = 0, \pm 1$ (if $\Omega = 0$ in both states then $\Delta J = 0$ is forbidden)

Effectively no selection rules apply to concomitant changes in vibrational quantum number for an electronic transition ($\Delta v = 0, \pm 1, 2, 3, 4....$).

The lowest lying electronically excited state of IO accessible from the groundstate (and the only non-ionic electronically excited state of IO to have received experimental investigation) is the $A^2\Pi$ state. Thus the detection of IO by LIF is limited to transitions of the type, $A^2\Pi_{3/2}$ $(v',J') \leftarrow X^2\Pi_{3/2}$ (v'',J''). In consideration of the concomitant vibrational transition, it is clear that the LIF transition must originate in $v'' = 0$ (as all other vibrational levels will have negligible population at room temperature), but the chosen terminal vibrational level of the $A^2\Pi$ state requires more careful consideration. Electronic transitions are also known as vertical transitions – in that the initial internuclear separation of the excited state will have the same geometry as that of the groundstate. This is due to the Franck-Condon principle that states: *as nuclei are so much more massive than the electrons, an electronic transition takes place very much faster than the nuclei can respond.* An electronic transition will therefore most probably terminate in the vibrational level that has an internuclear separation, which is closest to that of the groundstate. However, several nearby vibrational states will also have an appreciable probability of having the same internuclear separation as the groundstate, hence transitions will occur to all vibrational states around this region (see Fig. 3.4-1). The absolute intensity of absorption is proportional to the square of the overlap of the ground and excited state wavefunctions, or the Franck-Condon Factor (FCF). Fig. 3.3-2 displays an absorption spectrum of the $A^2\Pi_{3/2} \leftarrow X^2\Pi_{3/2}$ transition of IO. In the absorption spectrum, the "banded" structure is due to the vibrational progression of $A^2\Pi_{3/2}$ $(v') \leftarrow X^2\Pi_{3/2}$ $(v'' = 0)$ transitions. As can be seen, the (4,0) vibrational band is most intense, indicating that the FCF of the (4,0) transition is largest. Thus we might assume that the (4,0) band of the $A \leftarrow X$ transition will be most favourable for the LIF detection of IO. However, the $A^2\Pi_{3/2}$ state of IO is known to be highly predissociative[7,10] – the excited state potential energy surface is crossed by repulsive, unbound, electronic potential energy surfaces that results in the dissociation of the I – O bond. Furthermore, the rate of predissociation is found to be dependent on the vibrational level (and rotational level for $v' = 2$) of the electronically excited state. Predissociation of the $v' = 1$, 4 and 5 vibrational levels is found to be extremely rapid, resulting in excited state lifetimes of 0.88, 0.59 and 0.09 ps respectively[10]. Indeed, the lifetime of these states is so short that the absorption spectra exhibit no rotational structure. Thus LIF transitions terminating in any of these vibrational levels are undesirable (and would essentially be undetectable), irrespective of the magnitude of the FCF's, as the fluorescence quantum yield will be negligibly small.

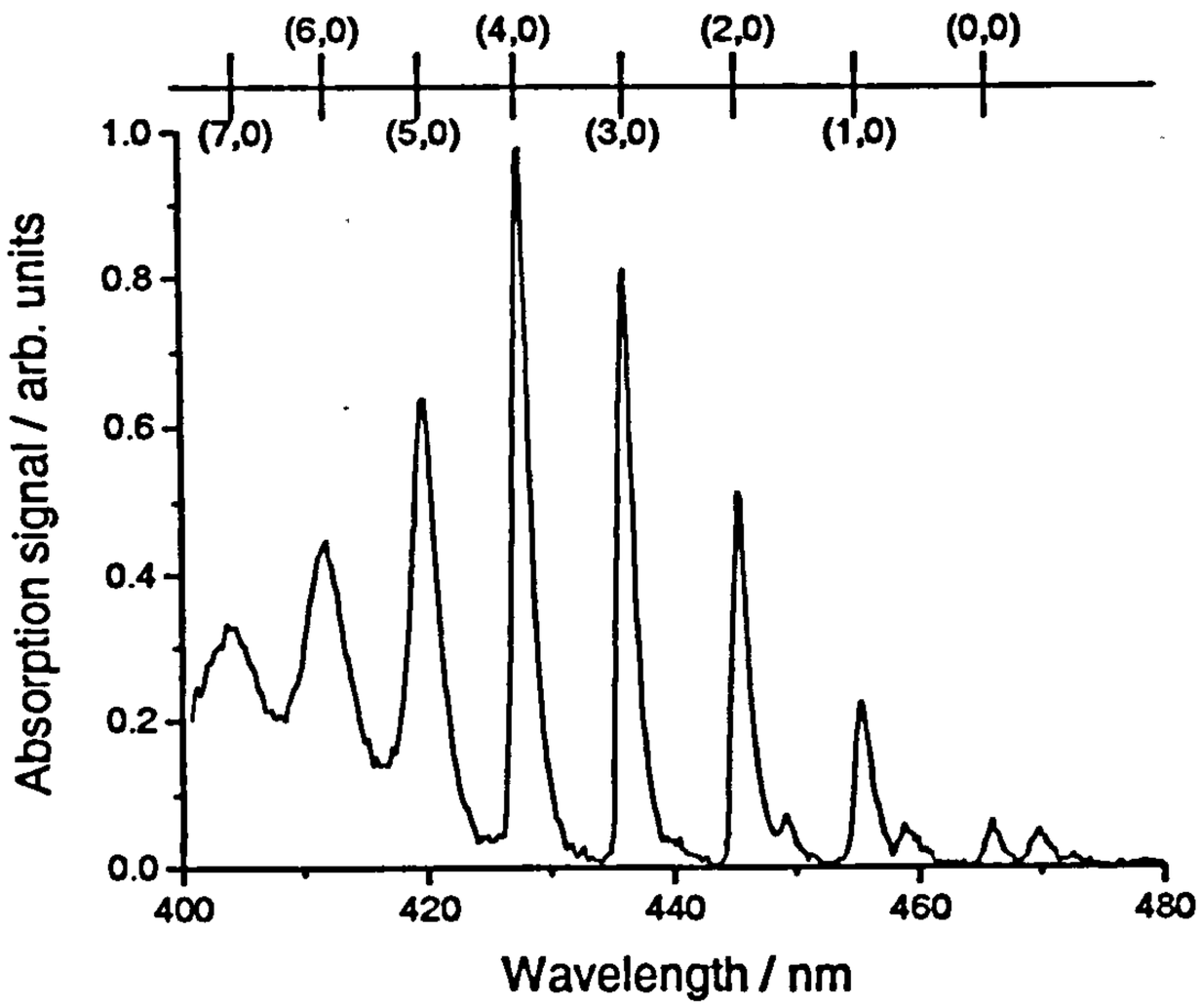

Fig. 3.3-2 – Assigned absorption spectrum of the $A^2\Pi_{3/2} \leftarrow X^2\Pi_{3/2}$ transition of IO. Only transitions originating from v' = 0 are labelled. The weak absorption bands that are evident to the red side of the (3,0), (2,0), (1,0) and (0,0) bands are the (4,1), (3,1), (2,1) and (1,1) hot bands respectively. The absorption spectrum was kindly provided by Dr. W. J. Bloss from the University of Leeds.

The v' = 0, 2 and 3 vibrational levels exhibit rotational structure and v' = 0 and 3 have *J'*-independent lifetimes of 17.6 and 6.6 ps respectively[10]. The lifetime of v' = 2 is found to be rotational level dependent, varying linearly with *J'*(*J'*+1) (rotational energy) from ~ 1 ns in *J'* = 1.5 to ~ 15 ps in *J'* = 50.5 [10]. Thus, although the FCF for the (3,0) vibrational transition is greater than that of the (2,0) band (and much greater than that of the (0,0) band – see Fig. 3.3-2), the (2,0) vibrational transition of the A ← X system of IO is the only rational choice for its LIF detection (where sensitivity is paramount, as in field measurements) due to the longer excited state lifetime (providing that the transition terminates in relatively low *J'* levels). Hence, the $A^2\Pi_{3/2}$ (v' = 2) ← $X^2\Pi_{3/2}$ (v'' = 0) transition possesses all requirements for the atmospheric measurement of IO by LIF – *viz.* relatively strong absorption, an appreciable fluorescence quantum yield and extensive rotational structure.

In selecting an appropriate rotational transition for the LIF detection of IO, several considerations should be made. For example, the ground rotational state should have a significant population. For a diatomic molecule, the rotational state of maximum population at temperature, T, can be approximated by E. 3.3-1 [9]

$$J_{max} = \sqrt{\frac{k_B T}{2hcB}} - \frac{1}{2} \qquad \text{E. 3.3-1}$$

where, B is the rotational constant (~ 0.34 cm^{-1} for the ground vibrational state of IO)[7]. From E. 3.3-1 it is found that the maximum rotational population of IO at 300 K is found in $J'' = 16.5$ (assuming the absorption cross-section is independent of J''). Thus transitions arising from this state will give maximum absorption intensity. However, as rotational transitions are limited by the selection rule, $\Delta J = \pm 1$ (the Q branch, $\Delta J = 0$, is of very weak intensity for a $^2\Pi - {}^2\Pi$ transition)[9] we must also consider the excited state lifetime of the rotational level populated by the LIF transition (as the fluorescence quantum yield will decrease with increasing J' due to enhanced predissociation). Thus there is a balance between the groundstate rotational population and the fluorescence quantum yield of the rotational level in the electronically excited state. Assuming (for now) no rotational energy transfer (RET) in the excited state, it is found that the optimum, single-line, LIF transition for the detection of IO is $P_1(5)$ (*i.e.* $A^2\Pi_{3/2}$ ($v' = 2$, $J' = 4.5$) ← $X^2\Pi_{3/2}$ ($v'' = 0$, $J'' = 5.5$)[11]. However, as the rotational constant of the $X^2\Pi_{3/2}$ $v'' = 0$ state is larger than that of the $A^2\Pi_{3/2}$ $v' = 2$ state (~ 0.27 cm^{-1})[10], it is found that the rotational spectrum of the (2,0) band has a vortex, or bandhead, in the R_1 branch, with a turning point in the spectrum where several rotational lines are separated by an energy that is smaller than the natural linewidth of the transitions. These transitions correspond to the $R_1(2)$ – $R_1(4)$ rotational lines, and the combined populations of these low J'' levels, combined with the longer fluorescence lifetime of the excited state rotational levels ($J' = 3.5 - 5.5$), means that the R_1 (2,0) bandhead yields optimum sensitivity for the LIF detection of IO. Fig. 3.3-3 displays a LIF spectrum of the (2,0) band of the A – X transition of IO, with a partial rotational assignment.

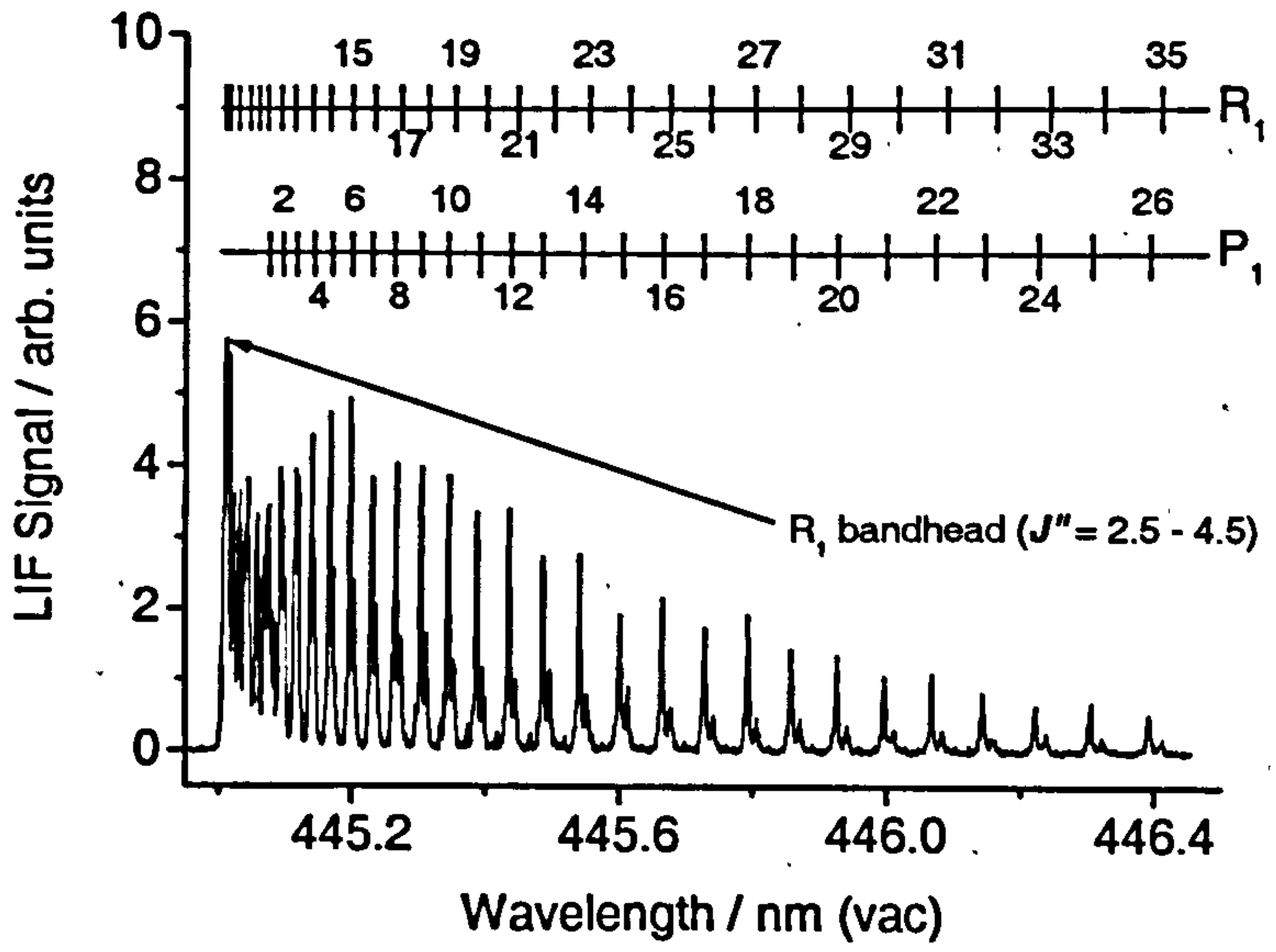

Fig. 3.3-3 – LIF spectrum of the (2,0) band of the $A^2\Pi_{3/2} \leftarrow X^2\Pi_{3/2}$ transition of IO. Experimental conditions: $P = 10$ Torr; $T = 296$ K; $[N_2O] = 1.1 \times 10^{15}$ molecule cm^{-3}; $[CH_3I] = 2.2 \times 10^{14}$ molecule cm^{-3}; $[N_2]$ = balance; $\lambda_{ex} = 193$ nm; $P_{ex} = 20$ mJ $pulse^{-1}$; $P_{pr} = 500$ μJ $pulse^{-1}$; $\Delta t = 200$ μs. Note that the rotational transitions are only partially labelled for clarity. As the J values of a $^2\Pi$ state are half-integral, the nomenclature of the rotational transitions is such that, for example, $R_1(27)$ corresponds to the rotational transition, $J' = 28.5 \leftarrow J'' = 27.5$, and $P_1(18)$ corresponds to the rotational transition, $J' = 17.5 \leftarrow J'' = 18.5$.

From the IO LIF spectrum, it can be seen that the most intense fluorescence signal is observed at the (2,0) bandhead, consistent with the spectroscopy of IO discussed above (note also that the most intense single-line transition is $P_1(5)$ – also in agreement with the above discussion). Further, as no rotational structure is present at the low wavelength side of the bandhead, this line is particularly suitable for the atmospheric detection of IO, where tuning the laser frequency on and off the IO transition is straightforward, and not subject to contamination by LIF from other close lying rotational transitions of IO.

3.4 Dispersed Fluorescence of the $A^2\Pi_{3/2}$ State of IO and the Determination of Relative FCF's for Various v' → v'' Transitions of the $A^2\Pi_{3/2} \rightarrow X^2\Pi_{3/2}$ System

Due to the rapid predissociation of the $A^2\Pi_{3/2}$ state, the fluorescence lifetime of IO is short ($\tau < 1$ ns) and fluorescence consequently occurs within the laser pulse employed to induce the LIF transition. Therefore, fluorescence of IO cannot be distinguished from laser radiation by temporal electronic gating of the PMT (as for OH), or by any other method, and must be collected off-resonantly (red-shifted to the laser wavelength) by the incorporation of interference filters. Fluorescence from the excited state of IO will occur in distinct "bands", corresponding to the wavelengths of the various v' = 2 → v'' transitions, and the relative intensity of the different bands will be governed by the appropriate FCF's. Although calculated FCF's for the (2,0) – (2,5) vibrational transitions of the $A^2\Pi_{3/2} \leftarrow X^2\Pi_{3/2}$ system of IO are reported in the literature[12], these calculations have only been compared to the results of one experimental study[13]. Further, fluorescence from v' = 2 of the $A^2\Pi_{3/2}$ state of IO has been reported to extend to wavelengths of up to 619.3 nm[14,15] (corresponding to the (2,10) vibrational transition), although only visual estimates of the fluorescence intensity could be achieved. As the collection of IO fluorescence in a LIF instrument requires the use of optical filters, which must successfully block light from both laser scatter and solar scatter (whilst transmitting the maximum fraction of IO fluorescence), knowledge of the relative intensity and wavelength of fluorescence from the different vibrational bands is required in order to design an appropriate filtering system. FCF's are also important from a fundamental point of view, allowing the comparison of theoretical and experimental data, and provide important information with respect to the potential energy surfaces of molecules. Thus an experimental investigation into the relative FCF's of various vibrational transitions in the $A^2\Pi_{3/2} \rightarrow X^2\Pi_{3/2}$ system of IO would provide a useful addition to the existing literature, and is the focus of this section.

A useful experimental technique for evaluating the relative FCF's of vibrational transitions is that of dispersed fluorescence. In a dispersed fluorescence experiment, the molecule of interest is excited from its groundstate to an excited vibrational level (often in an electronically

excited state, as in a typical LIF experiment) and the ensuing fluorescence is resolved as a function of wavelength by dispersion through a monochromator. For a large, polyatomic, molecule, the dispersed fluorescence spectrum will be relatively unstructured due to multiple transitions between a large density of states, and extracting useful information with regards to FCF's can be difficult. However, the bands of radiation corresponding to the vibrational progression of an electronic transition of a diatomic molecule can readily be resolved by a monochromator of moderate resolution.

Fig. 3.4-1 illustrates the fluorescence scheme of the $A^2\Pi_{3/2}$ ($v' = 2$) state of IO, once populated by laser radiation.

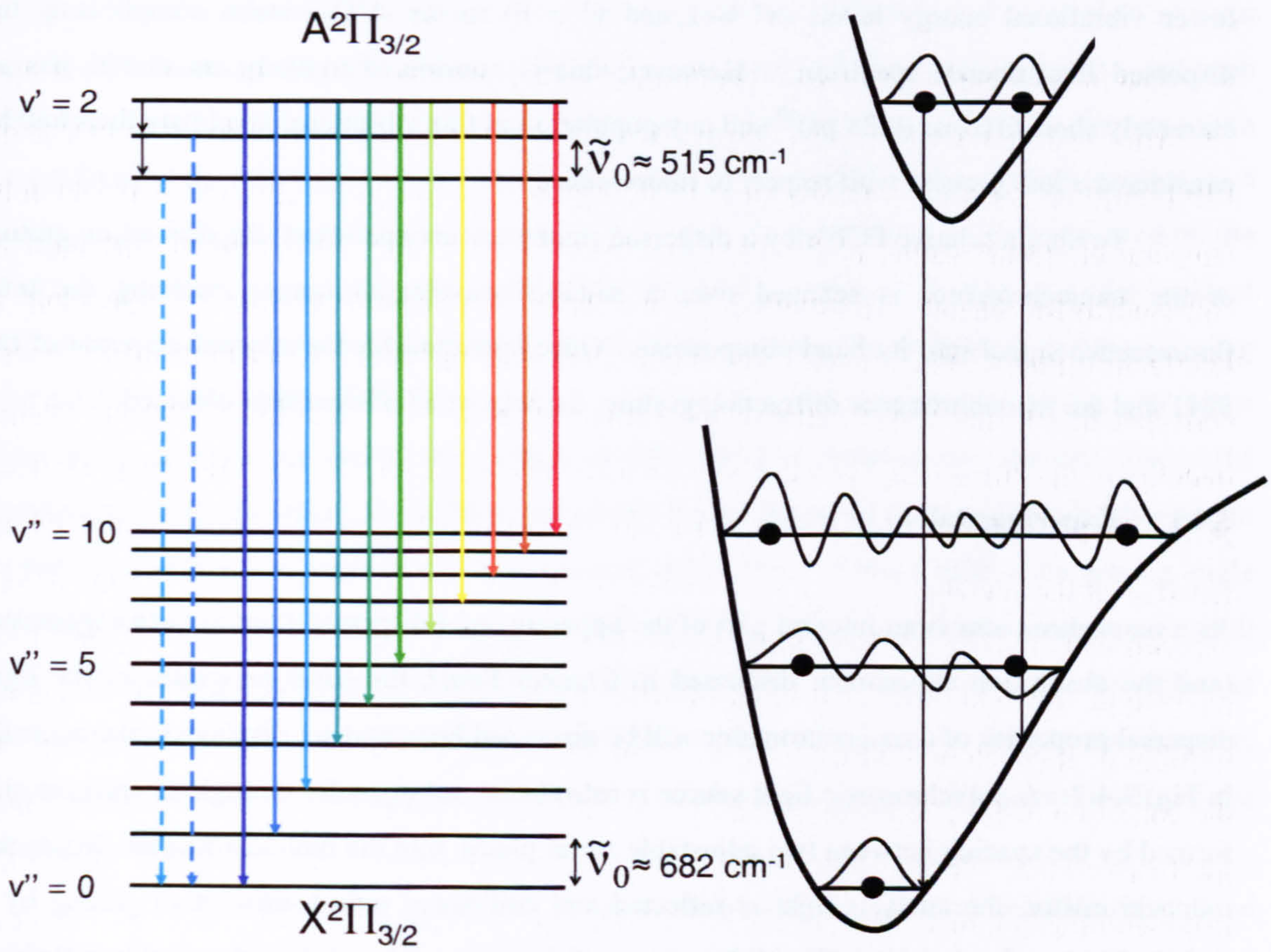

Fig. 3.4-1 – Fluorescence scheme for the $A^2\Pi_{3/2}$ ($v' = 2$) state of IO. The diagram on the left schematically represents the vibrational progression resulting from the $v' = 2 \rightarrow v''$ vibrational manifold (up to the (2,10) vibrational transition) of the $A^2\Pi_{3/2} \rightarrow X^2\Pi_{3/2}$ transition. The dashed arrows represent the possibility of fluorescence originating from other vibrational levels in the $A^2\Pi_{3/2}$ state, as a result of vibrational energy transfer (VET), although this is considered improbable for reasons discussed in the text. The potential energy surfaces of the ground and electronically excited states are represented on the right, and the approximate wavefunctions of several vibrational levels within them. Note that the solid black circles represent the most probable nuclear geometry for the different vibrational levels (*i.e.* the square of the wavefunction) and that these move towards the turning point of the potential energy curve, where the nuclear motion is slowest, as the vibrational quantum number increases.

Briefly, the excited state population can undergo collisional processes (RET, VET and quenching) and predissociation and fluorescence. Fluorescence will occur to all vibrational levels in the groundstate that have wavefunctions that exhibit appreciable overlap with that of the excited state (the (2,5) vibrational transition will have maximum intensity of those depicted in Fig. 3.4-1). The effective fluorescence intensity of any one vibrational band will be governed by the rate of radiative decay to the groundstate, which is governed by the FCF of the vibrational transition. Although VET, quenching and predissociation will result in an increased rate of excited state decay, reducing the fluorescence quantum yield, these processes will have an equal effect on all transitions of the vibrational manifold and the relative band intensities will be unaltered. Note that the occurrence of VET could result in fluorescence originating from lower vibrational energy levels (v' = 1 and v' = 0) in the $A^2\Pi_{3/2}$ state, complicating the dispersed fluorescence spectrum. However, this is considered unlikely, as v' = 1 has an extremely short lifetime (0.88 ps)[10] and any population of this vibrational level may therefore be considered a loss process with respect to fluorescence.

To obtain relative FCF's by a dispersed fluorescence experiment, the diffraction grating of the monochromator is scanned over a suitable wavelength range, resolving the total fluorescence signal into its band components. Once corrected for the spectral response of the PMT and the monochromator diffraction grating, the relative FCF's are thus obtained.

3.4.1 Experimental

As a monochromator is an integral part of the apparatus of a dispersed fluorescence experiment (and the absorption experiment discussed in Chapter Four), the basic principles of the light dispersal properties of a monochromator will be discussed here, and are displayed schematically in Fig. 3.4-2. A polychromatic light source is introduced orthogonally through an entrance slit, formed by the spacing between two adjustable metal plates, into the monochromator. Inside the monochromator, the analysis light is reflected and collimated onto a diffraction grating by a series of appropriate mirrors. The diffraction grating consists of a plate with a highly reflective Aluminium (or gold) coating. The grating surface (the blaze) contains many fine grooves, which are arranged in a tooth-like pattern, and as the collimated light source hits the grating, the light is reflected as from a point source from the long edge of the blaze, establishing a complex interference pattern from the wavefronts reflected from adjacent grooves on the grating. For any particular wavelength of light, constructive interference only occurs at specific angles (relative to the grating normal) given by the equation, $n\lambda = d\sin\theta$, where n is any integer, λ is the wavelength, d is the grating spacing (the length of a groove), and θ is the angle of diffraction. Although waves of a particular wavelength of light only become slightly out of

phase as the diffraction grating angle is moved away from the ideal, because there are so many grooves on the grating (> 300 per mm) the interference pattern is so chaotic that essentially no light intensity is transmitted at any other angle. The grating works most efficiently for first-order diffraction (n = 1), and the incident polychromatic radiation is thus resolved (or dispersed) into its individual components. The dispersed radiation is reflected from the grating onto another series of mirrors, which focus the light onto a second pair of slits at the monochromator exit. Although all wavelengths of light are reflected by the second series of mirrors, only light of a particular wavelength, to which the angle of the diffraction grating is set, will be focused onto the exit slit. All other wavelengths of light are dumped onto the back wall of the monochromator, which is blackened so as to minimise the internal scatter of radiation.

The absolute resolving power of a monochromator is defined by the number of grooves on the diffraction grating, the quality of the diffraction grating blaze, and the distance between diffraction grating and exit slits in the monochromator. However, experimentally, the resolution is predominantly determined by the exit (and entrance) slit widths of the monochromator, as a range of wavelengths will be focused onto the exit slit. The wavelength of light detected by the PMT is primarily governed by the angle of the diffraction grating with respect to the incident radiation. Thus, a dispersed spectrum is obtained by scanning the diffraction grating (altering the relative angle of the diffraction grating with respect to the incident radiation), and hence constantly changing the central wavelength of light which is focused onto the exit slits of the monochromator. However, it should be noted that higher orders of light will also be detected at a particular diffraction angle due to the equation, $n\lambda = d\sin\theta$. Thus a diffraction grating angle corresponding to a first-order diffraction of 600 nm light, will also transmit second-order (300 nm) diffracted light and third-order (200 nm) diffracted light, although first-order diffraction is usually most intense. In experiments where higher orders of diffraction may be problematic, appropriate filtering of the incident radiation can be employed prior to the entrance slits of the monochromator.

The monochromator employed in this study (Acton SpectraPro-2358) has three diffraction gratings, arranged on a triangular mount (as depicted in Fig. 3.4-2), of 300, 600 and 1200 grooves/mm, which are operated under computer control. For the 1200 grooves/mm diffraction grating, the absolute resolution of the spectrometer is 0.1 nm. The experimental resolution is controlled by altering the entrance and exit slit widths of the monochromator, which can be manually varied between ~ 10 and 3000 μm.

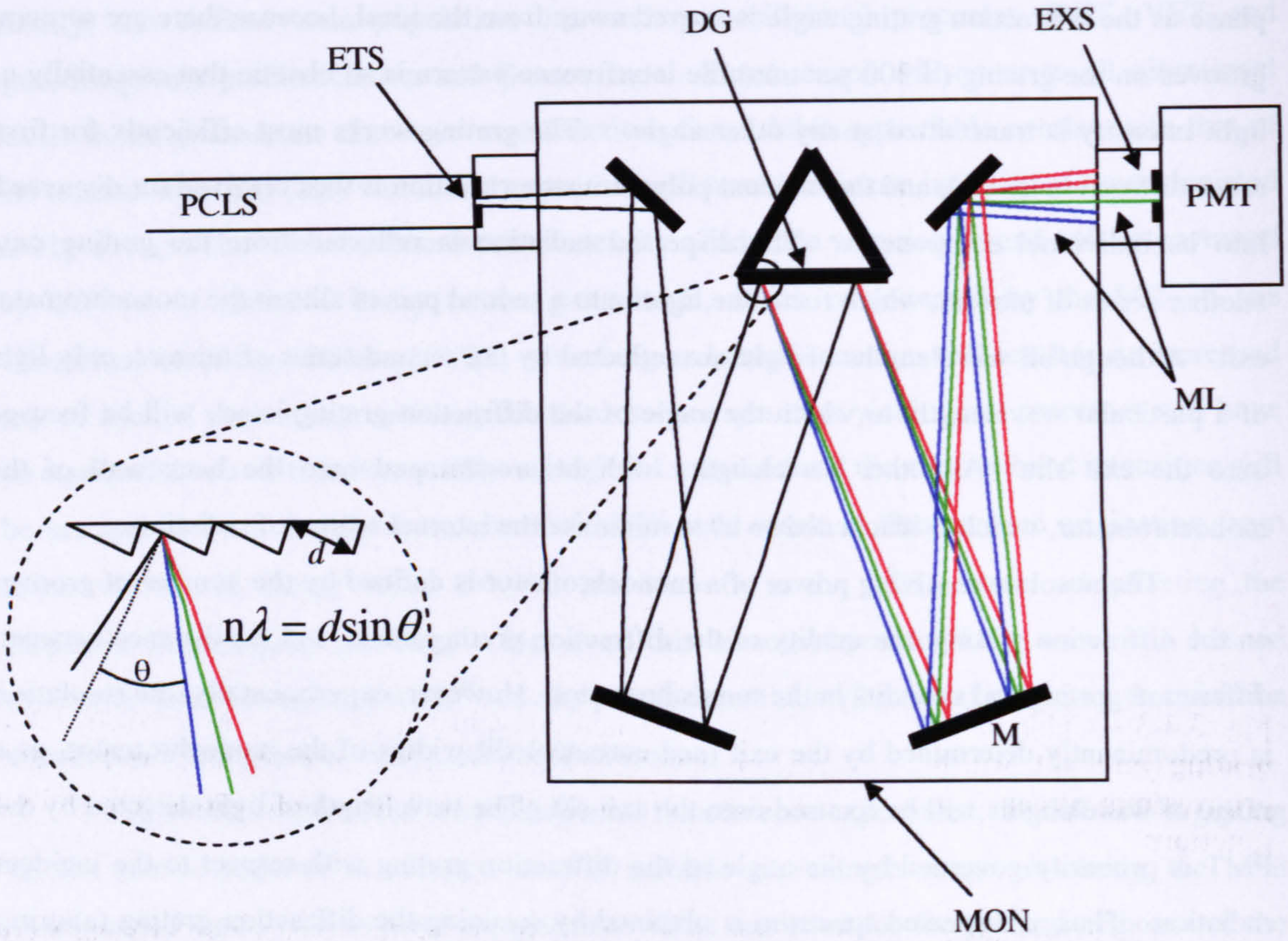

Fig. 3.4-2 – Schematic diagram showing the principal workings of a monochromator and diffraction grating. The inset displays a microscopic schematic of the diffraction grating blaze. PCLS = polychromatic light source, ETS = entrance slits, DG = diffraction grating, EXS = exit slits, PMT = photomultiplier tube, ML = monochromatic light, M = mirror, MON = monochromator housing.

In order to calibrate the resolution of the monochromator, light from a low pressure Hg Pen-Ray lamp was directed through the monochromator and the (full width at half maximum) FWHM of an Hg atomic emission line at 435.8335 nm was determined as a function of both monochromator slit width and diffraction grating. Note that the line width of an atomic emission line at low pressure is sufficiently small (a fraction of a pm), that the measurement of its FWHM is strictly indicative of the monochromator resolution. The monochromator grating was scanned at a constant speed over the Hg line, and the light intensity detected by the PMT was monitored on an oscilloscope. The time taken for the diffraction grating to scan over the FWHM of the signal observed by the PMT was converted into a wavelength range (by the scan speed of the experiment) to yield the resolution of the monochromator. The results are displayed in Fig. 3.4-3.

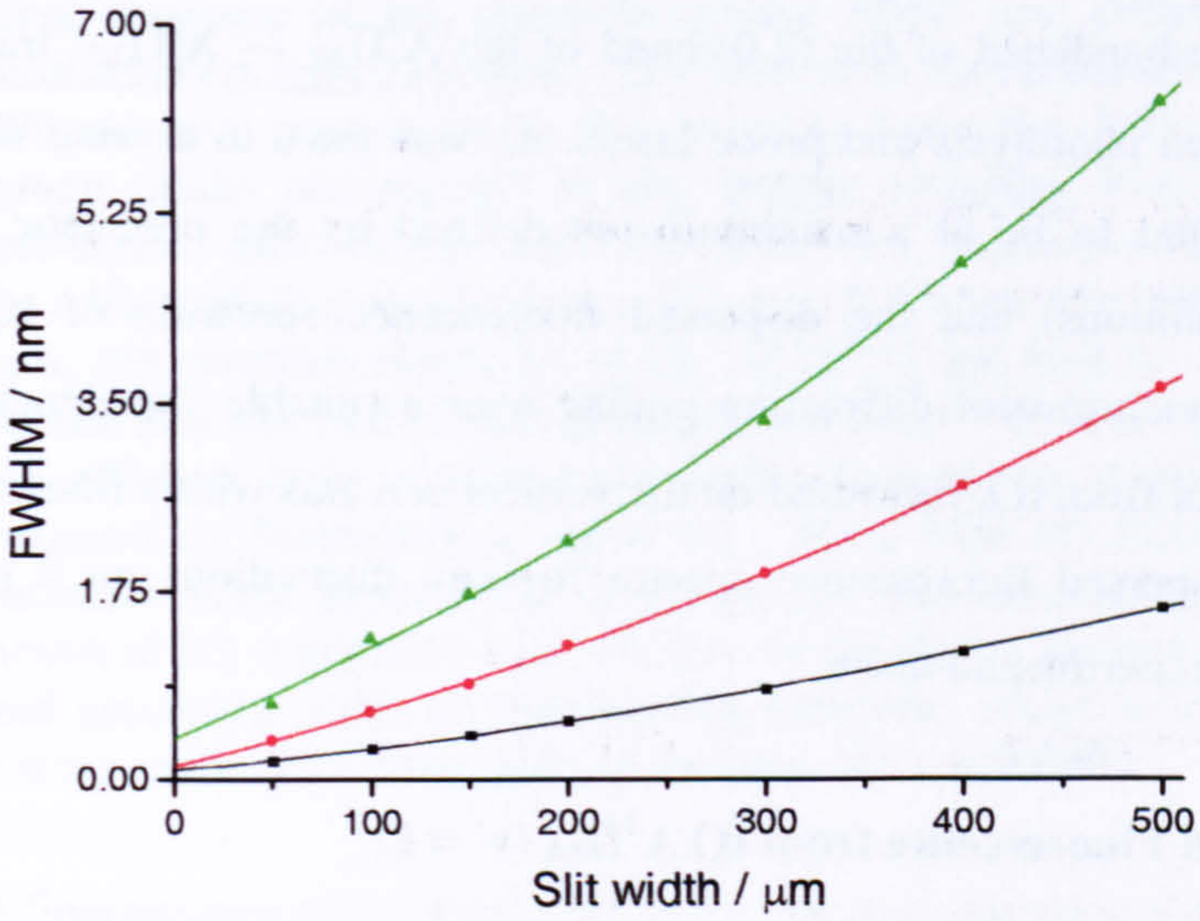

Fig. 3.4-3 – Calibration curves of monochromator resolution as a function of diffraction grating and slit width. Diffraction grating: black = 1200 grooves/mm, red = 600 grooves/mm, green = 300 grooves/mm. The data are fitted to second order polynomial functions.

The experimental apparatus employed for the dispersed fluorescence experiment were essentially the same as that described in section 2.4, with the notable exception that the reaction cell had two additional horizontal axes (which were both 45° with respect to the laser axes), one of which was used as the dispersed fluorescence axis. The total fluorescence signal from IO was, *via* the standard procedure, monitored by a PMT at the top port of the vertical cell axis, and fluorescence was collimated and softly focused into the monochromator by two plano-convex lenses situated in a cylindrical tube connecting the reaction cell to the monochromator entrance slit. Both ends of the optics tube were surrounded by black cloth to minimise the amount of scattered room light entering the monochromator. An Hg Pen-Ray lamp was placed outside the reaction cell, opposite the monochromator on the dispersed fluorescence axis, in order to provide a calibration source for the monochromator wavelength. The fourth horizontal reaction cell axis was redundant. The laser system consisted of an Excimer laser operating on an ArF exciplex at 193 nm, and an Nd:YAG pumped dye laser operating on a Coumarin 2 dye. The photolysis energy was typically 20 mJ pulse^{-1}, and the excitation energy was ~ 0.5 mJ pulse^{-1} at 445 nm. For all experiments described in this section, IO was generated by the reaction of O (^{3}P) atoms with CH_3I. Groundstate O atoms were generated by the 193 nm photolysis of N_2O in an excess of N_2 [to quench the initially formed O (^{1}D)]. All reagents were purified and administered to the reaction vessel by the normal procedure, and all concentrations of reagents were calculated from the appropriate mass flow rates and total reaction cell pressure. All experiments were conducted at a room temperature of 296 K.

To record a dispersed fluorescence spectrum, the frequency of the probe laser was tuned to the peak of the bandhead of the (2,0) band of the $A^2\Pi_{3/2} \leftarrow X^2\Pi_{3/2}$ transition of IO. The delay time between photolysis and probe lasers, Δt, was fixed to a value where the LIF signal from IO was found to be at a maximum (as defined by the precursor concentrations and experimental conditions) and the dispersed fluorescence spectrum of IO was obtained by scanning the monochromator diffraction grating over a suitable wavelength range. The total fluorescence signal from IO, measured on the vertical cell axis with a filtered PMT, was used to normalise the dispersed fluorescence spectra for any fluctuations on a point-to-point basis, originating from experimental noise.

3.4.2 Dispersed Fluorescence from IO $A^2\Pi_{3/2}$ (v' = 2)

For modest concentrations of IO (~ 10^{13} molecule cm^{-3}) the dispersed fluorescence spectrum originating from the $A^2\Pi_{3/2}$ (v' = 2) state of IO was readily observed. While the diffraction grating of the monochromator was scanned at constant speed, the raw analogue output from the monochromator PMT was sent to an oscilloscope, integrated by a boxcar averager and stored on a control PC, allowing the fluorescence intensity of IO to be determined as a function of wavelength. The integration gate of the boxcar was set to capture all fluorescence from IO (*i.e.* positioned over the entire probe laser pulse). Fig. 3.4-4 displays a dispersed fluorescence spectrum of IO thus obtained.

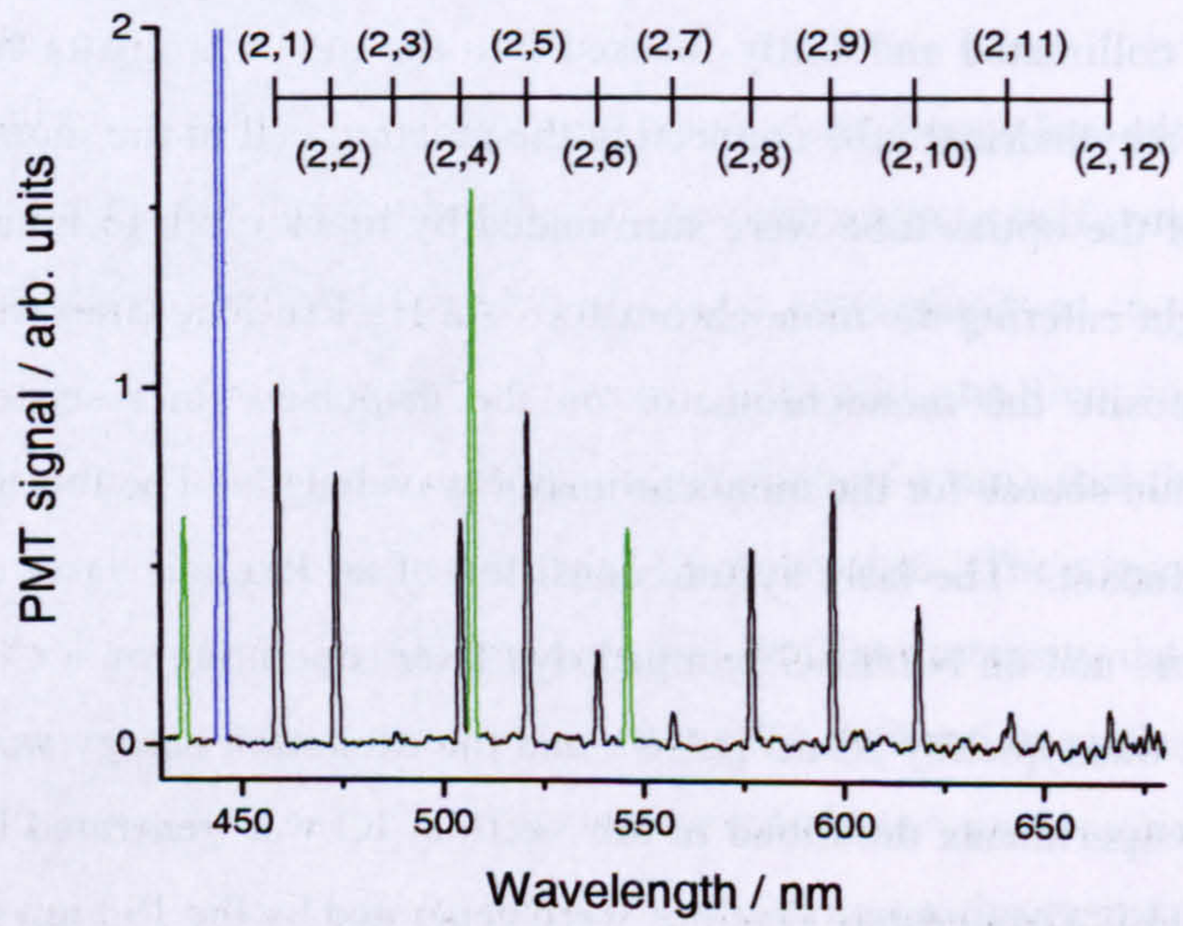

Fig. 3.4-4 – Dispersed fluorescence spectrum of the $A^2\Pi_{3/2}$ (v' = 2) state of IO. Experimental conditions: P = 50 Torr; T = 296 K; $[CH_3I]$ = 1.1 × 10^{15} molecule cm^{-3}; $[N_2O]$ = 1.2 × 10^{16} molecule cm^{-3}; $[N_2]$ = balance; Δt = 170 μs; λ_{pr} = 444.890 nm; P_{pr} = 500 μJ $pulse^{-1}$; λ_{ex} = 193 nm; P_{ex} = 20 mJ $pulse^{-1}$; M_g = 1200 grooves/mm; M_r = 0.55 nm; M_{ss} = 10 nm/min. Note that the dispersed fluorescence spectrum is normalised for the

total fluorescence signal of IO (which varied by < 10 % over the entire experiment) and also for the spectral response of the monochromator PMT and diffraction grating, as defined by the manufacturers specifications. The blue peak corresponds to the probe laser radiation at 444.890 nm and, consequently, fluorescence from the (2,0) band could not be observed. The green peaks correspond to Hg atomic emission lines at 435.8335 and 546.0750 nm (first-order diffraction) and 507.3042 nm (second-order diffraction of 253.6521 nm line). Although the second-order line is ~ 2.5 times the intensity of the first-order emission lines, the absolute intensity of the 253.6521 nm line is ~ 30 times greater than those at ~ 436 and 546 nm (which are of equal intensity)[16], thus first-order diffraction is ~ 12 times more efficient than second-order diffraction in the monochromator. The black peaks correspond to fluorescence from IO. Note that IO fluorescence was not observed for vibrational bands beyond the (2,12) band. The wavelength of the dispersed fluorescence spectrum of IO was calibrated relative to the three Hg emission lines and the laser radiation, and assuming a linear relationship between monochromator scan speed and diffraction grating angle (from the calibration plot, $R^2 = 0.999995$).

The intensity of IO fluorescence was normalised for the spectral response of the monochromator PMT and diffraction grating (which had a combined effect of altering the IO fluorescence signal by a factor of ~ three at the longest wavelength studied), and the total fluorescence signal of IO as recorded by a second channel on the boxcar averager. Fluorescence from the $A^2\Pi_{3/2}$ ($v' = 2$) state of IO was observed to extend up to a wavelength of 666.3 nm, attributed to the (2,12) vibrational band. All structure assigned to the dispersed fluorescence spectrum of IO was confirmed by recording "background" dispersed fluorescence spectra, in which IO was removed from the reaction cell by removing the O atom source (N_2O). With the exception of the laser radiation and the Hg emission lines, no other structure was present in the background spectra.

As a result of the short fluorescence lifetime of IO, fluorescence from the resonant transition (the (2,0) band) could not be observed due to the intense laser radiation. In order to overcome this limitation of the experiment, fluorescence from the (2,0) band was observed by LIF excitation in the (2,1) "hot band". As the vibrational constant of the $X^2\Pi_{3/2}$ state of IO is relatively small ($\nu_0 = 681.7$ cm^{-1})[8], a non-negligible equilibrium population exists in $v'' = 1$ at room temperature (~ 3 %). Thus if IO is excited from $v'' = 1 \rightarrow v' = 2$ in the electronic transition, the resonant transition is the (2,1) vibrational band, and fluorescence from the (2,0) band can be observed blue-shifted relative to the laser radiation. To excite IO in the (2,1) band the probe laser radiation was changed to a wavelength of ~ 459 nm by operating the probe laser on a Coumarin 47 dye. In order to sufficiently prevent the detection of probe laser radiation by the PMT (monitoring the total fluorescence signal of IO), the cut-on wavelength of the colour-glass interference filter had to be increased to 515 nm. Fig. 3.4-5 displays an LIF spectrum of part of the (2,1) band of IO, recorded after making the appropriate experimental changes.

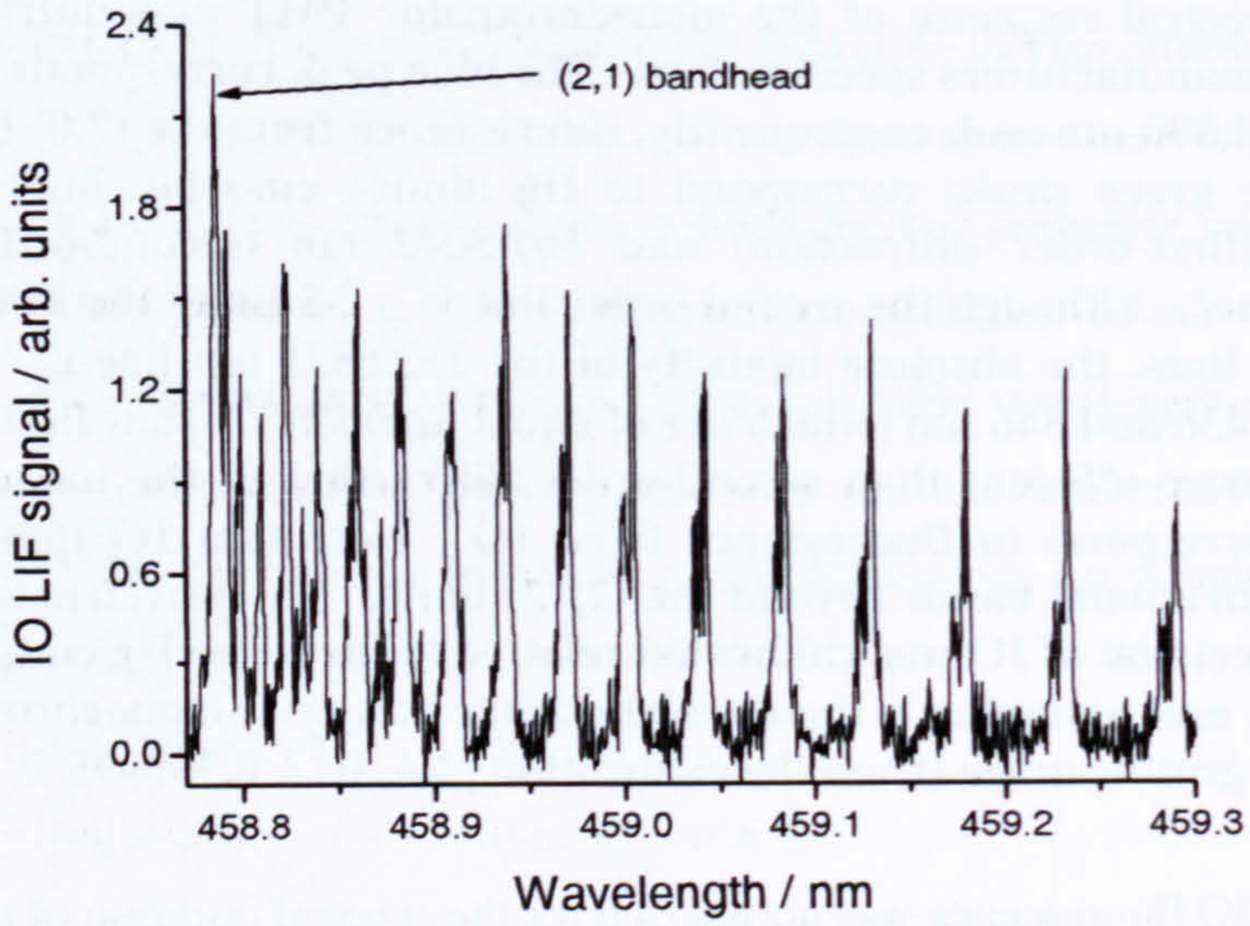

Fig. 3.4-5 – LIF spectrum of low *J''* region of the (2,1) $A^2\Pi_{3/2} \leftarrow X^2\Pi_{3/2}$ transition of IO. Experimental conditions: P = 50 Torr; T = 296 K; $[CH_3I] = 1.9 \times 10^{15}$ molecule cm^{-3}; $[N_2O] = 2.2 \times 10^{16}$ molecule cm^{-3}; $[N_2]$ = balance; Δt = 70 μs; P_{pr} = 500 μJ $pulse^{-1}$; λ_{ex} = 193 nm, P_{ex} = 20 mJ $pulse^{-1}$, PRF = 5 Hz. Note that the line on the extreme left of the LIF spectrum is the (2,1) R_1 bandhead at 458.736 nm.

In order to determine the relative intensity of (2,0) fluorescence, the dispersed fluorescence experiment was repeated by exciting IO at the (2,1) R_1 bandhead of the $A^2\Pi_{3/2} \leftarrow X^2\Pi_{3/2}$ transition. Fig. 3.4-6 displays the resulting dispersed fluorescence spectrum.

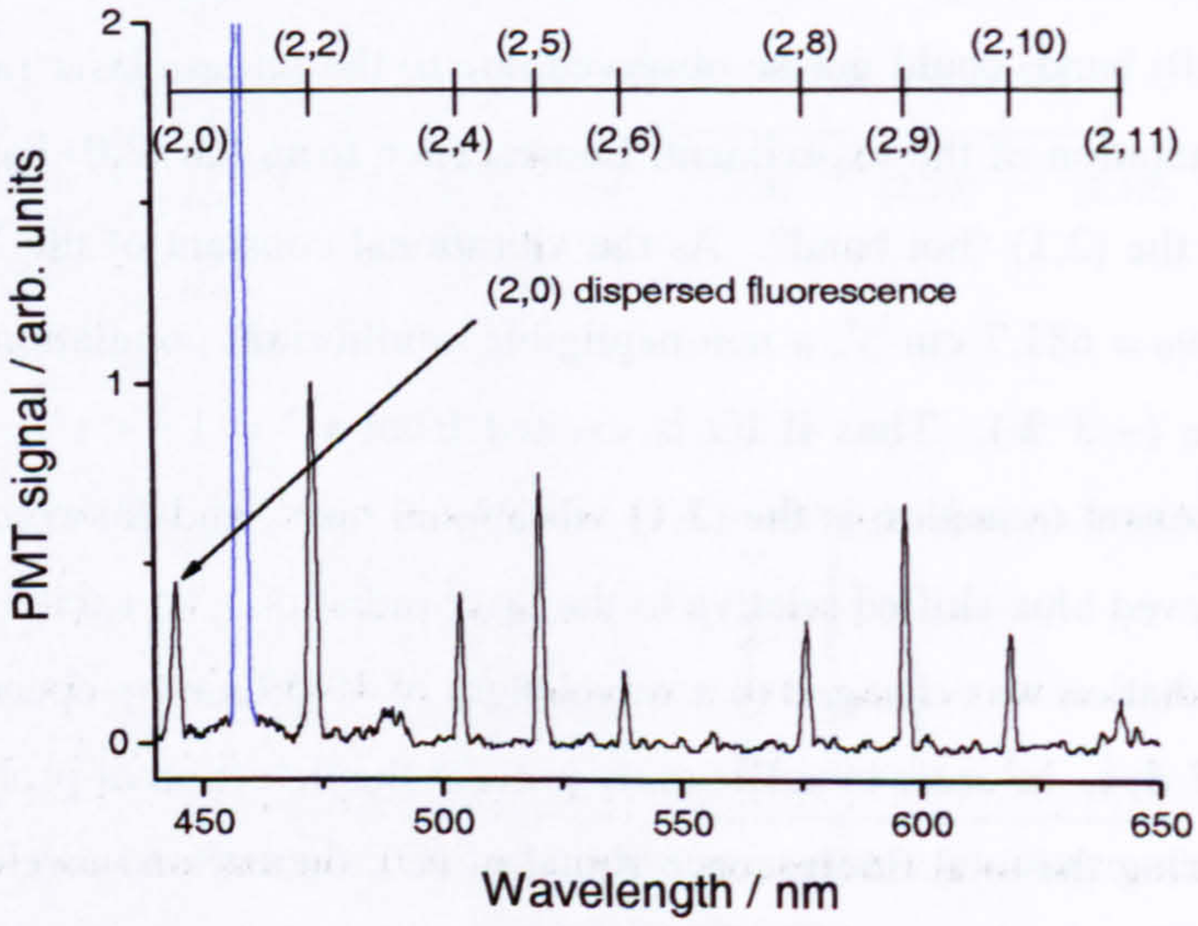

Fig. 3.4-6 – Dispersed fluorescence spectrum of the $A^2\Pi_{3/2}$ (v' = 2) state of IO, post excitation in the (2,1) band at 458.736 nm. Experimental conditions: P = 50 Torr; T = 296 K; $[CH_3I] = 1.9 \times 10^{15}$ molecule cm^{-3}; $[N_2O] = 2.2 \times 10^{16}$ molecule cm^{-3}; $[N_2]$ = balance; Δt = 70 μs; λ_{pr} = 458.736 nm; P_{pr} = 1.6 mJ $pulse^{-1}$; λ_{ex} = 193 nm; P_{ex} = 20 mJ $pulse^{-1}$; M_g = 1200 grooves/mm; M_r = 0.55 nm; M_{ss} = 10 nm/min. The blue peak corresponds to the probe laser wavelength and the black peaks correspond to the dispersed fluorescence spectrum of IO.

The blue-shifted fluorescence from the (2,0) band is clearly visible in the dispersed fluorescence spectrum, yielding the complete description of the (**v'** = 2 → **v''**) vibrational progression of the $A^2\Pi_{3/2} \rightarrow X^2\Pi_{3/2}$ system of IO.

To compare the relative intensities of the (2,1) – (2,12) vibrational transitions, the total area under each band of the vibrational progression was integrated in Microsoft Origin for three dispersed fluorescence spectra recorded under identical conditions, and where the LIF excitation of IO was at the (2,0) bandhead. In order to obtain the relative intensity of the (2,0) transition, the total area under the (2,0) and (2,2) vibrational bands was integrated for three dispersed fluorescence spectra, recorded under identical conditions and where IO excitation was in the (2,1) hot band, and the average values were normalised to the intensity of the (2,2) band as previously determined. Fig. 3.4-7 displays the relative FCF's determined in this study (once normalised to the FCF of the (2,1) band as calculated by Rao *et. al.*[12]), along with the calculated values of Rao *et. al.*.[12] and the relative FCF's determined experimentally by Spietz *et. al.*[13].

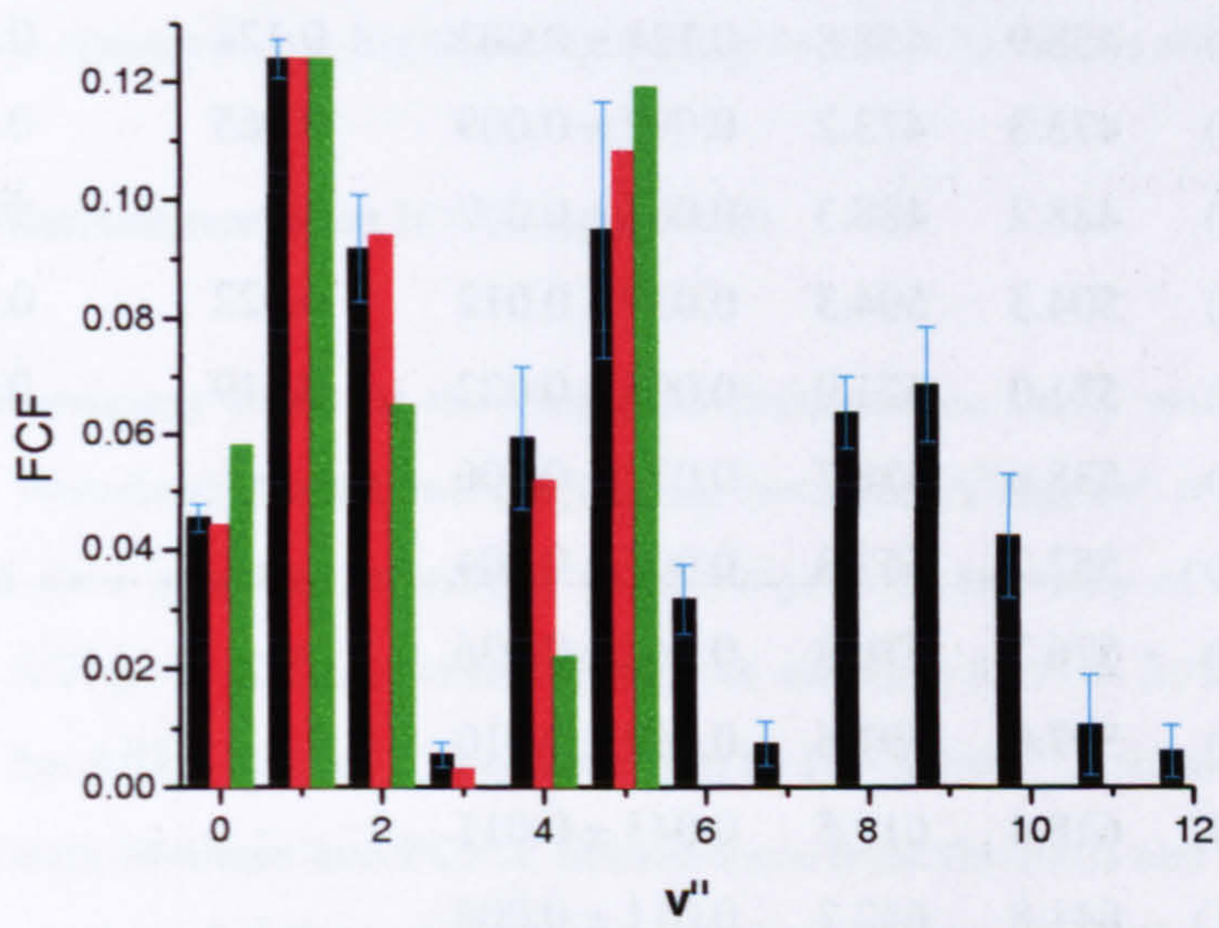

Fig. 3.4-7 – Experimental (black = this work, green = Spietz *et. al.*[13]) and theoretical FCF's for the (v' = 2 → v'') vibrational transitions of the $A^2\Pi_{3/2} \leftarrow X^2\Pi_{3/2}$ system of IO. The experimental fluorescence intensities, determined in this work, are converted to relative FCF's by normalisation of the most intense transition (the (2,1) band) to the FCF calculation of Rao *et. al.*[12]. The error bars represent the 2σ standard deviation of the average experimental fluorescence intensities. The relative FCF's of Spietz *et. al.*[13] were determined by absorption spectroscopy, and are also normalised to the (2,1) band. The theoretical FCF's are taken from Rao *et. al.*[12].

The relative FCF's of the (2 → **v''**) progression determined in this study are in excellent agreement with the FCF calculations of Rao *et. al.*[12]. In the experimental study of Spietz *et. al.*[13] vibrational band strengths were extracted from absorption spectra recorded in photolysis mixtures of I_2/O_3. Thus in their work relative FCF's could only be obtained for vibrational

progressions containing a common groundstate vibrational level, such as (v' ← 0), which explains why their results (presented in Fig. 3.4-7) only extend up to v'' = 5. The work of Spietz *et. al.*[13] was subject to interference from additional absorbers in the photolysis system (such as OIO) and also the weak intensity of transitions arising from higher groundstate vibrational levels (due to their weak population). The results obtained in this work should therefore be regarded as preferential. However, for a more rigorous treatment, further FCF calculations extending to higher vibrational levels in the groundstate are required. Table 3.4-1 lists the relative FCF's determined in the course of this work, along with the relevant experimental determinations of Spietz *et. al.*[13], and the calculations of Rao *et. al.*[12], for the (2 → v'') vibrational progression of the $A^2\Pi_{3/2} \leftarrow X^2\Pi_{3/2}$ system of IO. The experimental and theoretical wavelengths for the vibrational bands are also given.

Band	$\lambda_{exp}{}^1$	λ_{calc}	$FCF_{exp}{}^1$	$FCF_{exp}{}^2$	FCF_{calc}
(2,0)	444.9	445.0	0.045 ± 0.003	0.054	0.044
(2,1)	458.9	458.8	0.124 ± 0.003	0.124	0.124
(2,2)	473.3	473.2	0.092 ± 0.009	0.065	0.094
(2,3)	488.2	488.3	0.006 ± 0.002	-	0.003
(2,4)	504.3	504.3	0.059 ± 0.012	0.022	0.052
(2,5)	521.0	521.0	0.095 ± 0.022	0.119	0.108
(2,6)	538.6	538.7	0.032 ± 0.006	-	-
(2,7)	557.2	557.3	0.007 ± 0.004	-	-
(2,8)	576.7	576.9	0.064 ± 0.006	-	-
(2,9)	597.0	597.6	0.069 ± 0.010	-	-
(2,10)	618.4	619.5	0.043 ± 0.011	-	-
(2,11)	641.8	642.7	0.011 ± 0.008	-	-
(2,12)	666.3	667.2	0.006 ± 0.004	-	-

Table 3.4-1 – Relative FCF's ($FCF_{exp}{}^1$ = this work, $FCF_{exp}{}^2$ = Spietz *et. al.*[13]) and observed wavelengths ($\lambda_{exp}{}^1$ = this work) for the vibrational bands of the $A^2\Pi_{3/2}$ (v' = 2) → $X^2\Pi_{3/2}$ (v'') system of IO. The errors for the FCF's determined in this work are the 2σ standard deviation of the average fluorescence intensities of the vibrational bands. The estimated precision of the experimental wavelengths is ± 0.2 nm, as inferred from the reproducibility of the band positions in the dispersed fluorescence spectra. The calculated FCF's (FCF_{calc}) are taken from Rao *et. al.*[12] and the calculated wavelengths (λ_{calc}) are obtained using the spectroscopic data of Newman *et. al.*[10] and Miller *et. al.*[8].

The experimental and calculated wavelengths are in excellent agreement for the (2,0) – (2,8) vibrational transitions, although a discrepancy is apparent for transitions terminating in the v''

= 9 – 12 vibrational levels. However, it should be emphasised that the main aim of this study was to obtain the relative intensity of vibrational transitions originating from the $A^2\Pi_{3/2}$ (v' = 2) state of IO and less attention was accorded to the wavelength calibration of the monochromator, which was achieved with four points over the 430 – 550 nm range. Despite an R^2 value of 0.999995 from the calibration plot, the error associated with calculating a wavelength from the slope statistics was approximately ± 2 nm. Further, although the diffraction grating of the monochromator was found to scan linearly with wavelength over the 430 – 550 nm range, it is possible that a slight non-linearity ensued at higher wavelengths (corresponding to transitions terminating in higher v''). The high resolution studies of Newman *et. al.*[10] and Miller *et. al.*[8] were designed for the accurate determination of spectroscopic constants, which are very sensitive to the exact frequency of spectroscopic transitions, and are now well defined in the literature. In summary, the calculated wavelengths of the vibrational transitions (using the experimental data of Newman *et. al.*[10] and Miller *et. al.*[8]) should be preferred.

It should be stated that spectroscopic transitions between the (2,3), (2,7), (2,11) and (2,12) bands of the $A^2\Pi_{3/2} - X^2\Pi_{3/2}$ system of IO have not previously been observed in absorption or emission spectroscopy, highlighting the high sensitivity of this study.

3.4.3 Dispersed Fluorescence from IO $A^2\Pi_{3/2}$ (v' = 0)

Although the primary focus of the dispersed fluorescence study was to quantify the relative intensity of vibrational transitions originating from the $A^2\Pi_{3/2}$ (v' = 2) state, from a fundamental point of view it is also interesting to investigate the intensity of other vibrational progressions of the $A^2\Pi_{3/2} \rightarrow X^2\Pi_{3/2}$ system of IO. In addition to v' = 2, the v' = 0 and 3 vibrational levels of the $A^2\Pi_{3/2}$ state of IO are known to be LIF active[17-19]. Due to the combined effect of the excited state lifetimes and FCF's, fluorescence from the (0,0) and (3,0) bands is of comparable intensity, and 1 – 2 orders of magnitude weaker than that from the (2,0) band[18]. As the excitation wavelength required for LIF detection of IO in the (0,0) band (465 – 467 nm) could be generated with the Dye laser configuration employed for the (2,1) band experiments, an investigation into fluorescence originating from the $A^2\Pi_{3/2}$ (v' = 0) state of IO was carried out. Fig. 3.4-8 displays a LIF spectrum of the (0,0) band of IO obtained in this study.

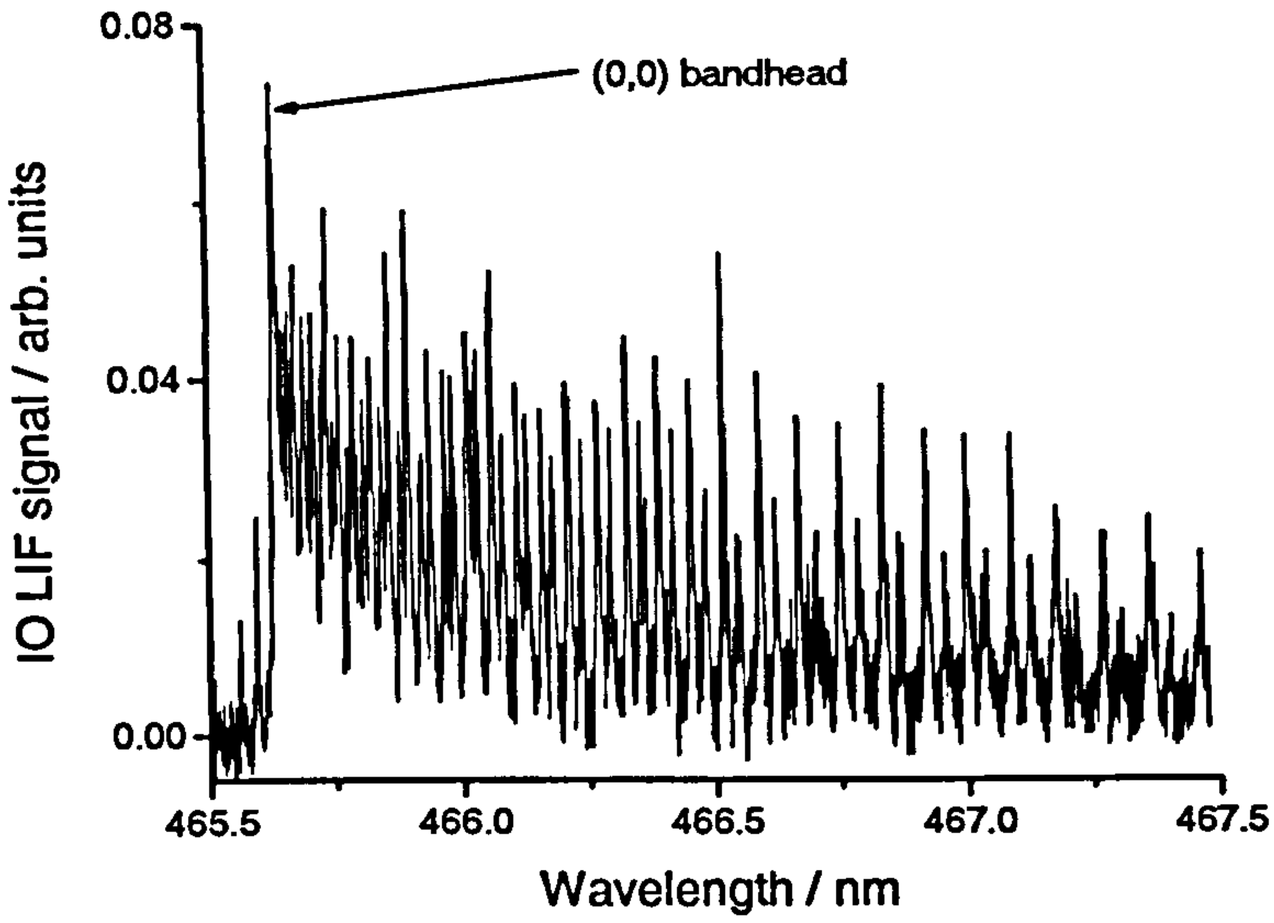

Fig. 3.4-8 – LIF spectrum of the (0,0) band of the $A^2\Pi_{3/2} \leftarrow X^2\Pi_{3/2}$ transition of IO. Experimental conditions: $P = 50$ Torr; $T = 296$ K; $[CH_3I] = 2.3 \times 10^{15}$ molecule cm^{-3}; $[N_2O] = 4.3 \times 10^{16}$ molecule cm^{-3}; $[N_2]$ = balance; $\Delta t = 50$ μs, $P_{pr} = 1.2$ mJ pulse^{-1}; $\lambda_{ex} = 193$ nm; $P_{ex} = 20$ mJ pulse^{-1}; PRF = 5 Hz. Note that the rotational lines of the (0,0) band are lifetime broadened (with respect to the (2,0) band) due to the short excited state lifetime, and are not fully resolved at low J' (near the bandhead) where the spacing between rotational transitions is small.

To record the dispersed fluorescence spectrum originating from $v' = 0$, the probe laser frequency was tuned to the bandhead of the (0,0) transition at 465.64 nm, and the experiment was conducted using the same procedure as previously described. Initially, only light from the excitation laser was detected by the monochromator PMT but after increasing the operating voltage of the PMT, widening the entrance and exit slits of the monochromator, and employing the lowest resolution diffraction grating of the monochromator, a low intensity band structure was observed in the dispersed fluorescence spectrum. To obtain the dispersed fluorescence spectrum of the ($0 \rightarrow v''$) vibrational progression of IO, the experiment was repeated in the presence and absence of N_2O (and hence IO). Although the band structure, attributable to spectroscopic transitions of IO, was not present in the absence of N_2O, an artefact signal with a central wavelength of ~ 523 nm was observed (as was the laser radiation). The source of this spurious signal is unknown, although once subtracted from the spectrum recorded in the presence of N_2O (and IO), its interference was minimised. Fig. 3.4-9 displays dispersed fluorescence spectra recorded in the absence and presence of IO, and the dispersed fluorescence spectrum of the ($0 \rightarrow v''$) vibrational progression of IO obtained from their residual.

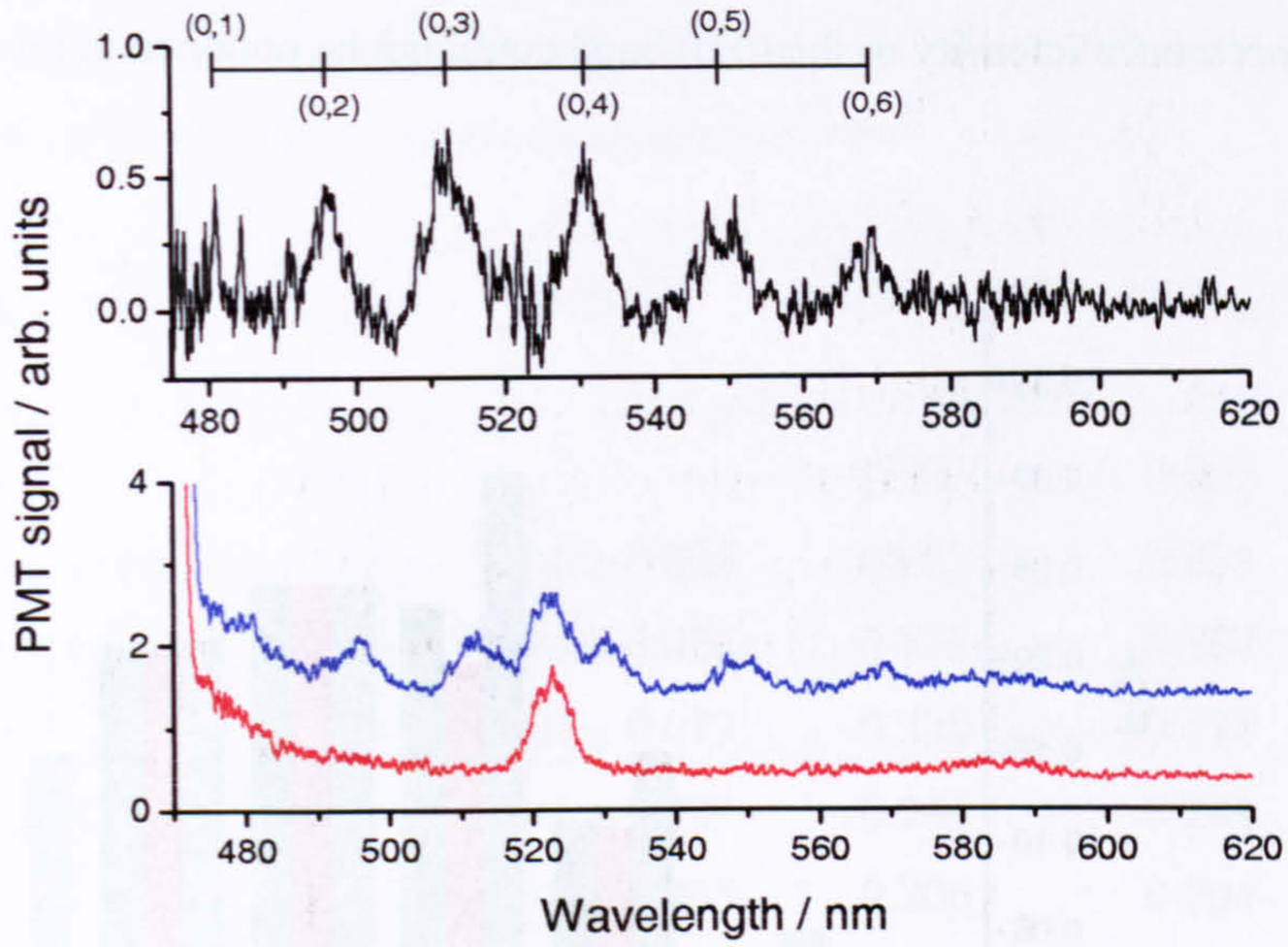

Fig. 3.4-9 – Dispersed fluorescence spectra obtained in the presence and absence of IO (bottom panel: + IO = blue; and, – IO = red) for a laser excitation wavelength of 465.64 nm, and the residual (v' = 0 → v'') vibrational progression of the $A^2\Pi_{3/2} \rightarrow X^2\Pi_{3/2}$ system of IO (top panel). Experimental conditions: P = 50 Torr; T = 296 K; $[CH_3I] = 2.3 \times 10^{15}$ molecule cm^{-3}; $[N_2O] = 4.3 \times 10^{16}$ molecule cm^{-3}; $[N_2]$ = balance; Δt = 50 μs; λ_{pr} = 465.64 nm; P_{pr} = 1.2 mJ $pulse^{-1}$; λ_{ex} = 193 nm; P_{ex} = 20 mJ $pulse^{-1}$; M_g = 300 grooves/mm, M_r = 6.26 nm, M_{ss} = 10 nm/min. The spectra are normalised for the total IO LIF signal (as monitored by a filtered PMT on a separate detection axis), and the spectral response of the monochromator diffraction grating and PMT.

Despite the residual spectrum having a relatively poor signal-to-noise ratio the (0 → v'') progression, originating from the $A^2\Pi_{3/2}$ state of IO, is clearly visible and extends up to a wavelength of 568.7 nm – corresponding to the (0,6) vibrational transition. The experiment was repeated a total of three times and the area under each vibrational band was integrated and averaged to obtain the relative fluorescence intensities. The fluorescence intensities were converted to FCF's by normalisation to the FCF of the (0,4) band, as calculated by Rao *et. al.*[12]. Note that the FWHM's of the vibrational bands obtained in this study are much greater than those observed in the v' = 2 investigation (*cf.* Figs. 3.4-4 and 3.4-6), reflecting the lower resolution of the monochromator. Fig. 3.4-10 displays the relative FCF's of the (0,1) – (0,6) vibrational transitions as determined in this study, along with the FCF calculations of Rao *et. al.*[12], and the experimental results of Spietz *et. al.*[13]. Although, in principle, the dispersed fluorescence from the (0,0) band could be measured by exciting IO in the (0,1) hot-band (similarly to the determination of the (2,0) fluorescence intensity in the v' = 2 experiments), the fluorescence intensity would be too weak to observe the dispersed fluorescence spectrum (due to the small vibrational population of v'' = 1 and the short excited state lifetime of v' = 0), and

the tuneable range of the Dye laser did not extend to the required wavelength (480.8 nm). Thus the relative fluorescence intensity of the (0,0) band could not be obtained in this work.

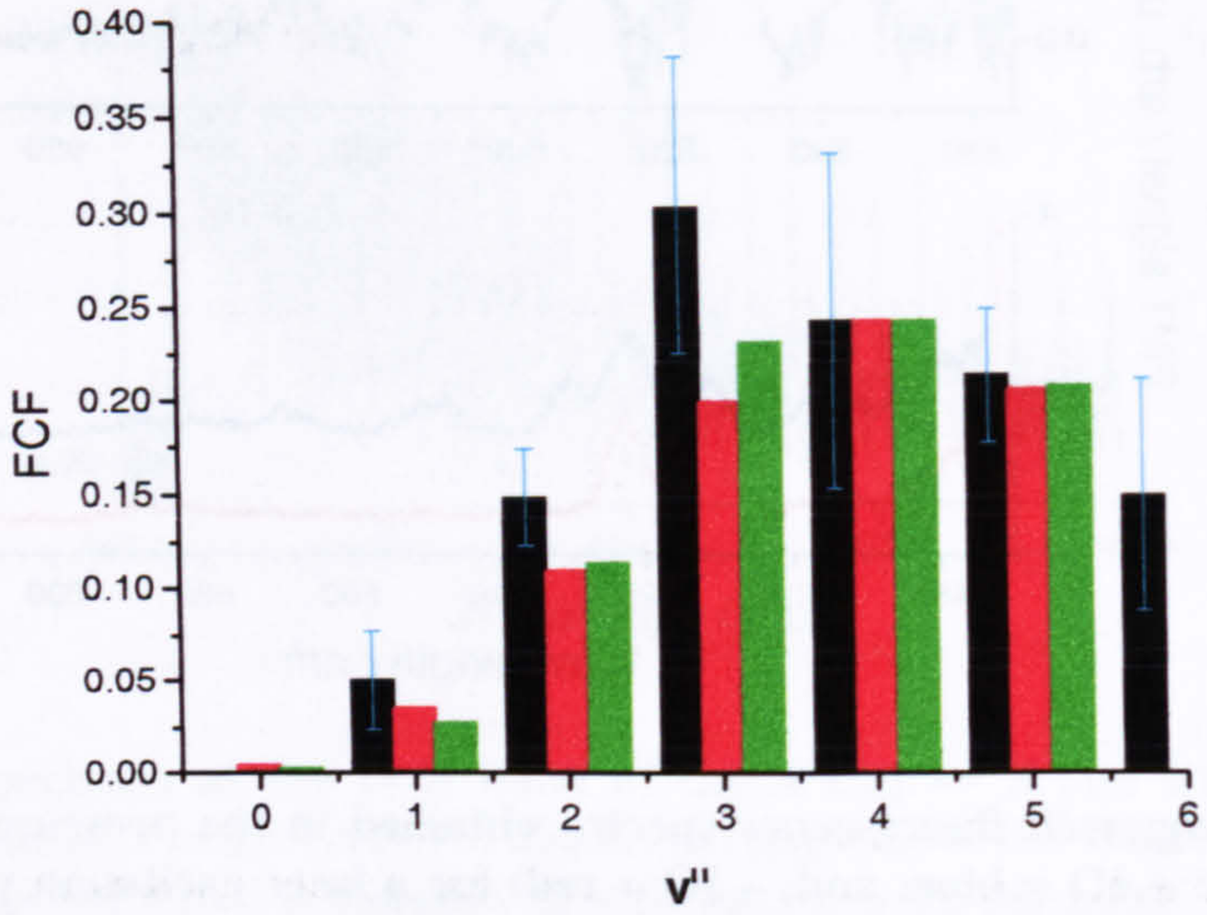

Fig. 3.4-10 – Experimental (black = this work, green = Spietz *et. al.*[13]) and theoretical (red = Rao *et. al.*[12]) FCF's for the (v' = 0 → v'') vibrational transitions of the $A^2\Pi_{3/2} \rightarrow X^2\Pi_{3/2}$ system of IO. The experimental fluorescence intensities have been converted to relative FCF's by normalisation to the FCF of the (0,4) band, as calculated by Rao *et. al.*[12]. The error bars represent the 2σ standard deviation of the average experimental fluorescence intensities.

From Fig. 3.4-10 it can be seen that the results of Rao *et. al.*[12] and Spietz *et. al.*[13] are in excellent agreement and that the FCF's determined in this study are significantly higher than those of the other two studies for vibrational transitions terminating in $v'' \leq 3$. However, if the experimental FCF's were obtained by normalisation of the relative fluorescence intensities to the (0,3) FCF calculation of Rao *et. al.*[12], this discrepancy would shift to higher v''. The artefact signal at 523 nm (Fig. 3.4-9) could have interfered with the determination of the (0,3) band intensity in this work, as could the laser radiation with the (0,1) and (0,2) bands, but the subtraction of the background spectrum should have accounted for contamination from these sources. Despite the relatively poor signal-to-noise ratio of the experimental data obtained in this study, the reproducibility of the dispersed fluorescence spectrum was reasonably satisfactory (as indicated by the 2σ error bars in Fig. 3.4-10) and as all spectra were corrected for the spectral response of the monochromator PMT and diffraction grating by the same procedure as that used in the v' = 2 study (the results of which were found to be in good agreement with the FCF calculations[12]), the reason for the observed discrepancy is unclear.

Table 3.4-2 lists the wavelengths and FCF's for the (v' = 0 → v'') vibrational progression of the $A^2\Pi_{3/2} \rightarrow X^2\Pi_{3/2}$ system of IO obtained in this study, along with the

calculated transition wavelengths and FCF's of Rao *et. al.*[12], and the experimental FCF's of Spietz *et.al.*[13]. All of the vibrational bands reported in Table 3.4-2 have been previously observed (as well as the (0,7) band) in emission spectroscopy[15].

Band	$\lambda_{exp}{}^1$	λ_{calc}	$FCF_{exp}{}^1$	$FCF_{exp}{}^2$	FCF_{calc}
(0,0)	-	465.7	-	0.003	0.005
(0,1)	480.9	480.8	0.050 ± 0.027	0.027	0.035
(0,2)	496.5	496.6	0.148 ± 0.026	0.113	0.109
(0,3)	512.5	513.3	0.302 ± 0.079	0.230	0.198
(0,4)	530.6	530.9	0.241 ± 0.089	0.241	0.241
(0,5)	549.7	549.6	0.212 ± 0.035	0.206	0.204
(0,6)	568.7	569.2	0.148 ± 0.062	-	-

Table 3.4-2 – Relative FCF's ($FCF_{exp}{}^1$) and observed wavelengths ($\lambda_{exp}{}^1$) of the vibrational bands of the $A^2\Pi_{3/2}$ (v' = 0) → $X^2\Pi_{3/2}$ (v'') system of IO determined in this work. Note the errors for the FCF's are the 2σ standard deviation of the average fluorescence intensity of the vibrational bands. The estimated error of the experimental wavelengths is ± 0.2 nm, as inferred from the reproducibility of the band positions in the dispersed fluorescence spectra. Relative FCF's ($FCF_{exp}{}^2$) determined by Spietz *et. al.*[13] are also presented. The calculated FCF's (FCF_{calc}) are taken from Rao *et. al.*[12] and the calculated wavelengths are obtained using spectroscopic data of Newman *et. al.*[10] and Miller *et. al.*[8].

3.4.4 Discussion

The work reported in this section represents the first quantitative investigation of the relative intensity of vibrational transitions originating from the $A^2\Pi_{3/2}$ state of IO. In total 19 vibrational transitions have been observed: 13 originating from v' = 2; and the remainder from v' = 0. The detection of fluorescence from the (2,3), (2,7), (2,11) and (2,12) vibrational bands represents the first experimental observation of these transitions in the $A^2\Pi_{3/2} - X^2\Pi_{3/2}$ system of IO, reflecting the high sensitivity of the experiment and the ease of detecting low intensity spectroscopic transitions on a low-noise background. The relative intensity of transitions originating from v' = 2 are in excellent agreement with existing FCF calculations[12], although calculations extending to higher groundstate vibrational levels (v'' = 6 – 12) are required for a more rigorous comparison. The results obtained are also in reasonable agreement with a recent absorption study[13], although the findings of this fluorescence study are considered preferential due to less potential experimental interferences. The band intensity of transitions arising in the ($A^2\Pi_{3/2}$) v' = 0 state of IO are not in as good agreement with the other studies[12,13], the reason for which is unclear. The results obtained in this work are useful for the development of an LIF

instrument for the detection of IO in the atmosphere, which is discussed in greater detail in section 3.6.

3.5 Fluorescence Quenching of the $A^2\Pi_{3/2}$ state of IO

In section 3.2 it was stated that an evaluation of the parameter, ϕ, is necessary in order to determine the theoretical sensitivity of an LIF instrument. ϕ is known as the fluorescence quantum yield, and is equal to the number of photons of radiation emitted as fluorescence by an excited state, per photon absorbed by the groundstate. More specifically, for a molecule which does not undergo ISC or internal conversion, ϕ is given by E. 3.5-1

$$\phi = \frac{k_f}{k_f + k_p + k_q[Q]} \qquad \text{E. 3.5-1}$$

where k_f is the natural rate of radiative decay of the excited state (*i.e.* the reciprocal of the natural radiative lifetime, $1/\tau_{rad}$), k_p is the predissociation rate of the excited state, and k_q is the bimolecular quenching rate coefficient for collisional deactivation of the excited state by quencher, Q (assuming that quenching is linear with pressure). An alternative way of writing E. 3.5-1 is, $\phi = \tau/\tau_{rad}$, where τ is the fluorescence lifetime of the excited state. Thus the fluorescence lifetime of an excited state is given by E. 3.5-2

$$\tau = \frac{1}{k_f + k_p + k_q[Q]} \qquad \text{E. 3.5-2}$$

If the fluorescence lifetime of a species can be directly determined, therefore, the various parameters of E. 3.5-2 can be investigated by a Stern-Volmer analysis, where the fluorescence lifetime is measured as a function of pressure of Q. Plotting the reciprocal fluorescence lifetime against [Q] thus yields a straight line, with gradient, k_q, and intercept, $(k_f + k_p)$. Commonly, $k_f >> k_p$, and the natural radiative lifetime of an excited state can be determined directly from a Stern-Volmer analysis.

Although predissociation of the $A^2\Pi_{3/2}$ state of IO has received experimental investigation[7,10], there are no reported investigations of the collisional quenching of excited state fluorescence in the existing literature. As the theoretical sensitivity of an IO LIF instrument is directly related to the fluorescence quantum yield, the aim of the work reported in this section was to investigate the importance of fluorescence quenching in the $A^2\Pi_{3/2}$ state of IO.

3.5.1 Experimental

As previously mentioned, the fluorescence lifetime of the $A^2\Pi_{3/2}$ state of IO cannot be determined directly because it is shorter than the width of a typical laser pulse. Therefore, a Stern-Volmer analysis (as described above) cannot be performed, and an alternative method must be devised to probe fluorescence quenching of the $A^2\Pi_{3/2}$ state of IO. From equations 3.2-2 and 3.2-3 it can be seen that the fluorescence signal from an excited state is directly proportional to the fluorescence quantum yield of that state. Thus if the fluorescence signal from a constant concentration of IO is measured as a function of total pressure, any changes in fluorescence signal must be attributable to quenching of the excited state (as ϕ and k_q are the only pressure dependent terms in equations 3.2-3 and 3.5-1 respectively). More specifically, the pressure dependent fluorescence signal of IO can be expressed by E. 3.5-3.

$$S_{IO} = \beta \frac{k_f}{k_f + k_p + k_q[Q]} \qquad \text{E. 3.5-3}$$

where, β is an experimental constant, $C_{IO}'[IO]$ (where $C_{IO}' = C_{IO}/\phi$). Thus a modified Stern-Volmer analysis can be performed by plotting the reciprocal of the fluorescence signal against the number density of Q, as expressed in E. 3.5-4 (providing that β is maintained at a constant value as a function of [Q]).

$$\frac{1}{S_{IO}} = \frac{k_f + k_p}{\beta} + \frac{k_q[Q]}{\beta} \qquad \text{E. 3.5-4}$$

The resultant plot should yield a straight line with intercept, $(k_f + k_p)/\beta$ and gradient, k_q/β. However, as β is an unknown constant (in the absence of absolute calibration of the LIF instrument) no direct information with regards to the quenching rate coefficient can be obtained from this procedure. Despite this limitation of the experiment, the relative rate of k_q (with respect to $k_f + k_p$) can be obtained by dividing E. 3.5-4 through by the intercept term yielding E. 3.5-5

$$\frac{1}{S_{IO}'} = 1 + \frac{k_q}{k_f + k_p}[Q] \qquad \text{E. 3.5-5}$$

where, $1/S_{IO}'$ is the normalised value of the reciprocal fluorescence signal. Now, a plot of $1/S_{IO}'$ against [Q] yields a straight line with unity intercept, and gradient, $k_q/(k_f+k_p)$. From the

gradient, the absolute quenching rate coefficient can be obtained by dividing through by the fluorescence lifetime of the excited state (as measured in the CRDS experiments of Newman *et. al.*[10], which were conducted at a low pressure of ~ 1 Torr – *i.e.* conditions of negligible collisional quenching). Thus, for a particular rotational level in the $A^2\Pi_{3/2}$ (v' = 2) state of IO, the quenching rate coefficient can be obtained from E. 3.5-6

$$k_q = \frac{k_q}{(k_f + k_p)\tau} \qquad \text{E. 3.5-6}$$

where τ can be calculated from the expression

$$\tau = \frac{1}{2\pi c\Gamma} \qquad \text{E. 3.5-7}$$

where, Γ is the Lorentzian line width of a rotational line, corresponding to J', and is calculated from the experimentally derived relationship expressed in E.3.5-8[20]

$$\Gamma = 0.004 + \kappa J'(J'+1) \qquad \text{E. 3.5-8}$$

where, Γ has units of cm^{-1}, and κ is a constant of proportionality (113×10^{-6}).

To perform a quenching experiment, therefore, requires generating a constant concentration of IO as a function of total pressure. To achieve this, IO was generated by the reaction of O atoms with either CH_3I or CF_3I. These reactions are known to be independent of pressure[21] thus providing a reactive system in which the temporal profile of IO is independent of pressure. Groundstate O atoms were generated by the 193 nm photolysis of N_2O in the presence of a large excess of N_2 (to rapidly quench O (^1D) to O (^3P)). Reagent mixtures of CH_3I (or CF_3I) and N_2O were prepared in N_2 *via* the normal procedure and administered to the reaction cell at different total pressures. The concentrations of N_2O and iodide were maintained constant as a function of total pressure *via* a combination of adjusting the total gas flow rate and throttling of the reaction cell vacuum system. The various processes determining the concentration of IO at any particular reaction time are as follows

N_2O + 193 nm	→	N_2 + O (^1D)	k_1
O (^1D) + N_2	→	O (^3P) + N_2	k_2
O (^3P) + RI	→	IO + R	k_3
IO + IO	→	products	k_4

$$IO \rightarrow \text{loss} \qquad k_5$$

where k_5 represents the pseudo-first-order rate coefficient for loss processes of IO other than the IO self-reaction. However, as the experimental conditions were arranged so that $k_2' >> k_3'$ and the concentration of IO was low enough (typically 1.8×10^{12} molecule cm^{-3}) to approximate its removal as first-order, the above reaction scheme can be simplified to

$$O + RI \rightarrow IO + R \qquad k_{growth}$$

$$IO \rightarrow \text{loss} \qquad k_{loss}$$

where k_{growth} is the pseudo-first-order rate coefficient for the rate of formation of IO, and k_{loss} is the pseudo-first-order rate coefficient for the loss of IO in the kinetic system. Solving the differential equations for the concentration of IO at a particular reaction time, t, yields E. 3.5-9

$$[IO]_t = \frac{k_{growth}[IO]_{max}}{(k_{growth} - k_{loss})}\left(e^{-k_{loss}t} - e^{-k_{growth}t}\right) \qquad \text{E. 3.5-9}$$

where $[IO]_{max}$ ($= \beta[O]_0$, *i.e.* the amount of O atoms generated by the excimer laser multiplied by some experimental constant) is effectively the peak IO LIF signal (S_{IO} in E. 3.5-3), which is directly proportional to the concentration of IO.

The same experimental apparatus as used for the dispersed fluorescence experiment was employed for the LIF detection of IO, with the exception that no monochromator was employed, and the fluorescence from IO was detected directly by a filtered PMT. The majority of experiments focused on quenching of the R_1 bandhead of the $A^2\Pi_{3/2}$ ($v' = 2$) $\leftarrow$ $X^2\Pi_{3/2}$ ($v'' = 0$) transition of IO in N_2, as this is the LIF transition to be used in the field instrument. However, a limited number of experiments were also performed in Ar and He bath gases, and for different rotational transitions and bands of excitation. All experiments were conducted at 296 K.

For a particular quenching experiment, kinetic traces of IO were recorded as a function of total pressure, and fitted to E. 3.5-9, returning a value for $[IO]_{max}$. The data points were collected in a random fashion so that kinetic traces were not recorded for consecutive pressure points, reducing the potential interference from systematic fluctuations of experimental variables. All data were normalised to the excimer laser power, which was measured at the rear reaction cell window after each kinetic trace was recorded. Fluctuations in the excimer laser power were observed to be relatively insignificant, deviating by no more than ~ 10 % over the course of a quenching experiment. Fig. 3.5-1 displays some kinetic traces recorded at different

total pressures, and Fig. 3.5-2 displays a plot of $[IO]_{max}$ against the total number density of N_2 obtained in a particular quenching experiment.

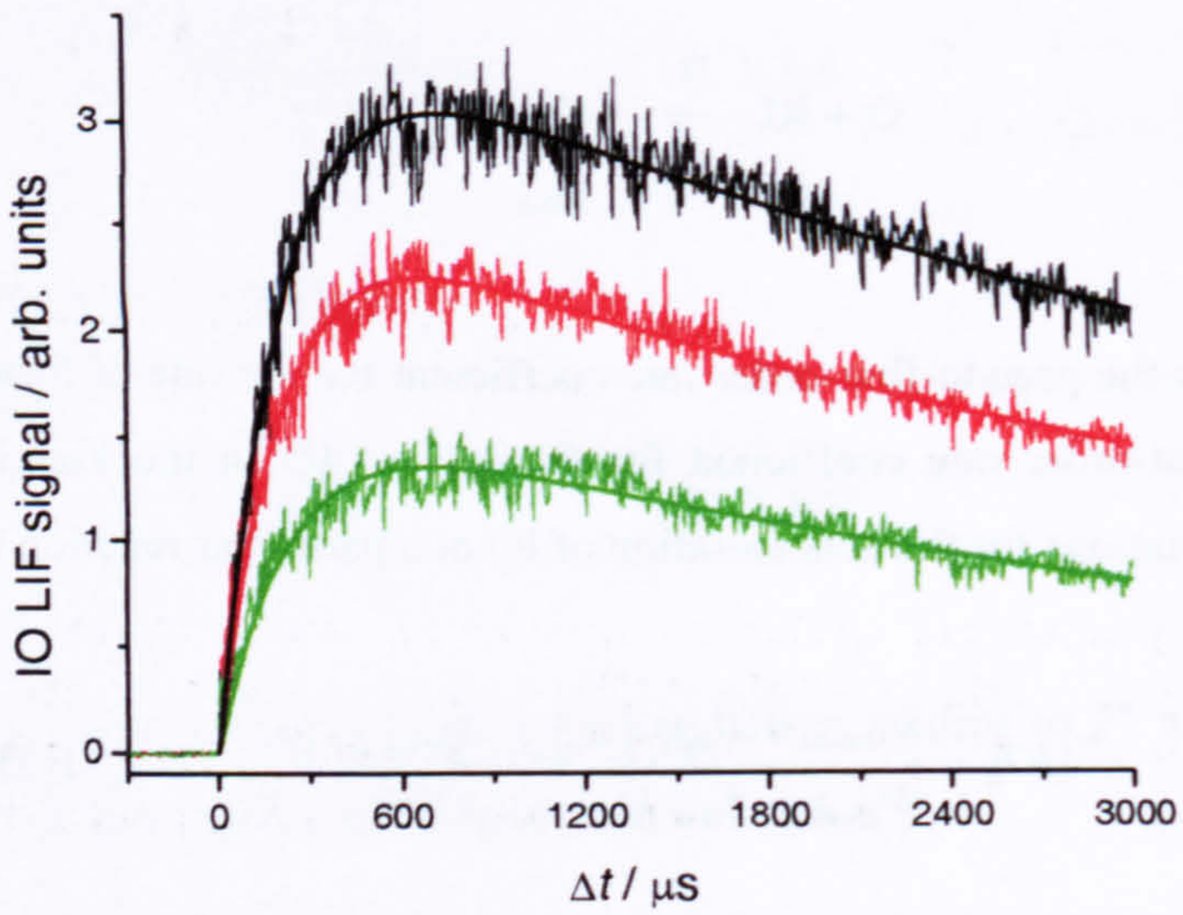

Fig. 3.5-1 – Kinetic traces of IO as a function of total N_2 pressure (black = 20.1 Torr, red = 302.7 Torr, green = 698.5 Torr). The solid lines are fits of E. 3.5-9 to the experimental data. From the fits: $[IO]_{max}$ = 3.45 ± 0.04 (black), 2.58 ± 0.03 (red) and 1.61 ± 0.03 (green); k_{growth} (s^{-1}) = 4670 ± 160 (black), 4930 ± 200 (red), 4250 ± 220 (green); k_{loss} (s^{-1}) = 180 ± 10, 210 ± 10, 235 ± 15. All errors are the 2σ standard error returned from the fitting procedure. Experimental conditions: T = 296 K; $[CF_3I] = 1.09 \times 10^{15}$ molecule cm^{-3}; $[N_2O] = 1.84 \times 10^{15}$ molecule cm^{-3}; $[N_2]$ = balance; λ_{ex} = 193 nm, P_{ex} = 37 mJ $pulse^{-1}$, P_{pr} = 340 μJ $pulse^{-1}$, λ_{pr} = 444.89 nm.

From, the kinetic traces of IO, and the plot of IO_{max} against $[N_2]$ (Fig. 3.5-2), it can clearly be seen that the fluorescence intensity is observed to decrease with increasing pressure. Further, the similarity in the temporal evolution of IO indicates that the concentration of species within the reaction cell – and most importantly IO – is relatively constant as a function of pressure and that the reduction in fluorescence intensity is likely to be due to fluorescence quenching, rather than a diminished concentration of IO at higher pressures. Values of k_{growth} and k_{loss} (obtained in the same experiment as the data presented in Fig. 3.5-2) are displayed in Fig. 3.5-3, emphasising the apparent independence of pressure to the kinetics of the system.

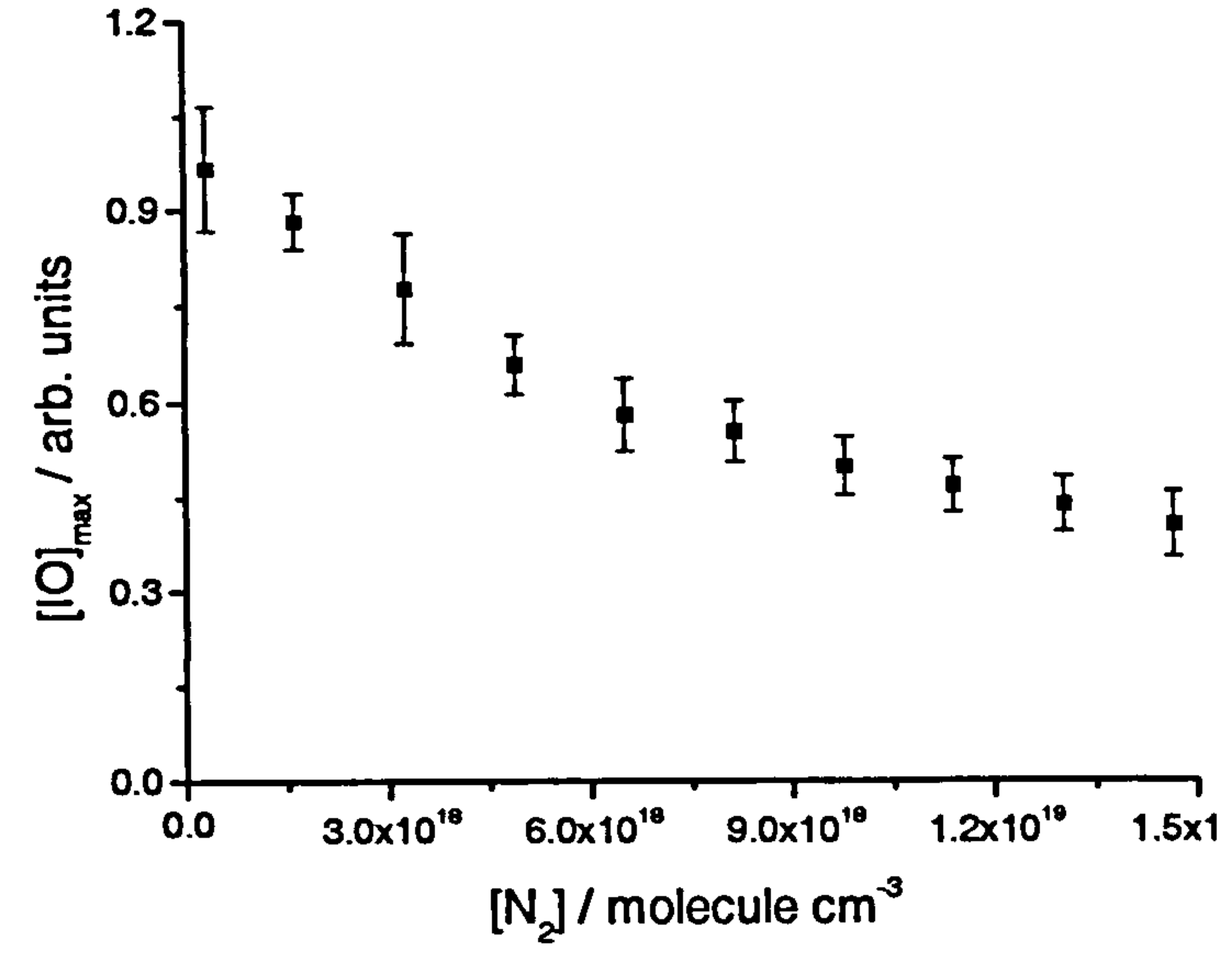

Fig. 3.5-2 – Dependence of IO fluorescence intensity on the total pressure of N_2. Excitation is at the R_1 (2,0) bandhead of the $A^2\Pi_{3/2} \leftarrow X^2\Pi_{3/2}$ electronic transition. Experimental conditions: $T = 296$ K; $[CF_3I] = 3.1 \times 10^{14}$ molecule cm^{-3}; $[N_2O] = 1.35 \times 10^{15}$ molecule cm^{-3}; $[N_2]$ = balance; $\lambda_{ex} = 193$ nm; $P_{ex} = 14$ mJ $pulse^{-1}$; $P_{pr} = 53$ μJ $pulse^{-1}$; $\lambda_{pr} = 444.89$ nm.

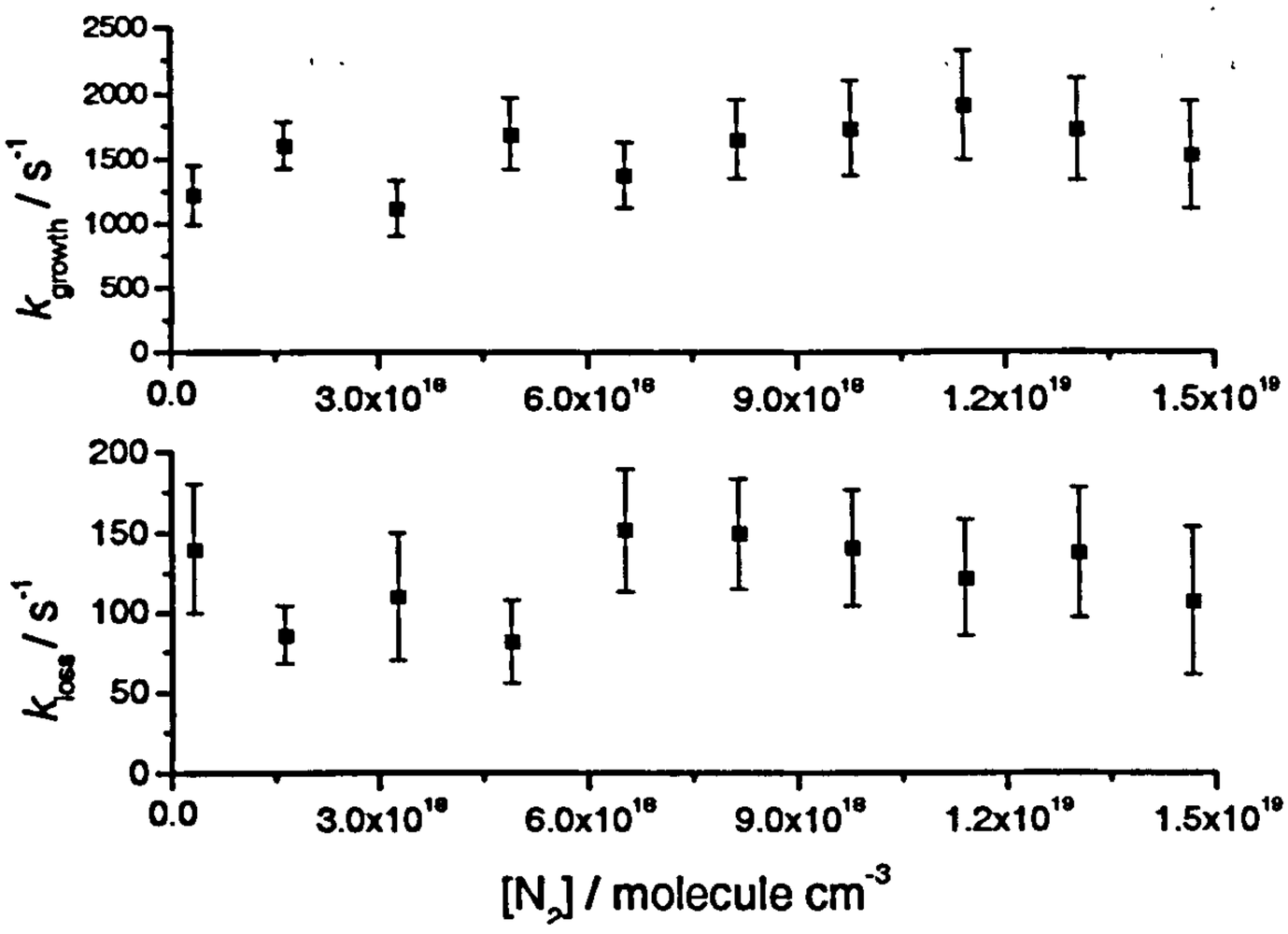

Fig. 3.5-3 – Formation and loss rates of IO, in the O + CF_3I system, as a function of $[N_2]$. The experimental conditions were identical to those given in the caption to Fig. 3.5-2.

3.5.2 Quenching of the $J' = 3.5 - 5.5$ Rotational Levels of the $A^2\Pi_{3/2}$ (v' = 2) State of IO

Fig. 3.5-4 displays the normalised Stern-Volmer plot of the data from the quenching experiment displayed in Fig. 3.5-2.

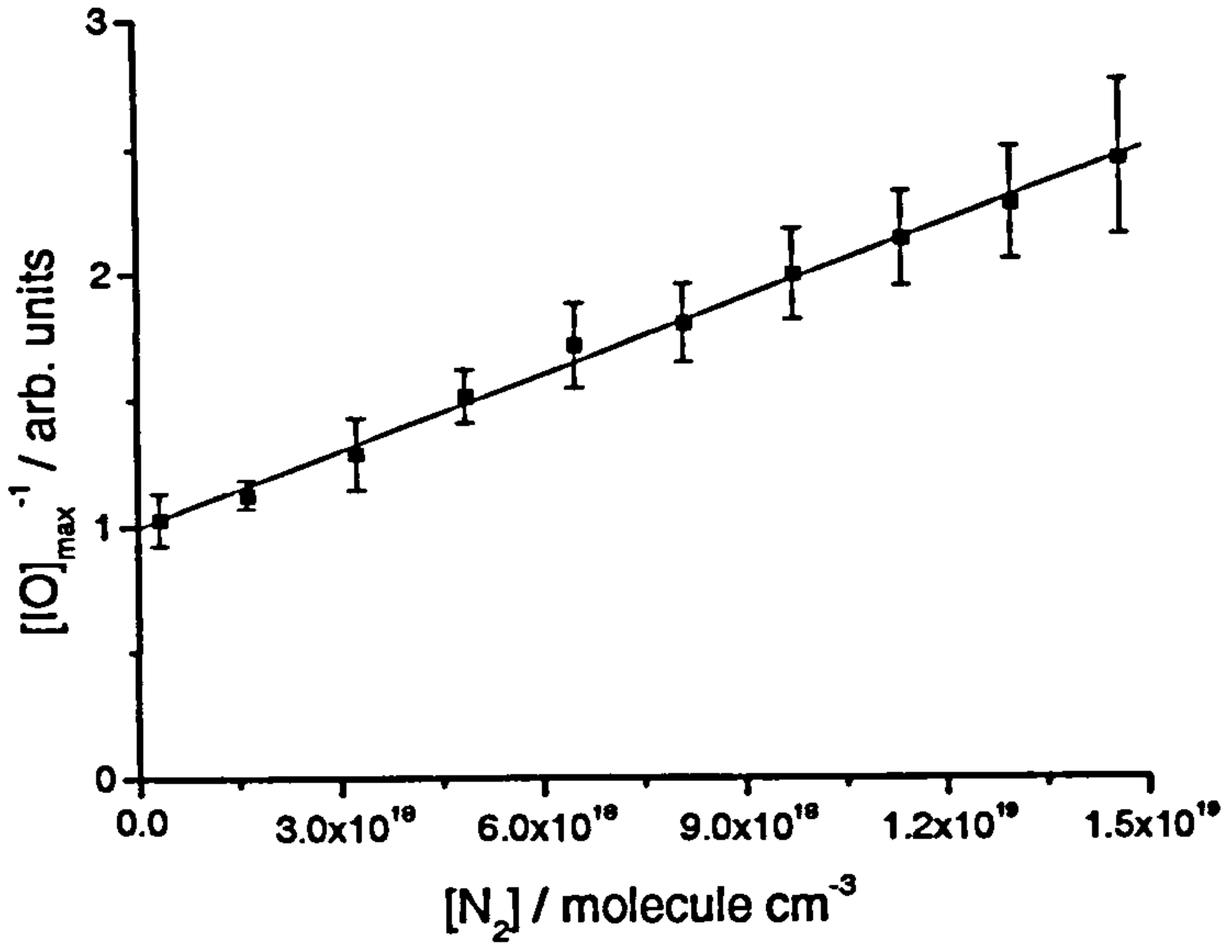

Fig. 3.5-4 – Stern-Volmer plot for quenching of the $A^2\Pi_{3/2}$ (v' = 2, J' = 3.5 – 5.5) state of IO by N_2. Excitation is at the R_1 (2,0) bandhead of the $A^2\Pi_{3/2} \leftarrow X^2\Pi_{3/2}$ electronic transition. The experimental conditions are identical to those given in the caption to Fig. 5.3-2. From the linear fit, $k_q/(k_f + k_p) = (1.00 \pm 0.06) \times 10^{-19}$ $cm^3 molecule^{-1} s^{-1}$.

Excitation of IO was at a wavelength of 444.89 nm, corresponding to the R_1 (2,0) bandhead of the $A^2\Pi_{3/2} \leftarrow X^2\Pi_{3/2}$ electronic transition. As stated in section 3.2, the R_1 bandhead is a blend of three rotational transitions, originating from the $J'' = 2.5 - 4.5$ groundstate rotational levels. Therefore, the $J' = 3.5 - 5.5$ rotational levels of the excited state are initially populated by the laser radiation. As discussed in the experimental section, in order to convert the relative rate coefficient obtained from the slope of the Stern-Volmer plot into an absolute quenching rate coefficient, the lifetime of the excited state (under conditions of negligible collisional quenching) is required. If it is assumed that the average lifetime of the excited state populated in the LIF transition can be approximated by the $J' = 4.5$ state, then from equations 3.5-8 and 3.5-7 we obtain, $\tau = 781$ ps. Thus, substituting the appropriate values into E. 3.5-6, we obtain the quenching rate coefficient for the (2,0) bandhead by N_2 at 296 K, $k_q = (12.8 \pm 0.8) \times 10^{-11}$ $cm^3 molecule^{-1} s^{-1}$. Note that this determination of the quenching rate coefficient assumes that RET (and VET) is of negligible consequence in the $A^2\Pi_{3/2}$ state of IO, prior to the emission of fluorescence, due to its short predissociative lifetime (this assumption is discussed in greater detail in section 3.5.3). Although this value is relatively large and consistent with typical electronically excited state quenching rate coefficients, because the fluorescence lifetime of IO

could not be observed directly, the quenching experiment was repeated under different experimental conditions in order to investigate any systematic dependencies of the quenching rate coefficient on the experimental conditions. All quenching rate coefficients obtained are presented in Table 3.5-1, along with the pertinent experimental conditions.

Band	$[N_2]$	[RI]	$[N_2O]$	P_{ex}	P_{pr}	$k_q/(k_f + k_p)$	k_q
(2,0)	1.3 – 22.7	7.8[a]	9.2	21	157	4.5 ± 0.7	5.8 ± 0.8
(2,0)	1.3 – 22.7	7.8[a]	9.2	112	157	12.5 ± 0.2	16.0 ± 0.2
(2,0)	1.3 – 22.7	1.7[a]	9.2	112	157	5.5 ± 0.4	7.1 ± 0.5
(2,0)	2.3 – 19.4	5.6[a]	2.0	103	340	6.5 ± 1.9	8.4 ± 2.4
(2,0)	2.3 – 19.4	5.6[a]	2.0	103	82	5.5 ± 0.4	7.1 ± 0.5
(2,0)	2.3 – 19.4	10.9[b]	18.4	37	340	6.4 ± 0.6	8.2 ± 0.8
(2,0)	0.3 – 16.2	7.4[b]	3.6	12	76	4.2 ± 1.3	5.3 ± 1.7
(2,1)	0.3 – 16.2	7.4[b]	3.4	12	111	6.7 ± 1.8	8.5 ± 2.3
(2,0)	0.3 – 14.6	7.4[b]	16.0	14	194	8.6 ± 3.4	11.0 ± 4.4
(2,0)	0.3 – 16.2	3.1[b]	4.6	16	53	10.7 ± 0.2	13.7 ± 1.8
(2,0)	0.3 – 16.2	3.1[b]	13.5	14	53	10.0 ± 0.1	12.8 ± 0.8

Table 3.5-1 – Summary of all quenching experiments performed on initial population of $J' = 3.5 – 5.5$ in the $A^2\Pi_{3/2}$ ($v' = 2$) state of IO. From left to right, the columns represent: the vibrational band of the electronic transition used to excite IO ($\lambda_{(2,0)} = 444.89$ nm; $\lambda_{(2,1)} = 458.74$ nm); the experimental pressure range of N_2 (10^{18} molecule cm^{-3}); the experimental concentration of RI (10^{14} molecule cm^{-3}, [a] = CH_3I, [b] = CF_3I); the experimental concentration of N_2O (10^{14} molecule cm^{-3}); the excimer laser power at 193 nm (mJ $pulse^{-1}$); the probe laser power (μJ $pulse^{-1}$); the gradient of the normalised Stern-Volmer plot (10^{-20} $cm^3 molecule^{-1} s^{-1}$); and the absolute quenching rate coefficient (10^{-11} $cm^3 molecule^{-1} s^{-1}$).

From the data in Table 3.5-1 it can be seen that, although there is a large range in the determined values of k_q, no systematic dependence on any of the experimental variables is apparent. Although this is indicative that the apparent quenching of IO fluorescence by N_2 is a genuine result, the large uncertainty in the average value of k_q is of concern [$k_q = (9.5 \pm 6.9) \times 10^{-11}$ $cm^3 molecule^{-1} s^{-1}$, where the error is the 2σ standard deviation of all independent determinations].

In order to investigate the possibility of the observed quenching being due to a decrease in the concentration of IO with increasing pressure, a quenching experiment was conducted where excitation was at the R_1 bandhead of the (0,0) band of the $A^2\Pi_{3/2} \leftarrow X^2\Pi_{3/2}$ transition of IO. The lifetime of the ($v' = 0$) state of IO is 17.6 ps[10], and independent of J'. Thus for the rate

of quenching, at 296 K and 760 Torr, to be equal to the rate of predissociation, the quenching rate coefficient would have to be, $k_q = 2.3 \times 10^{-9}$ $cm^3 molceule^{-1} s^{-1}$ – approximately an order of magnitude higher than the gas kinetic rate coefficient. Clearly, therefore, quenching of the $A^2\Pi_{3/2}$ ($v' = 0$) state of IO should not be apparent over the pressure range studied in this work. Fig. 3.5-5 displays kinetic traces of IO, from the (0,0) quenching experiment, recorded at total pressures of 10 and 500 Torr N_2.

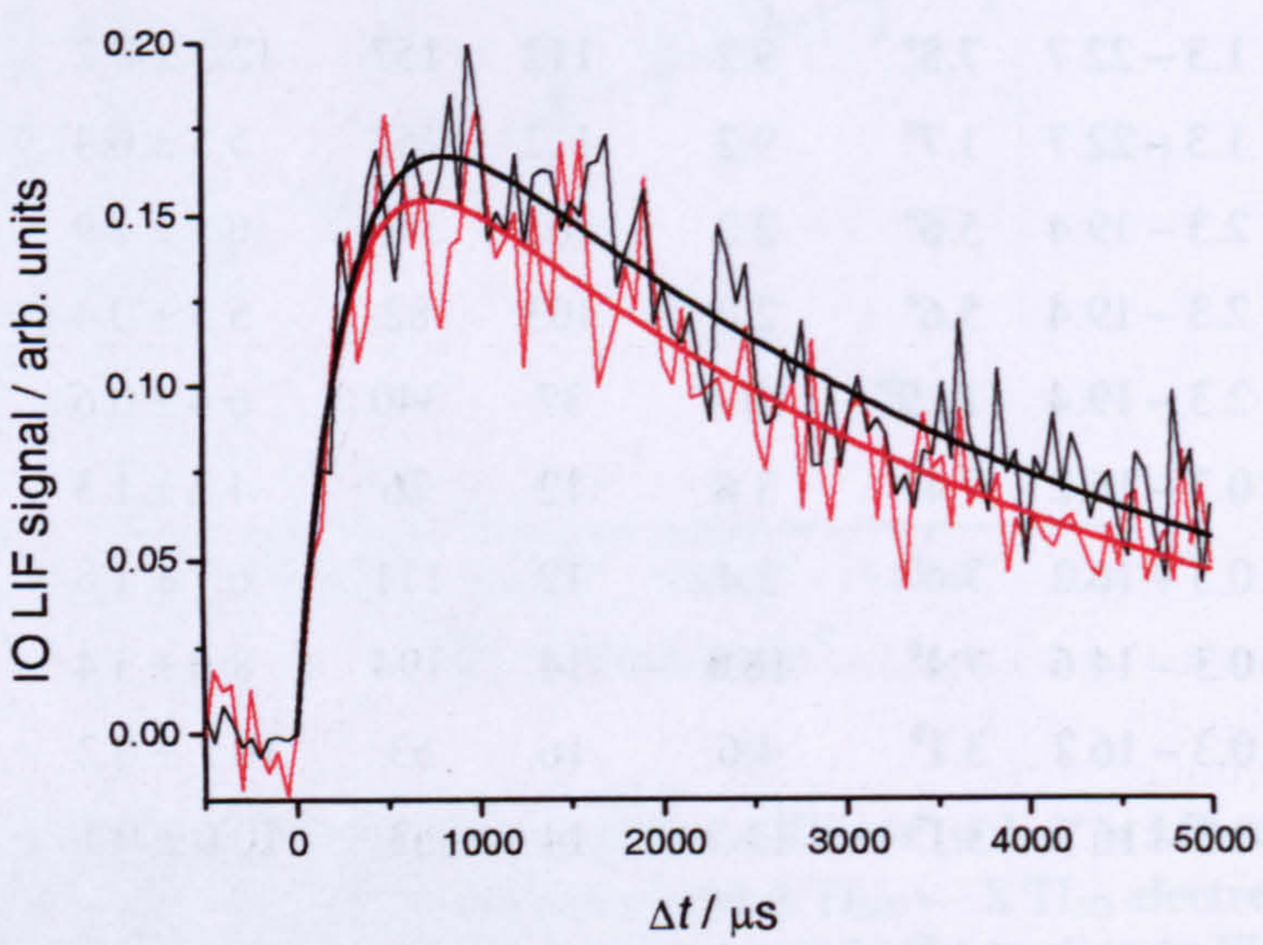

Fig. 3.5-5 – Kinetic traces of IO recorded at total pressures of 10 Torr (black) and 500 Torr (red) N_2, where LIF excitation is at the R_1 bandhead of the (0,0) band of the $A^2\Pi_{3/2} \leftarrow X^2\Pi_{3/2}$ electronic transition of IO. The solid lines are fits of E. 3.5-9 to the experimental data. From the fits: $[IO]_{max} = 0.21 \pm 0.02$ (black) and 0.19 ± 0.02 (red); k_{growth} (s^{-1}) $= 3300 \pm 660$ (black) and 3730 ± 850 (red); k_{loss} (s^{-1}) $= 280 \pm 40$ (black) and 300 ± 40 (red). All errors are the 2σ standard error returned from the fitting procedure. Experimental conditions: $T = 296$ K; $[CF_3I] = 8.2 \times 10^{14}$ molecule cm^{-3}; $[N_2O] = 3.2 \times 10^{15}$ molecule cm^{-3}; $[N_2]$ = balance; $\lambda_{ex} = 193$ nm; $P_{ex} = 17$ mJ $pulse^{-1}$; $P_{pr} = 340$ μJ $pulse^{-1}$; $\lambda_{pr} = 465.64$ nm.

From the kinetic traces it can clearly be seen that the LIF signal from IO has effectively no pressure dependence between 10 and 500 Torr N_2. Similarly to the (2,0) band experiments, the temporal evolution of IO does not display a pressure dependence, further substantiating that the experimental conditions are well defined and that the concentration of IO is relatively constant with total pressure. Fig. 3.5-6 displays the resultant Stern-Volmer plot from the (0,0) band quenching experiment. From the slope of the linear fit to the data, it can be seen that quenching of fluorescence from the $A^2\Pi_{3/2}$ ($v' = 0$) state of IO is negligible over the pressure range of the experiment, in agreement with the above discussion. (However, it is interesting that if the slope of the Stern-Volmer plot is converted into a quenching rate coefficient, a value of, $k_q = (9.7 \pm$

18.9) × 10^{-11} $cm^3molecule^{-1}s^{-1}$ is obtained – in excellent agreement with the results of the (2,0) experiments, albeit with a very large uncertainty).

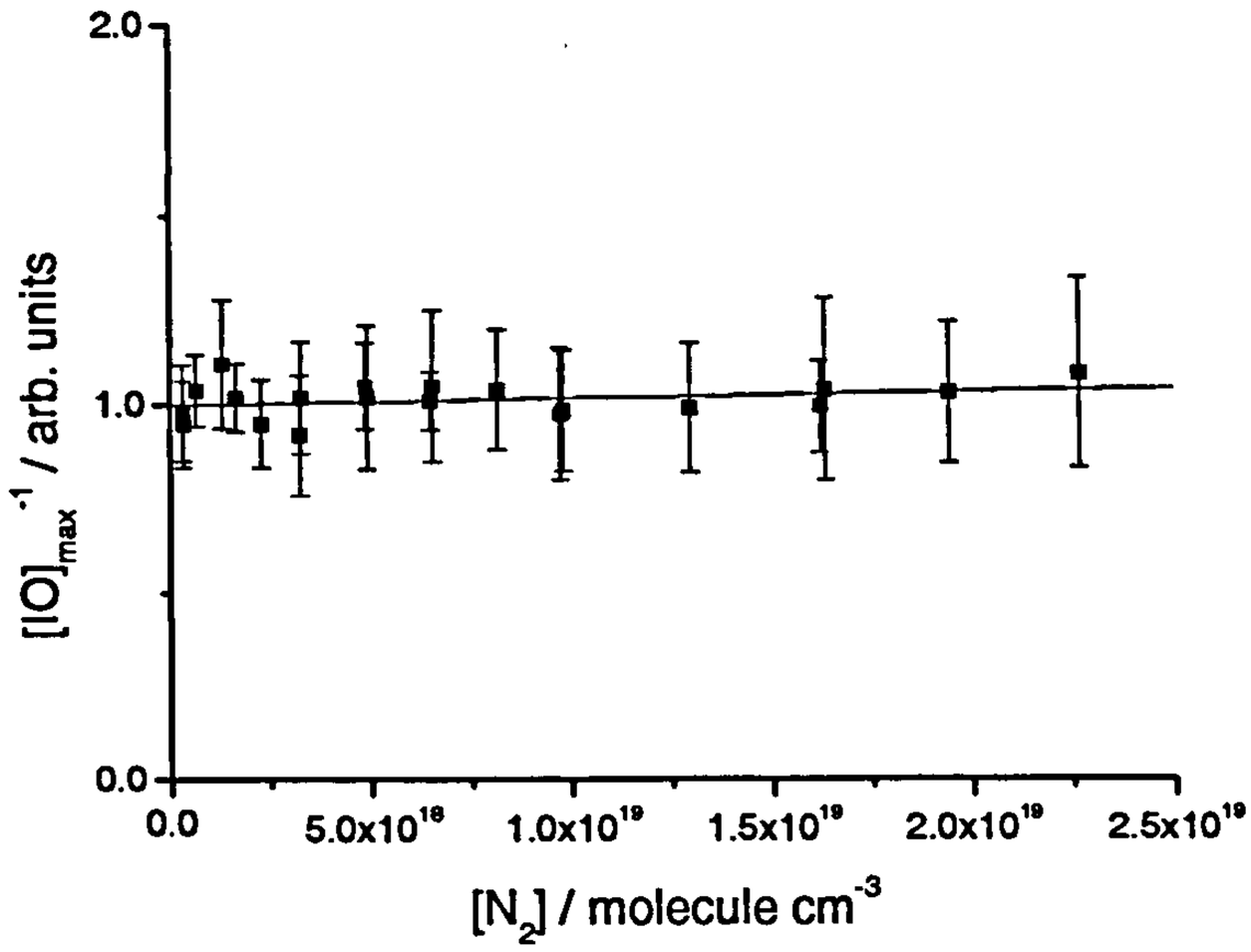

Fig. 3.5-6 – Stern-Volmer plot for quenching of the $A^2\Pi_{3/2}$ (v' = 0, J' = 3.5 – 5.5) state of IO by N_2. Excitation is at the R_1 (0,0) bandhead of the $A^2\Pi_{3/2} \leftarrow X^2\Pi_{3/2}$ electronic transition. The experimental conditions are identical to those given in the caption to Fig. 3.5-5. From the linear fit, $k_q/(k_f + k_p) = (1.7 \pm 3.3) \times 10^{-21}$ $cm^3molecule^{-1}s^{-1}$.

Thus, the negative result of the (0,0) quenching experiment is incontrovertible evidence that fluorescence quenching of the $A^2\Pi_{3/2}$ (v' = 2) state does indeed occur. In light of this, a reasoned argument must be drawn to explain the large range of k_q values determined in the (2,0) experiments. The most likely explanation is due to the fact that the bandhead of the (2,0) (and (2,1)) LIF excitations of IO are a blend of rotational transitions, resulting in the initial population of three different rotational levels in the excited state, possessing different excited state lifetimes due to the J'-dependent predissociation mechanism. This means that the observed quenching rate coefficient is likely to depend on the precise wavelength of the excitation laser (due to changes in the overlap of the energy distribution of the laser pulse and the groundstate rotational population as the laser wavelength is subtly altered). The quenching rate coefficient is also likely to have some form of J'-dependence, further exaggerating this effect. In addition, if significant pressure broadening of the rotational transitions occurs, the peak height of the bandhead will decrease with increasing pressure, altering the observed quenching rate coefficient as the precise wavelength of the excitation laser is altered. Some dependence of the quenching rate coefficient on laser line width may also be expected, therefore. In summary, the range of k_q values obtained in this study is predominantly attributed to slight changes (fractions of a wavenumber) in excitation wavelength between the independent quenching experiments.

As a final investigation in this section, quenching experiments were performed in Ar and He bath gases. LIF from IO was induced by excitation at the R_1 bandhead of the (2,0) band As quenching of O (^{1}D) is significantly less efficient in He and Ar (than N_2), approximately 7 Torr of N_2 was added to the reaction system, for each pressure studied, to ensure the rapid quenching of O (^{1}D) to O (^{3}P). For this reason, quenching was only investigated over the 100 – 700 Torr pressure range, so that N_2 was always a minor constituent of the reaction mixture. Fig. 3.5-7 displays the resulting Stern-Volmer plots, obtained in the noble-gas quenching experiments.

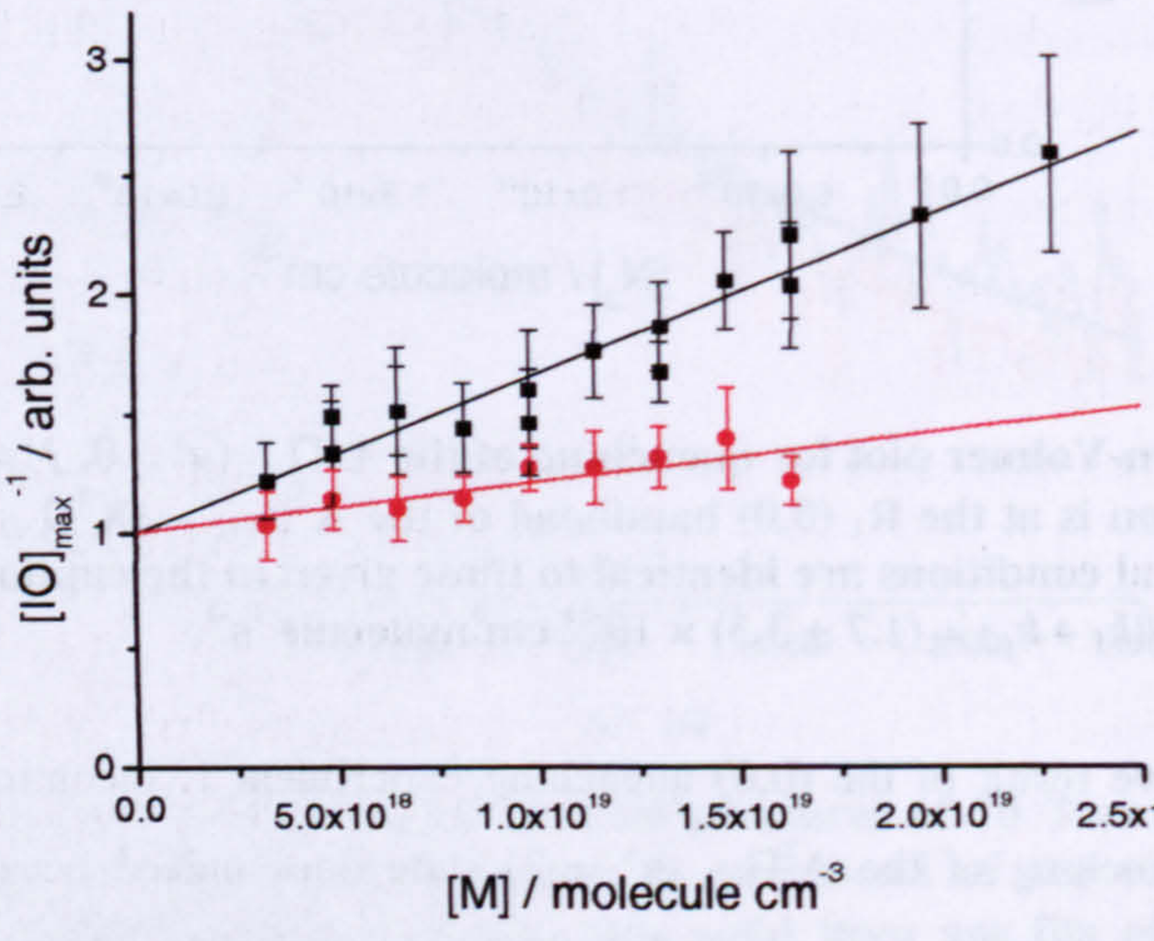

Fig. 3.5-7 – Stern-Volmer plots for quenching of the $A^2\Pi_{3/2}$ (v' = 2) state of IO in Ar (black) and He (red). Excitation is at the R_1 (2,0) bandhead of the $A^2\Pi_{3/2} \leftarrow X^2\Pi_{3/2}$ electronic transition. Experimental conditions: T = 296 K; [CF_3I] = 5.8 × 10^{14} molecule cm^{-3}; [N_2O] = 1.4 × 10^{15} molecule cm^{-3}; [N_2] = 2.3 × 10^{17} molecule cm^{-3}; [M] = balance; λ_{ex} = 193 nm; P_{ex} = 25 mJ pulse^{-1}; P_{pr} = 110 μJ pulse^{-1}; λ_{pr} = 444.89 nm. From the linear fits, $k_q/(k_f + k_p)$ = (6.7 ± 1.1) × 10^{-20} cm^{3}molecule^{-1}s^{-1} (Ar) and (2.1 ± 1.3) × 10^{-20} cm^{3}molecule^{-1}s^{-1} (He).

If the relative rate coefficients, returned from the slopes of the Stern-Volmer plots, are converted into absolute quenching rate coefficients then we obtain, k_q (Ar) = (8.6 ± 1.4) × 10^{-11} cm^{3}molecule^{-1}s^{-1}, and, k_q (He) = (2.7 ± 1.7) × 10^{-11} cm^{3}molecule^{-1}s^{-1}. This result is somewhat surprising, in that fluorescence quenching of the $A^2\Pi_{3/2}$ (v' = 2) state of IO is of comparable efficiency in N_2 and Ar, and, more significantly, unexpectedly efficient in He. Although the 2σ standard uncertainty of the He quenching rate coefficient is relatively large, the absolute quenching rate coefficient is statistically greater than, k_q = 1.0 × 10^{-11} cm^{3}molecule^{-1}s^{-1}, which is uncharacteristically high for collisional quenching rate coefficients of excited states by He. This result may be indicative that RET is involved in the quenching mechanism (as RET is a much more efficient process in He, with respect to other types of energy transfer). The involvement

of RET in the quenching mechanism is discussed at greater length in the next section of this chapter.

3.5.3 Mechanism and *J'*-dependent quenching of the $A^2\Pi_{3/2}$ (v' = 2) state of IO

In order to probe the mechanism of fluorescence quenching in the $A^2\Pi_{3/2}$ (v' = 2) state of IO, the quenching rate coefficient was determined for a number of values of *J'*. Experiments were conducted in an identical fashion to that described in the previous sections, with the exception that the probe laser was tuned to excitation wavelengths corresponding to different rotational transitions in the P_1 branch of the $A^2\Pi_{3/2}$ (v' = 2) ← $X^2\Pi_{3/2}$ (v' = 0) transition of IO. Fig. 3.5-8 displays some selected Stern-Volmer plots obtained from the experiments where excitation was in the $P_1(2)$, $P_1(6)$ and $P_1(18)$ transitions (corresponding to *J'* = 1.5, 5.5 and 17.5) respectively. From the slopes of the Stern-Volmer plots, and substitution of the excited state lifetime into E. 3.5-6, quenching rate coefficients of, $k_{q,J'}$ (10^{-11} $cm^3molecule^{-1}s^{-1}$) = (0.83 ± 0.43), (8.3 ± 1.4) and (16.7 ± 1.5) are obtained for the *J'* = 1.5, 5.5 and 17.5 rotational levels respectively. It should be noted that all rotational transitions, excited in the *J'*-dependent quenching experiments, result in the population of only one rotational level in the exited state, and the quenching rate coefficients obtained are therefore more state specific than was the case for the (2,0) bandhead. However, the relatively good agreement between the quenching rate coefficient for *J'* = 5.5 [k_q = (8.3 ± 1.4) × 10^{-11} $cm^3molecule^{-1}s^{-1}$], obtained in this study, with the average quenching rate coefficient obtained at the (2,0) bandhead [$J'_{average}$ = 4.5, $k_{q,J'average}$ = (9.5 ± 6.9) 10^{-11} $cm^3molecule^{-1}s^{-1}$] suggests that the method of data analysis for the bandhead experiments was justified, and that the relatively high degree of experimental scatter was largely due to the blend of excited state rotational levels and subtle changes in the excitation wavelength. Table 3.5-2 displays all quenching rate coefficients determined in the *J'*-dependent quenching experiments, along with the average value (for *J'* = 4.5) determined from the (2,0) bandhead experiments. In Fig. 3.5-9, the quenching rate coefficients are plotted against *J'*. From the data obtained, it would appear that the quenching rate coefficient of the $A^2\Pi_{3/2}$ (v' = 2) state of IO increases with *J'* – initially very rapidly, before exhibiting a weaker dependence at high *J'*. The observed trend is somewhat surprising. A quenching mechanism that could explain a positive *J'*-dependence to the quenching rate coefficient could be collisional predissociation (where the rate of predissociation increases with *J'*, as the energy separation between the curve crossing point and rotational energy level becomes smaller).

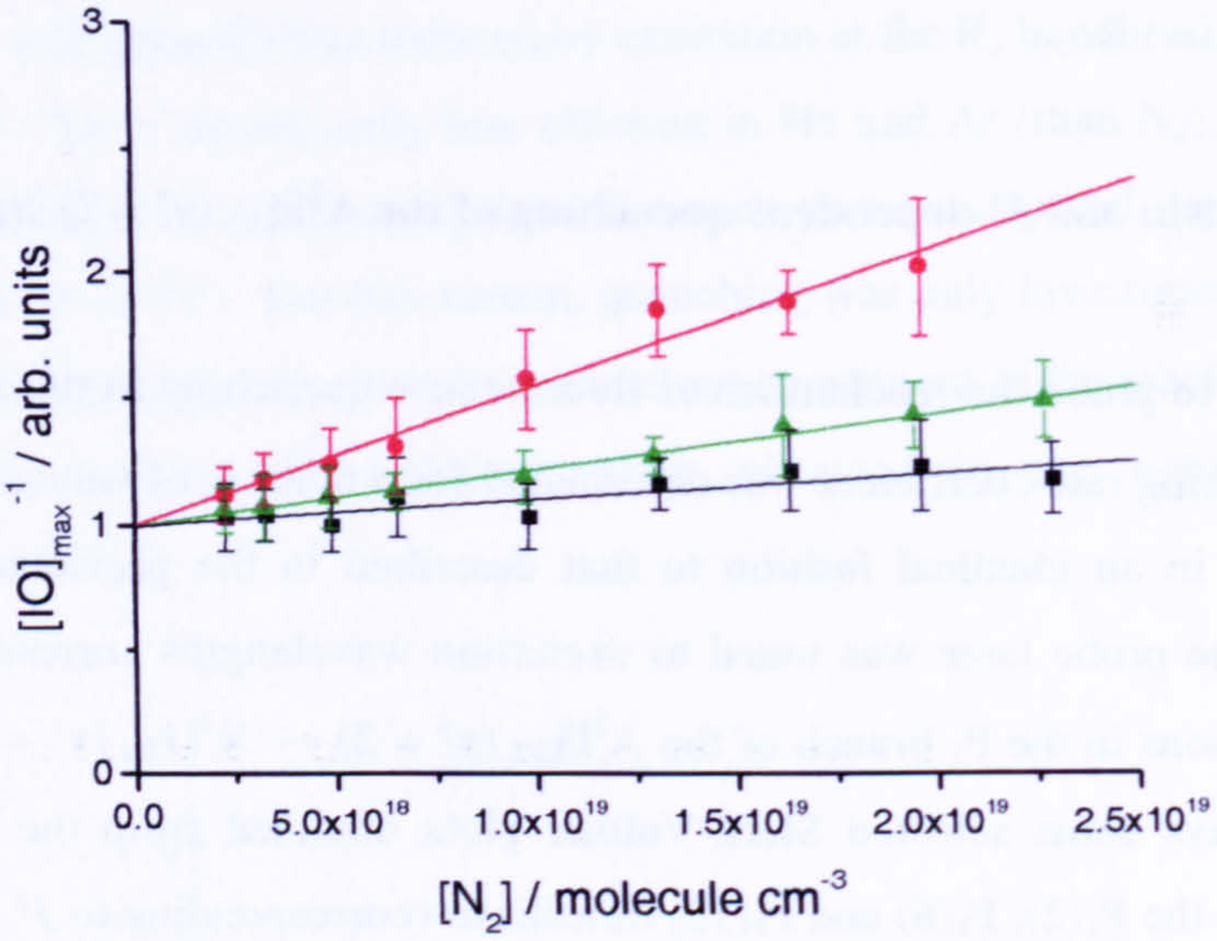

Fig. 3.5-8 – Stern-Volmer plots for quenching of various rotational levels in the $A^2\Pi_{3/2}$ (v' = 2) state of IO: J' = 1.5 (black), 5.5 (red) and 17.5 (green). From the linear fits, $k_q/(k_f + k_p)$ (10^{-20} cm^{3}molecule^{-1}s^{-1}) = (1.0 ± 0.6) (black), (5.5 ± 1.0)(red), and (2.2 ± 0.2) (green). The errors are the 2σ standard error from the linear fits. Experimental conditions: T = 296 K; [CH_3I] = 1.2 × 10^{14} molecule cm^{-3}; [N_2O] = 8.4 × 10^{14} molecule cm^{-3}; [N_2] = balance; λ_{ex} = 193 nm; P_{ex} = 45 mJ pulse^{-1}; P_{pr} = 151 μJ pulse^{-1}; λ_{pr} (nm) = 444.95 (black), 445.02 (red) and 445.53 (green).

λ_{pr}	Rot. Transition	J'	$k_q/(k_f + k_p)$	k_q
444.95	$P_1(2)$	1.5	1.0 ± 0.5	0.83 ± 0.43
444.89	Bandhead	3.5 – 5.5	7.4 ± 5.4	9.5 ± 6.9
445.02	$P_1(6)$	5.5	5.5 ± 0.9	8.3 ± 1.4
445.04	$P_1(7)$	6.5	7.0 ± 1.5	12.5 ± 2.7
445.14	$P_1(10)$	9.5	4.5 ± 0.5	13.1 ± 1.5
445.22	$P_1(12)$	11.5	4.2 ± 1.1	16.1 ± 4.2
445.31	$P_1(14)$	13.5	2.6 ± 0.6	12.6 ± 2.9
445.41	$P_1(16)$	15.5	2.9 ± 2.6	17.9 ± 15.9
445.53	$P_1(18)$	17.5	2.2 ± 0.2	16.7 ± 1.5
445.60	$P_1(19)$	18.5	2.5 ± 2.3	20.8 ± 19.0

Table 3.5-2 – J'-dependent quenching rate coefficients for the $A^2\Pi_{3/2}$ (v' = 2) state of IO. From left to right, the column headings represent: the excitation wavelength of the quenching experiment (nm); the corresponding rotational transition; the excited state rotational level(s) initially populated by the laser radiation; the slope of the Stern-Volmer plots from the experimental data (10^{-20} cm^{3}molecule^{-1}s^{-1}); the quenching rate coefficients (10^{-11} cm^{3}molecule^{-1}s^{-1}), determined from the slope of the Stern-Volmer plots and equations 3.5-6 – 3.5-8. Note that, with the exception of excitation energy, the experimental conditions for all experiments were essentially identical.

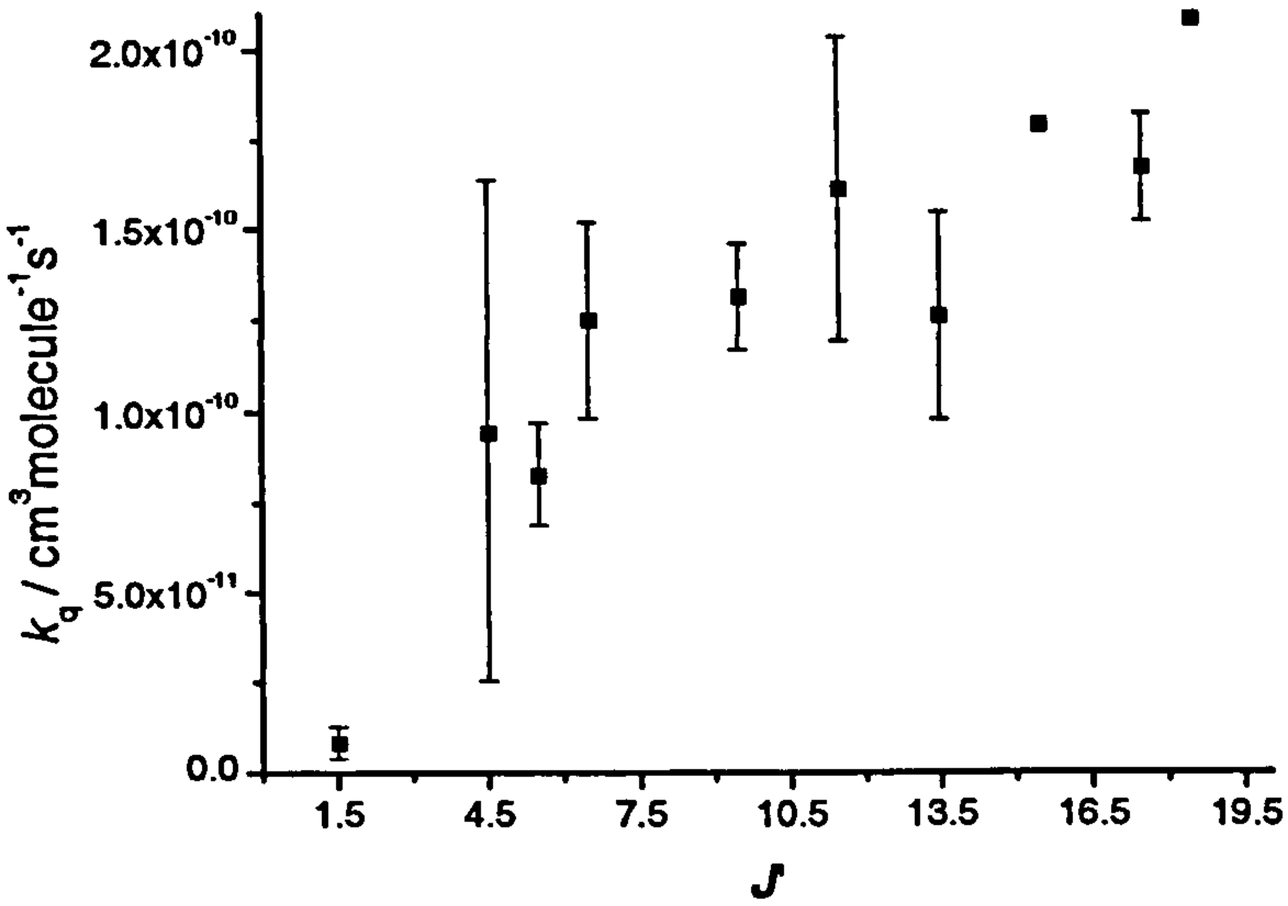

Fig. 3.5-9 – J'-dependent quenching rate coefficients for the $A^2\Pi_{3/2}$ (v' = 2) state of IO. Note that error bars are not shown for J' = 15.5 and 18.5, as the magnitude of error (see Table 3.5-2) would detract from the scale of the graph.

In an attempt to obtain a more complete description of the J'-dependent quenching rate coefficients, LIF spectra of the (2,0) band were recorded at total pressures of 10 Torr and 700 Torr N_2, and under identical experimental conditions (with the exception of total pressure). The spectra are displayed in Fig. 3.5-10 and illustrate the dramatic effect of pressure on the apparent rotational distribution. At low J', the fluorescence intensity of the rotational transitions is substantially reduced at higher pressure due to collisional quenching of the $A^2\Pi_{3/2}$ state of IO, and at high J' the effects of quenching become less apparent as competition with predissociation becomes less efficient. In order to investigate the J'-dependence of quenching, Stern-Volmer plots (albeit with only two data points) were constructed for every (resolved) rotational transition of the spectra. The slopes of the Stern-Volmer plots were then converted into quenching rate coefficients from the appropriate excited state lifetimes. Fig. 3.5-11 displays the results. Although there is a large degree of scatter in the data (as to be expected from a two-point Stern-Volmer analysis), the determined quenching rate coefficients are of a similar magnitude to those obtained in the more complete kinetic analyses displayed in Fig. 3.5-9. Further, the quenching rate coefficient is similarly observed to increase with J' (before apparently decreasing somewhere beyond the J' = 12.5 – 16.5 region).

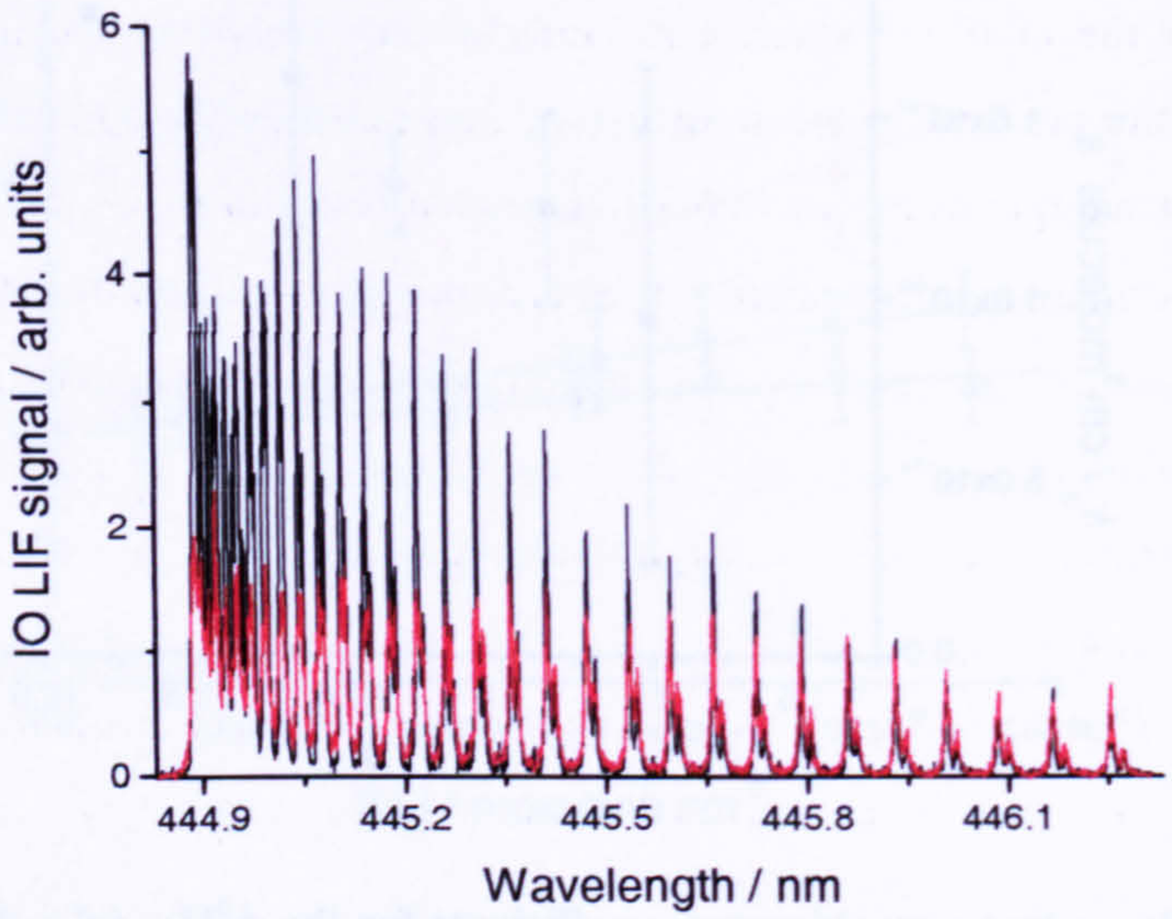

Fig. 3.5-10 – LIF spectra of the (2,0) band of the $A^2\Pi_{3/2} \leftarrow X^2\Pi_{3/2}$ transition of IO recorded at 10 Torr total pressure (black) and 700 Torr total pressure (red) N_2. The experimental conditions were identical to those given in the figure caption of Fig. 3.5-8, with the exception that the delay time between photolysis and probe lasers, Δt, was fixed at a constant value, where the LIF signal from IO was observed to be maximum (700 μs).

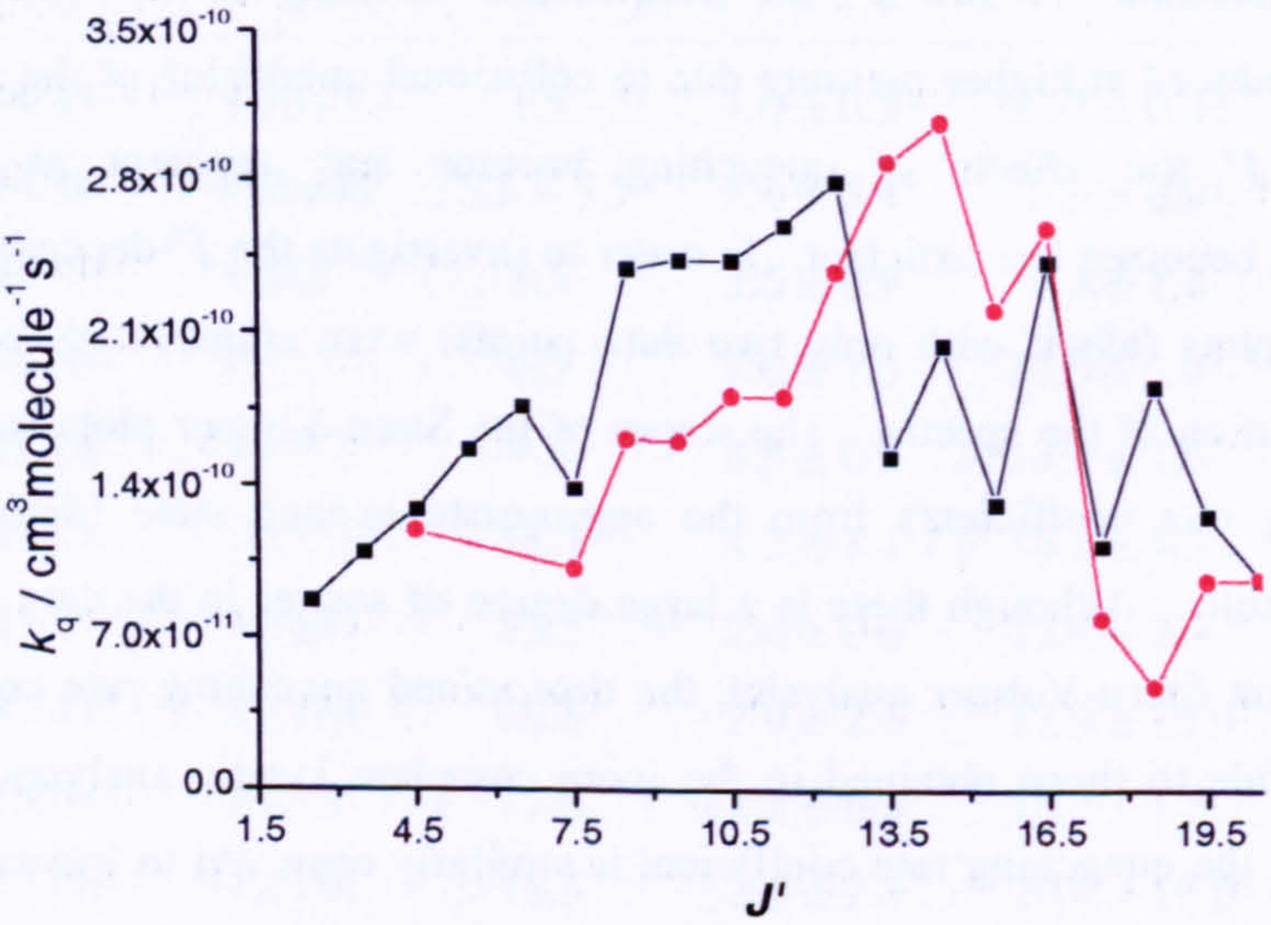

Fig. 3.5-11 – J'-dependent quenching rate coefficients for the $A^2\Pi_{3/2}$ (v' = 2) state of IO, obtained from a two-point Stern-Volmer analysis of the LIF spectra displayed in Fig. 3.5-10. The black data points correspond to LIF transitions of the P_1 branch, and the red data points the R_1 branch.

It must be commented that too much confidence should not be placed in the J'-dependence displayed in either Fig. 3.5-9 or Fig. 3.5-11 for two main reasons. The first is that, particularly for the high J' experiments, only a very small change in fluorescence signal is observed over the pressure range studied (see Fig. 3.5-8), which introduces a significant error into the determined quenching rate coefficients as a result of unavoidable experimental scatter. The second, and more significant reason, is a result of the method of determining the quenching rate coefficients. As discussed previously, the quenching rate coefficients are determined assuming no RET in the excited state, and that $(k_f + k_p)$ can be calculated from equations 3.5-7 and 3.5-8. However, if RET is not negligible, then the calculated lifetimes of the excited state will be erroneous, and especially so for low J'. The rate of RET would be expected to decrease with increasing J', as the spacing between successive rotational levels becomes greater, and also the extent of RET would be expected to decrease with increasing J', as the lifetime decreases due to the J'-dependent predissociation mechanism. If RET proceeds at the gas kinetic rate at 296 K, the rate of RET would be equal to the rate of predissociation for the $J' = 1.5$ level at a pressure of ~ 100 Torr, and would thus be the dominant process at higher pressures. It is, therefore, very likely that the assumption that RET is negligible in the $A^2\Pi_{3/2}$ ($v' = 2$) state of IO is incorrect and that the calculated lifetimes of the excited state are significantly overestimated at low J', resulting in the underestimation of the quenching rate coefficients. In fact one would expect the effect of RET to result in a decrease in the quenching rate coefficient with increasing J' for two reasons. First, that the rate of RET will decrease with increasing J', and secondly that the influence of RET will decrease with increasing J', due to the shorter lifetime of the rotational levels. This reasoning could explain why the quenching rate coefficient appears to decrease at higher J' in Fig. 3.5-11, which therefore may be a genuine result. As, at higher J', the rotational level initially populated by the laser radiation is nearer to the thermal equilibrium ($J'_{max,296\ K} = 19.5$), and the effects of RET will be less, the calculated lifetime (used for the determination of the quenching rate coefficient) is likely to be nearer to the true value than at low J'.

In order to investigate this hypothesis, a dispersed fluorescence experiment was performed. If the LIF excitation of IO is in the (2,0) R_1 bandhead, then the $J' = 3.5 - 5.5$ rotational levels are initially populated in the excited state. If we assume that RET is negligible then fluorescence will only occur at wavelengths corresponding to the absorption transitions: $R_1(3)$, $R_1(4)$, $R_1(5)$, $P_1(4)$, $P_1(5)$ and $P_1(6)$ (as these are the only rotational transitions allowed by the spectroscopic selection rules for a diatomic molecule characterised by Hund's case *a*, with a Q branch of negligible intensity), but in distinct bands corresponding to different groundstate vibrational levels. If we consider the (2,1) vibrational band, the wavelength range of the allowed transitions will fall in the 458.93 – 459.10 nm region (a spread of 0.17 nm). Conversely, if RET is not negligible fluorescence will occur over a much wider wavelength

range, as the number of populated rotational levels in the excited state, and hence the number of allowed transitions to the groundstate, is increased. Thus information with regards to the influence of RET in the $A^2\Pi_{3/2}$ ($v' = 2$) state of IO can be obtained by recording the dispersed fluorescence spectrum of a particular vibrational emission band at high resolution.

To perform this experiment, the dispersed fluorescence spectrum of the (2,1) band of the $A^2\Pi_{3/2} \rightarrow X^2\Pi_{3/2}$ transition of IO was recorded at a monochromator resolution of 0.3 nm. To record the spectrum, Δt is fixed at a constant value where the fluorescence signal from IO is maximum, and the excitation laser is tuned to the peak of the (2,0) bandhead. The monochromator grating is then scanned from 458 – 462 nm, at a scan speed of 1 nm/min, and the wavelength-resolved dispersed fluorescence intensity, as observed by the monochromator PMT, is recorded. The experiment was repeated at total pressures of 10 Torr and 600 Torr N_2, under otherwise identical conditions. The results are displayed in Fig. 3.5-12.

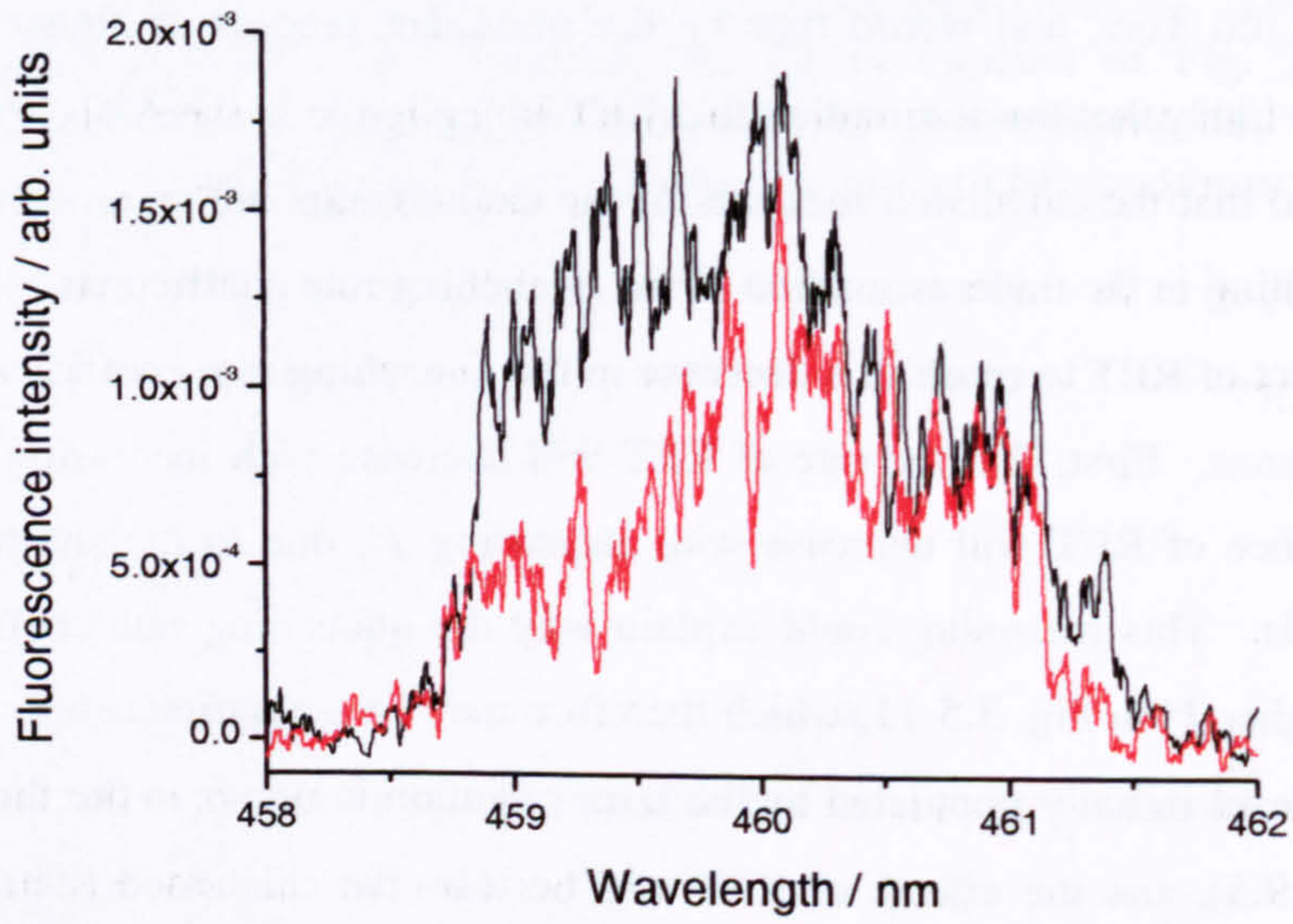

Fig. 3.5-12 – Dispersed fluorescence spectrum of the (2,1) band of the $A^2\Pi_{3/2} \rightarrow X^2\Pi_{3/2}$ transition of IO, recorded as a function of N_2 pressure: 10 Torr (black) and 600 Torr (red). Excitation is at the R_1 bandhead of the (2,0) transition. Experimental conditions: T = 296 K; $[CH_3I] = 5.6 \times 10^{14}$ molecule cm^{-3}; $[N_2O] = 3.4 \times 10^{15}$ molecule cm^{-3}; $[N_2]$ = balance; Δt = 200 μs; λ_{pr} = 444.890 nm; P_{pr} = 145 μJ pulse^{-1}; λ_{ex} = 193 nm, P_{ex} = 43 mJ pulse^{-1}; M_g = 1200 grooves/mm; M_r = 0.30 nm; M_{ss} = 1 nm/min.

The results of the dispersed fluorescence experiment are striking in that fluorescence is observed to extend over a 2 – 3 nm window – a much greater range than expected in the scenario of negligible RET (0.17 nm), and from the monochromator resolution (0.3 nm), unambiguously illustrating the influence of RET in the $A^2\Pi_{3/2}$ ($v' = 2$) state of IO. The fluorescence is observed to extend up to the 461 – 461.5 nm wavelength range, corresponding to transitions originating from J' levels of the order of 34.5 – 37.5, suggesting that RET is

extremely efficient and is competitive with predissociation at pressures as low as 10 Torr N_2. The second notable feature of the dispersed fluorescence spectra is that the low J' component of the fluorescence is significantly weaker at 600 Torr than 10 Torr, indicating that fluorescence quenching of the excited state is indeed occurring, and that this is likely to be attributable, at least partially, to RET. The fact that the fluorescence intensity exhibits less pressure dependence at high J' is in accord with the excited state lifetime being predominantly governed by predissociation at high J'.

The results of the dispersed fluorescence experiment imply that all quenching rate coefficients, determined in this study by Stern-Volmer analysis, are erroneous due to the incorrect assumption that the influence of RET is negligible in the excited state, and that the excited state lifetime could be accurately defined by the lifetime of the rotational state initially populated by the laser radiation.

3.5.3.i Boltzmann Analysis of LIF Spectra

In light of the above findings, a different approach was adopted to gain a more representative understanding of the true J'-dependence and absolute rate coefficient for collisional quenching in the $A^2\Pi_{3/2}$ ($v' = 2$) state of IO, which utilises Boltzmann analysis of LIF excitation spectra. The intensity of an absorption line, I_{abs}, is given by E. 3.5-10[9]

$$I_{abs} = \frac{I_0 N h\tilde{\nu} B_{if} g}{Q_T} \exp\left(-hc\varepsilon_{J''}/k_B T\right) \qquad \text{E. 3.5-10}$$

where, I_0 is the intensity of the excitation radiation; B_{if} is the Einstein coefficient of absorption of the spectroscopic transition; N is the total population of the groundstate, Q_T is the total partition function for the groundstate; $\tilde{\nu}$ is the transition frequency (cm^{-1}); g is the average degeneracy of the ground and excited states ($J' + J'' + 1$); and $\varepsilon_{J''}$ is the energy of the groundstate rotational level (cm^{-1}). As I_0 (providing the excitation energy is constant), N, h and Q_T are all constants (for a given temperature), if we wish to compare the relative intensity of rotational transitions in an electronic absorption spectrum, E. 3.5-10 can be simplified to E. 3.5-11

$$I_{abs}^{\cdot} = \tilde{\nu} B_{if} g \exp\left(-hc\varepsilon_{J''}/k_B T\right) \qquad \text{E. 3.5-11}$$

where $I_{abs}^{'} = \frac{I_{abs} Q_T}{I_0 N h}$, and manipulated to give the rotational temperature, T, from a Boltzmann plot of $\ln\left[I_{abs}^{'} / (\tilde{\nu} B_{if}\, g)\right]$ against $\varepsilon_{J''}$, yielding a straight line with negative gradient, $hc/k_B T$.

Providing that no J'-dependent processes affect the fluorescence quantum yield of the excited state, the rotational temperature of an LIF excitation spectrum can also be obtained by the Boltzmann analysis, as the fluorescence spectrum will effectively mirror that of absorption. For example, Fig. 3.5-13 displays a Boltzmann plot for the LIF spectrum of the (0,0) band of IO (displayed in Fig. 3.4-8) measured at 296 K (note that predissociation is not J'-dependent in the $A^2\Pi_{3/2}$ ($v' = 0$) state of IO[10], and that the fluorescence lifetime (17.2 ps) is too short for collisional quenching, which may be J'-dependent to have any significant effect).

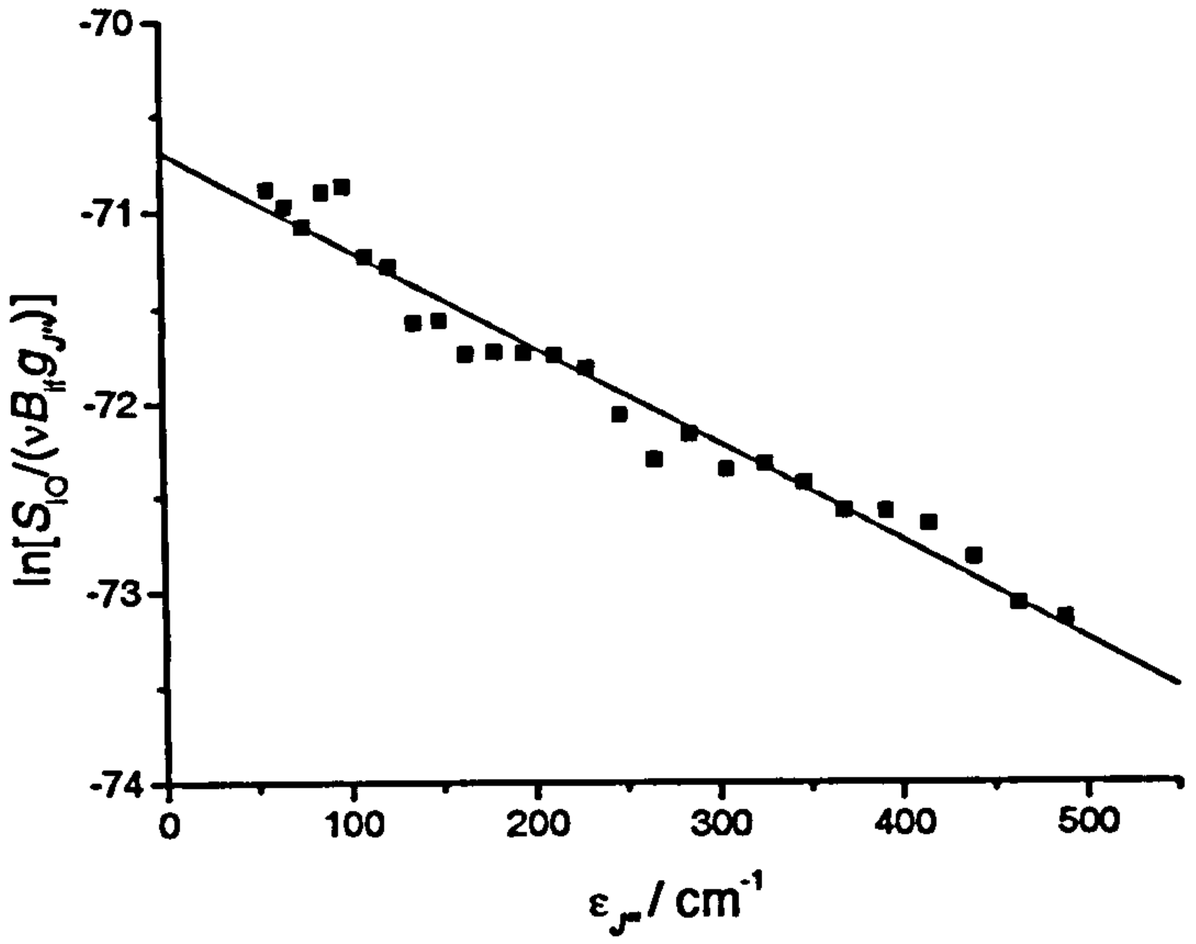

Fig. 3.5-13 – Boltzmann plot for the R_1 branch of the (0,0) band of the $A^2\Pi_{3/2} \leftarrow X^2\Pi_{3/2}$ transition of IO. From the linear fit, $hc/k_B T = 0.005 \pm 0.0005$, yielding a rotational temperature of (290 ± 30) K. The experimental conditions are identical to those given in the caption to Fig. 3.4-8.

From the slope of the Boltzmann plot of the (0,0) band, the rotational temperature is found to be (290 ± 30) K, in excellent agreement with the experimental temperature of 296 K.

Conversely, any deviation in the determined rotational temperature (from that at which the experiment was performed) by the Boltzmann analysis of a ro-vibrational band that exhibits a J'-dependent process will yield information with respect to that process. Fig. 3.5-14 displays a LIF spectrum of the (2,0) band of IO, recorded over a wide range of rotational transitions. The spectrum is normalised for the variation of probe laser power with wavelength.

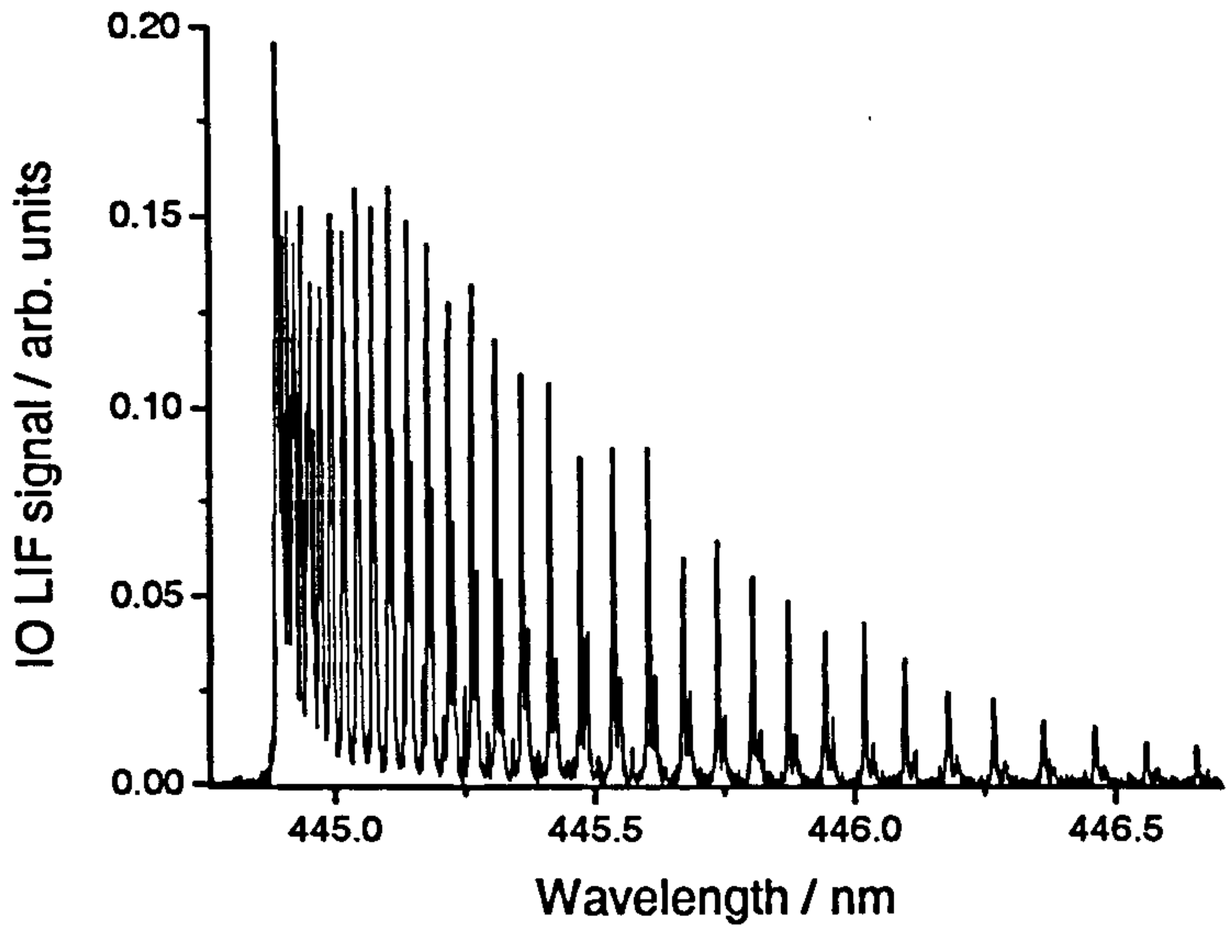

Fig. 3.5-14 – LIF spectrum of the (2,0) band of the $A^2\Pi_{3/2} \leftarrow X^2\Pi_{3/2}$ transition of IO. Experimental conditions: P = 30 Torr; T = 296 K; $[CH_2I_2] = 7.4 \times 10^{13}$ molecule cm^{-3}; $[O_2] = 1.2 \times 10^{16}$ molecule cm^{-3}; $[N_2]$ = balance; λ_{ex} = 248 nm; P_{ex} = 50 mJ pulse^{-1}; P_{pr} = 500 μJ pulse^{-1}; Δt = 2000 μs. NB. In this experiment IO was generated from the reaction, $O + CH_2I \rightarrow$ PRODUCTS. For more information with regards to the mechanism of this reaction, see Chapter Four.

Fig. 3.5-15 displays Boltzmann plots of the P_1 branch of the above LIF spectrum. The black data points represent a Boltzmann analysis of the uncorrected experimental line intensities, and the red data points correspond to a Boltzmann plot in which the experimental data have been normalised to account for the J'-dependent predissociation of the $A^2\Pi_{3/2}$ ($v' = 2$) state. The rotational temperatures returned from the different Boltzmann analyses are (107 ± 6) K for the uncorrected data and (266 ± 30) K for the data corrected for predissociation. The uncorrected data return a significantly lower rotational temperature (than the experimental temperature) because the fluorescence quantum yield decreases with increasing J'. Therefore, the intensity of spectral lines (with respect to an absorption spectrum) also decreases with increasing J', lowering the effective rotational temperature (essentially because the rotational population is underestimated at high J'). Although the discrepancy in rotational temperatures is much less when predissociation is considered, the Boltzmann analysis exhibits a systematic deviation from linearity. This deviation is most likely due to two factors. First, in correcting the data for predissociation we are assuming that RET is negligible in the excited state of IO and that the reduction of signal intensity at high J' is directly proportional to the predissociation rate of the J' state initially populated by the laser radiation. However, if RET is not negligible then this assumption will be incorrect because predissociation is J'-dependent (note that for a J'-independent predissociation mechanism, such as that in the $A^2\Pi_{3/2}$ ($v' = 0$) state of IO, the

influence of RET will not effect the Boltzmann analysis as the fluorescence lifetime of all ***J'*** states is equal and the LIF spectrum will map the Boltzmann population of the groundstate). Secondly, if the $A^2\Pi_{3/2}$ (**v'** = 2) state of IO undergoes some sort of conventional quenching mechanism, which exhibits a ***J'***-dependence, then this process will also effect the relative intensity of spectral lines. Thus any deviations from linearity (where the slope corresponds to the experimental temperature of 296 K) in the Boltzmann plot will provide information with regards to the relative rates of RET and ***J'***-dependent collisional quenching in the $A^2\Pi_{3/2}$ (**v'** = 2) state of IO.

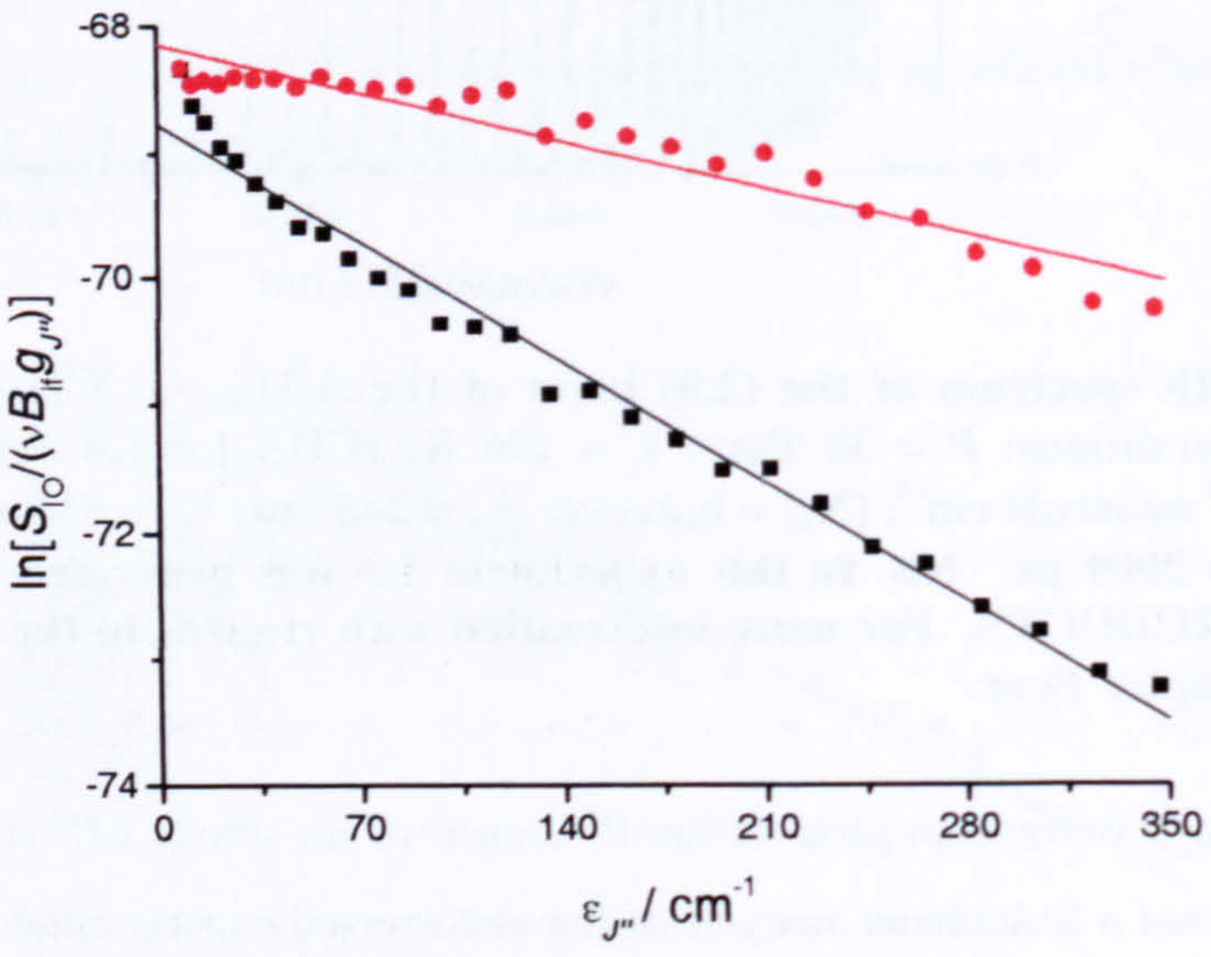

Fig. 3.5-15 – Boltzmann plots for the P_1 branch of the (2,0) band of the $A^2\Pi_{3/2} \leftarrow X^2\Pi_{3/2}$ transition of IO. The experimental conditions are identical to those given in the caption to Fig. 3.5-14. The black data points represent a Boltzmann analysis of the uncorrected experimental line intensities: from the linear fit; $hc/k_BT = 0.0135 \pm 0.0007$, yielding a rotational temperature of (107 ± 6) K. The red data points represent a Boltzmann analysis for which the experimental line intensities have been corrected for the *J'*-dependent predissociation of the $A^2\Pi_{3/2}$ (v' = 2) state of IO: from the linear fit; $hc/k_BT = 0.0054 \pm 0.0006$, yielding a rotational temperature of (266 ± 30) K.

To explore these effects, a 296 K absorption spectrum of the (2,0) band of the $A^2\Pi_{3/2} \leftarrow X^2\Pi_{3/2}$ system of IO was simulated in PGOPHER[22], a spectral simulation program. As well as simulating spectra, PGOPHER returns the relative intensity of the individual rotational transitions, allowing the construction of a Boltzmann plot. Fig. 3.5-16 displays the simulated spectrum and the generated Boltzmann plot from its output, which was found to be linear and returns a rotational temperature of (296 ± 1) K – in perfect agreement with the simulated temperature. Information regarding the ***J'***-dependent effects of collisional quenching and RET (at 30 Torr – the experimental pressure of the LIF spectrum displayed Fig. 3.5-14) can therefore be directly obtained from the ratio of the intensity of the simulated and experimental spectral

lines (once the experimental line intensities have been normalised for the J'-dependent predissociation).

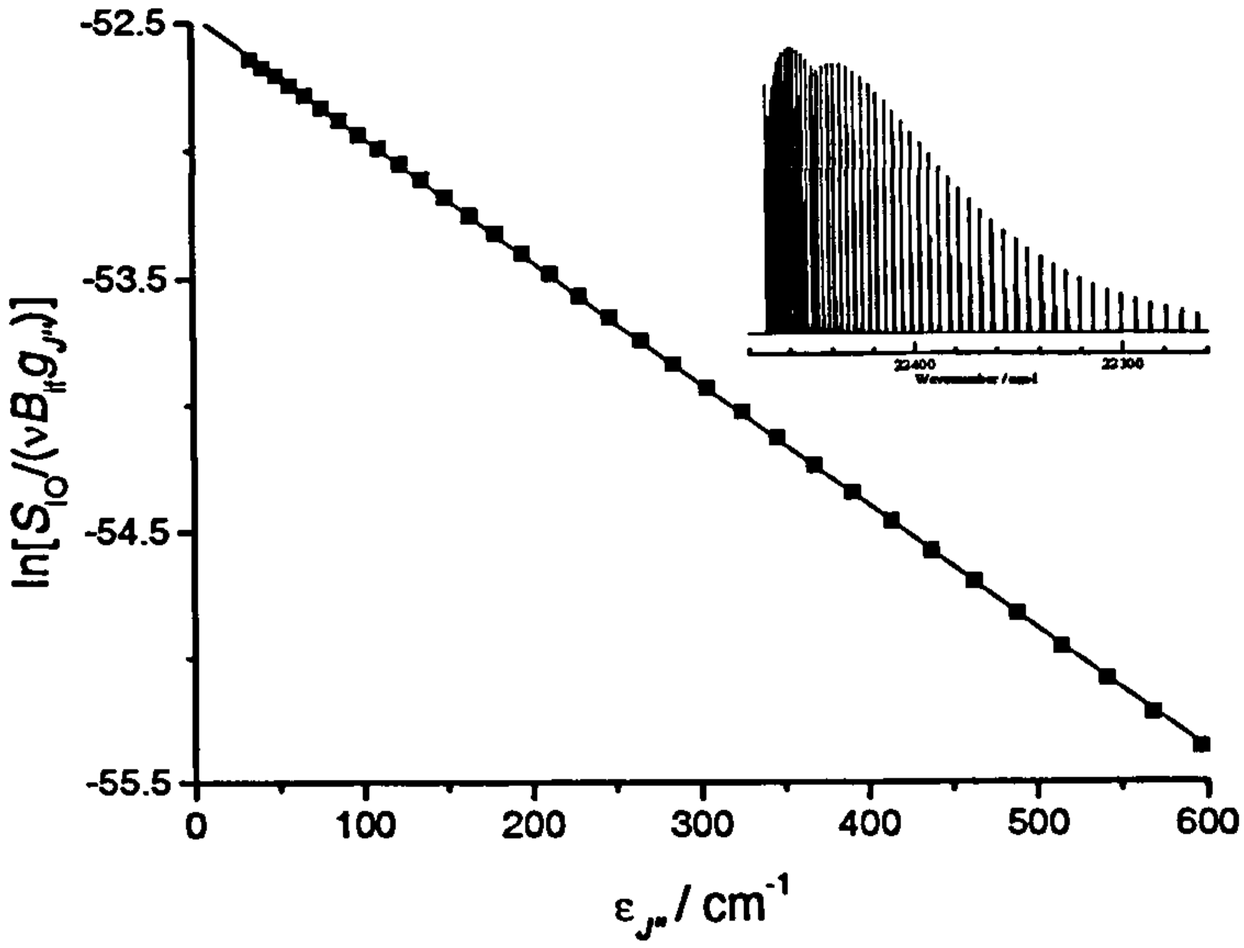

Fig. 3.5-16 – Simulated spectrum of the (2,0) band of the $A^2\Pi_{3/2} \leftarrow X^2\Pi_{3/2}$ transition of IO at 296 K and for a laser line width of 0.1 cm^{-1} (top right) and a Boltzmann plot generated from the returned line intensities of the P_1 branch (main panel). The spectrum is simulated over the J'' = 1.5 – 50.5 range. From the linear fit, $hc/k_BT = 0.00486 \pm 0.00002$, yielding a rotational temperature of (296 ± 1) K.

Fig. 3.5-17 displays the relative quenching rate coefficients (which can be considered to be composite of both RET and conventional quenching processes) determined by this procedure, and the resulting Boltzmann plot of the experimental LIF spectrum displayed in Fig. 3.5-14, once corrected for both predissociation and quenching. As can be seen from Fig. 3.5-17, the Boltzmann plot is linear and yields the correct experimental temperature. However, the apparent J'-dependence of the quenching rate, required for the correct transformation of the experimental data, is unexpected. It should be emphasised that this relationship is only representative of the relative effects of RET and some other quenching process in the $A^2\Pi_{3/2}$ (v' = 2) state of IO in 30 Torr N_2, and does not reflect the true J'-dependent relative rate coefficients of any one quenching mechanism. (Note that VET could also represent a quenching mechanism as the excited state lifetimes of v' = 1 and v' = 0 are shorter than that of v' = 2. However, the rate of VET is generally less than that of RET and collisional quenching in electronically excited states, and no evidence for fluorescence originating from v' = 1 and/or v' = 0 was evident in dispersed fluorescence spectra where excitation was in the (2,0) band, even at the highest pressure studied of 600 Torr N_2.) To investigate the apparent trend more thoroughly, an identical analysis was performed on LIF spectra recorded at 10, 200 and 700

Torr total pressure N_2. The returned relative quenching rate coefficients are plotted as a function of J' and total pressure in Fig. 3.5-18.

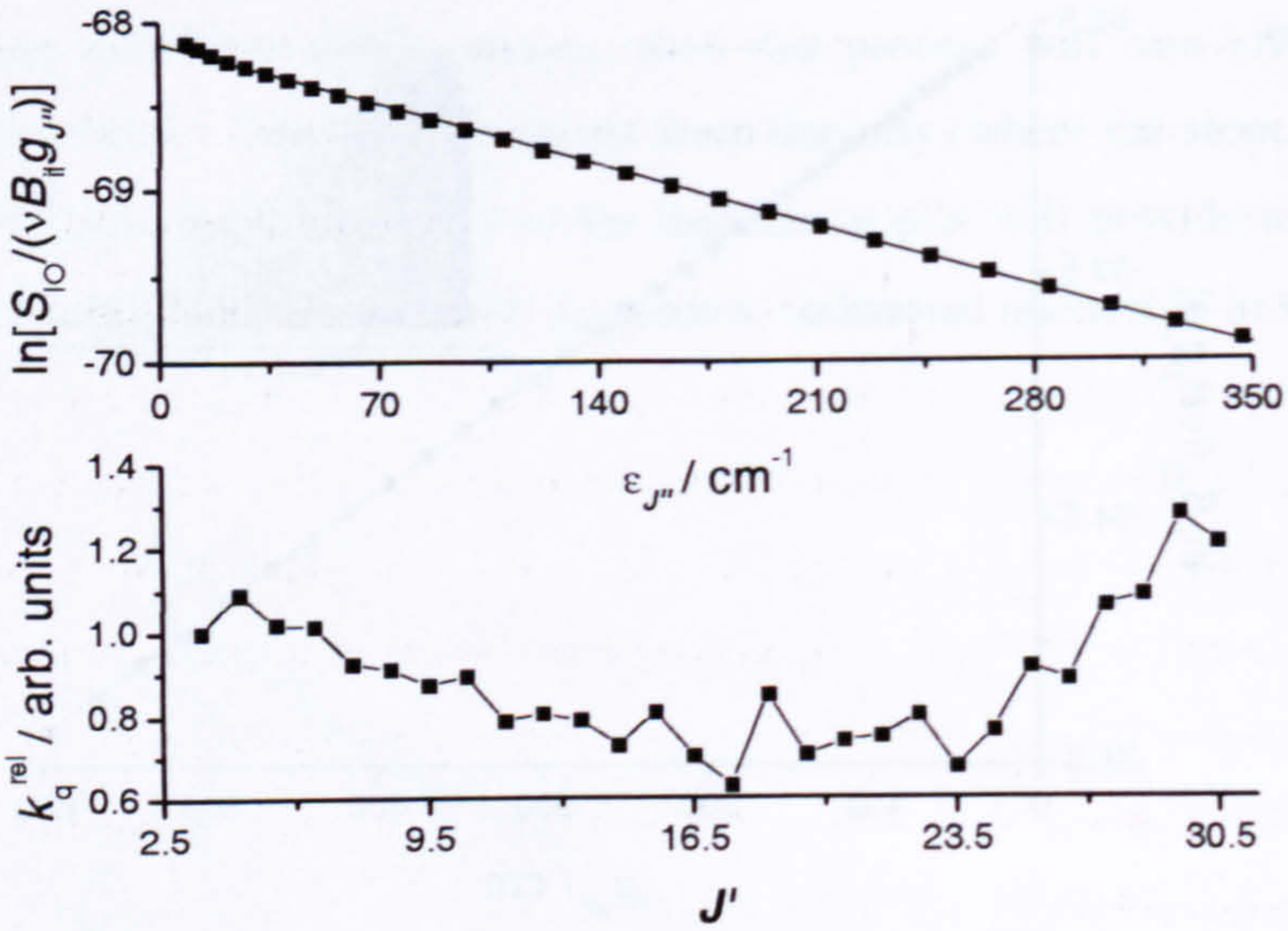

Fig. 3.5-17 – Relative J'-dependent quenching rate coefficients, k_q^{rel}, for the $A^2\Pi_{3/2}$ (v' = 2) state of IO (bottom panel), and a Boltzmann plot of the (2,0) LIF spectrum displayed in Fig. 3.5-14 (top panel), once corrected for J'-dependent predissociation and J'-dependent quenching in IO $A^2\Pi_{3/2}$ (v' = 2). Note that the quenching rate coefficients are relative to the value for the J' = 3.5 state, which is assigned a value of unity. From the linear fit to the Boltzmann plot, hc/k_BT = 0.00489 ± 0.00005, yielding a rotational temperature of (294 ± 3) K.

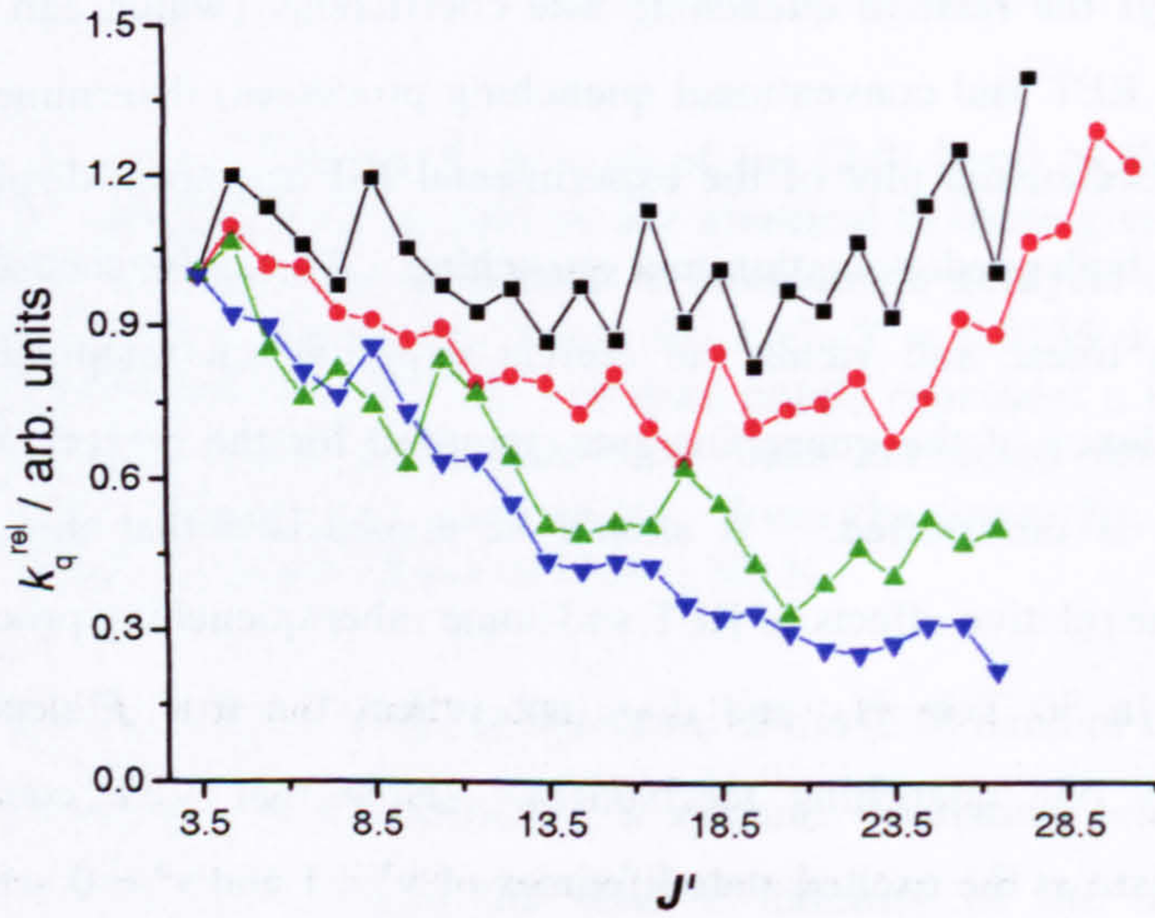

Fig. 3.5-18 – J'-dependent quenching rate coefficients required to transform LIF spectra recorded at 10 (black), 30 (red), 200 (green) and 700 Torr (blue) total pressure N_2 into a 296 K absorption spectrum, where the intensity of spectral lines is predominantly determined by the groundstate Boltzmann population. The LIF spectra recorded at 10 and 700 Torr are displayed in Fig. 3.5-10, and the 30 Torr spectrum is presented in Fig. 3.5-14. The 200 Torr LIF spectrum is not presented in this work but was recorded under identical experimental conditions to those in Fig. 3.5-10, with the exception of total pressure. In the data analysis, all spectra were normalised for the variation of excitation laser power with wavelength.

Interestingly, the apparent ***J'***-dependence of quenching becomes more pronounced with increasing pressure, with a significant negative dependence on ***J'***. This effect must be attributable to RET, as quenching by a conventional ***J'***-dependent mechanism will display the same relative ***J'***-dependence at any pressure. Thus, some conclusions can be drawn with respect to the quenching mechanism of the $A^2\Pi_{3/2}$ (**v'** = 2) state of IO. If we assume that, at a total pressure of 700 Torr N_2, RET in the $A^2\Pi_{3/2}$ state of IO is effectively complete (*i.e.* complete rotational thermalisation of the excited state occurs, no matter the initial ***J'*** state populated by the laser radiation) then the fluorescence lifetime of the excited state will be independent of the rotational transition of the electronic excitation, and hence the 700 Torr LIF spectrum does not need to be corrected for effects of ***J'***-dependent predissociation. Therefore, any deviations from the 296 K absorption spectrum, observed in the Boltzmann analysis of the 700 Torr LIF spectrum, must be attributable to genuine quenching of the $A^2\Pi_{3/2}$ (**v'** = 2) state of IO. Fig. 3.5-19 displays the relative ***J'***-dependent collisional quenching rate coefficients obtained by this reasoning

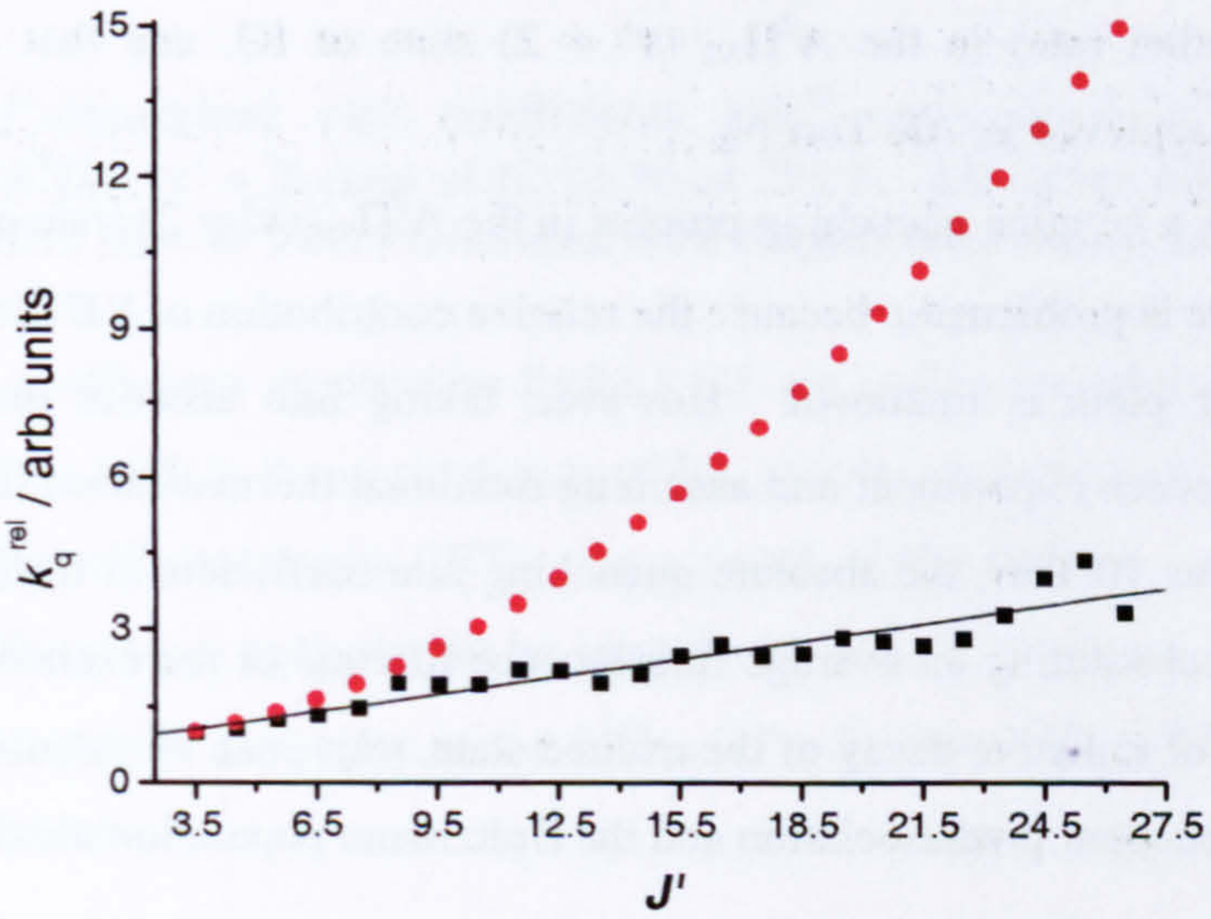

Fig. 3.5-19 – Relative *J'*-dependent collisional quenching rate coefficients (black) determined from a 700 Torr LIF spectrum of the (2,0) $A^2\Pi_{3/2} \leftarrow X^2\Pi_{3/2}$ transition of IO (Fig. 3.5-10), assuming that RET is much more efficient than predissociation in the $A^2\Pi_{3/2}$ (v' = 2) state, resulting in complete rotational thermalisation. The rate coefficients are relative to that of *J'* = 3.5, which is assigned a value of unity. The red data points represent the relative rate coefficients of predissociation[10] in the $A^2\Pi_{3/2}$ (v' = 2) state of IO, which are also relative to that of *J'* = 3.5, which is assigned a value of unity.

The data presented in Fig. 3.5-19 show that, assuming rotational thermalisation in the excited state, there is a quenching process occurring in the $A^2\Pi_{3/2}$ (**v'** = 2) state of IO, which has a linear positive dependence on ***J'***. Quenching rate coefficients of electronically excited states usually exhibit negative ***J'*** dependencies, which may suggest the presence of collisional predissociation

in the $A^2\Pi_{3/2}$ state of IO, albeit with a much weaker J'-dependence than that of the intrinsic predissociation mechanism. It should again be emphasised that this argument relies on the implicit assumption that RET is rapid with respect to predissociation in 700 Torr N_2. However, there is reasonably good evidence to support this assumption. The maximum J' state initially populated in the 700 Torr LIF spectrum (in the P_1 branch) is $J' = 26.5$. From the predissociation data[20], the lifetime of this state is ~ 61.5 ps. For equal rates of RET and predissociation at 296 K and 700 Torr, an RET rate coefficient of ~ 7.2×10^{-10} $cm^3 molecule^{-1} s^{-1}$ is required, which is not anomalously high. Further, in the dispersed fluorescence experiment (Fig. 3.5-12) it was shown that the influence of RET must be significant at pressures as low as 10 Torr N_2, where an extremely high RET rate coefficient of ~ 4×10^{-9} $cm^3 molecule^{-1} s^{-1}$ is required for equal rates of RET and predissociation (at $J' = 4.5$; the average excited state rotational level populated by the laser). At 600 Torr N_2, the dispersed fluorescence spectrum of the (2,1) band was not observed to extend to significantly higher wavelengths than that at 10 Torr (indicating that the excited state rotational levels may have been thermalised at the lower pressure). The conclusion is, therefore, that the rate of RET is extremely rapid (at least an order of magnitude higher than the gas kinetic collision rate) in the $A^2\Pi_{3/2}$ ($v' = 2$) state of IO, and that complete rotational thermalisation is achieved in 700 Torr N_2.

If there is a genuine quenching process in the $A^2\Pi_{3/2}$ ($v' = 2$) state of IO, the evaluation of its absolute rate is problematic because the relative contribution of RET towards the slopes of the Stern-Volmer plots is unknown. However, taking into account the inferences of the dispersed fluorescence experiment and assuming rotational thermalisation in the excited state at pressures as low as 10 Torr, the absolute quenching rate coefficient at the (2,0) bandhead may be estimated by substituting an average fluorescence lifetime of the excited state into E. 3.5-6. The average rate of radiative decay of the excited state, $\langle k_p \rangle$, can be calculated from E. 3.5-12, which takes into account predissociation and the Boltzmann population distribution.

$$\langle k_p \rangle = \frac{\sum k_{p,J'} \cdot (2J'+1) \exp[-hcBJ'(J'+1)/k_B T]}{q_{rot}} \qquad \text{E. 3.5-12}$$

where, $k_{p,J'}$ is the predissociation rate of rotational level, J'; B is the rotational constant of the $A^2\Pi_{3/2}$ ($v' = 2$) state of IO (0.269 cm^{-1})[10]; and q_{rot} is the rotational partition function at temperature, T ($q_{rot,\ 296\ K} = 1526$). From E. 3.5-12 we obtain, $\langle k_p \rangle = 8.5 \times 10^9$ s^{-1} for the thermalised $A^2\Pi_{3/2}$ ($v' = 2$) state of IO, corresponding to a lifetime of ~ 118 ps. Substituting this value in to E.3.5-6, along with the average quenching rate coefficient determined at the (2,0) bandhead by Stern-Volmer analysis, yields a quenching rate coefficient of, $k_{q(bandhead)} = (6.3 \pm 4.6) \times 10^{-10}$ $cm^3 molecule^{-1} s^{-1}$. Rate coefficients for collisional quenching of the $A^2\Pi_{3/2}$ (v'

= 2) state of IO by N_2 may therefore be estimated for $J' = 3.5 - 26.5$, by applying the relative J'-dependent quenching rates determined from the 700 Torr LIF spectrum (Fig. 3.5-19). Table 3.5-3 lists the quenching rate coefficients determined by this procedure.

J'	$k_{q,J'}$	J'	$k_{q,J'}$	J'	$k_{q,J'}$
3.5	5.8	11.5	13.0	19.5	16.5
4.5	6.3	12.5	12.8	20.5	16.1
5.5	7.3	13.5	11.4	21.5	15.6
6.5	7.7	14.5	12.4	22.5	16.4
7.5	8.6	15.5	14.4	23.5	19.1
8.5	11.3	16.5	15.7	24.5	23.3
9.5	11.2	17.5	14.4	25.5	25.2
10.5	11.3	18.5	14.7	26.5	19.3

Table 3.5-3 – J'-dependent rate coefficients (10^{-10} $cm^3molecule^{-1}s^{-1}$) for collisional quenching of the $A^2\Pi_{3/2}$ ($v' = 2$) state of IO by N_2 at 296 K. All values are derived with the assumption that RET in > 10 Torr N_2 is rapid with respect to predissociation.

Although the rate coefficients reported in Table 3.5-3 are highly speculative due to a lack of information regarding RET in the excited state of IO, clearly quenching of the $A^2\Pi_{3/2}$ ($v' = 2$) state of IO is highly efficient (as is RET). As a result of the findings of this work, future experimental and theoretical work should be carried out in order to obtain greater insight into fundamental energy transfer processes in the $A^2\Pi_{3/2}$ ($v' = 2$) state of IO, and to determine their absolute rate coefficients.

3.5.4 Discussion

This work represents the first detailed investigation into fluorescence quenching of the $A^2\Pi_{3/2}$ ($v' = 2$) excited state of IO. The only previous investigation was carried out by Dillon and reported in his PhD thesis[23]. In that work, the ratio of rates of quenching and predissociation, k_q/k_p, in the $A^2\Pi_{3/2}$ ($v' = 2$) state of IO was determined in N_2 at 294 K in an analogous experiment to that of the Stern-Volmer analysis reported in section 3.5.2. After exciting IO at the R_1 (2,0) bandhead of the $A^2\Pi_{3/2} \leftarrow X^2\Pi_{3/2}$ electronic transition, Dillon found the ratio of rate coefficients, $k_q/k_p = (9.0 \pm 2.3) \times 10^{-20}$ $cm^3molecule^{-1}s^{-1}$.

In this work the experiment of Dillon was repeated over a more extensive range of conditions and an average k_q/k_p value of $(7.4 \pm 5.6) \times 10^{-20}$ $cm^3molecule^{-1}s^{-1}$ was determined, slightly smaller but in reasonable agreement with that of Dillon. The influence of collisional quenching in the $A^2\Pi_{3/2}$ (v' = 2) state of IO was confirmed by performing quenching experiments after excitation in the (0,0) band of the $A^2\Pi_{3/2} \leftarrow X^2\Pi_{3/2}$ system, where essentially no decrease in IO LIF signal was observed with increasing pressure, due to inefficient quenching as a result of the short excited state lifetime. Quenching of v' = 2 was also observed in Ar (which was of a comparable rate to that by N_2) and in He (which was less efficient by a factor of approximately four). Experiments were also performed in N_2 for other initially populated rotational levels in the $A^2\Pi_{3/2}$ (v' = 2) state and k_q/k_p was found to decrease with increasing J' due to the rapid predissociation. However, once the ratio of rate coefficients were corrected for the predissociation rate of the excited rotational level (importantly assuming no RET) the quenching rate coefficient was found to increase with increasing J'.

LIF excitation spectra of the (2,0) band of the $A^2\Pi_{3/2} \leftarrow X^2\Pi_{3/2}$ transition of IO were observed to display a marked pressure dependence, increasing in rotational temperature with increasing pressure, indicating the influence of both RET and collisional quenching in the $A^2\Pi_{3/2}$ (v' = 2) state. To investigate the effects of RET in more detail, dispersed fluorescence spectra of the (2,1) band of the $A^2\Pi_{3/2} \rightarrow X^2\Pi_{3/2}$ transition of IO were recorded at relatively high resolution (0.3 nm) after exciting IO at the R_1 bandhead of the (2,0) band. At pressures as low as 10 Torr N_2 the fluorescence was observed to extend over a wide range of wavelengths, indicating extremely rapid RET in the excited state with a rate coefficient of the order of 4×10^{-9} $cm^3molecule^{-1}s^{-1}$. The small rotational constant of the $A^2\Pi_{3/2}$ state ($B \approx 0.27$ cm^{-1})[10] and the partial ionic character of IO may allow for very efficient rotational energy transfer. Fluorescence quenching is to be an expected result of RET in the $A^2\Pi_{3/2}$ (v' = 2) state of IO (when relatively low J' states are initially populated by the LIF excitation) as the maximum rotational population is found in J' = 19.5 where the fluorescence lifetime (and hence fluorescence quantum yield) are significantly smaller than at low J'. However, it is unknown whether RET alone can explain the experimental results and it is considered that an additional quenching process is occurring.

To investigate these possibilities further, a more rigorous examination of the pressure dependent LIF scans was performed. When the rotational lines of the LIF spectra were corrected for predissociation (assuming no RET in the excited state) it was found that the relative J'-dependence of the quenching rate coefficients, required to convert the observed rotational temperature to the correct value, displayed a marked pressure dependence – indicating the influence of RET. Assuming that RET results in complete thermalisation of the excited state in 700 Torr N_2 (regardless of the J' state initially populated by the excitation laser, up to J'

= 26.5) a positive J'-dependence was observed for a collisional quenching process in the excited state of IO, which displayed a linear dependence on J' and is considered to be a collisional predissociation mechanism. Assuming that rotational thermalisation of the excited state is complete in 10 Torr of N_2, the absolute collisional quenching rate coefficient of this process is estimated as, $k_q = (6.3 \pm 4.6) \times 10^{-10}$ cm^{3}molecule^{-1}s^{-1} for $J' = 4.5$, and $\sim 2 \times 10^{-9}$ cm^{3}molecule^{-1}s^{-1} for $J' = 26.5$. Although the effects of RET and collisional quenching could not be completely decoupled in this study, both processes must occur at extremely rapid rates (significantly faster than the gas kinetic collision frequency) and require further experimental and theoretical research.

Determining the absolute state-to-state rate coefficients of RET in the $A^2\Pi_{3/2}$ ($v' = 2$) state of IO is non-trivial. They could potentially be determined by recording the time dependent, rotationally resolved, dispersed fluorescence spectrum originating from the $A^2\Pi_{3/2}$ ($v' = 2$) state, after the initial population of a single rotational level. However, as the excited state lifetime of IO is so short (< 1 ns) this experiment could not be achieved with a typical commercial laser as the laser pulse width would be significantly longer than the lifetime of the excited state. In principle, the experiment could be performed with a ps laser, although a fluorescence detector with a greater temporal resolution than a conventional PMT would also be required. Further, the line width of a 1 ps laser is at least 5.3 cm^{-1} (due to the Heisenberg uncertainty principle) and multiple J' levels in the $A^2\Pi_{3/2}$ ($v' = 2$) state would be populated by the laser radiation (note that 5 cm^{-1} overlaps the first 12 rotational transitions of the R_1 branch of the $A^2\Pi_{3/2}$ ($v' = 2$) $\leftarrow$ $X^2\Pi_{3/2}$ ($v' = 0$) transition of IO). A quantitative study of RET could not be successfully studied by analysis of pressure dependent dispersed fluorescence spectra (even at a full rotational resolution) as RET could not be completely decoupled from a J'-dependent collisional quenching process. In summary, a quantitative investigation of RET in the $A^2\Pi_{3/2}$ ($v' = 2$) state of IO cannot be achieved by conventional laboratory techniques.

Information regarding RET in $^2\Pi_{3/2}$ states of IO could be obtained by investigating rotational energy transfer in the $X^2\Pi_{3/2}$ groundstate of IO. To achieve this, an IR pump laser could be used to excite groundstate IO to an excited vibrational level (*e.g.* $v'' = 2$ or $v'' = 3$), which could subsequently be excited to the $A^2\Pi_{3/2}$ state of IO, inducing fluorescence, by a second, UV probe laser. By recording LIF excitation spectra as a function of delay time between pump and probe lasers, the evolution of the rotational distribution in the groundstate could be monitored, allowing the determination of the absolute state-to-state rate coefficients of RET in the $X^2\Pi_{3/2}$ state of IO. Further, as the (0,2) and (0,3) bands of the $A^2\Pi_{3/2} \leftarrow X^2\Pi_{3/2}$ transition of IO have relatively large FCF's (see section 3.4.3) excitation of the groundstate population to $v' = 0$ would minimise interference to the data analysis from predissociation and RET in the $A^2\Pi_{3/2}$ state of IO (as predissociation in $v' = 0$ is not J'-dependent). An

experimental apparatus designed for studying the rate of reactions of vibrationally excited small free-radicals will soon be developed in our laboratory and could be used for the suggested study of RET in the $X^2\Pi_{3/2}$ state of IO.

In conclusion this study has provided important insight into energy transfer processes in the $A^2\Pi_{3/2}$ (v' = 2) state of IO and, despite only being informative at a semi-quantitative level, lays the foundation for future experimental and theoretical research.

3.6 LIF Instrument for the Detection of IO Radicals in the Atmosphere

Fig. 3.6-1 shows a diagram of the core components of the fluorescence cell that has been designed, and built, for the detection of IO in the atmosphere by LIF. As the initial testing and adaptation of the instrument is the focus of ongoing research, a detailed description of the instrument will be given in future work, and only the most fundamental details are discussed herein. The fluorescence cell is constructed from a 100 × 100 × 100 mm cube of aluminium, and is anodised in a matt black finish to minimise the scatter of laser and solar radiation. Ambient air is entrained into the fluorescence cell through a cone-shaped turret of 2" base diameter, which has a 1.5 mm diameter nozzle (see Fig. 3.6-3). The turret is situated on the top face of the fluorescence cell (as depicted in Fig. 3.6-1) and is held in place by the vacuum of the cell by means of an o-ring seal. The turret nozzle is raised ~ 10 mm above the fluorescence cell surface. The fluorescence cell is evacuated by a rotary vane pump that is attached to the cell *via* flexible steel bellows connected to a flange with a KF 25 fitting, which is fixed to the bottom face of the fluorescence cell (Fig. 3.6-1) and sealed with an o-ring. The fluorescence cell has four external connection points (ECP) that can be connected to ¼" swagelock fittings and the cell pressure is measured by a 0 – 1000 Torr capacitance manometer (connected to one of the ECP's). When all cell axes and ECP's are sealed (a blank is in place of the turreted nozzle) the base pressure of the reaction cell is < 10 mTorr. When the unrestricted pump draws ambient air through the 1.5 mm diameter nozzle, the reaction cell pressure stabilises at ~ 80 Torr.

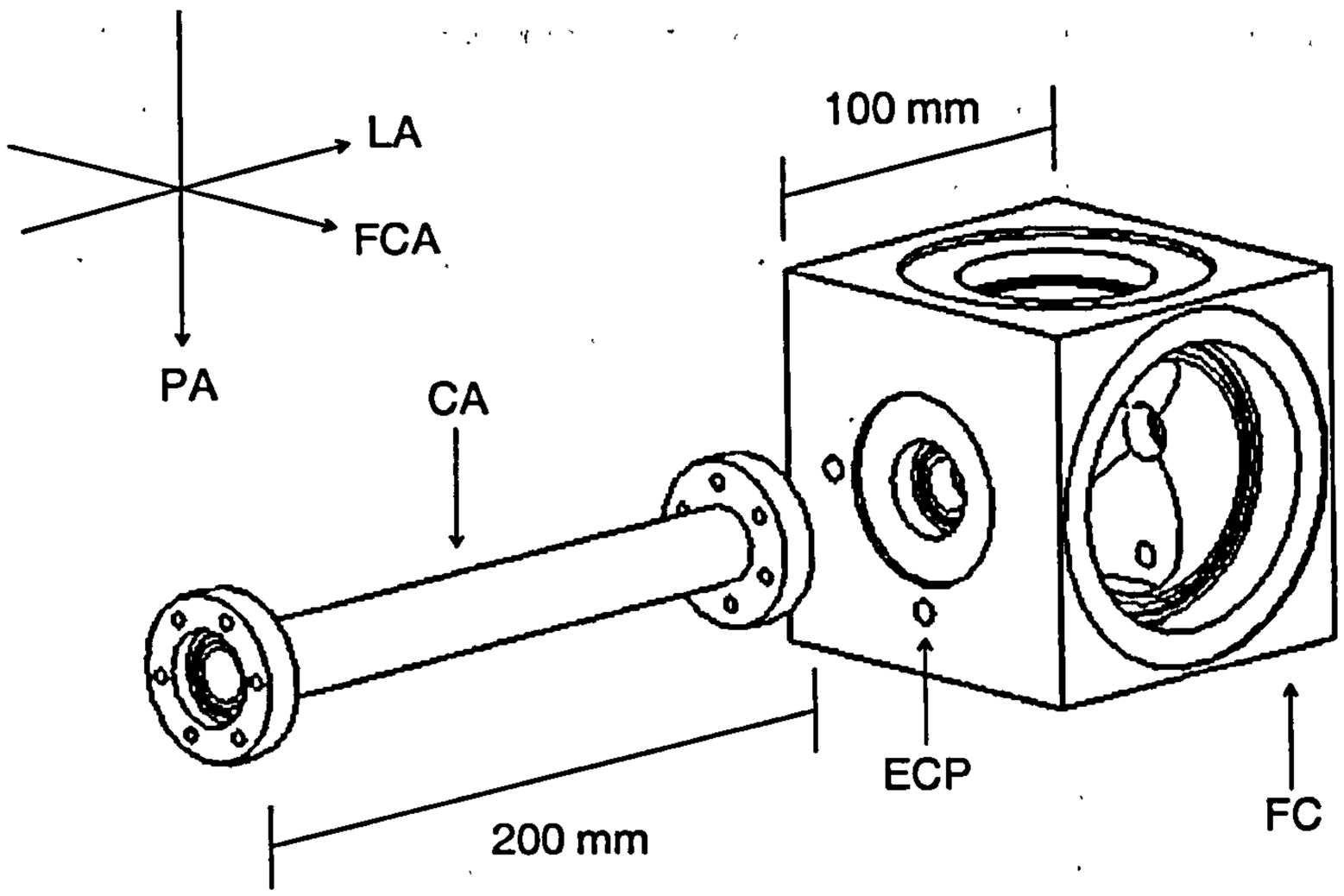

Fig. 3.6-1 – Basic diagram of the LIF cell built for the detection of IO in the atmosphere. The crossed arrows at the top left-hand-side of the figure represent the pumping (PA), lasing (LA), and fluorescence collection (FCA) axes of the fluorescence cell (FC). The additional structural components that are labelled are a cell arm (CA) and an external connection point (ECP).

Laser light is introduced into the fluorescence cell through an anodised aluminium arm of 200 mm length. The end of the arm connecting to the fluorescence cell has a plug with 1" external diameter that forms a seal with the socket of the fluorescence cell *via* an o-ring seal. The cell vacuum is maintained by a 1" diameter planoconvex glass lens that is sealed by an o-ring at the opposite end of the cell arm. The planoconvex lens has a nominal focal length of 400 mm, softly focusing the laser radiation at the LIF excitation region and reducing the amount of laser scatter within the fluorescence cell. The cell arms contain a series of baffles, constructed from matt black plastic, that are spaced at equal distances along the length of the arm and restrict the amount of scattered laser radiation entering the cell. A fibre optic is used to transport light from laser to cell arm and a fibre optic coupler, connected to the end of the cell arm *via* an anodised aluminium flange, collimates the laser radiation exiting the fibre optic into a beam of ~ 8 mm diameter. As defined by the focal length of the planoconvex lens, the laser beam diameter at the LIF excitation region (the centre of the fluorescence cell) is ~ 2 mm. A small o-ring, situated between fibre optic coupler and flange, allows the adjustment of the laser beam alignment through the fluorescence cell *via* the pressure exerted onto the o-ring from three small screws connecting the coupler to the flange.

Fluorescence from IO is collected on the horizontal cell axis, orthogonal to the laser beam. The optical arrangement for fluorescence collection is schematically represented in Fig. 3.6-2. Fluorescence passes through a 3" diameter glass window, forming the seal to the fluorescence cell vacuum, and into the fluorescence collection housing (FCH). Within the FCH, fluorescence from IO is collimated by two glass planoconvex lenses situated in series (and at the optimum distance from LIF excitation region) and each of 127 mm nominal focal length. The collimated fluorescence is then passed through a cut-on and a cut-off interference filter, before being refocused by two more identical planoconvex lenses onto the photocathode of the CPM (channel photomultiplier). The cut-on interference filter removes the fundamental 445 nm laser radiation and the cut-off interference filter removes any undoubled 890 nm IR laser radiation residing in the laser beam (see below). All optics within the FCH are fixed by a combination of interchangeable, variable thickness, anodised aluminium and matt black plastic spacers, allowing the relative position of the optics to be altered. The CPM is situated in a tight-fitting mount, and held in place by several tie wraps, at its optimum distance from the second set of planoconvex lenses. The opposite end of the fluorescence collection axis (to the FCH) is sealed by a second 3" diameter glass window, behind which is a spherically concave laser mirror (or backreflector), located at its optimum distance from LIF excitation region. The backreflector refocuses fluorescence to its source thus increasing the amount of fluorescence detected by the CPM by a factor of two. Further, as the backreflector is coated with a substrate that only reflects radiation between 495 – 605 nm, the S/N of the LIF instrument is enhanced as only fluorescence from IO (and not laser radiation) is reflected into the FCH. The CPM is powered by a high voltage power supply and operated at a voltage of 3 kV. The signal output from the CPM is sent to an oscilloscope and a computer controlled photon counter. The analogue CPM signal observed on the oscilloscope is used to set the gate width of the photon counter to temporally overlap with the laser pulse (in which all fluorescence from IO occurs). The fluorescence signal recorded by the photon counter is stored on the control PC for analysis at a later date.

An all solid-state, Nd:YAG-pumped, titanium sapphire laser is used for the generation of the 444.89 nm radiation required for excitation of IO at the R_1 (2,0) bandhead of the $A^2\Pi_{3/2} \leftarrow X^2\Pi_{3/2}$ electronic transition. The Nd:YAG laser is a diode-pumped, Q-switched, intra-cavity frequency doubled Nd:YAG laser which produces ~ 10 W of 532 nm radiation with a 25 ns pulse width, and 1 mm beam diameter, when operating at a PRF of 5 kHz. The 532 nm YAG laser radiation is used to pump a titanium sapphire crystal, generating a useful wavelength range of ~ 690 – 1000 nm. For the generation of 445 nm radiation, an IR wavelength of 890 nm is selected by the diffraction grating, and frequency doubled by a cerium lithium borate (CLBO) crystal. For an IR laser power of ~ 1 W at 890 nm, approximately 150 mW of 445 nm

excitation radiation can be generated. In a previous work[11] the laser line width of the 445 nm radiation was estimated as 0.065 cm^{-1} by comparison of experimental LIF excitation spectra with simulated spectra in PGOPHER[22]. For a more detailed description of the laser system see Bloss *et. al.*[1].

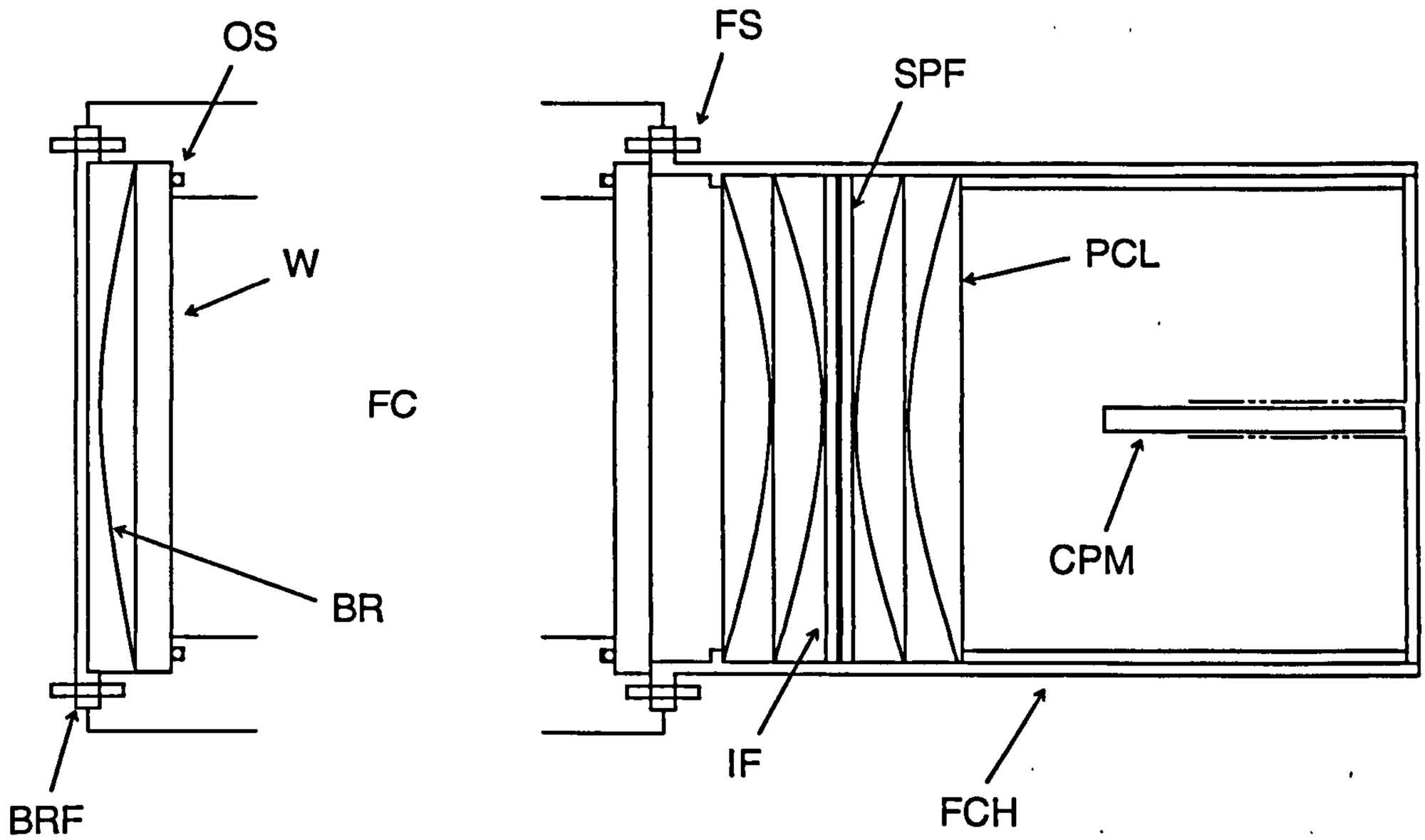

Fig. 3.6-2 – Schematic diagram of the fluorescence collection arrangement in the IO fluorescence cell. Note that the diagram is not to scale and only depicts the most essential features of the fluorescence detection. BR = back reflector, BRF = back reflector flange, CPM = channel photomultiplier, FC = fluorescence cell, FCH = fluorescence collection housing, FS = fixing screw, IF = interference filter, OS = o-ring seal, PCL = planoconvex lens, SPF = short pass filter, W = window.

3.6.1 Theoretical Sensitivity

As discussed in section 3.2, the theoretical sensitivity of an LIF field instrument is given by equation, E. 3.2-3. This section deals with evaluating the various parameters of the sensitivity equation for the IO LIF instrument described above, using the spectroscopic data obtained in this work, and comparing the determined sensitivity with the value previously estimated by Bloss *et. al.*[1].

3.6.1.i – The Einstein coefficient of absorption and fractional population of the groundstate, $B_{if}\frac{N_{(v'',J'')}}{N}$

As three rotational transitions are excited in the R_1 bandhead of the $A^2\Pi_{3/2}$ (v' =2) ← $X^2\Pi_{3/2}$ (v'' = 0) transition of IO, it is appropriate to evaluate B_{if} and $N_{(v'',J'')}/N$ as a product.

(In the work of Bloss *et. al.*[1], the fluorescence quantum yield, ϕ, was also considered in this term, although for reasons discussed in section 3.6.1.vii below, this treatment will not be extended to this work.) At the (2,0) bandhead the product of $B_{if}\frac{N_{(v'',J'')}}{N}$ will be equal to the sum of the values of the individual rotational transitions, as given by E. 3.6-1

$$B_{if}\frac{N_{(v'',J'')}}{N} = B_{(R_1(2))}\frac{N_{(v''=0,J''=2.5)}}{N} + B_{(R_1(3))}\frac{N_{(v''=0,J''=3.5)}}{N} + B_{(R_1(4))}\frac{N_{(v''=0,J''=4.5)}}{N} \qquad \text{E. 3.6-1}$$

For the $R_1(2)$, $R_1(3)$ and $R_1(4)$ rotational transitions, the Einstein coefficients of absorption are: 4.16×10^{23}; 4.36×10^{23} and 4.44×10^{23} $cm^3J^{-1}s^{-2}$ respectively[11]. The rotational populations of the groundstate levels are given by E. 3.6-2.

$$\frac{N_{(v'',J'')}}{N} = \frac{(2J''+1)\exp[-hcBJ''(J''+1)/k_BT]}{Q_{tot}} \qquad \text{E. 3.6-2}$$

where Q_{tot} is the total partition function ($q_{rot}q_{vib}$) of the $X^2\Pi_{3/2}$ (v' = 0) state of IO and is equal to 1263 at 296 K (where summation is over all Λ-doublets, which are excited by the laser radiation). From E 3.6-2, the fractional populations of the $J'' = 2.5$, 3.5 and 4.5 rotational levels in the groundstate of IO are evaluated to be 0.0047, 0.0062 and 0.0076 at 296 K respectively. Thus, substituting the appropriate values into E. 3.6-1, $B_{if}\frac{N_{(v'',J'')}}{N}$ is calculated to be equal to 8 $\times 10^{21}$ $cm^3J^{-1}s^{-2}$ for the R_1 (2,0) bandhead of the $A^2\Pi_{3/2} \leftarrow X^2\Pi_{3/2}$ system of IO at 296 K.

3.6.1.ii – Laser power, *P*

Although the laser system is capable of generating up to ~ 150 mW of 445 nm radiation, a value of 1 mW is used in the theoretical calculation as it is more meaningful to compare sensitivities in the absence of experimental variables (*i.e.* the sensitivity is expressed per mW of laser power).

3.6.1.iii – The laser, $\Delta\tilde{\nu}_L$, and IO transition, $\Delta\tilde{\nu}_D$, line widths

As previously stated, the laser line width of the 445 nm radiation generated by the Nd:YAG pumped titanium sapphire laser is estimated as 0.065 cm^{-1}. The natural line width of a spectroscopic transition corresponding to absorption in the UV-visible region of the

electromagnetic spectrum is predominantly determined by Doppler broadening and is essentially due to the range of translational energies that a molecule possesses. The Doppler width of a spectral line is given by E. 3.6-3

$$\Delta\nu = \frac{2\nu}{c}\left(\frac{2k_B T \ln 2}{m}\right)^{1/2} \qquad \text{E. 3.6-3}$$

For a frequency corresponding to the R_1 (2,0) bandhead of the $A^2\Pi_{3/2} \leftarrow X^2\Pi_{3/2}$ transition of IO (6.74×10^{14} s^{-1}), the Doppler width is calculated to be ~ 700 MHz, or 0.023 cm^{-1}. However, as the bandhead consists of three rotational transitions, which have an energy distribution of ~ 0.082 cm^{-1}, the natural line width of the IO transition is taken as 0.105 cm^{-1}.

3.6.1.iv – Length of the laser beam overlapping the ambient sample, ℓ

Although the laser beam is overlapping with the ambient air sample across the entire length of the fluorescence cell, only fluorescence originating from near to the centre of the cell will be efficiently focused onto the CPM. Therefore the active length of the laser beam can be approximated by the beam diameter, which is 2 mm at the centre of the fluorescence cell. Thus, $\ell = 0.2$ cm.

3.6.1.v – Collection efficiency of the optics, ε

The collection efficiency of the optics is defined by the fraction of fluorescence detected by the CPM, with respect to the total solid angle of fluorescence (4 π). The solid angle of fluorescence detected by the CPM, 0 is given by E. 3.6-4

$$0 = \frac{2A}{f^2} \qquad \text{E. 3.6-4}$$

where, A is the area defined by the radius of the clear aperture of the fluorescence cell windows (31.6 mm) and f is the nominal focal length of the planoconvex lenses (63.5 mm). Note that the factor of 2, in E. 3.6-4, accounts for the increased fraction of fluorescence collected as a result of the back reflector. Thus, for the fluorescence cell, $\varepsilon = 0.124$.

3.6.1.vi – Fluorescence transmission efficiency, T, and quantum efficiency of the CPM, η

For the interference filters incorporated in the fluorescence collection housing, IO fluorescence from the (2,5) – (2,10) vibrational bands of the $A^2\Pi_{3/2} \rightarrow X^2\Pi_{3/2}$ system is efficiently detected by the CPM. However, as the quantum efficiency of the CPM is wavelength dependent, as is the transmission of the colour glass cut-on filter in the 515 – 545 nm range, it is useful to evaluate the product of these parameters as a function of vibrational band, also taking into account the relative band strengths. Note that the short-pass filter has an approximately constant transmission of 60 % in the 500 – 630 nm region and all windows and lenses are anti-reflected coated in the 425 – 675 nm region, yielding a transmission of > 99.5 %. Thus, the term ηT can be evaluated from E. 3.6-5

$$\eta T = 0.6 \sum_{v''=5}^{v''=10} I_{(2,v'')} \eta_{(2,v'')} T_{(2,v'')} \qquad \text{E. 3.6-5}$$

where: $I_{(2,v'')}$ is the fractional fluorescence intensity of vibrational band (2,v''), *i.e.* $FCF_{(2,v'')}/FCF_{TOTAL}$ (as determined from the experimental data reported in section 3.4); $\eta_{(2,v'')}$ is the CPM quantum efficiency at the wavelength corresponding to the vibrational band (2,v''); and $T_{(2,v'')}$ is the percentage transmission (expressed as a fraction) of the cut-on colour glass filter at the wavelength corresponding to vibrational band (2,v''). Note that the factor of 0.6 accounts for the wavelength independent transmission efficiency of the short-pass interference filter. Table 3.6-1 lists the appropriate values of I, η and T for the (2,5) – (2,10) vibrational bands.

Band	λ	$I_{(2,v'')}$	$\eta_{(2,v'')}$	$T_{(2,v'')}$	$(I\eta T)_{2,v''}$
(2,5)	521.0	0.145	0.72	0.098	0.0103
(2,6)	538.7	0.049	0.96	0.088	0.0041
(2,7)	557.3	0.011	0.99	0.078	0.0008
(2,8)	576.9	0.098	0.99	0.067	0.0065
(2,9)	597.6	0.106	0.99	0.057	0.0059
(2,10)	619.5	0.066	0.99	0.046	0.0030

Table 3.6-1 – Wavelength dependence of the CPM quantum efficiency, η, the colour glass filter transmission efficiency, T, and the relative band strength, I, of the various (2,v'') vibrational transitions. NB. η and T are evaluated by the manufacturer's specifications and I is evaluated using the dispersed fluorescence data obtained in section 3.4.

Substituting the appropriate values into E. 3.6-5, ηT is calculated to be 0.018.

3.6.1.vii – Fluorescence quantum yield, ϕ

The fluorescence quantum yield, ϕ, is evaluated from E. 3.5-1. In the work of Bloss *et. al.*[1], ϕ was evaluated in conjunction with B_{if} and $N_{(v'',J'')}/N$ as it was assumed that RET is insignificant in the $A^2\Pi_{3/2}$ (v' = 2) state of IO and that the excited state lifetime could be calculated from the predissociation rate of the rotational level initially populated by the laser radiation. However, in consideration of the work discussed in section 3.5, it is likely that the excited state population has undergone significant rotational redistribution as a consequence of RET in 80 Torr N_2, and probably to the extent of complete rotational thermalisation. Thus the predissociation rate of the excited state can be evaluated from E. 3.5-12 and is calculated as, $k_p = 8.5 \times 10^9$ s^{-1} at 296 K. The natural radiative lifetime of the $A^2\Pi_{3/2}$ state of IO is unknown, although Bekooy *et. al.*[7] estimated it as 10 – 100 ns by extrapolation of the corresponding electronic transition moment of ClO. Taking the mid-estimate value, we obtain, $k_f = 1.82 \times 10^7$ s^{-1}. Using the estimated quenching rate coefficient obtained in section 3.5.3 for quenching of the R_1 (2,0) bandhead by N_2 ($k_q = 6.3 \times 10^{-10}$ $cm^3 molecule^{-1} s^{-1}$), $k_q[Q]$ is thus evaluated as 1.64×10^9 s^{-1} in 80 Torr air (assuming that the quenching rate coefficient is comparable in air and N_2). Thus the fluorescence quantum yield at 296 K and 80 Torr air is calculated to be 0.0018 for excitation of IO in the R_1 (2,0) bandhead of the $A^2\Pi_{3/2} \leftarrow X^2\Pi_{3/2}$ electronic transition.

3.6.1.viii – The ratio of densities inside and outside the fluorescence cell, ρ_{in}/ρ_{out}

Assuming that the rotational temperatures are equal inside and outside of the fluorescence cell, ρ_{in}/ρ_{out} is given by the ratio of fluorescence cell and ambient pressures. Hence, for a typical ground-level ambient pressure of 760 Torr, and a fluorescence cell pressure of 80 Torr, ρ_{in}/ρ_{out} = 0.105 at 296 K.

3.6.1.ix – The fractional reduction in [IO] due to heterogeneous loss processes between the fluorescence cell nozzle and LIF excitation region, γ_{IO}

As the extent of heterogeneous IO loss processes in the fluorescence cell are unknown, γ_{IO} is assumed to be unity (*i.e.* no losses occur). This assumption is very likely to be incorrect and is one reason why an absolute experimental calibration of the LIF instrument is paramount in order to determine its true sensitivity.

3.6.1.x – Evaluation of the theoretical calibration constant, C_{IO}, and detection limit, LOD_{IO}, of the IO LIF field instrument

Substituting all values into E. 3.2-3, the theoretical calibration constant for the IO LIF instrument is calculated to be, $C_{IO} = 5.7 \times 10^{-9}$ cts cm^3 molecule^{-1} s^{-1} mW^{-1}. For a laser power of 50 mW; a total averaging time of 60 s ($m = n = 1$, $t = 30$ s); a S/N of 1; and estimated laser, solar and dark background count rates of 200, 100 and 5 cts s^{-1} respectively, the detection limit of the instrument is found to be, $LOD_{IO} = 1.6 \times 10^7$ molecule cm^{-3} (or 0.7 ppt at ground-level). Although the theoretical LOD is sensitive enough to detect IO in the MBL (assuming the DOAS-reported mixing ratios), it is almost three orders of magnitude smaller than that reported by Bloss *et. al.*[1]. Table 3.6-2 lists the values of all variable parameters in E. 3.2-3 determined in this work, and in the work of Bloss *et. al.*[1].

Parameter	(Units)	Bloss *et. al.*[1], 2003	This work, 2006
$B_{if}\phi N_{(v'',J'')}/N$	(cm^{3}J^{-1}s^{-2})	2.5×10^{20}	1.44×10^{19}
P	(W)	0.001	0.001
$\left[\sqrt{\left(\Delta\tilde{\nu}_L^{\,2} + \Delta\tilde{\nu}_D^{\,2}\right)}\right]^{-1}$	(cm)	14.3	8.1
ℓ	(cm)	0.35	0.2
ε		0.125	0.124
ηT		0.0375	0.018
ρ_{in}/ρ_{out}		0.53	0.105
C_{IO}	(cts cm^3 molecule^{-1} s^{-1} mW^{-1})	3.3×10^{-6}	5.7×10^{-9}
LOD_{IO}	[molecule cm^{-3} (ppt)]	2.7×10^4 (0.001)	1.6×10^7 (0.7)

Table 3.6-2 – Theoretical parameters of E. 3.2-3, theoretical calibration constants, and theoretical detection limits for an IO LIF field instrument as determined in this work, and in that of Bloss *et. al.*[1]. Note that for the LOD_{IO} calculation in the work of Bloss *et. al.*[1], the following values were used: $S/N = 1$, $P = 50$ mW, $m = n = 1$, $t = 30$ s, $S_{lb} = 1000$ cts s^{-1}, $S_{sb} = 500$ cts s^{-1} and $S_{db} = 0$ cts s^{-1}. In this work the same values were used with the exceptions: $S_{lb} = 200$ cts s^{-1}, $S_{sb} = 100$ cts s^{-1} and $S_{db} = 5$ cts s^{-1}. Note that although $B_{if}N_{(v'',J'')}/N$ and ϕ were evaluated separately in this work, their product is given in this table for comparison with the work of Bloss *et. al.*[1]. Conversely, η and T were evaluated separately in the work of Bloss *et. al.*[1] but are expressed as their product herein for ease of comparison to this work (from Bloss *et. al.*[1], $\eta = 0.15$ and $T = 0.25$).

The largest discrepancy found between any one parameter in this work and the work of Bloss *et. al.*[1] is a factor of approximately 20 in $B_{if}\phi N_{(v'',J'')}/N$. As the same values for the

groundstate populations and Einstein coefficients of absorption were used in both works, the discrepancy is solely attributable to differences in the fluorescence quantum yield, ϕ, highlighting the importance of considering RET and fluorescence quenching in the $A^2\Pi_{3/2}$ (v' = 2) state of IO, which were ignored in the work of Bloss *et. al.*[1] but experimentally investigated in this work. The second largest discrepancy in the theoretical sensitivities, a factor of ~ 5, is found in ρ_{in}/ρ_{out}. The magnitude of this parameter is governed by the pressure of the fluorescence cell at which the experiment is performed. Discerning the optimum pressure for the field experiment is non-trivial, requiring future experimental research, and is discussed further in section 3.6.3. The sensitivity of the LIF instrument evaluated in this work is reduced by a factor of ~ 2 by the parameters, ηT, because the relative intensities of the vibrational bands of the (2 → v'') progression were previously unknown and had to be estimated. The dispersed fluorescence data determined in section 3.4 have thus facilitated the accurate evaluation of these parameters. The other parameters resulting in a reduced theoretical sensitivity of the LIF instrument are $\left[\sqrt{\left(\Delta\tilde{\nu}_L^{\,2}+\Delta\tilde{\nu}_D^{\,2}\right)}\right]^{-1}$ and ℓ. In the work of Bloss *et. al.*[1], the range of frequencies of the rotational transitions constituting the R_1 (2,0) bandhead were not considered and ℓ was estimated in accordance with the appropriate value for the Leeds HO_x FAGE instrument (which is not comparable to the IO LIF cell described above).

This work has shown that evaluating the theoretical sensitivity of an LIF instrument in the absence of information regarding spectroscopic and energy transfer processes in excited states should be treated with caution. However, even with the significantly reduced sensitivity determined herein it would appear that LIF is a viable technique for the detection of IO in the MBL.

3.6.2 Absolute Calibration of the IO LIF instrument

The large discrepancy between the calculated theoretical sensitivity of the IO LIF field instrument reported in this work and that of Bloss *et. al.*[1] emphasises the uncertainty involved with such an evaluation. Although the theoretical sensitivity determined in this work should be regarded as preferable due to a more comprehensive understanding of the physical properties of the $A^2\Pi_{3/2}$ (v' = 2) state of IO, the sensitivity analysis still requires estimating some parameters of E. 3.2-3, such as γ_{IO}, ℓ and k_f (which is essential for an accurate evaluation of ϕ) and it would be unwise to base the absolute sensitivity of the instrument at the theoretical limit. The absolute experimental calibration of the instrument is therefore of fundamental importance. However, as IO is a reactive radical species that cannot be purchased commercially, absolute calibration of the instrument requires *in situ* generation of a quantifiable source of IO, which is non-trivial,

particular as relatively low concentrations of IO (> 10^{11} molecule cm^{-3}) will rapidly diminish due to self-reaction.

Fig. 3.6-3 shows a schematic diagram of the calibration cell designed for the experimental determination of the absolute sensitivity of the IO LIF instrument. In the calibration experiment, a mixture of $CF_3I/N_2O/N_2$ is flowed at a total flow rate of ~ 20 slm[24] (atmospheric pressure) through a Pyrex flow tube (PFT) of ~ 25 mm internal diameter. At a region near the bottom of the PFT, a circular hole of ~ 10 mm diameter is drilled through the calibration cell, allowing the irradiation of the gas in the photolysis region (PR) of the PFT with light from an unfiltered Hg Pen-Ray lamp. Light from an Hg atomic emission line at 184.9 nm photolyses N_2O in the gas mixture generating O (^1D) atoms, which are quickly quenched to the groundstate (O ^3P) configuration by the large excess of N_2. The O (^3P) atoms react with CF_3I in the PFT generating IO with a yield of > 80 %[25]. Gas from the calibration cell is drawn into the fluorescence cell under vacuum, where IO is excited at the LIF excitation region, and the ensuing fluorescence detected by the CPM. The calibration cell has four ¼ " excess gas ports (EGP's), which allow any excess gas not entering the fluorescence cell to escape. By attaching a static cell to the EGP's it is found that a total flow rate of ~ 15 slm is required to balance the flow rate in the fluorescence cell. Evaluating the concentration of IO excited at the LIF excitation region fundamentally requires knowledge of the O atom concentration generated by the photolysis of N_2O. The lamp flux at 184.9 nm is determined in a separate experiment by flowing air (at an equal flow rate) through the PFT, generating O_3. The excess gas from the calibration cell is sent to a commercial O_3 analyser, which yields the concentration of O_3 (and hence O atoms) generated under the experimental conditions. Thus from knowledge of the concentration of O_2 in the PFT, the total flow rate in the PFT (allowing the evaluation of the residence time of the gas mixture in the PR) and the absorption cross section of O_2 at 184.9 nm, the 184.9 nm lamp flux can be evaluated and is found to be, $F_{(184.9\ nm)} \approx 3 \times 10^{14}$ photons cm^{-2} for the Hg lamp operating at full power (20 mA DC).

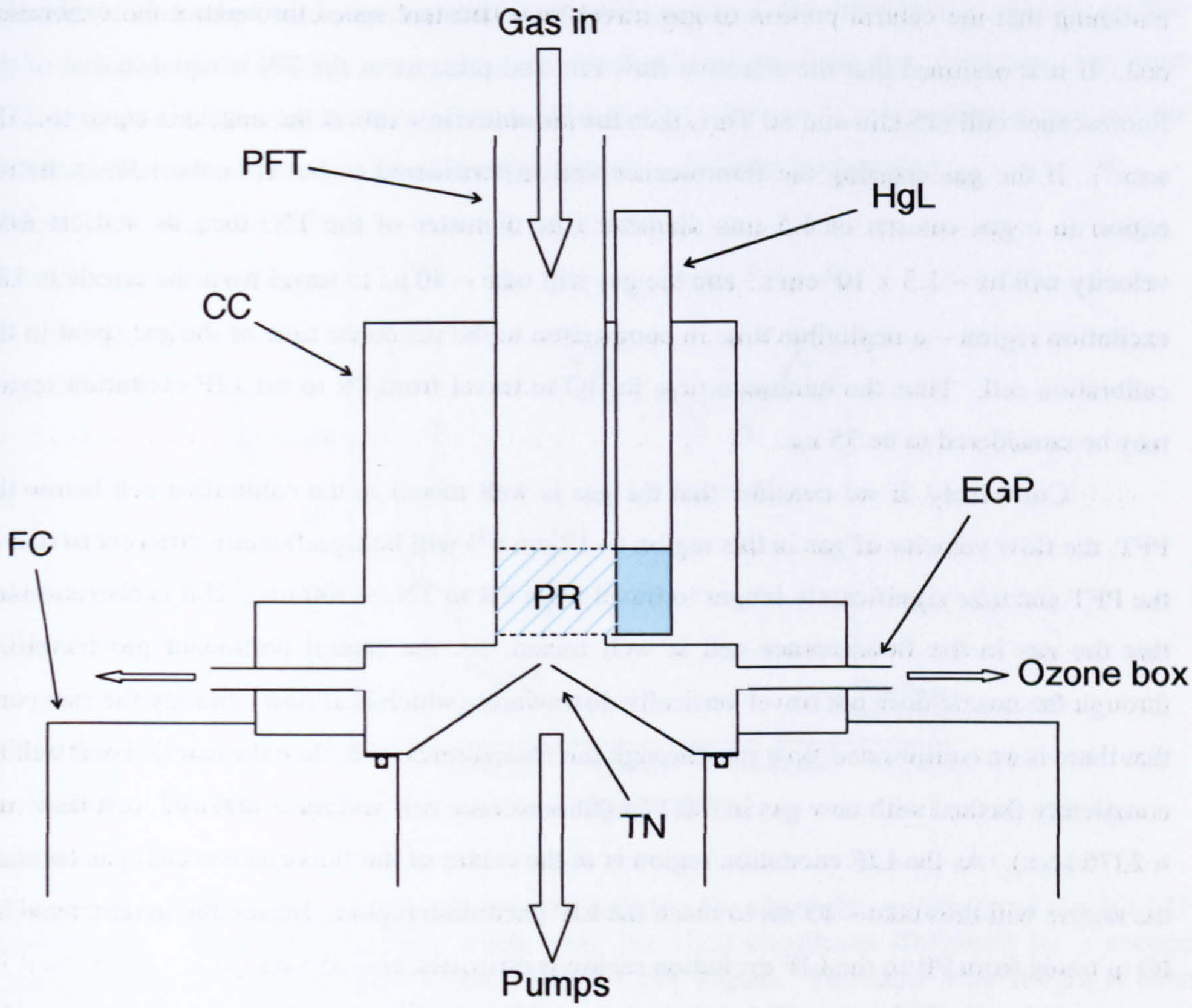

Fig. 3.6-3 – Calibration cell for the IO LIF field instrument. Note that the turreted nozzle (TN) forms the vacuum with the fluorescence cell (FC) *via* an o-ring seal and that the calibration cell (CC) is fixed onto the fluorescence cell *via* a flange with screws. EGP = excess gas port, HgL = low pressure Hg Pen-Ray lamp, PFT = Pyrex flow tube, PR = photolysis region.

The flux of O atoms generated by the photolysis of N_2O can thus be calculated from the concentration of N_2O in the PFT, the absorption cross-section of N_2O at 184.9 nm, the lamp flux at 184.9 nm, and the residence time, t_{PR}, of the gas mixture in the PR of the flow tube. For the conditions of a typical calibration experiment: T = 296 K, P = 760 Torr, $[N_2O] = 4 \times 10^{17}$ molecule cm^{-3}, $[CF_3I] = 2 \times 10^{15}$ molecule cm^{-3}, $[N_2]$ = balance, flow rate = 20 slm, t_{PR} = 15 ms, $F_{(184.9\ nm)} = 3 \times 10^{14}$ photons cm^{-2}; approximately 2.6×10^{11} molecule cm^{-3} of O atoms are generated by the photolysis of N_2O. Once the concentration of O atoms is known, the concentration of IO at the LIF excitation region can then be estimated by the time taken for the gas mixture to travel from the PR to the LIF excitation region, assuming that in that time IO is only removed by self-reaction. However, estimating the time for the gas mixture to reach the LIF excitation region is not straight-forward. In the PFT, a cross-section with 1 cm^3 depth is cleared in ~ 15 ms (*i.e.* the flow velocity is ~ 70 cm s^{-1}). As the bottom of the PFT is ~ 5 cm above the fluorescence cell nozzle, the gas mixture will therefore reach the nozzle after ~ 75 ms,

assuming that the central portion of gas travels at a constant speed throughout the calibration cell. If it is assumed that the effective flow rate and pressure at the TN is equal to that of the fluorescence cell (15 slm and 80 Torr) then the absolute flow rate at the nozzle is equal to 2375 sccs[26]. If the gas entering the fluorescence cell is considered to travel to the LIF excitation region in a gas column of 1.5 mm diameter (the diameter of the TN) then its vertical flow velocity will be ~ 1.3×10^5 cm s^{-1} and the gas will take ~ 40 μs to travel from the nozzle to LIF excitation region – a negligible time in comparison to the residence time of the gas spent in the calibration cell. Thus the minimum time for IO to travel from PR to the LIF excitation region may be considered to be 75 ms.

Conversely, if we consider that the gas is well mixed in the calibration cell below the PFT, the flow velocity of gas in this region (~ 17 cm s^{-1}) will be significantly different to that in the PFT and take significantly longer to travel from PR to TN (~ 300 ms). If it is also assumed that the gas in the fluorescence cell is well mixed, *i.e.* the central portion of gas travelling through the nozzle does not travel vertically downwards (which is almost certainly the case) and that there is an equilibrated flow rate through the fluorescence cell, then the reaction cell will be completely flushed with new gas in ~ 0.17 s (fluorescence cell volume = 400 cm^3, cell flow rate = 2375 sccs). As the LIF excitation region is at the centre of the fluorescence cell, gas entering the nozzle will thus take ~ 85 ms to reach the LIF excitation region. Hence, the longest time for IO to travel from PR to the LIF excitation region is estimated as ~ 385 ms.

After 75 ms, an initial IO concentration of 2.6×10^{11} molecule cm^{-3} (assuming a unity branching ratio for the reaction, $O + CF_3I \rightarrow IO + CF_3$) will be diminished to ~ 5.4×10^{10} molecule cm^{-3} by self-reaction, and for a residence time of 385 ms this value will be reduced to ~ 1.4×10^{10} molecule cm^{-3}. Thus there is almost a factor of five uncertainty in the calibration procedure and it should be emphasised that the outlined calibration methodology does not consider additional losses of IO such as wall losses, photolysis in the PR of the PFT, or reaction with impurities/photochemical species present in the calibration cell. In order to accurately define the transit time of IO from generation to detection, the flow rate and pressure gradients in the calibration and fluorescence cells should be investigated. However, as an initial evaluation of the experimental sensitivity of the IO LIF instrument (and its comparison to the theoretical sensitivity) the calibration experiment outlined above is sufficient.

Fig. 3.6-4 displays the results of a calibration experiment. The experimental procedure is performed in the following manner. The gas mixture of $CF_3I/N_2O/N_2$ is flowed past the 184.9 nm radiation from the Hg lamp, resulting in a constant flux of IO at the LIF excitation region. The wavelength of the excitation laser is then scanned under computer control in steps of 0.001 nm over the first two rotational lines of the (2,0) band [the bandhead and a second line (corresponding to the $R_1(1)$ and $R_1(5)$ rotational transitions)]. Once the scan is complete, the diffraction grating of the laser is instructed to return the laser to the wavelength where

maximum fluorescence signal was observed (the peak of the bandhead), and an on-line measurement cycle (*m*) ensues. Once the on-line measurements are complete, the laser wavelength is tuned to an off-line position (444.70 nm) where no IO absorption occurs and the off-line measurement cycle (*n*) is performed, obtaining the laser background.

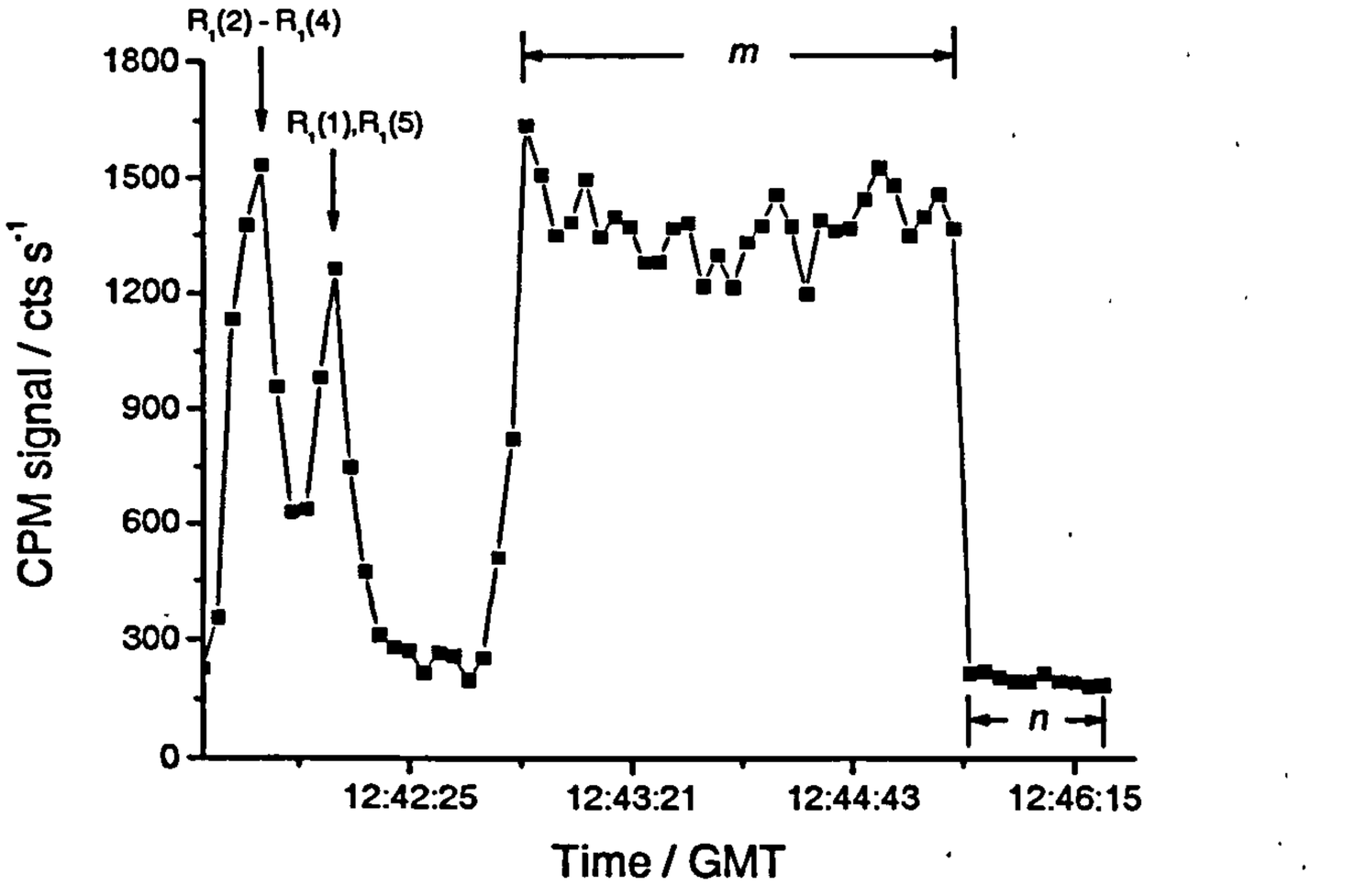

Fig. 3.6-4 – Calibration experiment for determining the absolute sensitivity of the IO LIF instrument. Note that the laser scans over the (2,0) bandhead (followed by a second spectral line) in order to observe the peak IO LIF signal. The laser wavelength is then retuned to the peak signal (λ_m = 444.889 nm) and the on-line (*m*) LIF signal is averaged over a user-defined range (*t*). When the on-line cycle is complete the laser wavelength is tuned to an off-resonant wavelength (λ_n = 444.70 nm) where no IO absorption occurs and the background signal is recorded in the off-line regime (*n*). Experimental conditions: P_{PFT} = 760 Torr; P_{FC} = 80 Torr; T = 296 K; flow rate$_{PFT}$ = 20 slm; $[N_2O]_{PFT} = 4 \times 10^{17}$ molecule cm^{-3}; $[CF_3I]_{PFT} = 2 \times 10^{15}$ molecule cm^{-3}; $[N_2]_{PFT}$ = balance; $F_{(184.9\ nm)} = 3 \times 10^{14}$ photons cm^{-2}; λ_m = 444.889 nm; λ_n = 444.700 nm; P = 15 mW; m = 30; n = 10; t = 30 s. From the experimental data: $m_{avg} = (1382 \pm 190)$ cts s^{-1}, and $n_{avg} = (200 \pm 25)$ cts s^{-1}. Hence the IO fluorescence signal, $S_{IO} = (1182 \pm 192)$ cts s^{-1}. The above calibration experiment was performed by Dr. Lisa Whalley and Kate Furneaux.

From the calibration experiment, the number of counts attributable to IO LIF is found to be 1182 cts s^{-1}. Thus for the estimated range of IO concentrations, the calibration factor is determined as, $C_{IO} = (1.5 - 5.6) \times 10^{-9}$ cts cm^3 molecule^{-1} s^{-1} mW^{-1}, in remarkably good agreement with the theoretical evaluation (5.7×10^{-9} cts cm^3 molecule^{-1} s^{-1} mW^{-1}). Assuming that the transit time for IO to reach the LIF excitation region of the fluorescence cell is somewhere between the best and worst case scenarios, a mid-estimate value of $C_{IO} = 3.6 \times 10^{-9}$ cts cm^3 molecule^{-1} s^{-1} mW^{-1} may therefore be most representative of the true experimental sensitivity of the IO LIF instrument. Thus for a *S/N* of 1; a total integration time of 60 s ($m = n = 1$, t = 30 s); a laser power of 50 mW; and background counts of, S_{lb} = 667 cts s^{-1} (taking the value of 200 cts s^{-1} for a laser power of 15 mW and assuming that laser scatter scales linearly

with laser power), S_{sb} = 70 cts s^{-1} (measured independently), and S_{db} = 5 cts s^{-1} (manufacturers specifications); the absolute detection limit of the apparatus is calculated to be, $LOD_{IO} = 3.9 \times 10^7$ molecule cm^{-3} (or 1.6 ppt). Note that this sensitivity is sufficient for the detection of IO in the MBL and is representative of the IO LIF instrument in its infancy. The sensitivity could be enhanced, with no instrumental modifications, by increasing the averaging time of the experiment. With further development of the LIF instrument (see section 3.6.3) it is expected that the detection limit of the instrument could be improved by at least a factor of three.

3.6.3 Discussion

After reassessing the theoretical detection limit of an LIF instrument for the detection of IO in the atmosphere, it is found that the projected theoretical sensitivity is 2 – 3 orders of magnitude less sensitive than previously estimated[1]. The decrease in sensitivity is predominantly associated with the decreased fluorescence quantum yield of the $A^2\Pi_{3/2}$ (v' = 2) state of IO as a result of rotational energy transfer and fluorescence quenching in the excited state, which have been experimentally investigated for the first time in the course of this work. The theoretical sensitivity is also decreased as a result of the smaller fraction of the total fluorescence detected by the instrument, which has been evaluated accurately in this study by consideration of the relative band strengths of the $A^2\Pi_{3/2}$ (v' = 2) → $X^2\Pi_{3/2}$ (v'') vibrational progression that has been quantified for the first time by a dispersed fluorescence experiment.

Under realistic experimental conditions, the theoretical detection limit of the instrument has been calculated to be 1.6×10^7 molecule cm^{-3} (0.7 ppt) for a total integration time of one minute – sufficient for the measurement of IO in the MBL. From an initial calibration experiment the absolute detection limit of the instrument is determined to be ~ 3.9×10^7 molecule cm^{-3} (~ 1.6 ppt), in good agreement with the theoretical evaluation suggesting that the fluorescence quantum yield of the $A^2\Pi_{3/2}$ (v' = 2) state of IO is fairly well characterised by the results obtained in this work. The determined sensitivity of the LIF instrument implies that LIF will be an important diagnostic tool for the measurement of local IO concentrations in the atmosphere, improving our quantitative understanding of iodine chemistry in the MBL and providing a meaningful comparison with the average IO concentrations reported by the DOAS technique. However, it should be emphasised that the calibration method is susceptible to considerable uncertainties and must be developed more rigorously in order for IO LIF signals obtained in the field to be converted into absolute IO concentrations.

It is envisaged that the detection limit of the LIF instrument could be significantly enhanced, with respect to the preliminary estimates, by future research and development. For

example, Fig. 3.6-5 displays the pressure dependence to the theoretical sensitivity as determined by the evaluation of the pressure dependent parameters in E. 3.2-3

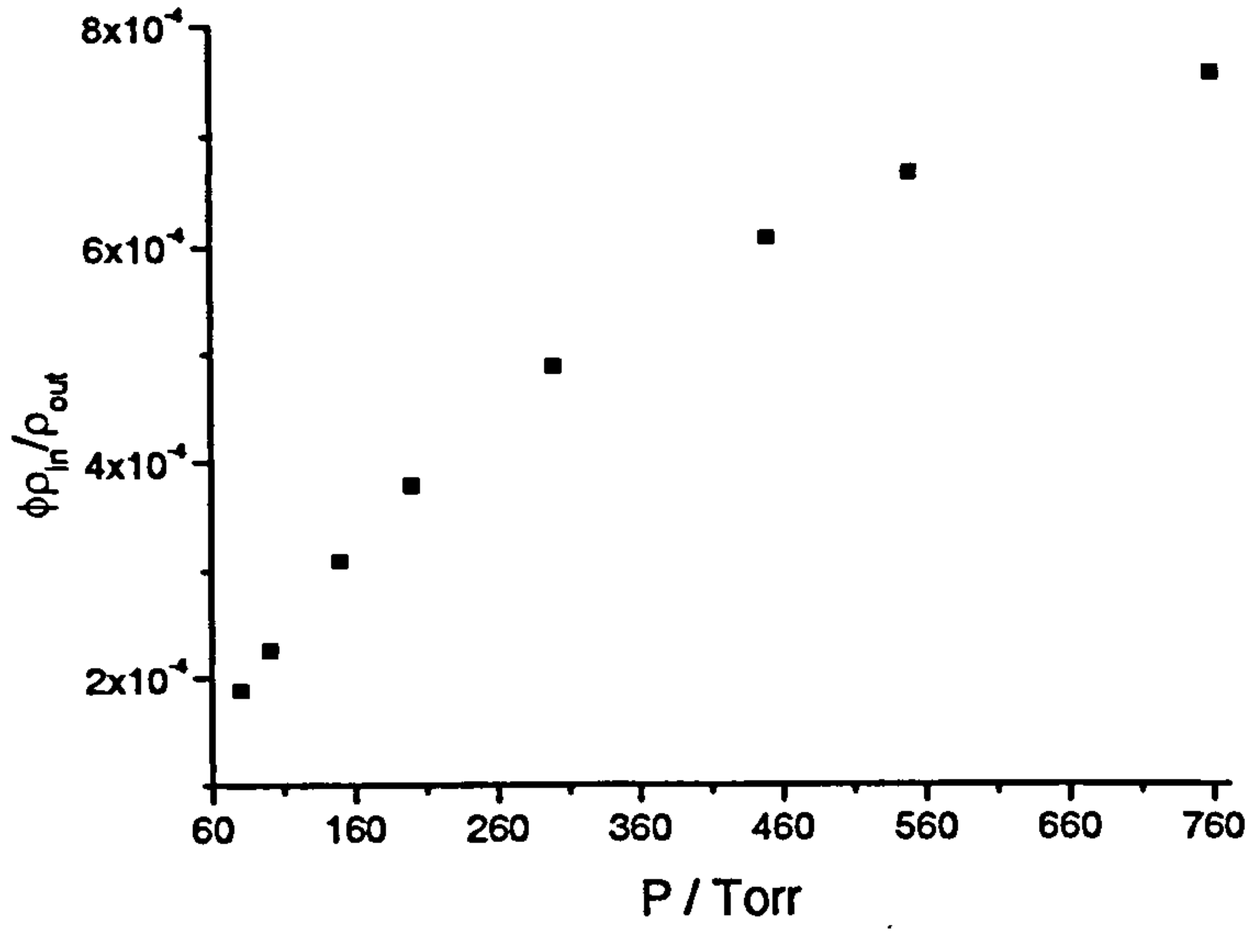

Fig. 3.6-5 – Pressure dependence of the theoretical sensitivity of an IO LIF field instrument determined by consideration of the pressure dependent parameters in E. 3.2-3, ϕ and ρ_{in}/ρ_{out}. Note that ρ_{in}/ρ_{out} is evaluated from the ratio of fluorescence cell and ambient pressures and ϕ is evaluated from E. 3.5-1 ($k_f = 1.82 \times 10^7$ s^{-1}, $k_p = 8.5 \times 10^9$ s^{-1}, $k_q = 6.3 \times 10^{-10}$ cm^{3}molecule^{-1}s^{-1}) assuming that RET results in the complete rotational thermalisation of the $A^2\Pi_{3/2}$ (v' = 2) state of IO at pressures of 80 Torr and above after LIF excitation in the R_1 (2,0) bandhead.

As can be seen, the theoretical sensitivity increases with pressure as the reduction in fluorescence quantum yield is overcompensated by the increase in number density at higher pressures. Hence, the theoretical sensitivity at atmospheric pressure is approximately four times greater than that at 80 Torr. However, the adopted pressure of the field experiment is dependent on several other factors. First, as the excitation laser operates at a PRF of 5 kHz, a laser pulse is produced every 200 μs. In order to prevent potential photolytic interferences (such as the production and excitation of IO from the photolysis of $IONO_2$ within the same laser pulse for example) a fresh gas parcel must therefore travel a vertical distance of > 2 mm (*i.e.* the diameter of the laser beam at the LIF excitation region) in 200 μs. As discussed in section 3.6-2, the flow rate inside the fluorescence cell at 80 Torr is 2365 sccs. For the worst case scenario, where the vertical flow velocity in the fluorescence cell is equal at all positions, the gas will take ~ 3.4 ms to travel through the LIF excitation region. However, for the best case scenario, where the gas travels through the cell in a collimated jet of 1.5 mm diameter (corresponding to the nozzle diameter) the LIF excitation region will be replenished with fresh gas in 0.6 μs. Clearly, some sort of intermediate value will be representative of the true flow rate. In order to increase the fluorescence cell pressure, the pumping rate would have to be reduced thus decreasing the flow

rate through the cell, ultimately leading to longer residence times. In summary, efficient flushing of the LIF excitation region with fresh gas is uncertain even at low pressures and extreme caution should be taken if higher reaction cell pressures are adopted. However, the same total flow rate through the fluorescence cell could be maintained at higher pressures *via* a combination of reducing the fluorescence cell nozzle diameter and reducing the total pumping rate. Clearly, the gas flow within the fluorescence cell requires experimental, or theoretical, characterisation. In deciding the optimum fluorescence cell operating pressure, the pressure dependence of the scatter of laser and solar radiation also needs to be considered. Both of these relationships should be characterised and quantified in order to asses the true pressure dependence of the theoretical sensitivity of the IO LIF instrument.

Further improvements to the sensitivity of the IO LIF instrument could be achieved by reducing the scatter of laser and solar radiation. Presently, the fluorescence collection system incorporates a filter system allowing a wide range of wavelengths to be detected by the PMT ($500 < \lambda < 650$ nm). Although the wide fluorescence window ensures maximum collection of IO fluorescence, the fluorescence from IO only occurs in discrete bands according to the vibrational transitions, whereas scatter from solar radiation and red-shifter laser scatter (note that some laser scatter may also be attributed to red-shifted LIF from the colour glass filter) may occur at all wavelengths. Thus, the background may be improved by employing a narrow band-pass filter, specifically designed to capture fluorescence from only one vibrational band of the $A^2\Pi_{3/2} \rightarrow X^2\Pi_{3/2}$ transition of IO. For example, a narrow band-pass filter with central wavelength of 521.0 nm, peak transmission of ~ 50 %, and FWHM of 2 – 3 nm would essentially collect all fluorescence from the (2,5) vibrational band while successfully discriminating the vast majority of solar (and laser) scattered radiation. If such a filter were employed, the parameter ηT (see Table 3.6-2) would be reduced from it current value of 0.018 to a value of 0.0071. However, this reduction in sensitivity is likely to be overcompensated for by the reduction in background. The laser background could also be reduced further by more efficient baffling in the fluorescence cell arms. Assuming the incorporation of such a narrow-band interference filter, more efficient discrimination of the laser scatter, and an operating pressure of 300 Torr, the detection limit of the IO LIF instrument is calculated to be 6.7×10^6 molecule cm^{-3} (0.27 ppt) for a $S/N = 1$, $m = n = 1$, $t = 30$ s, $P = 50$ mW, $S_{lb} = 50$ cts s^{-1}, $S_{sb} = 7$ cts s^{-1}, $S_{db} = 0$ cts s^{-1}. The magnitude of the background count rates are considered to be upper limits, once the appropriate adaptations have been made, and the calculated detection limit is considered to be a conservative estimate for the optimised IO LIF instrument.

A previously unmentioned factor, that could affect the sensitivity of the IO LIF field instrument, is the contribution to the background signal from NO_2 fluorescence. Nitrogen dioxide absorbs relatively strongly at 445 nm and fluoresces over the entire fluorescence

window of the $A^2\Pi_{3/2} \rightarrow X^2\Pi_{3/2}$ transition of IO. To address this potential interference, an absolute calibration of the LIF instrument should be performed with respect to NO_2 detection. As NO_2 is a stable molecule, its *in situ* generation is not required and the calibration experiment would be very straight-forward. However, NO_2 fluorescence is not considered to be a major potential interference to the IO field measurements due to the low concentrations found in the remote MBL (~ 1 – 100 ppt) and the fact that NO_2 fluorescence is rapidly quenched by N_2 at the envisaged operating pressures of the field experiment ($P > 80$ Torr). Further, the incorporation of a narrow-band interference filter would help to minimise interference from NO_2 fluorescence as the majority of its fluorescence will be discriminated. If the LIF cell is found to be particularly sensitive for NO_2 detection, it is conceivable that the instrument could be used to determine the concentration of NO_2 in the MBL. There are surprisingly few direct detection methods for the measurement of NO_2 at low concentration and, in principle therefore, the IO LIF instrument could prove a useful tool for its detection in the clean marine atmosphere.

The IO LIF instrument described in section 3.6 was designed and constructed as part of this PhD and is currently making point measurements of IO in the MBL at a coastal site in Brittany (France), as part of the RHaMBLE (Reactive Halogens in the Marine Boundary Layer Experiment) field campaign. The preliminary results suggest that IO concentrations in excess of 20 ppt have been detected – higher than any other measurement of IO in the atmosphere to date.

References

1. W. J. Bloss, T. J. Gravestock, D. E. Heard, T. Ingham, G. P. Johnson and J. D. Lee, "Application of a compact all solid-state laser system to the in situ detection of atmospheric OH, HO_2, NO and IO by laser-induced fluorescence", *J. Environ. Monit.*, **5**, 21 – 28, 2003.
2. D. J. Creasey, P. A. Halford-Maw, D. E. Heard, M. J. Pilling and B. J. Whitaker, "Implementation and initial deployment of a field instrument for measurement of OH and HO_2 in the troposphere by laser-induced fluorescence", *J. Chem. Soc., Faraday Trans.*, **93**, 2907-2913, 1997.
3. A. Hofzumahaus, U. Aschmutat, M. Hessling, F. Holland and D. H. Ehhalt, "The measurement of tropospheric OH radicals by laser-induced fluorescence spectroscopy during the POPCORN field campaign", *Geophys. Res. Lett*, **23**, 2541-2544, 1996.
4. P. S. Stevens, J. H. Mather and W. H. Brune, "Measurement of tropospheric OH and HO_2 by laser-induced fluorescence at low pressure", *J. Geophys. Res.*, **99**, 3542-3557, 1994.
5. Y. Kanaya, Y. Sadanaga, J. Hirokawa, Y. Kajii and H. Akimoto, "Development of a ground-based LIF instrument for measuring HO_x radicals: Instrumentation and calibrations", *J. Atmos. Chem.*, **38**, 73-110, 2001.
6. M. K. Gilles, M. L. Polak and W. C. Lineberger, "Photoelectron spectroscopy of IO^-", *J. Chem. Phys.*, **95**, 4845 – 4853, 1991.
7. J. P. Bekooy, W. L. Meerts and A. Dymanus, "High-Resolution Laser-rf Spectroscopy on the $A^2\Pi_{3/2} - X^2\Pi_{3/2}$ System of Iodine Oxide (IO)", *J. Mol. Spectrosc.*, **102**, 320 – 343, 1983.

8. C. E. Miller and E. A. Cohen, "Rotational spectroscopy of IO $X^2\Pi_i$", *J. Chem. Phys.*, 115, 6459 – 6470, 2001.
9. G. Herzberg, "*Molecular Spectra and Molecular Structure: I. Spectra of Diatomic Molecules*", Second Edition, D. Van Nostrand Company, Inc., New York, 1950.
10. S. M. Newman, W. H. Howie, I. C. Lane, M. R. Upson and A. J. Orr-Ewing, "Predissociation of the $A^2\Pi_{3/2}$ state of IO studied by cavity ring-down spectroscopy", *J. Chem. Soc. Faraday Trans.*", 94, 2681 – 2688, 1998.
11. T. Gravestock, "*The Detection of Free-Radicals in the Atmosphere by LIF*", Masters thesis, University of Leeds, 2002.
12. M. L. P. Rao, D. V. K. Rao and P. T. Rao, "Dissociation Energies, r-Centroids and Franck-Condon Factors of IO Molecule", *Phys. Lett.*, 50, 341 – 342, 1974.
13. P. Spietz, J. C. Gomez-Martin and J. P. Burrows, "Spectroscopic studies of the I_2/O_3 photochemistry Part 2. Improved spectra of iodine oxides and analysis of the IO absorption spectrum", *J. Photochem. Photobiol. A.*, 176, 50 – 67, 2005.
14. R. A. Durie and D. A. Ramsay, "Absorption Spectra of the Halogen Monoxides", *Can. J. Phys.*, 36, 35 – 53, 1958.
15. R. A. Durie, F. Legay and D. A. Ramsay, "An Emission System of the IO Molecule", *Can. J. Phys.*, 38, 444 – 452, 1960.
16. C. J. Sansonetti, M. L. Salit and J. Reader, "Wavelengths of spectral lines in mercury pencil lamps", *Applied Optics*, 35, 74 – 77, 1996.
17. G. Inoue, M. Suzuki and N. Washida, "Laser induced fluorescence of iodine oxide (IO) radicals and rate constant for the reaction of iodine oxide (IO) + nitric oxide", *J. Chem. Phys.*, 79, 4730 – 4735, 1983.
18. A. A. Turnipseed, M. K. Gilles, J. B. Burkholder and A. R. Ravishankara, "LIF detection of IO and the rate coefficients for I + O_3 and IO + NO reactions", *Chem. Phys. Lett.*, 242, 427 – 434, 1995.
19. D. Hoelscher, C. Fockenberg and R. Zellner, "LIF detection of the IO radical and kinetics of the reactions I + O_3 → IO + O_2, O (^{3}P) + I_2 → IO + I, O (^{3}P) + CH_3I → IO + CH_3, and O (^{3}P) + CF_3I → IO + CF_3 in the temperature range 230 to 310 K", *Berichte der Bunsen-Gesellschaft*, 102, 716 – 722, 1998.
20. A. J. Orr-Ewing, University of Bristol, personal communication 2006.
21. M. A. Teruel, T. J. Dillon, A. Horowitz and J. N. Crowley, "Reaction of O(^{3}P) with the alkyl iodides: CF_3I, CH_3I, CH_2I_2, C_2H_5I, 1-C_3H_7I and 2-C_3H_7I", *Phys. Chem. Chem. Phys.*, 6, 2172 – 2178, 2004.
22. PGOPHER spectral simulation program written by C. M. Western. A summary of the program and the Hamiltonian used is given in M. E. Green and C. M Western, *J. Chem. Phys.*, 104, 808, 1996.
23. T. J. Dillon, "", PhD Thesis, University of Leeds, 2002.
24. slm = standard litre per minute at 1 bar and 0 °C.
25. M. K. Gilles, A. A. Turnipseed, R. K. Talukdar, Y. Rudich, P. W. Villalta, L. G. Huey, J. B. Burkholder and A. R. Ravishankara, "Reactions of O(^{3}P) with Alkyl Iodides: Rate Coefficients and Reaction Products", *J. Phys. Chem.*, 100, 14005 – 14015, 1996.
26. sccs = standard cubic centimetre per second at 1 bar and 0 °C.

Chapter Four: A Multidimensional Study of the Reaction $CH_2I + O_2$: Products and Atmospheric Implications

4.1 Introduction

As discussed in Chapter One, the radiative balance and climate of the Earth's atmosphere are partially influenced by cloud formation and therefore the presence of aerosol particles that lead to the formation of cloud condensation nuclei (CCN). It is now well established that iodine oxide chemistry leads to the formation of new particles in the marine boundary layer (MBL)[1-5]. Iodine monoxide (IO) is the precursor to higher iodine oxides (such as OIO and I_2O_2) in the MBL, and the processes leading to its formation are thus relevant to the production of new particles. Although molecular iodine (I_2) is now thought to be the main precursor to IO and particle formation at Mace Head, Ireland[6-8], diiodomethane (CH_2I_2) has recently been observed at high concentration at a separate coastal location, where I_2 was not detected[9]. In the troposphere CH_2I_2 is rapidly photolysed ($\tau \approx 5$ minutes)[10] to CH_2I and I[11]. The iodine atoms react with O_3, forming IO, and the CH_2I radicals will rapidly be consumed by reaction with O_2

$$CH_2I_2 + h\nu \rightarrow CH_2I + I \qquad \text{(P4-1)}$$

$$I + O_3 \rightarrow IO + O_2 \qquad \text{(R4-1)}$$

$$CH_2I + O_2 \rightarrow \text{products} \qquad \text{(R4-2)}$$

A recent study[12] reported that IO is formed directly in reaction R4-2 with a unity yield, which could therefore influence particle production in the MBL under localised conditions. The main aim of the work reported in this chapter was to determine the mechanism by which IO is formed after the photolysis of CH_2I_2 in the presence of O_2, and whether or not this process could be of atmospheric significance.

4.2 Previous Investigations of the $CH_2I + O_2$ Reaction

There are few studies of the $CH_2I + O_2$ reaction reported in the literature. An indirect study of reaction R4-2 by Sehested *et. al.*[13] reported the absorption spectrum of CH_2IO_2 over a wavelength range of 220 – 400 nm and estimated the reaction kinetics of its self-reaction. In that study[13] CH_2I radicals were generated by reaction of fluorine atoms with methyl iodide in 1 bar of SF_6 at 295 K. Absorption profiles of the reaction mixture were recorded in the absence and presence of 40 mbar O_2 at various wavelengths, and the observed differences (in absorption intensity and temporal evolution) were attributed to the presence of peroxy species (CH_2IO_2,

CH_3O_2 and FO_2). After making several assumptions regarding the chemistry occurring within the system, the rate coefficient of the CH_2IO_2 self-reaction was estimated as 9×10^{-11} $cm^3molecule^{-1}s^{-1}$. Once corrected for absorption by CH_3O_2 and FO_2, the absorption spectrum of CH_2IO_2 was obtained and found to have a broad, "unusual peroxy spectrum". In the work of Sehested *et. al.*[13], the absorption spectrum and self-reaction kinetics of the CH_2I radical were also reported. The absorption spectrum of CH_2I was found to have two predominant peaks; at 280 nm and 337.5 nm. The peak at 280 nm was of greatest intensity with an absorption cross-section of 8.5×10^{-18} $cm^2molecule^{-1}$. The rate coefficient for the self-reaction of CH_2I was estimated as 4×10^{-11} $cm^3molecule^{-1}s^{-1}$.

The first direct study of the $CH_2I + O_2$ reaction to appear in the literature was that of Masaki *et. al.*[14]. The authors measured rate coefficients for the reaction of several substituted methyl radicals with O_2 at 298 K, and the reaction of $CH_2I + O_2$ was investigated between total pressures of 2 – 15 Torr (N_2) by following the temporal evolution of CH_2I in an excess of O_2 by mass spectrometry (MS). CH_2I radicals were generated by the Excimer laser photolysis of CH_2ICl at 193 nm. The authors found a pressure independent rate coefficient of $(1.6 \pm 0.2) \times 10^{-12}$ $cm^3molecule^{-1}s^{-1}$, suggesting that the reaction may proceed *via* a bimolecular process, such as $CH_2I + O_2 \rightarrow CH_2O + IO$, although this hypothesis is clearly in disagreement with the findings of Sehested *et. al.*[13].

A study by Cotter *et. al.*[15], designed to investigate the fate of oxidation products of alkyl iodides in the atmosphere, monitored the products of the chlorine initiated oxidation of CH_3I by FTIR spectroscopy. The reaction sequence was initiated by the photolysis of a Cl_2/CH_3I/air mixture at atmospheric pressure and temperature by a continuous 360 nm light source. Under their experimental conditions the reaction of $Cl + CH_3I$ predominantly produces $HCl + CH_2I$ (see Chapter Five) and the chemically generated CH_2I radicals subsequently react with O_2. The observed reaction products were CH_3Cl, HCl, CH_2O and CO. Hydrochloric acid (HCl) and methyl chloride (CH_3Cl) are primary and secondary products of the $Cl + CH_3I$ reaction (see Chapter Five) and formaldehyde (CH_2O) and carbon monoxide (CO) were attributed to end products of the reaction of $CH_2I + O_2$. In analogy to the known chemistry of bromine peroxy (CH_2BrO_2)[16] and bromine alkoxy (CH_2BrO)[17] species, the authors suggested that their experimental results could be explained by the following chemical mechanism

$$Cl + CH_3I \rightarrow HCl + CH_2I \qquad \text{(R4-3)}$$

$$CH_2I + O_2 + M \rightarrow CH_2IO_2 + M \qquad \text{(R4-2a)}$$

$$CH_2IO_2 + CH_2IO_2 \rightarrow CH_2IO + CH_2IO + O_2 \qquad \text{(R4-4a)}$$

$$CH_2IO \rightarrow CH_2O + I \qquad \text{(R4-5)}$$

$$CH_2O + Cl \rightarrow HCl + HCO \qquad \text{(R4-6)}$$

$$HCO + O_2 \rightarrow HO_2 + CO \qquad \text{(R4-7)}$$

Cotter *et. al.*[15] conclude that (assuming all CH_2I is converted to CH_2IO) effectively all of the iodine alkoxy radical decomposes to $CH_2O + I$ with a yield of 0.88 ± 0.14.

An experimental investigation by Enami *et. al.*[12] employing CRDS detection of IO, reported the direct formation of IO in the reaction of $CH_2I + O_2$. In their experiment, CH_2I was generated by the 266 nm photodissociation of CH_2I_2 using an Nd:YAG laser, and reacted with an excess of O_2 in a N_2 buffer between total pressures of 5 – 80 Torr and over a temperature range of 278 – 313 K. By following the temporal evolution of IO, the authors reported a pressure and temperature independent rate coefficient for the reaction of $CH_2I + O_2$ of $(4.0 \pm 0.4) \times 10^{-13}$ $cm^3molecule^{-1}s^{-1}$, suggesting a bimolecular reaction mechanism in agreement with the hypothesis of Masaki *et. al.*[14] but in quantitative disagreement over the rate coefficient. In the study of Enami *et. al.*[12], the yield of IO from reaction R4-2 was estimated as unity by comparing the concentration of IO generated from the reactions of $O + CH_3I$ and $O + CF_3I$. The reaction of $O + CF_3I$ is known to produce IO in high yield (83 ± 9) %[18], whereas the reaction of $O + CH_3I$ has several product channels[18]

$$\begin{aligned}
O + CH_3I &\rightarrow CH_3 + IO && \text{(R4-8a = 44 \%)} \\
&\rightarrow CH_2I + OH && \text{(R4-8b = 16 \%)} \\
&\rightarrow H + I + CH_2O && \text{(R4-8c = 7 \%)} \\
&\rightarrow I + CH_3O && \text{(R4-8d < 3 \%)} \\
&\rightarrow HI + CH_2O && \text{(R4-8e < 5 \%)}
\end{aligned}$$

Enami *et. al.*[12] compared the concentration of IO from reacting equal amounts of O atoms with excesses of CH_3I and CF_3I in the presence of O_2, which were observed to be approximately equal. The authors conclude that the yield of $CH_2I + OH$ (from reaction R4-8b) must be significantly larger than previously reported (51 ± 20) % – *cf.* above – and that "it is safe to say" that the yield of IO from the reaction of $CH_2I + O_2$ is unity. As a further test to the formation of IO in reaction R4-2, the detection of IO was sought and found in mixtures of $Cl_2/CH_3I/O_2/N_2$ post photolysis at 355 nm thus proving that CH_2I_2 is not required for the formation of IO and that CH_2I is a direct precursor to its formation. Note that these observations are not necessarily in disagreement with those of Cotter *et. al*[15] as the co-product to IO in the reaction of $CH_2I + O_2$ is, by definition, CH_2O.

A very recent study by Eskola *et. al.*[19] investigated the temperature and pressure dependencies of the reaction kinetics of the CH_2Br and CH_2I reactions with O_2 by photoionisation MS. For the reaction of $CH_2I + O_2$, no dependence in the rate coefficient was observed between total pressures of 0.6 – 46 Torr He at 298 K, with an average value of $(1.37 \pm$

0.32) × 10^{-12} $cm^3molecule^{-1}s^{-1}$, in good agreement with the findings of Masaki *et. al.*[14]. Reaction R4-2 was found to have a negative temperature dependence over the 220 – 450 K range, described by Arrhenius parameters of, $k(T) = (1.39 \pm 0.01) \times 10^{-12} (T/300)^{-1.55 \pm 0.06}$ $cm^3molecule^{-1}s^{-1}$. The reaction kinetics were determined by following the temporal profile of CH_2I, generated by the 193 nm photolysis of CH_2ICl or the 248 nm photolysis of CH_2I_2, in an excess of O_2. Eskola *et. al.*[19] observed the formation of I atoms and IO on the same timescale as CH_2I removal and found an average I atom yield of 0.91 ± 0.34. A weak signal from HI was also observed but no definitive formaldehyde signal was apparent in their experiment. With respect to the reaction of $CH_2Br + O_2$, the reaction kinetics were found to be pressure dependent and display a negative temperature dependence in accordance with an association reaction mechanism, forming CH_2BrO_2. The high pressure limit for the reaction of $CH_2Br + O_2$ was estimated as, $k_\infty = 4.9 \times 10^{-12}$ $cm^3molecule^{-1}s^{-1}$ by extrapolation of the data obtained. To explain the difference in reactivity between CH_2I and CH_2Br (and to satisfy the results of the previous studies) the authors proposed the following mechanism for reaction R4-2

$$CH_2I + O_2 \rightarrow CH_2IOO^*$$
$$CH_2IOO^* + M \rightarrow CH_2IOO + M$$
$$CH_2IOO^* \rightarrow CH_2OO + I$$
$$\rightarrow CH_2O + IO$$
$$\rightarrow CHIO + OH$$

where, CH_2IOO^* represents an excited peroxy species that can undergo collisional stabilisation at higher pressures (accounting for the observation of CH_2IO_2 in the work of Sehested *et. al.*[13]) or decompose to several different products. Small amounts of HI detected in the reaction system of Eskola *et. al.*[19] are attributed to the decomposition of CHIO.

Clearly, there are large discrepancies between the studies of the reaction of $CH_2I + O_2$ with regards to the reaction kinetics, reaction mechanism and reaction products. Coupled with the incomplete knowledge of the gas-phase chemistry of iodine species in the atmosphere and the importance of iodine chemistry in the formation of new particles in the MBL, possibly involving the photolysis of CH_2I_2, the reaction of $CH_2I + O_2$ warrants further experimental and theoretical investigation. In this study the reaction products of the reaction of $CH_2I + O_2$ have been investigated by absorption spectroscopy, laser induced fluorescence (LIF) and MS. Analysis of the kinetic behaviour of IO, CH_2O, I and an unknown species, possibly CH_2IO_2, provide important information regarding the reaction mechanism and potential influence of the reaction of $CH_2I + O_2$ in the marine atmosphere.

4.3 Investigation of the Products of the $CH_2I + O_2$ Reaction by Absorption Spectroscopy

The principal aim of the work reported in this section was to investigate whether IO is formed directly from the reaction of $CH_2I + O_2$ as suggested by Enami *et. al.*[12] (and Eskola *et. al.*[19]) or by secondary chemistry within the reaction system. The experimental apparatus was a typical pulsed laser photolysis single-pass absorption (PLP-SPA) system, similar to that described in section 2.5. Briefly, collimated UV-visible light from a Xe arc lamp was passed through a cylindrical Pyrex reaction cell (of 110 cm length and 25 mm internal diameter), with sealed silica windows at each end. A photolysis laser beam, generated by an Excimer laser (operating at 248 or 193 nm), was passed counter propagated to the analysis light through the reaction cell. The two beams were aligned to result in their complete overlap along the entire light path through the Pyrex vessel and the analysis light exiting the reaction cell was steered into a monochromator using an appropriate optical arrangement. All reagent mixtures were prepared on a gas handling line and introduced into the reaction cell *via* calibrated MFC's and through ¼" PTFE tubing. The Excimer laser was triggered at a constant pulsed repetition frequency (PRF) by a delay generator, producing radical species within the reaction cell. The diffraction grating and entrance and exit slit width of the monochromator were adjusted to allow analysis light of an appropriate frequency and band width to be detected by the monochromator PMT. The analogue PMT signal was digitised on an oscilloscope, which was also triggered by the delay generator, and stored on a control PC for analysis at a later date. The exhaust of the reaction cell consisted of ½" PTFE tubing leading to a fume cupboard. Experiments were generally performed at atmospheric pressure and temperature although some experiments were executed at low pressure (~ 4 Torr) by connecting a rotary pump to the exhaust of the reaction cell.

4.3.1 Generation and Detection of IO

A reference reaction was initially required to generate IO radicals in order to optimise the sensitivity of the apparatus and select the correct wavelength at which to monitor the analysis light. The reaction of $O + I_2 \rightarrow IO + I$ was chosen. Oxygen atoms were generated by the 248 nm photolysis of O_3, which was produced by flowing a small flow of O_2 over a Hg Pen-Ray lamp prior to the reaction cell inlet. Molecular iodine was introduced to the Pyrex cell by passing a small flow of N_2 over a few crystals of I_2 suspended in a sealed vessel containing glass wool. IO was produced by the following sequence of reactions:

$$O_3 + 248\ nm \rightarrow O(^1D) + O_2 \qquad (R4\text{-}9)$$

$$O(^1D) + N_2 \rightarrow O(^3P) + N_2 \qquad (R4\text{-}10)$$

$$O(^3P) + I_2 \rightarrow IO + I \qquad (R4\text{-}11)$$

The experimental conditions were arranged so that electronically excited O (^{1}D) atoms were rapidly quenched to the groundstate, O (^{3}P), which were primarily consumed by I_2.

It is well known that the absorption maxima of the $A^2\Pi_{3/2} \leftarrow X^2\Pi_{3/2}$ electronic transition of IO occurs at ~ 427.2 nm, the peak of the (4,0) vibrational band (see Fig. 3.3-2). Fig. 4.3-1 shows an absorption trace recorded at 427.2 nm after the 248 nm photolysis of an $I_2/O_3/O_2/N_2$ mixture. As can be seen, the peak IO absorption signal is rapidly reached (as the O atoms are consumed) before it is observed to diminish as the self-reaction of IO (and other loss processes) dominate. Note that as IO is formed the light intensity detected by the PMT is reduced (as the PMT operates on a negative voltage, a larger negative signal corresponds to a greater intensity of light) as absorption of the analysis light by IO occurs.

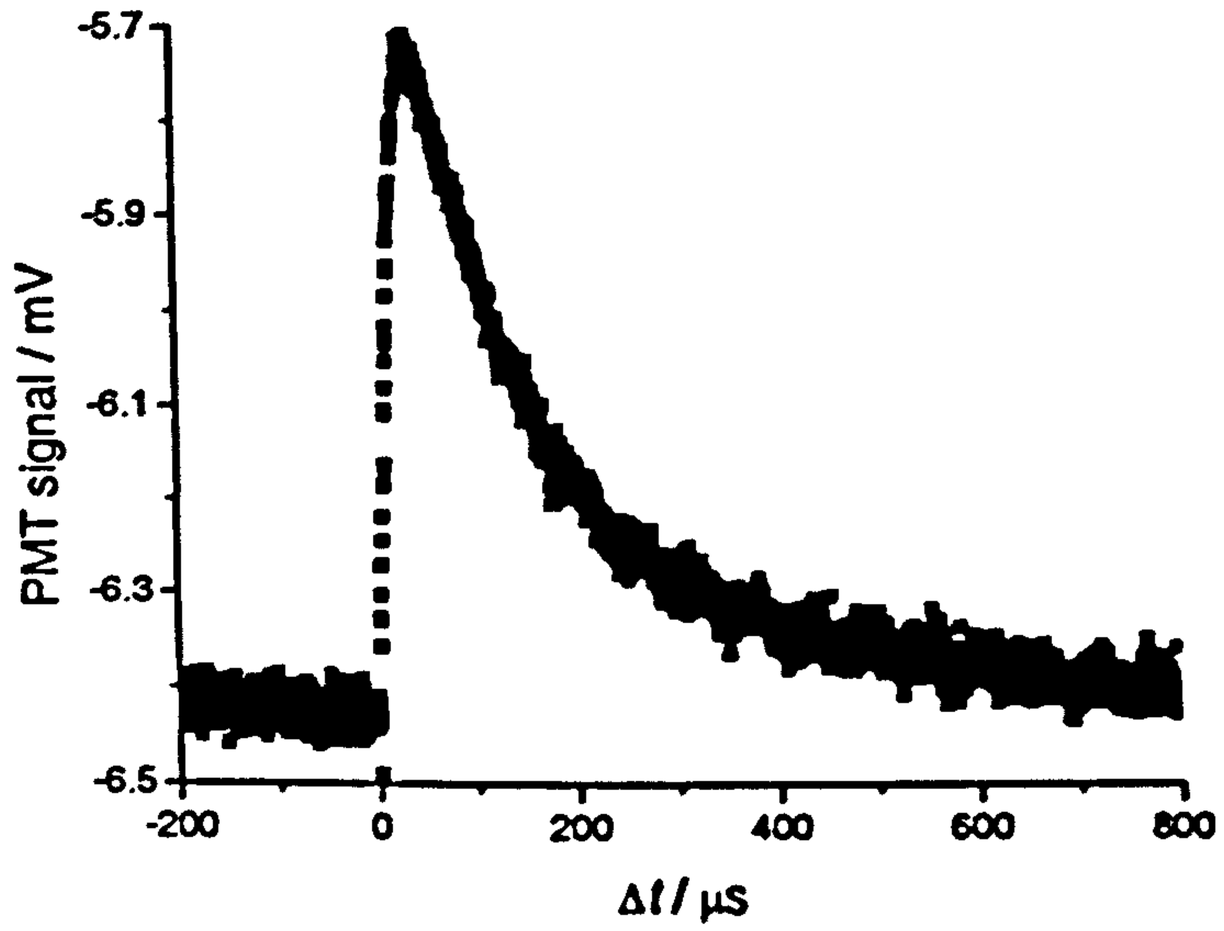

Fig. 4.3-1 - Absorption trace of IO recorded in a 248 nm photolysis mixture of $I_2/O_3/N_2/O_2$. Experimental conditions: P = 760 Torr; T = 296 K; [I_2] = 2.9 × 10^{14} molecule cm^{-3}; [O_3] ≈ 2× 10^{14} molecule cm^{-3}; [O_2] = 5.0 × 10^{17} molecule cm^{-3}; [N_2] = balance; F = 1.2 × 10^{17} photons cm^{-2}; λ_m = 427.2 nm; M_g = 1200 g/mm; M_r = 1.6 nm. The IO signal is an average of 50 laser shots. Note that the abbreviations in all figure captions in this thesis are defined in the Glossary of Terms (p. xxvii).

The species responsible for the absorption signal observed in Fig. 4.3-1 could be confirmed as IO by obtaining an absorption spectrum of the reaction mixture, which was measured by recording absorption traces whilst scanning the diffraction grating of the monochromator in 0.3 nm steps from 414.6 – 441.6 nm, the most intense region of IO absorption. The monochromator resolution was enhanced to 0.3 nm to reduce the possibility of

overlapping absorption from different vibrational bands in the electronic transition of IO and the absorption intensity, I_{abs}, was calculated from the Beer-Lambert law (E. 2.5-1), $I_{abs} = \ln(I_0/I)$, where I_0 is the average intensity of analysis light before the Excimer laser is triggered, and I is the intensity of analysis light at a later time, Δt, when IO is absorbing, which is averaged over a small range of reaction times where the IO signal was found to be of greatest intensity (Δt = 20 – 50 μs). Fig. 4.3-2 displays the resulting absorption spectrum of IO.

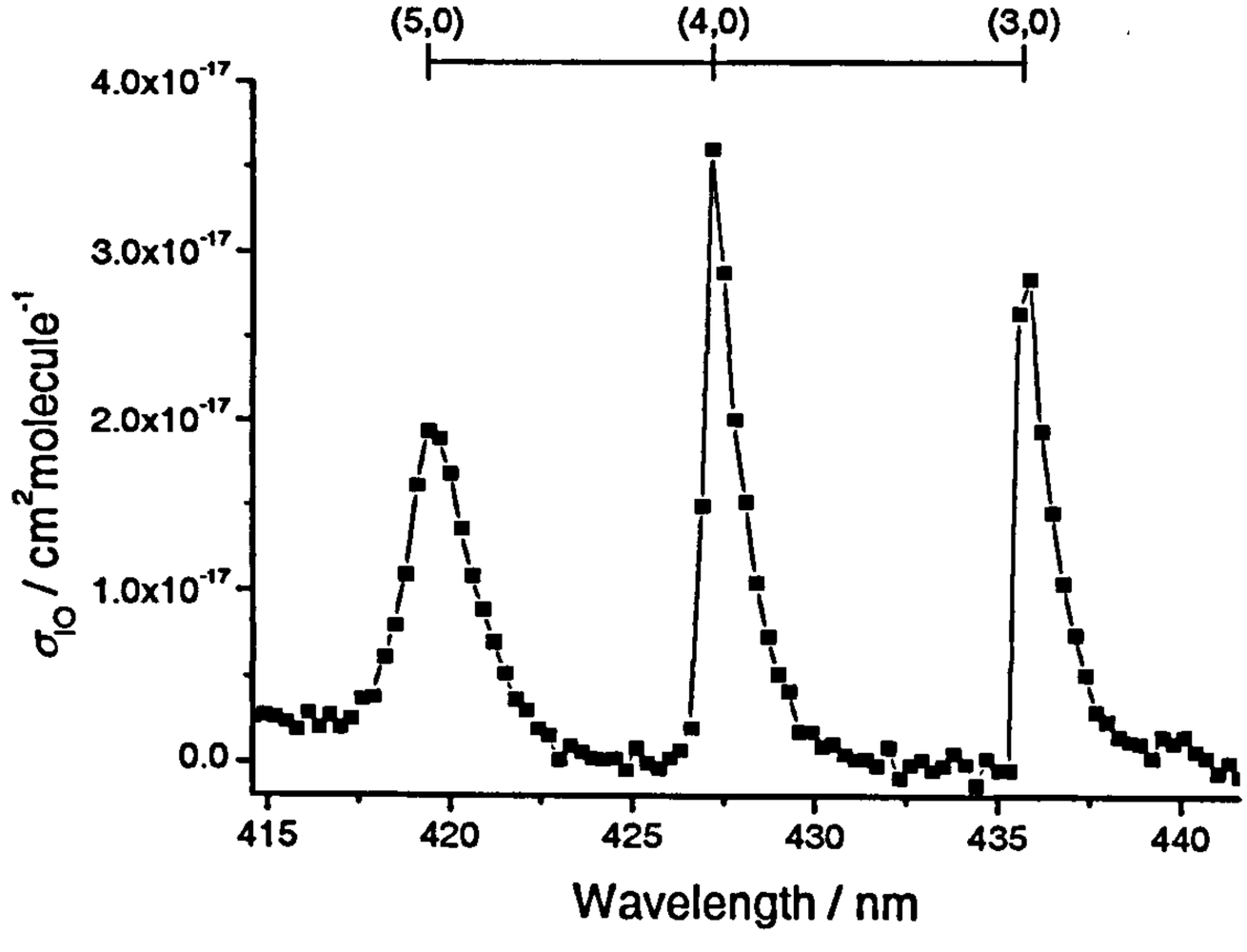

Fig. 4.3-2 – Absorption spectrum of IO between 414.6 – 441.6 nm obtained by the procedure outlined in the text. The vibrational transitions (v',v'') of the electronic transition are assigned. The experimental conditions are the same as previously given with the exception of an enhanced monochromator resolution of 0.3 nm FWHM. Note that the IO absorption, I_{abs}, has been converted to an absolute absorption cross-section, σ_{IO}, by normalisation of the peak absorption signal at 427.2 nm to a value of 3.6×10^{-17} $cm^2molecule^{-1}$. The absorption cross-sections are tabulated in Appendix II.

In Fig. 4.3-2, the IO absorption, I_{abs}, has been converted to an absolute absorption cross-section, σ_{IO}, by scaling the peak absorption at 427.2 nm to a value of, $\sigma_{IO(427.2nm)} = 3.6 \times 10^{-17}$ $cm^2molecule^{-1}$, which is well defined in the literature[20-22]. The absorption spectrum obtained can unambiguously be assigned to IO (see Fig. 3.3-2) and, in agreement with the most recent studies[21,22], verifies that the absorption cross-section of IO tends to zero between subsequent vibrational transitions over the (5,0) – (2,0) range. The reagent mixture of $I_2/O_3/N_2/O_2$ is a relatively clean system to measure the absorption spectrum of IO due to the lack of other chemical species which absorb in the same spectral window as IO (over the wavelength range investigated in this work).

In order to accurately investigate the reaction kinetics of IO in absorption experiments with relatively high concentrations, σ_{IO} must be accurately known at the studied wavelength and

monochromator resolution in order to convert the IO absorption into an absolute concentration, *via* the Beer-Lambert law, so that the second-order, self-reaction kinetics of IO can be treated in the correct manner (as described in section 2.2). As the absorption spectrum of IO is highly structured, the measured absorption cross-section will depend on monochromator resolution and it is therefore useful to quantify this relationship. To obtain this information, absorption traces of IO were recorded at 427.2 nm as a function of monochromator slit width (and hence resolution – see Fig. 3.4-3). The results are shown in Fig. 4.3-3. Note that the IO absorptions were converted to absorption cross-sections by scaling the value obtained at a monochromator resolution of 0.3 nm to the well defined literature value of 3.6×10^{-17} $cm^2 molecule^{-1}$[20].

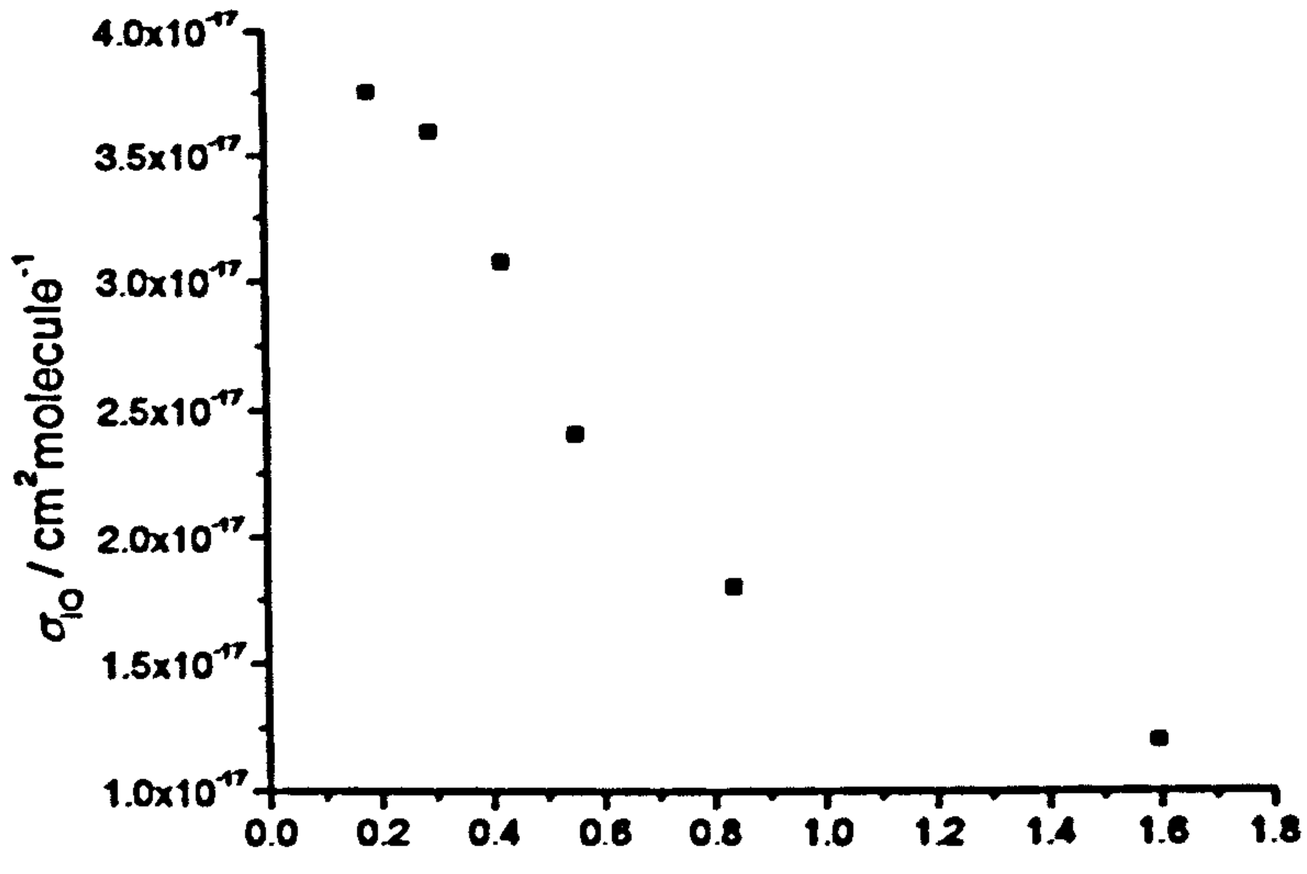

Fig. 4.3-3 – Absorption cross-sections of IO (at 427.2 nm and 298 K) as a function of monochromator resolution. All experimental conditions were identical to those previously stated. In order of increasing monochromator FWHM the monochromator slit widths were set at 50, 100, 150, 200, 300 and 500 μm respectively.

Using the data obtained, the peak concentration of IO for the absorption trace displayed in Fig. 4.3-1 is evaluated as ~ 9×10^{13} molecule cm^{-3}, in sensible accord with the experimental conditions. The absorption trace was modelled in FACSIMILE, once converted to an absolute IO concentration, to return a rate coefficient of $(9.4 \pm 0.3) \times 10^{-11}$ $cm^3 molecule^{-1} s^{-1}$ for the self-reaction of IO, in good agreement with the recommended literature value of 9.9×10^{-11} $cm^3 molecule^{-1} s^{-1}$[23].

4.3.2 The Production of IO from Photolysis of $CH_2I_2/O_2/N_2$ Reagent Mixtures at 248/193 nm

After characterising the experimental system, it was attempted to detect IO after the photolysis of a reagent mixture of $CH_2I_2/O_2/N_2$ at 248 nm. Diiodomethane was introduced to

the reaction cell by passing a small flow of N_2 through a glass vessel containing the purified liquid. The room temperature vapour pressure of CH_2I_2 (~ 1.1 Torr) is sufficient to allow ample transfer of reagent into the reaction cell (typically 10^{14} – 10^{15} molecule cm^{-3}). Upon the photolysis of the reaction mixture the production of IO was readily observed. As stated in section 4.2, the previous two studies[12,19] that have detected IO in similar reaction systems have reported IO as a direct product from the reaction of $CH_2I + O_2$. To investigate this claim, absorption traces of IO were recorded for a range of initial CH_2I_2 (and hence CH_2I) concentrations in a very large excess of O_2. Fig. 4.3-4 displays the results.

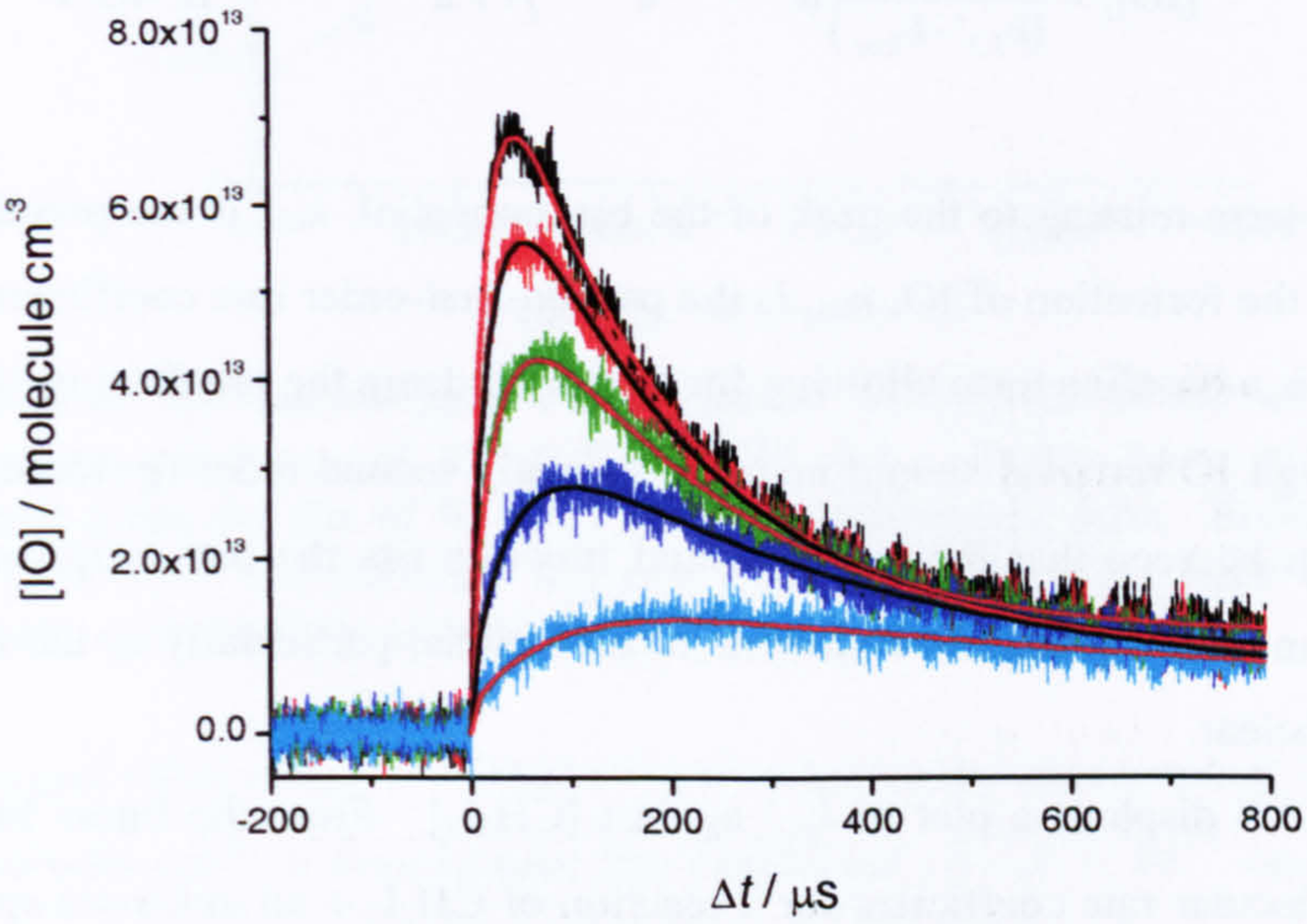

Fig. 4.3-4 – Absorption traces of IO recorded as a function of $[CH_2I_2]$. Experimental conditions: P = 760 Torr; T = 296 K; $[CH_2I_2]$ (molecule cm^{-3}) = 1.35×10^{15} (black), 1.07×10^{15}(red), 7.76×10^{14}(green), 4.73×10^{14} (blue), 1.84×10^{14} (cyan); $[O_2] = 2.04 \times 10^{18}$ molecule cm^{-3}; $[N_2]$ = balance; $F = 1.2 \times 10^{17}$ photons cm^{-2}; λ_m = 427.2 nm; M_g = 1200 g/mm; M_r = 1.6 nm. The absorption traces are an average of 50 laser shots. Note that all CH_2I_2 concentrations were determined absolutely by absorption spectroscopy (by recording the intensity of analysis light at 290 nm in the presence and absence of CH_2I_2) and were always found to be within 15 % of the calculated values from the mass flow rates and vapour pressure of CH_2I_2. The IO absorptions have been converted to absolute IO concentrations using the correct absorption cross-section of IO for the monochromator resolution as previously determined. The solid lines are fits of E. 4.3-1 to the experimental data.

Two striking features are apparent from the absorption traces. First, that the peak IO concentration is directly proportional to the initial concentration of CH_2I_2. This is indicative that IO is generated from a photolysis product of CH_2I_2, as all other variables were constant throughout the experiment. From the laser fluence and the absorption cross-section of CH_2I_2 at 248 nm ($\sigma = 1.57 \times 10^{-18}$ $cm^2 molecule^{-1}$)[11] it can be calculated that ~ 19 % of the initial CH_2I_2 concentration is photolysed by the photolysis pulse. By comparing the peak IO concentrations with the corresponding calculated initial CH_2I concentrations it is found that, assuming IO is

generated from the reaction of $CH_2I + O_2$, the yield of IO is ~ 30 – 40 %. This is in disagreement with the findings of Enami *et. al.*[12] who report a unity yield. The second important inference to be drawn from Fig. 4.3-4 is that the rate of formation of IO is strongly dependent on the concentration of CH_2I_2. This fact is strongly indicative that IO is not generated directly from the reaction of $CH_2I + O_2$, as the concentration of O_2 is in such excess to CH_2I (at least by a factor of 17000) that first-order reaction conditions are present. The fits to the IO absorption traces are of the form

$$[IO]_t = \frac{P1}{(k_{IO}' - k_{loss})}\left(e^{-k_{loss}t} - e^{-k_{IO}'t}\right) + P2 \qquad \text{E. 4.3-1}$$

where $P1$ is a term relating to the peak of the biexponential, k_{IO}' is the pseudo-first-order rate coefficient for the formation of IO, k_{loss} is the pseudo-first-order rate coefficient for the removal of IO, and $P4$ is a baseline term allowing for any offset from the pre-Excimer laser background signal. Although IO removal should be predominantly second-order (governed by the IO self-reaction) it can be seen that the biexponential function fits the data surprisingly well and is sufficient for an initial quantitative analysis of the results, particularly as the mechanism to IO formation is unclear.

Fig. 4.3-5 displays a plot of k_{IO}' against $[CH_2I_2]$. From the linear fit to the data, the effective bimolecular rate coefficient for a reaction of CH_2I_2 + an unknown species to form IO is, $k = (3.7 \pm 0.5) \times 10^{-11}$ $cm^3 molecule^{-1} s^{-1}$. Note that this does not necessarily imply that IO is formed from a reaction involving CH_2I_2. The non-zero intercept to the bimolecular plot, $c = (7800 \pm 3600)$ s^{-1}, probably indicates that additional loss processes to the IO precursor are occurring. As stated above, the significant dependence of the rate of formation of IO on the CH_2I_2 concentration is effectively incontrovertible evidence that IO is not formed directly from the reaction of $CH_2I + O_2$. Although the potential of interference from secondary chemistry is great – a large fraction of CH_2I_2 is photolysed by the Excimer laser and, for the highest CH_2I_2 concentration, ~ 20 % of the Excimer laser radiation will be absorbed along the length of the reaction cell (resulting in a high and non-uniform radical concentration distribution) it is still highly unlikely that IO is a direct reaction product of the $CH_2I + O_2$ reaction.

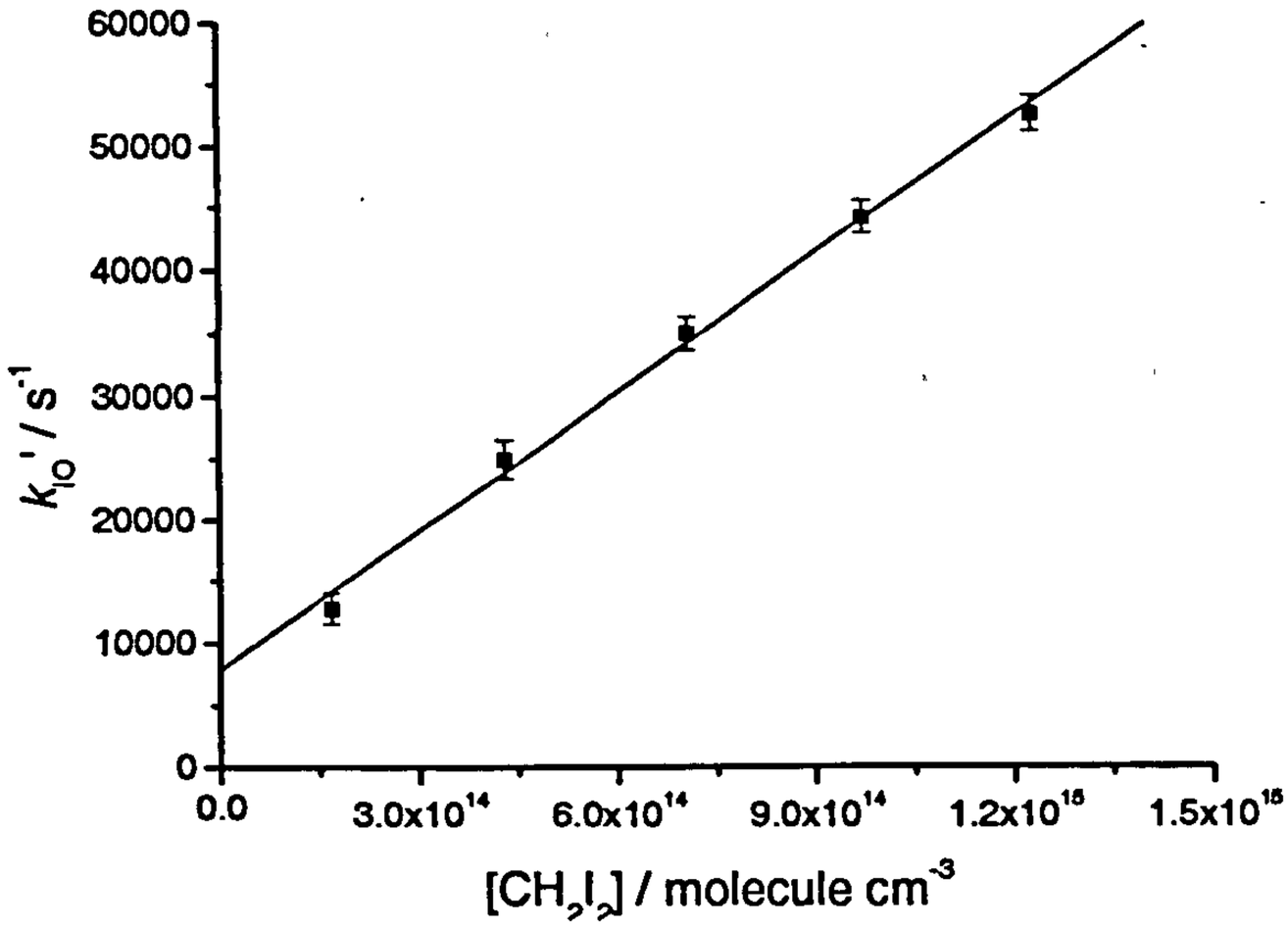

Fig. 4.3-5 – Plot of the pseudo-first-order rate of formation of IO as a function of [CH_2I_2] in reactive mixtures of $CH_2I_2/O_2/N_2$/248 nm. Error bars are 2σ standard error as returned from the fits of E. 4.3-1 to the experimental data. From the linear fit, m = (3.7 ± 0.5) × 10^{-11} $cm^3molecule^{-1}s^{-1}$, c = (7800 ± 3600) s^{-1}. Note that the CH_2I_2 concentrations are corrected for photolysis by the excimer laser pulse.

If the largest value of k_{IO}' (~ 52000 s^{-1}) is divided by the experimental O_2 concentration (~ 2 × 10^{18} molecule cm^{-3}) a bimolecular rate coefficient of 2.6 × 10^{-14} $cm^3molecule^{-1}s^{-1}$ is obtained, approximately 15 times smaller than that determined by Enami *et. al.*[12] and almost 60 times smaller than the MS determinations of Masaki *et. al.*[14] and Eskola *et. al.*[19] for the reaction of $CH_2I + O_2$. If IO is produced directly from reaction R4-2 then very efficient recycling of IO would have to occur to explain this observation. It is interesting that the rate coefficient determined by Enami *et. al.*[12] (which was determined by following the temporal behaviour of IO) is a factor of ~ 4 smaller than that determined by the MS studies of reaction R4-2. Further, in contrast to the results obtained herein, Enami *et. al.*[12] found that the rate of formation of IO was independent of CH_2I_2 concentration, when varied by a factor of three. A notable difference between the experimental conditions of this study and that of Enami *et. al.*[12] was the much lower concentrations of O_2 used in their work. This fact is explored in section 4.4.1.

Similarly to its rate of formation, the rate of removal of IO, k_{loss}, was found to be directly proportional to the concentration of CH_2I_2. This observation is consistent with the peak concentration of IO (and therefore its loss rate due to self-reaction) being proportional to the initial concentration of CH_2I_2. Although other IO losses were probably occurring (as the IO decays were not observed to be strictly second-order) the removal of IO from the chemical system is beyond the scope of the present study and was not investigated further.

4.3.2.1 Absorption Spectrum of the $CH_2I_2/O_2/N_2$/248 nm System

As the results discussed in section 4.3.2 indicated that IO is not formed directly from the reaction of $CH_2I + O_2$, a time dependent absorption spectrum of the reaction mixture was recorded to search for additional species: products of the $CH_2I + O_2$ reaction and/or potential precursors of the IO radical. Absorption traces of the reaction mixture were recorded in 10 nm intervals between 297 – 597 nm. Fig. 4.3-6 displays the time dependent absorption spectra obtained.

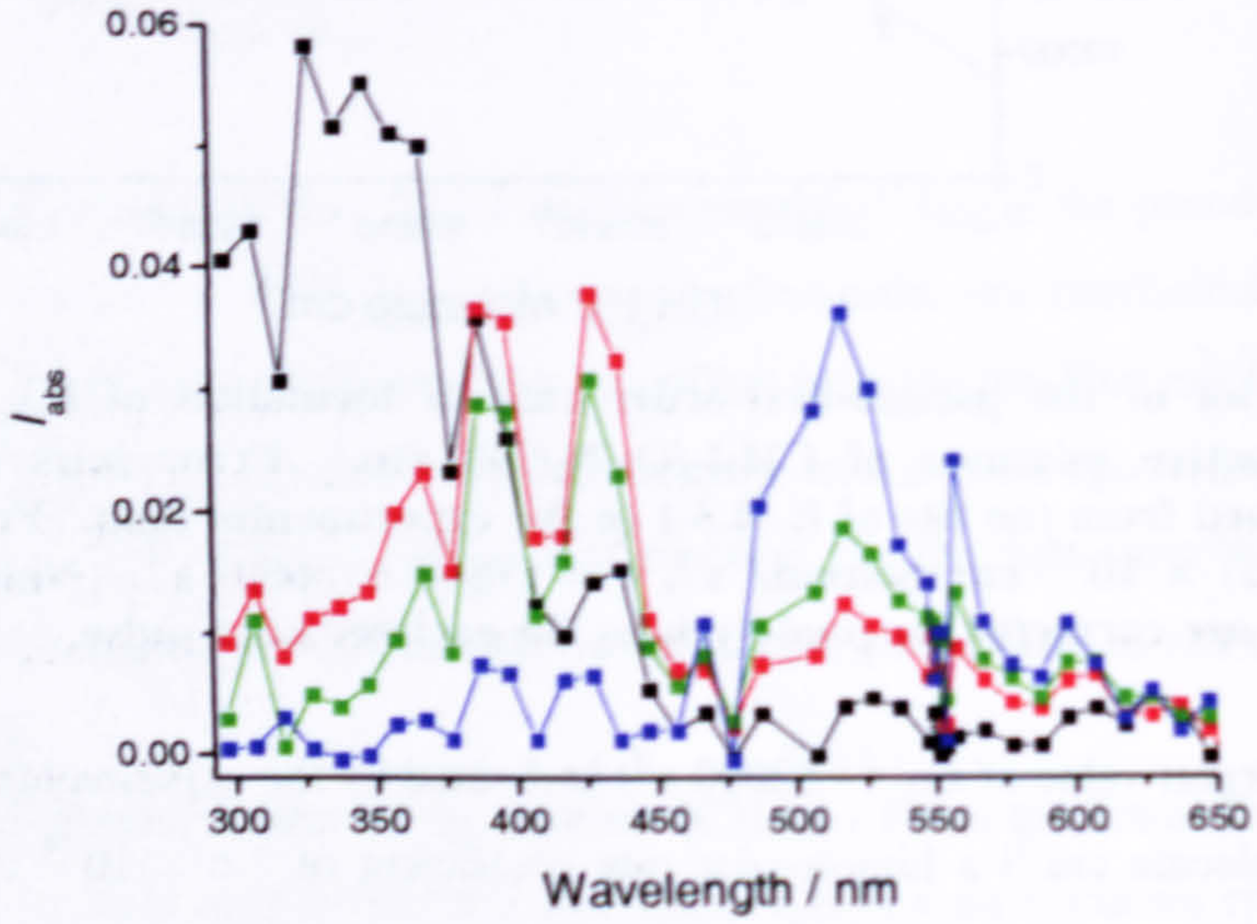

Fig. 4.3-6 – Time dependent absorption spectra of a $CH_2I_2/O_2/N_2$/248 nm reaction mixture. The absorption spectra were recorded by the same procedure outlined in section 4.3.1: I_0 was taken as the pre-Excimer laser background (with the exception of the 297 – 347 nm region – see caption to Fig. 4.3-7) and I was averaged over a range of reactions times after the Excimer laser was triggered (black = 2.5 – 12.5 μs, red = 40.5 – 90.5 μs, green = 100.5 – 150.5 μs, blue = 700.5 – 800.5 μs). The experimental conditions were identical for all wavelengths and the same as those given for the IO absorption trace recorded at maximum $[CH_2I_2]$ in Fig. 4.3-4, with the exception of an enhanced monochromator resolution of 0.4 nm. Analysis wavelengths were selected in a random manner to minimise systematic uncertainty.

At very early reaction times (2.5 – 12.5 μs) the absorption spectrum was observed to be dominated by a species absorbing in the 300 – 400 nm range. At intermediate reaction times (40.5 – 150.5 μs) the maximum absorption intensity was found to shift to the 400 – 450 nm region, and at long reaction times (700 – 800 μs) absorption was only observed in the 500 – 600 nm window. The absorption traces recorded at analysis wavelengths of 337 nm, 427 nm and 517 nm are displayed in Fig. 4.3-7.

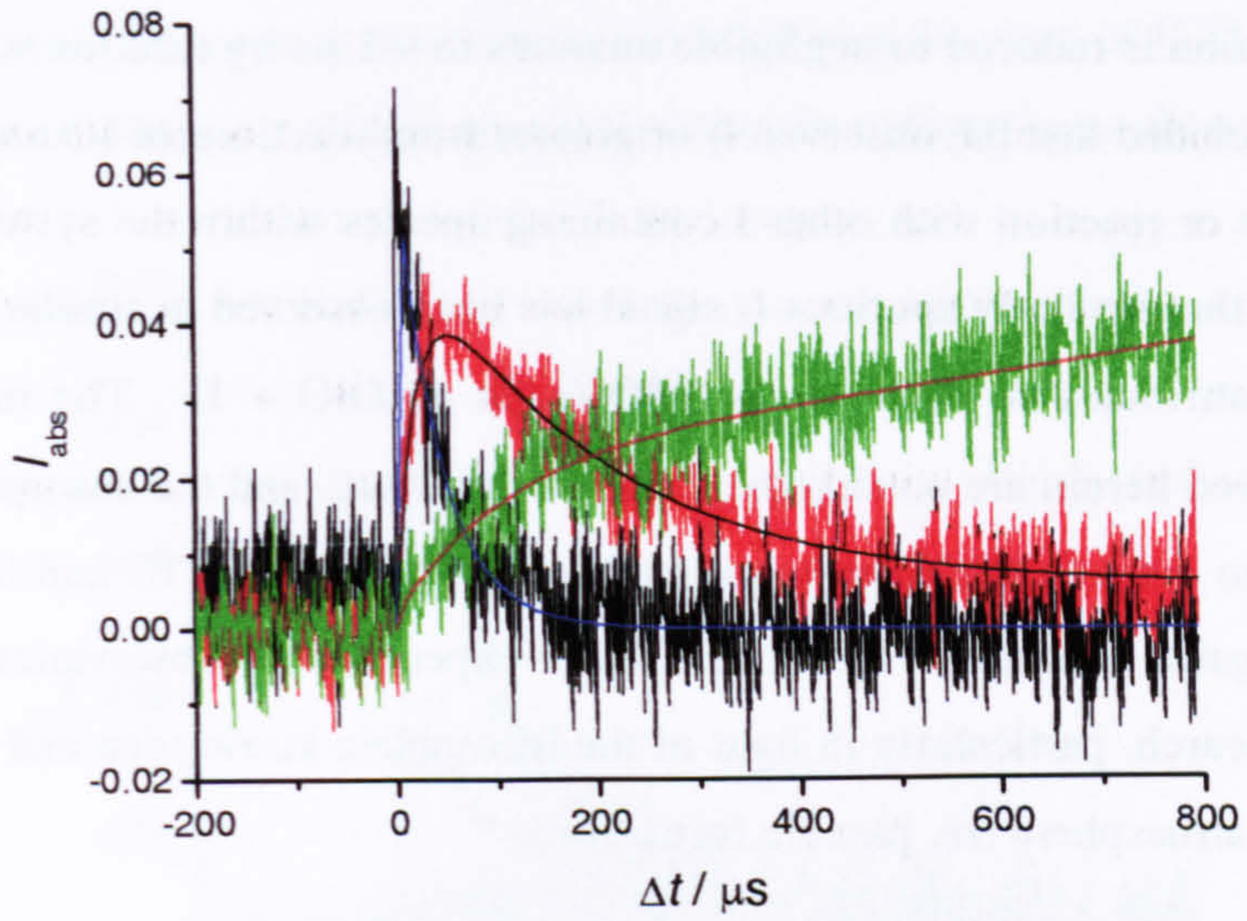

Fig. 4.3-7 – Absorption traces for the reaction mixture of $CH_2I_2/O_2/N_2$/248 nm recorded at 337 nm (black), 427 nm (red) and 517 nm (green). The experimental conditions were are as previously stated. The solid lines are fits of E. 4.3-1 to the experimental data. From the fits: k_{IO}' (or rather, k_{growth}) (s^{-1}) = 2.34 ×10^6 (337 nm), 4.8 × 10^4 (427 nm) and 9.2 × 10^3 (517 nm); k_{loss} (s^{-1}) = 2.3 × 10^4 (337 nm), 5.3 × 10^3 (427 nm) and -620 (517 nm). Note that at a wavelength of 337 nm CH_2I_2 absorbs analysis light and the post-excimer laser background is negative due to CH_2I_2 photolysis by the Excimer laser. For this reason, I_0 was taken as the long-time post-excimer baseline (Δt = 600 – 800 ms) for all data points between 297 – 347 nm as displayed in Fig. 4.3-6, and explains why the pre-Excimer baseline is positive for the 337 nm absorption trace displayed above.

It can be seen that there would appear to be some correlation between the decay of the absorber at 337 nm (black) and the growth of the absorbing species at 427 nm (red), and the decay of the absorber at 427 nm and the growth of the species absorbing at 517 nm. The absorbing species at 427 nm has already been identified as IO and the species responsible for absorption at 517 nm is most likely I_2 or OIO, as inferred from the approximate shape of the absorption spectrum over the 500 – 600 nm region (see Fig. 4.3-6) and the fact that they are both products of the IO self-reaction. For further confirmation of this hypothesis an absorption trace was recorded at 549.1 nm, a peak in the absorption spectrum of OIO[24], which is displayed in Fig. 4.3-8. The temporal profile of the absorption trace recorded at 549.1 nm is very different to that recorded at 517 nm, exhibiting a rapid growth and decay, and is therefore attributed predominantly to OIO. The absorption at 517 nm is thus attributed mainly to the production of I_2. It is perhaps surprising that strong I_2 absorption is witnessed on a timescale comparable to IO_x chemistry within the system as the production of I_2 from the IO self-reaction is well known to be only a minor product channel (< 5 %). Further, despite the large I atom concentration and the relatively high pressure, recombination of I atoms to form I_2 should occur on a much slower timescale than that observed (and may partially account for the slow, secondary I_2 growth observed in the 517 nm

absorption trace, k_{loss} = - 620 s^{-1}). Molecular iodine cannot be produced from reactions of CH_2I (as its concentration is reduced to negligible amounts in ~ 1 μs by reaction with O_2) and it must therefore be concluded that the observed I_2 originates from reactions of IO and OIO, *i.e.* by self- or cross-reaction or reaction with other I containing species within the system (I or CH_2I_2). It should be noted that similarly spurious I_2 signal has been observed in similar reaction systems[25] and have been attributed to reactions of OIO (such as OIO + I). The intricacies of the I_2 formation observed herein are outside the scope of this work, and the absorption observed over the 500 – 600 nm range is attributed to products of the reactions of IO and OIO. Neither topic will be investigated further. However, these experimental observations warrant future experimental research, particularly in light of the incomplete knowledge and importance of IO_x chemistry in the atmosphere (*re.* particle formation).

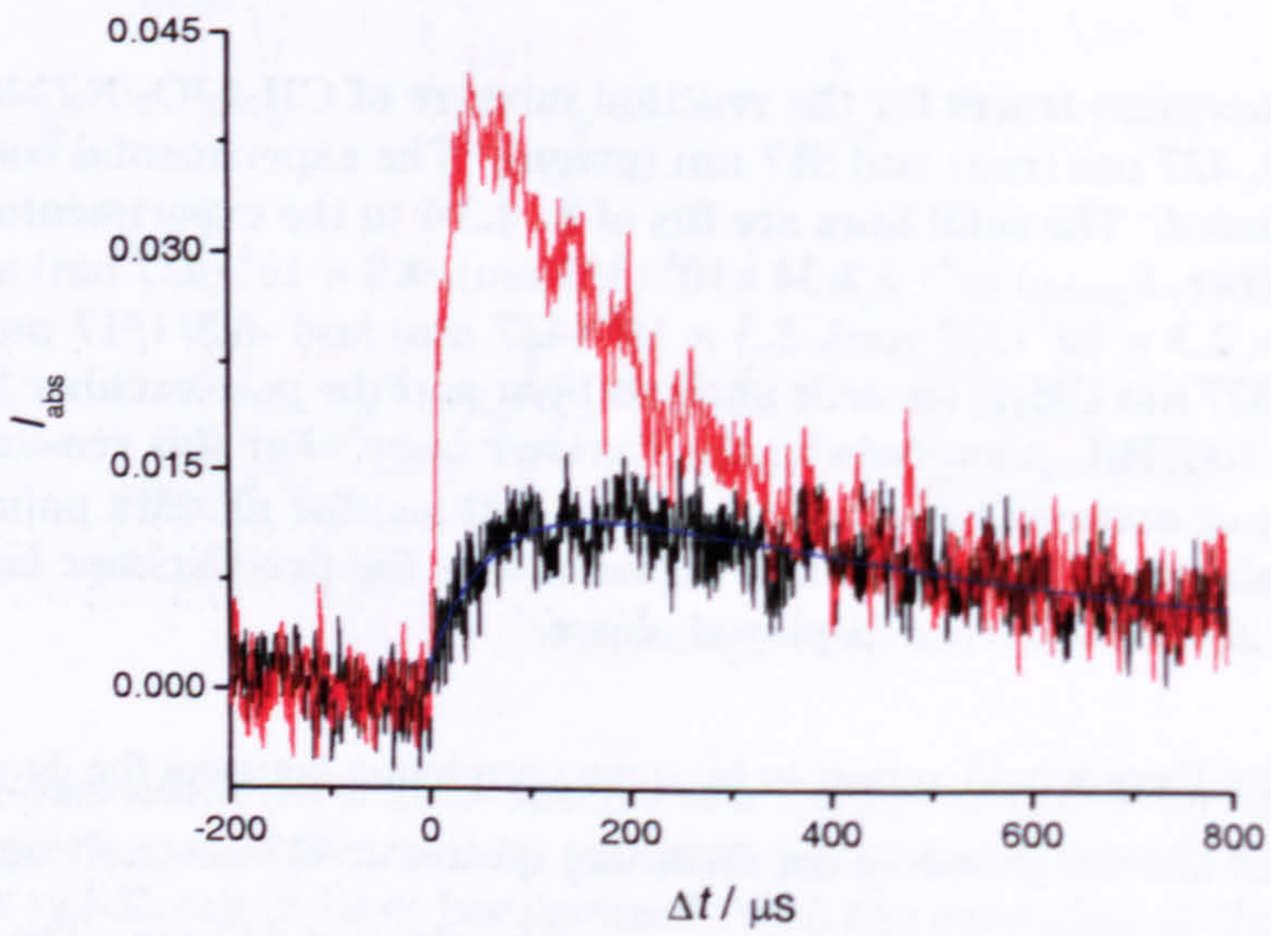

Fig. 4.3-8 – Absorption traces recorded at 427 nm (red) and 549.1 nm (black). The experimental conditions are as previously stated. The solid blue line is a fit of E. 4.3-1 to the 549.1 nm absorption trace. From the fit, $k_{growth} = 1.6 \times 10^4$ s^{-1} and $k_{loss} = 1.5 \times 10^3$ s^{-1}.

With respect to the current research, a more interesting feature of the absorption spectrum displayed in Fig. 4.3-6 is the absorption of an unknown species (subsequently referred to as species "X") in the 300 – 400 nm region. In the work of Sehested *et. al.*[13] the absorption spectrum of CH_2IO_2 was reported to exhibit continuous absorption over the 220 – 400 nm wavelength range. From the fit of E. 4.3-1 to the 337 nm absorption trace (see Fig. 4.3-7) the pseudo-first-order rate coefficient for the formation of species X is, k_{growth} = (2.34 ± 1.13) ×10^6 s^{-1}. Dividing this value by the experimental O_2 concentration yields a bimolecular rate coefficient of, $k = (1.1 \pm 0.6) \times 10^{-12}$ $cm^3 molecule^{-1} s^{-1}$, in reasonably good agreement with the determination of the rate coefficient for the reaction of $CH_2I + O_2$ by the MS studies[14,19], perhaps suggesting that X is formed directly from reaction R4-2 and is indeed the CH_2IO_2

peroxy radical. To investigate whether the kinetics of species X had any dependence on the concentration of CH_2I_2, absorption traces were recorded as a function of $[CH_2I_2]$ at an analysis wavelength of 350 nm. Fig. 4.3-9 displays some of the absorption traces obtained

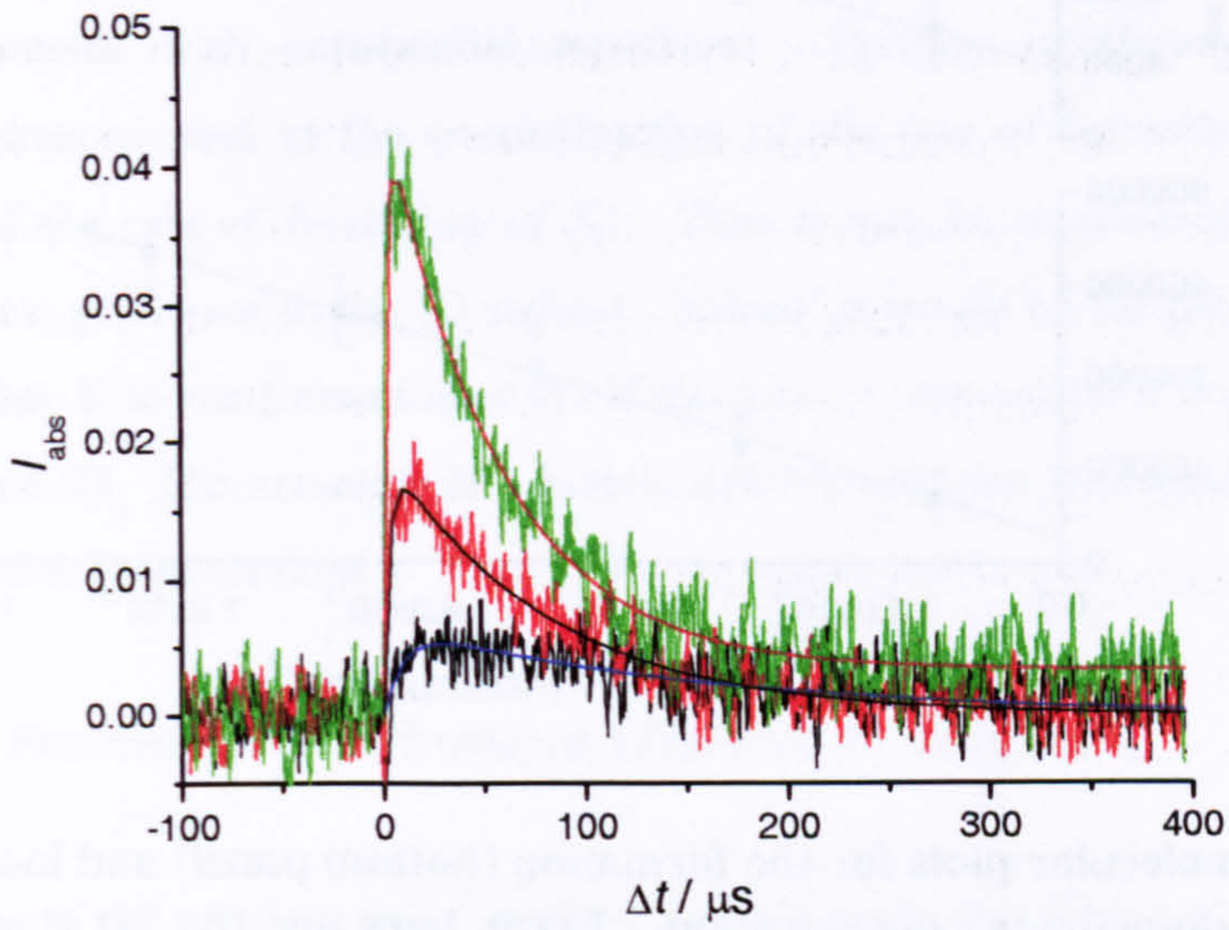

Fig. 4.3-9 – Absorption traces of species X recorded as a function of $[CH_2I_2]$. Experimental conditions are the same as previously stated with the exception: $[CH_2I_2]$ (molecule cm^{-3}) = 1.35×10^{15} (green), 7.76×10^{14}(red) and 1.84×10^{14} (black); M_r = 0.4 nm; λ_m = 350 nm. The solid lines are fits of E. 4.3-1 to the experimental data. From the fits: k_{growth} (s^{-1}) = 5.0×10^5 (green), 3.2×10^5 (red) and 1.1×10^5 (black); k_{loss} (s^{-1}) = 1.8×10^4 (green), 1.2×10^4 (red) and 6.0×10^3 (black) s^{-1}.

Similarly to IO, the peak concentration of X was found to be directly proportional to the concentration of diiodomethane, as was its rate of formation. Bimolecular plots for the pseudo-first-order formation and loss rates of species X are displayed in Fig. 4.3-10. It is interesting that both the formation and loss rates of X exhibit such a strong dependence on CH_2I_2 concentration, and would initially suggest that species X cannot be CH_2IO_2 (or any direct product of the reaction of $CH_2I + O_2$). If the largest pseudo-first-order rate coefficient, k_{growth}, obtained in the experiment (~ 50000 s^{-1}) is divided by the experimental O_2 concentration (~ 2×10^{18} molecule cm^{-3}), a bimolecular rate coefficient of, $k = (2.5 \pm 0.3) \times 10^{-13}$ $cm^3 molecule^{-1} s^{-1}$ is obtained, significantly smaller than that of the reaction of $CH_2I + O_2$, and in direct contrast to the value determined previously for the 337 nm absorption trace. Upon analysing the kinetic traces recorded between 297 – 347 nm (in the absorption spectrum experiment) it is found that both the rates of formation and loss of species X systematically decrease in moving to longer wavelengths. This finding can be explained by the presence of multiple absorption.

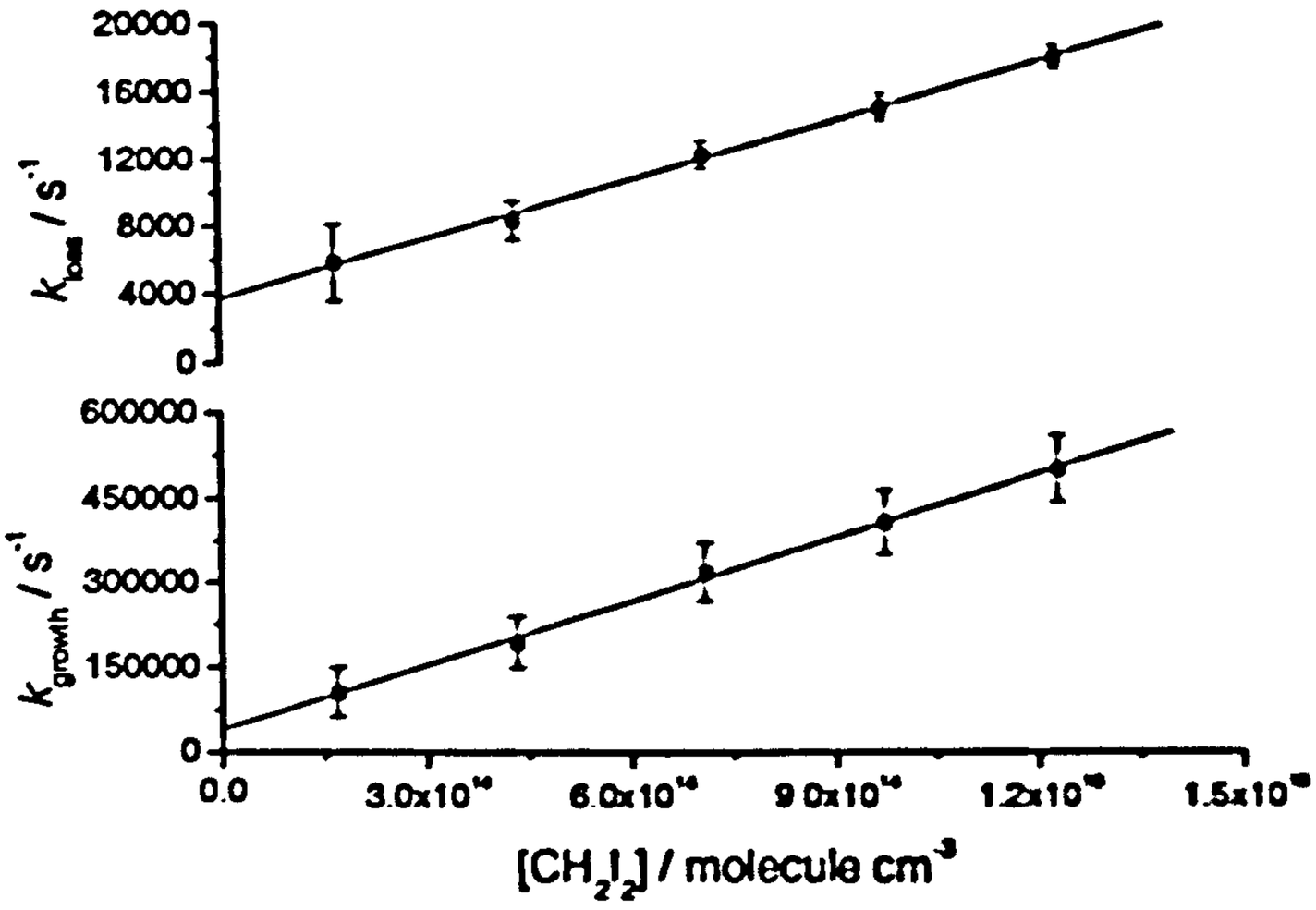

Fig. 4.3-10 – Bimolecular plots for the formation (bottom panel) and loss of species X as a function of diiodomethane concentration. Error bars are the 2σ standard uncertainty returned from the fitting procedure. From the linear fits, k = (3.79 ± 0.34) × 10^{-10} $cm^3 molecule^{-1} s^{-1}$ (formation) and, k = (1.17 ± 0.11) × 10^{-11} $cm^3 molecule^{-1} s^{-1}$ (loss). The intercepts (s^{-1}) are (3750 ± 900) and (40000 ± 27000) for the loss and growth plots respectively.

At wavelengths greater than ~ 340 nm, IO begins to absorb the analysis light and any observed absorption will thus be the sum of that due to species X and IO (and any other species that may absorb at that wavelength). As IO is formed at a lesser rate (see Fig. 4.3-7) the apparent rate of formation of X will therefore be underestimated. Conversely, as the analysis light is changed to shorter wavelengths, the CH_2I radical will begin to absorb. In fact, the absorption spectrum of CH_2I is known to have maxima at 337.5 nm and 280 nm[13]. As CH_2I is a photolytic species in the reaction system (it is formed in the Excimer laser pulse), the presence of CH_2I at early reaction times will have the effect of increasing the apparent rate of formation of species X. Unhelpfully, the unknown species cannot be studied in the absence of either IO or CH_2I as they are both intrinsic species in the reaction system. Further, absorption from CH_2I cannot be deconvoluted from that of species X by recording absorption traces in the absence and presence of O_2 (and therefore the mystery absorber) as this would result in altering the temporal profile of CH_2I. In summary, it is not possible at this stage to conclude whether or not species X is a direct product of the $CH_2I + O_2$ reaction. This topic is returned to in section 4.3.2.3.

With respect to the hypothesis that absorber X is the precursor to IO in the reaction system, it can be seen from the bimolecular plot in Fig. 4.3-10 that the rate of removal of X has a CH_2I_2 dependence of , k = (1.17 ± 0.11) × 10^{-11} $cm^3 molecule^{-1} s^{-1}$ (at an analysis wavelength of 350 nm). In section 4.3.2, the rate of formation of IO was found to have a dependence on the

concentration of CH_2I_2 that was approximately three times greater (k = (3.7 ± 0.5) × 10^{-11} $cm^3molecule^{-1}s^{-1}$). However, it should be noted that the formation rate of OIO (k_{growth} = 1.6 × 10^4 s^{-1}, see Fig. 4.3-8) was approximately three times greater than the decay rate of its precursor, IO (k_{loss} = 5.3 × 10^3 s^{-1}, see Fig. 4.3-7), highlighting the problems associated with analysing second-order processes with exponential equations. Further, interference from multiple absorption may have resulted in the overestimation of the rate of formation of IO (and the underestimation of the rate of formation of X). Thus it may be considered fairly likely that species X is a direct precursor to the IO radical. Indeed, it would be far more difficult to link the decay of species X to the formation of IO if the rate of removal of X was greater than the rate of formation of IO. The presence of a kinetic link between the two species is examined in greater detail in subsequent sections.

4.3.2.2 Potential Sources of IO in Photolysis Mixtures of $CH_2I_2/O_2/N_2$

The results of the previous two sections clearly indicate that IO is not a direct product of the CH_2I + O_2 reaction, R4-2. The possibility that IO is generated from sources other than chemistry initiated by reaction R4-2 was therefore investigated.

The photolysis of CH_2I_2 at 248 nm is known to generate a variety of chemical species in both multi-photon and single-photon processes. For example, the multi-photon dissociation of CH_2I_2 produces CH_2 + I_2 in a concerted elimination process at photolysis wavelengths as long as 310 nm[26]. At shorter wavelengths (λ < 200 nm) CH_2 + I_2 can be produced by the single-photon dissociation of CH_2I_2[27]. Although these processes often require high intensity radiation a study by Baughcum and Leone[27] found that unfocused Excimer laser radiation can result in the formation of CH_2 radicals, and other ionised products, from the photolysis of diiodomethane at 248 nm. Thus it is entirely possible, and indeed likely, that some multiphoton dissociation of CH_2I_2 will occur in our experimental system, generating CH_2 radicals. In the presence of a large excess of O_2, CH_2 radicals are rapidly consumed generating CH_2O + O (amongst other products)[28]. The subsequent production of IO from the reaction, O + CH_2I_2 → IO + CH_2I (R4-12) is therefore a possibility, and could explain the observed dependence of the rate of formation of IO on the concentration of CH_2I_2. The rate coefficient for R4-12 has only been reported by one experimental investigation[29]. In that study, the rate coefficients for a number of O + RI reactions were determined by following the temporal profile of O atoms, in an excess concentration of alkyl iodide, by resonance fluorescence. Reaction R4-12 was found to be independent of total pressure and temperature with a bimolecular rate coefficient of, k = 7.4 × 10^{-11} $cm^3molecule^{-1}s^{-1}$. Although IO has not been reported as a product of reaction R4-12, the relatively high yields of IO from the reactions of O + CH_3I (R4-8a) and O + CF_3I indicate that IO would be expected in significant yield from the reaction, O + CH_2I_2 → products. Further,

the rate coefficient for reaction R4-12, determined by Tereul *et. al.*[29], is only a factor of two greater than the rate coefficient inferred from the CH_2I_2 dependence of the rate of formation of IO in the $CH_2I_2/O_2/N_2$/248 nm reaction system determined in section 4.3.2.

In order to investigate the potential production of O atoms in our system an experiment was performed to infer their presence. An excess of Br_2 was added to a reaction mixture of $CH_2I_2/O_2/N_2$/248 nm by passing a small flow of N_2 through a glass vessel containing liquid bromine. Any O atoms would thus rapidly be converted to BrO by the reaction O (^{3}P) + Br_2 → BrO + Br[30]. The detection of BrO was attempted at an analysis wavelength of 338.9 nm – the peak of the (9,0) vibrational band of the $A^2\Pi_{3/2} \leftarrow X^2\Pi_{3/2}$ electronic transition[24]. Fig. 4.3-11 displays the absorption trace obtained, along with a second trace recorded under identical conditions but at an analysis wavelength of 427.2 nm.

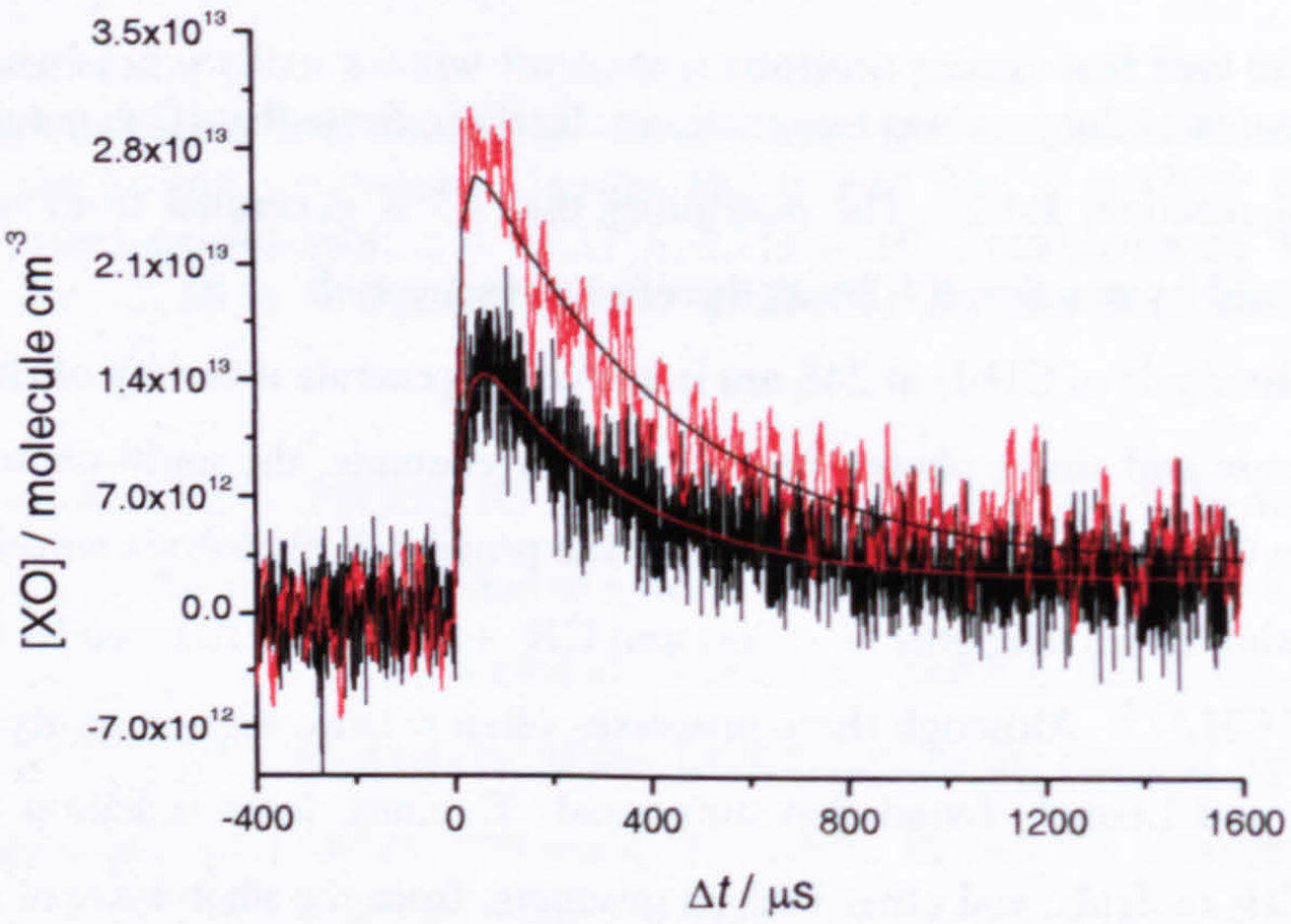

Fig. 4.3-11 – Absorption traces of BrO (red) and IO (black) in a $CH_2I_2/Br_2/O_2/N_2$/248 nm reaction mixture recorded at 338.9 nm and 427.2 nm respectively. Experimental conditions: P = 760 Torr; T = 296 K; $[CH_2I_2] = 1.11 \times 10^{15}$ molecule cm^{-3}; $[Br_2] = 1.83 \times 10^{16}$ molecule cm^{-3}; $[O_2] = 2.74 \times 10^{18}$ molecule cm-3; $[N_2]$ = balance; $F = 1.25 \times 10^{17}$ photons cm^{-2}; M_r = 0.3 nm, M_g = 1200 g/mm. Note that the Br_2 concentration was determined absolutely by absorption spectroscopy. The absorption signals of BrO and IO were converted into absolute concentrations using the appropriate absorption cross-sections. The solid lines are fits of E. 4.3-1 to the experimental data. From the fits, k_{growth} (s^{-1}) = (5.8 ± 1.7) × 10^4 (BrO) and (4.4 ± 0.8) × 10^4 (IO).

The absorption traces clearly show the presence of both BrO and IO after photolysis of the reaction mixture. The absorption at 338.9 nm could be assigned to BrO by recording an "off-line" absorption trace at 337.7 nm (a wavelength where BrO does not absorb), which is displayed in Fig. 4.3-12.

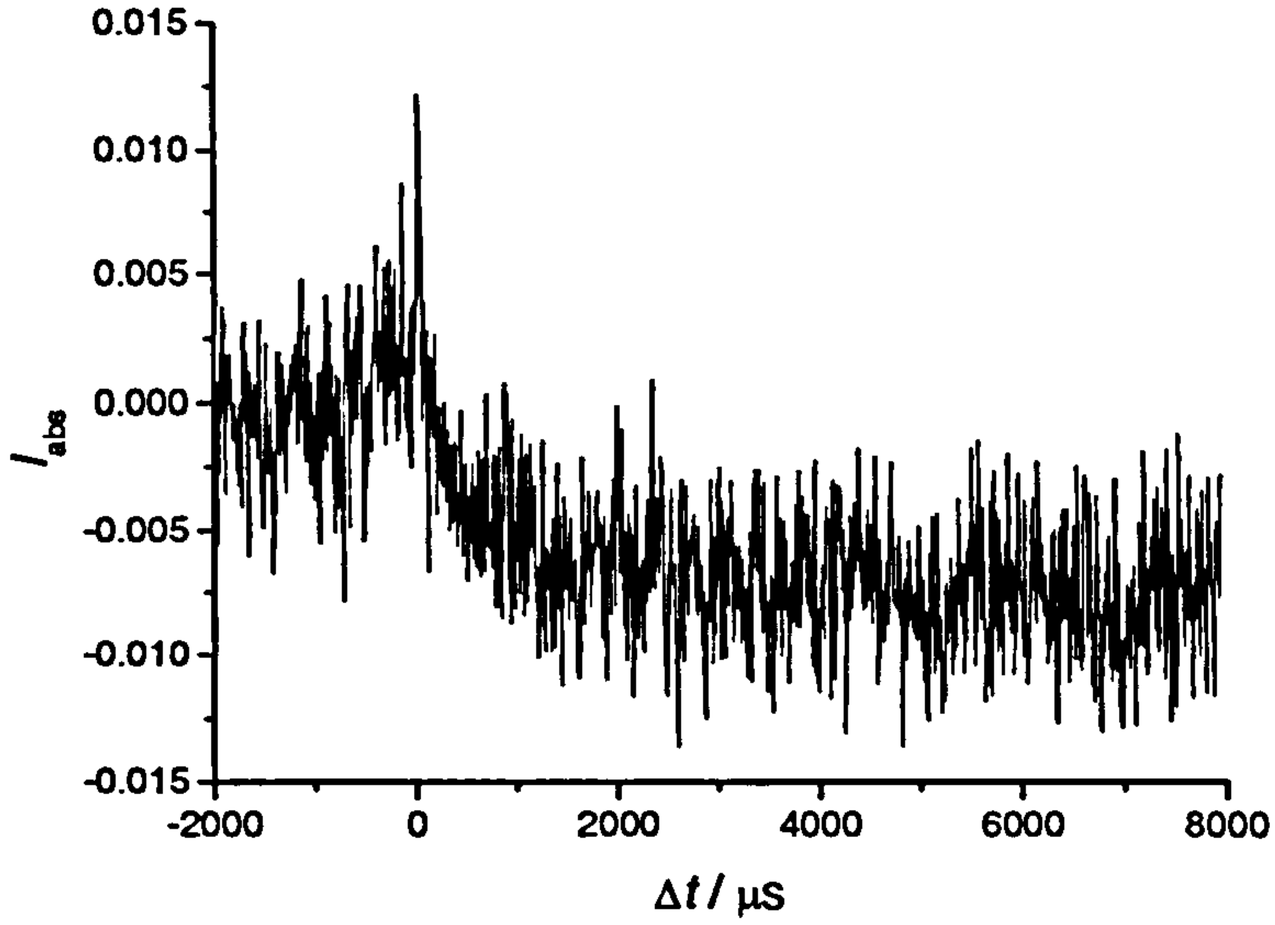

Fig. 4.3-12 – Absorption trace recorded at 337.7 nm in a $CH_2I_2/Br_2/O_2/N_2$/248 nm reaction mixture. The experimental conditions are the same as given in the previous figure caption.

In the off-line absorption trace, the strong absorption previously observed – and attributed to BrO – is clearly absent. However, absorption structure is still evident in the off-line trace. The negative absorption, observed at longer reaction times, can be attributed to the photolysis of CH_2I_2 and Br_2 by the Excimer laser, which is masked at earlier reaction times by the weak absorption of other trace species (such as CH_2I and species X, which are rapidly consumed – see previous section). Although the off-line absorption signal will also have contaminated the absorption trace recorded at 338.9 nm, it should be noted that the absorption signal, $I_{abs} = I_0/I$, giving rise to the BrO signal displayed in Fig. 4.3-11 was of much greater intensity (I_{abs} (max) ≈ 0.05), and that this contamination was therefore negligible.

The presence of BrO may therefore be thought to infer the presence of O atoms within the reaction system. However, a more careful analysis of the absorption traces displayed in Fig. 4.3-11 suggests that this is not the case. First, if BrO and IO are produced by the reaction of O atoms with Br_2 and CH_2I_2 respectively, the ratio of their peak concentrations should be approximately equal to

$$\frac{[BrO]_{max}}{[IO]_{max}} = \frac{k_{(O+Br_2)}[Br_2]}{k_{(O+CH_2I_2)}[CH_2I_2]} = 4.2$$

which is more than a factor of two greater than observed. Secondly, and more informatively, BrO and IO are not observed to form on a timescale consistent with the consumption of O atoms by Br_2 and CH_2I_2. If IO and BrO are formed from O atoms then their rates of formation should

be equivocal and equal to the total rate of consumption of O $\left(k_{tot}' = k_{(O+Br_2)}[Br_2] + k_{(O+CH_2I_2)}[CH_2I_2] \approx 10^6\, s^{-1}\right)$. Although the observed rates of formation of BrO and IO are comparable (see caption to Fig. 4.3-11), suggesting that both species are formed by the same reaction mechanism, they are much too small to infer the reaction of O atoms with Br_2 and CH_2I_2. Thus, it would appear that O atoms are not present (at significant concentration) in the reaction system.

To further investigate the hypothesis of O atom formation in reaction mixtures of $CH_2I_2/O_2/N_2/h\nu$, experiments were performed at a photolysis wavelength of 193 nm. Initially, the yield of IO from the reaction of O + CH_2I_2 (R4-12) was determined. To achieve this, N_2O was photolysed in the presence of an excess of O_2 and N_2. The experimental conditions were such that all O (^1D) atoms (initially produced by the 193 nm photolysis of N_2O) were rapidly quenched to O (^3P), which were subsequently converted to O_3 by the reaction, O + O_2 + M→ O_3.+ M. The absolute concentration of O_3 was then measured by absorption spectroscopy at an analysis wavelength of 255 nm ($\sigma(O_3)$ = 1.17 × 10^{-17} $cm^2 molecule^{-1}$)[11]. In back-to-back experiments, O_2 was replaced with CF_3I or CH_2I_2, which consumed the O atoms, generating IO. Thus by comparison of the peak IO concentrations to [O_3], the branching ratios for the formation of IO from the reactions of O + CF_3I and O + CH_2I_2 are determined. The results of this experiment are displayed in Fig. 4.3-13.

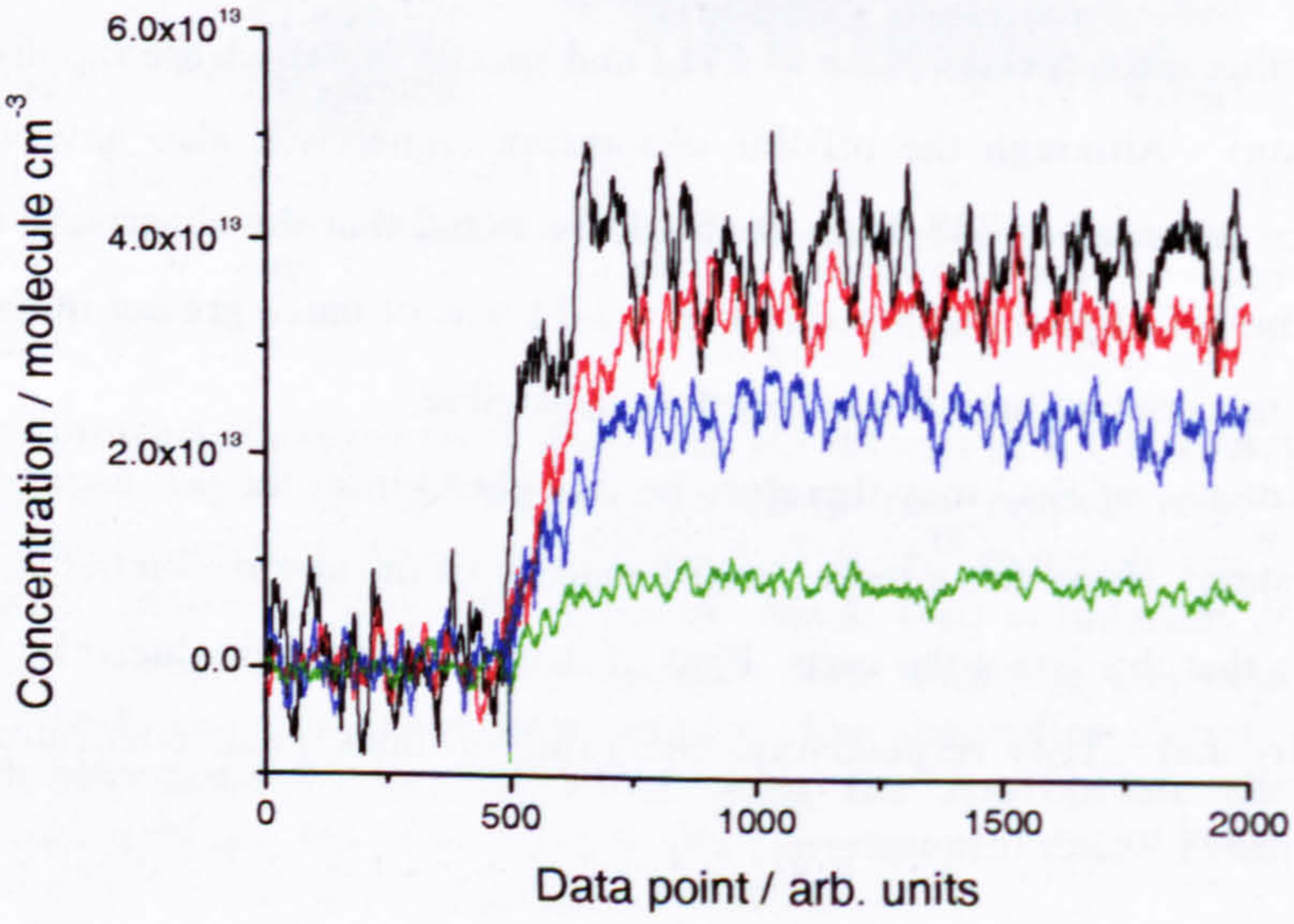

Fig. 4.3-13 – Absorption traces of O_3 (black) and IO for various mixtures of O + RI. Experimental conditions: [N_2O] = 2.75 × 10^{17} molecule cm^{-3} (all); [O_2] = 4.36 × 10^{17} molecule cm^{-3} (black); [CF_3I] = 2.61 × 10^{17} molecule cm^{-3} (red and blue); [CH_2I_2] = 6.96 × 10^{14} molecule cm^{-3} (blue and green); [N_2] = balance; F = 5.8 × 10^{16} photons cm^{-2}. All other conditions are as previously stated. Note that as the various reactions proceed at different rates the absorption traces were collected over different time spans and the x-axis is therefore displayed as arbitrary data point, rather than reaction time.

After converting the absorption signals into absolute concentrations, the branching ratio for IO production from the reaction of O + CF_3I was determined as (87 ± 15) %, in good agreement with the literature value[18], and the branching ratio for IO formation from the reaction of O + CH_2I_2 was determined as (22 ± 4) %. This is somewhat of a surprising result. As stated previously, the branching ratio for IO formation from the reaction, O + CH_3I → products is known to be ~ 40 %[18]. One would intuitively expect the branching ratio for IO formation from the reaction of O + CH_2I_2 to be greater, as two sites are available for I atom transfer. A possible reason for this apparently anomalous result is the absorption of photolysis radiation by CH_2I_2. To investigate this hypothesis, an IO absorption trace was recorded where both CF_3I and CH_2I_2 were present in the reaction mixture (represented by the blue absorption trace in Fig. 4.3-13). Under the experimental conditions ~ 96 % of the O atoms (generated by the photolysis of N_2O) should be consumed by CF_3I. Therefore, the peak IO concentration should be approximately equal to that where only CF_3I was present in the reaction mixture. However, it was found that the peak IO signal observed when both iodides were present was only ~ 73 % of that when only CF_3I was in the reaction system. Under the experimental conditions ~ 20 % of the photolysis light will be absorbed by CH_2I_2, reducing the initial O atom concentration produced from N_2O photolysis. It is thus more appropriate to determine the branching ratio for IO formation from reaction R4-12 by comparing the peak IO concentration from the absorption trace where only CH_2I_2 was present to that where both CF_3I and CH_2I_2 were present (rather than to the O_3 absorption trace, where absorption of the photolysis radiation by CH_2I_2 was not occurring). In this manner, the branching ratio for IO formation from reaction R4-12 is determined as (30 ± 5) % (where the branching ratio of IO formation from the reaction O + CF_3I → products has been accounted for). The corrected value is still somewhat smaller than may be expected, probably because photolysis products of CH_2I_2 (such as CH_2I) are reacting with O atoms to generate species other than IO (note that when CF_3I is present, almost all O atoms are consumed by reaction with the trifluoromethyliodide, which does not significantly absorb at 193 nm due to its small absorption cross-section)[11]. The branching ratio of 30 % should therefore be regarded as a lower limit in absolute terms.

In a subsequent experiment an absorption trace of IO was recorded in a mixture of $CH_2I_2/O_2/N_2$/193 nm, and in a back-to-back experiment a large excess of CF_3I was added to the reaction mixture. According to the results obtained above, if IO is predominantly produced from O atoms within the system, the peak IO concentration should increase by a factor of approximately three (*i.e.* the ratio of the branching ratios for IO formation from the reactions of O + CF_3I and O + CH_2I_2) upon the addition of a large excess of CF_3I. Additionally, IO would be expected to form at a much enhanced rate due to the high concentration of CF_3I and rapid consumption of O atoms. An absorption trace was also recorded where only $CF_3I/O_2/N_2$/193

nm were present in the reaction mixture, to quantify the extent of O atom production from the 193 nm photolysis of O_2. The results are shown in Fig. 4.3-14.

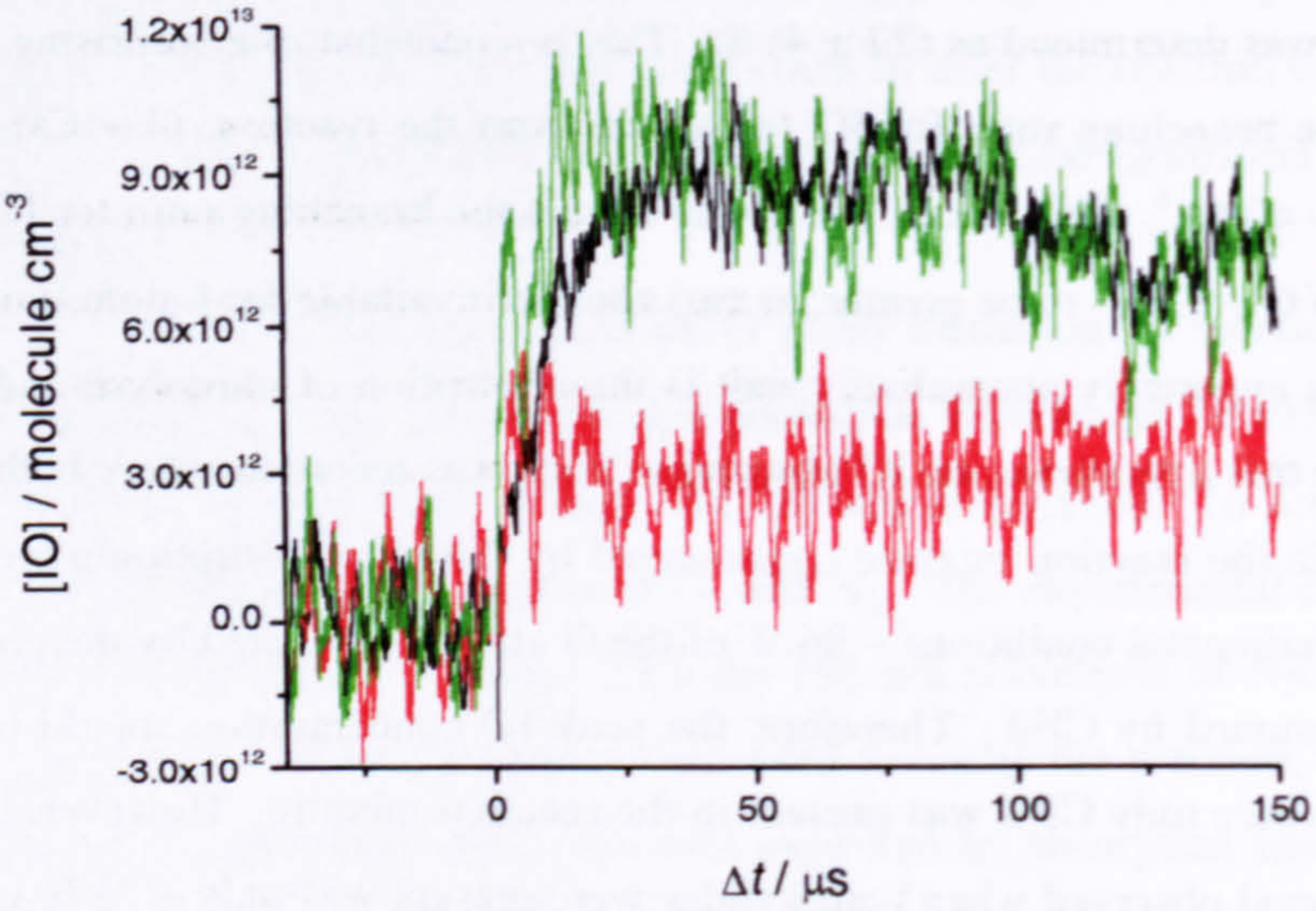

Fig. 4.3-14 – Absorption traces of IO, recorded at 427.2 nm, in a reaction mixture of $CH_2I_2/CF_3I/O_2/N_2$/193 nm. Experimental conditions: $[O_2] = 1.05 \times 10^{18}$ molecule cm^{-3} (all); $[CH_2I_2] = 5.45 \times 10^{14}$ molecule cm^{-3} (black and green); $[CF_3I] = 2.53 \times 10^{17}$ molecule cm^{-3} (red and black); $[N_2]$ = balance. All other experimental conditions are as previously stated.

From the results it can be seen that the peak IO concentration is only marginally increased when CF_3I was added to the reaction mixture (black *vs.* green absorption traces in Fig. 4.3-14). The rate of formation of IO is enhanced upon the addition of CF_3I, although this is most likely due to the rapid consumption of a small amount of O atoms generated by the 193 nm photolysis of O_2 (red absorption trace) by CF_3I.

The unequivocal conclusion of the results presented in this section is that oxygen atoms are not the predominant precursor of IO in photolytic reaction mixtures of $CH_2I_2/O_2/N_2$.

4.3.2.3 Low Pressure Investigation of the $CH_2I_2/O_2/N_2/h\nu$ Reaction System

As a final part of the investigation by absorption spectroscopy, the possibility of any pressure dependence to the most pertinent previous findings was investigated. A rotary pump was connected to the exhaust of the reaction cell and an appropriate flow of O_2 was passed through a MFC to allow the total reaction cell pressure to stabilise at a few Torr. A small flow of N_2 was passed through a glass vessel containing purified CH_2I_2 and entrained into the bulk O_2 flow. The glass vessel was separated from the vacuum of the reaction cell by a needle valve, allowing variable amounts of the iodide into the reaction system. The CH_2I_2 concentration was

determined absolutely by absorption spectroscopy. The total pressure of the reaction cell was maintained at ~ 4 Torr, and measured with a 0 – 10 Torr capacitance manometer.

The absorption spectrum of a reaction mixture of $CH_2I_2/O_2/N_2$/193 nm was recorded (by the same procedure outlined in section 4.3.2.1) at ~ 4 Torr total pressure to investigate whether IO and the unknown absorber, species X, exhibit any pressure dependence in the reaction system. Absorption traces were recorded in 10 nm intervals, at a monochromator resolution of 0.3 nm, between 247.2 – 457.2 nm. Similarly to the atmospheric pressure system, strong absorption from both IO and species X was observed. Fig. 4.3-15 displays the absorption traces recorded at analysis wavelengths of 337.2 and 427.2 nm.

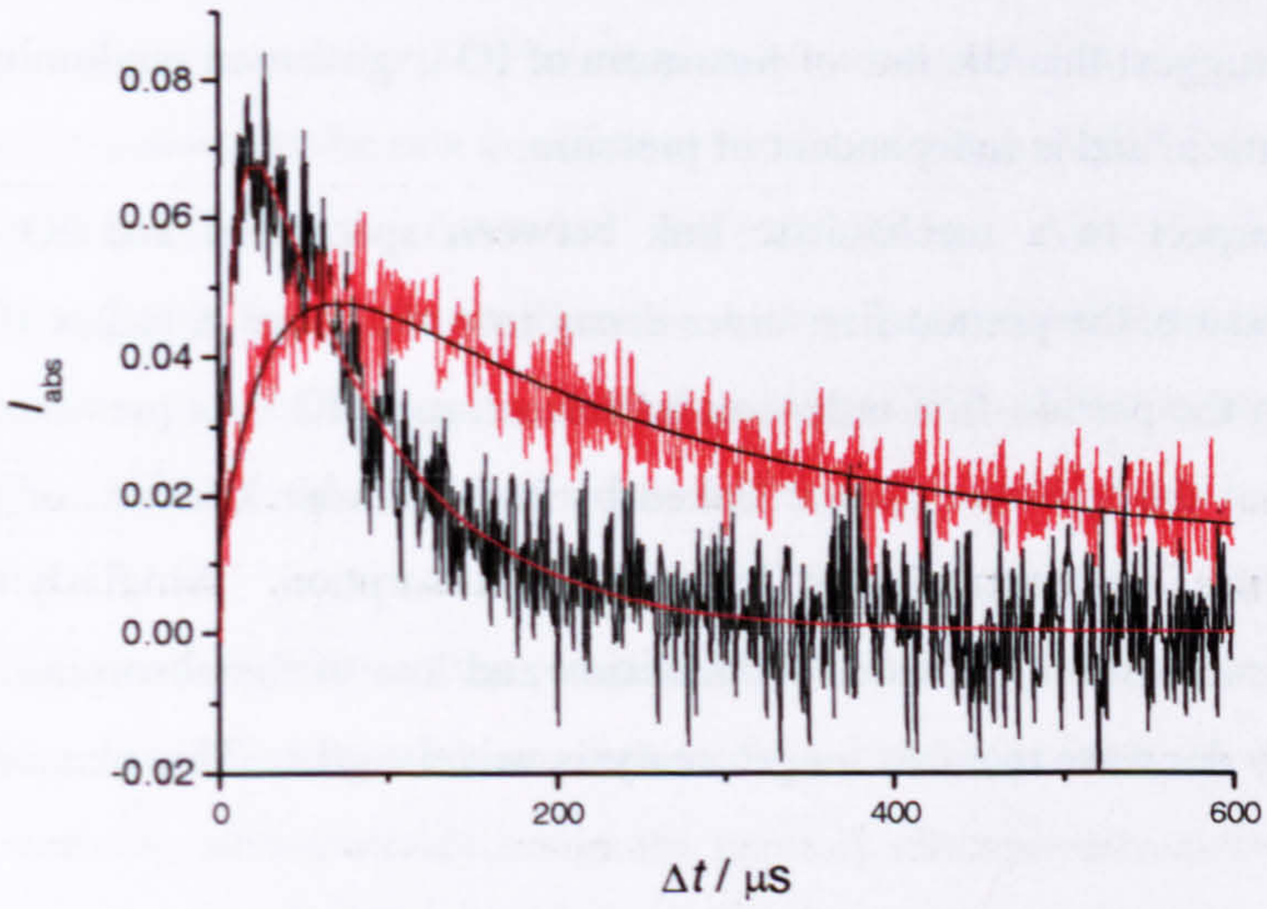

Fig. 4.3-15 – Absorption traces of IO (red) and species X (black) recorded at analysis wavelengths of 427.2 nm and 337.2 nm respectively in a $CH_2I_2/O_2/N_2$/193 nm reaction mixture at low pressure. Experimental conditions: P = 4.1 Torr; T = 296 K; $[CH_2I_2] = 8.19 \times 10^{14}$ molecule cm^{-3}; $[O_2] = 1.06 \times 10^{17}$ molecule cm^{-3}; $[N_2]$ = balance; $F = 5.8 \times 10^{16}$ photons cm^{-2}; The solid lines are fits of E. 4.3-1 to the experimental data. From the fits: $k_{IO}' = (3.4 \pm 0.3) \times 10^4$ s^{-1} and $k_X' = (1.1 \pm 0.1) \times 10^5$ s^{-1}; $k_{loss}(IO) = (4.3 \pm 0.6) \times 10^3$ s^{-1} and $k_{loss}(X) = (1.2 \pm 0.1) \times 10^4$ s^{-1}.

As observed at atmospheric pressure, there appears to be some correlation between the decay of species X and the formation of IO, suggesting that the temporal profiles of the two species are connected. If the pseudo-first-order rate coefficient for the formation of species X (1.13×10^5 s^{-1}) is divided by the experimental O_2 concentration (1.06×10^{17} molecule cm^{-3}), an effective bimolecular rate coefficient of, $k = 1.1 \times 10^{-12}$ cm^{3}molecule^{-1}s^{-1} is obtained. This value is in exact agreement with that obtained at atmospheric pressure (for the absorption trace recorded at 337 nm). If the pseudo-first-order rate coefficient for the formation of X is divided by the experimental CH_2I_2 concentration (8.19×10^{14} molecule cm^{-3}) an effective bimolecular rate coefficient of, $k = 1.4 \times 10^{-10}$ cm^{3}molecule^{-1}s^{-1} is obtained. This value is somewhat smaller, although of the same order of magnitude, of that obtained at atmospheric pressure (3.8×10^{-10}

$cm^3molecule^{-1}s^{-1}$). These observations would tend to suggest that the reaction kinetics of species X have a greater dependence on the experimental O_2 concentration than $[CH_2I_2]$, and are largely independent of pressure.

From the absorption trace recorded at 427.2 nm, the pseudo-first-order rate of formation of IO is found to be $(3.4 \pm 0.3) \times 10^4$ s^{-1}, yielding a bimolecular rate coefficient of, $k = 3.8 \times 10^{-11}$ $cm^3molecule^{-1}s^{-1}$, once divided by the experimental CH_2I_2 concentration, again in excellent agreement with the previous findings. If divided by the experimental O_2 concentration, the rate of formation of IO yields an effective bimolecular rate coefficient of, $k = 3.2 \times 10^{-13}$ $cm^3molecule^{-1}s^{-1}$, significantly greater than that obtained at atmospheric pressure, but still much smaller than the MS determinations of the rate coefficient for the reaction of $CH_2I + O_2$. The above findings suggest that the rate of formation of IO is governed predominantly by the initial CH_2I_2 concentration, and is independent of pressure.

With respect to a mechanistic link between species X and IO, as was found at atmospheric pressure, the pseudo-first-order decay rate of species X (1.2×10^4 s^{-1}) is a factor of ~ 3 smaller than the pseudo-first-order rate of formation of IO. As previously stated, this may be indicative that the two species are linked by second-order kinetics, or that their apparent absorption profiles are contaminated by multiple absorption. Similarly to at atmospheric pressure, the pseudo-first-order rates of formation and loss of the absorption traces were found to systematically decrease towards longer analysis wavelengths. This phenomenon is displayed in Fig. 4.3-16.

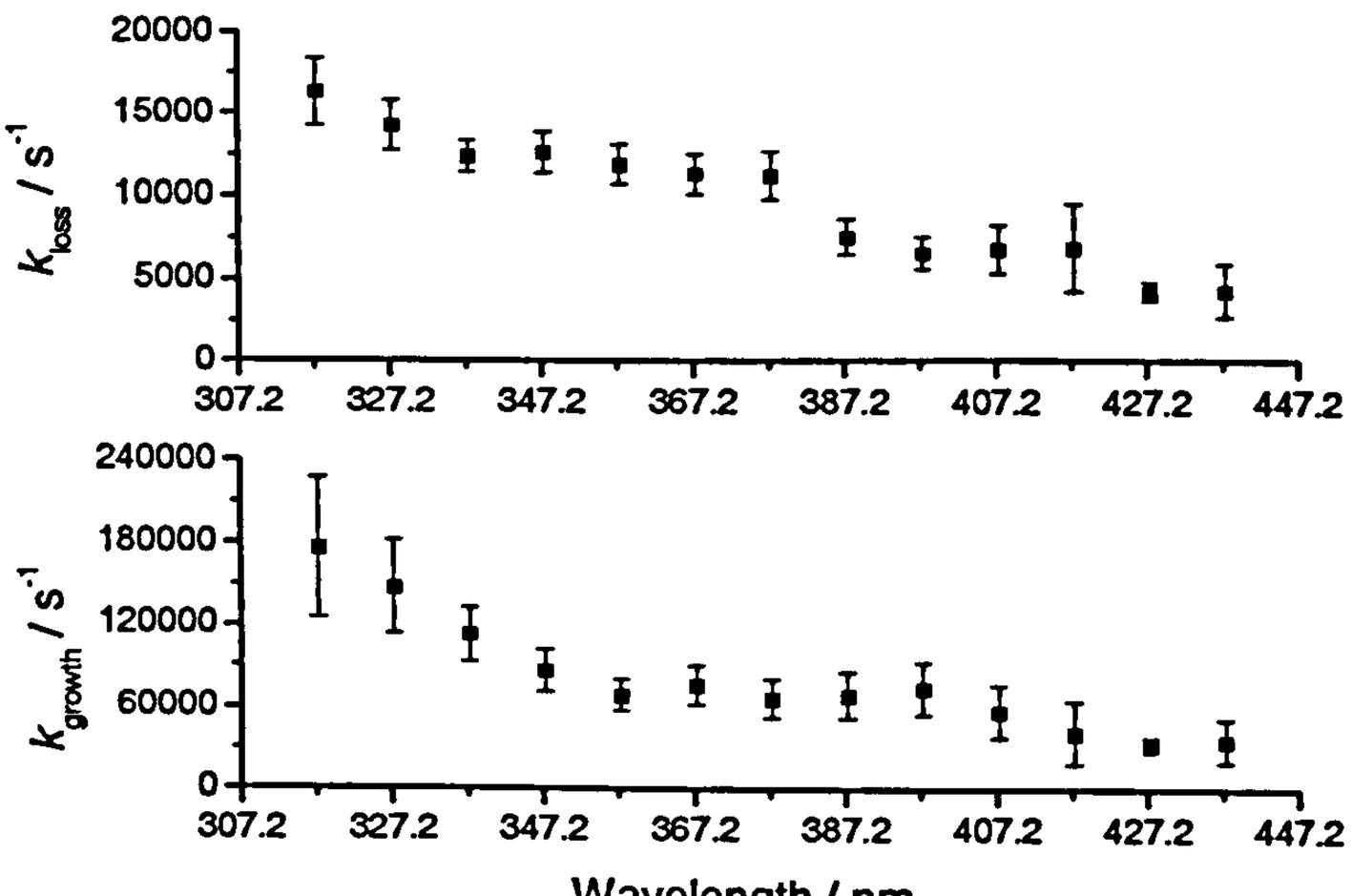

Fig. 4.3-16 – Plot of the pseudo-first-order rates of formation (bottom panel) and loss (top panel) of the absorption traces as a function of analysis wavelength. All rate coefficients were determined from fits of E. 4.3-1 to the experimental data and the error bars are the 2σ standard error returned from the fitting procedure. The experimental conditions were identical for all absorption traces (with the exception of analysis wavelength) and as stated in the caption to the previous figure.

Fig. 4.3-16 clearly indicates the effect of multiple absorption on determining the reaction kinetics of the system. In the absence of distinct spectral features, the presence of multiple absorption from different chemical species means that the true rate of formation of any one absorber cannot be uniquely determined. It is therefore difficult to ascertain whether species X is a direct product of the $CH_2I + O_2$ reaction, or is formed from secondary chemistry within the system. For example, the absorption cross-section of the CH_2I radical, reported by Sehested *et. al.*[13], is of comparable magnitude at wavelengths of 320 nm (1.11×10^{-18} $cm^2molecule^{-1}$) and 360 nm (1.05×10^{-18} $cm^2molecule^{-1}$) but the pseudo-first-order formation rates of the absorption traces (as displayed in Fig. 4.3-16) are different by a factor of nearly three. If the effective bimolecular rate coefficient (with respect to O_2) is determined for the 317.2 nm absorption trace, a value of, $k = 1.7 \times 10^{-12}$ $cm^3molecule^{-1}s^{-1}$ is obtained, comparable to the mass spectrometric determinations of the rate coefficient for the reaction of $CH_2I + O_2$. At 357.2 nm, however, this value is reduced to, $k = 6.6 \times 10^{-13}$ $cm^3molecule^{-1}s^{-1}$. Although IO absorbs weakly at 357.2 nm, it is unlikely that such a difference to the determined kinetics could be solely attributable to IO, and as the absorption cross-section of the CH_2I radical is approximately equal at both wavelengths, this is highly indicative that additional absorbing species are also present in the reaction system.

Considering the complexity of the reaction system and the fact that the formation rate of species X is roughly consistent (to within a factor of two or three) with the expected decay of CH_2I by reaction with O_2, we tentatively assign the mystery absorption to a direct product of the $CH_2I + O_2$ reaction. In consideration of the preceding literature, we consider species X to be either CH_2IO_2 or CH_2O_2 (the co-product to I atoms, as reported in near-unity yield by Eskola *et. al.*[19]).

Fig. 4.3-17 displays the absorption spectrum of the reaction mixture, averaged over a reaction time of 17 – 34 μs, the temporal window where maximum absorption from species X was observed. To calculate the absorption signal, I_{abs}, the initial light intensity, I_0, was taken as the pre-Excimer laser baseline for absorption traces recorded at wavelengths of 357.5 nm and above, and the average of the long-reaction time baseline (500 – 600 μs) for the absorption traces recorded at 347.5 nm and below (due to the absorption of analysis light by CH_2I_2). Contamination of the uncorrected absorption spectrum from IO absorption at 427.2 nm is evident, despite the early reaction times over which the spectrum is averaged. No other distinct spectral features due to IO absorption are present as all other absorption traces were recorded off the peak of IO transitions.

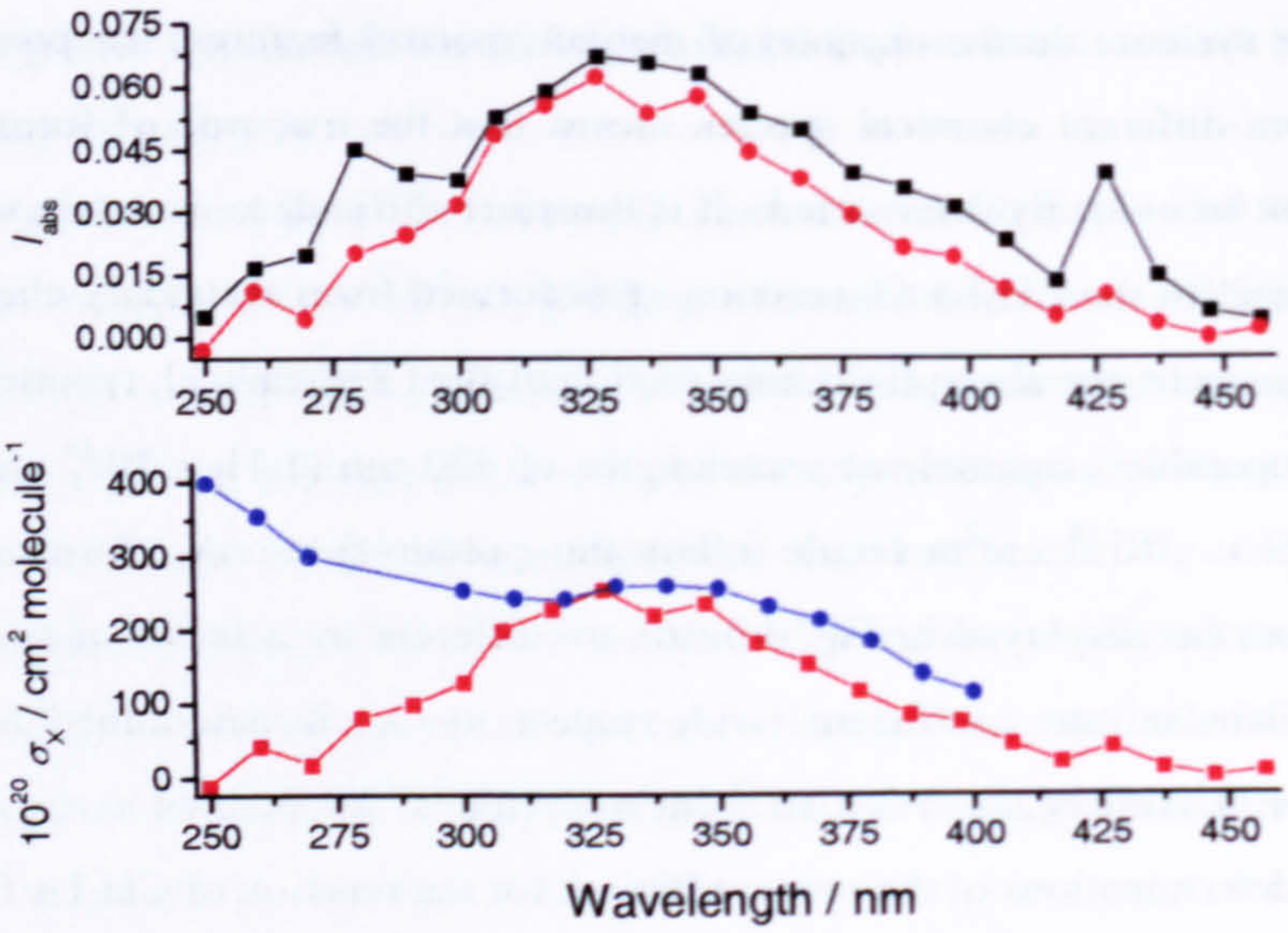

Fig. 4.3-17 – Absorption spectrum of the $CH_2I_2/O_2/N_2$/193 nm reaction mixture averaged between 17 – 34 μs after the photolysis pulse. The top panel shows the uncorrected absorption signal (black) and the absorption spectrum of species X (red), once corrected for absorption by IO and CH_2I (as described in the text). The bottom panel displays the absorption spectrum of species X (red) scaled to the reported absorption spectrum of the CH_2IO_2 radical[13] (blue) so that the peak signals are equal at 330 nm. Experimental conditions are as previously stated.

In order to correct the absorption spectrum for contamination from IO, an absorption spectrum was averaged over the 500 – 600 μs temporal window (where the concentration of species X is zero) between 357.5 – 457.5 nm (IO absorbs only weakly below 360 nm). It was then assumed that the true absorption intensity, I_{abs}, of species X was 0.01 at 427.2 nm in the absorption spectrum shown in Fig. 4.3-17 (black), and that all additional absorption was due to IO. The long-time absorption spectrum was then scaled to this value at 427.2 nm and subtracted from the uncorrected spectrum.

A second peak in the uncorrected absorption spectrum is apparent at a wavelength of 277.5 nm, consistent with the absorption maximum of the CH_2I radical. The entire absorption spectrum (up to 400 nm) was therefore corrected for CH_2I absorption using the absorption cross-sections reported by Sehested *et. al.*[13], and assuming that the true absorption intensity of the species X was 0.02 at 277.5 nm. The corrected absorption spectrum of species X (red) displays broad, unstructured absorption between 250 – 450 nm with a peak at ~ 330 nm.

In the bottom panel of Fig. 4.3-17, the corrected absorption spectrum of species X is scaled to the reported spectrum of CH_2IO_2[13]. Between 310 – 400 nm the scaled spectra are in good agreement, particularly as the absorption spectrum of Sehested *et. al.*[13] was not corrected for absorption by IO (which will have been present in their reaction system). Indeed, over the 310 – 400 nm range the absorption spectrum of Sehested *et. al.*[13] is essentially in perfect

agreement with our uncorrected spectrum. It is concluded therefore that the same species is responsible for the observed absorption between 310 – 400 nm in both studies. At wavelengths below 310 nm, however, the spectra become strongly divergent, which cannot be explained by the presence of the CH_2I radical. A noticeable difference in the work of Sehested *et. al.*[13] was their method of CH_2I generation ($F + CH_3I \rightarrow HF + CH_2I$). It is well known that halogen atoms form stable adducts with the alkyl iodides[31,32], and the CH_3I-Cl adduct has been shown (see Chapter Five) to absorb strongly over the 345 – 375 nm region. It is reasonable to expect the absorption spectrum of CH_3I-F to be significantly blue shifted to that of CH_3I-Cl, and we suspect that the "CH_2IO_2" absorption spectrum of Sehested *et. al.*[13] is contaminated by CH_3I-F absorption between 220 – 310 nm. Indeed, in their paper, Sehested *et. al.*[13] comment that their CH_2IO_2 absorption spectrum is "an unusual peroxy spectrum".

Fig. 4.3-18 displays an absorption trace recorded in this experiment at 290 nm, the peak of the CH_2I_2 absorption spectrum[11]. The absorption signal has been converted into a CH_2I_2 concentration using the absorption cross-section of CH_2I_2 at 290 nm ($\sigma = 3.8 \times 10^{-18}$ $cm^3 molecule^{-1} s^{-1}$)[11] and the negative signal indicates the extent of CH_2I_2 photolysis by the Excimer laser.

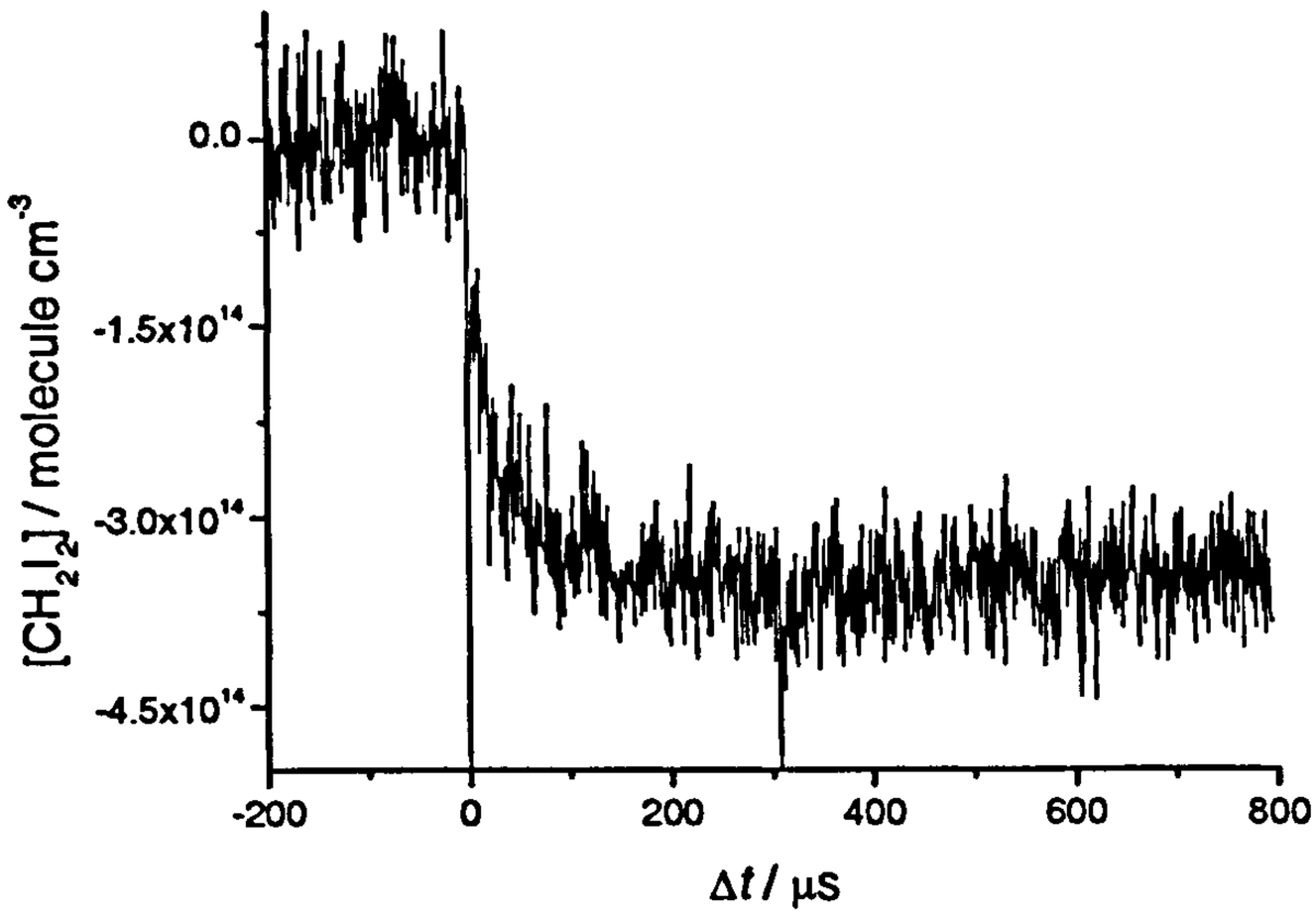

Fig. 4.3-18 – Absorption trace recorded at 290 nm. All experimental conditions are as previously stated. Note that the negative concentration corresponds to the amount of CH_2I_2 photolysed by the Excimer laser. The negative signal is not instantaneous due to absorption of the analysis light by CH_2I and species X at early reaction times.

Averaging the CH_2I_2 concentration over a reaction time of 400 – 800 μs (where it is assumed that no other species are absorbing at 290 nm) it is calculated that $(3.48 \pm 0.61) \times 10^{14}$ molecule cm^{-3} of the initial CH_2I_2 concentration is photolysed by the Excimer laser (corresponding to ~ 30 %). If it is assumed that species X is produced in a 100 % yield from the reaction of $CH_2I + O_2$

(whether directly or not), a lower limit to its absorption cross-section at 327.2 nm can therefore be assigned as, $\sigma_{(327.2\ nm)} = 1.7 \times 10^{-18}$ $cm^2 molecule^{-1}$. This value is consistent with the reported absorption cross-section of CH_2IO_2 at 330 nm ($\sigma = 2.57 \times 10^{-18}$ $cm^2 molecule^{-1}$)[13]. (Note that the extent of CH_2I_2 photolysis places a lower limit to the yield of IO, originating from CH_2I, of ~ 4 %, much less than that suggested by Enami *et. al.*[12] and estimated in section 4.3.2). Fig. 4.3-19 displays the absorption spectrum of species X determined in this study, along with the known absorption spectra of the CH_2ClO_2[33] and CH_2BrO_2[16] peroxy species.

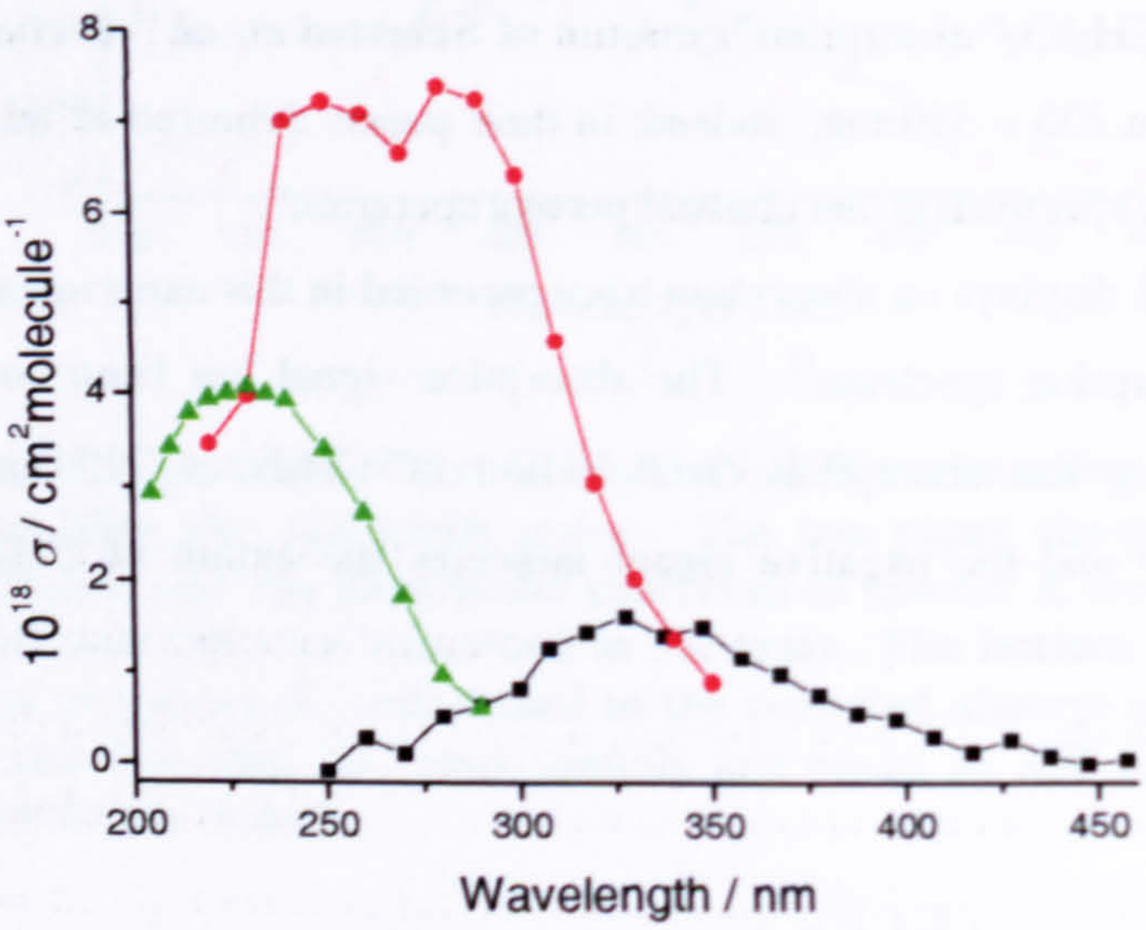

Fig. 4.3-19 – Ultraviolet absorption spectra of the CH_2ClO_2[33] (green) and CH_2BrO_2[16] (red) peroxy species, and species X (black) as determined in this study. Note that the absorption intensity of species X has been converted to an absorption cross-section by normalisation to the lower limit estimated at 327.2 nm (1.7×10^{-18} $cm^2 molecule^{-1}$). The estimated absorption cross-sections of species X are tabulated in Appendix III.

The absorption spectrum of species X determined in this work is of similar spectral structure to those of the CH_2ClO_2 and CH_2BrO_2 peroxy radicals. Further, the peak of the absorption spectrum is significantly red-shifted, consistent with the presence of a large, electron-rich, iodine atom (note that the absorption maxima of CH_2BrO_2 is similarly red-shifted to that of CH_2ClO_2). It is considered unlikely that the absorption spectrum determined in this work belongs to any isomeric form of CH_2O_2. The electronic absorption spectrum of formic acid (HCOOH) does not extend beyond ~ 260 nm[34]. Further, HCOOH is a stable molecule and highly active in the infra-red. Formic acid was not reported in the FTIR study of Cotter *et. al.*[15] or in the MS investigation of Eskola *et. al.*[19]. Other isomeric forms of CH_2O_2 include formaldehyde carbonyl oxide (H_2COO) and dioxirane (H_2CO_2), in which the C and O atoms form a three-membered ring. Formaldehyde carbonyl oxide is highly unstable and largely isomerises to dioxirane[35]. In turn, dioxirane is also unstable at room temperature[36] and decomposes to formic acid, HCO, OH, CO_2, H_2, CO and H_2O[37]. No decomposition products of

dioxirane were reported in the studies of Cotter *et. al.*[15] or Eskola *et. al.*[19]. However, it is worth mentioning that the theoretical study of Aplincourt *et. al.*[35] predicted an electronic transition for formaldehyde carbonyl oxide at a wavelength of either 334 nm or 435 nm (depending on the level of theory used).

In conclusion, we consider it very likely that the absorption spectrum of species X is attributable to the CH_2IO_2 peroxy species. However, the reaction kinetics of species X were found to be inconsistent with those expected for a product formed directly in the reaction, $CH_2I + O_2 \rightarrow$ products. The observed discrepancies are attributed to second-order chemistry and interference from the absorption of multiple species within the reaction system. Species X is also considered to be a direct precursor to IO formation in the reaction system. These ideas are explored further in subsequent sections of this chapter.

4.3.2.4 Discussion

The photolysis of CH_2I_2 in the presence of O_2 has been investigated at 248 nm and 193 nm by absorption spectroscopy, revealing important information with regards to the reaction $CH_2I + O_2 \rightarrow$ products. First, and foremost, that IO is not formed as a direct reaction product, in direct contrast to the findings of two recent studies[12,19]. This conclusion could be drawn from the significant $[CH_2I_2]$ dependence to the rate of formation of IO ($k = (3.7 \pm 0.5) \times 10^{-11}$ $cm^3molecule^{-1}s^{-1}$) in a large excess of O_2. It has also been definitively proved that IO is not formed by the reaction $O + CH_2I_2$ (initiated by the multi-photon dissociation of CH_2I_2) in the reaction mixture. However, a lower limit of 0.3 for the branching ratio of IO formation in the reaction $O + CH_2I_2 \rightarrow$ products has been determined. In disagreement with the findings of Enami *et. al.*[12] the yield of IO produced from CH_2I (generated by photolysis) was found to be much less than unity and in the range of 4 – 40 %. The yield of IO may be pressure dependent, although its reaction kinetics are not. Upon the addition of Br_2 to the reaction system, the production of BrO was observed with a similar temporal profile to IO – indicative that both species are formed from a common precursor, and by similar reaction mechanisms.

The second significant finding of this study was the broad absorption of an unknown species, "X", between 250 – 450 nm in the reaction mixture. The absorption maximum of X occurred at 327.2 nm, for which a lower limit to its absorption cross-section, $\sigma = 1.7 \times 10^{-18}$ $cm^2molecule^{-1}$ has been determined. By comparison of the absorption spectrum obtained (once corrected for absorption by IO and CH_2I) with the known spectra of CH_2ClO_2 and CH_2BrO_2, it is considered that species X is most probably the CH_2IO_2 peroxy radical. The reaction kinetics of absorber X were found to be independent of pressure but complicated by absorption by CH_2I and IO (and possibly other species) and probably second-order processes (that were not considered in the data analysis). Consequently, species X cannot unambiguously be identified

as CH_2IO_2. As a result of the anti-correlation between the temporal profiles of species X and IO, it is considered that X is the direct precursor to IO in the reaction system.

It must be emphasised that the results presented in this study of $CH_2I_2/O_2/N_2/h\nu$ reaction mixtures by absorption spectroscopy should be interpreted at a semi-quantitative level only, for several important reasons. First, that the extent of CH_2I_2 photolysis was very large (20 – 30 %) resulting in high and non-uniform radical concentrations. Secondly, that the data was contaminated from the absorption of multiple species; and thirdly that the chemical reactions occurring within the reaction system are not well defined and probably involve a mixture of first- and second-order processes that may have resulted in recycling of the monitored species.

4.4 Laser Induced Fluorescence Study of $CH_2I_2/O_2/h\nu$ Reaction Mixtures

In order to gain a more quantitative understanding of processes occurring within the $CH_2I_2/O_2/h\nu$ reaction system an LIF investigation was performed. As shown in Chapter Three, LIF is a sensitive detection method for IO and is therefore a useful tool for studying its reaction kinetics under conditions where effects from radical-radical chemistry and interference from the IO self-reaction are negligible. In addition, LIF is more specific than absorption spectroscopy as many absorbing species will not fluoresce. Although many LIF experiments were performed in the course of this work, only the most pertinent and relevant findings are reported in order to prevent this chapter becoming too exhaustive to read.

4.4.1 LIF Study of the IO Radical

In this study, the LIF detection of IO was achieved with a similar apparatus used for the quenching experiments described in Chapter Three. Diiodomethane was purified on a gas handling line and diluted and stored in a glass bulb, which was blackened to prevent the photolysis of CH_2I_2 by room light. All concentrations within the reaction cell were calculated from the calibrated mass flow rates of the reagents and the total reaction cell pressure. Fig. 3.5-14 shows a LIF spectrum of the (2,0) band of the $A^2\Pi_{3/2} \leftarrow X^2\Pi_{3/2}$ system of IO obtained in a photolysis mixture of $CH_2I_2/O_2/N_2$. Fig. 4.4-1 displays "on-line" and "off-line" kinetic traces recorded in a $CH_2I_2/O_2/N_2/248$ nm reaction mixture, confirming the presence of IO.

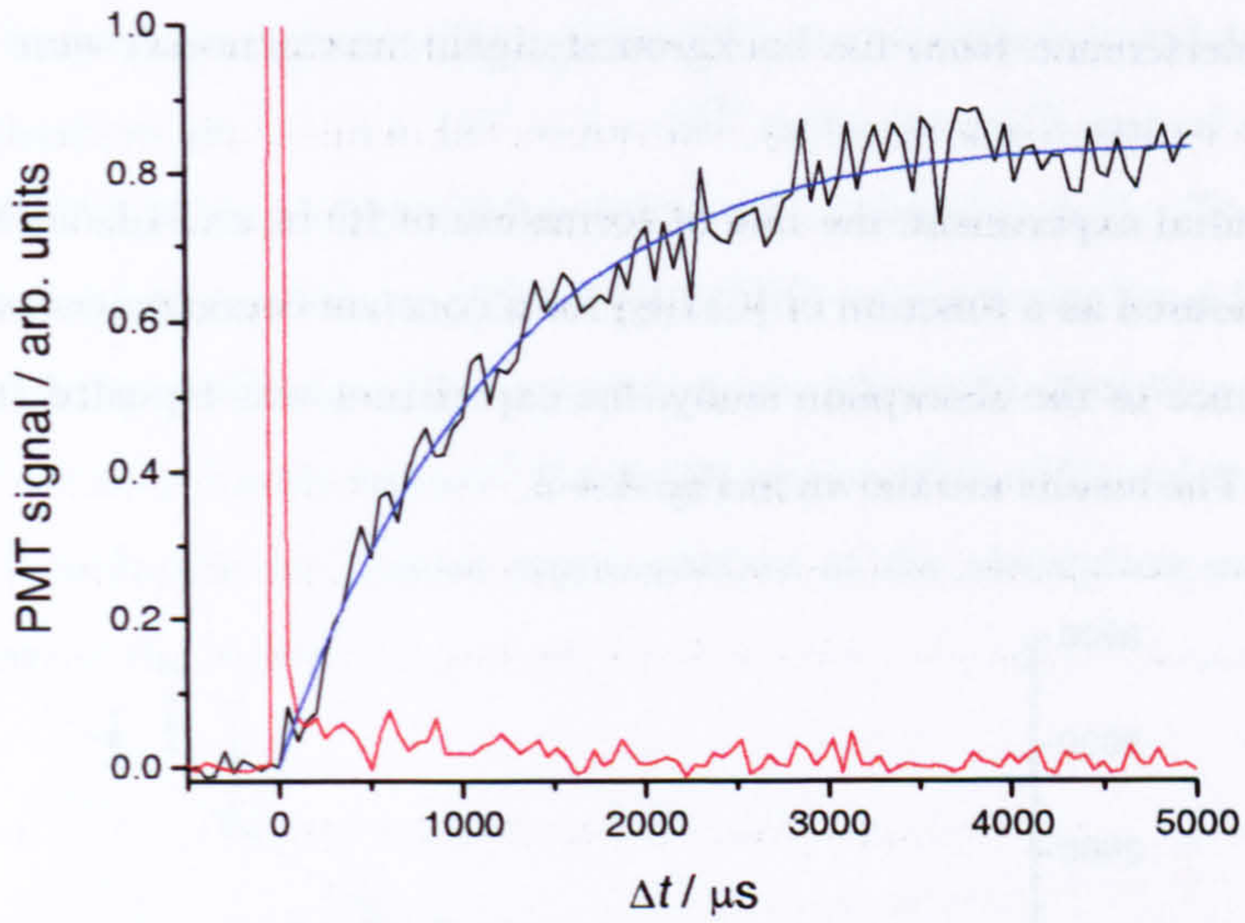

Fig. 4.4-1 – Kinetic traces recorded in a $CH_2I_2/O_2/N_2$/248 nm reaction mixture by LIF, confirming the presence of IO. Experimental conditions: P = 30 Torr; T = 296 K; $[CH_2I_2]$ = 1.63×10^{14} molecule cm^{-3}; $[O_2]$ = 6.15×10^{14} molecule cm^{-3}; $[N_2]$ = balance; λ_{pr} = 444.89 nm (black) and 444.70 nm (red); P_{pr} = 0.8 mJ $pulse^{-1}$; P_{ex} = 20 mJ $pulse^{-1}$; PRF = 2 Hz. The black data points represent the temporal profile of IO, excited at the peak of (2,0) bandhead, and the red data points are an off-line kinetic trace recorded at an excitation wavelength (444.70 nm) where IO does not absorb. The solid blue line is a fit of E. 4.3-1 to the on-line trace. From the fit, k_{IO}' = (800 ± 52) s^{-1} and k_{loss} is fixed to a value of 10 s^{-1}, determined independently from a kinetic trace extending to larger values of Δt.

Kinetic traces were only recorded over a range of values of Δt where the production of IO was observed as the aim of this study was to deduce its mechanism of formation in the reaction system. However, from kinetic traces extending to longer reaction times, the removal rate of IO was found to be very small (typically 10 - 30 s^{-1}) and consistent with a low concentration of IO ($<< 10^{12}$ molecule cm^{-3}). Interference from the self-reaction of IO to the analysis of the kinetic traces will therefore have been negligible. In the off-line kinetic trace displayed in Fig. 4.4-1, a very large PMT signal is observed at $\Delta t = 0$ (note that this was also the case for the on-line trace) and the post-Excimer laser signal does not fully recover to the pre-Excimer laser background. It is well known that I_2 exhibits intense fluorescence, which extends over a wide range of the visible part of the spectrum, after Excimer laser excitation at 193 nm. In fact, this fluorescence is so intense that it can be observed as a blue/green flash by the naked eye (illustrating the non-negligible timescale of fluorescence). In these experiments, a red flash was observed by eye when the reaction cell was irradiated with a pulse of 248 nm Excimer laser radiation. CH_2I_2 has many excited states[27] and transitions arising from their population will be numerous and complex. The spurious off-line signal is therefore attributed to fluorescence from CH_2I_2 (and possibly I_2) induced by the absorption of 248 nm Excimer laser radiation. However, as this background signal was always much weaker than fluorescence from IO, off-line traces

were not recorded under all experimental conditions and the first few points of the IO kinetic traces (where interference from the background signal was greatest) were discarded prior to their analysis.

As an initial experiment, the rate of formation of IO in a $CH_2I_2/O_2/N_2$/248 nm reaction mixture was measured as a function of $[CH_2I_2]$ for a constant concentration of O_2. However, in a notable difference to the absorption study, the experiment was repeated for two different O_2 concentrations. The results are shown in Fig. 4.4-2.

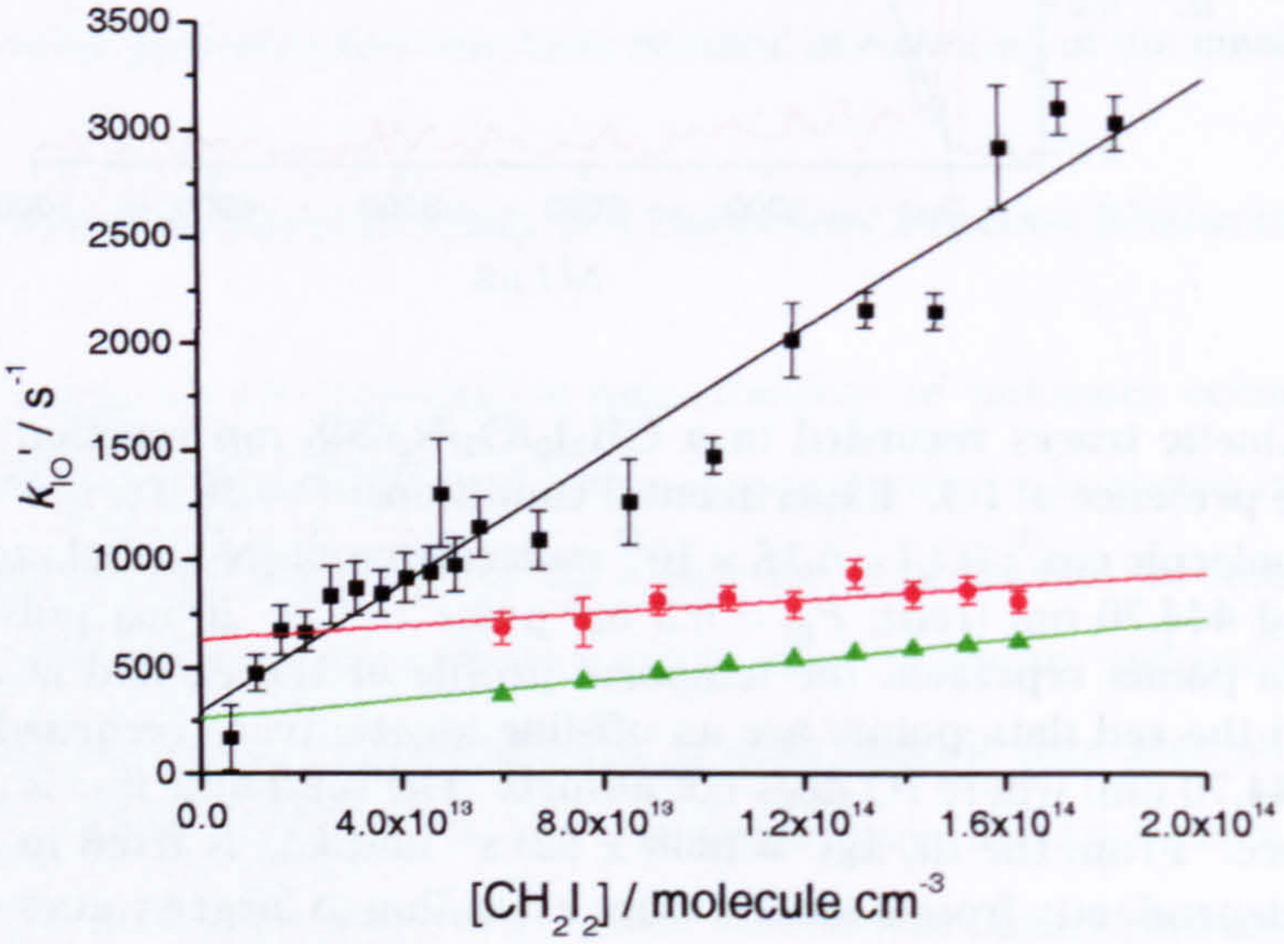

Fig. 4.4-2 – Bimolecular plots displaying the rate of formation of IO as a function of $[CH_2I_2]$ in a $CH_2I_2/O_2/N_2$/248 nm reaction mixture for different experimental O_2 concentrations. Experimental conditions: P = 30 Torr (black and red) and 100 Torr (black); T = 296 K; $[O_2]$ = 2.5 ×10^{16} molecule cm^{-3} (black) and 6.2 ×10^{14} molecule cm^{-3} (red); $[N_2]$ = balance. All other experimental conditions are as previously stated. The green data points are model simulations of the experiment performed with the lower O_2 concentration, as described in the text. Error bars are 2σ standard error returned from fits of E. 4.3-1 to the experimental data. From the linear fits, k ($cm^3 molecule^{-1} s^{-1}$) = (1.46 ± 0.17) × 10^{-11} (black), (1.47 ± 1.36) × 10^{-12} (red) and (2.28 ± 0.35) × 10^{-12} (green).

In the experiment containing the higher O_2 concentration ($[O_2] = 2.5 \times 10^{16}$ molecule cm^{-3}), the rate of formation of IO was found to be strongly dependent on $[CH_2I_2]$ in agreement with the findings of the absorption experiment (note that the smaller value of, $k = (1.46 \pm 0.17) \times 10^{-11}$ $cm^3 molecule^{-1} s^{-1}$ determined by LIF is of minor significance and is discussed further in section 4.4.2). The experiment was repeated at total pressures of 30 and 100 Torr and no apparent change to the $[CH_2I_2]$ dependence of the rate of formation of IO was observed. All data points obtained are displayed in the same bimolecular plot in Fig. 4.4-2 (black data points).

When the O_2 concentration was reduced, however, an interesting result was observed: the $[CH_2I_2]$ dependence to the rate of formation of IO was greatly reduced. This finding becomes more significant when the results of Enami *et. al.*[12] are considered. In their experiment

the rate of formation of IO was not observed to depend on $[CH_2I_2]$, when the concentration of CH_2I_2 was varied by a factor of three (although the O_2 concentration is not stated). The range of $[O_2]$ studied by Enami *et. al.*[12] (~ $1 \times 10^{14} - 3 \times 10^{15}$ molecule cm^{-3}) was of the same order of magnitude as that used in this study ($[O_2] = 6.2 \times 10^{14}$ molecule cm^{-3}). To investigate these observations more thoroughly, the rate of formation of IO was measured as a function of $[O_2]$ at a constant concentration of CH_2I_2. The experiment was executed over two distinct ranges of $[O_2]$: i) ~ $2 \times 10^{14} - 3 \times 10^{15}$ molecule cm^{-3} (a similar range to that of Enami *et. al.*[12]); and ii) ~ $1 \times 10^{16} - 1 \times 10^{17}$ molecule cm^{-3} (more representative of the absorption experiments). The results are displayed in Fig. 4.4-3.

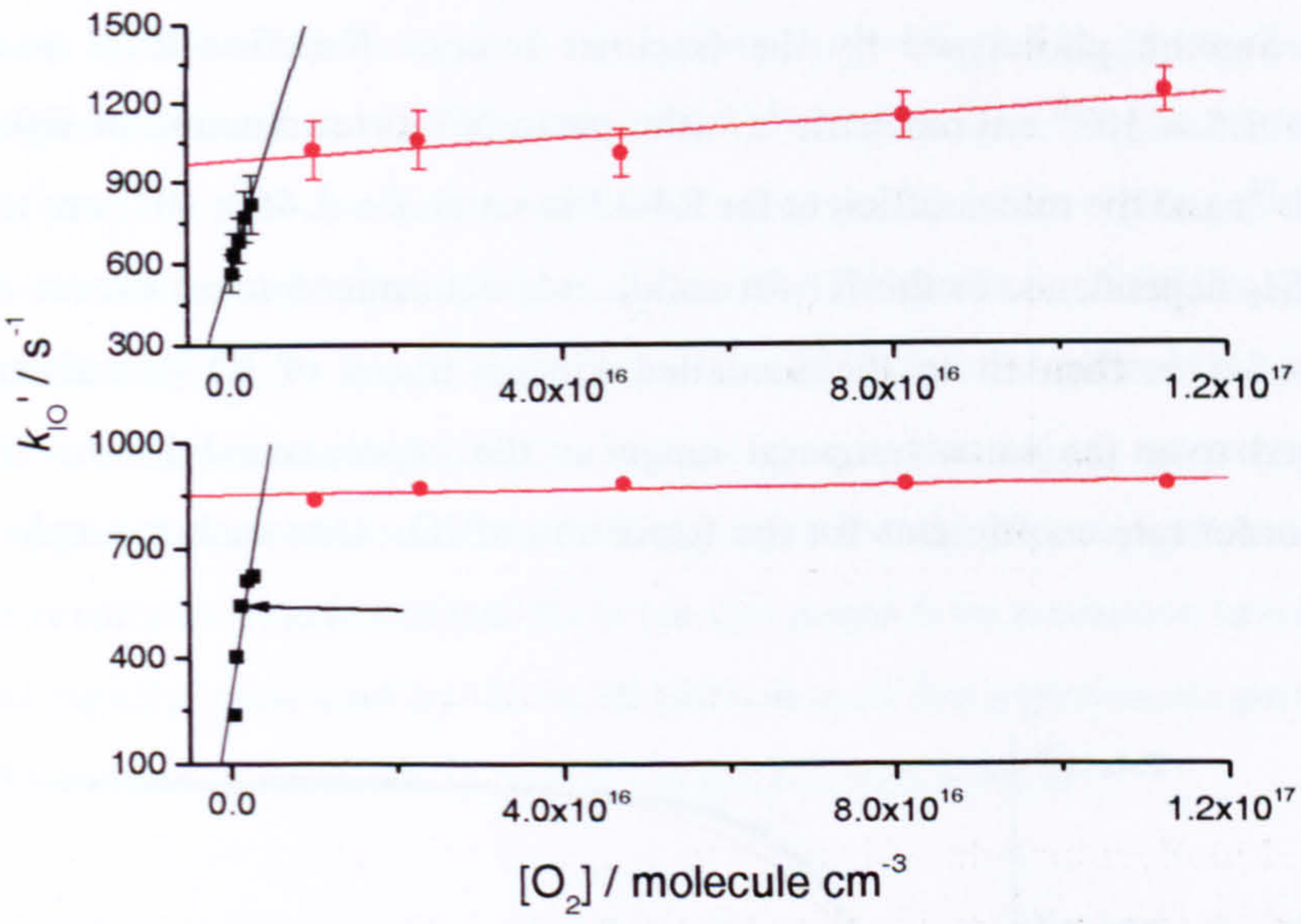

Fig. 4.4-3 – Dependence of the rate of formation of IO on $[O_2]$ in $CH_2I_2/O_2/N_2$/248 nm reaction mixtures. Experimental conditions: P = 30 Torr; T = 296 K; $[CH_2I_2] = 6 \times 10^{13}$ molecule cm^{-3}. All other experimental conditions are as previously stated. The top panel displays the experimental data and the bottom panel displays model simulations described in the text. From the linear fits to the data, k ($cm^3 molecule^{-1} s^{-1}$) = $(1.0 \pm 0.3) \times 10^{-13}$ (black, experiment) and $(1.4 \pm 0.2) \times 10^{-13}$ (black, model); and $(2.2 \pm 1.8) \times 10^{-15}$ (red, experiment) and $(3.7 \pm 5.5) \times 10^{-16}$ (red, model).

For the experiment conducted at higher $[O_2]$, very little dependence of the rate of formation of IO is observed, $k = (2.2 \pm 1.8) \times 10^{-15}$ $cm^3 molecule^{-1} s^{-1}$. However, in the experiment employing lower concentrations of O_2, a much enhanced dependence to the rate of formation of IO on $[O_2]$ was found ($k = (1.0 \pm 0.3) \times 10^{-13}$ $cm^3 molecule^{-1} s^{-1}$), approaching that determined by Enami *et. al.*[12] ($k = (4.0 \pm 0.4) \times 10^{-13}$ $cm^3 molecule^{-1} s^{-1}$). The intuitive inference is that a product of the reaction of $CH_2I + O_2$ is reacting with another species within the system (that is in someway related to the concentration of CH_2I_2), generating IO:

$$CH_2I + O_2 \rightarrow X \qquad \text{(R4-2)}$$

$$X + CH_2I_2 \rightarrow IO \qquad \text{(R4-13)}$$

Thus at low $[O_2]$, reaction R4-2 is rate determining, whereas R4-13 determines the overall reaction kinetics of IO at higher concentrations of O_2. Note that reaction R4-13 does not necessarily involve diiodomethane directly (but some species whose concentration is directly proportional to that of CH_2I_2). In an attempt to explain the experimental results *via* this mechanism, a simple model was created in FACSIMILE. The model consists of reactions R4-2 and R4-13 and initial conditions of $[CH_2I_2]_0$, $[CH_2I]_0$ and $[O_2]_0$. The initial concentrations of CH_2I_2 and O_2 are set to the experimental values, and $[CH_2I]_0$ is set as 4 % of $[CH_2I_2]_0$ (the approximate amount photolysed by the Excimer laser). Reaction R4-2 is assigned a rate coefficient of 1.5×10^{-12} $cm^3 molecule^{-1} s^{-1}$ (the mean MS determination of Eskola *et. al.*[19] and Masaki *et. al.*[14]) and the rate coefficient for R4-13 is set at, $k = 1.46 \times 10^{-11}$ $cm^3 molecule^{-1} s^{-1}$ (the effective CH_2I_2 dependence to the IO formation rate determined in an excess of O_2 – see Fig. 4.4-2). E. 4.3-1 is then fit to the modelled kinetic traces of IO (simulated for the same conditions and over the same temporal range as the experimental kinetic traces) to return pseudo-first-order rate coefficients for the formation of IO. One such example is given in Fig. 4.4-4.

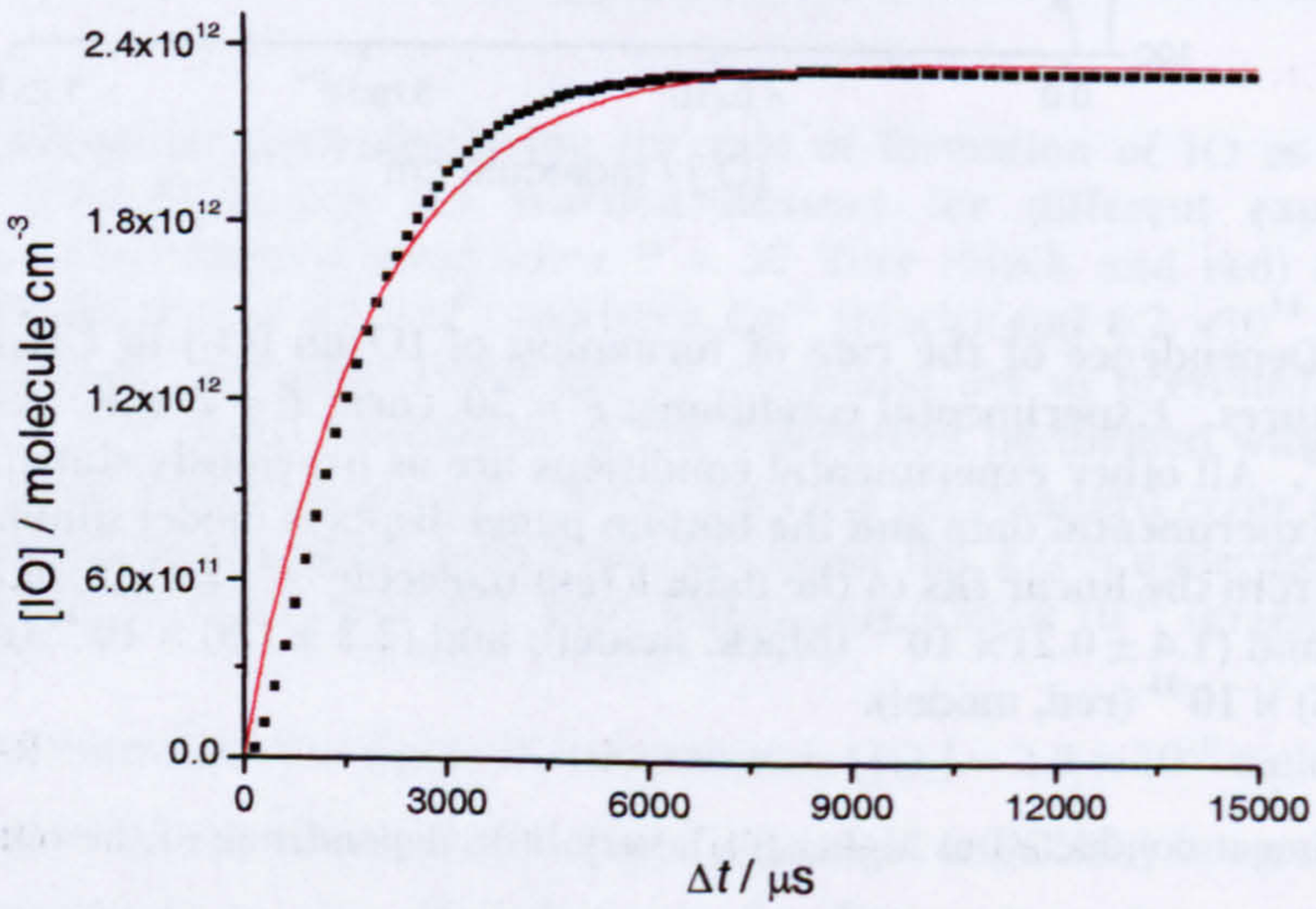

Fig. 4.4-4 – Simulated kinetic trace of IO by the FACSIMILE model described in the text (black squares). The initial parameters, $[O_2]_0$, $[CH_2I_2]_0$ and $[CH_2I]_0$ were (molecule cm^{-3}) 1.17×10^{15}, 5.81×10^{13} and 2.32×10^{12} respectively. The solid red line is a fit of E. 4.3-1 to the modelled kinetic trace. From the fit, $k_{IO}' = (543 \pm 24)$ s^{-1}. The data point generated from this simulation is represented by the arrow in Fig. 4.4-3. Note that the simulated kinetic trace is not exponential in nature. The experimental traces did not display a deviation from exponential form as pronounced as that shown here (see Fig. 4.4-1) although the interference from the spurious signal, tentatively assigned to CH_2I_2 fluorescence, meant that the true temporal behaviour of IO could not be observed at early reaction times.

From Fig. 4.4-3 it can be seen that the experimental and model results are in reasonably good agreement, particularly as the model only consists of two reactive processes and the chemistry occurring in the experimental system will be far more complex. The same model was used to generate pseudo-first-order formation rates of IO for the experiment displayed in Fig. 4.4-2, where $[CH_2I_2]$ was varied at a relatively low, constant concentration of O_2. Again, the model results ($k = (2.3 \pm 0.4) \times 10^{-12}$ $cm^3 molecule^{-1} s^{-1}$) are in reasonable agreement with experiment ($k = (1.5 \pm 1.4) \times 10^{-12}$ $cm^3 molecule^{-1} s^{-1}$), illustrating the reduced dependence to the rate of formation of IO on $[CH_2I_2]$ at low O_2 concentrations. Therefore, it would appear that we have arrived at a mechanism which can largely explain the results of Enami *et. al.*[12] and the work reported in this chapter thus far.

The focus of research now turns to two questions: i) what is the predominant product of reaction R4-2, species X; and ii) what species, which is connected to the concentration of CH_2I_2, reacts with X to produce IO? In relation to the first question, a review of the previous literature, and the results obtained in this work so far, indicate that the products of the reaction $CH_2I + O_2 \rightarrow$ products are either $CH_2O_2 + I$, or CH_2IO_2 (note that CH_2IO_2 is considered more likely due its possible detection in the absorption study). With respect to the second question, three species within the reaction system are a function of $[CH_2I_2]$ (with the obvious exception of itself): CH_2I, I and X. It can readily be concluded that IO is not generated from a reaction involving CH_2I, as this radical was rapidly consumed by O_2 in all but a few of the experiments performed in this study. Thus, the following reactions may occur in the reaction system

$$CH_2O_2 + CH_2O_2 \rightarrow 2\,CH_2O + O_2 \quad \text{(R4-14)}$$

$$CH_2O_2 + CH_2I_2 \rightarrow IO + CH_2O + CH_2I \quad \text{(R4-15)}$$

$$CH_2O_2 + I \rightarrow IO + CH_2O \quad \text{(R4-16)}$$

$$CH_2IO_2 + CH_2IO_2 \rightarrow 2\,CH_2IO + O_2 \quad \text{(R4-4a)}$$

$$CH_2IO_2 + CH_2I_2 \rightarrow IO + CH_2IO + CH_2I \quad \text{(R4-17)}$$

$$CH_2IO_2 + I \rightarrow IO + CH_2IO \quad \text{(R4-18)}$$

$$CH_2IO \rightarrow CH_2O + I \quad \text{(R4-5)}$$

Of the reactions identified above, only the processes involving CH_2I_2 or I may be expected to generate IO. It is considered unlikely that the reactions involving CH_2I_2 will be thermodynamically favourable, due to the relatively high enthalpy of formation of CH_2I (~ 230 kJ mol^{-1})[23], and it is therefore concluded that IO is probably produced by reaction R4-16 or R4-18. To investigate this hypothesis the dependence of the rate of formation of IO on photolysis energy should be determined. As I is a photolytic product of CH_2I_2, the concentration of I will

increase with photolysis energy (for a constant concentration of CH_2I_2) as would the rate of formation of IO, if the suggested reactions are responsible for its formation. Note that, assuming 100 % conversion of CH_2I to CH_2O_2 or CH_2IO_2, the postulated reactions are second-order processes. It was attempted to determine the rate of formation of IO as a function of Excimer laser power, which could only be varied by a factor of two. Although the rate of formation of IO was observed to increase with photolysis photon flux, suggesting the involvement of I atoms in its formation, an insufficient number of data points were collected over the narrow Excimer power range studied to allow a quantitative interpretation of the results.

As both of the postulated mechanisms to IO formation involve the concomitant formation of CH_2O (note that CH_2IO is expected to decompose to CH_2O + I, R4-5) our attention was directed towards an LIF study of formaldehyde.

4.4.2 LIF study of CH_2O

As the results presented in this section represent the first experimental investigation of formaldehyde in this thesis, pertinent details of the experimental apparatus are discussed here. Formaldehyde has a structured UV absorption spectrum in the 250 – 360 nm spectral window originating from vibronic transitions of the $\tilde{A}^1A_2-\tilde{X}^1A_1$ band system, an $n \rightarrow \pi^*$ electronic transition in the C-O bond[38]. As the pure electronic transition is forbidden by electric dipole selection rules, a concomitant vibrational transition must occur to allow sufficient intensity. The 4_0^1 vibrational band of this system, centred at ~ 353 nm, is well known to exhibit intense fluorescence and has been extensively exploited as a diagnostic tool for CH_2O in combustion chemistry[39]. The vibrational transition of the $\tilde{A}^1A_2-\tilde{X}^1A_1 4_0^1$ band corresponds to a $1 \leftarrow 0$ excitation of the out-of-plane bending mode, ν_4. Fluorescence from this transition extends to a wavelength of ~ 600 nm[40] and has a natural radiative lifetime of the order of 70 ns[41]. In this study, CH_2O was detected by LIF of the $\tilde{A}^1A_2-\tilde{X}^1A_1 4_0^1$ band at an excitation wavelength of ~ 353.16 nm, near the band origin.

Excitation radiation was generated by an Excimer pumped Dye laser system. Approximately 50 mJ pulse^{-1} of 308 nm radiation (generated by a XeCl Excimer laser) was directed into a Dye laser operating on DMQ dye. The emission range of DMQ dye is ~ 340 – 375 nm and at 353.16 nm, approximately 3 mJ pulse^{-1} of excitation energy could be generated. The lasing wavelength of the Dye laser was manually selected at the laser control panel and could be scanned at constant speed over a programmed wavelength range. Radiation from the Dye laser was aligned through the reaction cell *via* a series of aluminium laser mirrors and terminated at a beam dump located at the rear cell window. A photolysis laser pulse of 248 nm,

generated by a KrF Excimer laser, was passed through the reaction cell, orthogonal to the excitation laser beam, and terminated at a beam dump. An iris, situated at the front cell window was used to shape the Excimer laser beam to a circular profile of ~ 7 mm diameter. The Excimer laser power was measured intermittently with a power meter, which was interchanged with the beam dump at the rear cell window. At full power, approximately 60 mJ pulse^{-1} of 248 nm radiation was measured at the rear cell window. The photolysis radiation could be attenuated to powers as low as 3 mJ pulse^{-1} *via* a combination of reducing the operating voltage of the Excimer laser and by placing a series of fine mesh metal gauzes over the Excimer laser output. The reaction cell was a stainless steel vessel consisting of a six-way cross of cylindrical arms and ~ 500 cm^3 in volume. The main bulk of the reaction cell was encased in an insulated steel cube, which could be filled with a cooling agent, allowing experiments to be conducted below room temperature. The two horizontal cell axes were used as the laser axes, and fluorescence from CH_2O was detected at the top port of the vertical cell axis by a PMT surrounded by black cloth in order to minimise the detection of room light. All ports on the horizontal cell axes, and the fluorescence detection port, were covered with 50 mm diameter silica windows and sealed by o-rings. A Perspex interference filter (~ 3 cm thick) was placed prior to the PMT, in order to discriminate laser light from CH_2O fluorescence. The analogue signal from the PMT was sent to an oscilloscope and gated integrator and boxcar averager, before being digitised and stored on a control PC. The bottom port on the vertical cell axis was connected to a pumping system and the cell pressure (measured by a 0 – 1000 Torr capacitance manometer) was regulated by means of the total gas flow rate through the reaction vessel and throttling of the pumping system. Reagent gas mixtures were prepared on a gas handling line and introduced into the reaction cell *via* ¼ " stainless steel swagelock tubing. All reagent concentrations were calculated from the gas flow rates, dilution factors and total reaction cell pressure and temperature. The KrF and XeCl Excimer lasers were triggered by a delay generator operating under computer control, allowing the time interval between photolysis and probe lasers, Δt, to be varied to obtain kinetic data. The oscilloscope and boxcar averager were also triggered by the delay generator, at the same time as the XeCl (probe) laser.

As a reference, CH_2O was generated from the reaction of Cl atoms with methanol (MeOH or CH_3OH) in the presence of O_2. Chlorine atoms were produced by the 248 nm photolysis of thionyl chloride (Cl_2SO). The reaction sequence is given below, and a LIF excitation spectrum of the most intense region of the $\tilde{A}^1A_2-\tilde{X}^1A_1 4_0^1$ system of CH_2O is displayed in Fig. 4.4-5.

$$Cl_2SO + 248\ nm \rightarrow Cl + ClSO \qquad \text{(R4-19)}$$

$$Cl + CH_3OH \rightarrow HCl + CH_2OH \qquad \text{(R4-20)}$$

$$CH_2OH + O_2 \rightarrow CH_2O + HO_2 \qquad \text{(R4-21)}$$

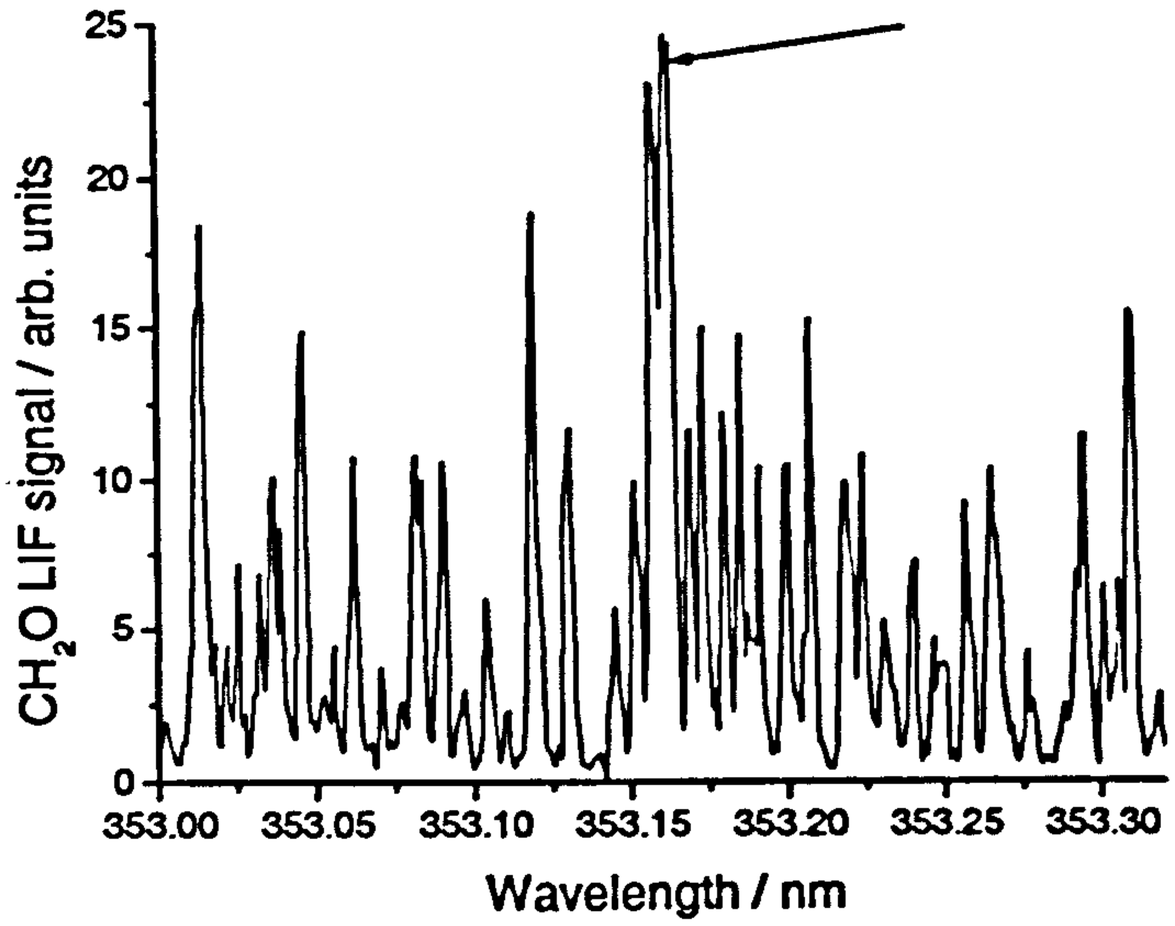

Fig. 4.4-5 – LIF spectrum of part of the $\tilde{A}^1A_2 - \tilde{X}^1A_1 4_0^1$ system of CH_2O. Experimental conditions: P = 100 Torr; T = 296 K; [Cl_2SO] = 1×10^{13} molecule cm^{-3}; [MeOH] = 1.2×10^{14} molecule cm^{-3}; [O_2] = 1.6×10^{16} molecule cm^{-3}; [N_2] = balance; F = 6.1×10^{16} photons cm^{-2}; Δt = 500 μs; PRF = 10 Hz. Note that the rotational line at 353.16 nm, indicated by the arrow, was used for all kinetic measurements of CH_2O reported in this section and corresponds to a blend of rotational transitions, predominantly in the $^rQ_3$ sub-band of the system[42].

It was found that the Perspex interference filter did not completely discriminate detection of probe laser radiation by the PMT, but as fluorescence from CH_2O was generally more intense and of longer lifetime than the laser pulse, the LIF detection of CH_2O was relatively unhindered. The fluorescence collection gate, set by the boxcar averager, was thus placed over the entire temporal span of the laser pulse and CH_2O fluorescence. Taking into account the significant probe laser background, the detection limit of the apparatus was estimated as 1×10^{11} molecule cm^{-3} (CH_2O) for no averaging of the fluorescence signal. Fig. 4.4-6 displays the signal output from the PMT, as recorded by the oscilloscope, in the presence and absence of Excimer laser radiation (and therefore CH_2O).

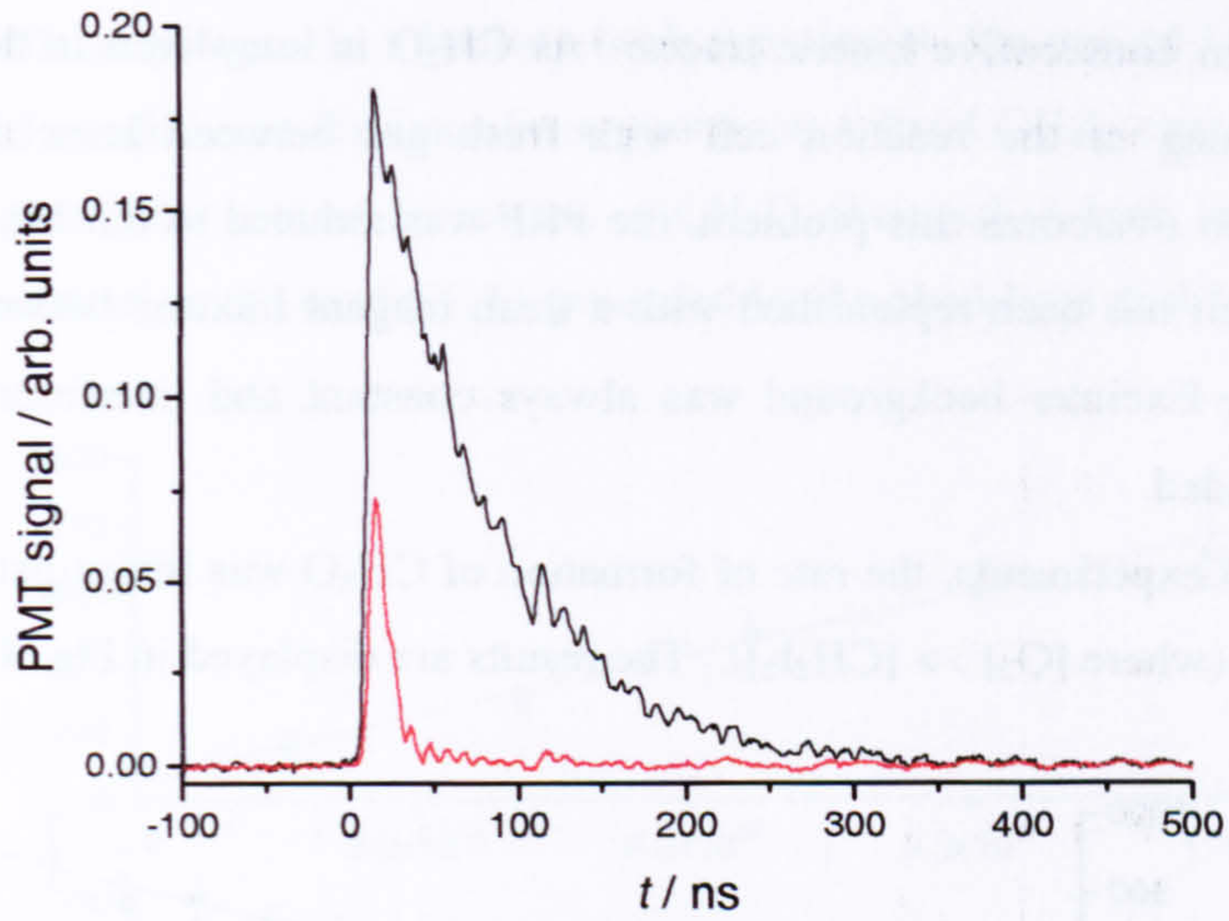

Fig. 4.4-6 – PMT signal in the presence (black) and absence (red) of Excimer laser radiation (and hence CH_2O) recorded by the oscilloscope. Experimental conditions are the same as given in the previous figure caption and the signal was averaged over 10 laser shots.

To investigate whether CH_2O is formed by the photolysis of diiodomethane in the presence of O_2, a reagent mixture of $CH_2I_2/O_2/N_2$ was introduced into the reaction cell and photolysed at 248 nm. LIF from CH_2O was readily observed and a kinetic trace displaying the formation of formaldehyde is displayed in Fig. 4.4-7.

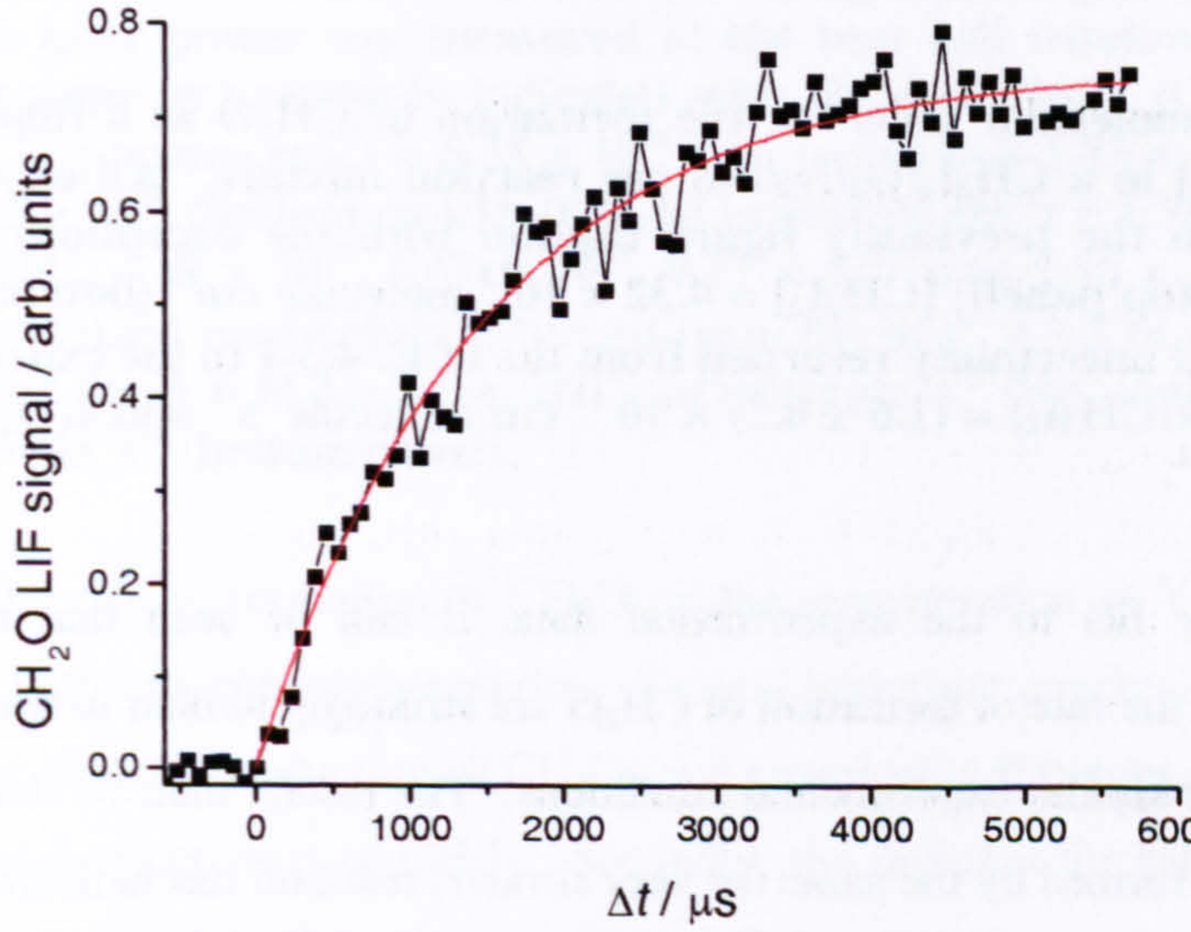

Fig. 4.4-7 – Kinetic trace showing the formation of formaldehyde in a $CH_2I_2/O_2/N_2$/248 nm reaction mixture. Experimental conditions: P = 100 Torr; T = 296 K; $[CH_2I_2] = 3.88 \times 10^{13}$ molecule cm^{-3}; $[O_2] = 2.84 \times 10^{16}$ molecule cm^{-3}; $[N_2]$ = balance; λ_{pr} = 353.16 nm; P_{pr} = 2.7 mJ pulse^{-1}; P_{ex} = 60 mJ pulse^{-1}; PRF = 0.5 Hz. The solid red line is a fit of E. 4.3-1 to the experimental data. From the fit, $k' = (647 \pm 68)$ s^{-1}. The removal of CH_2O from the system was found to be negligible (in some experiments a small secondary CH_2O growth was observed at long reaction times) and consequently k_{loss} and P4 are set to zero in the fitting procedure.

At a laser PRF of 2 Hz it was found that the pre-Excimer laser background systematically increased between consecutive kinetic traces. As CH_2O is long-lived in the reaction system, incomplete flushing of the reaction cell with fresh gas between laser shots results in its accumulation. To overcome this problem, the PRF was reduced to 0.5 Hz, in which time the entire reaction cell has been replenished with a fresh reagent mixture between laser shots. At this PRF the pre-Excimer background was always constant and interference to the reaction kinetics was avoided.

As initial experiments, the rate of formation of CH_2O was investigated as a function of $[CH_2I_2]$ and $[O_2]$ (where $[O_2] >> [CH_2I_2]$). The results are displayed in Fig. 4.4-8.

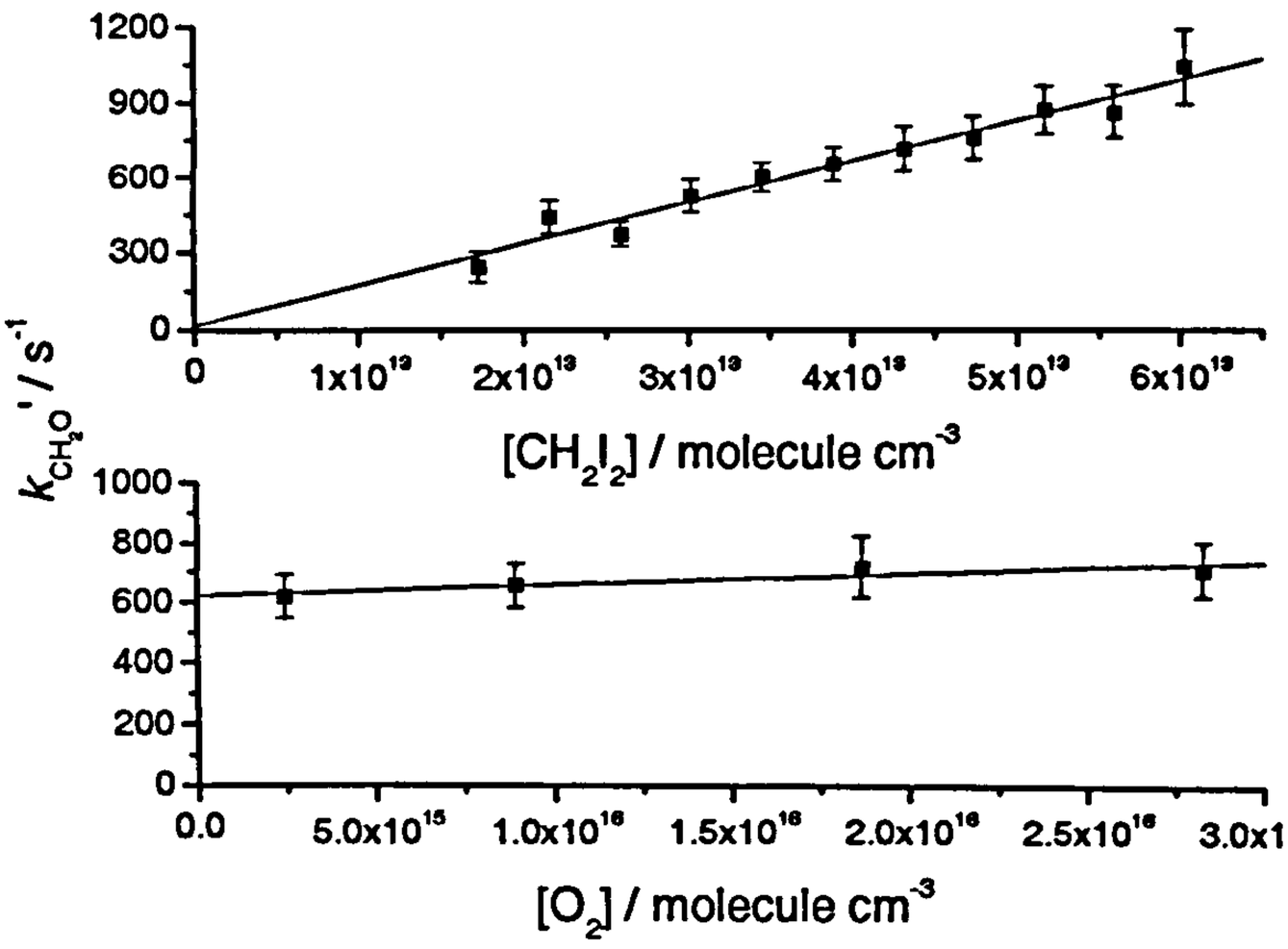

Fig. 4.4-8 – Bimolecular plots for the formation of CH_2O as a function of $[CH_2I_2]$ (top panel) and $[O_2]$ in a $CH_2I_2/O_2/N_2$/248 nm reaction mixture. All experimental conditions are as given in the previously figure caption with the exceptions: $[O_2] = 2.84 \times 10^{16}$ molecule cm^{-3} (top panel); $[CH_2I_2] = 4.32 \times 10^{13}$ molecule cm^{-3} (bottom panel). Error bars are 2σ standard uncertainty returned from fits of E. 4.3-1 to the experimental data. From the linear fits, $k(CH_2I_2) = (1.6 \pm 0.2) \times 10^{-11}$ $cm^3 molecule^{-1} s^{-1}$ and $k(O_2) = (3.6 \pm 5.6) \times 10^{-15}$ $cm^3 molecule^{-1} s^{-1}$.

From the linear fits to the experimental data, it can be seen that the $[CH_2I_2]$ and $[O_2]$ dependencies to the rate of formation of CH_2O are strikingly similar to that of IO (*cf.* Figs. 4.4-2 and 4.4-3) under similar experimental conditions. The results indicate that, although CH_2O and IO are probably formed by the same (or very similar) reaction mechanisms, CH_2O is not a direct product of the $CH_2I + O_2$ reaction, R4-2 (in disagreement with Enami *et. al.*[12]). As discussed in section 4.4.1, it is expected that CH_2O is generated in the reaction system by either self-reaction of peroxy species (produced from reaction R4-2) or from reaction of the peroxy species with I atoms (or CH_2I_2). As the power of the Excimer laser employed in this study could be varied by a factor of ~ 20, an experiment was performed in order to investigate this hypothesis. The rate

of formation of CH_2O was measured for five different CH_2I_2 concentrations (in an excess of O_2) at a fixed Excimer laser power. In a back-to-back experiment, the rate of formation of CH_2O was measured for four different Excimer laser powers at a fixed CH_2I_2 concentration. In Fig. 4.4-9 the pseudo-first-order rate of formation of CH_2O observed in both scenarios is plotted against Y, the concentration of I (and CH_2I) generated by the photolysis of diiodomethane.

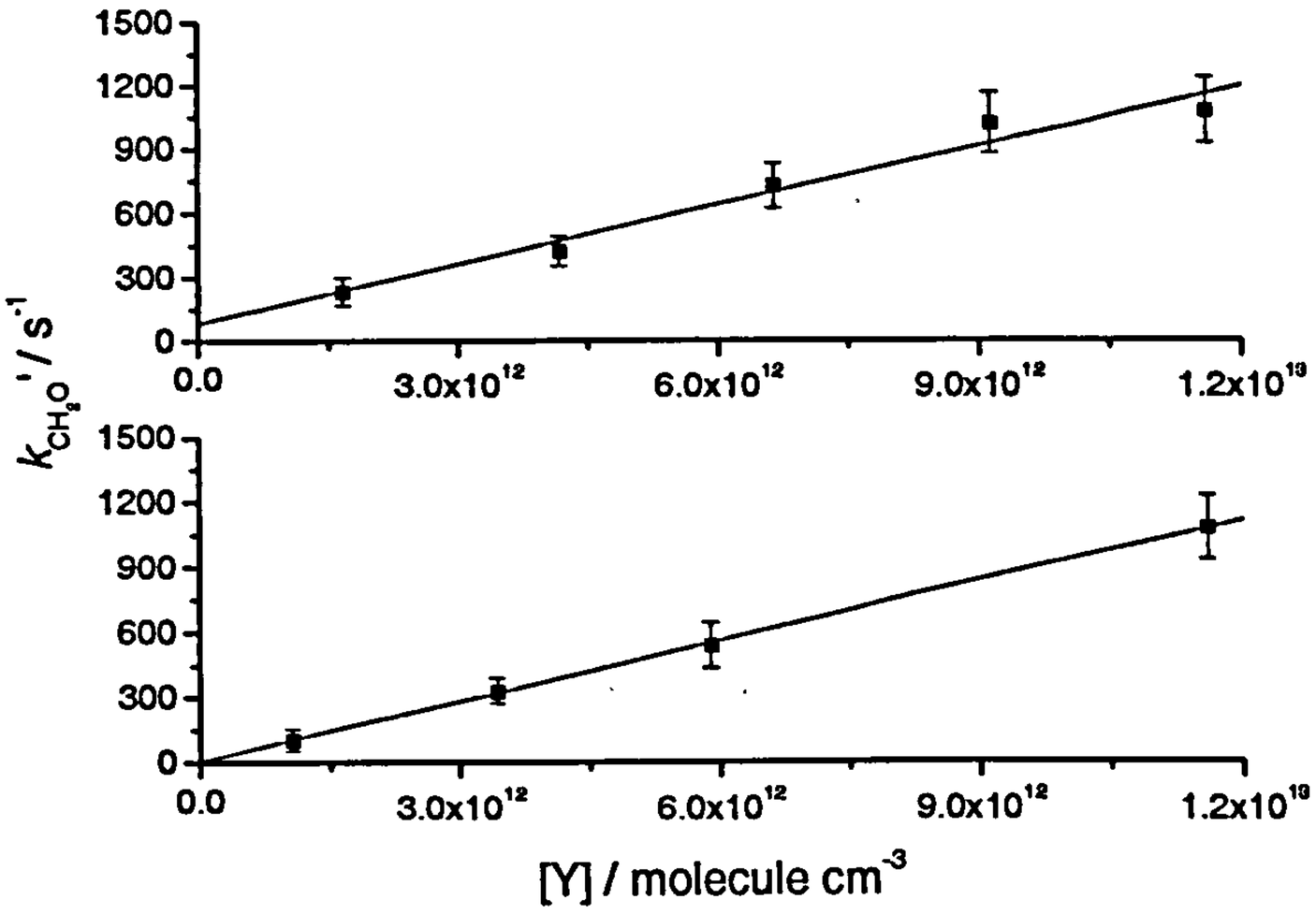

Fig. 4.4-9 – Bimolecular plots for the rate of formation of CH_2O as a function of Y, the radical concentration generated from CH_2I_2 photolysis. The top panel displays the data obtained when $[CH_2I_2]$ was varied at a fixed Excimer laser power, and the bottom panel displays the data obtained when the Excimer laser power was varied for a fixed $[CH_2I_2]$. The concentration of Y was evaluated from E. 2.3-1 (using a photolysis quantum yield of 1) and the Excimer laser power was measured at the rear cell window. Experimental conditions were the same as previously indicated with the exceptions: $[O_2] = 1.17 \times 10^{16}$ molecule cm^{-3} (all); F (photons cm^{-2}) $= 6.35 \times 10^{16}$ (top panel) and 5.83×10^{15}, 1.87×10^{16}, 3.23×10^{16} and 6.35×10^{16} (bottom panel); $[CH_2I_2]$ (molecule cm^{-3}) $= 1.16 \times 10^{14}$ (bottom panel) and 1.67×10^{13}, 4.18×10^{13}, 6.67×10^{13}, 9.17×10^{13} and 1.16×10^{14} (top panel). Error bars are 2σ standard uncertainty returned from fits of E. 4.3-1 to the experimental data. From the linear fits, $k = (9.2 \pm 3.1) \times 10^{-11}$ cm^3molecule$^{-1}s^{-1}$ (top panel) and $k = (9.2 \pm 0.7) \times 10^{-11}$ cm^3molecule$^{-1}s^{-1}$ (bottom panel).

The dependence of the rate of formation of CH_2O on the concentration of Y was found to be exactly the same for both experimental scenarios. Several important conclusions can be drawn from this result. First, that the production of CH_2O (and presumably IO) does not involve CH_2I_2 directly, rather a photolysis product of CH_2I_2. Secondly, the fact that the rate of formation of CH_2O is directly proportional to the concentration of Y (as was the peak CH_2O LIF signal) demonstrates that this photolysis product is formed in a single photon process, and must either be I or the product of the $CH_2I + O_2$ reaction. It is interesting that the rate coefficient obtained from the bimolecular plots ($k = 9.2 \times 10^{-11}$ cm^3molecule$^{-1}s^{-1}$) is similar to the estimated rate coefficient of the self-reaction of CH_2IO_2 ($k = 9 \times 10^{-11}$ cm^3molecule$^{-1}s^{-1}$) as reported by

Sehested *et. al.*[13]. If it is assumed that CH_2IO_2 is the only product of the $CH_2I + O_2$ reaction, then CH_2O must be formed from reaction R4-4a or R4-18 (or both). The self-reaction of CH_2IO_2 (R4-4a) is not expected to produce IO radicals, and we must therefore conclude that the reaction $I + CH_2IO_2$ (R4-18) must be occurring within the reaction system. In fact, it is known that ClO is produced from the reaction of Cl atoms with the CH_3O_2 peroxy species, and that this reactions proceeds at a rapid rates[43]. Indeed, if CH_2IO_2 were also to react with Br atoms, producing BrO, then the observation of BrO in the absorption experiment could be accounted for. However, we now arrive at an anomaly in that the yield of IO produced from CH_2I (generated by the photolysis of CH_2I_2) was estimated to be in the 4 – 40 % range in the absorption study. To explore this result, an experiment was performed in order to quantify the yield of CH_2O (produced from CH_2I) in the experimental system.

As stated previously, CH_2O was generated as a reference by the reaction of Cl atoms with MeOH in the presence of O_2. Under the experimental conditions, this process should result in the quantitative conversion of Cl atoms into CH_2O. The reaction of Cl atoms with CH_3I is known to produce CH_2I radicals in high yield (~ 80 %)[44] at room temperature. Thus an experiment was performed where equal amounts of Cl atoms were reacted with either CH_3OH or CH_3I (in a large excess of O_2) and the peak CH_2O LIF signals were compared. Assuming the removal of CH_2O to be negligible in both reaction systems (which was observed to be the case) the yield of CH_2O, $\Phi(CH_2O)$, produced from CH_2I is given by

$$\Phi_{CH_2O} = \frac{P_{CH_3I}}{0.8 \times P_{CH_3OH}} \qquad \text{E. 4.4-1}$$

where, Φ_{CH_2O} is the branching ratio for CH_2O formation from the initial CH_2I concentration, P_{CH_3I} and P_{CH_3OH} are the peak CH_2O LIF signals observed in the CH_3I and CH_3OH experiments respectively, and 0.8 is a factor accounting for the non-unity yield of CH_2I produced from the reaction of $Cl + CH_3I$.

When Cl atoms were reacted with CH_3I, extremely intense fluorescence, that could not be attributable to CH_2O, was observed at early reaction times, which decayed to a non-zero baseline at larger values of Δt. Fluorescence from this unknown species was independent of the presence of O_2 and was observed to form with the correct kinetics for a product of the reaction $Cl + CH_3I \rightarrow$ products. When the excitation wavelength of the probe laser was altered to 355 nm (a wavelength where CH_2O absorbs weakly in comparison to 353.16 nm) the intense fluorescence was still observed, although the PMT signal returned to the pre-Excimer laser background at longer reaction times. It was inferred that the species responsible for this unexpected fluorescence was the CH_3I-Cl adduct, recently observed in a CRDS absorption

experiment[31]. A spectroscopic and kinetic investigation of this species is the subject of Chapter Five of this thesis. As fluorescence from CH_3I-Cl was found to be relatively independent of excitation wavelength, subtraction of the 355 nm kinetic trace from that obtained at 353.16 nm was found to yield the temporal evolution of CH_2O in the reaction system. The results are displayed in Fig. 4.4-10.

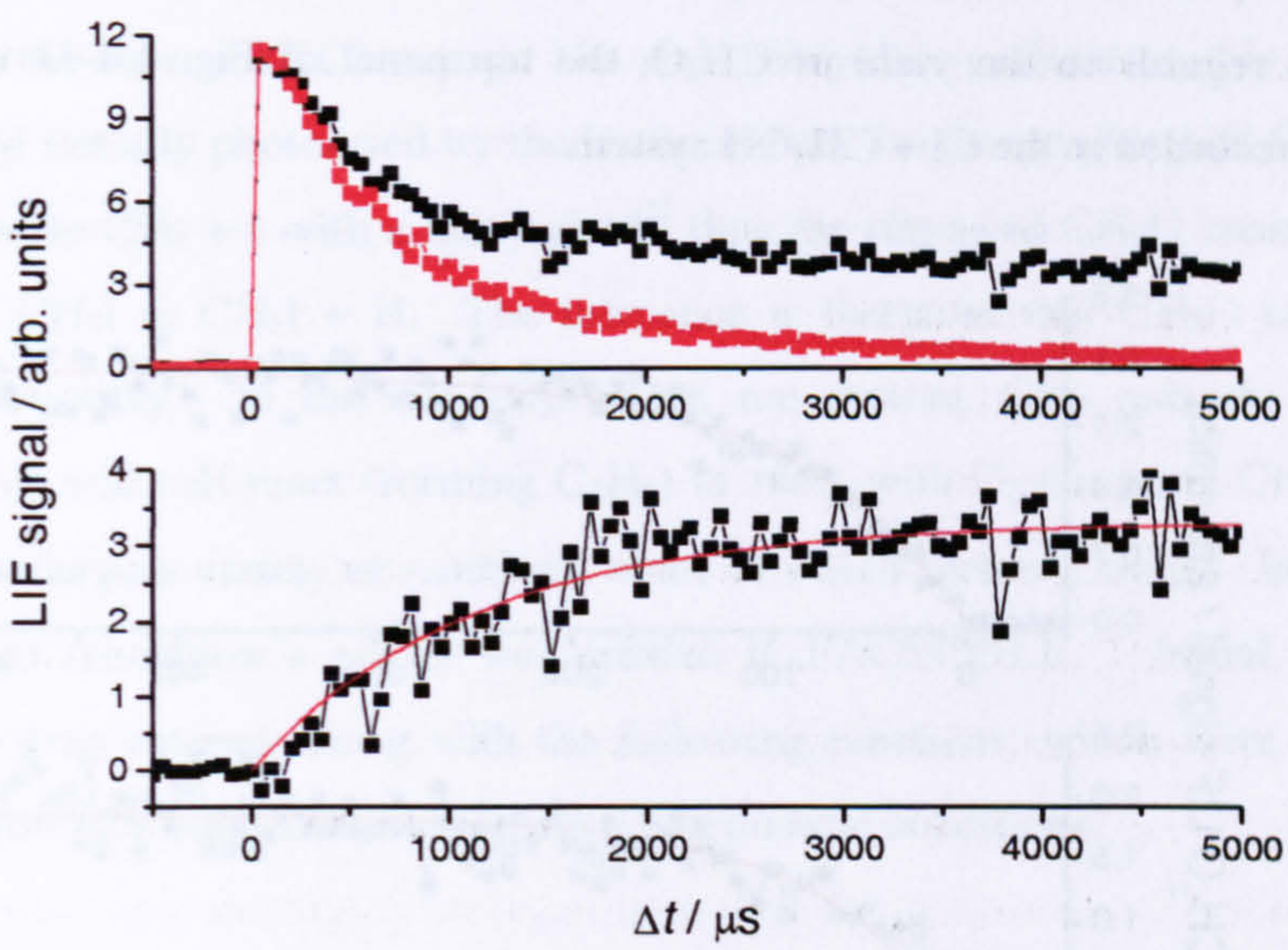

Fig. 4.4-10 – Kinetic traces recorded in a $Cl_2SO/CH_3I/O_2/N_2$/248 nm reaction mixture. The top panel displays the traces obtained at 353.16 nm (black) and 355 nm (red) showing fluorescence from the CH_3I-Cl adduct, and the bottom panel displays the residual CH_2O kinetic trace obtained by subtracting the 355 nm trace from the 353.16 nm trace. Experimental conditions: P = 100 Torr; T = 296 K; $[Cl_2SO] = 2.23 \times 10^{13}$ molecule cm^{-3}; $[CH_3I] = 8.8 \times 10^{14}$ molecule cm^{-3}; $[O_2] = 2.43 \times 10^{16}$ molecule cm^{-3}; $[N_2]$ = balance; $F = 6.0 \times 10^{16}$ photons cm^{-2}; PRF = 0.5 Hz; P_{pr} = 2.6 mJ pulse^{-1}. The solid red line is a fit of E. 4.3-1 to the residual CH_2O trace. From the fit, $P1$ = (2990 ± 200), k_{growth} = (920 ± 160) s^{-1}.

Before the yield of CH_2O is discussed, an interesting result from the residual CH_2O kinetic trace must be mentioned. In the $CH_2I_2/O_2/N_2$/248 nm experiments, information as to the relative extent of reactions R4-4a and R4-18 cannot be obtained as the concentration of I and CH_2IO_2 are expected to be equal (as they are both produced by the photolysis of CH_2I_2). However, in the Cl + CH_3I (+ O_2) system we have a chemical source of CH_2I, and a photolytic source of I (from the 248 nm photolysis of CH_3I), which are of unequal concentration. The pseudo-first-order rate of formation of CH_2O, determined from the fit to the trace displayed in the bottom panel of Fig. 4.4-10 is, $k(CH_2O)' = (920 \pm 160)$ s^{-1}. If this value is divided by the experimental CH_2I concentration ($0.8 \times [Cl]_0 = 7.5 \times 10^{12}$ molecule cm^{-3}) an effective bimolecular rate coefficient of, $k = (1.2 \pm 0.2) \times 10^{-10}$ cm^{3}molecule^{-1}s^{-1} is obtained for the self-reaction of CH_2IO_2 (R4-4a). This is comparable to the Y-dependence to the rate of formation of CH_2O determined previously ($k = 9.2 \times 10^{-11}$ cm^{3}molcule^{-1}s^{-1}). When the rate of formation of

CH_2O is divided by the I atom concentration ($[I]_0 = 4.6 \times 10^{13}$ molecule cm^{-3}), however, a significantly smaller effective bimolecular rate coefficient of, $k = (2.0 \pm 0.3) \times 10^{-11}$ $cm^3 molecule^{-1} s^{-1}$ is obtained for R4-18. Thus we can conclude that, although the reaction of I + CH_2IO_2 must occur (to explain the formation of IO), the self-reaction of peroxy radicals is predominant in the reaction system. This finding is discussed in greater detail at the end of this section. Note also that the presence of CH_2O in this experiment is unambiguous proof that CH_2I_2 is not required for its formation.

With regards to the yield of CH_2O, the top panel of Fig. 4.4-11 displays the CH_2O kinetic trace recorded in the Cl + CH_3OH system.

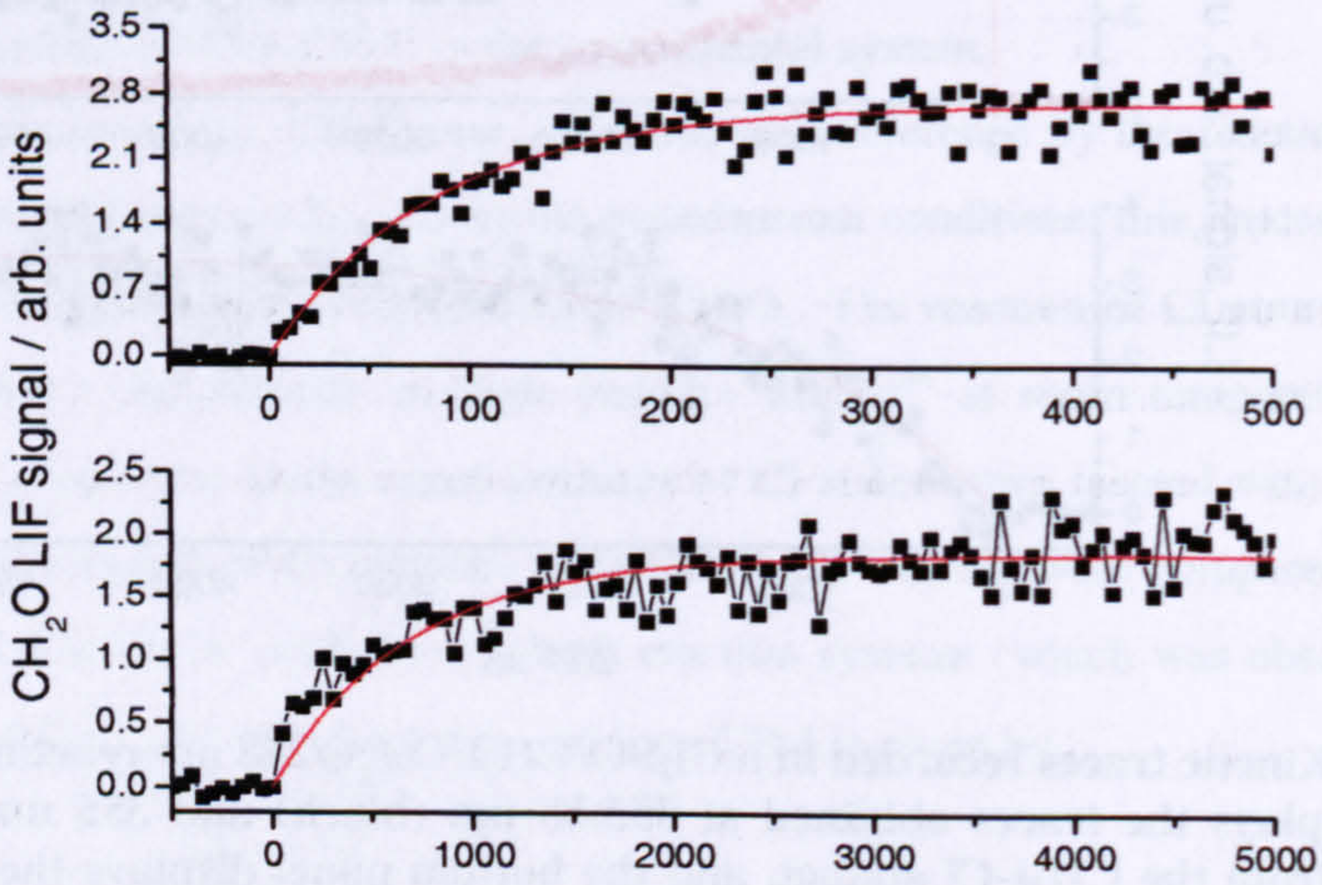

Fig. 4.4-11 – Kinetic traces showing the formation of CH_2O in a $Cl_2SO/CH_3OH/O_2/N_2$/248 nm reaction mixture (top panel) and a $CH_3I/O_2/N_2$/248 nm reaction mixture (bottom panel). Note that the experimental conditions were identical to those given in the previous figure caption, with the exceptions that CH_3I was replaced with 2.08×10^{14} molecule cm^{-3} of CH_3OH (top panel) and no Cl_2SO was present in the experiment conducted with CH_3I (bottom panel). The solid red lines are fits of E. 4.3-1 to the experimental data. From the fits: $P1$ = (31400 ± 3100) and k_{growth} = (11900 ± 1400) s^{-1} (top panel); $P1$ = (2600 ± 400), k_{growth} = (1440 ± 240) s^{-1} (bottom panel).

Substituting the appropriate values for P ($P = P1/k_{growth}$) into E. 4.4-1, a CH_2O yield of (150 ± 70) % is obtained. Thus the yield of CH_2O is significantly greater than that of IO, which is in agreement with the above conclusion that the CH_2IO_2 self-reaction must have a larger rate coefficient than that of I + CH_2IO_2. However, although within statistical uncertainty, it is surprising that the determined yield of CH_2O is significantly greater than unity. To explore this result, the CH_3I experiment was repeated in the absence of thionyl chloride (the chlorine atom precursor). Although fluorescence from CH_3I-Cl was not observed, LIF from CH_2O was detected and surprisingly at approximately half the intensity to that when Cl atoms were present.

The CH_2O kinetic trace, recorded in the $CH_3I/O_2/N_2$/248 nm reaction mixture, is displayed in the bottom panel of Fig. 4.4-11. After correcting the peak CH_2O LIF signal (observed in the Cl + CH_3I experiment) for that observed in the absence of Cl atoms, the CH_2O yield from CH_2I is thus revised to (70 ± 80) %, where the large error reflects the extended propagation of errors. Nevertheless, the yield of CH_2O is almost certainly larger than that of IO.

Although detracting from the aims of the current research, the presence of CH_2O in photolysis mixtures of $CH_3I/O_2/N_2$/248 nm is puzzling (note that no CH_2O was observed in the CH_3OH system in the absence of Cl atoms). If a yield analysis is performed, it is found that (14 ± 7) % of the CH_3I initially photolysed by the Excimer laser is converted to CH_2O. At 248 nm, CH_3I is photolysed to CH_3 + I with a unity yield[27] thus the observed CH_2O cannot result from the photolysis of CH_3I to CH_2I + H. The inference is therefore that CH_2O is produced by peroxy radical chemistry. In the $CH_3I/O_2/N_2$/248 nm system, CH_3 radicals (produced by photolysis of CH_3I) will self-react (forming C_2H_6) or react with O_2 (forming CH_3O_2 radicals). CH_3O_2 can then undergo a variety of reactions, some of which forming CH_2O. In an attempt to simulate the CH_2O formation a model was created in FACSIMILE. Initial parameters of $[CH_3]_0$ and $[O_2]_0$ were entered, along with the following reactions, which were assigned their appropriate literature rate coefficients under the experimental conditions[45].

$CH_3 + CH_3 + M$	→	$C_2H_6 + M$	(R4-22)
$CH_3 + O_2 + M$	→	$CH_3O_2 + M$	(R4-23)
$CH_3O_2 + CH_3$	→	$2\ CH_3O$	(R4-24)
$CH_3O_2 + CH_3O$	→	$CH_2O + CH_3OOH$	(R4-25a)
	→	other products	(R4-25b)
$CH_3O_2 + CH_3O_2$	→	$2\ CH_3O + O_2$	(R4-26a)
	→	$CH_2O + CH_3OH + O_2$	(R4-26b)

The model was instructed to simulate CH_2O production for the same conditions, and over the same temporal range, as the experiment. The CH_2O formation observed in experiment could not be reproduced by the FACSIMILE model, possibly indicating the presence of iodine chemistry. A study by Shah *et. al.*[46] determined the room temperature rate coefficient for the reaction of I + CH_3O (probably forming HI and CH_2O) as, $k = 8.5 \times 10^{-11}$ $cm^3 molecule^{-1} s^{-1}$ at 298 K. This reaction was thus entered into the model (as was the initial parameter $[I]_0$) and the CH_2O formation was re-simulated. The results are displayed in Fig. 4.4-12.

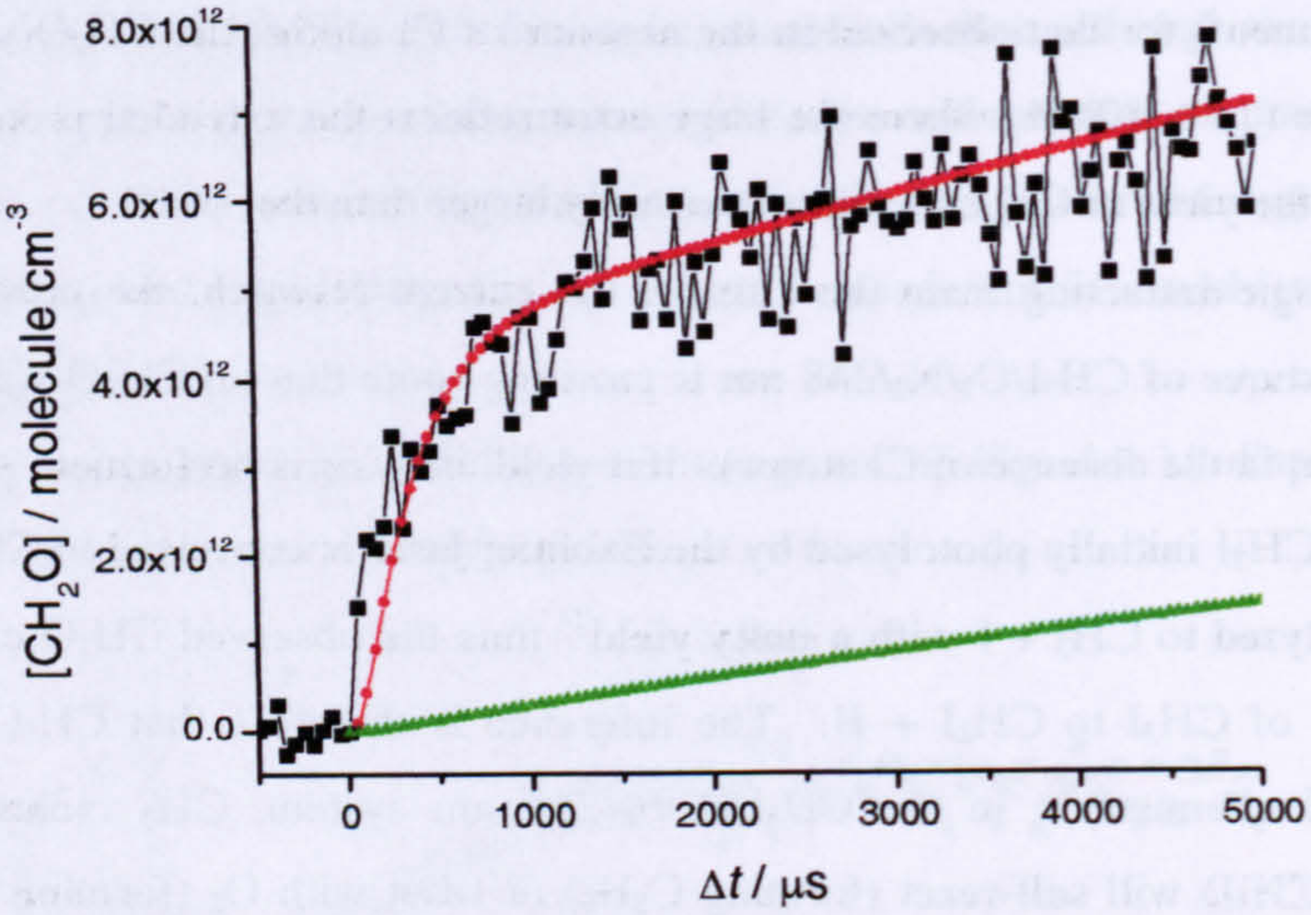

Fig. 4.4-12 – Experimental and modelled CH_2O production in a $CH_3I/O_2/N_2$/248 nm reaction mixture. The model outputs are shown by the red (including $I + CH_3O \rightarrow HI + CH_2O$) and green (no iodine chemistry) data points. Pertinent experimental conditions: $[CH_3]_0 = [I]_0 = 4.59 \times 10^{13}$ molecule cm^{-3}; $[O_2] = 2.43 \times 10^{16}$ molecule cm^{-3}. Note that the experimental CH_2O LIF signal was converted to an absolute concentration by calibrating the signal to that observed in the $Cl/CH_3OH/O_2/N_2$/248 nm system, where quantitative conversion of $[Cl]_0$ (calculated from the experimental conditions) to CH_2O was assumed.

The agreement between experimental and modelled CH_2O production is remarkable (for the model simulation including the iodine reaction) in terms of both absolute yield and temporal evolution, especially considering that the peroxy and alkoxy chemistry of the reaction system is likely to be more complex than considered by the model. The results are indicative that the reaction of $I + CH_3O$ does indeed produce $HI + CH_2O$ (as suggested by Shah *et. al.*[46]) and that no additional (unknown chemistry) needs to be evoked to explain the CH_2O formation observed in the $CH_3I/O_2/N_2$/248 nm reaction system.

4.4.3 Estimated Rate Coefficients for the Reactions $CH_2IO_2 + CH_2IO_2 \rightarrow 2\ CH_2IO + O_2$ and $I + CH_2IO_2 \rightarrow IO + CH_2IO$ at 296 K

Let us assume that reactions R4-4a and R4-18 are responsible for the observed production of CH_2O (from the unimolecular dissociation of CH_2IO) and IO in $CH_2I_2/O_2/N_2/h\nu$ reaction mixtures. It was previously concluded that the rate coefficient of R4-4a is greater than that of R4-18 for two main reasons: i) that the yield of CH_2O is apparently greater than that of IO; and ii) that in a $Cl_2SO/CH_3I/O_2/N_2$/248 nm reaction mixture, the rate of formation of CH_2O is probably more dependent on the concentration of CH_2I (chemically generated) than I (photolytically generated). The relative rates of R4-4a and R4-18 cannot be investigated from

the CH_2O data obtained in $CH_2I_2/O_2/N_2$/248 nm reaction mixtures because CH_2IO_2 (produced from CH_2I) and I are present at equal concentration. Although it is incorrect to assume that CH_2O is produced only from these reactions in mixtures of $Cl_2SO/CH_3I/O_2/N_2$/248 nm (as it has been shown that CH_2O is also formed from reactions involving CH_3O_2, produced as a result of CH_3I photolysis), in want of more informative results with respect to the question at hand, we will start with the assumption that other reactions forming CH_2O in this reaction system are of negligible consequence to its overall reaction kinetics.

In order to try and assign rate coefficients to the $CH_2IO_2 + CH_2IO_2$ and $I + CH_2IO_2$ reactions, a model was created in FACSIMILE. Initial parameters of $[CH_2I]_0$, $[I]_0$ and $[O_2]_0$ are entered into the model, along with the following reactions:

$$CH_2I + O_2 \rightarrow CH_2IO_2 \qquad \text{(R4-2)}$$

$$CH_2IO_2 + CH_2IO_2 \rightarrow 2\,CH_2O + 2\,I + O_2 \qquad \text{(R4-4a)}$$

$$I + CH_2IO_2 \rightarrow IO + CH_2O + I \qquad \text{(R4-18)}$$

Note that in this reaction scheme it is assumed that any CH_2IO will spontaneously decompose to $CH_2O + I$. The rate coefficient for R4-2 was fixed at, $k = 1.5 \times 10^{-12}$ $cm^3molecule^{-1}s^{-1}$ (the mean MS determination of Masaki *et. al.*[14] and Eskola *et. al.*[19]), and the rate coefficients for R4-4a and R4-18 were assigned initial values of 1.2×10^{-10} $cm^3molecule^{-1}s^{-1}$ and 2.0×10^{-11} $cm^3molecule^{-1}s^{-1}$ respectively.

The model was then used to simulate a CH_2O kinetic trace for the same initial conditions as the experiment displayed in the bottom panel of Fig. 4.4-10 and E. 4.3-1 was fit to the output, returning a pseudo-first-order rate coefficient for the formation of CH_2O. Initially, the formation rate of CH_2O was significantly overestimated by the model (with respect to the experimental value of 920 s^{-1}) and the initial values for the bimolecular rate coefficients of R4-4a and R4-18 were therefore adjusted in a trial and error procedure until a reasonable agreement between experimental and modelled formation rates was found (and where the ratio of rate coefficients was sufficient for CH_2O to be formed in significantly higher yield than IO). In this manner it was found that rate coefficients for R4-4a and R4-18 of 6×10^{-11} $cm^3molecule^{-1}s^{-1}$ and 1×10^{-11} $cm^3molecule^{-1}s^{-1}$ respectively, satisfied the experimental observations reasonably well. The simulated profile of CH_2O (and IO) is displayed in the top panel of Fig. 4.4-13.

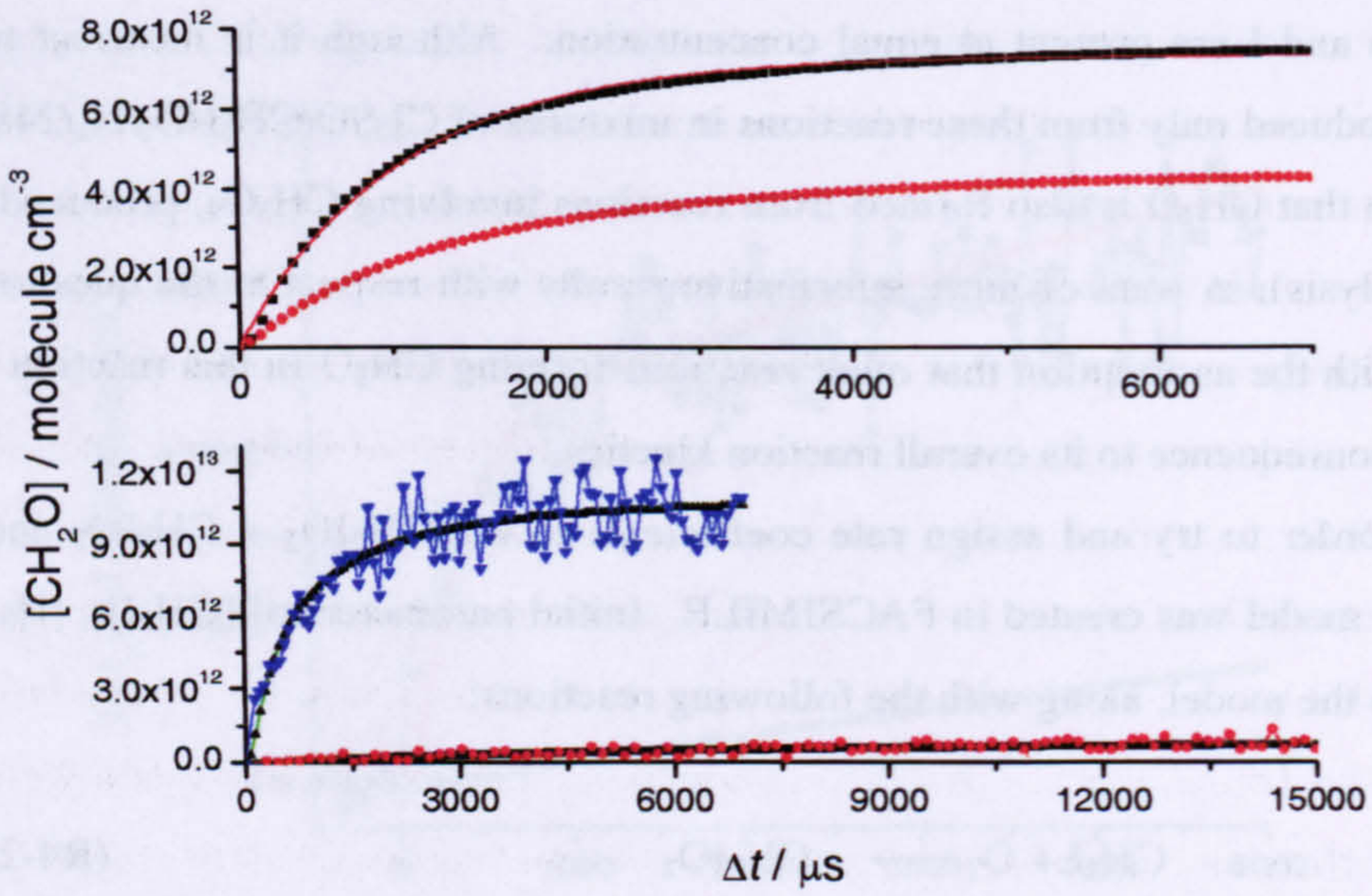

Fig. 4.4-13 – Top panel: simulated kinetic traces of CH_2O (black squares) and IO (red circles) in a $Cl/CH_3I/O_2/N_2$/248 nm reaction mixture using the FACSIMILE model described in the text, and employing rate coefficients of 6×10^{-11} $cm^3molecule^{-1}s^{-1}$ and 1×10^{-11} $cm^3molecule^{-1}s^{-1}$ for the reactions of $CH_2IO_2 + CH_2IO_2$ and $I + CH_2IO_2$ respectively. Experimental conditions: $[CH_2I]_0 = 7.49 \times 10^{12}$ molecule cm^{-3}, $[I]_0 = 4.59 \times 10^{13}$ molecule cm^{-3} and $[O_2]_0 = 2.43 \times 10^{16}$ molecule cm^{-3}. The solid red line is a fit of E. 4.3-1 to the simulated CH_2O. From the fit, $k(CH_2O)' = (948 \pm 18)$ s^{-1}. Bottom panel: model fitting (black) of the experimental data obtained in the $CH_2I_2/O_2/N_2$/248 nm Excimer power dependence experiments (see p. 41), performed at the highest (blue) and lowest (red) Excimer laser powers. Experimental conditions: $[CH_2I] = [I] = 1.16 \times 10^{13}$ molecule cm^{-3} (blue) and 1.06×10^{12} molecule cm^{-3} (red); $[O_2] = 1.17 \times 10^{16}$ molecule cm^{-3} (both). From the model output: $k(CH_2IO_2 + CH_2IO_2) = (7.7 \pm 1.5) \times 10^{-11}$ $cm^3molecule^{-1}s^{-1}$ (high power) and $(6.8 \pm 3.1) \times 10^{-11}$ $cm^3molecule^{-1}s^{-1}$ (low power). Note that the experimental kinetic traces illustrate the magnitude of the Excimer power dependence on both the rate of formation and peak concentration of CH_2O.

As a test of the estimated rate coefficients the FACSIMILE model was used to fit the experimental data obtained in the Excimer laser power dependence study of the $CH_2I_2/O_2/N_2$/248 nm reaction system (see pages 179 – 180). In this modelling study the experimental kinetic traces were converted from LIF signal into estimated $[CH_2O]$ by normalising the data so that the peak CH_2O signal was equal to the calculated concentration of CH_2I radicals generated by the Excimer laser. The experimental data was then entered into the FACSIMILE model, which was instructed to return a rate coefficient for the self-reaction of CH_2IO_2 (the rate coefficient for R4-18, $I + CH_2IO_2$ was fixed to 1×10^{-11} $cm^3molecule^{-1}s^{-1}$) after the appropriate experimental conditions had been assigned. The model fits to the experimental data, obtained for the highest and lowest Excimer laser power experiments, are displayed in the bottom panel of Fig. 4.4-13. For the four different Excimer laser powers studied rate coefficients for R4-4a of, k (10^{-11} $cm^3molecule^{-1}s^{-1}$) = (7.7 ± 1.5), (5.1 ± 0.9), (4.7 ± 1.8), and $(6.8 \pm 3.1) \times 10^{-11}$ $cm^3molecule^{-1}s^{-1}$ were obtained, essentially in very good agreement with that

estimated from the $Cl_2SO/CH_3I/O_2/N_2$/248 nm data. However, it must be emphasised that the estimated rate coefficients are highly speculative and their accuracy is dependent upon many assumptions. As the potential for chemical recycling of formaldehyde is great in chemical systems containing peroxy radicals, we prefer to quote the rate coefficients as lower limits.

Although it was stated that the kinetic data obtained in the absorption experiments should only be treated at a semi-quantitative level, in a final modelling investigation it was attempted to link the temporal profiles of species X (considered to be the CH_2IO_2 peroxy radical) and IO. Initially, the decay of species X was investigated. The absorption profiles of species X recorded at 350 nm (some of which are displayed in Fig. 4.3-9) were converted into absolute CH_2IO_2 concentrations using the appropriate absorption cross-section determined in section 4.3.2.3 ($\sigma_{350nm} = 1.4 \times 10^{-18}$ $cm^2molecule^{-1}$). The experimental data were entered into the FACSIMILE model, which was instructed to simulate the CH_2IO_2 growth and decay and return a rate coefficient for the self-reaction of CH_2IO_2, R4-4a. The initial concentrations of CH_2I and I were set at equal values and allowed to float, and the initial concentration of O_2 was fixed to the experimental value. In the absorption study it was found that species X did not form with the correct reaction kinetics for a product of the $CH_2I + O_2$ reaction (possibly because of multiple absorption), thus the rate coefficient for R4-2 was allowed to float in the model simulation. The rate coefficient for the reaction of $I + CH_2IO_2$ was fixed at 1×10^{-11} $cm^3molecule^{-1}s^{-1}$. After repeating this procedure for all five absorption traces, self-reaction rate coefficients of, k (10^{-11} $cm^3molecule^{-1}s^{-1}$) = (4.8 ± 0.1), (9.4 ± 0.3), (11.4 ± 0.4), (9.3 ± 0.5) and (10.8 ± 0.8) were returned. With the exception of the smallest value, the rate coefficients are in excellent agreement and have an average value of, $k = (10.2 \pm 2.1) \times 10^{-11}$ $cm^3molecule^{-1}s^{-1}$, which is in reasonable agreement with the lower limit estimated by the CH_2O LIF data. Fig. 4.4-14 displays the model fit to one of the absorption traces. It should again be emphasised that the results obtained in this modelling exercise are speculative, primarily because there is no definitive evidence that species X is CH_2IO_2. Having investigated the removal of species X, its possible link to the formation of IO was sought. For this purpose, the IO absorption trace obtained under identical experimental conditions to those given in the caption of Fig. 4.4-14 was entered into the FACSIMILE model. The initial CH_2I and I concentrations were fixed to the value returned from the previous modelling exercise ($[CH_2I]_0 = [I]_0 = 1.7 \times 10^{14}$ molecule cm^{-3}), as were the rate coefficients for reactions R4-2 and R4-4a (6.9×10^{-14} $cm^3molecule^{-1}s^{-1}$ and 11.4×10^{-11} $cm^3molecule^{-1}s^{-1}$ respectively). The model was then instructed to simulate the IO absorption trace, returning a value for the rate coefficient of the $I + CH_2IO_2$ reaction. The only pertinent alteration to the model was the addition of the IO self-reaction, which was assigned the literature rate coefficient of, $k = 9.9 \times 10^{-11}$ $cm^3molecule^{-1}s^{-1}$. The model fit to the experimental data is displayed in Fig. 4.4-15.

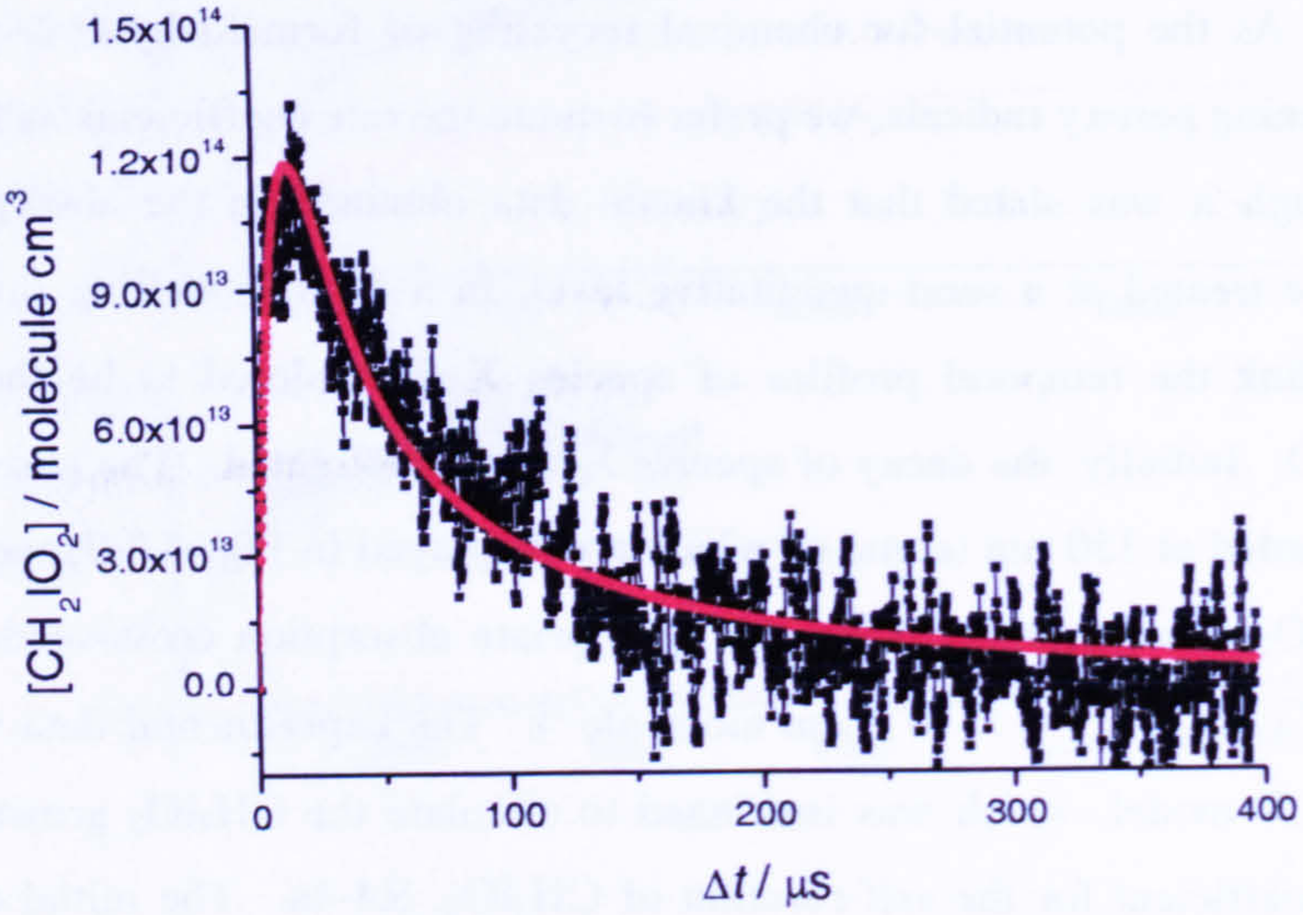

Fig. 4.4-14 – Model fit to the absorption profile of species X, speculated to be CH_2IO_2, by the FACSIMILE model described in the text. Experimental conditions: P = 760 Torr; T = 296 K; $[CH_2I_2] = 7.76 \times 10^{14}$ molecule cm^{-3}; $[O_2] = 2.04 \times 10^{18}$ molecule cm^{-3}; $[N_2]$ = balance; $F = 1.2 \times 10^{17}$ photons cm^{-2}. From the model output: $[CH_2I]_0 = [I]_0 = (1.7 \pm 0.1) \times 10^{14}$ molecule cm^{-3}; $k(CH_2I + O_2) = (6.9 \pm 0.5) \times 10^{-14}$ cm^{3}molecule^{-1}s^{-1}; $k(CH_2IO_2 + CH_2IO_2) = (11.4 \pm 0.4) \times 10^{-11}$ cm^{3}molecule^{-1}s^{-1}. Note that the model determinations of $k(CH_2I + O_2)$ ranged from $(6.9 \pm 0.5) \times 10^{-14}$ cm^{3}molecule^{-1}s^{-1} to $(7.7 \pm 0.8) \times 10^{-13}$ cm^{3}molecule^{-1}s^{-1} over the five absorption traces studied.

From Fig. 4.4-15 it can be seen that the model fit to the IO absorption trace is not particularly good. This may indicate that the temporal profiles of species X and IO are not linked (as described by the mechanism entered into the FACSIMILE model). However, the absorption experiments were prone to considerable interferences, such as the very high and non-uniform radical concentrations present, and the results obtained should be treated with caution. Further, the model simulation was allowed very little flexibility as $k(I + CH_2IO_2)$ was the only floated parameter. The rate coefficient for the reaction $I + CH_2IO_2 \rightarrow IO + CH_2IO$ returned by the model was, $k = (5.7 \pm 0.1) \times 10^{-11}$ cm^{3}molecule^{-1}s^{-1}, significantly larger than that estimated from the CH_2O LIF data. However, the accumulation of I_2 in the absorption cell may have provided an additional I atom source (to the photolysis of CH_2I_2) and the modelled rate coefficient for reaction R4-18 could therefore be significantly overestimated. Any mechanistic link between the temporal profiles of species X and IO was not investigated further.

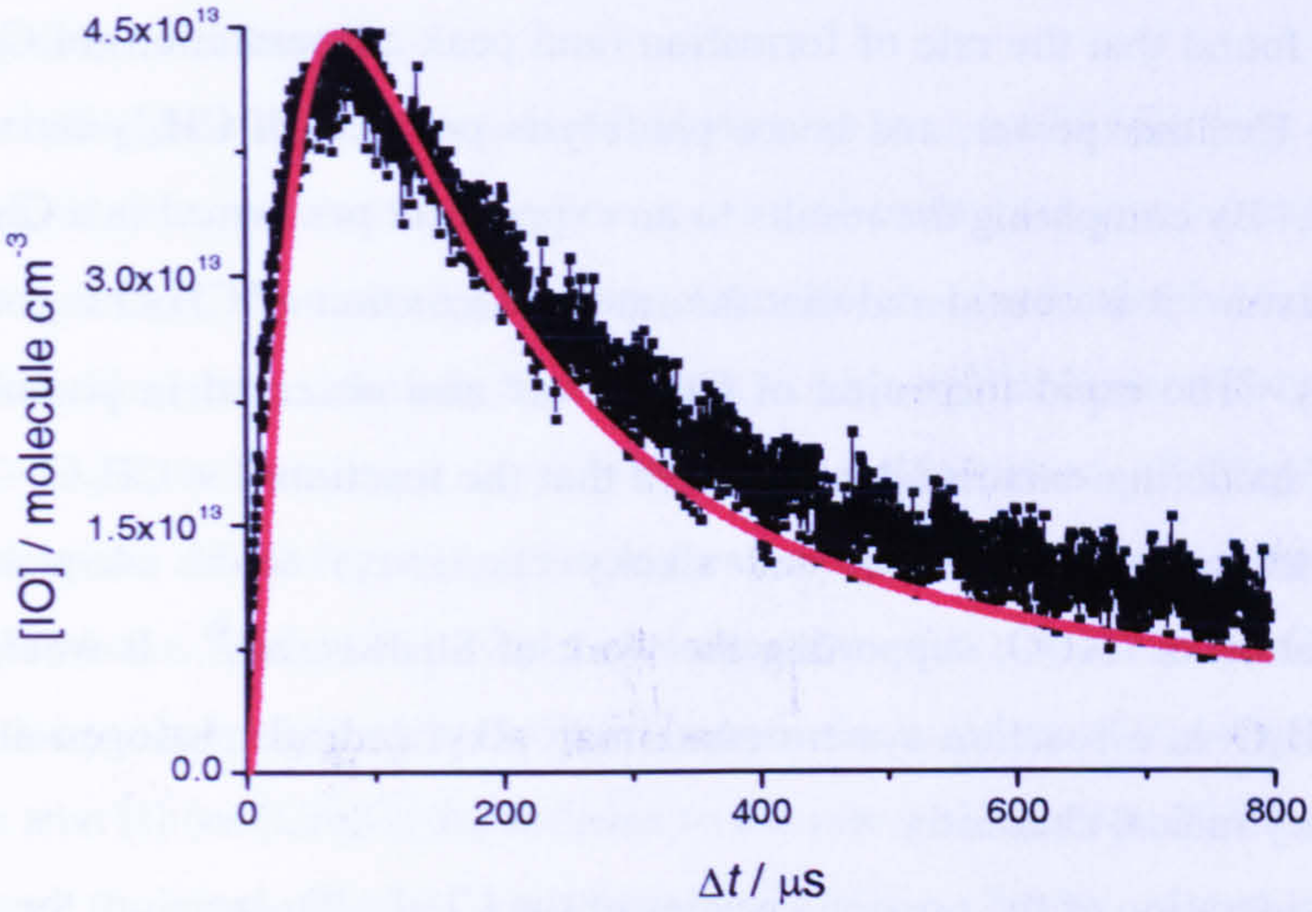

Fig. 4.4-15 – Model fit (red circles) to an IO absorption trace recorded under identical experimental conditions to that of species X shown in the previous figure. From the model output; $k(I + CH_2IO_2) = (5.7 \pm 0.1) \times 10^{-11}$ cm^{3}molecule^{-1}s^{-1}.

In line with the upper and lower limits determined in this modelling exercise, we choose to quote a range of values for the room temperature rate coefficient of the self-reaction of CH_2IO_2 of, $k = (6 - 12) \times 10^{-11}$ cm^{3}molecule^{-1}s^{-1}. For the reaction $I + CH_2IO_2 \rightarrow IO + CH_2IO$ the room temperature rate coefficient is of the order of, $k = (1 - 6) \times 10^{-11}$ cm^{3}molecule^{-1}s^{-1}.

4.4.4 Discussion

The results obtained in this LIF study have provided important information with regards to the products and mechanism of the $CH_2I + O_2$ reaction, R4-2. It has been definitively proved that IO and CH_2O are not formed as direct products of the $CH_2I + O_2$ reaction, in disagreement with the findings of Enami *et. al.*[12] (and with regards to IO, Eskola *et. al.*[19]). In a large excess of O_2 ($[O_2] > 10^{16}$ molecule cm^{-3}), the formation rates of IO and CH_2O have very little dependence on the experimental O_2 concentration but significant dependencies on $[CH_2I]$ and [I]. At relatively low concentrations of O_2, however, the $[O_2]$ dependence to the rate of formation of IO was observed to significantly increase and the $[CH_2I_2]$ dependence (in a CH_2I_2/O_2/248 nm reaction mixture) significantly decrease, providing an explanation for the experimental results of Enami *et. al.*[12] who conducted their study under low $[O_2]$ conditions. A primary conclusion, therefore, is that the rate coefficient of the $CH_2I + O_2$ reaction determined in the MS studies[14,19] should be used for purposes of atmospheric modelling and we would suggest the mean value of the two literature determinations, $k = 1.5 \times 10^{-12}$ cm^{3}molecule^{-1}s^{-1}.

From an Excimer power dependence study conducted in a CH_2I_2/O_2/248 nm reaction mixture it was found that the rate of formation (and peak concentration) of CH_2O had a linear dependence on Excimer power, and hence photolysis products of CH_2I_2 derived from a single photon process. By comparing the results to an experiment performed in a $Cl_2SO/CH_3I/O_2$/248 nm reaction mixture it is considered that the rate of formation of CH_2O is more dependent on $[CH_2I]$ than [I]. The rapid formation of CH_2O was also observed in photolysis mixtures of CH_3I/O_2 and a modeling exercise demonstrated that the reaction, $I + CH_3O \rightarrow CH_2O + HI$ (in conjunction with additional peroxy and alkoxy chemistry) could adequately describe the observed formation of CH_2O, supporting the work of Shah *et. al.*[46]. It would appear that the presence of CH_2O in a reaction system containing alkyl radicals, halogen atoms and O_2 is a marker of peroxy radical chemistry.

In consideration of the previous studies of the $CH_2I + O_2$ reaction, the known chemistry of CH_2ClO_2 and CH_2BrO_2, and the speculative detection of CH_2IO_2 in the absorption experiment reported in this work, it is hypothesised that CH_2O is formed in the experimental system by the self-reaction of CH_2IO_2 (R4-4a) and that IO is produced by the reaction of I + CH_2IO_2 (R4-18), which also produces CH_2O. The yield of CH_2O (deriving from CH_2IO_2) was estimated at (70 ± 80) %, significantly greater than that of IO (4 – 40 %), suggesting that reaction R4-4a has a larger rate coefficient than R4-18. A modelling exercise found that rate coefficients of, $k(CH_2IO_2 + CH_2IO_2) = 6 \times 10^{-11}$ $cm^3molecule^{-1}s^{-1}$, and $k(I + CH_2IO_2) = 1 \times 10^{-11}$ $cm^3molecule^{-1}s^{-1}$ could adequately describe the observations of the CH_2O LIF study. However, the chemical recycling of CH_2O (which was ignored by the model) is likely to have occurred and these rate coefficients should be regarded as lower limits. Although not aforementioned, the IO formation observed in the LIF study was unsatisfactorily reproduced by the same model, where the [I] dependence to the rate of formation of IO was overestimated by around an order of magnitude. However, the IO LIF study was performed at a laser pulsed repetition frequency of 2 Hz. Although any IO would have been completely removed from the reaction system between consecutive laser shots, the reaction cell was not completely replenished with a fresh reagent mixture and the accumulation of I_2 in the reaction cell is considered likely. It is probable, therefore, that an ill-defined I atom concentration was present in the IO LIF study, and the CH_2O investigation (performed at a lower laser PRF) should be considered more reliable. In a final modelling investigation, the rate coefficient for the self-reaction of the absorbing species speculated to be CH_2IO_2 was determined to be of the order of 1×10^{-10} $cm^3moleule^{-1}s^{-1}$, in reasonable agreement with the lower limit set from the CH_2O LIF experiments, and of that reported by Sehested *et. al.*[13]. An attempt to model IO production from CH_2IO_2 chemistry, using data obtained in the absorption experiment, was inconclusive and yielded a rate coefficient for R4-18 of, $k(I + CH_2IO_2) = 5.7 \times 10^{-11}$ $cm^3molecule^{-1}s^{-1}$, significantly greater

than that estimated from the CH_2O LIF data. However, the accumulation of I_2 in the absorption cell is also likely to have occurred.

Before ending this discussion several further points should be made. First, that it is difficult to deconvolute a reaction mechanism containing more than one reaction involving the same chemical species. Not enough information has been obtained to suggest that IO definitively derives from the reaction, I + CH_2IO_2. Although it is considered unlikely, it is possible that IO could be generated directly from the self-reaction of CH_2IO_2. In order to deduce the mechanism of IO formation, further experimental work is required. An Excimer laser power dependence study of the rate of formation of IO in CH_2I_2/O_2/248 nm reaction mixtures should be performed (under conditions where the build-up of I_2 cannot occur) in order to determine the true [I] (or [CH_2I]) dependence to the rate of formation of IO, and confirm that IO originates from the single-photon dissociation of CH_2I_2. Clearly, investigating the rate of formation of IO in reaction systems containing different initial concentrations of CH_2I and I would be informative. The second point to highlight is that, in the mechanism postulated for the formation of CH_2O in this work, it is assumed that CH_2IO spontaneously decomposes to CH_2O + I (in analogy to the CH_2BrO alkoxy species)[17]. If CH_2IO were to have a non-negligible lifetime (> 100 μs) CH_2O could be produced in higher yield but at a slower rate than IO, potentially accounting for some of the observed discrepancies in this work. Finally, in the course of this work, intense LIF from OH was observed after the 248 nm photolysis of CH_2I_2 in the presence of O_2. The source of OH is unknown but may imply the presence of dioxirane (see p.166) and/or CH_2IO_2 (see p.142). Unhelpfully, unforeseen problems with the laser system meant that the reaction kinetics of OH could not be determined. However, this work represents the first report of the detection of OH in the $CH_2I + O_2$ system and opens a further avenue for research in this complex reaction system.

In section 4.4.1 it was suggested that IO and CH_2O may be formed by the reaction $CH_2O_2 + I \rightarrow CH_2O + IO$ (R4-16). The reason why this reaction has not been discussed further is stated in the following section.

4.5 Mass Spectroscopic Investigation of the Products of the $CH_2I + O_2$ Reaction

In a final attempt to deduce the products of the $CH_2I + O_2$ reaction a mass spectrometric investigation was performed. It should be noted that we consider the reaction kinetics of the title reaction to be well characterised by the MS studies of Masaki *et. al.*[14] and Eskola *et. al.*[19]. CH_2I was generated by the 248 nm photolysis of CH_2I_2 in the presence of O_2. All experiments were performed in a He bath gas at a total pressure of ~ 1 Torr. The experimental apparatus was very similar to that described in Chapter Two, and is only briefly discussed here. The reagent mixture, prepared on a gas handling line, was introduced into the reaction flow tube *via*

calibrated MFC's and through ¼" copper tubing. A KrF Excimer laser irradiated the reaction mixture (along the entire length of the reaction tube) with a 50 mJ pulse of 248 nm radiation. The reaction mixture effuses through the flow tube pinhole, into the vacuum chamber where the gas sample is photoionised by a VUV laser pulse, generated by frequency tripling the output of a Nd:YAG pumped Dye laser in Xe. Approximately 200 – 400 nJ pulse^{-1} of photoionisation radiation was generated, over a tuneable wavelength range of 113.6 – 120 nm. Effusion through the pinhole is rapid (~ 10000 s^{-1}) in relation to the chemical reaction (typically 100 – 1000 s^{-1}) and the concentration of species was approximately equal at the photoionisation region and in the reaction flow tube at any particular time, Δt. Ions, generated by the VUV radiation are introduced into the mass spectrometer by a series of electric fields and detected by an ion detector, which is interfaced to an ion counting card on the control PC. The maximum reaction time over which the chemical system can be studied is ~ 15 ms and is governed by the flow velocity in the reaction cell (~ 25 ms^{-1}). The photolysis (Excimer) and probe (Nd:YAG) lasers are triggered by a delay generator, which also triggers the ion counting card and an oscilloscope that monitors the analogue signal from the ion detector, allowing a discriminator level to be set for the detection of ions by the card on the PC. The time of flight (TOF) of an ion within the mass spectrometer is related to its mass by E. 4.5-1

$$TOF = \frac{\ell}{\sqrt{\frac{2E}{m}}} \qquad \text{E. 4.5-1}$$

where ℓ is the length of the flight chamber and E is the electric field strength of the mass spectrometer, and m is the mass of the ion.

Fig. 4.5-1 displays the mass spectrum of a $CH_2I_2/O_2/He/248$ nm reaction mixture obtained in this study. Initially, a photoionisation wavelength of 113.67 nm was employed (corresponding to a fundamental dye laser wavelength of 682.00 nm) in order to confirm the production of CH_2O. Formaldehyde has an ionisation potential of 10.88 eV[47] and cannot be detected by ionisation wavelengths longer than 114.11 nm therefore. At a fixed value of Δt, ion signals were detected at TOF's attributed to CH_2^+, CH_2O^+, I^+, CH_2I^+, I_2^+ and $CH_2I_2^+$. A weak ion signal was also detected at a TOF of ~ 11.8 μs, corresponding to $CH_3COCH_3^+$. A trace amount of acetone is always detected in the instrument due to contamination from leak testing and cleaning of the experimental apparatus. The spectrum displayed in Fig. 4.5-1 was used to calibrate the MS instrument, as given in Fig. 4.5-2.

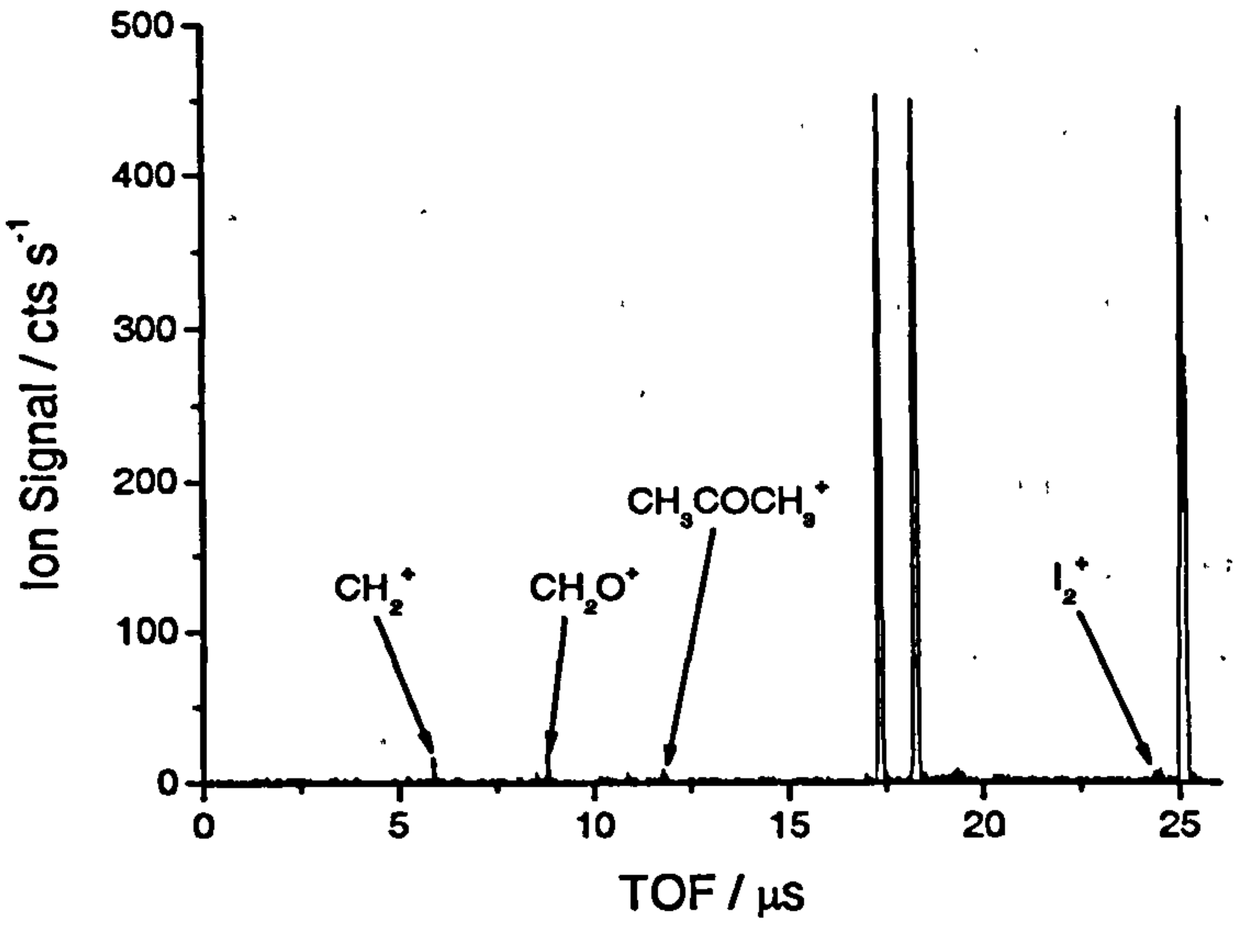

Fig. 4.5-1 – Mass spectrum of a CH_2I_2/O_2/He/248 nm reaction mixture. Experimental conditions: P = 1.1 Torr; T = 296 K; $[CH_2I_2] = 1.2 \times 10^{12}$ molecule cm^{-3}; $[O_2] = 7.6 \times 10^{14}$ molecule cm^{-3}; [He] = balance; P_{ex} = 50 mJ pulse^{-1}; λ_i = 113.67 nm; P_i = 5 mJ pulse^{-1}; Δt = 750 μs. Note that the largest peaks correspond to I^+, CH_2I^+ and $CH_2I_2^+$ in order of increasing TOF respectively. Some of the smaller peaks are labelled on the mass spectrum.

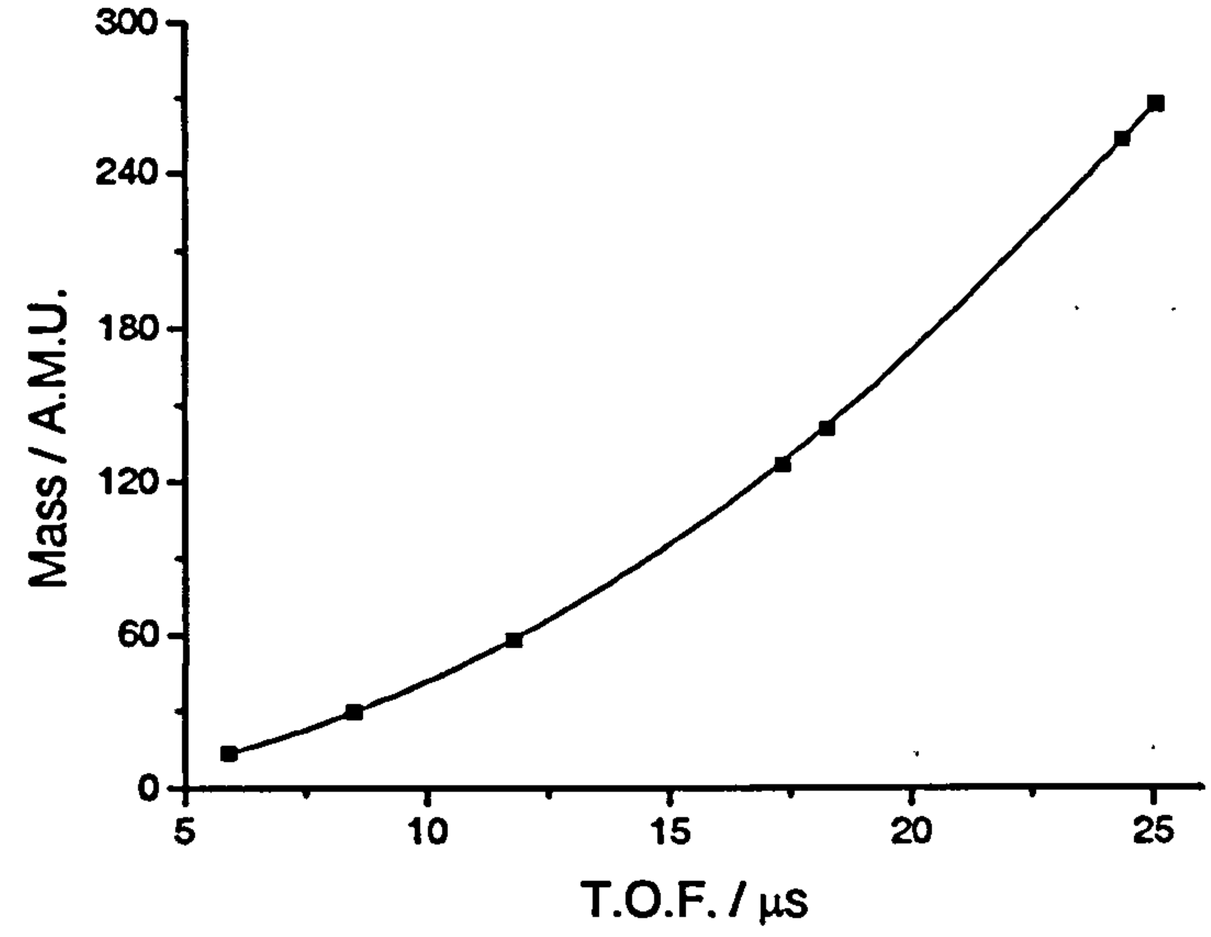

Fig. 4.5-2 – Calibration graph for the MS instrument. A simplified form of E. 4.5-1 is fit to the data: mass = $(TOF/a)^2 + b$, where a is an experimental constant and b is an offset term allowing for a non-zero intercept. From the fit, a = 1.529 ± 0.003 and b = -(1.19 ± 0.72) μs. The instrument was calibrated to the TOF of ions corresponding to CH_2, CH_2O, CH_3COCH_3, I, CH_2I, I_2 and CH_2I_2. The calibration graph is non-linear as the TOF of an ion is proportional to the square-root of its mass.

Experiments conducted for a photoionisation wavelength of 113.67 nm were subject to considerable interference from the photofragmentation of CH_2I_2 by the ionisation laser pulse, and informative kinetic experiments could not be performed. At wavelengths below 113.67 nm, CH_2^+, CH_2I^+ and I^+ are produced directly by the photofragmentation of CH_2I_2 and a large pre-Excimer laser background was observed for these species. However, the CH_2O ion signal was observed to increase after the photolysis pulse, as can be seen in Fig. 4.5-6, indicating that CH_2O is generated in the reaction system. Eskola *et. al.*[19] did not report the definitive assignment of CH_2O in their MS investigation, although a signal observed at $m/z = 30$ allowed an upper limit for the yield of CH_2O (originating from the $CH_2I + O_2$) reaction to be set at 33 %.

In this work (in addition to the species indicated in Fig. 4.5-1) small ion signals were observed at the notable masses of 46 ($CH_2O_2^+$), 128 (HI^+), and 143 (IO^+). In order to investigate the temporal profile of these species, the ionisation wavelength was increased to 118.33 nm (corresponding to a fundamental dye laser wavelength of 710 nm), where photofragmentation of CH_2I_2 was less significant. At this ionisation wavelength the resulting mass spectrum was again dominated by signals attributed to I, CH_2I and CH_2I_2. To investigate the reaction kinetics of CH_2I and I, experiments were performed where Δt (the delay between photolysis and ionisation lasers) was varied under identical experimental conditions, with the exception of $[O_2]$. A kinetic trace, observed at $m/z = 141$ is displayed in Fig. 4.5-3, showing the removal of CH_2I from the system.

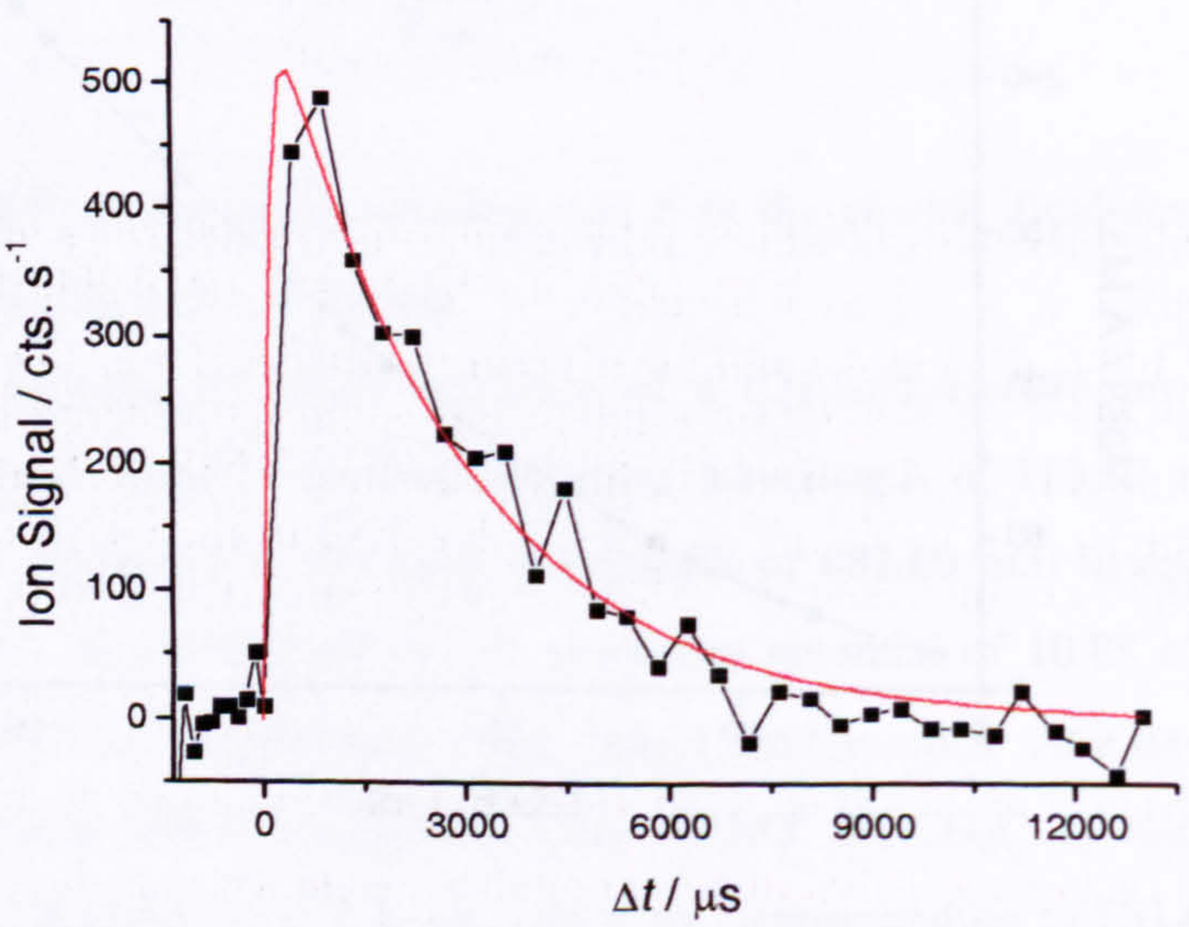

Fig. 4.5-3 – Kinetic trace recorded at $m/z = 141$ showing the removal of CH_2I in the reaction system. Note that a CH_2I^+ pre-Excimer laser background was observed (due to photofragmentation of CH_2I_2 by the ionisation laser) but has been subtracted from the kinetic trace in this figure. The solid red line is a fit of E. 4.3-1 to the kinetic trace, where k_{growth} is fixed to a value of 10000 s^{-1} (accounting for effusion through the pinhole). From the fit: $k_{loss} = (316 \pm 84)$ s^{-1}. Experimental conditions: $P = 1.1$ Torr; $T = 296$ K; $[CH_2I_2] = 1.19 \times 10^{12}$ molecule cm^{-3}; $[O_2] = 8.66 \times 10^{13}$ molecule cm^{-3}; [He] = balance; $\lambda_i = 118.33$ nm.

The pseudo-first-order rate of removal of CH_2I, k_{loss}, is displayed as a function of $[O_2]$ in the bottom panel of Fig. 4.5-4. From the linear fit, $k = (2.4 \pm 2.7) \times 10^{-12}$ $cm^3molecule^{-1}s^{-1}$, significantly larger but within statistical uncertainty of the previous MS[14,19] investigations. As stated, determining the rate coefficient for the reaction $CH_2I + O_2$ was not a principle aim of this study. In agreement with the findings of Eskola *et. al.*[19], the ion signal corresponding to a mass of 127 (I^+) was observed to increase at longer reaction times, over that initially generated by the Excimer laser. Kinetic traces showing the temporal profile of I atoms are displayed in Fig. 4.5-5 and the pseudo-first-order rates of formation determined from their kinetic analysis are given in the top panel of Fig. 4.5-4.

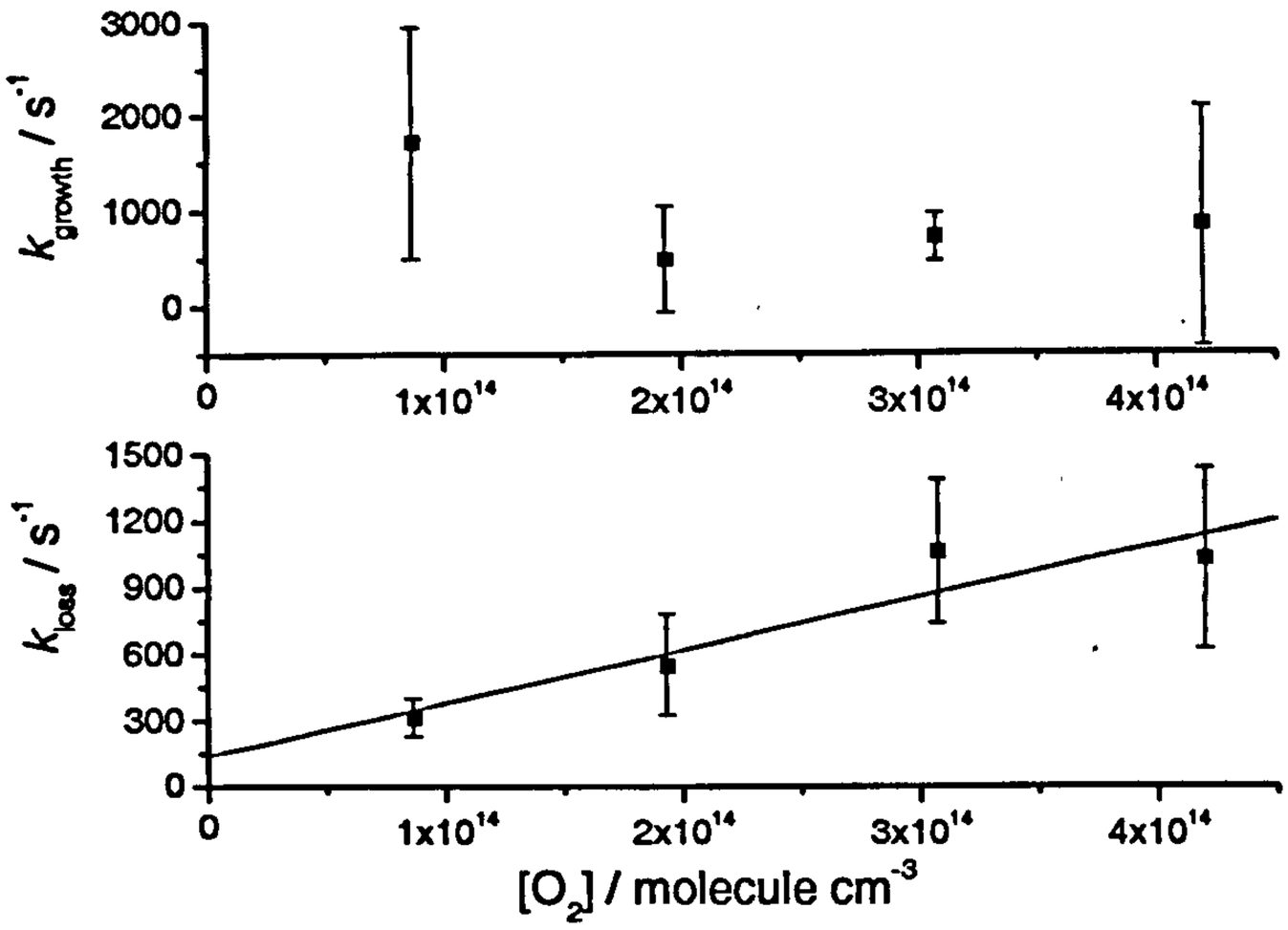

Fig. 4.5-4 – Bimolecular plots displaying the pseudo-first-order rates of formation of I (top panel) and removal of CH_2I as a function of $[O_2]$ in a $CH_2I_2/O_2/He/248$ nm reaction mixture. Error bars are the 2σ standard errors returned from fits to the appropriate exponential functions. No systematic relationship could be inferred between the rate of formation of I and concentration of O_2, largely because of the relatively high degree of experimental scatter (see Fig. 4.5.5). From the linear fit to the CH_2I data, $k(CH_2I + O_2) = (2.4 \pm 2.7) \times 10^{-12}$ $cm^3molecule^{-1}s^{-1}$. The experimental conditions are as previously indicated.

From the data presented in Fig 4.5-4, it can be seen that the I atom data are inconclusive. The pseudo-first-order rate of formation of I is of similar magnitude for all concentrations of $[O_2]$ and it cannot be determined if I atoms are formed directly from the reaction $CH_2I + O_2$ (as suggested by Eskola *et. al.*[19]) or from secondary chemistry within the system. However, a yield analysis of the peak I atom signal (in comparison to that generated by the Excimer laser, which will be equal to the initial concentration of CH_2I) shows that the conversion of CH_2I to I is high. Using values obtained from the fitting procedure, the average I atom yield was found to be (0.71 ± 0.47), in reasonable agreement with that determined by Eskola *et. al.*[19] (0.91 ± 0.34).

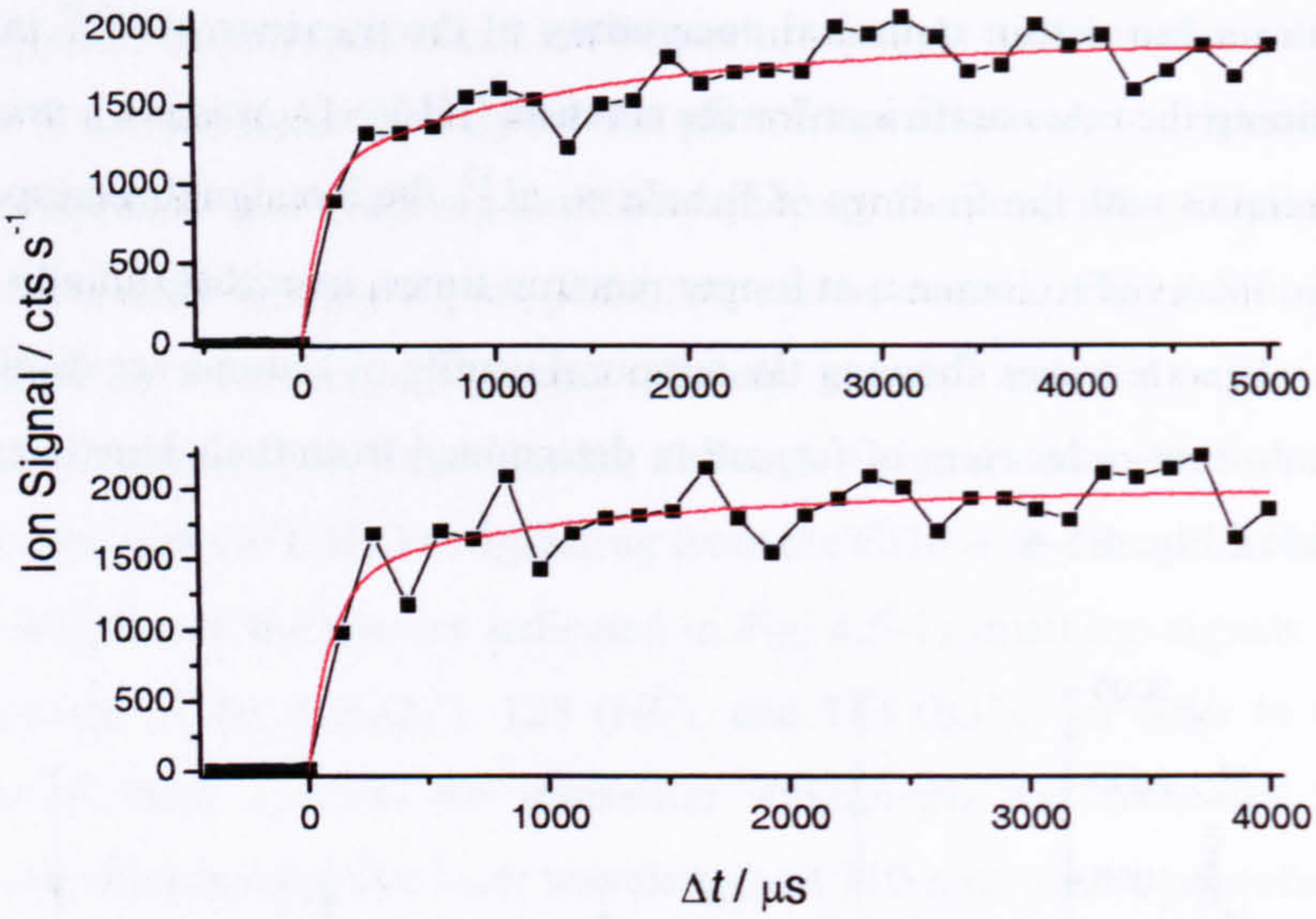

Fig. 4.5-5 – Kinetic traces displaying the photolytic, and secondary, formation of I atoms in the CH_2I_2/O_2/248 nm reaction system. The experimental data are fitted to a modified form of E. 5.3.2.1, allowing for the instant I atom signal generated by the photolysis of CH_2I_2. Note that the values returned from this fitting procedure allow the evaluation of the I atom yield. From the fittings, k_{growth} = (710 ± 252) s^{-1} (top panel) and (844 ± 1270) s^{-1} (bottom panel). Experimental conditions are the same as previously indicated with the exception, $[O_2]$ = 3.08 × 10^{14} molecule cm^{-3} (top panel) and 4.20 × 10^{14} molecule cm^{-3} (bottom panel).

In fact, it is this observation that leads us to the conclusion that the reaction I + CH_2O_2 → IO + CH_2O does not occur in the reaction system. If the reaction of CH_2I + O_2 were to generate I + CH_2O_2, which subsequently react to form IO + CH_2O, no I atom growth would be observed. Further, no co-product to I was observed in the experiment of Eskola *et, al.*[19] and we therefore conclude that I must be formed in a secondary process, involving CH_2IO_2. Note that the formation of IO almost certainly involves an I atom and that the reaction I + CH_2IO_2 → IO + CH_2IO does not result in the removal of I atoms (as they are catalytically regenerated by the dissociation of CH_2IO). Thus reactions of CH_2IO_2 can explain the formation of both I atoms and IO, without contradicting the experimental results of any of the CH_2I + O_2 studies. Although Eskola *et. al.*[19] reported the formation of I atoms on the same timescale as CH_2I removal in their system, this finding was based on the results of a single kinetic trace, which is not enough information to define a reaction mechanism. Further, IO was reported to appear on the same timescale as CH_2I removal and it has been definitively proved in this study that this is not the case. The formation of I atoms in the CH_2I + O_2 reaction system needs to be investigated more rigorously.

In addition to the detection of CH_2I, I and CH_2I_2 in the kinetic experiments, weak ion signals were also observed at m/z = 14, 46, 128, 143 and 254, probably corresponding to CH_2,

CH_2O_2, HI, IO and I_2 respectively. The signal from the species assumed to be HI, IO and I_2 were non-photolytic, increasing over the timescale of the experiment. No CH_2O was observed, consistent with an insufficient ionisation wavelength (118.33 nm) for its photoionisation. No signal was observed at m/z = 173, corresponding to the CH_2IO_2 peroxy radical. Fig. 4.5-6 displays the temporal evolution of the indicated species. Note that the kinetic traces displayed in the figure do not all correspond to the same kinetic experiment and it should not be attempted to correlate the temporal profiles of the species involved.

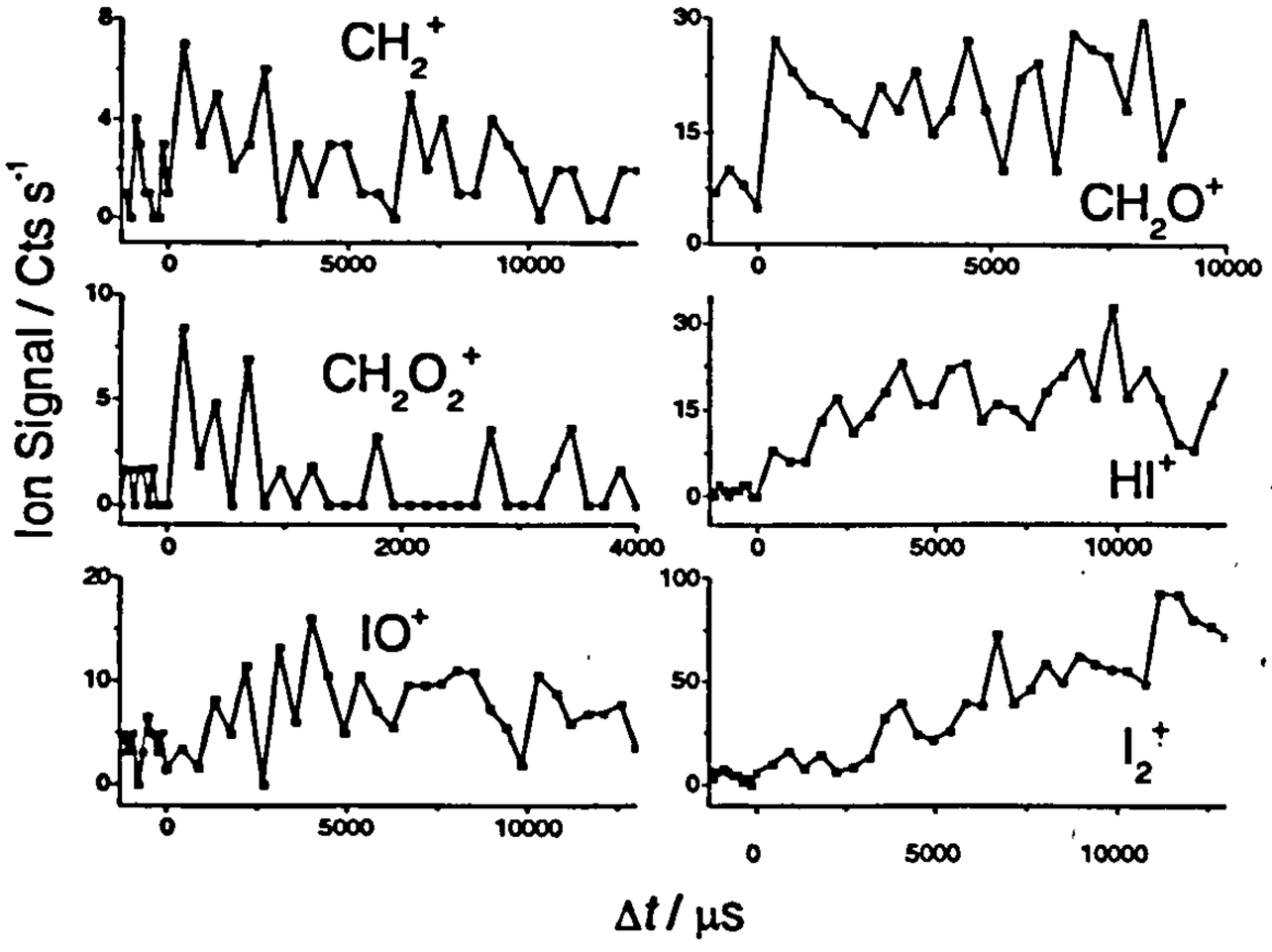

Fig. 4.5-6 – Kinetic traces obtained at m/z = 14, 30, 46, 128, 143 and 254. Note that the CH_2O kinetic trace was obtained at an ionisation wavelength of 113.67 nm. The concentration of CH_2I_2 was equal for all experiments, although $[O_2]$ was variable. No comparison between the temporal profiles of the different species should be drawn.

The first point to note about the kinetic traces displayed in Fig. 4.5-6 is that (with the exception of I_2) the peak signal of all species is very weak in comparison to that of CH_2I and I, crudely indicating that the concentration of these species are small. Analyses of the kinetic traces were not performed due to the small signals and high degree of scatter in the experimental data. However, the fact that the signal of all species is observed to increase after the Excimer laser pulse (Δt = 0) is indicative that they are all formed in the reaction system to some extent, and not by photofragmentation processes induced by the ionisation laser. The photolytic signal of CH_2 shows that, at 248 nm, a small fraction of CH_2I_2 undergoes multiphoton dissociation to CH_2 + I_2. The fact that CH_2 is present in the reaction system means that some CH_2O and IO formation can be expected from the reactions, $CH_2 + O_2 \rightarrow CH_2O + O$ and $O + CH_2I_2 \rightarrow IO + CH_2I$. However, it must be emphasised that the concentration of CH_2 will be very small and the concentrations of CH_2O and IO will be significantly smaller still (due to the appropriate branching ratios of the above reactions). The presence of a very weak signal at m/z = 46,

indicates that some isomeric form of CH_2O_2 is present in the reaction system. The signal is only present at very early reaction times and would appear to be photolytic in origin. The reason for this observation is unclear. Eskola *et. al.*[19] did not detect any isomeric form of CH_2O_2 in their experimental study. The presence of HI may indicate the presence of CHIO, potentially formed in a minor channel of the self-reaction of CH_2IO_2 (R4-4b), which can undergo unimolecular dissociation to CO + HI[48]. Eskola *et. al.*[19] also observed the formation of HI in their experiment but could not determine its kinetic formation. In the MS study of Masaki *et. al.*[14], HI was the only species (other than CH_2I and I) reported to be present in their reaction system. Although of very weak intensity, the presence of CH_2O and IO are not unexpected. The relatively intense I_2 signal is more difficult to explain. The formation rate of I_2 could not be determined as the asymptote of its exponential growth lies well outside the maximum experimental reaction time. However, assuming the I_2 signal cannot exceed half of the peak I signal, a lower limit to its pseudo-first-order rate of formation of 5 s^{-1} can be determined. Although small, this rate coefficient is orders of magnitude greater than that expected from the recombination of I atoms (or the reaction $I + CH_2I_2 \rightarrow CH_2I + I_2$) under the experimental conditions. Eskola *et. al.*[19] do not report the formation of I_2 in their study. The origin of I_2 is thus unclear, although it may be a marker of IO_x chemistry as speculated in the absorption experiment and discussed in section 4.3.2.1. In this study, no evidence of the CH_2IO_2 peroxy species at $m/z = 173$ was found. This may be because its ionisation potential is too high (note that HO_2 is not ionised beyond wavelengths of 109.4 nm)[47] or that it was completely photofragmented by the ionisation laser (CH_3O_2 may ionise at wavelengths as long as 168.7 nm)[49], which may be considered more likely.

4.5.1 Discussion

This results of this MS investigation are largely inconclusive. In fact, the only species forming in significant yield with respect to CH_2I in the reaction system was I atoms, with a yield of (71 ± 47) %. This result is in agreement with the findings of Eskola *et. al.*[19]. Although the appearance of I atoms approximately coincided with the removal of CH_2I, it could not be ascertained whether they are produced directly from the reaction $CH_2I + O_2$, or from secondary chemistry within the system. Only very weak signal was observed at $m/z = 46$, corresponding to CH_2O_2 – the presumable co-product of I atoms, and the temporal profile of this species did not coincide with that of I . In addition, CH_2O, HI, IO and I_2 were observed to form in the reaction system. No evidence for the CH_2IO_2 peroxy species was found. It is speculated that I atoms are most likely formed by secondary chemistry within the reaction system.

4.6 Reaction Products of $CH_2I + O_2$: Conclusions

This work represents the most comprehensive study to date of the reaction products of the $CH_2I + O_2$ reaction. By investigating multiple species by a variety of experimental techniques, a wealth of information has been obtained, providing insight into anomalies between the previous experimental studies. The most definitive conclusion found is that IO (and CH_2O) are not formed directly from the reaction of $CH_2I + O_2$, in contrast to the reports of two recent investigations[12,19]. However, IO and CH_2O display similar temporal behaviour in the reaction system and it is considered very likely that the two species are formed by the same (or closely related) reaction mechanisms. Specifically, after photolysing CH_2I_2 in the presence of a large excess of O_2 at 248 nm, the rate of formation of both species is found to be dependent upon the concentration of CH_2I_2 but only very weakly dependent on the concentration of O_2. When the concentration of O_2 is reduced, however, the rate of formation of IO is found to be more dependent on the experimental O_2 concentration. The rate of formation, and concentration, of CH_2O was found to be directly proportional to the concentration of photolysis products of CH_2I_2, indicating that I atoms, or the reaction products of the $CH_2I + O_2$ reaction, are involved in its formation. In observing the formation of CH_2O in reaction mixtures of $Cl_2SO/CH_3I/O_2/248$ nm, the rate of formation of CH_2O is considered to have a greater dependence on the concentration of CH_2I, than that of I atoms.

It has been definitively proved that IO is not produced by the reaction of O atoms (produced by the multi-photon dissociation of CH_2I_2) with CH_2I_2 in the reaction system. This finding was confirmed by adding large excesses of Br_2 and CF_3I to the reaction system, which had little effect on the observed IO (and BrO) production. Upon addition of Br_2 to the reaction system, the formation of BrO is observed in addition to that of IO, and it is considered that both species are formed by similar reaction mechanisms. No apparent pressure dependencies to the reaction kinetics of any species studied in this work were found.

In consideration of the previous literature, the reaction mechanisms of the $CH_2I + O_2$ reaction, previously postulated by Enami *et. al.*[12] and Eskola *et. al.*[19] can be discounted. Enami *et. al.*[12] reported that IO and CH_2O are formed directly in a bimolecular reaction mechanism by $CH_2I + O_2$. From the experimental findings of this work, this is clearly not the case. Eskola *et. al.*[19] conclude that CH_2I and O_2 react to produce a short lived CH_2IOO^* intermediate, which can decompose to several reaction products, predominantly $I + CH_2O_2$ (but also $IO + CH_2O$) in a unimolecular process, or be stabilised at high pressures forming the CH_2IO_2 peroxy radical. This mechanism can be discounted as, in such a system, the rates of formation of IO and CH_2O will be independent of the concentration of CH_2I_2 under pseudo-first-order conditions ($[O_2] >> [CH_2I_2]$).

The observation that I atoms are produced in the reaction system at high yield (~ 70 %) leads us to the conclusion that the $CH_2I + O_2$ reaction proceeds *via* one of two mechanisms:

$$CH_2I + O_2 \rightarrow CH_2IO_2 \qquad \text{(R4-2a)}$$

$$CH_2I + O_2 \rightarrow I + CH_2O_2 \qquad \text{(R4-2b)}$$

and that IO, CH_2O and I atoms can potentially be produced by the following reactions

$$CH_2IO_2 + CH_2IO_2 \rightarrow 2\,CH_2IO + O_2 \qquad \text{(R4-4a)}$$

$$CH_2IO \rightarrow CH_2O + I \qquad \text{(R4-5)}$$

$$I + CH_2IO_2 \rightarrow CH_2IO + IO \qquad \text{(R4-18)}$$

$$I + CH_2O_2 \rightarrow IO + CH_2O \qquad \text{(R4-16)}$$

Although we have no definitive evidence to suggest that the reaction of $CH_2I + O_2$ proceeds *via* either channel R4-2a or channel R4-2b, several pieces of information lead us to the conclusion that CH_2IO_2 formation is most likely, and that IO and CH_2O are therefore formed through reactions R4-4a, R4-5 and R4-18. (Note that an analogous reaction to R4-18 could also explain the formation of BrO, upon the addition of bromine to the reaction system). In the mass spectrometric investigation the formation of CH_2O_2 was not observed. Although the rates of formation of CH_2O and IO would display a dependence on the concentration of CH_2I_2 if produced by reaction R4-16, the net production of I atoms would not occur. Although CH_2IO_2 was not detected in the mass spectroscopic study (possibly due to its entire photofragmentation), the absorption spectrum of an unknown species in the 250 – 450 nm wavelength range obtained in this work is considered to be compatible with the known spectra of the CH_2ClO_2 and CH_2BrO_2 peroxy species, and was in good agreement (between 310 – 400 nm) with the previously reported CH_2IO_2 absorption spectrum[13]. The formation of this species was apparently independent of total pressure in the 4 – 760 Torr range. An attempt to verify the absorbing species as a direct product of the $CH_2I + O_2$ reaction was unsuccessful, although interference from multiple absorption and secondary chemistry may have been problematic. The only other species that this absorption could tentatively be assigned to are CH_2IO or CH_2O_2, neither of which are considered likely.

In an attempt to model the most important findings of this study, a complete quantitative consistency between the kinetic behaviour of IO, CH_2O and the species believed to be the CH_2IO_2 peroxy radical could not be achieved by a mechanism consisting of reactions R4-2a, R4-4a, R4-5 and R4-18, the largest discrepancy being found with regards to IO. By the confines of the experimental data we were able to set a limit range to the room temperature rate coefficient for reaction R4-4a of , $k = (6 - 12) \times 10^{-11}$ $cm^3 molecule^{-1} s^{-1}$, and a limit range of $k =$

$(1-6) \times 10^{-11}$ $cm^3molecule^{-1}s^{-1}$ for the room temperature rate coefficient for R4-18. The range of values for R4-4a are in good agreement with the estimated value of, $k = 9 \times 10^{-11}$ $cm^3molecule^{-1}s^{-1}$, reported by Sehested *et. al.*[13].

To confirm the predictions of this work, further experimental research should be carried out. First, a detailed spectroscopic and kinetic investigation of the absorbing species, speculated to be CH_2IO_2, should be performed. Secondly, the kinetics of IO in the $CH_2I + O_2$ reaction system should be investigated as a function of $[CH_2I]$ and [I]. If the reaction of $CH_2I + O_2$ does produce CH_2IO_2, it is interesting that the reaction is observed to be independent of pressure (although the reaction was found to have a negative activation energy by Eskola *et. al.*[19], supporting an association reaction mechanism). The presence of a heavy, electron rich I atom may provide a mechanism by which excess energy can be dissipated in the internal modes of CH_2IO_2, although we do not know whether this could explain the observed difference in the pressure dependencies of the $CH_2I + O_2$ and $CH_2Br + O_2$ reactions[19]. Future theoretical research could perhaps help resolve this discrepancy. In addition to the above findings, the formation of both OH and I_2 were observed after photolysing CH_2I_2 in the presence of O_2 at 248 nm, and the kinetic behaviour of these two chemical species within the reaction system should receive future experimental attention.

A final comment to make is that the chemistry occurring after the 193/248 nm photolytically initiated reaction of $CH_2I + O_2$ is clearly complex. Extrapolation of the findings of experimental investigations of reaction systems with high radical concentrations, and short photolysis wavelengths, to the chemistry of the atmosphere should be treated with caution. It is interesting that in the particle studies involving the photolysis of CH_2I_2 in the presence of O_3 (at wavelengths more appropriate to the troposphere), particle formation was only observed in the presence of both light and O_3. Particle formation involving iodine chemistry is thought to be initiated by the self-reaction of OIO, which in turn is controlled by the self-reaction of IO radicals. The fact that particle formation was only observed in the presence of O_3 essentially proves that IO is not formed directly from the reaction of $CH_2I + O_2$, and also that reactions R4-16 and R4-18 were not occurring at a significant enough extent to produce IO concentrations high enough to initiate particle formation. This observation supports our hypothesis that CH_2IO_2 is the major product of the $CH_2I + O_2$ reaction, and that CH_2IO_2 radicals are predominantly removed by self-reaction, producing CH_2O and I (and not IO).

4.7 Products of the $CH_2I + O_2$ Reaction: Atmospheric Implications

In considering the atmospheric implications of this work, the key question over the potential influence to particle formation in the MBL is whether $CH_2I + O_2$ reacts to form I + CH_2O_2, or CH_2IO_2. If I atoms are produced directly from the reaction, then the immediate

release of active iodine will result in enhanced formation of IO, OIO and particle production. Conversely, if CH_2IO_2 is formed, the release of active I into the atmosphere will be delayed and governed by the photolysis and reactions of CH_2IO_2. Particle formation, initiated by the OIO self-reaction, will therefore be less substantial if CH_2IO_2 is the reaction product of $CH_2I + O_2$. In order to demonstrate this effect, a simple model was FACSIMILE in created. The following processes are entered into the model and assigned the rate coefficients given in parentheses

$CH_2I_2 + h\nu$	$\rightarrow$	$CH_2I + I$	$(J = 4.24 \times 10^{-2}\ s^{-1})$
$I + O_3$	$\rightarrow$	$IO + O_2$	$(k = 1.2 \times 10^{-12}\ cm^3 molecule^{-1} s^{-1})$[45]
$CH_2I + O_2$	$\rightarrow$	CH_2IO_2	$(k = 1.5 \times 10^{-12}\ cm^3 molecule^{-1} s^{-1})$
	$\rightarrow$	$CH_2O_2 + I$	$(k = 1.5 \times 10^{-12}\ cm^3 molecule^{-1} s^{-1})$
$CH_2IO_2 + CH_2IO_2$	$\rightarrow$	$2\ CH_2O + 2\ I + O_2$	$(k = 9 \times 10^{-11}\ cm^3 molecule^{-1} s^{-1})$
$CH_2IO_2 + h\nu$	$\rightarrow$	I + products	$(J = 2.1 \times 10^{-2}\ s^{-1})$
$IO + IO$	$\rightarrow$	$OIO + I$	$(k = 3.5 \times 10^{-11}\ cm^3 molecule^{-1} s^{-1})$[7]
	$\rightarrow$	I_2O_2	$(k = 6.5 \times 10^{-11}\ cm^3 molecule^{-1} s^{-1})$[7]
$OIO + OIO$	$\rightarrow$	I_2O_4	$(k = 5 \times 10^{-11}\ cm^3 molecule^{-1} s^{-1})$[7]

The model was then run for two scenarios: that the reaction of $CH_2I + O_2$ produces either, i) CH_2IO_2 (in which case the, $I + CH_2O_2$ product channel is switched off) or, ii) $I + CH_2O_2$ (where the CH_2IO_2 product channel is turned off). All reactions were assigned the appropriate literature rate coefficients and photolysis rates were calculated using typical actinic flux data for the Mace Head site at 12.00 noon on 21st June. Note that the rate coefficient of the $CH_2I + O_2$ reaction is assigned the mean value of the MS determinations[14,19] ($k = 1.5 \times 10^{-12}\ cm^3 molecule^{-1} s^{-1}$) and the CH_2IO_2 self-reaction is assigned a rate coefficient of $9 \times 10^{-11}\ cm^3 molecule^{-1} s^{-1}$ (the mid-estimate value obtained in this study). Initial concentrations of 30 ppb and 20 ppt[9] for O_3 and CH_2I_2 respectively were entered into the model. At time zero, CH_2I_2 photolysis is initiated, and the resulting chemistry of IO and OIO is allowed to evolve as the gas mixture ages. The temporal profiles of IO and OIO, simulated for each scenario, are displayed in Fig. 4.7-1.

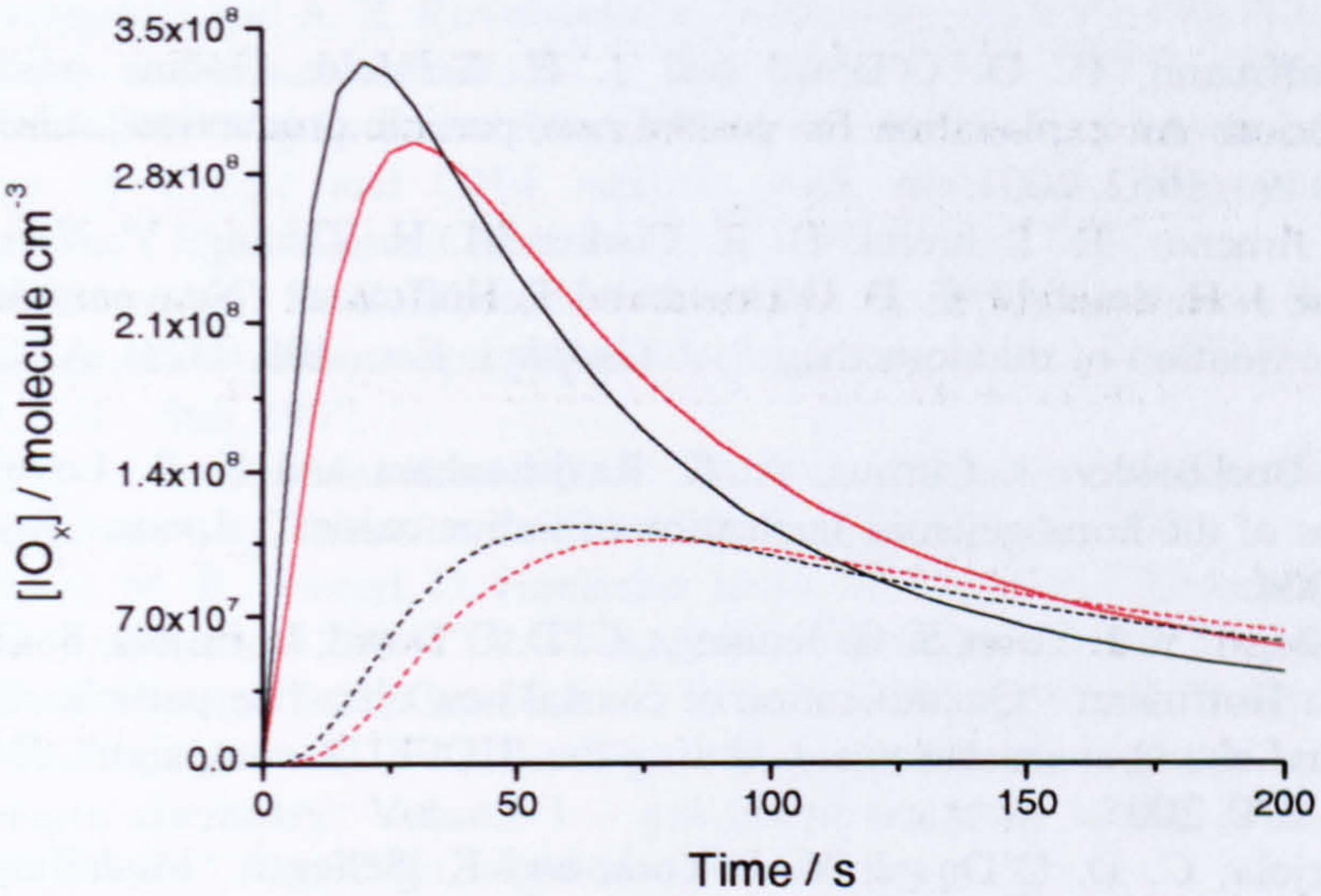

Fig. 4.7-1 – Atmospheric model simulations for the production of IO (solid lines) and OIO (broken lines) for the scenarios: i) $CH_2I + O_2 \rightarrow CH_2IO_2$ (red), and ii) $CH_2I + O_2 \rightarrow I + CH_2O_2$ (black). Note that for scenario (i) the model was also ran with the reaction $I + CH_2IO_2 \rightarrow IO + CH_2O + I$ ($k = 3 \times 10^{-11}$ $cm^3 molecule^{-1} s^{-1}$) included, which had no effect on the observed IO or OIO production as any I atoms within the system are rapidly consumed by O_3 (and not CH_2IO_2).

From the model output it can clearly be seen that the rates of production of IO and OIO are reduced, as are their peak concentrations, when CH_2IO_2 is defined as the product of the reaction $CH_2I + O_2$. Although the effects are relatively small, if the photolysis of CH_2IO_2 (or its reactions with other species, such as CH_3O_2 and NO) do not result in the immediate release of I atoms in the atmosphere, then the influence of this chemistry will be further exaggerated. This modelling exercise was not intended to quantify the effects of the $CH_2I + O_2$ reaction on the atmospheric chemistry of IO_x, merely to illustrate that including the formation, and subsequent chemistry, of CH_2IO_2 in atmospheric models (which is not currently the case) will have a noticeable effect on the production of IO, OIO, and particle production in the MBL under conditions where CH_2I_2 is the most important source of active iodine.

From the results obtained in this work we consider it almost certainly to be the case that the reaction of $CH_2I + O_2$ produces CH_2IO_2 in high (if not unity) yield. Future experimental research, as suggested throughout the course of this chapter, is required to substantiate this conclusion and better quantify the atmospheric significance of the CH_2IO_2 peroxy radical.

References

1. T. Hoffmann, C. D. O'Dowd and J. H. Seinfeld, "Iodine oxide homogeneous nucleation: An explanation for coastal new particle production", *Geophys. Res. Lett.*, 28, 1949 – 1952, 2001.
2. J. L. Jimenez, R. Bahreini, D. R. Cocker III, H. Zhuang, V. Varutbangkul, R. C. Flagan, J. H. Seinfeld, C. D. O'Dowd and T. Hoffmann, "New particle formation from photooxidation of diiodomethane", *J. Geophys. Res.*, 108 (D23), AAC5/1 – AAC5/25, 2003.
3. J. B. Burkholder, J. Curtius, A. R. Ravishankara and E. R. Lovejoy, "Laboratory studies of the homogeneous nucleation of iodine oxides", *Atmos. Chem. Phys.*, 4, 19 – 34, 2004.
4. K. Sellegri, Y. J. Yoon, S. G. Jennings, C. D. O'Dowd, L. Pirjola, S. Cautenet, H. Chen and T. Hoffmann, "Quantification of coastal new ultra-fine particles formation from in situ and chamber measurements during the BIOFLUX campaign", *Environ. Chem.*, 2, 260 – 270, 2005.
5. L. Pirjola, C. D. O'Dowd, Y. J. Yoon and K. Sellegri, "Modelling Iodine Particle Formation and Growth from Seaweed in a Chamber", *Environ. Chem.*, 2, 271 – 281, 2005.
6. A. Saiz-Lopez and J. M. C. Plane, "Novel iodine chemistry in the marine boundary layer", *Geophys. Res. Lett.*, 31, L04112, 2004.
7. A. Saiz-Lopez, J. M. C. Plane, G. McFiggans, P. I. Williams, S. M. Ball, M. Bitter, R. L. Jones, C. Hongwei and T. Hoffman, "Modelling molecular iodine emissions in a coastal marine environment: the link to new particle formation", *Atmos. Chem. Phys.*, 6, 883 – 895, 2006.
8. A. Saiz-Lopez, J. A. Shillito, H. Coe and J. M. C. Plane, "Measurements and modelling of I_2, IO, OIO, BrO and NO_3 in the mid-latitude marine boundary layer" *Atmos. Chem. Phys.*, 6, 1513 – 1528, 2006.
9. C. Peters, S. Pechtl, J. Stutz, K. Hebestreit, G. Honninger, K. G. Heumann, A. Schwarz, J. Winterlik and U. Platt, "Reactive and organic halogen species in three different European coastal environments", *Atmos. Chem. Phys.*, 5, 3357 – 3375, 2005.
10. L. J. Carpenter, W. T. Sturges, S. A. Penkett, P. S. Liss, B. Alicke, K. Hebestreit and U. Platt, "Short-lived alkyl iodides and bromides at Mace Head, Ireland: Links to biogenic sources and halogen oxide production", *J. Geophys. Res.*, 104, 1679 – 1689, 1999.
11. S. P. Sander, R. R. Friedl, A. R. Ravishankara, D. M. Golden, C. E. Kolb, M. J. Kurylo, R. E. Huie, V. L. Orkin, M. J. Molina, G. K. Moortgat and B.J. Finlayson-Pitts, *"Chemical Kinetics and Photochemical Data for Use in Atmospheric Studies: Evaluation Number 14"*, JPL Publication 02-25, February 1, 2003.
12. S. Enami, J. Ueda, M. Goto, Y. Nakano, S. Aloisio, S. Hashimoto and M. Kawasaki, "Formation of Iodine Monoxide Radical from the Reaction of CH_2I with O_2", *J. Phys. Chem. A.*, 108, 6347-6350, 2004.
13. J. Sehested, T. Ellermann and O. J. Nielsen, "A Spectrokinetic Study of CH_2I and CH_2IO_2 Radicals", *Int. J. Chem. Kin.*, 26, 259-272, 1994.
14. A. Masaki, S. Tsunashima and N. Washida, "Rate Constants for Reactions of Substituted Methyl Radicals (CH_2OCH_3, CH_2NH_2, CH_2I, and CH_2CN) with O_2", *J. Phys. Chem.*, 99, 13126 – 13131, 1995.
15. E. S. N. Cotter, N. J. Booth, C. E. Canosa-Mas and R. P. Wayne, "Release of iodine in the atmospheric oxidation of alkyl iodides and the fates of iodinated alkoxy radicals", *Atmos. Environ.*, 35, 2169 – 2178, 2001.
16. O. J. Nielson, J. Munk, G. Locke and T. J. Wallington, "Ultraviolet absorption spectra and kinetics of the self-reaction of CH_2Br and CH_2BrO_2 radicals in the gas phase at 298 K", *J. Phys. Chem.*, 95, 8714 – 8719, 1991.
17. J. J. Orlando, G. S. Tyndall and T. J. Wallington, "Atmospheric oxidation of CH_3Br: chemistry of the CH_2BrO radical", *J. Phys. Chem.*, 100, 7026 – 7033, 1996.

18. M. K. Gilles, A. A. Turnipseed, R. K. Talukdar, Y. Rudich, P. W. Villalta, L. G. Huey, J. B. Burkholder and A. R. Ravishankara, "Reactions of $O(^3P)$ with Alkyl Iodides: Rate Coefficients and Reaction Products", *J. Phys. Chem.*, **100**, 14005 – 14015, 1996.
19. A. J. Eskola, D. Wojcik-Pastuszka, E. Ratajczak and R. S. Timonen, "Kinetics of the reactions of CH_2Br and CH_2I radicals with molecular oxygen at atmospheric temperatures", *Phys. Chem. Chem. Phys.*, **8**, 1416 – 1424, 2006.
20. M. H. Harwood, J. B. Burkholder, M. Hunter, R. W. Fox and A. R. Ravishankara, "Absorption cross-sections and self-reaction kinetics of the IO radical", *J. Phys. Chem. A.*, **101**, 853 – 863, 1997.
21. P. Spietz, J. Gomez-Martin and J. P. Burrows, "Spectroscopic studies of the I_2/O_3 photochemistry", *J. Photochem. Photobiol., A.*, **176**, 50 – 67, 2005.
22. T. J. Dillon, M. E. Tucceri, D. Hoelscher and J. N. Crowley, "Absorption cross-section of IO at 427.2 nm and 298 K", *J. Photochem. Photobiol. A.*; **176**, 3 – 14, 2005.
23. Atkinson R., Baulch D.P., Cox R.A., Crowley J.N., Hampson R.F., Hynes R.G., Jenkin M.E., Rossi M.J. and J. Troe, "Evaluated kinetic and photochemical data for atmospheric chemistry: Volume I – gas phase reactions of O_x, HO_x, NO_x and SO_x species", *Atmos. Chem. Phys.*, **4**, 1461-1738, 2004.
24. S. Himmelmann, J. Orphal, H. Bovensmann, A. Richter, A. Ladstaetter-Weissenmayer and J. P. Burrows, "First observation of the OIO molecule by time-resolved flash photolysis absorption spectroscopy", *Chem. Phys. Lett.*, **251**, 330 – 334, 1996.
25. D. M. Joseph, S. H. Ashworth and J. M. C. Plane, "The absorption cross-section and photochemistry of OIO", *J. Photochem. Photobiol. A.*, **176**, 68 – 77, 2005.
26. Q. Zhang, U. Marvet and M. Dantus, "Concerted elimination dynamics from highly excited states", *Faraday Discuss.*, **108**, 63 – 80, 1997.
27. S. L. Baughcum and S. R. Leone, "Photofragmentation infrared emission studies of vibrationally excited free radicals CH_3 and CH_2I", *J. Chem. Phys.*, **72**, 6531 – 6545, 1980.
28. R. A. Alvarez and C. B. Moore, "Absolute yields of CO, CO_2, and H_2CO from the reaction $CH_2(X^3B_1) + O_2$ by IR diode laser flash kinetic spectroscopy, *J. Phys. Chem.*, **98**, 174 – 183, 1994.
29. M. A. Teruel, T. J. Dillon, A. Horowitz and J. N. Crowley, "Reaction of $O(^3P)$ with the alkyl iodides: CF_3I, CH_3I, CH_2I_2, C_2H_5I, 1-C_3H_7I and 2-C_3H_7I", *Phys. Chem. Chem. Phys.*, **6**, 2172 – 2178, 2004.
30. M. H. Harwood, D. M. Rowley, R. A. Cox and R. L. Jones, "Kinetics and mechanism of the BrO self-reaction: temperature- and pressure-dependent studies", *J. Phys. Chem. A.*, **102**, 1790 – 1802, 1998.
31. S. Enami, T. Yamanaka, S. Hashimoto, M. Kawasaki and K. Tonokura, "Direct Observation of Adduct Formation of Alkyl and Aromatic Iodides with Cl Atoms Using Cavity Ring-Down Spectroscopy", *J. Phys. Chem. A.*, **109**, 6066 – 6070, 2005.
32. S. Enami, T. Yamanaka, S. Hashimoto, M. Kawasaki and K. Tonokura, "Direct Observation of Adduct Formation of Alkyl and Aromatic Iodides with Cl Atoms Using Cavity Ring-Down Spectroscopy", *J. Phys. Chem. A.*, **109**, 6066 – 6070, 2005.
33. V. Catoire, R. Lesclaux, P. D. Lightfoot and M. Rayez, "Kinetic Study of the Reactions of CH_2ClO_2 with Itself and with HO_2 and Theoretical Study of the Reactions of CH_2ClO, between 251 and 600 K", *J. Phys. Chem.*, **98**, 2889 – 2898, 1994.
34. D. L. Singleton, G. Paraskevopoulos and R. S. Irwin, "UV Absorption cross-sections of the monomer and dimmer of formic acid", *J. Photochem.*, **37**, 209 – 216, 1987.
35. P. Aplincourt, E. Henon, F. Bohr and M. F. Ruiz-Lopez, "Theoretical study of photochemical processes involving singlet excited states of formaldehyde carbonyl oxide in the atmosphere", *Chem,. Phys.*, **285**, 221 – 231, 2002.
36. D. Cremer, E. Kraka and P. G. Szalay, "Decomposition modes of dioxiran, methyldioxirane and dimethyldioxirane – a CCSD(T), MR-AQCC and DFT investigation", Chem. Phys. Lett., 292, 97 – 109, 1998.

37. S. A. Kafafi, R. I. Martinez and J. T. Herron, "Molecular structure and energetics", in *Un-conventional Chemical Bonding*, vol. 6, Eds. J. F. Liebman and A. Greenberg, VCH Publishers, New York, 1988.
38. D. J. Clouthier and D. A. Ramsay, "The spectroscopy of formaldehyde and thioformaldehyde", *Ann. Rev. Phys. Chem.*, 34, 31 – 58, 1983.
39. J. E. Harrington and K. C. Smyth, "Laser induced fluorescence measurements of formaldehyde in a methane/air diffusion flame", *Chem. Phys. Lett.*, 202, 196 – 202, 1993.
40. R. J. H. Klein-Douwel, J. Luque, J. B. Jeffries, G. P. Smith and D. R. Crosley, "Laser-induced fluorescence of formaldehyde hot bands in flames", *App. Optics*, 39, 3712 – 3715, 2000.
41. Y. Yamasaki and A. Tezaki, "Non-linear pressure dependence of A-state fluorescence lifetime of formaldehyde", *Appl. Phys. B*, 80, 791 – 795, 2005.
42. G. H. Dieke and G. B. Kistiakowsky, "The Structure of the Ultraviolet Absorption Spectrum of Formaldehyde. I" *Phys. Rev.*, 45, 4 – 28, 1934.
43. M. M. Maricq, J. J. Szente, E. W. Kaiser and J. Shi, "Reaction of chlorine atoms with methylperoxy and ethylperoxy radicals", *J. Phys. Chem.*, 98, 2083 – 2089, 1994.
44. A. Aranda, G. Laverdet, G. Le Bras and G. Poulet, "Kinetic study of the CH_3O_2 + Br reaction at 298 K", *J. Chim. Phys.*, 95, 963 – 972, 1998.
45. M. Bilde and T. J. Wallington, "Atmospheric Chemistry of CH_3I: Reaction with Atomic Chlorine at 1 – 700 Torr Total Pressure and 295 K", *J. Phys. Chem. A.*, 102, 1550 – 1555, 1998.
46. NIST Chemical Kinetics Database: http://kinetics.nist.gov/kinetics/index.jsp
47. D. Shah, C. E. Canosa-Mas, N. J. Hendy, M. J. Scott, A. Vipond and R. P. Wayne, "Discharge-Flow Studies of the Kinetics of the Reactions of CH_3O with Cl, Br, I, ClO, BrO and IO Using Laser-Induced Fluorescence and Resonance-Fluorescence Detection", *Phys. Chem. Chem. Phys.*, 3, 4932 – 4938, 2001.
48. NIST Chemistry WebBook: http://webbook.nist.gov/chemistry/
49. I. Barnes, K. H. Becker and J. Starcke, "The gas-phase infrared spectra of formyl iodide and carbonyl iodide", *Chem. Phys. Lett.*, 246, 594 – 600, 1995.
50. Y. Cheung and W. Li, "A Gaussian-2 ab initio study of isomeric CH_3O_2 and $CH_3O_2^+$", *Chem. Phys. Lett.*, 223, 383 – 389, 1994.

Chapter Five: A Spectrokinetic Study of the CH_3I-Cl and ICH_2I-Cl Adducts

5.1 Introduction

Since chlorine atoms were highlighted as a potential oxidant in the marine boundary layer (MBL)[1] there have been numerous studies on their reaction with organic molecules[2-9]. The removal of saturated hydrocarbons from the troposphere is governed almost entirely by reaction with OH (and Cl) due to their relatively long photolysis lifetimes. The removal of alkyl iodides from the atmosphere, however, is thought to largely proceed *via* C-I bond cleavage initiated by solar radiation. The photolysis lifetime of the alkyl iodides ranges from a few minutes (CH_2I_2) to a few days (CH_3I)[10]. This photolysis is important due to the release of active iodine atoms into the MBL which can initiate catalytic O_3 depleting cycles (see Chapter One). Estimates of Cl atom concentrations in the atmosphere range from $10^2 - 10^5$ molecule cm^{-3} [11-13]. For a mid-estimate [Cl] value, the removal of CH_3I from the atmosphere by reaction with Cl is approximately an order of magnitude less efficient than that by reaction with OH, which itself only accounts for about 5 % of the total CH_3I removal[14]. This implies that towards the upper end of the [Cl] range, removal of CH_3I by reaction with Cl can be as important as that by reaction with OH, with a combined reactive loss of about 10 %. It has also been shown that reaction with Cl can become the predominant loss rate (more important than photolysis) for higher chain alkyl iodides, such as 1-C_3H_7I, in the atmosphere if the upper Cl atom concentration is assumed, due to the higher rate coefficients of these reactions[14]. In addition to knowledge of the atmospheric concentrations, two other factors are required in order to assess the atmospheric significance of the reaction of Cl atoms with the alkyl iodides, namely i) the rate coefficient of reaction under atmospherically relevant conditions, and ii) the mechanism and products of reaction.

The first kinetic study of the reaction of chlorine atoms with methyl iodide to appear in the literature was that by Kambanis *et. al.*[15]. The authors employed the very low pressure reactor (VLPR) technique with mass spectrometric detection of both reactants and products to determine the reaction kinetics. The reaction was studied over the temperature range 273 – 363 K at a total pressure of ~ 2 mTorr. A positive activation energy was found, yielding an Arrhenius relationship of $k(T) = (1.33 \pm 0.49) \times 10^{-11} \exp[-(690 \pm 120)/T]$ $cm^3 molecule^{-1} s^{-1}$. A quantitative conversion of Cl to HCl was observed suggesting that the reaction proceeds exclusively *via* a hydrogen atom transfer mechanism. The small, temperature-independent, kinetic isotope effect observed in the experiment ($k_H/k_D = 1.09 \pm 0.04$) was interpreted as evidence for the reaction proceeding *via* the formation of a CH_3I-Cl intermediate, which undergoes unimolecular dissociation at low pressure to yield HCl and CH_2I. A subsequent

theoretical paper from the same research group explored the formation of adducts in the reaction of Cl with HI, CH_3I and CH_3OCH_2I[16]. The paper predicts the formation of weakly bound adducts in all cases with standard enthalpies of adduct formation reactions at 298 K of -31.056, -52.409 and -51.337 kJ mol^{-1} respectively. All adducts involve two-centre three-electron interactions originating from charge transfer of electron density from non-bonding orbitals of iodine to bonding orbitals of the I-Cl bond, resulting in "a bond of significant covalent character". For all adducts, the I-Cl bond length is around 2.8 Å (~ 0.5 Å longer than in ICl), the R-I-Cl bond angle is found to be close to 80° and little distortion of the CH_3I molecule is observed. The authors note that spectroscopic studies of the adducts are required in order to determine their structures and verify the theoretical predictions.

The next significant study of CH_3I + Cl was that of Ayhens *et. al.*[17]. In that work, the reaction was studied by resonance fluorescence detection of Cl atoms over an extensive range of temperature (218 – 694 K) and pressure (5 – 500 Torr N_2). Between $363 < T < 694$ K the reaction was found to be pressure independent with a positive temperature dependence ($k(T) = 5.44 \times 10^{-11} \exp[-1250/T]$ $cm^3 molecule^{-1} s^{-1}$) and a significant kinetic isotope effect was observed (k_H/k_D = 4.3 and 3.6 at 373 and 419 K respectively). These results are strongly indicative that the reaction proceeds *via* a bimolecular H atom transfer mechanism, not involving the formation of an adduct, between 363 and 694 K. Over the $263 < T < 309$ K range, Cl atom regeneration was observed *via* a secondary process and was interpreted as evidence for the reversible formation of an adduct, which was further confirmed by the lack of a kinetic isotope effect on the overall reaction kinetics at room temperature. At temperatures below 250 K the reaction was observed to be pressure dependent, and proceed predominantly *via* adduct formation. At 218 K and 500 Torr > 99.4 % of the reactivity is attributed to adduct formation. According to Ayhens *et. al.*[17] the reaction mechanism can largely be described by the following reaction scheme

$$CH_2I + HCl \xleftarrow{k_{bi}} CH_3I + Cl \underset{k_{-a}}{\overset{k_a}{\rightleftharpoons}} (CH_3I\text{-}Cl)^* \xrightarrow{k_c[M]} CH_3I\text{-}Cl$$

where, k_{bi} is the bimolecular rate coefficient for the formation of CH_2I + HCl, k_a is the rate coefficient for adduct formation, k_{-a} is the rate of adduct decomposition back to reactants, and k_c is the pressure dependent rate coefficient of adduct stabilisation. The equilibrium constant for the process of adduct formation is given by $K_p = k_a/(k_{-a}RT) = \exp[(\Delta S/R)-(\Delta H/RT)]$, where ΔS

and ΔH are the entropy and enthalpy of adduct formation respectively. Ayhens *et al.*[17] determine the thermochemical parameters as ΔH^0_{298K} = (-53.6 ± 3.4) kJ mol^{-1} and ΔS^0_{298K} = (-88 ± 11) J mol^{-1} K^{-1}. The authors include a theoretical study of the CH_3I-Cl adduct and generally find very similar results to the study of Lazarou *et al.*[16]. Under typical MBL conditions of temperature and pressure, Ayhens *et al.*[17] concludes the total rate of reaction of CH_3I + Cl to be ~ 2.5×10^{-11} cm^{3}molecule^{-1}s^{-1}.

Goliff and Rowland[18] performed a product study of the methyl iodide + chlorine reaction by radiogas chromatography. In their study, CH_3I was reacted with ^{38}Cl (produced by the thermal neutron irradiation of gaseous $CClF_3$) and the products were monitored by gas chromatography. Although the quantification of inorganic products (HCl) could not be determined due to wall and exchange reactions, $CH_3{}^{38}Cl$ was detected with yields ranging from ~ 3 % at 343 K to ~ 10 % at 273 K. At 295 K no change in the $CH_3{}^{38}Cl$ yield was observed with increasing total pressure from 760 to 4000 Torr. The authors concluded that methyl chloride formation proceeds *via* either i) the direct substitution of Cl for I atoms or ii) the intramolecular rearrangement of a short-lived CH_3I-Cl intermediate.

The next chronological study of the CH_3I + Cl reaction, by Bilde and Wallington[19], involved FTIR detection of reactants and products at 1 and 700 Torr in a smog chamber. The reaction was observed to have a large kinetic isotope effect at 1 Torr and 295 K (k_H/k_D = 6) with a k_H rate coefficient of (9.0 ± 1.8) × 10^{-13} cm^{3}molecule^{-1}s^{-1}. In addition, the lack of any significant CH_3Cl production (< 4 %) and the effective 100 % conversion of CH_3I to CH_2Cl_2 ($CH_3I + Cl \rightarrow CH_2I + HCl$, $CH_2I + Cl_2 \rightarrow CH_2ICl + Cl$, $CH_2ICl + Cl \rightarrow CH_2Cl + ICl$, $CH_2Cl + Cl_2 \rightarrow CH_2Cl_2 + Cl$) were concluded by the authors to imply that at 1 Torr, the reaction of CH_3I + Cl proceeds exclusively *via* a bimolecular H atom abstraction mechanism (note that Cl_2 was used as the Cl atom source in their experiment). At 700 Torr total pressure the rate coefficient was observed to increase to (1.3 ± 0.4) × 10^{-12} cm^{3}molecule^{-1}s^{-1} and found to be independent of bath gas (N_2/O_2). In the study of Bilde and Wallington[19], the reaction kinetics is determined *via* monitoring the decomposition of CH_3I, in the constant presence of Cl atoms, over a timescale of minutes. Therefore, the much smaller rate coefficient obtained than in the study of Ayhens *et. al.*[17] is attributed to adduct formation, followed by a small fraction of unimolecular decomposition (~ 2 %) to products other than CH_3I + Cl. At 700 Torr the major products were observed to be CH_3Cl and CO, both of which displayed a complex dependence on [CH_3I]. The authors conclude that CH_3Cl is produced by two processes: i) the intramolecular rearrangement of the CH_3I-Cl adduct and ii) reaction of the CH_3I-Cl adduct with CH_3I. Under atmospherically relevant conditions an upper limit of 20 % is quoted for the CH_3Cl yield from the reaction of methyl iodide with chlorine atoms. The CO product is assumed to originate from oxidation of

formaldehyde by Cl ($CH_3I + Cl \rightarrow HCl + CH_2I$, $CH_2I + O_2 \rightarrow CH_2IO_2$, $2(CH_2IO_2) \rightarrow CH_2IO + CH_2IOOO$, $CH_2IO \rightarrow CH_2O + I$, $Cl + CH_2O + O_2 \rightarrow HCl + HO_2 + CO$).

Cotter *et. al.*[14] investigated the reaction of Cl atoms with a number of alkyl iodides, including CH_3I, by the fast-flow discharge flow technique coupled to resonance fluorescence detection of Cl atoms. The reaction of $CH_3I + Cl$ was studied at 298 K and between total pressures of 1.5 – 12 Torr (He). The authors found a pressure independent rate coefficient of, $k = (1.51 \pm 0.15) \times 10^{-12}$ $cm^3molecule^{-1}s^{-1}$ and concluded that the reaction proceeds *via* either direct hydrogen atom abstraction or the formation of a CH_3I-Cl adduct that is not stabilised to any significant extent over the range of experimental pressures (or that the reaction has already reached the high-pressure limit by 1.5 Torr).

Finally, two recent studies by Enami *et. al.*[20,21] reported the direct observation of a number of RI-Cl (R = CH_3, CH_3CH_2, CH_2Cl, CH_2Br, CH_2I, *n*-C_3H_7, *n*-C_4H_9, *cyclo*-C_6H_{11}, C_6H_5, C_6F_5 and *p*-$CH_3C_6H_4$) adducts by CRDS. No adduct formation was observed for the reaction of Cl atoms with CF_3I, CH_3Br or C_6H_5Br. The absorption cross-section of some of the adducts were reported at four wavelengths between 405 – 532 nm. For the CH_3I-Cl and ICH_2I-Cl adducts the absorption maxima were found to be at 405 nm with absorption cross-sections of $2.1 \times 10^{-17}cm^2molecule^{-1}$ and 4.7×10^{-18} $cm^2molecule^{-1}$ respectively. The reaction kinetics of the $CH_3I + Cl$ reaction were investigated at 250 K between total pressures (N_2) of 25 – 125 Torr and reasonable agreement was found with the results of Ayhens *et. al.*[17]. On addition of 5 – 10 Torr O_2, no additional removal of the adduct was observed, indicative of no reaction between the CH_3I-Cl adduct and molecular oxygen. Theoretical calculations on the CH_3I-Cl adduct were in accord with the previous theoretical studies[16,17], and the observed absorption was assigned to the red end of the $3^2A' \leftarrow 1^2A'$ and $4^2A' \leftarrow 1^2A'$ electronic transitions originating at 339.32 and 307.06 nm respectively. The two electronic transitions are assigned to σ-σ^* and σ^*-σ^* transitions in the I-Cl bond. Very recently, the CH_3I-Cl adduct has received experimental investigation by Wine *et. al.*[22] although the results are unpublished at the time of writing.

Although there have been no kinetic investigations of the reaction of chlorine atoms with diiodomethane (probably due to its atmospheric insignificance as a result of the short photolysis lifetime of CH_2I_2) there have been two notable studies on the reaction of Cl atoms with chloroiodomethane (CH_2ICl). Bilde *et. al.*[23] studied the reaction by two experimental techniques: i) laser flash photolysis coupled with resonance fluorescence detection of Cl atoms, and ii) FTIR detection of reactants and products in a continuous photolysis smog chamber. Both techniques found the rate coefficient to be (largely) independent of total pressure (5 – 700 Torr N_2/O_2) with a room temperature rate coefficient of 8.5×10^{-11} $cm^3molecule^{-1}s^{-1}$. Employing the former technique, the reaction was observed to have a negative temperature dependence over the range 206 – 432 K with an Arrhenius expression $k(T) = 4.4 \times 10^{-11} \exp(195/T)$ $cm^3molecule^{-1}s^{-1}$. The FTIR-smog chamber study included a product analysis, which determined an effective

100 % yield of CH_2Cl_2. This result implied that the mechanism of reaction was either direct halogen substitution or iodine atom transfer to form ICl + CH_2Cl (which will react with Cl_2 to form CH_2Cl_2). By adding varying amounts of O_2 to the system the authors showed that the yield of CH_2Cl_2 was directly proportional to the ratio $[Cl_2]/[O_2]$, indicating that the mechanism proceeds *via* I atom transfer (as CH_2Cl reacts with O_2 to form CH_2ClO_2, rather than with Cl_2 to form CH_2Cl_2). An upper limit of 8 % was attributed to the direct halogen substitution reaction, with the remainder being attributable to ICl + CH_2Cl formation. The experimental findings were rationalised by the formation of a CH_2ClI-Cl adduct (to explain the high rate coefficient) whose fate is decomposition to ICl + CH_2Cl, rather than back to reactants (or HCl + CHICl) on energetic grounds. The ICl forming channel is not energetically feasible for the reaction of other alkyl iodides with Cl, perhaps with the exception of CH_2I_2[24] – see section 5.5. With regards to atmospheric relevance, the authors conclude that for the higher end of reported Cl atom concentrations, the loss of CH_2ICl by reaction with Cl can compete with photolysis.

The second study of the reaction of chloroiodomethane with Cl was a combined experimental and theoretical investigation[25]. Experimentally the reaction was studied by the VLPR technique coupled to mass spectrometric analysis of reactants and products. The reaction was found to be independent of temperature (273 – 363 K) with a rate coefficient of $(3.13 \pm 0.27) \times 10^{-11}$ $cm^3 moloecule^{-1} s^{-1}$ at total pressures of 0.6 – 1.5 mTorr (He). The rate of formation of ICl was found to be equal to the rate of loss of Cl, indicating that it is formed directly by the reaction mechanism, and no CH_2Cl_2 was observed suggesting that the reaction does not proceed *via* halogen atom substitution. The theoretical investigation derived findings largely in accord with other RI-Cl adducts: an I-Cl bond length of 2.738 Å and a C-I-Cl bond angle of 76.21°. The adduct RI-Cl bond enthalpy was calculated as 54.8 kJ mol^{-1} and the 298 K enthalpy of adduct formation was calculated to be 79.1 kJ mol^{-1}. The authors conclude that for the reaction of CH_2ICl with Cl atoms, the ICl + CH_2Cl reaction pathway becomes energetically accessible and that dissociation of the CH_2ClI-Cl adduct to ICl + CH_2Cl, rather than HCl + CHICl, is favoured on entropic grounds. Reaction scheme, S5-2 summarises the conclusions. The scheme can explain the discrepancy between the rate coefficients obtained in the two studies of the CH_2ICl + Cl reaction (due to the higher pressures employed in the study of Bilde *et. al.*[23]) and also the lack of agreement with the temperature dependencies, as the internal energy distribution of the CH_2ClI-Cl adduct may have been non-thermal in the VLPR study (due to the low pressure of the experiment) resulting in a reduced temperature dependence to its rate of dissociation.

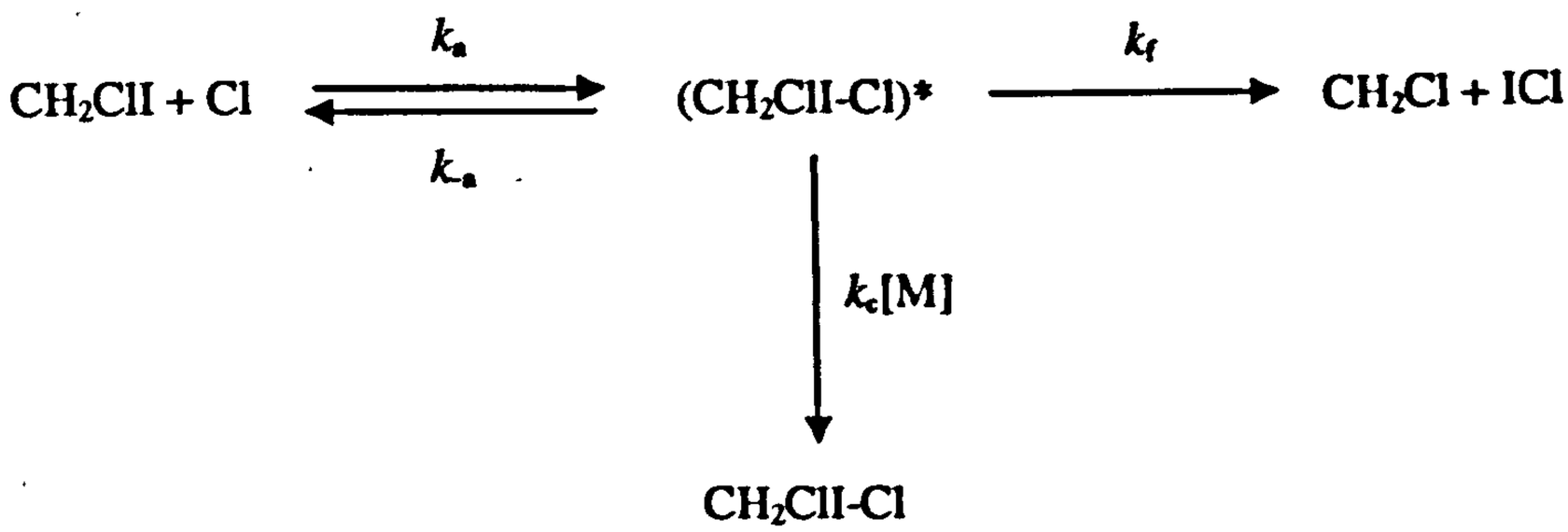

In summary, there is enough disagreement within the literature over the reaction kinetics of the reaction of atomic chlorine with methyl iodide; particularly with respect to the reaction products and fate of the CH_3I-Cl adduct, to warrant further experimental investigation. As there have been no kinetic studies of the reaction of chlorine atoms with diiodomethane, there is clearly scope to investigate the reaction kinetics, mechanism and products of this reaction (despite the lack of atmospheric significance) to further elucidate the reaction routes by which the alkyl iodides can react with atomic chlorine. In this study, we report the direct detection of the CH_3I-Cl and ICH_2I-Cl adducts for the first time by laser induced fluorescence (LIF). The reaction kinetics of the reactions of CH_3I and CH_2I_2 with Cl have been determined at ~ 206 K and 296 K, providing further insight into the mechanism of Cl + RI reactions. LIF excitation spectra, dispersed fluorescence spectra and fluorescence lifetime and quenching measurements of the two adducts are reported, providing useful information to further probe the internal energy distributions and electronic states of these interesting molecules. A detailed comparison to the existing literature is given.

5.2 Experimental

As described in the previous chapter, fluorescence from the chloro-iodomethane adduct was observed in an experimental system arranged for the detection of CH_2O by LIF. The experimental apparatus employed in the work discussed in this chapter is therefore essentially the same as previously outlined. For all experiments, chlorine atoms were generated *via* the 248 nm photolysis of thionyl chloride (Cl_2SO). At 248 nm, the major photolysis channel of thionyl chloride yields Cl atoms and ClSO radicals (96.5 %), although a minor channel also produces SO radicals and molecular chlorine[26]. It is believed that a small fraction of the internally excited ClSO radicals may further dissociate to Cl and SO[27]. As the photolysis wavelength is near the absorption maxima of CH_3I ($\sigma_{(248.4\ nm)} = 8.64 \times 10^{-19}$ $cm^2 molecule^{-1}$)[28]

and CH_2I_2 ($\sigma_{(248.4\ nm)} = 1.57 \times 10^{-18}$ $cm^2 molecule^{-1}$)[28] a low photolysis power of ~ 2 mJ $pulse^{-1}$ was employed for kinetic experiments, ensuring minimum generation of radical species from the photolysis of methyl iodide (< 0.5 %) and diiodomethane (< 1 %). For spectroscopic experiments, where the chemistry occurring is of less significance, the photolysis energy was typically 50 mJ $pulse^{-1}$.

Although LIF from the adducts was observed over the entire useful wavelength range of the probe laser dye (~ 345 – 375 nm), an excitation wavelength of ~ 360 nm was chosen for the majority of experiments (and ~ 365 nm for the ICH_2I-Cl adduct) as the probe laser energy (and adduct fluorescence) was most intense and contamination of the LIF signal from CH_2O was avoided (for experiments containing O_2). Similarly to LIF detection of CH_2O, the probe laser pulse was not completely removed by the Perspex filter and remained a background interference, decreasing the instrumental sensitivity. As the fluorescence lifetimes of the adducts were found not to be significantly longer than the pulse-width of the probe laser (see section 5.4.3), the fluorescence collection gate on the oscilloscope was placed over the entire probe laser pulse, where most of the adduct fluorescence was occurring. However, fluorescence from the adducts (particularly the CH_3I-Cl adduct) was extremely intense and generally much more so than the probe laser background. In fact, the observed fluorescence was so intense that the PMT had to be operated at relatively modest voltages (1100 – 1300 V) to avoid electronic saturation. Fig. 5.2-1 displays a typical kinetic trace of the CH_3I-Cl adduct.

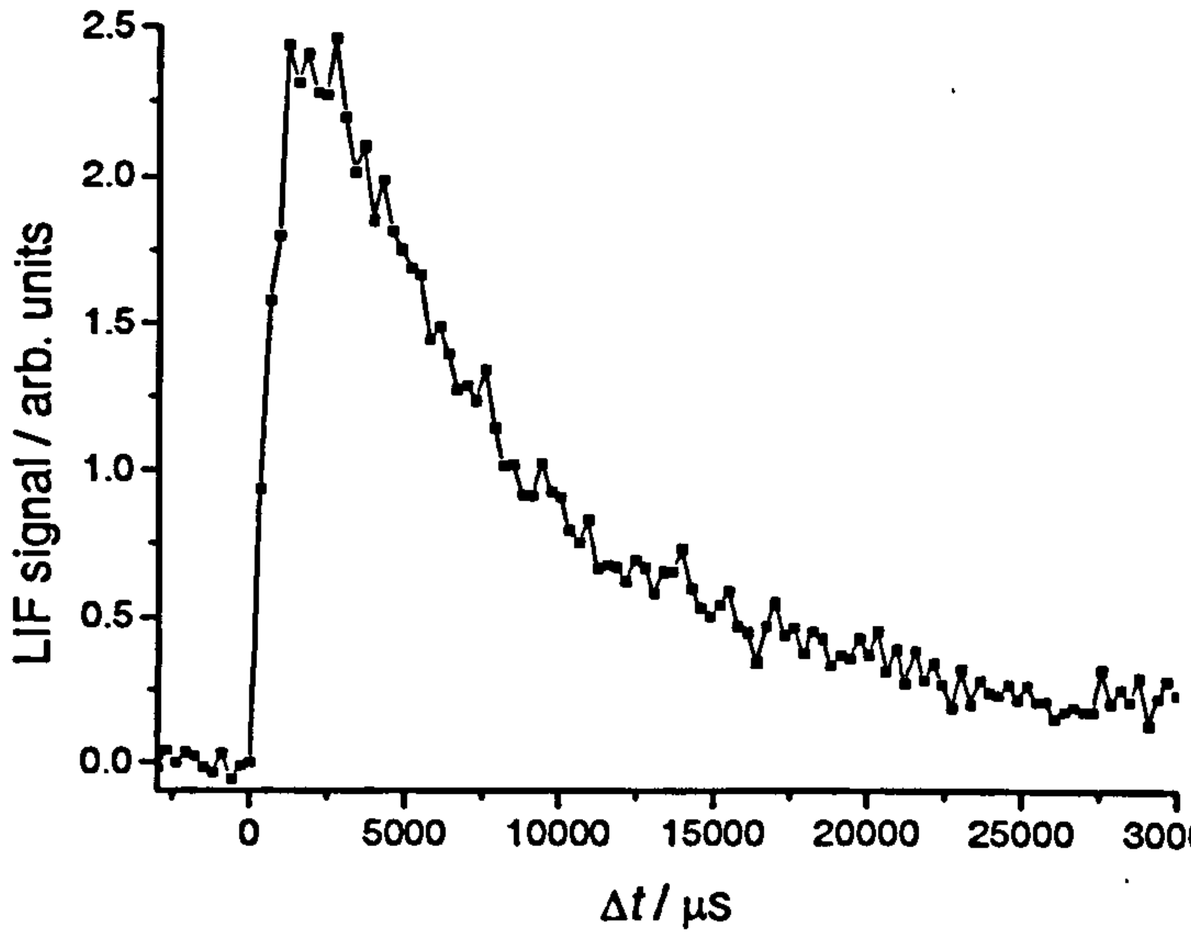

Fig. 5.2-1 – Kinetic trace of the CH_3I-Cl adduct. Experimental conditions: $T = 202$ K, $P = 70.8$ Torr; $[Cl_2SO] = 6.8 \times 10^{12}$ molecule cm^{-3}; $[CH_3I] = 8.01 \times 10^{13}$ molecule cm^{-3}; $[N_2]$ = balance; $\lambda_{pr} = 360.57$ nm, $F = 2.61 \times 10^{15}$ photons cm^{-2}.

The *S/N* ratio of the apparatus was determined by dividing the peak fluorescence signal from ten randomly selected kinetic traces (similar to that displayed in Fig. 5.2-1) by the 2σ standard deviation of the pre-Excimer laser background. Dividing the calculated initial Cl atom concentration (derived from the product of laser fluence, *F*, concentration and absorption cross-section of Cl_2SO [$\sigma_{(248.4\ nm)} = 7.02 \times 10^{-18}$ $cm^2 molecule^{-1}$][29]) by the experimental *S/N* ratio gives the detection limit of the apparatus for the CH_3I-Cl adduct of $(3.7 \pm 2.0) \times 10^9$ molecule cm^{-3} for an average of fifteen laser shots (assuming 100 % of Cl atoms are converted into the adduct). In itself, this represents a very sensitive detection limit but considering that the detection efficiency could be significantly enhanced by more effective filtering of the probe-laser background, increased probe laser power and a more sophisticated optical arrangement for fluorescence collection, it is entirely feasible that this detection limit could be improved by two orders of magnitude or more.

Fluorescence from the ICH_2I-Cl adduct was considerably weaker than that from its methyl iodide analogue (Fig. 5.2-2), consistent with the di-substituted alkyl iodide adduct having a weaker absorption cross section[20]. The detection limit of the apparatus with respect to ICH_2I-Cl was estimated at $(4.7 \pm 3.3) \times 10^{10}$ molecule cm^{-3} for an average of 25 laser shots.

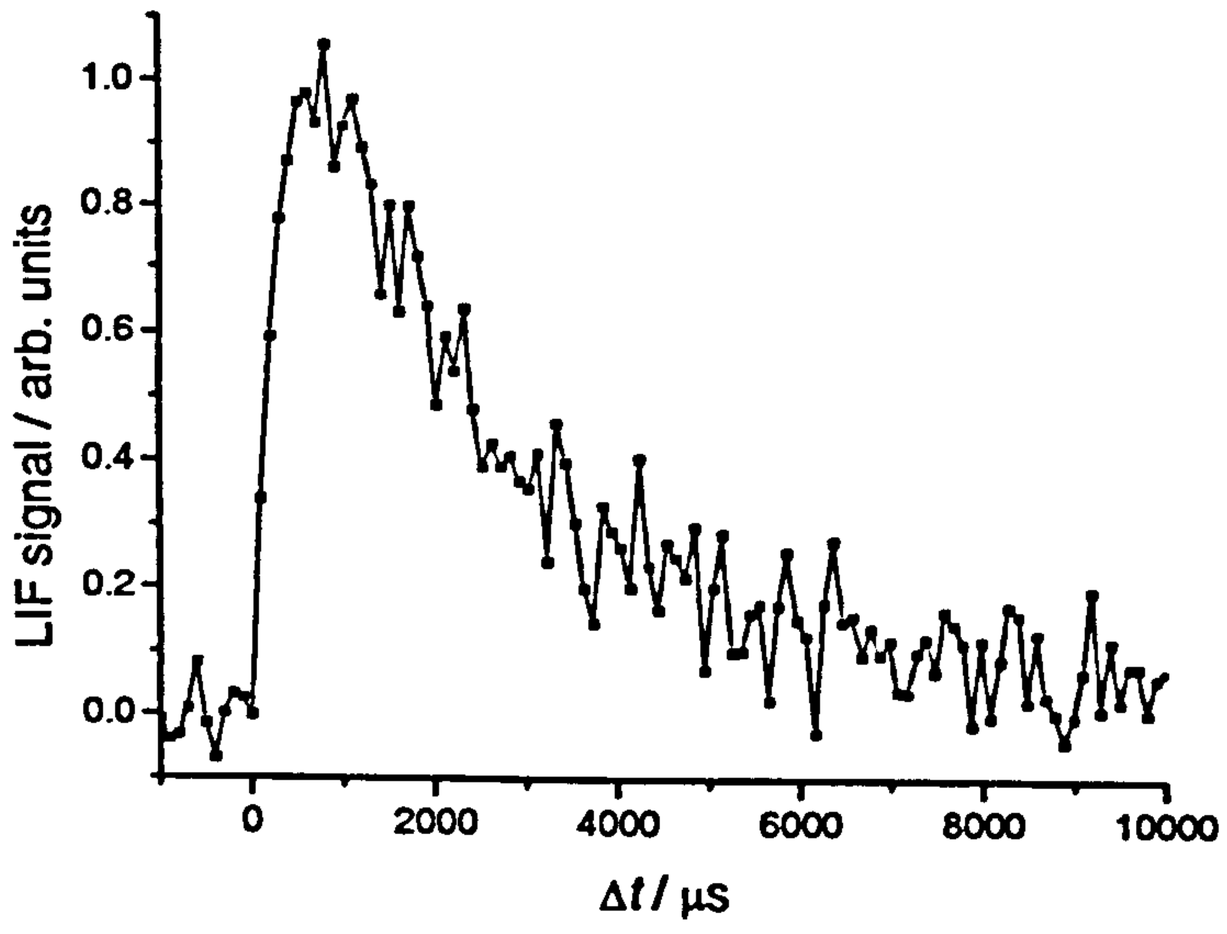

Fig. 5.2-2 – Kinetic trace of the ICH_2I-Cl adduct. Experimental conditions: $T = 202$ K; $P = 100.5$ Torr; $[Cl_2SO] = 1.66 \times 10^{13}$ molecule cm^{-3}; $[CH_2I_2] = 6.29 \times 10^{13}$ molecule cm^{-3}; $[N_2]$ = balance; $\lambda_{pr} = 365.57$ nm; $F = 4.17 \times 10^{15}$ photons cm^{-2}.

The adduct reaction kinetics were observed to be independent of laser pulsed repetition frequency (PRF) and experiments were typically conducted at 5 Hz. Each recorded kinetic trace was the average of several individual traces repeated in a cycle. The temporal range over which

a kinetic trace is recorded can be selected according to what information is desired (growth or decay kinetics).

The spectroscopic experiments were generally performed at a PRF of 10 Hz. To record a LIF spectrum, the dye laser was manually programmed to scan over a selected wavelength range at a constant scan speed (typically 0.03 nm s^{-1}) and the LIF signal was recorded at a fixed delay time, Δt, between photolysis and probe lasers. All experimental conditions remained constant, with the exception of excitation energy. The probe laser power was monitored as a function of wavelength so that the LIF signal could be normalised for laser power. Background LIF spectra (in the absence of iodide, chloride or excimer laser) were also obtained to ensure that the observed fluorescence was solely attributable to that of the adduct. Adduct dispersed fluorescence spectra were obtained with the incorporation of a monochromator (Applied Photophysics, f/3.4) to the experimental apparatus, which was situated on the cell LIF detection port, prior to the PMT. The monochromator grating could not be electronically controlled and had to be manually scanned by hand. To record a dispersed fluorescence spectrum, the adduct was excited at a particular wavelength and Δt and the fluorescence intensity was monitored as a function of wavelength, by altering the position of the monochromator grating. The PMT voltage was increased to compensate for the loss of photons inside the monochromator. The monochromator wavelength was calibrated relative to the probe laser radiation, assuming linear wavelength dependence. Fluorescence lifetime and quenching data were collected by recording the temporal profile of adduct fluorescence on the oscilloscope as a function of total reaction cell pressure. The temporal profile of the probe laser pulse was also recorded for its deconvolution from adduct fluorescence.

Thionyl chloride (Aldrich, 99+ %), methyl iodide (Aldrich, 99 %) and diiodomethane (Aldrich, 99 %) were purified by several freeze-pump-thaw cycles at 77 K prior to preparing the appropriate gas mixtures in 5 litre glass bulbs. The bulbs were completely covered in black tape to avoid photolytic degradation of the precursors and, with the exception of Cl_2SO, reagent mixtures were prepared daily. Nitrogen (Air Products, Premier grade) and He (BOC, CP grade) were administered directly from their gas cylinders without purification. All concentrations were evaluated by means of the individual gas flow rates, through calibrated MFC's, and total reaction cell pressure and temperature. Although photolysis of the iodide precursors was minimal in the majority of experiments, all concentrations were corrected for photolysis prior to kinetic analyses. The low temperature experiments were performed by enclosing the reaction cell core in an insulated jacket filled with a cardice/propan-2-ol slurry. Temperature measurements were made with a K-type thermocouple located near to the centre of the reaction cell which was calibrated both at room temperature (relative to a standard Hg thermometer) and at 195 K by directly immersing the thermocouple probe in a cardice/propan-2-ol slurry.

5.3 Reaction Kinetics of $CH_3I + Cl$

As briefly discussed in Chapter Four, the intense fluorescence observed from irradiating $CH_3I + Cl$ mixtures in the 350 – 360 nm region could almost certainly be inferred to originate from the CH_3I-Cl adduct. However, in order to definitively assign the observed LIF to adduct formation a kinetic investigation was required. Studying the reaction of methyl iodide and chlorine atoms *via* direct observation of the CH_3I-Cl adduct provides complementary data to the existing literature. If agreement is found between the results of the reaction kinetics determined by following the temporal profile of Cl atoms or CH_3I-Cl for example then the mechanism of reaction can be substantiated. In this study we have chosen to study the reaction kinetics of the $CH_3I + Cl$ reaction at two temperatures: i) ~ 206 K, where *irreversible* adduct formation should occur and ii) 296 K, where reversible adduct formation should be observed. For the kinetic analysis of the experimental data outlined below, it is assumed that the $CH_3I + Cl$ reaction proceeds *via* the mechanism proposed by Ayhens *et. al.*[17] (S5-1), due to the extensive range of conditions investigated (and quality of data obtained) in that study. Further, reaction scheme, S5-1 is consistent with the bulk of the existing literature on the $CH_3I + Cl$ reaction.

5.3.1 Kinetic Treatment of the Experimental Data

At 206 K, the kinetic system of $CH_3I + Cl$ is relatively simple as the bimolecular reaction (k_{bi}) and adduct dissociation (k_{-a}) are negligible in comparison to the association reaction, k_a. Extrapolation of the Arrhenius parameters obtained in the study of Ayhens *et. al.*[17] yields a bimolecular rate coefficient of $k_{bi(206\ K)} = 1.26 \times 10^{-13}$ $cm^3 molecule^{-1} s^{-1}$. At 5 Torr total pressure (N_2) this corresponds to < 4 % of the association reaction rate coefficient (Table 5.3-1) and at 500 Torr < 0.5 % of the total reactivity can be ascribed to the bimolecular reaction. Calculation of the dissociation rate coefficient, using the equilibrium data provided by Ayhens *et. al.*[17], shows that dissociation of the CH_3I-Cl adduct back to reactants is also negligible at low temperature ($k_{-a(206\ K)} = 0.8 - 7.2\ s^{-1}$ over the range of 5 – 500 Torr). Therefore, in the kinetic analysis of the CH_3I-Cl adduct at 206 K the following processes need only be considered

$CH_3I + Cl + M$	→	CH_3I-Cl + M	k_a
Cl	→	loss	k_{Cl}
CH_3I-Cl	→	loss	k_{loss}

where, k_a is the bimolecular rate coefficient for the reaction of $CH_3I + Cl$ at a given pressure [M], k_{Cl} is the first order rate coefficient for loss of Cl atoms due to diffusion and reaction with

trace constituents in the reaction mixture (other than CH_3I) and k_{loss} is the first order rate coefficient for loss of the CH_3I-Cl adduct due to diffusion and reaction with species within the system. A kinetic analysis of the above reaction scheme for $[CH_3I\text{-}Cl]_t$ (the concentration of adduct at reaction time, t yields the following expression

$$[CH_3I-Cl]_t = \frac{k_a'[Cl]_0}{(k_{loss}-(k_a'+k_{Cl}))}\left(e^{-(k_a'+k_{Cl})t}-e^{-k_{loss}t}\right) \qquad \text{E. 5.3-1}$$

where k_a' is the pseudo-first-order rate coefficient for the association reaction ($k_a' = k_a[CH_3I]$) and $[Cl]_0$ is the concentration of Cl atoms at $\Delta t = 0$ (the concentration of Cl atoms generated in the photolysis pulse). (NB. It should be noted that in this analysis k_a is really the sum of k_a and $k_c[M]$ as given in reaction scheme, **S5-1**). Thus E. 5.3-1 can be fit to a CH_3I-Cl kinetic trace obtained for a particular $[CH_3I]$ in the form of a generic biexponential equation

$$LIF = \frac{P1}{(P2-P3)}\left(e^{-P3t}-e^{-P2t}\right)+P4 \qquad \text{E. 5.3-2}$$

where, *LIF* is the time-dependent laser-induced fluorescence signal (proportional to the concentration of CH_3I-Cl), $P1 = k_a'\beta[Cl]_0$ (where β is the calibration constant of the LIF instrument), $P2 = k_{loss}$, $P3 = k_a' + k_{Cl}$, and *P4* is an additional parameter allowing for slight baseline deviations from the pre-Excimer laser background signal at large Δt. Fig. 5.3-1 displays some kinetic traces of CH_3I-Cl obtained at ~ 216 K with fits of E. 5.3-2 to the experimental data.

To obtain the rate coefficient, k_a, at a given pressure, the pseudo-first-order rate coefficient was measured as a function of $[CH_3I]$. A plot of k_a' against $[CH_3I]$ yields a straight line with slope k_a and intercept k_{Cl} (assuming k_{Cl} does not vary with the concentration of methyl iodide). For each determination of k_a kinetic traces were recorded for seven different methyl iodide concentrations over a range of approximately one order of magnitude (Table 5.3-1). For every concentration of methyl iodide two kinetic traces were recorded back-to-back: one over long reaction time capturing several lifetimes of adduct decay, and one at short Δt to accurately determine the adduct growth (Fig. 5.3-1). In fitting the small Δt data, k_{loss} was fixed to the accurate value obtained from the longer timescale experiment. All data points were incorporated for determinations of k_a.

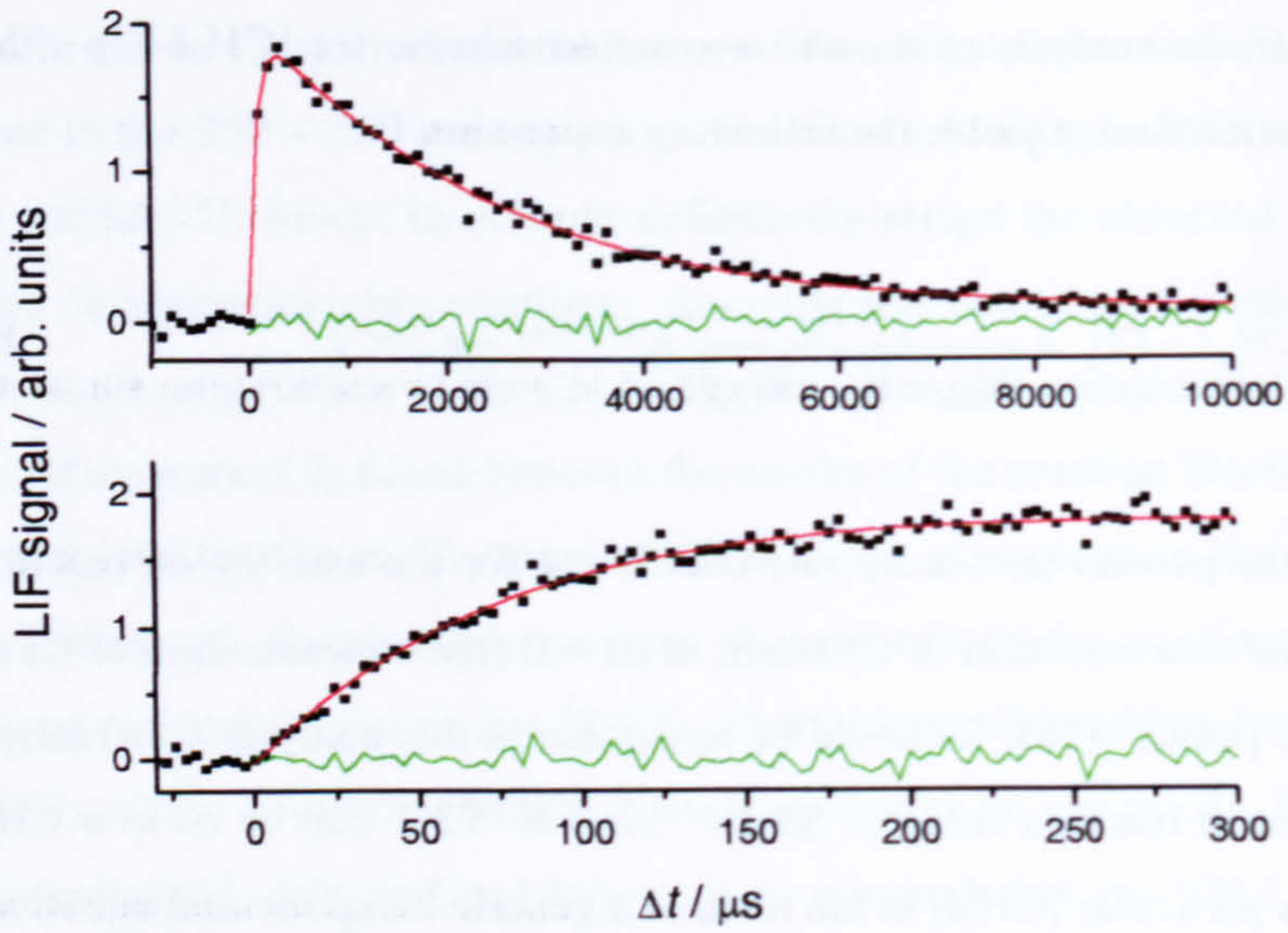

Fig 5.3-1 – Experimental CH_3I-Cl kinetic traces (black squares) with fits of E. 5.3-2 to the experimental data (solid red lines). The residuals of the fits to the data are given by the solid green lines. Experimental conditions: T = 215.9 K; P = 494.0 Torr; $[Cl_2SO]$ = 1.43 × 10^{13} molecule cm^{-3}; $[CH_3I]$ = 3.71 × 10^{14} molecule cm^{-3}; $[N_2]$ = balance; F = 2.4 × 10^{15} photons cm^{-2}; λ_{pr} = 360.57 nm.

A positive, long-time, baseline signal was observed above the pre-Excimer laser background under all conditions. This baseline discrepancy was independent of total pressure, $[Cl_2SO]$, $[CH_3I]$, $[O_2]$, laser PRF or Excimer fluence, and was observed to vary from (0.3 ± 1.1) – (8.1 ± 1.6) % of the peak adduct LIF signal. Unfortunately, the origin of the background signal could not be investigated due to the continuous LIF spectrum of the CH_3I-Cl adduct (see section 5.4.1) meaning that an off-line kinetic trace could not be recorded. In fitting E. 5.3-2 to the data it was essentially assumed that a species, generated by the Excimer laser, fluoresced weakly with a constant intensity over the timescale of the experiment. However, it is possible that the baseline deviation was due to the accumulation of fluorescing species generated by secondary chemistry within the reaction system, or recycling of the CH_3I-Cl adduct at large Δt by secondary processes. These possibilities are explored in greater detail in section 4.3.2 and were found to be of negligible consequence to the determined reaction kinetics.

At room temperature the kinetic analysis is complicated by dissociation of the adduct back to reactants and the higher rate of the bimolecular reaction channel of the CH_3I + Cl reaction ($k_{bi(296\ K)} = 7.97 \times 10^{-13}$ $cm^3 molecule^{-1} s^{-1}$)[17]. The following processes must therefore be considered:

$CH_3I + Cl$	$\rightarrow$	$HCl + CH_2I$	k_{bi}
$CH_3I + Cl + M$	$\rightarrow$	$CH_3I\text{-}Cl + M$	k_a
Cl	$\rightarrow$	loss	k_{Cl}
$CH_3I\text{-}Cl + M$	$\rightarrow$	$CH_3I + Cl + M$	k_{-a}
$CH_3I\text{-}Cl$	$\rightarrow$	loss	k_{loss}

and kinetic analysis of the above reaction scheme yields the following solution to $[CH_3I\text{-}Cl]_t$

$$[CH_3I-Cl]_t = \frac{k_a[Cl]_0}{(\lambda_+ - \lambda_-)}\left(e^{\lambda_+ t} - e^{\lambda_- t}\right) \qquad \text{E. 5.3-3}$$

where $\lambda_\pm$ is given by E. 5.3-4:

$$\lambda_\pm = \frac{-(k_a + k_{bi} + k_{Cl} + k_{-a} + k_{loss}) \pm \sqrt{(k_a + k_{bi} + k_{Cl} + k_{-a} + k_{loss})^2 - 4[(k_a + k_{bi} + k_{Cl})(k_{-a} + k_{loss}) - k_a k_{-a}]}}{2}$$

Thus, similarly to the low temperature analysis, the room temperature kinetic data can be fit with a generic function of the form

$$LIF = \frac{P1}{(P2 - P3)}\left(e^{P2t} - e^{P3t}\right) + P4 \qquad \text{E. 5.3-5}$$

where $P1 = k_a'\beta[Cl]_0$, $P2 = \lambda_+$ and $P3 = \lambda_-$

Fig. 5.3-2 displays two kinetic traces of the CH_3I-Cl adduct obtained at room temperature, with fits of E. 5.3-5 to the experimental data. Note the increase in adduct yield with increasing $[CH_3I]$. It is generically true that the temporal profile of a chemical species (that is determined by first-order processes) can be described by the sum of the individual exponential terms of the processes involved. From the above definition of λ, it can be seen that the sum of λ_+ and λ_- is equal to the negative sum of all first-order rate coefficients defined in the room temperature reaction mechanism. Therefore, a plot of $(\lambda_+ + \lambda_-)$ against $[CH_3I]$ should yield a negative straight line, with a slope equal to the negative sum of all rate coefficients which depend on $[CH_3I]$ and an intercept equal to the negative sum of all rate coefficients that do not depend on $[CH_3I]$.

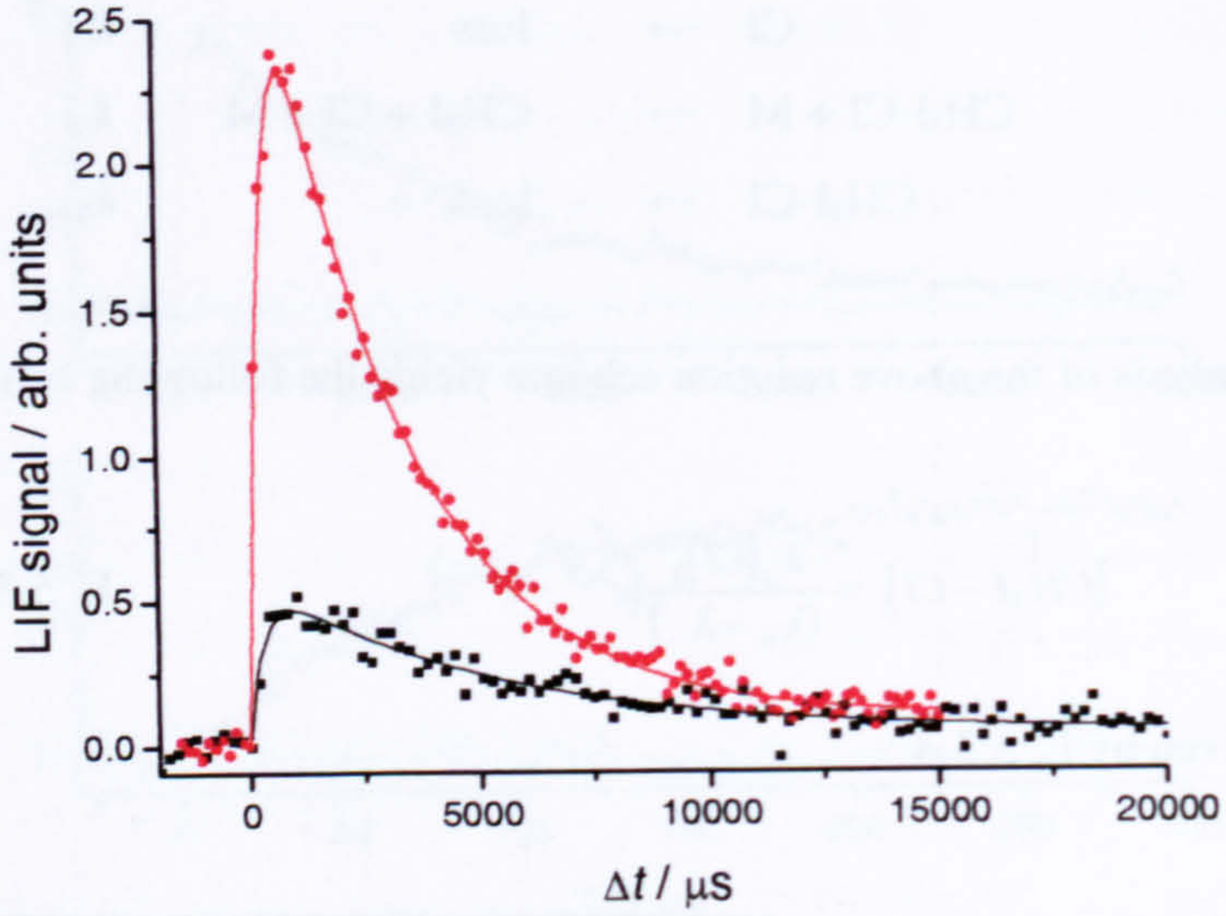

Fig. 5.3-2 – Experimental CH_3I-Cl kinetic traces (scattered points) with fits of E. 5.3-5 to the data (solid lines). Experimental conditions: Black; T = 296 K, P = 100.0 Torr, $[Cl_2SO]$ = 2.09×10^{13} molecule cm^{-3}, $[CH_3I]$ = 1.94×10^{13} molecule cm^{-3}, $[N_2]$ = balance. Red: T = 296 K, P = 102.0 Torr, $[Cl_2SO]$ = 2.05×10^{13} molecule cm^{-3}, $[CH_3I]$ = 1.34×10^{14} molecule cm^{-3}, $[N_2]$ = balance. Both: F = 2.34×10^{15} photons cm^{-2}, λ_{pr} = 360.57 nm.

5.3.2 Reaction Kinetics of the CH_3I + Cl Reaction at ~ 206 K

A. Adduct Formation

Fig. 5.3-3 displays some bimolecular plots for the CH_3I + Cl reaction as a function of pressure at low temperature. Table 5.3-1 lists all low temperature determinations of k_a obtained in this work along with selected data from other studies. The intercepts of all bimolecular plots were of similar magnitude and no systematic relationship to the experimental conditions was evident. The average intercept value was (229 ± 285) s^{-1}, where the error represents 2σ uncertainty. Thus it can be concluded that diffusion of Cl atoms and their reaction with species other than CH_3I were of slight but negligible consequence. It should be noted that the rate coefficients determined in this study are really the sum of k_a and k_{bi} but as the statistical error associated with each determination of k_a is significantly larger than the extrapolated bimolecular rate coefficient at 206 K (1.26×10^{-13} $cm^3 molecule^{-1} s^{-1}$) the bimolecular process can be regarded as negligible with respect to the overall reaction kinetics ($k_a >> k_{bi}$). It was mentioned in section 5.3.1 that a positive baseline deviation was observed in the kinetic traces at large Δt and was taken into account in the kinetic analyses. However, the excellent agreement between the rate coefficients determined in this study and those obtained in the study of Ayhens *et. al.*[17] suggests that this interference had little effect on the kinetics being determined. The close agreement

between the two studies may be taken as incontrovertible evidence that the fluorescing species observed in this study is indeed a product of the CH_3I + Cl reaction, and therefore the CH_3I-Cl adduct.

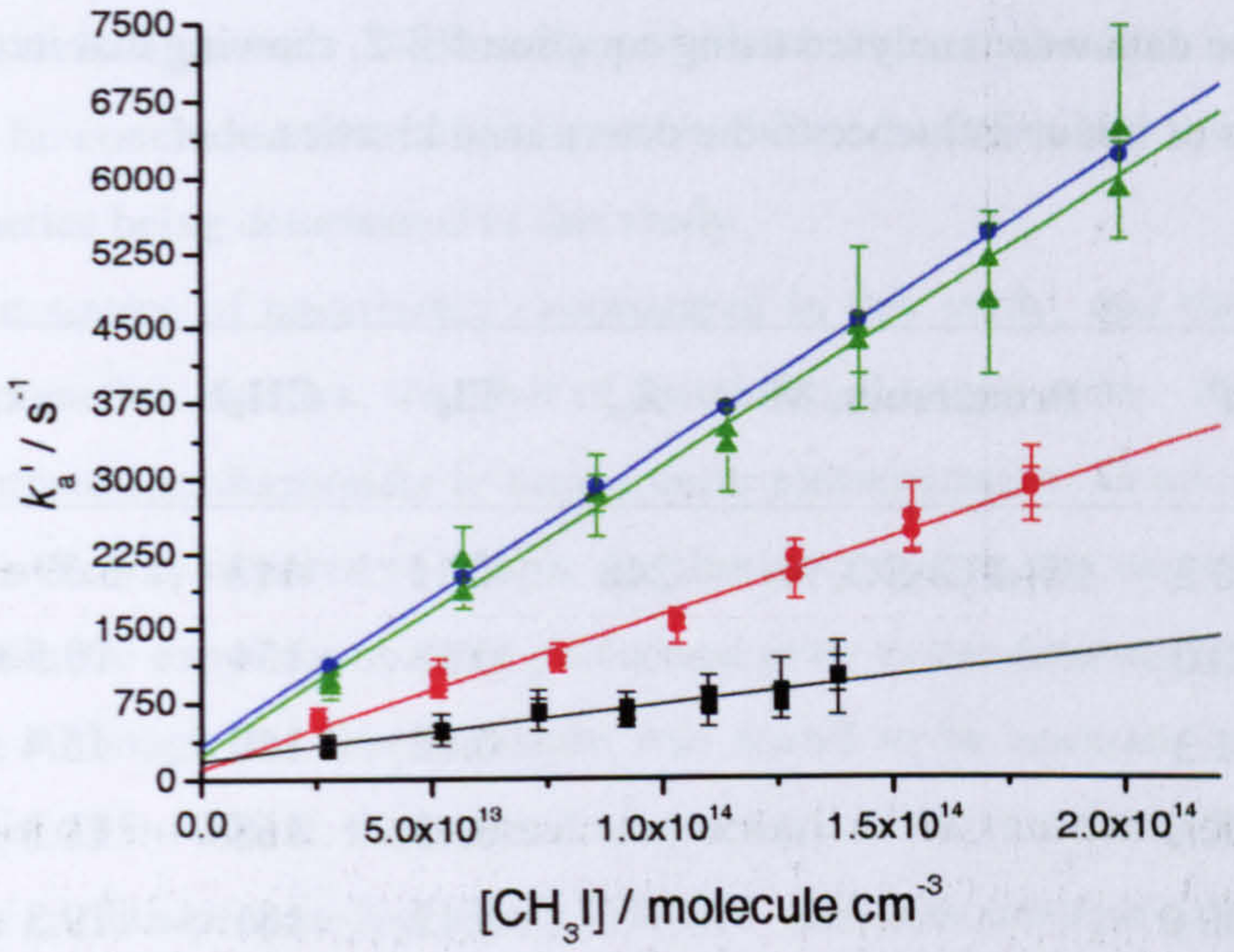

Fig. 5.3-3 – Bimolecular plots for the reaction CH_3I + Cl. Black: T = 200 K, P = 10.2 Torr. Red: T = 202 K, P = 71.3 Torr. Green: T = 216 K, P = 251.0 Torr. Additional experimental conditions are given in Table 5.3-1. The blue data points are model simulations for the 250 Torr experiment as described in the text.

However, it was considered prudent to investigate interference from the baseline discrepancy. The data from the 500 Torr experiment were reanalysed with a modified version of E 5.3-2, allowing for the exponential growth of a species other than CH_3I-Cl, which also fluoresces at the excitation wavelength

$$LIF = \frac{P1}{(P2 - P3)}\left(e^{-P3t} - e^{-P2t}\right) + P4\left(1 - e^{-P5t}\right) \qquad \text{E. 5.3-6}$$

where *P4* is related to the fluorescence signal from the unknown species at infinite reaction time (assuming no loss of this species) and *P5* is the pseudo-first-order rate coefficient for its formation. When the large Δt data were reanalysed with E. 5.3-6 a unique solution was only obtained once from the seven data points due to the obvious difficulty of generating unique solutions to multi-parameter functions. In the other six analyses *P5* was returned with a value equal to that of *P3* (or k_{loss}). It will be shown that the adduct removal is predominantly governed by reaction with radicals within the system (even for the very low concentrations present) and the above findings may therefore be indicative that the adduct is reacting with species within the reaction system that generate products which fluoresce at the excitation

wavelength, although with much weaker intensity than the adduct itself. Possible candidates may be considered to be ICl or CH_3Cl. Fluorescence by I-Cl may be considered particularly likely as it is considered that electronic transitions within this bond are responsible for the adduct fluorescence. Analysing the data by this procedure returned a k_a value < 2 % greater than that when the data were analysed using equation 5.3-2, showing that interference from such a mechanism was of minor influence to the determined kinetics.

T	P	Precursors, M	λ_{ex}	Cl_0	CH_3I	k_a	Ref.
200.0	10.2	CH_3I/Cl_2SO, N_2	248	0.11	113	5.59 ± 1.20	a
200.4	40.0			0.13	154	10.5 ± 1.6	a
201.9	71.3			0.12	160	15.4 ± 1.2	a
203.8	100.2			0.13	168	18.3 ± 1.7	a
203.8	100.0			0.12	181	19.3 ± 1.9	a
216.2	251.0			0.12	189	28.8 ± 2.3	a
215.9	497.4			0.24	371	35.1 ± 3.5	a
218	5.1	CH_3I/Cl_2, N_2	355	0.11	1140	3.31 ± 0.52	17
218	10			0.11	982	5.04 ± 0.26	17
218	30			0.10	1160	10.2 ± 0.7	17
218	100			0.14	983	19.8 ± 1.9	17
218	250			0.16 - 0.33	722	25.0 ± 1.3	17
218	500			0.36	662	29.7 ± 2.6	17
250	10			0.19	990	3.25 ± 0.21	17
250	100			0.10	830	14.3 ± 0.7	17
250	500			0.30	356	24.5 ± 1.9	17
250	25			1 – 10	9000	4.0 ± 1.0	20
250	125			1 – 10	9000	20.0 ± 3.0	13

Table 5.3-1 – Kinetic data obtained in this work[a] and other selected studies of the CH_3I + Cl reaction for $T \leq 250$ K. The provided experimental conditions include: T (K), P (Torr), nature of the chlorine precursor and bath gas, photolysis wavelength (nm), estimated initial Cl atom concentration and range of CH_3I concentrations employed (10^{12} molecule cm^{-3}), and association rate coefficients k_a (10^{-12} $cm^3 molecule^{-1} s^{-1}$). Note that this study and that of Enami *et. al.*[20] employed spectroscopic detection of the CH_3I-Cl adduct, and Ayhens *et. al.*[17] employed resonance fluorescence detection of Cl atoms.

Another possible explanation for the observed baseline deviation is that secondary chemistry not involving the adduct was responsible. For the one data point where a unique solution to

E. 5.3-6 was obtained, the formation rate of the unknown fluorescing species (*P5* = (317 ± 2603) s^{-1}) was approximately 30 % smaller than that of adduct removal (*P3*). The 500 Torr data were therefore reanalysed with a fixed value for *P5* of 317 s^{-1} (assuming no dependence on [CH_3I]). Similarly, the returned k_a rate coefficient was < 2 % greater than that where the baseline deviation was ignored. Ultimately, whatever the mechanism responsible for its occurrence, it can be concluded that the observed baseline deviation had no appreciable effect on the reaction kinetics being determined in this study.

The largest source of uncertainty encountered in this study, and therefore the largest interference to the reaction kinetics, was that of reaction cell temperature. Kinetic experiments could not be performed simultaneously to temperature measurements, as a reaction cell port on the Excimer laser axis was required to couple the thermocouple to the experimental apparatus. Consequently the kinetic experiments were performed prior to the determination of the reaction cell temperature. Although the thermocouple was found to be accurate to ± 1 K over the temperature range of 195 – 296 K, the internal temperature of the reaction cell was not observed to equal that of the cardice/propan-2-ol slurry (195 K). Between reaction cell pressures of 10 – 100 Torr the cell temperature was in the region of 200 – 204 K but at pressures of 250 and 500 Torr, the reaction cell temperature was found to be ~ 216 K. The most likely explanation for this observation is that the relatively small heat capacity of N_2 did not allow the thermalisation of gas from room temperature to 195 K within its residence time in the reaction cell. The inconsistent temperature measurements raise two potential sources of error to the determined rate coefficients. As the number density of a gas is inversely proportional to its temperature at a fixed volume, determining concentrations from gas flow rates and pressures requires accurate knowledge of the temperature. In this work, [CH_3I] is required in order to evaluate k_a and so uncertainty with regards to temperature ultimately leads to uncertainty in k_a. Further, the pressure dependence of an association reaction should be investigated at a constant temperature as the reaction kinetics will also vary with *T* (*cf.* 218 and 250 K data in Table 5.3-1). As the absolute calibration of the thermocouple was accurate, however, the first interference is considered unlikely.

The pressure dependence of an association reaction is commonly expressed by E. 5.3-7, which describes how the effective bimolecular rate coefficient varies with pressure for a specified temperature and bath gas

$$k([M],T) = \frac{k_0 k_\infty [M] F_c^{\,X}}{(k_\infty + k_0[M])} \qquad \text{E. 5.3-7}$$

where $X = \left\{1 + [\log(k_0[M]/k_\infty)]^2\right\}^{-1}$

Here k_0 is the third-order rate coefficient of the association reaction, k_∞ is the high pressure limit (the bimolecular rate coefficient at infinite pressure), and F_c is a broadening parameter which allows for changes in the internal energy distribution of the association complex with pressure. Fig. 5.3-4 displays all low temperature determinations of k_a from this study and the data of Ayhens *et.al.*[17] at 218 K. Due to the imprecise reaction cell temperature in this study, E. 3.5-7 is fit to all data in Fig. 5.3-4 and the parameters obtained from the fit are quoted for the mean experimental temperature of (212 ± 16) K.

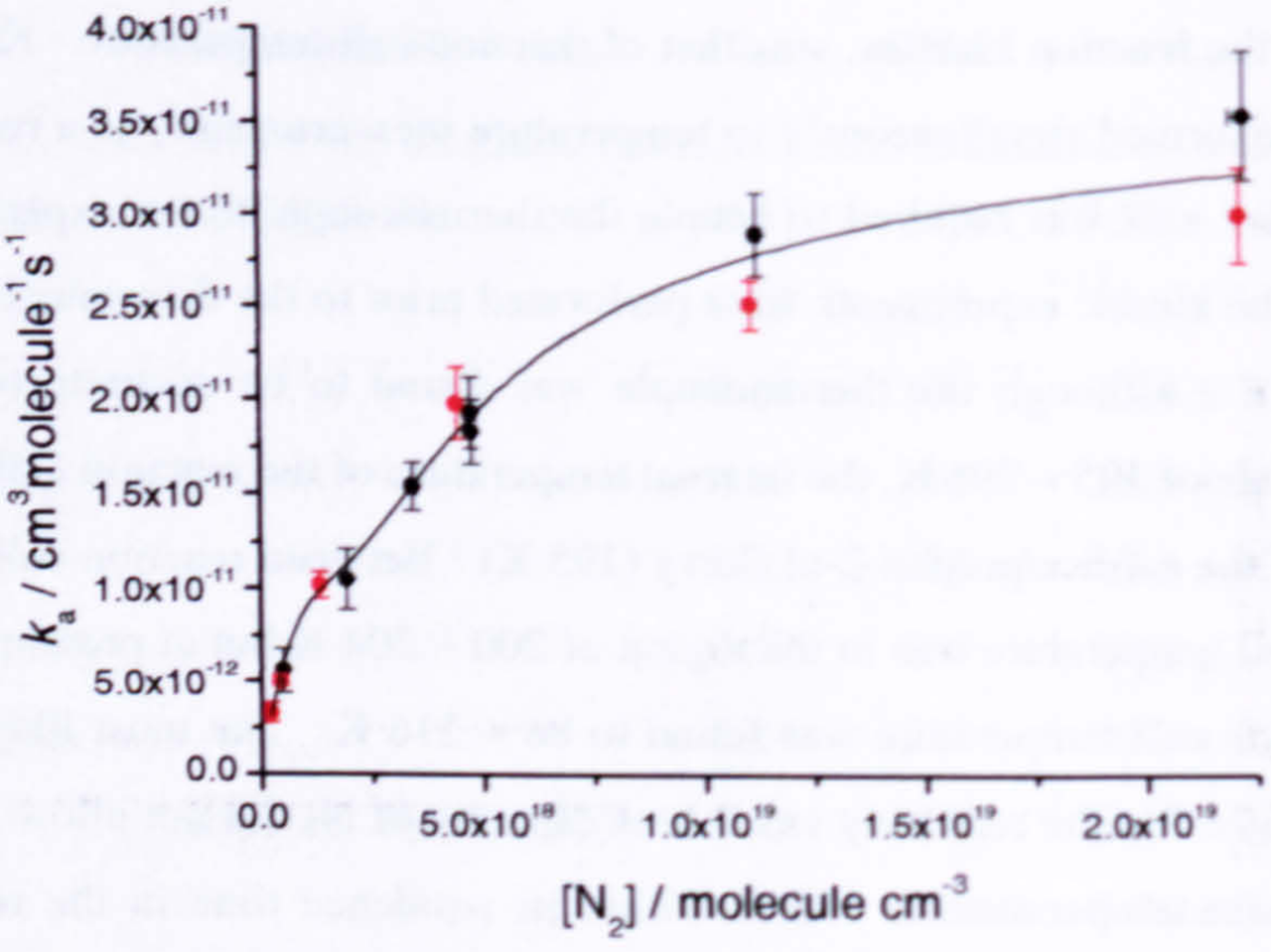

Fig. 5.3-4 – Pressure dependence of the CH_3I + Cl reaction at ~ 212 K. The black data points represent the k_a determinations from this work and the red data points are the 218 K data taken from Ayhens *et. al.*[17]. The solid black line is a fit of E. 5.3-7 to all data presented.

From the fit of E. 5.3-7 to the data in Fig. 5.3-4, the kinetic parameters obtained are:

$$k_0 = (1.64 \pm 0.92) \times 10^{-29} \text{ cm}^6\text{molecule}^{-2}\text{s}^{-1}$$
$$k_\infty = (3.79 \pm 0.33) \times 10^{-11} \text{ cm}^3\text{molecule}^{-1}\text{s}^{-1}$$
$$F_c = 0.64 \pm 0.27$$

where all errors are 2σ uncertainty. The results are in good agreement with those reported in the work of Ayhens *et. al.*[17] of 2.0×10^{-29} $\text{cm}^6\text{molecule}^{-2}\text{s}^{-1}$, 4.0×10^{-11} $\text{cm}^3\text{molecule}^{-1}\text{s}^{-1}$ and 0.63 for k_0, k_∞, and F_c respectively.

B. Adduct Removal

An interesting observation from the kinetic analysis was that the adduct loss rate (*P3* or k_{loss}) increased with [CH_3I] at a given total pressure. Fig. 5.3-5 displays a plot of k_{loss} against [CH_3I] for the 250 Torr data. Note that only one experimental data point for each methyl iodide concentration is included (as the small Δt kinetic traces did not extend to a reaction time where the adduct decay is observed).

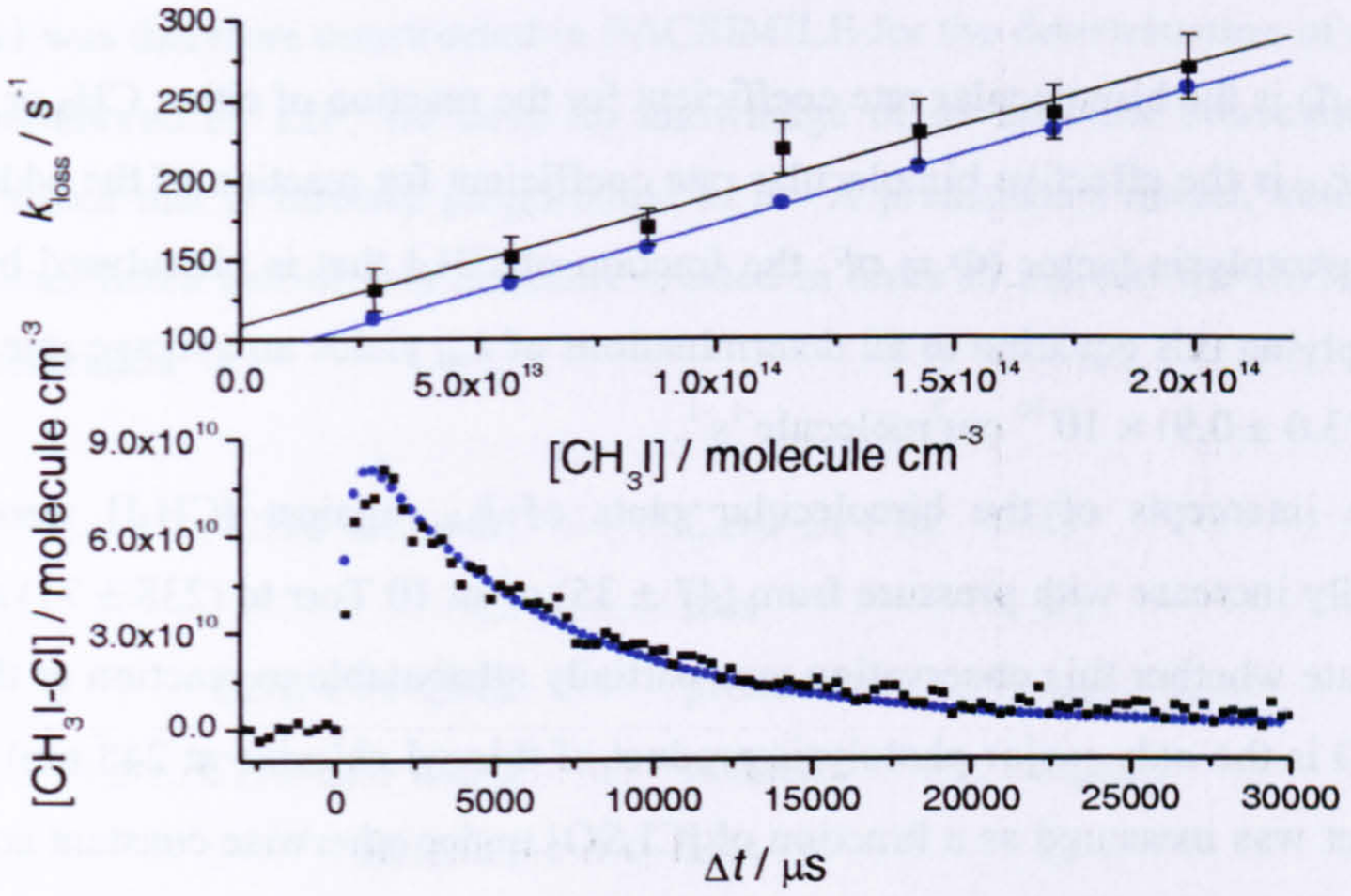

Fig. 5.3-5 – Top panel: bimolecular plot for k_{loss} at 216 K and 251 Torr. From the slopes: k_{eff} (cm^{3}molecule^{-1}s^{-1}) = (8.12 ± 1.64) × 10^{-13} (black) and 8.37 × 10^{-13} (blue). Bottom panel: kinetic trace for [CH_3I] = 8.5 × 10^{13} molecule cm^{-3}. Black squares represent experimental data and blue circles indicate model simulations (explained in the text).

The [CH_3I] dependence of k_{loss} was found to be independent of total pressure with an average effective bimolecular rate coefficient, k_{eff} = (6.93 ± 1.89) × 10^{-13} cm^{3}molecule^{-1}s^{-1}. This phenomenon could be explained by one of two mechanisms. First, that the adduct reacts with methyl iodide, as proposed by Bilde and Wallington[19]. In that work the authors reported an effective rate coefficient for adduct formation of (4.6 ± 1.4) × 10^{-13} cm^{3}molecule^{-1}s^{-1}, derived from the increased reactivity of the system in moving from 1 – 700 Torr total pressure. As the reaction kinetics in the experiment of Bilde and Wallington[19] were determined by monitoring the loss of CH_3I on a timescale of minutes in a continuous photolysis smog chamber, this effective rate coefficient can be interpreted as the sum of adduct loss processes that do not regenerate the reactants. Bilde and Wallington[19] observed the yield of CH_3Cl to display a complex dependence on [CH_3I] in their experiment ($\gamma(CH_3I)$ = 20 – 80 %). If the reaction of CH_3I-Cl + CH_3I exclusively produces CH_3Cl (+ products) then the yield of CH_3Cl should be equal to $k_{eff}/(k_{eff}+k_{bi})$ ≈ 37 %, and independent of CH_3I. Thus the results of Bilde and

Wallington[19] are not consistent with this mechanism and indicate the presence of complex secondary chemistry. The alternative explanation, to the observed dependence of k_{loss} on [CH_3I], is that the adduct is reacting with photolysis products of CH_3I (methyl radicals or iodine atoms). If it is assumed that the adduct reacts with only one of these species, the bimolecular rate coefficient of the reaction can be evaluated from equation 5.3-8.

$$k_{CH_3/I} = \frac{k_{eff}}{\Phi} \qquad \text{E. 5.3-8}$$

Here, $k(CH_3/I)$ is the bimolecular rate coefficient for the reaction of either CH_3 or I radicals with the adduct, k_{eff} is the effective bimolecular rate coefficient for reaction of the adduct with CH_3I, and Φ is a photolysis factor ($\Phi = \sigma F$, the fraction of CH_3I that is photolysed by the Excimer laser). Applying this equation to all determinations of k_{eff} yields an average rate coefficient of, $k(CH_3/I) = (3.0 \pm 0.9) \times 10^{-10}$ $cm^3 molecule^{-1} s^{-1}$.

The intercepts of the bimolecular plots of k_{loss} against [CH_3I] were observed to systematically increase with pressure from (47 ± 35) s^{-1} at 10 Torr to (238 ± 71) s^{-1} at 500 Torr. To investigate whether this observation was partially attributable to reaction of the adduct with ClSO (ClSO is the only major photolysis product of thionyl chloride at 248 nm) the decay rate of the adduct was measured as a function of [Cl_2SO] under otherwise constant conditions. Fig. 5.3-6 shows the resulting kinetic traces.

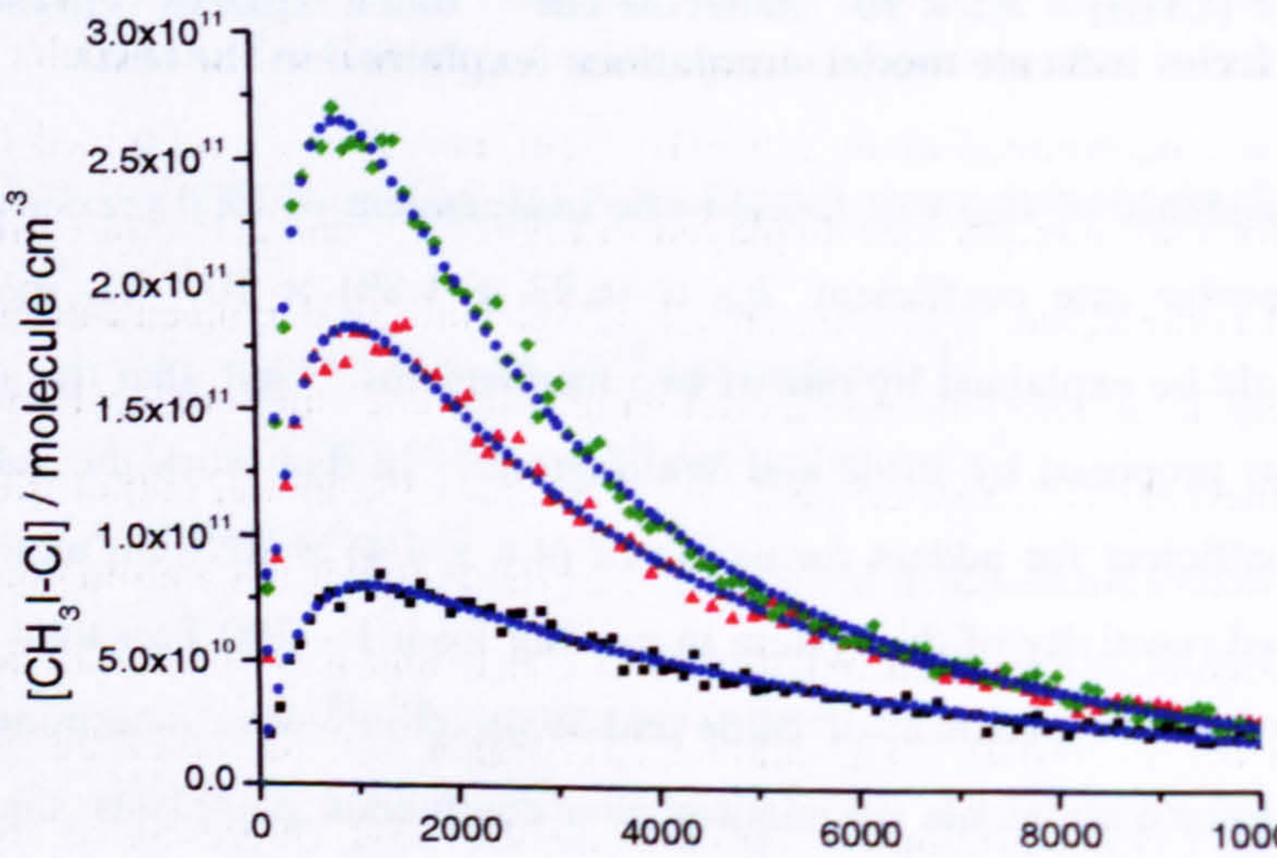

Fig. 5.3-6 – Kinetic traces of the CH_3I-Cl adduct recorded as a function of [Cl_2SO]. Experimental conditions: T = 204 K; P = 100 Torr; [CH_3I] = 1.17×10^{14} molecule cm^{-3}; [Cl_2SO] (molecule cm^{-3})= 7.04×10^{12} (black), 1.76×10^{13} (red) and 2.81×10^{13} (green); [N_2] = balance; $F = 2.40 \times 10^{15}$ photons cm^{-2}; λ_{pr} = 360.57 nm. The scattered points represent the experimental data and the solid blue circles represent the model fit to the data (explained in the text).

From the results of this experiment it can be seen that the peak adduct LIF signal increases with Cl_2SO (and hence Cl) concentration, as expected. The adduct decay rate is also observed to increase with [Cl_2SO]. This fact primarily indicates that the CH_3I-Cl adduct reacts with ClSO to some extent (NB. see section C). Assuming that dissociation of the adduct back to reactants (or any other products) at 204 K is negligible (this is almost certainly the case due to the linearity, and small intercepts, of the bimolecular plots of k_a' and k_{loss} against [CH_3I]) the rate coefficient for the reaction of the adduct with ClSO radicals, k_{ClSO} cannot be obtained from a plot of k_{loss} against [CH_3I] as the reaction is effectively a second order process ([ClSO] ≈ [Cl] ≈ [CH_3I-Cl]). A model was therefore constructed in FACSIMILE for the determination of k_{ClSO}. As the adduct was monitored by LIF, we have no knowledge of its absolute concentration, only a fluorescence signal that is directly proportional to it. A preliminary model, consisting of the various processes listed below, was therefore created in order to convert the LIF signal into an absolute concentration

$CH_3I + Cl + M$	→	CH_3I-Cl + M	k_a
Cl	→	loss	k_{Cl}
CH_3I-Cl + CH_3I	→	products	k_{eff}
CH_3I-Cl + ClSO	→	products	k_{ClSO}
CH_3I-Cl	→	loss	k_d

where k_d is the first order rate coefficient for adduct removal by diffusion. In the model k_a, k_{Cl}, k_{eff}, k_{ClSO} and k_d are given the values 1.88×10^{-11} $cm^3molecule^{-1}s^{-1}$ (the average 100 Torr determination), 229 s^{-1} (the average intercept value to the growth bimolecular plots), 6.93×10^{-13} $cm^3molecule^{-1}s^{-1}$ (determined above), 5×10^{-10} $cm^3molecule^{-1}s^{-1}$ (obtained from a plot of k_{loss} against [ClSO] for the kinetic traces displayed in Fig. 5.3.6) and 20 s^{-1} (a realistic estimation of diffusive losses) respectively. The initial Cl, ClSO and CH_3I concentrations for a particular kinetic experiment are entered into the model which simulates the temporal profile of the adduct over the same timescale as the experiment. By examining the model output file, the peak adduct concentration is determined (which is naturally less than the initial Cl atom concentration due to loss of Cl by processes other than reaction with CH_3I, and loss of the adduct by the various mechanisms illustrated above). The adduct LIF signal can therefore be converted into an (estimated) absolute concentration by normalising the peak fluorescence signal to the peak concentration value returned from the model output file.

The model was then used to fit the normalised experimental data and return a value for k_{ClSO}. In the model fitting, two parameters are set as variable to allow the model calculation sufficient flexibility. The floated parameters are either k_{ClSO} and $[Cl]_0$, or k_{ClSO} and k_{Cl}. Both versions of the model were fit to the kinetic traces, retuning a total of six values for k_{ClSO}. The average k_{ClSO}

value obtained was (9.0 ± 0.3) × 10^{-10} $cm^3molecule^{-1}s^{-1}$, where the error is the 2σ standard deviation. The excellent precision (> 96 %) of the determined rate coefficient is definitive proof of the reaction of the CH_3I-Cl adduct with ClSO radicals within the system. When the variable parameter in the model (other than k_{ClSO}) was the initial Cl atom concentration, the returned value for $[Cl]_0$ was always within 99 % of the calculated value. When k_{Cl} was the second floated parameter, an average k_{Cl} value of (253 ± 16) s^{-1} was returned, in excellent agreement with the experimental determination of (229 ± 289) s^{-1}. The model fit to the experimental data is shown in Fig. 5.3-6.

Despite the high precision of k_{ClSO} returned by the model, the accuracy of the rate coefficient determination is subject to considerable uncertainty. The absorption cross section of thionyl chloride at 248 nm is required in order to evaluate the initial concentrations of both Cl atoms and ClSO. As the temperature dependence of the Cl_2SO absorption cross section has not been reported, it is therefore assumed that the absorption cross section does not change significantly between 296 and 204 K. An additional uncertainty associated with estimating the initial concentrations of Cl and ClSO arises from the, relatively minor, disagreement over the photolysis product yields of the 248 nm laser dissociation of thionyl chloride[26,27]. For calculating the concentrations of Cl and ClSO we use the yields reported by Baum *et. al.*[26]. A final source of uncertainty over the radical concentrations is that of laser fluence. The excimer laser power was measured at the rear cell window and reflective losses of laser radiation from the window may, therefore, underestimate the true photon density at the photolysis/LIF axis of the reaction cell. It is also possible that significant concentrations of SO could be present (~ 10 % of [ClSO]) and account for some of the observed adduct reactivity. We choose to quote an accuracy of ± 50 % in k_{ClSO}, to account for all possible uncertainties, thus giving a value of (9.0 ± 4.5) × 10^{-10} $cm^3molecule^{-1}s^{-1}$ at 204 K. It should also be noted that this rate coefficient may reflect the reaction of the adduct with non-thermal ClSO, due to a high degree of internal excitation from the excimer laser (although at 204 K and 100 Torr N_2, any internally excited ClSO should be rapidly thermalised). Despite the large error, the determined rate coefficient for the reaction of CH_3I-Cl with ClSO is extremely high and significantly greater than the gas kinetic bimolecular rate coefficient at 204 K (~ 2 × 10^{-10} $cm^3molecule^{-1}s^{-1}$). This may be indicative of the presence of long-range attractive forces on the reaction potential energy surface. To our knowledge, this is the first reported rate coefficient for a reaction involving the ClSO radical. The modeling exercise has demonstrated that the adduct can react extremely rapidly with radical species. It is therefore considered most likely that the observed increase in k_{loss} with $[CH_3I]$ is attributable to reaction of the CH_3I-Cl adduct with photolysis products of methyl iodide (indeed, in the next section, it will be shown definitively that this is the case). Further, if it is assumed that the most likely candidate is I atoms, then a mechanism is provided whereby the generation of ICl at long reaction time could perhaps explain the positive baseline

deviation encountered in the experiments. At 298 K, the reaction enthalpies for the reactions of $CH_3 + CH_3ICl \rightarrow CH_3Cl + CH_3I$ and $I + CH_3I\text{-}Cl \rightarrow ICl + CH_3I$ are calculated to be -296.5 kJ mol^{-1} and -157.4 kJ mol^{-1} respectively.

In the low temperature experiments, for each bimolecular determination of k_a at a specific pressure, all conditions were maintained at constant values except $[CH_3I]$. Therefore, as the concentration of CH_3I increases so does the ratio of (CH_3 or I)/Cl. This means that the reaction of the adduct with photolysis products of methyl iodide may not be strictly pseudo-first-order over a bimolecular data set and may result in curvature to the bimolecular plots of k_{loss} against CH_3I, thus underestimating k_{eff} (and hence k(CH_3 or I)). To investigate this effect, model simulations were ran for the 250 Torr kinetic experiment, the results of which are displayed in Fig. 5.3-5. To generate the model data points, kinetic traces are simulated in FACSIMILE (using the model outlined above) for the exact experimental conditions of each of the seven experiments with different methyl iodide concentrations. The model output is then fitted to E. 5.3-2 to generate values for k_{loss} (and k_a'). From Fig. 5.3-5 it can be seen that no curvature in the linear fit of the model output data is evident (similarly to the experimental observations) and the determined value of k_{eff} is ~ 3 % greater than that of the experimental determination. This result indicates that second-order chemistry is not predominant and does not significantly effect the determination of k_{eff} (and k(CH_3/I)). Also displayed in Fig. 5.3-5 is a model output kinetic trace generated for a particular concentration of methyl iodide, along with its corresponding experimental trace (normalised to the peak concentration of the model output). It can be seen that the agreement between experiment and model is remarkably good, especially considering that the experimental data are not fitted by the model, rather the model is simply a simulation of the experimental conditions. The y-axis offset between the model and experimental bimolecular plots (and the greater deviation between experimental and model data points at long reaction time in the kinetic traces) can be explained by the fact that the model does not account for the experimental baseline deviation. The pseudo-first-order adduct decay rate is therefore slightly underestimated by the model for a particular methyl iodide concentration. However, the fact that the slopes are in excellent agreement further substantiates the fact that the baseline deviation has little effect on the determined reaction kinetics. In Fig. 5.3-1 the model k_a' values for the 250 Torr experiment are plotted alongside the experimental data. From the slope, $k_a = (2.96 \pm 0.07) \times 10^{-11}$ $cm^3molecule^{-1}s^{-1}$, < 3 % greater than the experimentally determined (and model input) value of $(2.88 \pm 0.23) \times 10^{-11}$ $cm^3molecule^{-1}s^{-1}$. This reiterates the fact that the baseline deviation had little effect on the experimental determinations of k_a; neither did the reaction of the adduct with the low concentration of radicals within the system.

A final test of the chemistry occurring within the system and the reaction mechanism of methyl iodide and chlorine at ~ 206 K can be made from comparing the adduct yield as a

function of $[CH_3I]$. As $[Cl_2SO]$, and hence [Cl], is maintained at a constant value across a bimolecular data set, the peak adduct LIF signal in a kinetic trace should remain constant with $[CH_3I]$ if the adduct does not undergo unimolecular dissociation (as assumed in the kinetic analysis of the data). However, in reality the yield will change with $[CH_3I]$ due to loss of Cl atoms by processes other than reaction with CH_3I, and reaction of the adduct with radicals within the system. Fig. 5.3-7 displays the peak experimental adduct LIF signal for each methyl iodide concentration (relative to that at the highest concentration) for the 100.2 Torr experiment. The peak LIF signal is determined by taking the average of 10 – 20 data points at the peak of the kinetic traces recorded for small Δt. Also included in the figure are the peak adduct concentrations (also relative to the value returned for the highest methyl iodide concentration), obtained from the model output files of the FACSIMILE simulation described previously (adapted to the 100 Torr conditions), represented by the blue data points. The red data points are also model calculations, but with the adduct-radical reactions switched off.

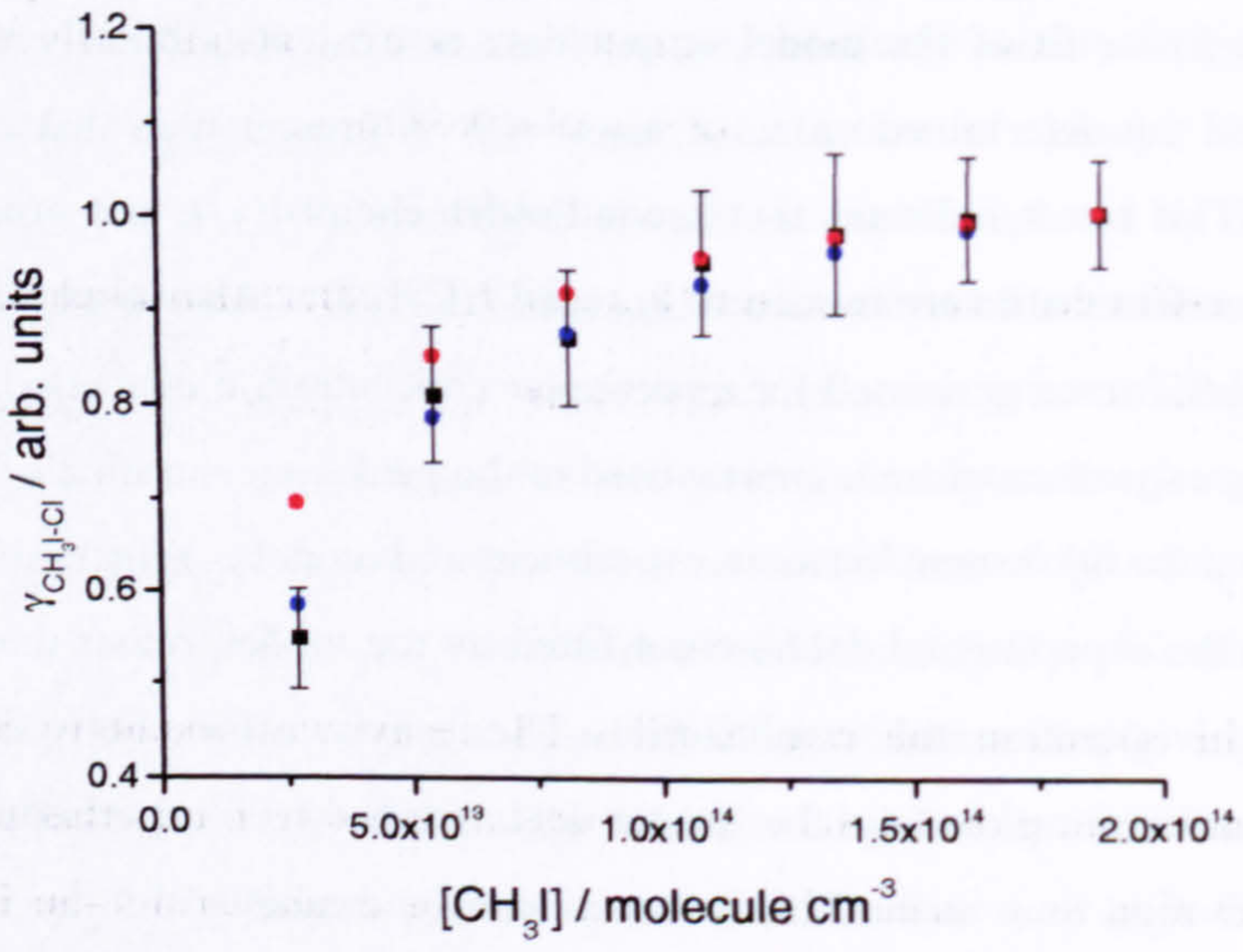

Fig. 5.3-7 – CH_3I-Cl yield plot for the reaction of CH_3I with Cl at 100 Torr and 204 K. The black squares represent the experimental data points (with 2σ uncertainty). The model calculations are represented by the blue circles (full model) and red circles (model without adduct-radical reactions).

The excellent agreement between the experimental data and the full model output is thus strongly indicative of the reaction mechanism being correctly identified (*i.e.* unimolecular dissociation of the adduct at 204 K is negligible) and the full chemistry of the system being understood, particularly as omitting the adduct-radical chemistry significantly overestimates the adduct yield at low methyl iodide concentrations.

As a final investigation at low temperature, the adduct removal rate was measured as a function of $[O_2]$ to discern whether any significant reaction between CH_3I-Cl and O_2 occurs.

Experiments were performed at 100 Torr total pressure and 204 K. The decay of the adduct was monitored in the absence and presence of up to ~ 5×10^{16} molecule cm^{-3} of O_2 and no significant change in the adduct decay rate was observed. Fig. 5.3-8 displays the measured adduct decay, k_{loss}, as a function of $[O_2]$.

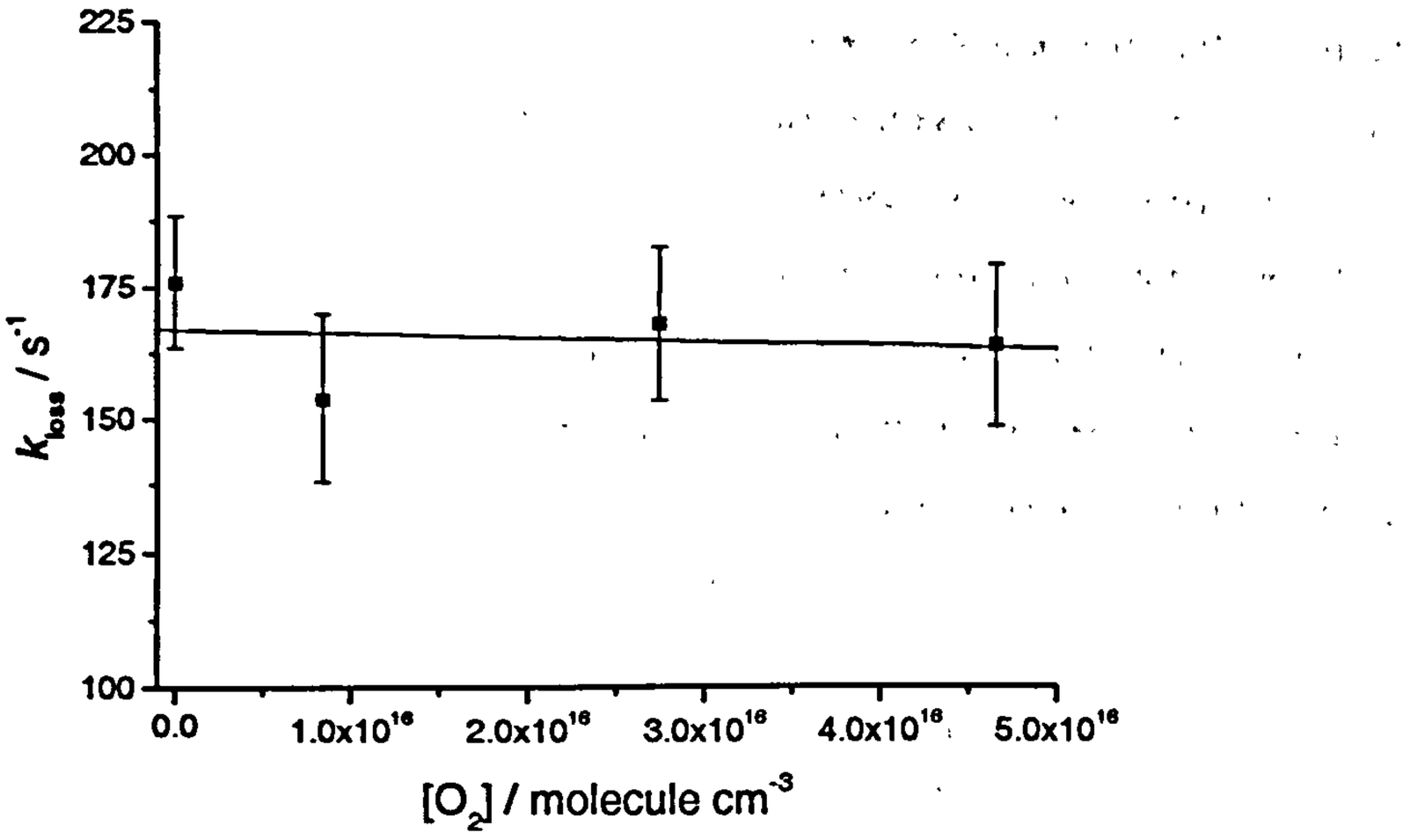

Fig. 5.3-8 – CH_3I-Cl decay rate as a function of $[O_2]$. Experimental conditions: T = 204 K, P = 100.2 Torr, $[CH_3I] = 1.24 \times 10^{14}$ molecule cm^{-3}, $[Cl_2SO] = 7.09 \times 10^{12}$ molecule cm^{-3}, $[O_2]$ = as indicated, $[N_2]$ = balance, $F = 2.4 \times 10^{15}$ photons cm^{-2}, λ_{pr} = 360.57 nm.

C. Note in Proof

In this investigation the rate of CH_3I-Cl decay was found to increases with the experimental concentration of $[Cl_2SO]$, which was assumed to imply that the CH_3I-Cl adduct reacts with ClSO radicals. Since this work was executed and written-up it has come to our attention that a subsequent kinetic and spectroscopic investigation of the CH_3I-Cl adduct by absorption spectroscopy[22] has reported a rate coefficient for the self-reaction of CH_3I-Cl of $k = (3.5 \pm 0.3) \times 10^{-10}$ $cm^3 molecule^{-1} s^{-1}$ at 250 K and 300 Torr N_2. As the concentration of Cl atoms, and therefore the adduct, are also dependent on the initial concentration of $[Cl_2SO]$, self-reaction of CH_3I-Cl will also have accounted for some of the observed adduct reactivity in this work. It should be emphasised that this result will have very little effect on the rate coefficients reported in this chapter (as the self-reaction is accounted for by the rate coefficient assigned to the CH_3I-Cl + ClSO reaction). Initial revision of the results suggests that the correct rate coefficient for the CH_3I-Cl + ClSO reaction is also of the order of $k = 3.5 \times 10^{-10}$ $cm^3 molecule^{-1} s^{-1}$ at ~ 206 K. Note that the ICH_2I-Cl adduct is also likely to self-react at a rapid rate.

5.3.3 Reaction Kinetics of the CH_3I + Cl Reaction at 296 K

As discussed is section 5.3.1, at room temperature, reversible adduct formation means that the experimental data must be fitted to E. 5.3-5, where the sum of the exponential terms is equal to the negative sum of all rate coefficients for all processes occurring within the reaction system. Therefore, a plot of $(\lambda_+ + \lambda_-)$ against $[CH_3I]$ should yield a straight line where the slope is equal to $-(k_a + k_{bi} + k_{eff})$ and the intercept is equal to $-(k_{-a} + k_{Cl} + k_{ClSO} + k_d)$. In order to evaluate the rate coefficients governing reversible adduct formation, k_a and k_{-a}, prior knowledge of the other rate coefficients is therefore required. Experiments were therefore performed in order to evaluate k_{eff} (*i.e.* $k(CH_3/I)$) and k_{ClSO} at 296 K. Fig. 5.3-9 displays two plots of $(\lambda_+ + \lambda_-)$ against $[CH_3I]$ for two experiments conducted under identical conditions other than excimer laser power, which was varied by more than an order of magnitude.

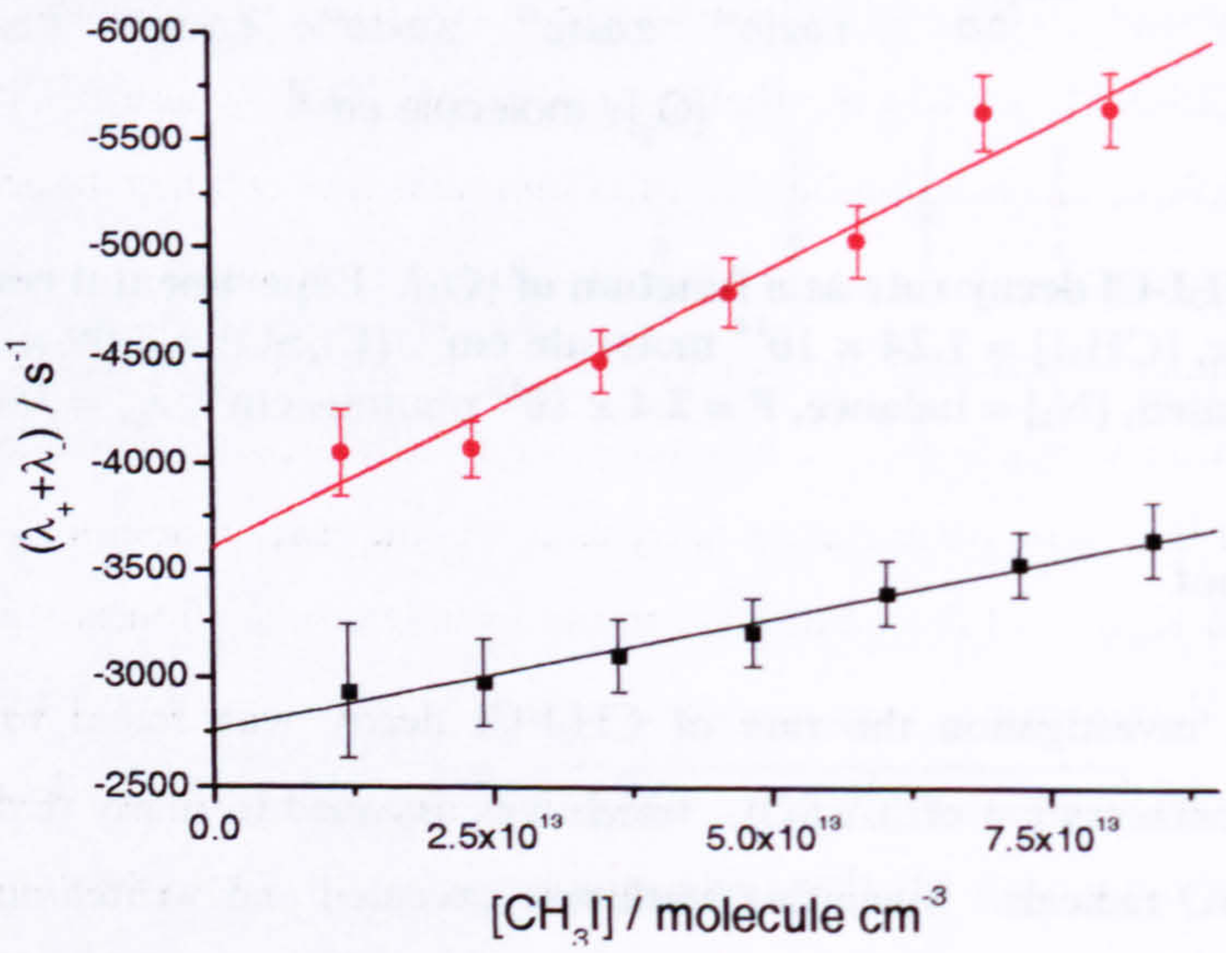

Fig. 5.3-9 – Bimolecular plots for CH_3I + Cl at 296 K. Experimental conditions: P = 100 Torr, $[Cl_2SO] = 7.21 \times 10^{12}$ molecule cm^{-3}, $[N_2]$ = balance, λ_{pr} = 360.57 nm, $F = 4.64 \times 10^{15}$ photons cm^{-2} (black) and 5.21×10^{16} photons cm^{-2} (red). From the linear fits: $m = -(1.03 \pm 0.15) \times 10^{-11}$ $cm^3 molecule^{-1} s^{-1}$, $c = -(2756 \pm 83)$ s^{-1} (black) and $m = -(2.61 \pm 0.59) \times 10^{-11}$ $cm^3 molecule^{-1} s^{-1}$, $c = -(3605 \pm 306)$ s^{-1} (red).

From Fig. 5.3-9 it can clearly be seen that both intercept and slope increase significantly with excimer laser fluence. This is conclusive evidence that the adduct reacts with photolysis products of both CH_3I and Cl_2SO. As $[Cl_2SO]$ is maintained at a constant value across the range of CH_3I concentrations it follows that the enhanced slope from the experiment utilising the higher excimer laser fluence is solely attributable to reaction of the adduct with photolysis products of methyl iodide. Thus simple modification of E. 5.3-8 gives

$$k_{(CH_3I)} = \frac{\Delta m}{\Delta \Phi} \qquad \text{E. 5.3-9}$$

where, Δm is the difference of the slopes from the plots of $(\lambda_+ + \lambda_-)$ against $[CH_3I]$, and $\Delta\Phi$ is the difference in photolysis factors from the two experiments. Thus we derive the value, $k(CH_3 / I) = (3.82 \pm 1.48) \times 10^{-10}$ cm^{3}molecule^{-1}s^{-1}. This value is in good agreement with that determined from the low temperature study of $(3.0 \pm 0.9) \times 10^{-10}$ cm^{3}molecule^{-1}s^{-1}, providing evidence that the increasing adduct loss rate with $[CH_3I]$ observed at low temperature was solely attributable to this process (and not reaction of the adduct with CH_3I). The fact that $k(CH_3/I)$ was found to be independent of pressure at low temperature indicates that the reaction is a bimolecular process. Therefore, although the values of $k(CH_3/I)$ at 296 and 216 K are within statistical uncertainty of each other, the slightly higher room temperature determination may be a genuine result and attributable to a weak barrier to reaction.

The difference in the intercepts of the slopes displayed in Fig. 5.3-9 is (848 ± 317) s^{-1}. As at the y-intercept, $[CH_3I] = 0$, this increase in reactivity of the adduct must be ascribed to reaction with ClSO. If we assume that $k_{ClSO} = \Delta c / \Delta[ClSO]$ (where $\Delta[ClSO]$ is the calculated difference in ClSO concentration between the high and low excimer laser power experiments), then we obtain k_{ClSO} (296 K) $= (3.66 \pm 1.37) \times 10^{-10}$ cm^{3}molecule^{-1}s^{-1}. Note that determining k_{ClSO} in this manner is assuming the reaction of CH_3I-Cl + ClSO to be occurring under pseudo-first-order reaction conditions. At low temperature, the reaction of ClSO radicals with the CH_3I-Cl adduct had to be treated essentially as a second order reaction as $[ClSO] \approx [CH_3I\text{-}Cl]$. However at 296 K, loss of the adduct *via* unimolecular dissociation is significantly high ($k_a \approx 2500$ s^{-1} at 100 Torr) that its concentration is always substantially lower than the initial Cl atom concentration (and hence [ClSO]). A simple modeling exercise, the details of which are not pertinent here, demonstrated that determining k_{ClSO} in the procedure described above underestimates the true rate coefficient by < 5 %. Thus, to a good approximation, the reaction of adduct with ClSO at 296 K can be treated as a pseudo-first-order process under the experimental conditions of this study. The finding that k_{ClSO} (296 K) is substantially lower than that at 204 K ($k_{ClSO} = (9.0 \pm 4.5) \times 10^{-10}$ cm^{3}molecule^{-1}s^{-1}) is in agreement with the reaction involving long-range attractive forces. Treating the k_{ClSO} determinations to an Arrhenius analysis (albeit only with two data points) yields a temperature dependence that can be described by the expression, $k_{ClSO}(T) = 4.94 \times 10^{-11} \exp(590/T)$.

Thus, for any plot of $(\lambda_+ + \lambda_-)$ against $[CH_3I]$ we have a method for the evaluation of k_a and k_{-a}:

$$k_a = -(m - k_{bi} - k_{eff}) \qquad \text{E. 5.3-10}$$

$$k_{-a} = -(c - k_{Cl} - k_{ClSO}' - k_d) \qquad \text{E. 5.3-11}$$

where, k_{bi} (296 K) = 7.97×10^{-13} $cm^3molecule^{-1}s^{-1}$ (taken from Ayhens *et. al*[17]), k_{eff} is calculated for the experimental conditions ($k_{eff} = (\Delta k(CH_3/I)')/\Delta[CH_3I]$), k_{Cl} is assumed to be independent of temperature and given the average value obtained from the low temperature experiments of 229 s^{-1}, k_{ClSO}' is calculated for the experimental conditions ($k_{ClSO}' = k_{ClSO}[ClSO]$), and k_d is given the nominal value of 20 s^{-1} for consistency with previous treatment of the data. Fig. 5.3-10 displays a plot of ($\lambda_+ + \lambda_-$) against $[CH_3I]$ at 500 Torr.

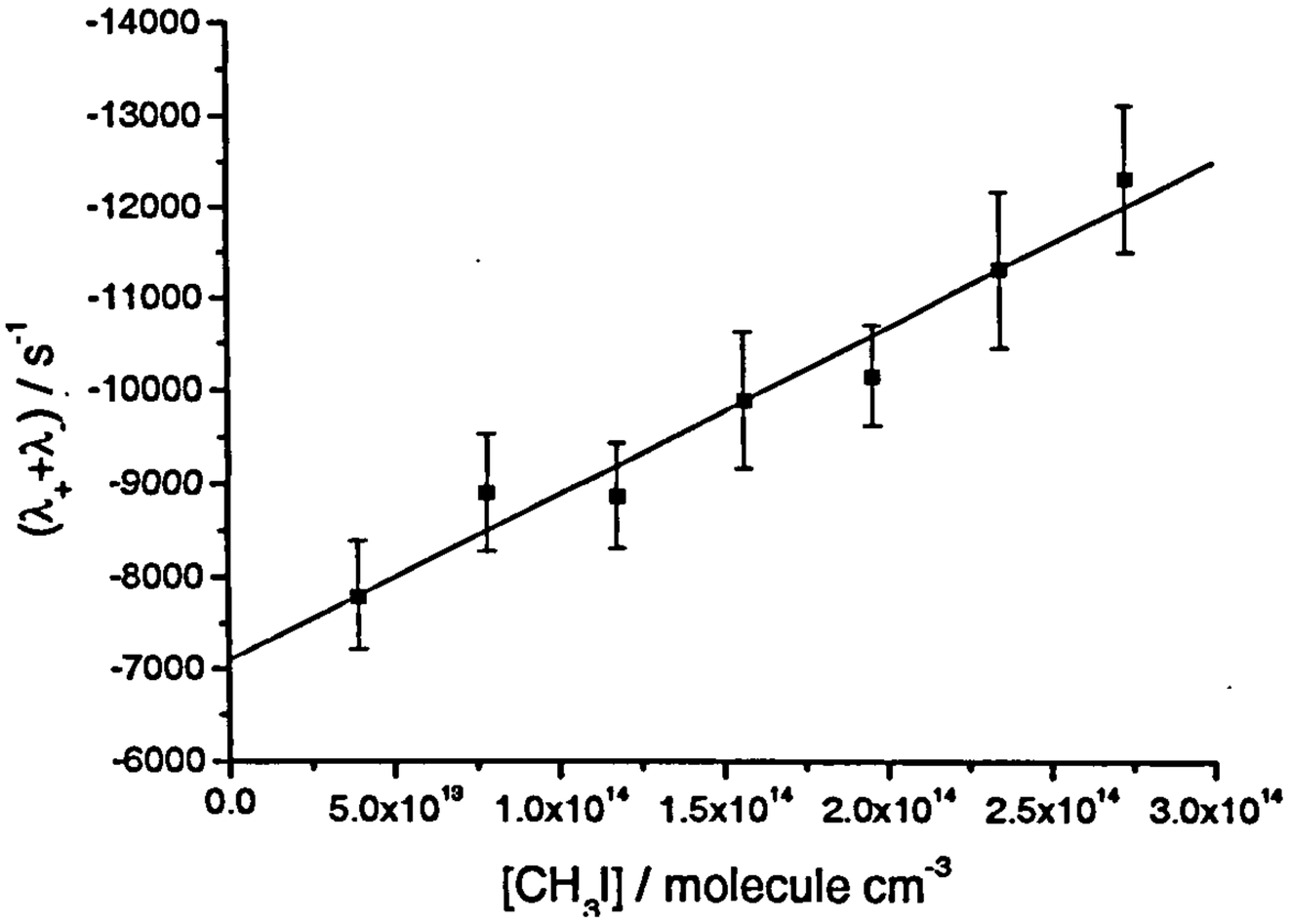

Fig. 5.3-10 – Bimolecular plot for CH_3I + Cl at 500 Torr and 296 K. Experimental conditions: $\Delta[CH_3I] = 2.34 \times 10^{14}$ molecule cm^{-3} ($\Delta[CH_3/I] = 5.19 \times 10^{11}$ molecule cm^{-3}), $[Cl_2SO] = 2.09 \times 10^{13}$ molecule cm^{-3} ($[ClSO] = 3.62 \times 10^{11}$ molecule cm^{-3}), $[N_2]$ = balance, $F = 2.55 \times 10^{15}$ photons cm^{-2}, λ_{pr} = 360.57 nm. From the linear fit to the data, $m = -(1.79 \pm 0.42) \times 10^{-11}$ $cm^3molecule^{-1}s^{-1}$ and $c = -(7100 \pm 727)$ s^{-1}.

Therefore,

$$k_a \text{ (296 K, 500 Torr)} = -[(-1.79 \times 10^{-11})-(7.97 \times 10^{-13})-(8.47 \times 10^{-13})]$$
$$= (1.63 \pm 0.38) \times 10^{-11} \text{ cm}^3\text{molecule}^{-1}\text{s}^{-1}$$

$$k_{-a} \text{ (296 K, 500 Torr)} = -[-7100-229-132-20]$$
$$= (6720 \pm 690) \text{ s}^{-1}.$$

The equilibrium constant, K_p is thus calculated to be $(58.3 \pm 14.8) \times 10^3$ atm^{-1}. Table 5.3-2 lists all determinations of k_a, k_{-a} and K_p obtained at 296 K in this study

P	$[Cl_2SO]$	$\Delta[CH_3I]$	F	$-m$	$-c$	k_{eff}	k_{ClSO}'	k_a	k_{-a}	K_p
21.5	3.10	439	24.5	12.6	37.7	8.31	18.8	3.53	16.4	52.0 ± 41.7
101.1	3.16	248	3.13	10.3	37.1	1.04	2.45	8.41	32.2	63.1 ± 36.5
101.6	0.72	7.26	4.64	10.3	27.6	1.54	0.83	7.97	24.2	79.4 ± 12.0
101.8	0.72	7.26	52.1	26.1	36.0	17.3	9.32	7.97	24.2	79.4 ± 19.3
100.4	2.06	11.5	2.55	10.8	24.7	0.85	1.30	9.11	24.7	89.0 ± 25.4
501.4	2.09	23.4	2.55	17.9	71.0	0.85	1.32	16.2	67.2	58.3 ± 14.8
101.0[a]	2.20	81.9	24.5	12.1	26.3	8.31	13.3	3.00	10.5	69.0 ± 27.3

Table 5.3-2 – Experimental conditions and determinations of k_a, k_{-a} and K_p for $CH_3I + Cl \leftrightarrow CH_3I$-Cl at 296 K. All experiments were conducted in N_2 with the exception of [a], in which the bath gas was He. Units: [] = 10^{13} molecule cm^{-3}; $F = 10^{15}$ photons cm^{-2}; (m, k_{eff}, k_a) = 10^{-12} cm^{3}molecule^{-1}s^{-1}; (c, k_{ClSO}', k_{-a}) = 10^2 s^{-1}; $K_p = 10^3$ atm^{-1}.

From the data in Table 5.3-2 it can be seen that at 296 K, K_p is independent of pressure and bath gas (as expected) within the error limits, with an average value of $(70.2 \pm 29.0) \times 10^3$ atm^{-1}, in excellent agreement with the value of 72.6×10^3 atm^{-1} calculated from the thermochemical data of Ayhens *et. al.*[17]. Considering the wide range of conditions employed in the 296 K kinetic experiments, this result is thus strongly indicative that the mechanism used to interpret the kinetic data is correct and that the rate coefficients for the adduct-radical reactions are well defined. It was noted in section 5.2 that the peak LIF adduct signal at 296 K was strongly dependent on $[CH_3I]$. This observation can be interpreted in terms of the adduct loss rate being comparable, and thus competitive, to adduct formation (under the experimental conditions). Thus modeling the variation of the adduct yield as a function of $[CH_3I]$ is a further test of the chemical system and the reaction mechanism. Fig. 5.3-11 displays the experimental peak adduct LIF signal as a function of methyl iodide concentration for the 101.1 Torr kinetic experiment. Also displayed in Fig. 5.3-11 are model calculations of the peak CH_3I-Cl concentration as a function of $[CH_3I]$. The experimental yields were analysed in the same way as described in section 5.3.2.B and the model used to calculate the theoretical yields was essentially the same as that described previously but with the addition of the bimolecular, k_{bi}, and adduct dissociation, k_{-a}, rate coefficients. The model input parameters are set to the exact experimental conditions of each methyl iodide concentration and all rate coefficients are adjusted to their appropriate value at 100 Torr and 296 K.

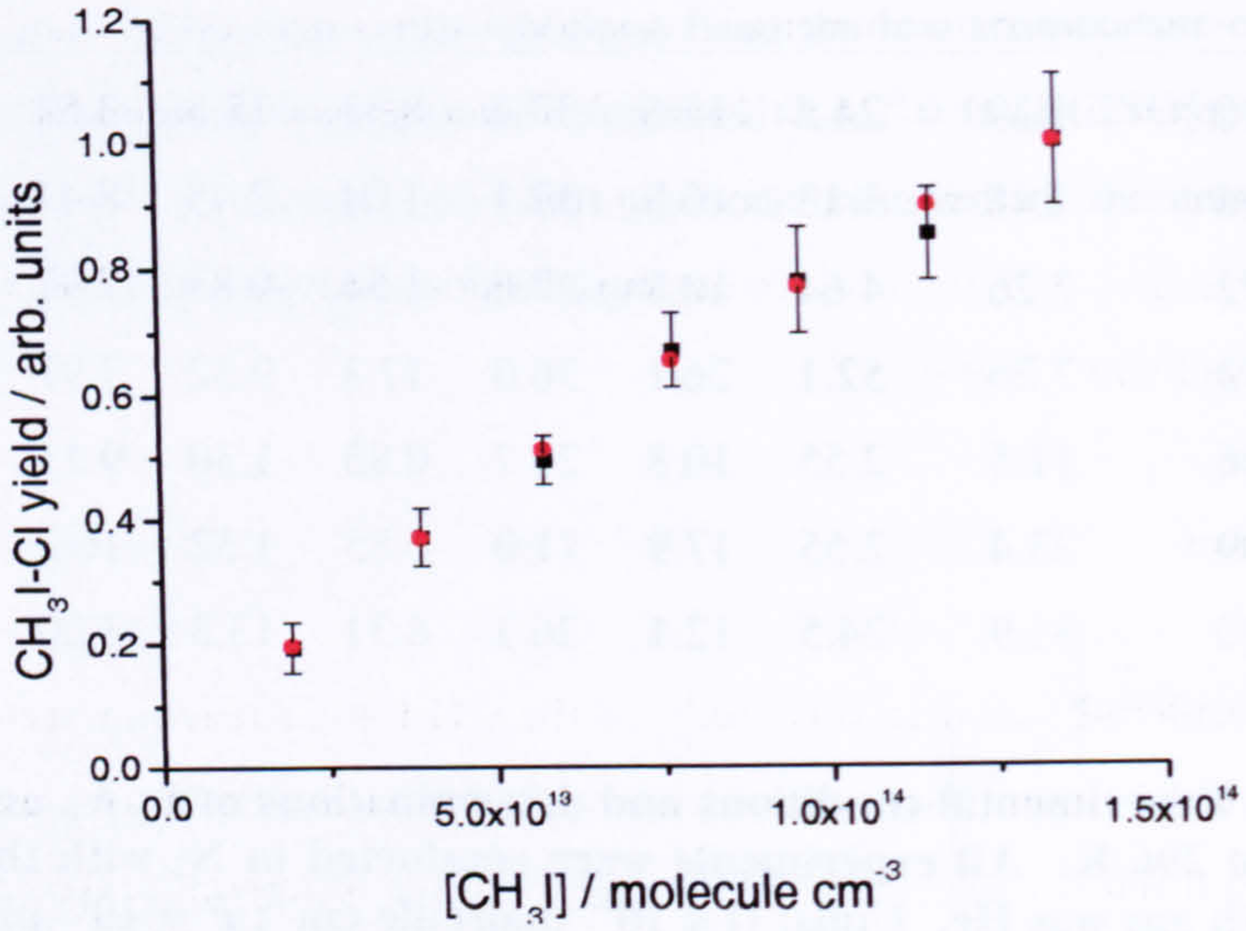

Fig. 5.3-11 – CH_3I-Cl yield plot for the reaction of CH_3I with Cl at 100 Torr and 296 K. The black squares represent the experimental data points (with 2σ uncertainty). The model calculations are represented by the red circles.

The exceptional agreement between experimental and model yields is highly indicative of the chemistry of the system being fully understood. It should be noted, however, that despite the fact that the rates of all processes determining the formation and removal of the adduct are well defined, the mechanism of adduct dissociation cannot be ascertained from this study. The CH_3I-Cl yield changes appreciably with [CH_3I] at 296 K as a result of the relatively high degree of unimolecular adduct dissociation. Whether this dissociation is back to reactants, or to products such as HCl + CH_2I or ICl + CH_3, will have very little effect on the overall adduct yield. In summary, the adduct yield is governed by the extent of adduct dissociation, and not by its mechanism. Despite this limitation of the current study, there is very good reason why the room temperature dissociation of CH_3I-Cl can be assumed to, almost exclusively, regenerate CH_3I + Cl. The study of Ayhens *et. al.*[17] employed resonance fluorescence detection of chlorine atoms. At room temperature, regeneration of Cl was observed, thus indicating that the adduct must, at least partially, dissociate back to reactants. As previously stated, in the study of Bilde and Wallington[19], the reaction kinetics of the CH_3I + Cl reaction were determined by monitoring the removal of CH_3I on a timescale of minutes in a continual photolysis smog chamber. The fact that the apparent rate coefficient for the reaction of methyl iodide with chlorine only increased by a small amount in moving from 1 – 700 Torr total pressure (4.6×10^{-13} $cm^3 molecule^{-1} s^{-1}$) indicates that the vast majority of the adduct decomposes back to reactants under atmospheric conditions. From the 296 K results obtained in this study (along with the results of Ayhens *et. al.*[17]), the total rate coefficient for the reaction of CH_3I + Cl can be estimated as, $k = 2.1 \times 10^{-11}$

$cm^3molecule^{-1}s^{-1}$ under typical atmospheric conditions. If it is assumed that the entire effective rate coefficient for adduct formation observed in the study of Bilde and Wallington[19] is attributable to unimolecular adduct dissociation to products other than CH_3I + Cl (which is unlikely), an upper limit of (0.046/2.1) = 2.2 % can be placed on adduct dissociation channels that do not regenerate methyl iodide and chlorine.

In agreement with the low temperature kinetic study, the CH_3I-Cl adduct was not observed to react with O_2 at 296 K.

5.3.4 Discussion

The results obtained in this study of the CH_3I + Cl reaction are essentially in perfect agreement with the findings of Ayhens *et. al.*17. Primarily, this provides conclusive evidence that the observed fluorescence from CH_3I + Cl mixtures following 360.57 nm laser excitation is attributable to the CH_3I-Cl adduct, which has not previously been reported to fluoresce (or experimentally absorb below 405 nm). At ~ 206 K the reaction of methyl iodide with atomic chlorine proceeds *via* irreversible adduct formation, as inferred from the linearity and small intercepts of the bimolecular plots, and the adduct yield as a function of [CH_3I]. Typical of an association complex reaction mechanism, the reaction kinetics of CH_3I + Cl display a marked pressure dependence. The adduct removal from the chemical system has been shown to be predominantly governed by reaction with radicals within the system. This observation suggests that the CH_3I-Cl adduct does not react with CH_3I, contrary to prior belief[19]. An interesting implication of the extremely rapid bimolecular reactions of the CH_3I-Cl adduct with radicals is that the CH_3I component of the adduct may act as an intramolecular third body in reactions which may be expected to display a pressure dependence, such as $CH_3 + Cl \rightarrow CH_3Cl$ or $I + Cl \rightarrow ICl$.

At room temperature, the adduct is observed to undergo reversible formation, as inferred from the large intercepts of the bimolecular plots and the significant dependence of adduct yield on [CH_3I]. Under atmospheric conditions typical of the MBL, the reaction of CH_3I + Cl proceeds with a total rate coefficient of ~ 2.1×10^{-11} $cm^3molecule^{-1}s^{-1}$. The study of Bilde and Wallington[19] places an upper limit on adduct dissociation channels that do not produce CH_3I + Cl, of 2.2 % at 296 K. If it is assumed that that this dissociation is exclusively to CH_3Cl + I, then a CH_3Cl yield of ~ 37 % should be observed at room temperature. The CH_3Cl yield in the study of Bilde and Wallington[19] was found to range from ~ 20 – 80 % and displayed a complex dependence on [CH_3I]. It is therefore most likely that the majority of the increased reactivity observed in their experiment in moving from 1 – 700 Torr total pressure is attributable to reaction of the CH_3I-Cl adduct with radicals within the system that generate CH_3Cl. In the study of Goliff and Rowland[18], a CH_3Cl yield of ~ 9 % was observed for the reaction of methyl

iodide and chlorine at 760 Torr and 298 K. The CH_3Cl yield was observed to decrease with increasing temperature, consistent with a decrease in the equilibrium constant, K_p, with increasing temperature. The yield was not observed to increase significantly in moving from 760 – 4000 Torr total pressure, probably because the association rate coefficient, k_a, has almost reached the high pressure limit in one atmosphere of bath gas. If it is assumed that the CH_3I-Cl adduct does not dissociate to any other products than CH_3Cl + I, the fate of the adduct at room temperature is almost exclusively (> 99.5 %) dissociation back to reactants.

The fact that Cotter *et. al.*[14] observed no pressure dependence in the reaction of CH_3I + Cl is most likely due to the narrow pressure range employed in a He bath gas in that study. Therefore, an apparent increase in the rate coefficient is indistinguishable from the experimental noise. However, the rate coefficient reported by Cotter *et. al.*[14] is significantly larger than the more reliable literature values for the bimolecular, HCl + CH_2I, forming channel of the reaction of CH_3I + Cl. This result is therefore indicative of some degree of adduct formation in their experiment.

The one significant discrepancy within the literature, therefore, is the fact that Kambanis *et. al.*[15] observed no significant kinetic isotope effect for the reaction of CH_3I + Cl → HCl + CH_2I, in contrast to the findings of Ayhens *et. al.*[17] and Bilde and Wallington[19], and also reported a smaller activation energy than Ayhens *et. al.*[17]. The notable experimental difference in the work of Kambanis *et. al.*[15] was the very low pressure employed in that study (~ 2 mTorr). The authors rationalise the anomalous result as implying that HCl formation arises from dissociation of the CH_3I-Cl adduct, which is not thermalised at low pressure, resulting in a smaller barrier to reaction. However, if this were the case then the effective rate coefficient for adduct formation reported in the study of Bilde and Wallington[19] would be much larger due to faster adduct formation at higher pressure. The reason for this discrepancy in the literature is thus unclear.

In the course of this study, it was found that the CH_3I-Cl adduct does not react with O_2, in agreement with the findings of Bilde and Wallington[19] and Enami. *et. al.*[20]. Therefore, it can be concluded that the reaction of CH_3I and Cl is of little atmospheric significance. Even if the reported Cl atom concentrations in the MBL are towards the upper estimates, the reaction of Cl with CH_3I cannot compete with the photolytic removal of methyl iodide from the atmosphere. Further, the atmospheric fate of the adduct will be decomposition back to reactants (with a small but insignificant amount of CH_3Cl + I formation). Although, in this study, the CH_3I-Cl adduct has been shown to react gas kinetically with radical species, there are no radicals present in the marine atmosphere at significant enough concentration that could compete with dissociation for adduct removal. If NO were to react at the gas kinetic rate with the CH_3I-Cl adduct, then adduct removal *via* this reaction could only compete with dissociation under conditions of extreme pollution. The effective rate coefficient for the reaction of CH_3I + Cl in the atmosphere is

therefore ~ 1×10^{-12} $cm^3 molecule^{-1} s^{-1}$ with > 90 % of the product yield being attributable to HCl and CH_2I.

5.4 Spectroscopic Study of the CH_3I-Cl Adduct

5.4.1 LIF Excitation Spectrum of the CH_3I-Cl Adduct

Fig. 5.4-1 displays the LIF excitation spectra of the CH_3I-Cl adduct recorded at 296 and 204 K. The spectra are normalised for probe laser power and represent the adduct fluorescence signal (as a function of excitation wavelength) relative to the background electronic signal of the apparatus, which is set to zero. Background LIF spectra of thionyl chloride and methyl iodide displayed no fluorescence signal in the presence or absence of excimer laser radiation (for the experimental Δt value). As can be seen from the spectra, the CH_3I-Cl adduct was observed to fluoresce strongly over the entire tuneable range of the dye laser. No significant difference is apparent in the spectra in moving from 296 – 204 K; suggesting that the adduct is thermalised rapidly in 100 Torr of nitrogen (< 150 μs) and that the electronic transition, occurring in the LIF excitation scheme, originates from the ground state of the adduct. As expected, the fine structure of the LIF spectrum at 204 K is more apparent, probably indicating the narrower rotational and vibrational distribution at low temperature. A slight difference between the spectra is that the fluorescence signal is slightly more intense at the extreme ends of the 296 K LIF spectrum, relative to that at 204 K. At the "red end" of the spectrum this feature may be attributable to hot band electronic transitions originating from excited vibrational levels in the adduct ground state, which have greater population at the higher temperature. Towards shorter wavelengths this observation may be attributable to the red wing of a transition originating at higher energy ($\lambda < 345$ nm) than the fundamental absorbance responsible for the majority of the observed fluorescence. Indeed, a second, relatively broad peak in the CH_3I-Cl LIF spectrum was observed at ~ 340 nm. However, a reproducible spectrum of the structure of this feature could not be obtained as 340 nm represents the extreme edge of the efficiency of the DMQ dye, on which the dye laser was operating. Although fluorescence from the CH_3I-Cl adduct is continuous (*i.e.* never returns to the baseline) over the 345 – 375 nm region, considerable spectral structure can be observed. Fig. 5.4-2 displays two expanded regions of the 204 K LIF spectrum, highlighting some of the structural features present.

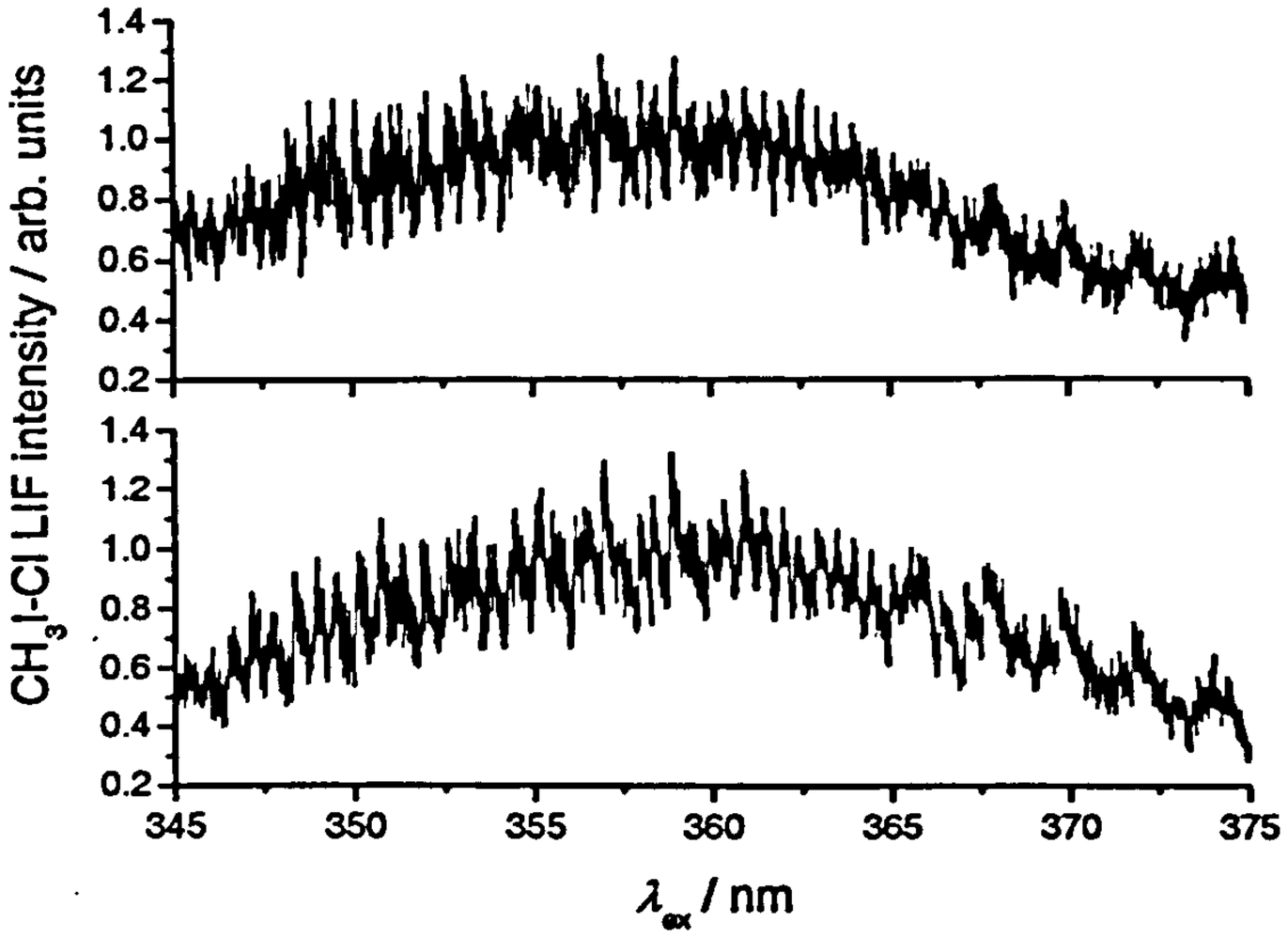

Fig. 5.4-1 – LIF spectra of the CH_3I-Cl adduct at 296 K (top panel) and 204 K (bottom panel). Experimental conditions: P = 100 Torr, $[Cl_2SO]$ = 6.3 × 10^{13} molecule cm^{-3}, $[CH_3I]$ = 4.3 × 10^{14} molecule cm^{-3}, $[N_2]$ = balance, Δt = 150 μs, F = 5.21 × 10^{16} photons cm^{-2}.

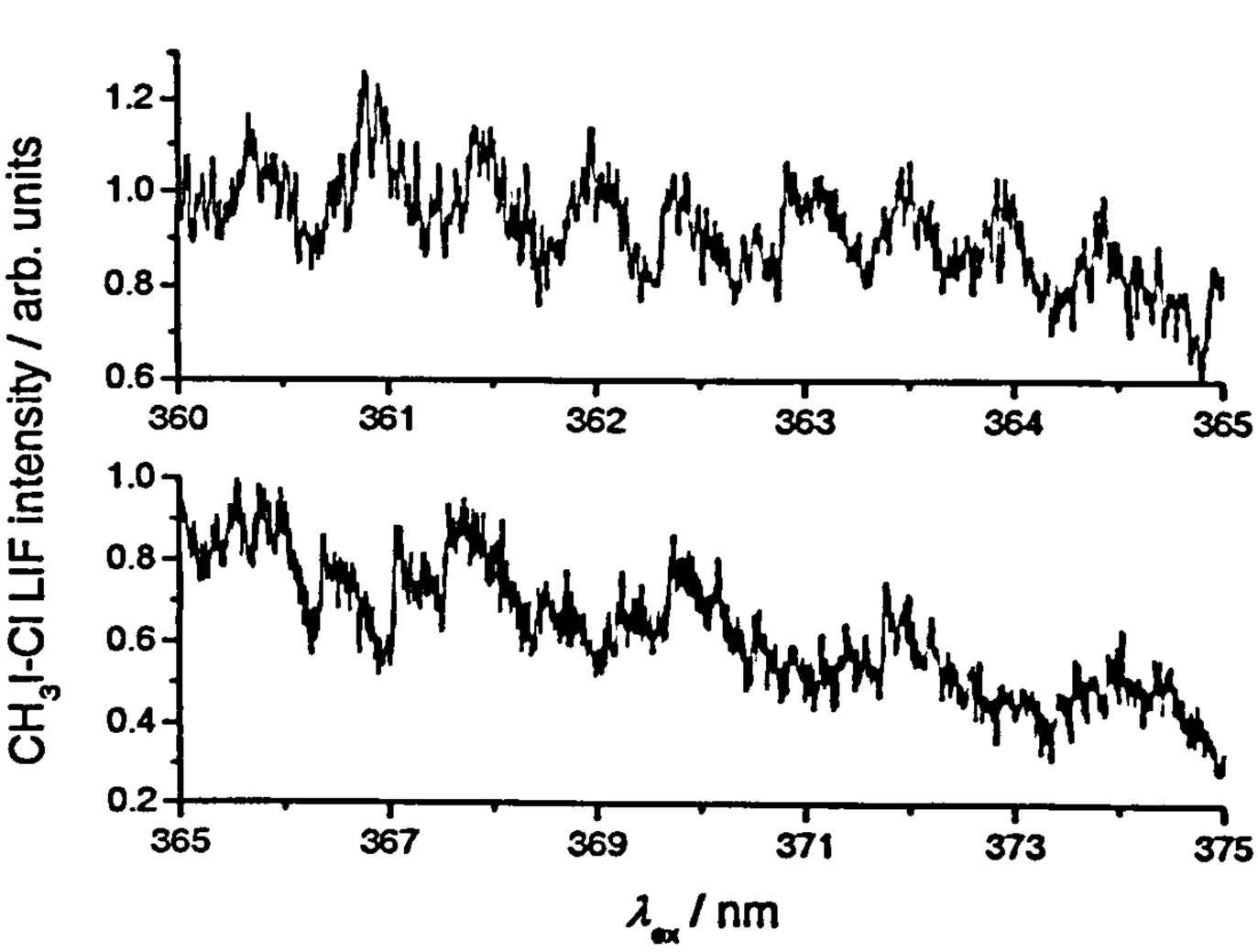

Fig. 5.4-2 – Expanded regions of the 204 K CH_3I-Cl LIF spectrum displayed in Fig. 5.4-1 displaying considerable structural features.

From Fig. 5.4-2 it can be seen that there are two regularly spaced structural features. The average separation between peaks in the spectral region shown in the top panel is ~ 0.5 nm, corresponding to an energy spacing of (40 ± 10) cm^{-1}. The regular spacing of the structure displayed in the bottom panel of ~ 2 nm corresponds to an energy separation of (150 ± 20) cm^{-1}.

Energy spacings of this magnitude are consistent with the vibrational frequencies of polyatomic molecules. In the theoretical calculations of Lazarou *et. al.*[16] the lowest ground state vibrational frequency of the CH_3I-Cl adduct is calculated to be 141.12 cm^{-1}. Ayhens *et. al.*[17] calculate the two lowest ground state CH_3I-Cl vibrational frequencies as 89 and 171 cm^{-1}. Thus the structural features present in Fig. 5.4-2 may be attributable to vibrational transitions in the CH_3I-Cl adduct. It would appear that there is a general change in spectral structure at ~ 370 nm. That is, only the 150 cm^{-1} spaced structure appears to wavelengths longer than 370 nm, whereas greater spectral structure is present at blue shifted wavelengths. This may be indicative that the origin of the electronic transition responsible for the observed adduct fluorescence is ~ 370 nm. For this scenario, structure to the red of the origin is attributable to hot bands of the electronic transition, and the more intense structure at shorter wavelengths is most likely attributable to electronic transitions terminating in highly excited vibrational levels of the adduct excited state. The presence of hot bands would not necessarily be indicative of the adduct having a non-thermal vibrational distribution as, for a small vibrational spacing of ~ 150 cm^{-1}, significant vibrational population (> 1 %) will be present for levels up to v'' = 6 at 296 K (and v'' = 4 at 204 K). The excitation scheme proposed is schematically represented in Fig. 5.4-3. The proposed excitation scheme could thus account for the observed structural features in the CH_3I-Cl LIF spectrum and the changes observed at the extreme ends of the spectrum at different temperature. It should be noted, however, that this excitation scheme is likely to be an extremely simplified description of the adduct spectroscopy due to the large density of states of a polyatomic molecule such as CH_3I-Cl. In the CRDS studies[20,21], absorption of the CH_3I-Cl adduct between 405 – 532 nm was ascribed to the red wing of transitions originating at 307 and 339 nm. The difference in wavelength between the two transitions (~ 30 nm) is therefore of similar magnitude to the proposed electronic transition origins in Fig. 5.4-3 (although with a ~ 30 nm displacement to the red).

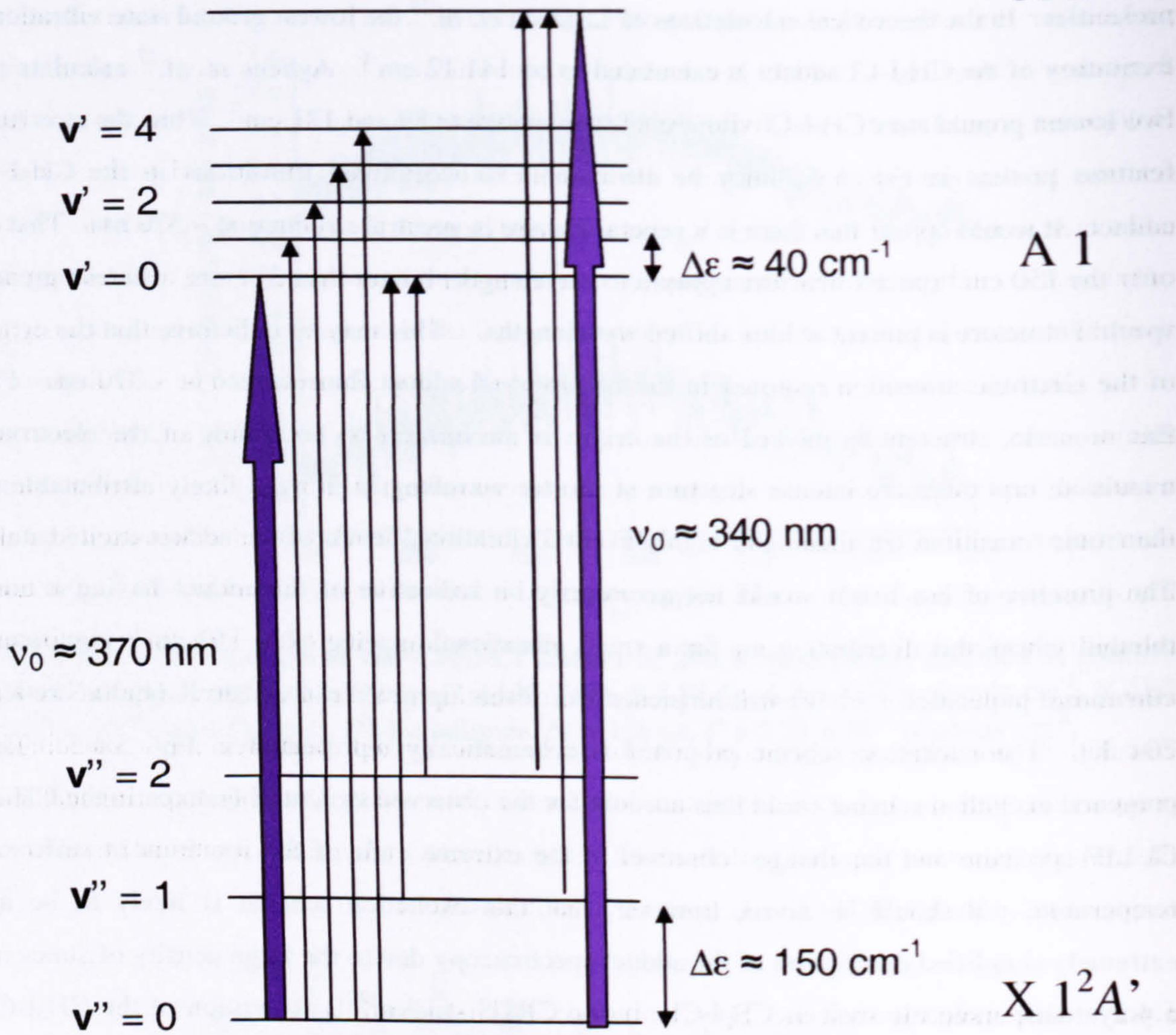

Fig. 5.4-3 – Possible LIF excitation scheme for the CH_3I-Cl adduct in the 340 – 370 nm spectral window. Transitions originate in the $X1^2A'$ adduct groundstate and terminate in various vibrational levels of unknown electronically excited states of the adduct, A1 and A2, with symmetry *A'* or *A''*. Note that this scheme will be for a particular vibrational mode of the adduct.

As the structure of the CH_3I-Cl LIF excitation spectrum reported in this work shows no significant temperature dependence, and because the adduct decay rate was not observed to change with pressure in the kinetic investigation, it is likely that the ground state of the adduct is thermalised rapidly in less than 10 Torr of N_2 (the lowest pressure studied in the kinetic investigation). If it is assumed that the 339 nm transition (the lower energy transition), calculated by Enami *et. al.*[20], is responsible for the observed adduct absorption in the CRDS experiments then, for an excitation wavelength of 405 nm, ~ 5000 cm^{-1} of ground state adduct excitation is required to undergo the designated transition. The exothermicity for CH_3I-Cl formation is calculated to be ~ 50 kJ mol^{-1} [16,17] (~ 4200 cm^{-1}) and so, even if all energy released

from adduct formation is transferred into internal excitation of CH_3I-Cl, an energy deficit is present for the assigned electronic transition. At 532 nm, > 10000 cm^{-1} of internal adduct excitation is required to satisfy the energetic requirements of the 339 nm transition. The Boltzmann population of a state lying 10000 cm^{-1} above the groundstate at 298 K is ~ 1×10^{-21}, relative to the groundstate. Further, the potential energy well of the CH_3I-Cl adduct is calculated to be ~ 60 kJ mol^{-1} [16] (~ 5000 cm^{-1}). Therefore, if the adduct possessed 10000 cm^{-1} of internal excitation, it would exist only for a very short period of time before dissociating and would not be detectable by absorption spectroscopy. Clearly, the electronic transitions assigned to the CH_3I-Cl absorption reported in the CRDS studies are incorrect. The calculations of Enami *et. al.*[20] are wholly inconsistent with their experimental observations, and the observed adduct absorption is most likely due to transitions terminating in lower lying electronic states than those identified in their study. Very few details to the theoretical calculations of the transition frequencies and probabilities are presented in the studies of Enami *et. al.*[20,21] and their reliability can therefore not be assumed. Calculating the electronic structure of iodine-containing molecules is notoriously difficult due to the high electron density. The theoretical calculations are therefore concluded not to be of great enough accuracy for a meaningful comparison with the experimental results obtained in this study. Further experimental and theoretical studies are required to definitively assign the electronic (and vibrational) transitions responsible for the CH_3I-Cl LIF spectrum reported in this work.

5.4.2 Dispersed Fluorescence Spectrum of the CH_3I-Cl Adduct

To further probe the transitions occurring within the CH_3I-Cl adduct the dispersed fluorescence spectrum was recorded at 296 K. As aforementioned, the monochromator grating could not be operated under computer control and had to be manually scanned by hand. Fig. 5.4-4 shows a dispersed fluorescence spectrum of the CH_3I-Cl adduct over a 320 – 600 nm spectral window, following 360.57 nm excitation. The first peak in the spectrum corresponds to the probe laser at ~ 360 nm. Fluorescence from the adduct consists of a strong peak at ~ 430 nm and a second, much weaker, peak at ~ 480 nm. Beyond ~ 500 nm, essentially no adduct fluorescence was observed. The observed fluorescence could be unambiguously assigned to the CH_3I-Cl adduct as the signal at ~ 430 nm was so intense that a kinetic trace could be recorded through the monochromator, as displayed in Fig. 5.4-5. Under the experimental conditions, the observed adduct reaction kinetics are in very good agreement with calculation using the previously determined adduct kinetics at 296 K and 20 Torr [$(\lambda_+ + \lambda_-)_{calc} = (0.89 \pm 0.14) \times (\lambda_+ + \lambda_-)_{exp}$].

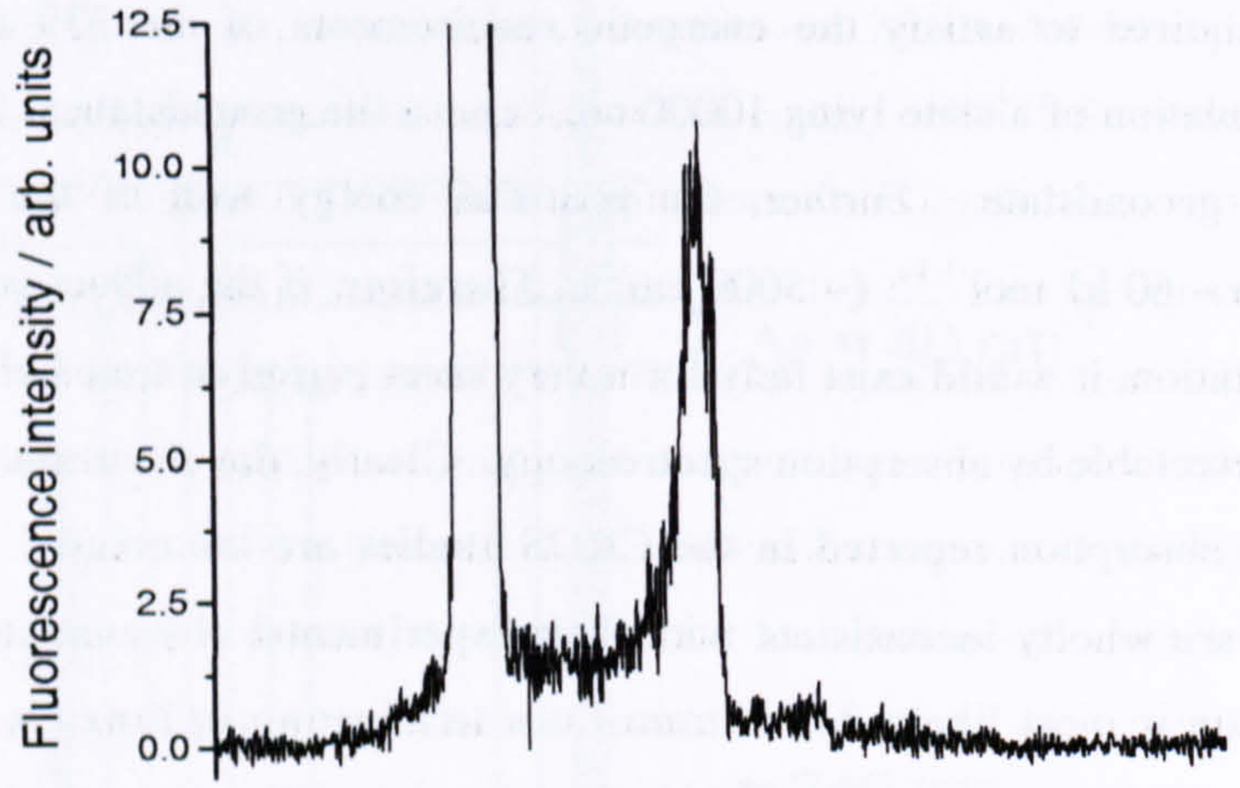

Fig. 5.4-4 – Dispersed fluorescence spectrum of the CH_3I-Cl adduct over the 320 – 600 nm range at 296 K. Experimental conditions: P = 287 Torr, $[Cl_2SO] = 6.0 \times 10^{13}$ molecule cm^{-3} , $[CH_3I] = 2.3 \times 10^{15}$ molecule cm^{-3} , $[N_2]$ = balance, Δt = 40 μs, $F = 3.3 \times 10^{16}$ photons cm^{-2}, λ_{pr} = 360.57 nm. Note that no wavelength scale is given as the monochromator grating had to be manually scanned by hand at an approximately constant rate.

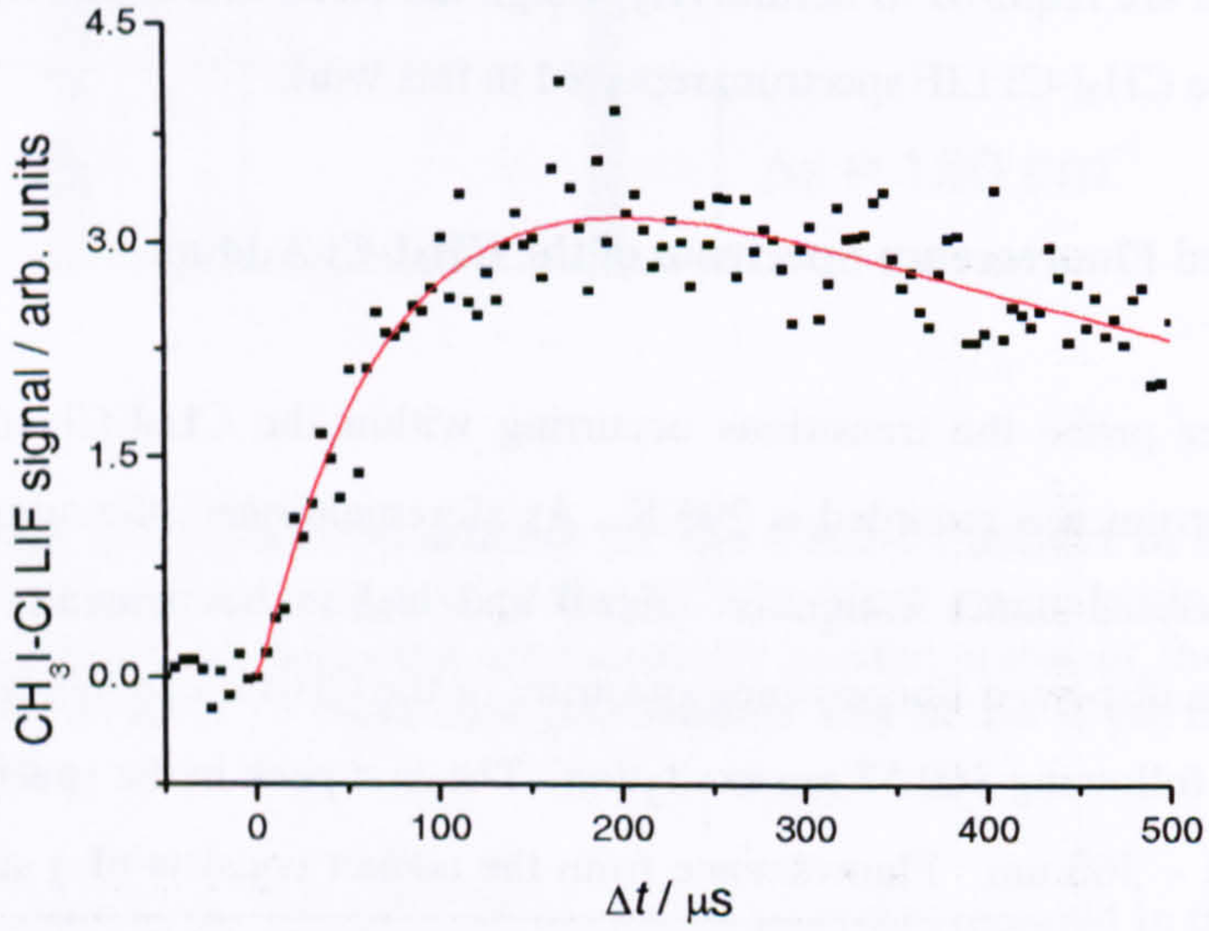

Fig. 5.4-5 – CH_3I-Cl kinetic trace recorded from monitoring adduct fluorescence at ~ 430 nm through the monochromator. Experimental conditions: T = 296 K, P = 20.2 Torr, $[Cl_2SO] = 2.6 \times 10^{13}$ molecule cm^{-3} , $[CH_3I] = 5.3 \times 10^{14}$ molecule cm^{-3} , $[N_2]$ = balance, F = 3.3×10^{16} photons cm^{-2}, λ_{pr} = 360.57 nm. The solid red line is a fit of E. 5.3-5 to the experimental data. From the fit, $(\lambda_+ + \lambda_-)_{exp} = -(13620 \pm 2154)$ s^{-1}. From the experimental conditions and the data in Table 5.3-2, $(\lambda_+ + \lambda_-)_{calc} = -12120$ s^{-1}.

The fact that little fluorescence is observed blue-shifted to the excitation wavelength in the dispersed fluorescence spectrum (Fig. 5.4-4) suggests that adduct excitation is not in the red

wing of an electronic transition between ground and excited states of CH_3I-Cl. If the electronic transition, responsible for adduct fluorescence, originated at 307 or 339 nm some blue shifted fluorescence relative to the excitation laser pulse at 360.57 nm would be expected. Further, this observation suggests that the groundstate of the adduct is thermalised prior to excitation.

The dispersed fluorescence spectrum of the CH_3I-Cl adduct was determined over the 375 – 475 nm range by recording the fluorescence signal of the adduct in 5 nm intervals. The probe laser background was also recorded (in the absence of excimer laser radiation) under the same experimental conditions in order for its subtraction from the fluorescence signal. The fluorescence signal for each wavelength was averaged for ~ 500 laser shots. The FWHM resolution of the monochromator was found to be ~ 5 nm for a 3 mm slit width. Fig. 5.4-6 displays the dispersed fluorescence spectra of CH_3I-Cl at 30 and 300 Torr. The fluorescence spectrum is observed to have a significant pressure dependence, shifting to longer wavelengths with increasing pressure, which is indicative of vibrational energy transfer in the excited state of the adduct. Presumably VET is relatively fast, thus a greater fraction of fluorescence originates from lower vibrational energy levels in the adduct excited state, and tends towards longer wavelengths. The behaviour also suggests that the rate of VET is competitive with that of electronic quenching.

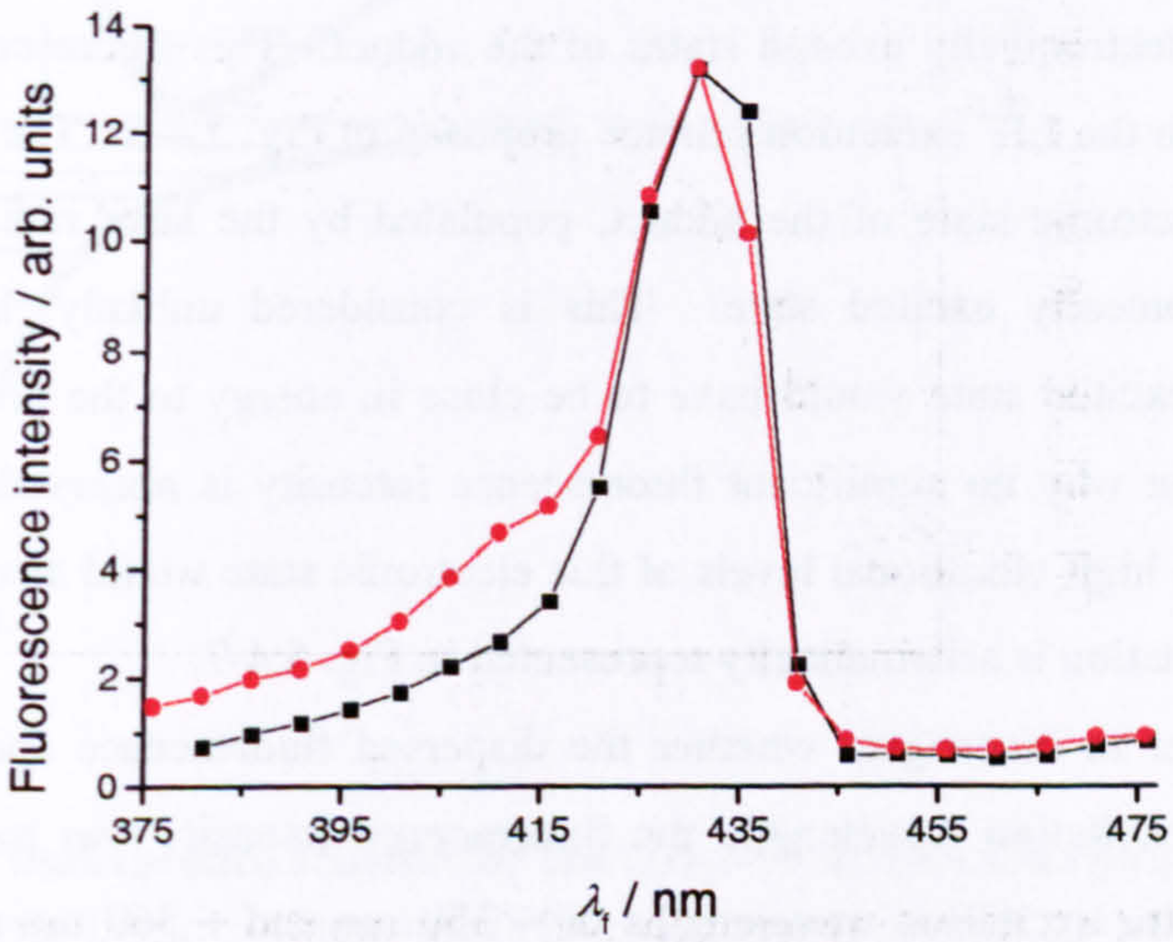

Fig. 5.4-6 – Dispersed fluorescence spectra of the CH_3I-Cl adduct at 296 K and 30 Torr (red) and 300 Torr (black). Experimental conditions: $[Cl_2SO] = 6.0 \times 10^{13}$ molecule cm^{-3}, $[CH_3I] = 2.3 \times 10^{15}$ molecule cm^{-3}, $[N_2]$ = balance, $\Delta t = 40$ μs, $F = 3.3 \times 10^{16}$ photons cm^{-2}, $\lambda_{pr} = 360.57$ nm. Note that the data have been normalised so that the peak fluorescence signals of the spectra are equal at ~ 430 nm. The fluorescence signal is relative to zero, *i.e.*, fluorescence is occurring at all wavelengths.

The largest fluorescence peak loses intensity for $\lambda > 445$ nm. This wavelength cannot represent the origin of the electronic transition as the CH_3I-Cl absorption spectrum reported by Enami *et. al.*[20] would be expected to display a similar structure to the dispersed fluorescence spectrum reported herein, which is not the case. Further, according to the LIF excitation scheme proposed in Fig. 5.4-3 (where ν_0 for the A1 ← X $1^2A'$ transition is altered to 445 nm) excitation at ~ 360 nm would correspond to extremely high vibrational excitation of the adduct excited state (v' ≈ 130, assuming a vibrational frequency of 40 cm^{-1} and not allowing for anharmonicity), *via* a transition which may be expected to have a small Franck Condon factor and terminate above the dissociation energy of the excited state. Therefore, the dispersed fluorescence spectrum can be interpreted in one of two ways. The first scenario is that fluorescence occurs between the same two electronic states that are responsible for the adduct absorption, and therefore terminates in the ground electronic state of CH_3I-Cl. If we assume that the electronic origin of the observed transition is ~ 370 nm, as previously predicted, then fluorescence at ~ 445 nm will terminate in a groundstate vibrational level with ~ 4500 cm^{-1} of energy (*i.e.* assuming that fluorescence originates from the ground vibrational level of the electronically excited state). This energy is of similar magnitude to the predicted binding energy of the adduct and may therefore provide a logical explanation as to why no significant fluorescence signal is observed at longer wavelengths. The weak fluorescence signal observed beyond 445 nm is perhaps attributable to the blue end of an electronic transition originating at ~ 480 nm, which is probably a transition between two electronically excited states of the adduct. This fluorescence scheme is entirely compatible with the LIF excitation scheme proposed in Fig. 5.4-3. The second scenario is that the excited electronic state of the adduct, populated by the laser radiation, is fluorescing to another electronically excited state. This is considered unlikely, however, as the lower electronically excited state would have to be close in energy to the ground electronic state in order to explain why no significant fluorescence intensity is observed beyond ~ 445 nm (as fluorescence to high vibrational levels of this electronic state would also be expected to occur). The first explanation is schematically represented in Fig. 5.4-7.

In order to investigate whether the dispersed fluorescence spectrum of CH_3I-Cl was dependent on excitation wavelength, the fluorescence intensity was measured over the 405 – 445 nm range for excitation wavelengths of ~ 350 nm and ~ 360 nm at 300 Torr. Fig. 5.4-8 displays the resulting spectra. Note that the data are not corrected for the probe laser background, explaining why the fluorescence signal does not tend towards the baseline at shorter wavelength. The close agreement between the two spectra indicates that fluorescence of CH_3I-Cl is essentially independent of excitation wavelength between 350 and 360 nm, consistent with the fluorescence scheme postulated in Fig. 5.4-7, and that the same electronic transition between ground and excited states is excited at both laser wavelengths.

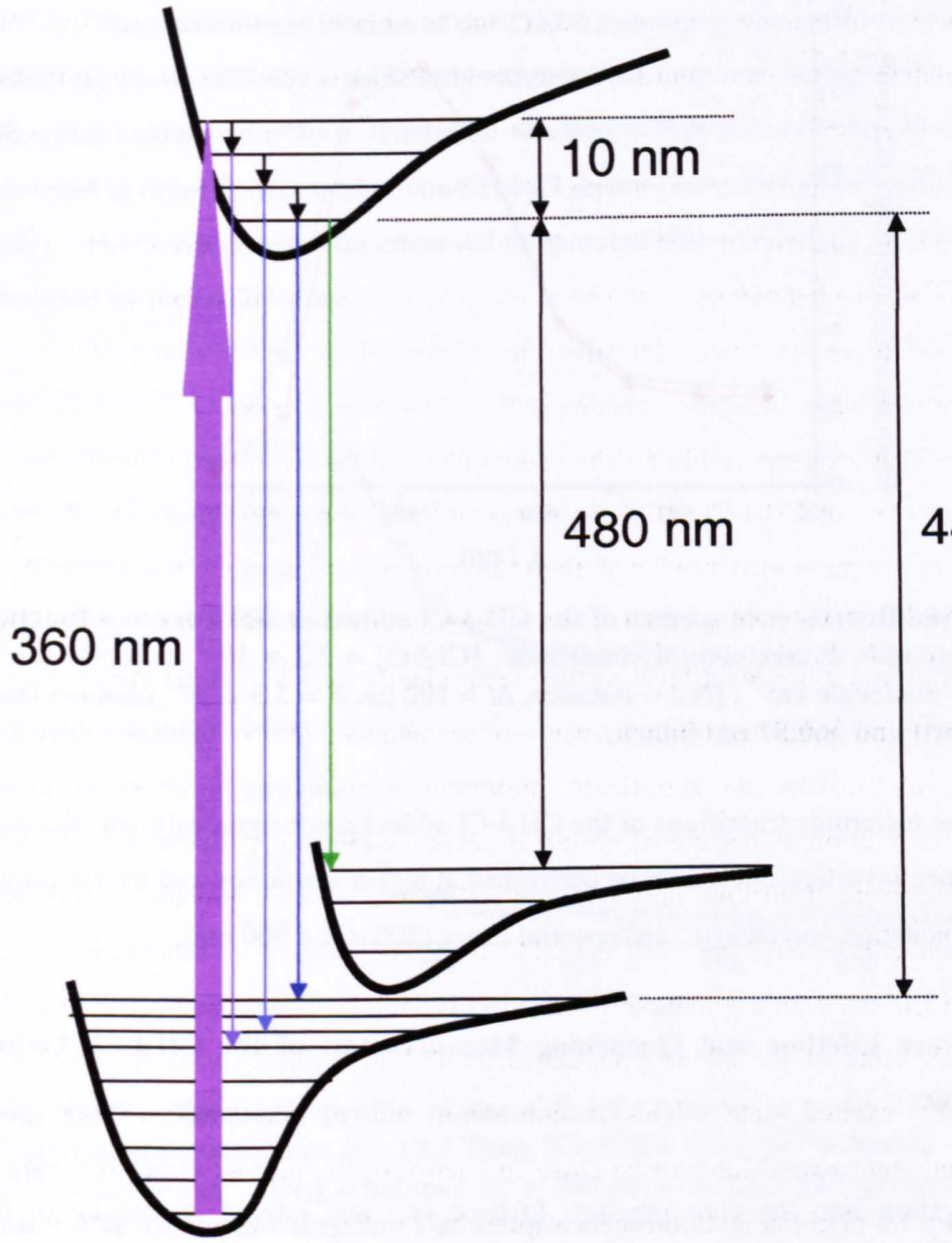

Fig. 5.4-7 – Proposed fluorescence scheme for the CH_3I-Cl adduct following ~ 360 nm laser excitation.

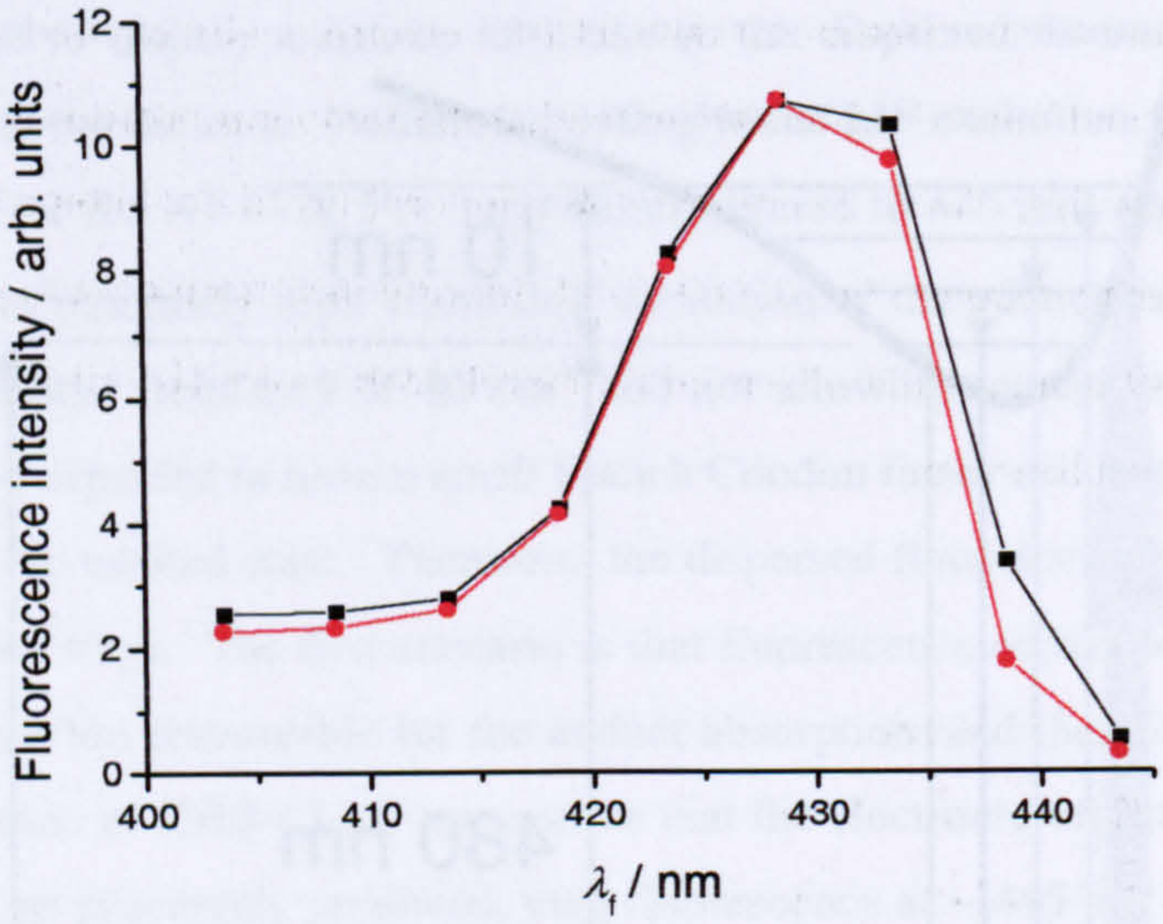

Fig. 5.4-8 – Dispersed fluorescence spectra of the CH_3I-Cl adduct at 300 Torr as a function of excitation wavelength. Experimental conditions: $[Cl_2SO] = 3.2 \times 10^{13}$ molecule cm^{-3}, $[CH_3I] = 7.8 \times 10^{14}$ molecule cm^{-3}, $[N_2]$ = balance, $\Delta t = 100$ μs, $F = 3.3 \times 10^{16}$ photons cm^{-2}, $\lambda_{pr} = 350.57$ nm (red) and 360.57 nm (black).

To probe the electronic transitions of the CH_3I-Cl adduct more rigorously, an extensive dispersed fluorescence investigation should be performed at higher resolution and over a greater range of pressure, excitation wavelength, and spectral range ($200 < \lambda < 900$ nm).

5.4.3 Zero Pressure Lifetime and Quenching Measurements of the CH_3I-Cl Adduct Excited State

An investigation into the zero pressure lifetime (τ_0) and rate of quenching of the electronically excited state of the CH_3I-Cl adduct by N_2 was performed at 296 K. Measurement of these processes can yield valuable information as to the nature of the potential energy surfaces of molecules. To quantify these parameters, the fluorescence lifetime of the CH_3I-Cl adduct was recorded as a function of total pressure (N_2) for an excitation wavelength of 360.57 nm. The fluorescence lifetime of a species, τ(s) at a given pressure of gas is given by E. 5.4-1

$$\tau = \frac{1}{A_f + A_p + A_q[Q]} \qquad \text{E. 5.4-1}$$

where, A_f is the inverse natural radiative lifetime ($1/\tau_0$) (s^{-1}), A_p is the predissociation rate (s^{-1}), A_q is the bimolecular quenching rate coefficient ($cm^3 molecule^{-1} s^{-1}$), and [Q] is the concentration of quencher Q (molecule cm^{-3}). Thus if the fluorescence lifetime of a species is measured as a

function of a pressure ([Q]), a plot of $1/\tau$ against [Q] should yield a straight line with slope A_q and intercept $(A_f + A_p)$.

The fluorescence lifetime of the CH_3I-Cl electronically excited state was observed to be relatively short, and only significantly extended the temporal profile of the probe laser pulse at pressures below ~ 100 Torr. Therefore, the temporal profile of the probe laser pulse was also recorded in order to deconvolute the CH_3I-Cl fluorescence from the temporal profile of the laser pulse. Fig. 5.4-9 displays the observed temporal profile of CH_3I-Cl fluorescence at ~ 10 Torr, recorded by the oscilloscope.

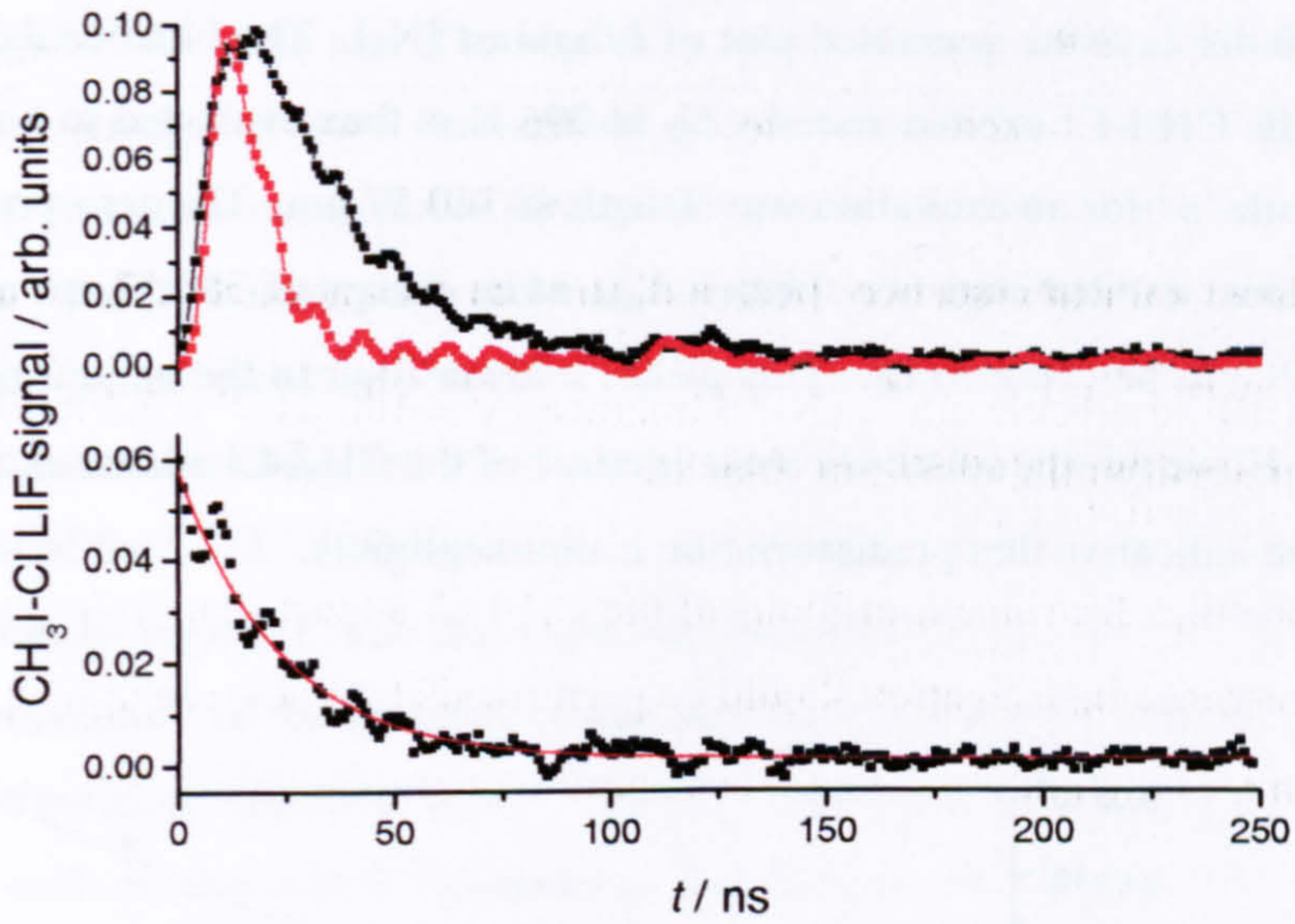

Fig. 5.4-9 – Temporal profile of the CH_3I-Cl adduct at ~ 10 Torr total pressure N_2. Experimental conditions: P = 10.2 Torr, $[Cl_2SO] = 4.1 \times 10^{13}$ molecule cm^{-3} , $[CH_3I] = 5.1 \times 10^{14}$ molecule cm^{-3} , $[N_2]$ = balance, Δt = 500 μs, $F = 3.3 \times 10^{16}$ photons cm^{-2}, λ_{pr} = 360.57 nm. The top panel displays the temporal profile of the CH_3I-Cl fluorescence (black squares) and the probe laser pulse (red squares), normalised to the peak adduct LIF signal. The bottom panel displays the residual of the CH_3I-Cl fluorescence with a fit to E. 5.4-2. From the fit $k_f = (4.14 \pm 0.17) \times 10^8$ s^{-1} ($\tau = (24.2 \pm 1.0)$ ns).

To obtain the fluorescence lifetime of the adduct at a given pressure, the temporal profile of the probe laser background is subtracted from that of the CH_3I-Cl fluorescence profile (after normalising the peak signal of the probe laser to that of the adduct fluorescence). From the probe laser background, it is found that the FWHM of the dye-laser pulse is ~ 15 ns. At all pressures investigated, the fluorescence of the adduct was found to be completely resolved from that of the probe laser at a time of 25 ns after the rising edge of the probe laser pulse. The residual CH_3I-Cl fluorescence profile is then fitted to a single exponential decay, E. 5.4-2, to obtain the inverse fluorescence lifetime of the adduct, k_f

$$S_t = S_0 \exp(-k_f t) \qquad \text{E. 5.4-2}$$

where, S_t and S_0 are the fluorescence intensities of CH_3I-Cl at time, t, and $t = 0$ respectively. The procedure for determining k_f as a function of pressure is displayed in Fig. 5.4-9.

The fluorescence lifetime of the CH_3I-Cl adduct was observed to decrease significantly with increasing pressure and, for all pressures investigated, the temporal profile of the CH_3I-Cl fluorescence was observed to follow monoexponential behaviour. Although, the precursor concentrations were not maintained at constant values across the study, their low values ($[CH_3I]_{max}$ < 20 mTorr and $[Cl_2SO]_{max}$ < 2 mTorr) means that quenching of CH_3I-Cl fluorescence must be solely attributed to collisional deactivation of the adduct excited state by N_2. Fig. 5.4-10 displays the generated plot of k_f against $[N_2]$. The bimolecular quenching rate coefficient of the CH_3I-Cl excited state by N_2 at 296 K is thus evaluated to be $(1.28 \pm 0.24) \times 10^{-11}$ $cm^3 molecule^{-1} s^{-1}$ for an excitation wavelength of 360.57 nm. The zero-pressure lifetime of the CH_3I-Cl adduct excited state (*i.e.* $1/(A_f + A_p)$), at an energy of 360.57 nm above the ground state, is evaluated to be (28 ± 3) ns. This places a lower limit to the natural radiative lifetime, τ_{rad}, of 28 ns. However, the relatively short lifetime of the CH_3I-Cl adduct excited state at zero pressure may be indicative that predissociation is non-negligible.

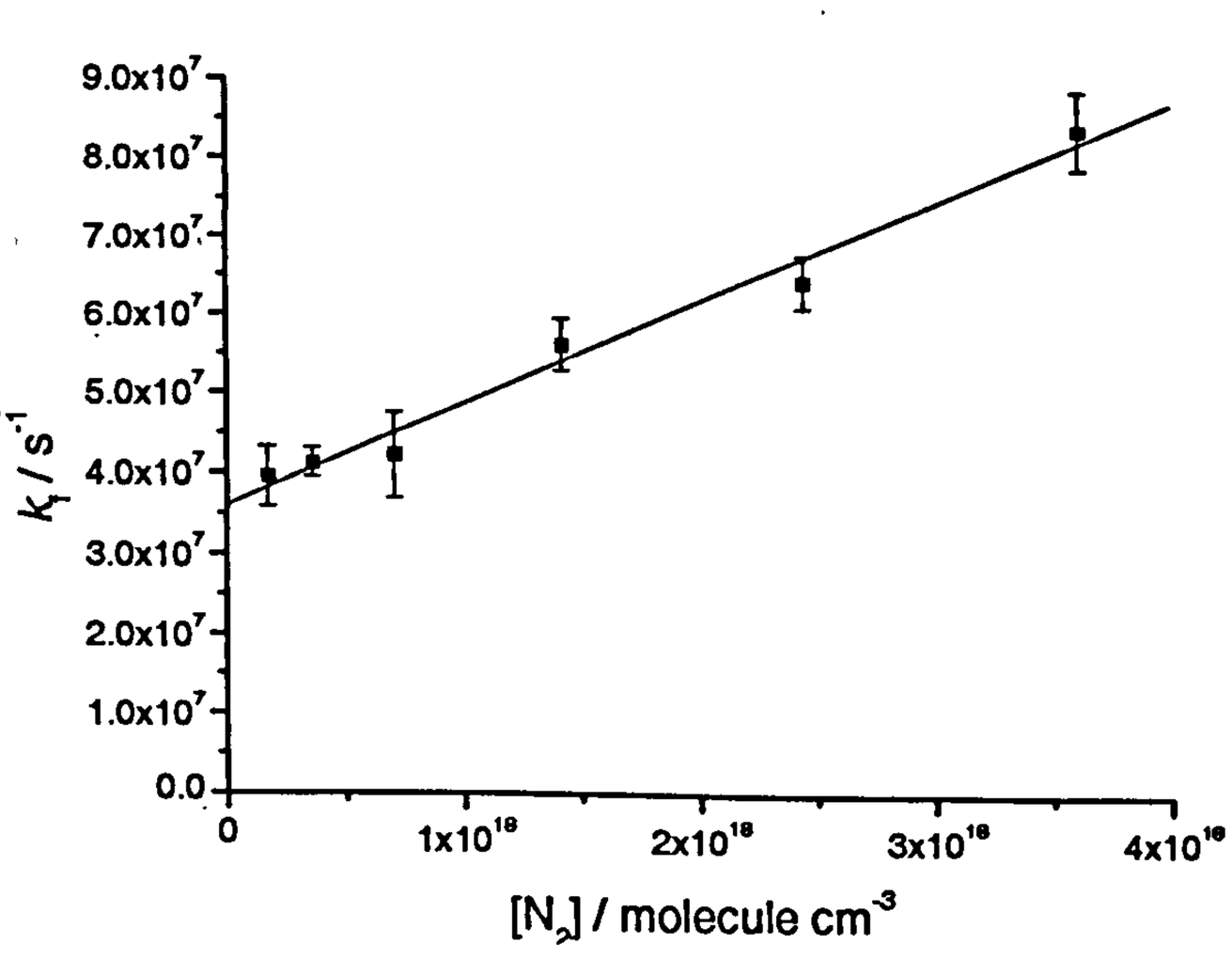

Fig. 5.4-10 – Plot of the inverse fluorescence lifetime of the CH_3I-Cl adduct, k_f, against $[N_2]$ for an excitation wavelength of 360.57 nm. From the linear fit, $k(N_2, 296\ K) = (1.28 \pm 0.24) \times 10^{-11}$ $cm^3 molecule^{-1} s^{-1}$ and $(A_f + A_p) = (3.61 \pm 0.45) \times 10^7$ s^{-1}.

As the pressure dependence of the CH_3I-Cl dispersed fluorescence spectrum may be indicative of VET in the adduct excited state, the mechanism for fluorescence quenching may be vibrational relaxation to states which lie close to the potential energy surface of a repulsive electronic state (that crosses the potential energy surface of the bound CH_3I-Cl electronic state

at relatively low vibrational levels) and results in the dissociation of the CH_3I-Cl adduct. This hypothesis could be tested by measuring the quenching rate coefficient, and zero pressure lifetime, of the CH_3I-Cl excited state as a function of excitation wavelength (*i.e.* if the postulated mechanism is correct, the quenching rate coefficient and zero pressure lifetime should decrease and increase respectively with increasing excitation energy).

5.4.4 Discussion

The LIF excitation spectrum of the CH_3I-Cl adduct has been reported for the first time. The chloro-iodomethane adduct is observed to fluoresce strongly over the entire investigated wavelength range of 345 – 375 nm. The similarity in the LIF spectra at 204 and 296 K indicates that the adduct is excited from a thermalised groundstate in 100 Torr of N_2 diluent. Two regularly spaced structural components of the LIF spectra were identified with energy spacing of (40 ± 10) cm^{-1} and (150 ± 20) cm^{-1} and may correspond to the lowest vibrational frequencies of the excited and ground electronic states of the CH_3I-Cl adduct respectively. The origin of the electronic transition responsible for the observed fluorescence is tentatively assigned at ~ 370 nm. Absorption of the CH_3I-Cl adduct over the wavelength range investigated in this study has not been previously reported and the experimental observations do not agree with recent theoretical calculations[20] of the energies of the electronic states of the CH_3I-Cl adduct, or the probability of transitions between them. The LIF spectrum recorded in this work requires assignment by refined theoretical calculations and further experiment. The adduct is now known to absorb over an extensive wavelength range (~ 340 – 540 nm) and the LIF spectrum of CH_3I-Cl should be recorded over as wider wavelength range as experimentally possible to further probe the electronic structure of this molecule. The pressure dependence of the LIF spectrum should also be investigated. A high resolution study of the structural components of the LIF spectrum at low temperature should be performed in order to more accurately determine the spectroscopic constants of the CH_3I-Cl adduct.

The dispersed fluorescence spectrum of CH_3I-Cl is also reported. The fluorescence intensity increases from the excitation wavelength up to ~ 430 nm, where an intense fluorescence peak is observed. The 430 nm fluorescence peak has a sharp cut off wavelength of ~ 445 nm, beyond which only weak fluorescence is observed. Essentially no CH_3I-Cl fluorescence is observed at wavelengths longer than ~ 500 nm. The dispersed fluorescence spectrum is pressure dependent with enhanced fluorescence intensity at shorter wavelengths at low pressure, possibly indicating the occurrence of vibrational energy transfer in the excited state of the adduct. No discernible difference in the dispersed fluorescence spectrum was observed in moving from an excitation wavelength of ~ 360 nm to ~ 350 nm. The most likely mechanism of CH_3I-Cl fluorescence is resonant fluorescence, of the electronic transition excited

by the laser, to highly excited vibrational levels in the adduct groundstate. The apparent cut off wavelength (~ 445 nm) of the intense fluorescence peak probably corresponds to the difference in energy between the ground vibrational level of the electronically excited state and the dissociation limit of the ground electronic state. To further probe the electronic transitions of CH_3I-Cl, the dispersed fluorescence spectrum should be recorded over a greater spectral region for an extensive range of excitation wavelengths and pressures. The dispersed fluorescence of CH_3I-Cl should be recorded under higher resolution than the present study (~ 5 nm FWHM) to identify any structural components of the spectrum.

The bimolecular quenching rate coefficient for the excited state of CH_3I-Cl by N_2, initially populated at ~ 360 nm above the ground state, has been directly measured by fluorescence lifetime measurements to be, $k = (1.28 \pm 0.24) \times 10^{-11}$ $cm^3 molecule^{-1} s^{-1}$ at 296 K. The zero pressure lifetime of the excited state is relatively short [(28 ± 3) ns], possibly indicating the influence of predissociation. The mechanism of excited state quenching probably involves vibrational energy transfer, possibly resulting in interaction with repulsive electronic states of CH_3I-Cl. For a more detailed investigation, quenching rate coefficients and the zero pressure lifetime of the CH_3I-Cl adduct excited state should be studied as a function of excitation energy and for a variety of quenchers.

5.5 Reaction Kinetics of the CH_2I_2 + Cl Reaction

In the introduction it was discussed that the reaction of chloroiodomethane with Cl atoms is known to produce ICl and CH_2I with an effective 100 % yield. Table 5.5-1 lists the standard enthalpies of reaction, $\Delta H^0_{r,298}$, for the formation of either HCl or ICl (and their co products) from the reaction of Cl atoms with CH_3I, CH_2ICl and CH_2I_2. Thus we can see that, while the ICl forming channel is inaccessible for the reaction of CH_3I + Cl, this reaction pathway becomes energetically accessible for the reaction of chlorine atoms with both chloroiodomethane and diiodomethane. Further, there are large errors associated with the enthalpies of reaction for the HCl forming channel of the CH_2ICl and CH_2I_2 reactions with Cl (due to the indirect methods of obtaining the enthalpies of formation of $CHICl$ and CHI_2). Therefore, the enthalpies of reaction for the HCl and ICl product channels may be much closer to one another than indicated. As ICl is known to be the exclusive reaction product of the Cl + CH_2ICl reaction[23,25], a significant ICl yield may therefore be expected for the reaction of diiodomethane with atomic chlorine. ICl has been detected as a product of the Cl + CH_2I_2 reaction in a reactive scattering study[24].

Iodoalkane	$\Delta H^0_{r,298}$ (HCl)	$\Delta H^0_{r,298}$ (ICl)
CH_3I	2.3	28.4
CH_2ICl	-8.7	6.4
CH_2I_2	-7.4	8.3

Table 5.5-1 – Reaction enthalpies (kJ mol^{-1}) for the formation of HCl / ICl from the reaction of relevant alkyl iodides with atomic chlorine at 298 K. The enthalpies are calculated from the known standard enthalpies of formation, $\Delta H^0_{f,298}$, of the various products and reactants[30]. No experimental determinations of $\Delta H^0_{f,298}$ for CHICl (CH_2ICl + Cl → HCl + CHICl) or CHI_2 (CH_2I_2 + Cl → HCl + CHI_2) are reported in the literature. $\Delta H^0_{f,298}$ (CHICl) has been theoretically calculated to be 212 kJ mol^{-1} [25]. $\Delta H^0_{f,298}$ (CHI_2) has been estimated by extrapolating a plot of $\Delta H^0_{f,298}$ (CH_2X) against $\Delta H^0_{f,298}$ (CHX_2) for F, Cl and Br, yielding a value for $\Delta H^0_{f,298}$ (CHI_2) of (324.2 ± 188.2) kJ mol^{-1}.

5.5.1 Reaction Kinetics of CH_2I_2 + Cl at ~ 206 K

Similarly to the CH_3I + Cl investigation, the reaction kinetics of the CH_2I_2 + Cl reaction were studied between 10 – 500 Torr total pressure (N_2) at ~ 206 K and by monitoring the temporal evolution of the ICH_2I-Cl adduct by LIF (λ_{pr} = 365.57 nm). At low temperature the data were analysed using equation 5.3-2. Note that whether the reaction mechanism proceeds to HCl or ICl products is irrelevant if we assume that both the bimolecular reaction channel and adduct dissociation are negligible at low temperature. Fig. 5.5-1 displays some kinetic traces of the CH_2I_2 adduct recorded over different ranges of Δt. The biexponential function, E. 5.3-2 was found to satisfactorily fit the experimental data and, similarly to the CH_3I-Cl adduct LIF signal, a small, positive baseline deviation was observed at large Δt. The rate of formation of the ICH_2I-Cl adduct, in the reaction of diiodomethane with Cl, was found to be pressure dependent. Fig. 5.5-2 displays bimolecular plots of k_a' against [CH_2I_2].

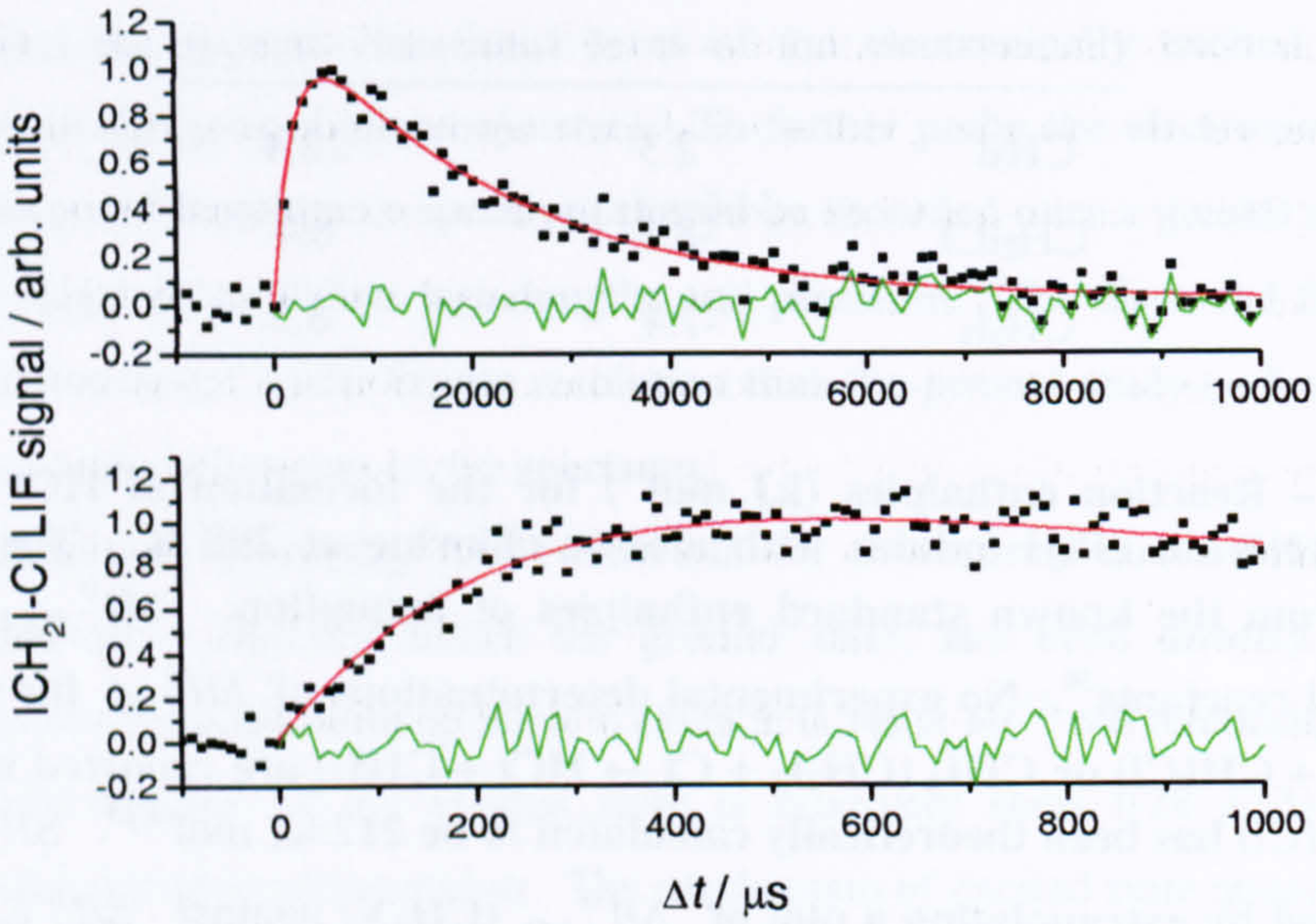

Fig. 5.5-1 – Experimental kinetic traces of the ICH_2I-Cl adduct and their respective fits to E. 5.3-2. The residuals of the fits to the data are given by the solid green line. Experimental conditions: T = 203.8 K, P = 100.2 Torr, $[Cl_2SO] = 1.56 \times 10^{13}$ molecule cm^{-3}, $[CH_2I_2] = 7.90 \times 10^{13}$ molecule cm^{-3}, $[N_2]$ = balance, $F = 4.2 \times 10^{15}$ photons cm^{-2}, λ_{pr} = 365.57 nm.

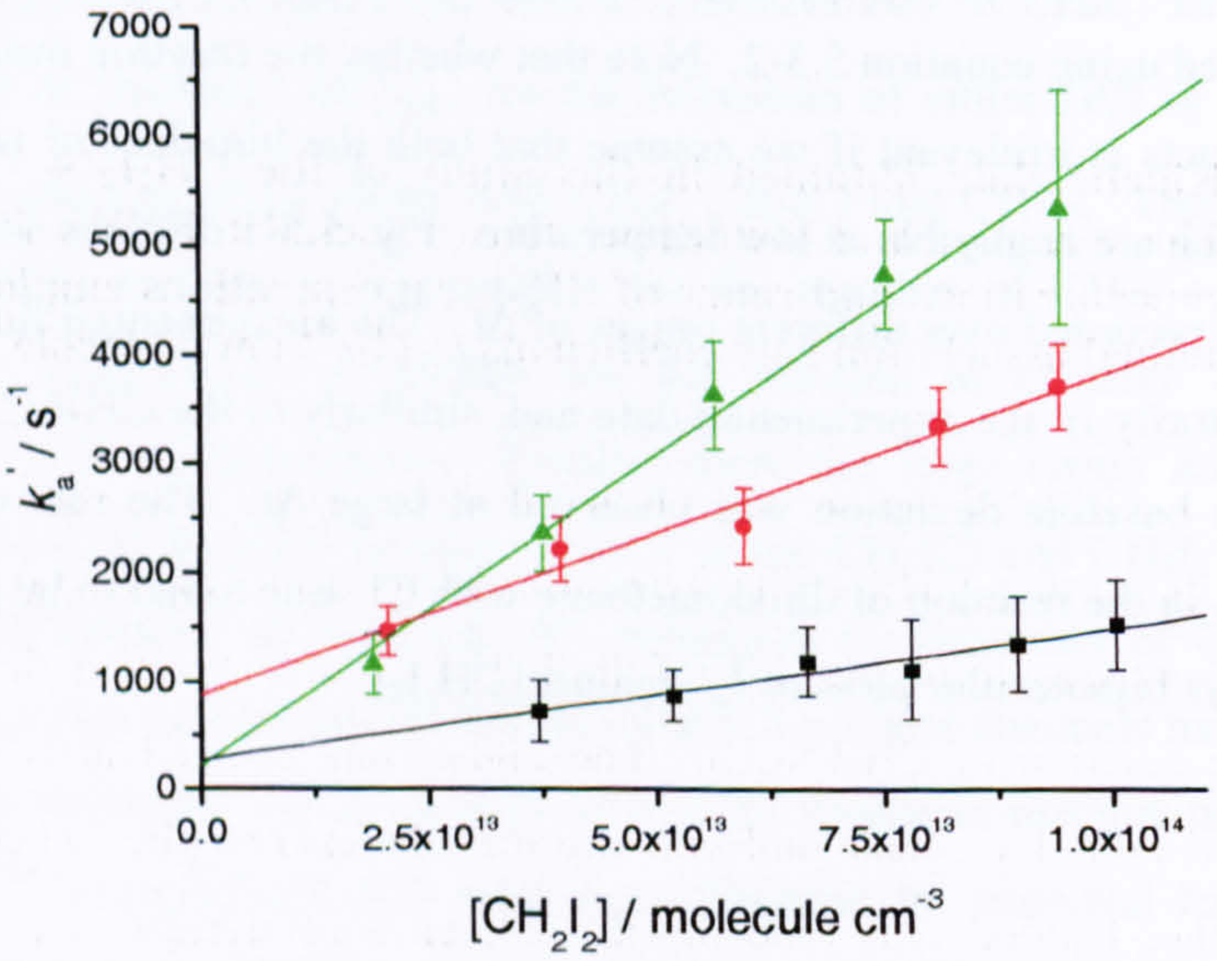

Fig. 5.5-2 – Bimolecular plots for the reaction of Cl + CH_2I_2. Black: T = 200.0 K, P = 10.3 Torr. Red: T = 201.9 K, P = 69.5 Torr. Green: T = 216.2 K, P = 248.3 Torr. Other experimental conditions are given in Table 5.5-2.

As can be seen in Fig. 5.5-2, all bimolecular plots were observed to be linear. Although the experimental scatter was relatively large, no systematic dependence on pressure was observed in the bimolecular y-axis intercepts, with an average value of (740 ± 767) s^{-1}. The larger average intercept value, relative to the CH_3I + Cl data, may be indicative that the Cl atom loss is dependent on [Cl_2SO] (as higher Cl_2SO concentrations were employed in the CH_2I_2 study). The experimental scatter was greater in this study compared with that of CH_3I + Cl, due to the weaker fluorescence of the ICH_2I-Cl adduct and the collection of a fewer number of data points. Diiodomethane concentrations had to be kept relatively low as the iodide was observed to condense (which could be seen in the form of liquid deposits on the cell windows) at concentrations above ~ 1×10^{14} molecule cm^{-3}. Table 5.5-2 lists all determinations of k_a obtained in this study along with pertinent experimental conditions.

T	P	Cl_0	CH_2I_2	k_a
200.0	10.3	0.75	80.5	12.3 ± 4.2
200.2	20.1	0.83	98.7	21.0 ± 11.9
200.4	39.8	0.44	75.1	29.2 ± 4.6
201.9	69.5	0.45	73.6	30.9 ± 5.4
203.8	100.2	0.45	79.3	48.6 ± 10.7
216.2	248.3	0.42	75.3	57.6 ± 7.6
215.9	496.7	0.85	75.2	60.4 ± 21.9

Table 5.5-2 – Kinetic data obtained in this study of the CH_2I_2 + Cl reaction at low temperature. The experimental conditions shown include: T (K), P (Torr), estimated initial Cl atom concentrations and range of CH_2I_2 concentrations employed (10^{12} molecule cm^{-3}), and determined association rate coefficients k_a (10^{-12} cm^3molecule$^{-1}s^{-1}$).

From the data in Table 5.5-2, it can be seen that adduct formation is significantly faster in the reaction of CH_2I_2 + Cl than CH_3I + Cl. The different reaction kinetics observed is conclusive evidence that we are monitoring the LIF of the ICH_2I-Cl adduct, rather then the same species monitored in the reaction of CH_3I + Cl. The higher rate coefficient would seem to be an intuitive result, as a diiodomethane molecule presumably has two sites where adduct formation can occur (at either I atom) thus reducing the influence of steric factors. At ~ 206 K, the reaction of diiodomethane with atomic chlorine shows a significant pressure dependence. This result is in agreement with the reaction kinetics of CH_3I + Cl but in disagreement with the reaction kinetics of CH_2ICl + Cl, where a pressure independent rate coefficient is observed

(with a negative temperature dependence)[23,25]. Fig. 5.5-3 shows a plot of k_a against total pressure.

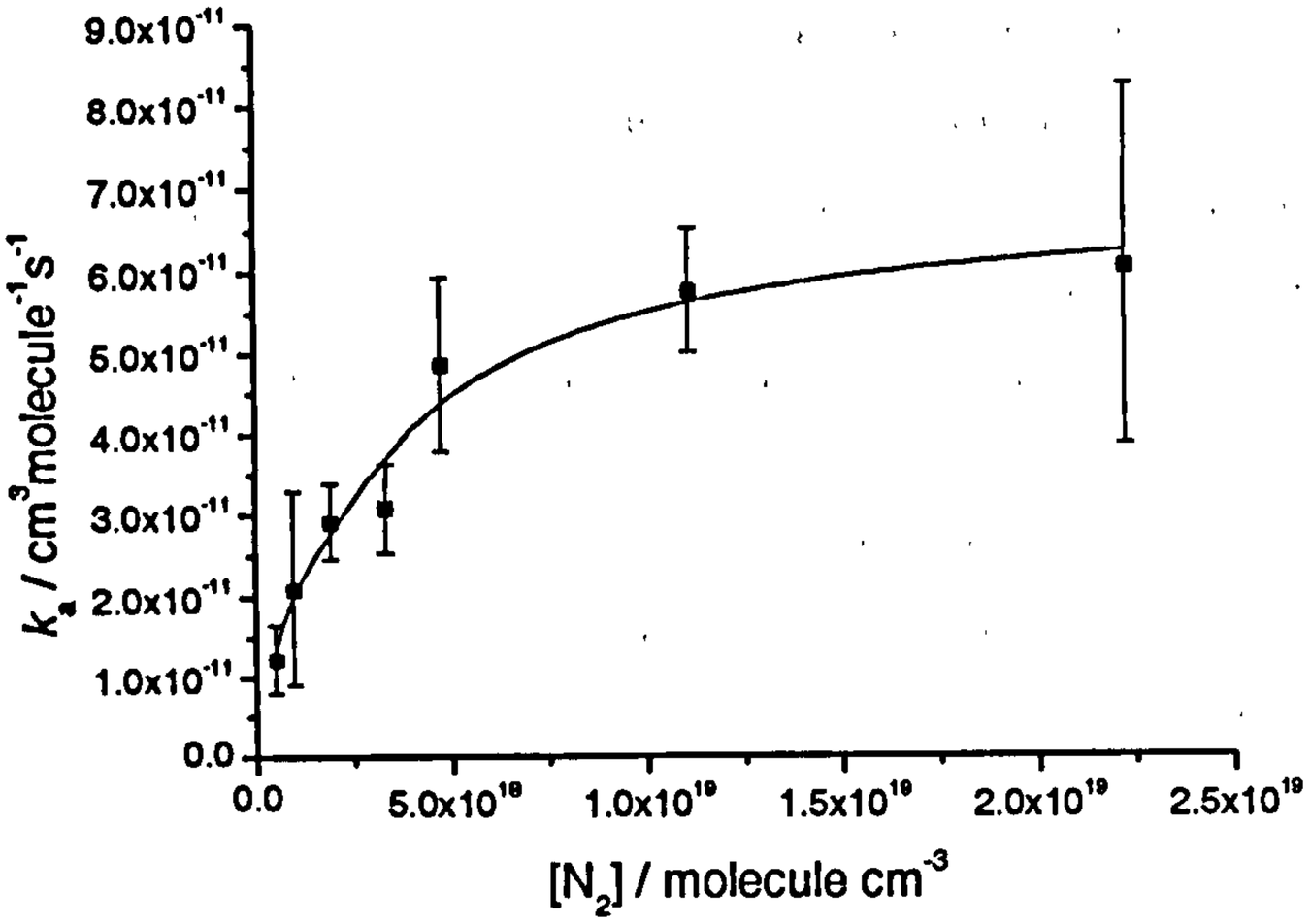

Fig. 5.5-3 – Pressure dependence of the CH_2I_2 + Cl reaction at ~ 206 K. The solid black line is a fit of E. 5.3-7 to the data.

From the fit of E. 3.5-7 to the experimental data the following parameters are obtained:

$$k_0 = (3.6 \pm 4.1) \times 10^{-29}\ \text{cm}^6\text{molcule}^{-2}\text{s}^{-1}$$
$$k_\infty = (7.0 \pm 1.1) \times 10^{-11}\ \text{cm}^3\text{molecule}^{-1}\text{s}^{-1}$$
$$F_c = 0.80 \pm 0.57$$

Thus the rate coefficient at the high pressure limit is approximately twice as high for the reaction of CH_2I_2 + Cl than that for CH_3I + Cl. At 206 K and 50 Torr, the rate coefficient for the reaction of CH_2ICl + Cl is reported as $(11.4 \pm 0.3) \times 10^{-11}$ $\text{cm}^3\text{molecule}^{-1}\text{s}^{-1}$ [23], *i.e.* significantly higher than the high pressure limit of either of the other reactions. This could be interpreted as evidence for the reaction of CH_2I_2 + Cl proceeding *via* the same mechanism as CH_3I + Cl. However, this hypothesis will be disproved in due course, by showing that the reaction of CH_2I_2 + Cl would appear to progress *via* a mechanism which lies somewhere between the two different mechanisms of the reactions of CH_3I and CH_2ICl with Cl.

As was the case for the reaction kinetics of CH_3I-Cl, the decay rate of the ICH_2I-Cl adduct, k_{loss}, was observed to increase with the concentration of the iodide. The average effective bimolecular rate coefficient for the reaction of the ICH_2I-Cl adduct with CH_2I_2 was found to be, $k_{eff} = (3.11 \pm 2.42) \times 10^{-12}$ $\text{cm}^3\text{molecule}^{-1}\text{s}^{-1}$, and independent of pressure. Applying equation 5.3-8 to the k_{loss} data returns a rate coefficient for reaction of the adduct with CH_2I or I

radicals of, $k(CH_2I + I) = (4.9 \pm 3.9) \times 10^{-10}$ $cm^3 molecule^{-1} s^{-1}$. The large error reflects the relatively high degree of experimental scatter. Taking the large uncertainty into account, the derived value for $k(CH_2I + I)$ is in reasonable agreement with that of $k(CH_3 + I)$, determined in section 5.3.2.B. The theoretical calculations[16,17,20,21,25] of the various RI-Cl adducts show that their structure and bond enthalpies are similar and there is no obvious reason, therefore, why the ICH_2I-Cl adduct should react more rapidly with I radicals (or CH_2I radicals) than the CH_3I-Cl adduct, consistent with the observations here No systematic pressure dependence was observed to the intercepts of the bimolecular plots of k_{loss} against $[CH_2I_2]$, with an average value of (310 ± 197) s^{-1}. This larger value obtained than in the CH_3I + Cl experiments is likely to reflect the higher concentrations of Cl_2SO employed in the CH_2I_2 study.

Fig. 5.5-4 shows a plot of the experimental peak ICH_2I-Cl LIF signal as a function of $[CH_2I_2]$ (normalised to unity for the highest diiodomethane concentration) at two different total pressures. Also included are model reproductions of the peak ICH_2I-Cl concentrations. The model is essentially the same as that described in section 6.3.2.B. In the model, the rate coefficient for adduct formation, k_a, is adjusted to the appropriate value determined in this study, k_{Cl} is altered to 740 s^{-1} (the average intercept value of the bimolecular plots), and the adduct-radical reaction rate coefficients are left unaltered to that of the CH_3I-Cl values. The model assumes no adduct dissociation or bimolecular reaction of CH_2I_2 + Cl.

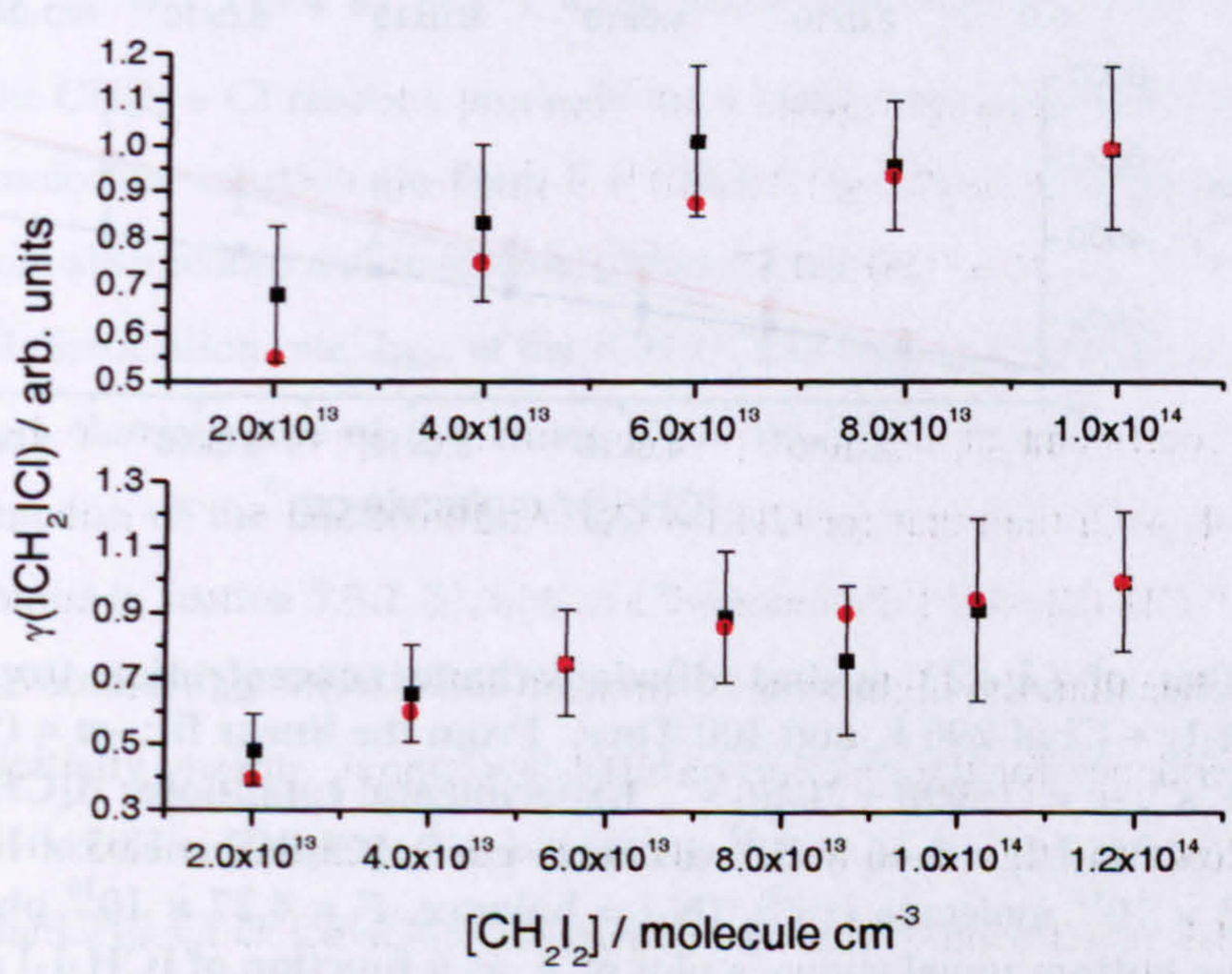

Fig. 5.5-4 – ICH_2I-Cl yield plots for the reaction of CH_2I_2 with Cl at 100 Torr (top panel) and 20 Torr at ~ 206 K. The black squares represent the experimental data points (with 2σ uncertainty) and the model calculations are represented by the red circles.

As can be seen from Fig. 5.5-4, there is reasonable agreement between the experimental and modelled yields. However, the model values tend to slightly overestimate the loss of ICH_2I-Cl,

particularly at lower [CH_2I_2]. This is indicative that the loss processes are overestimated in the model. It is most likely that the relatively high k_{Cl} value of 740 s^{-1} is responsible for this result. The experimental ICH_2I-Cl yields, in conjunction with the modeling exercise, demonstrate that dissociation of the ICH_2I-Cl adduct is negligible at low temperature (~ 206 K).

Experiments performed with, and without, up to ~ 2 Torr of O_2 showed that the ICH_2I-Cl adduct does not react with molecular oxygen, similarly to the CH_3I-Cl and other chloroalkyliodide adducts[21].

5.5.2 Reaction Kinetics of CH_2I_2 + Cl at 296 K and 100 Torr

The temporal profile of the ICH_2I-Cl adduct was determined as a function of diiodomethane concentration at 100 Torr total pressure (N_2) and 296 K. The data were analysed using E. 5.3-5 and the resulting plot of (λ_++λ_-) against [CH_2I_2] is displayed in Fig. 5.5-5.

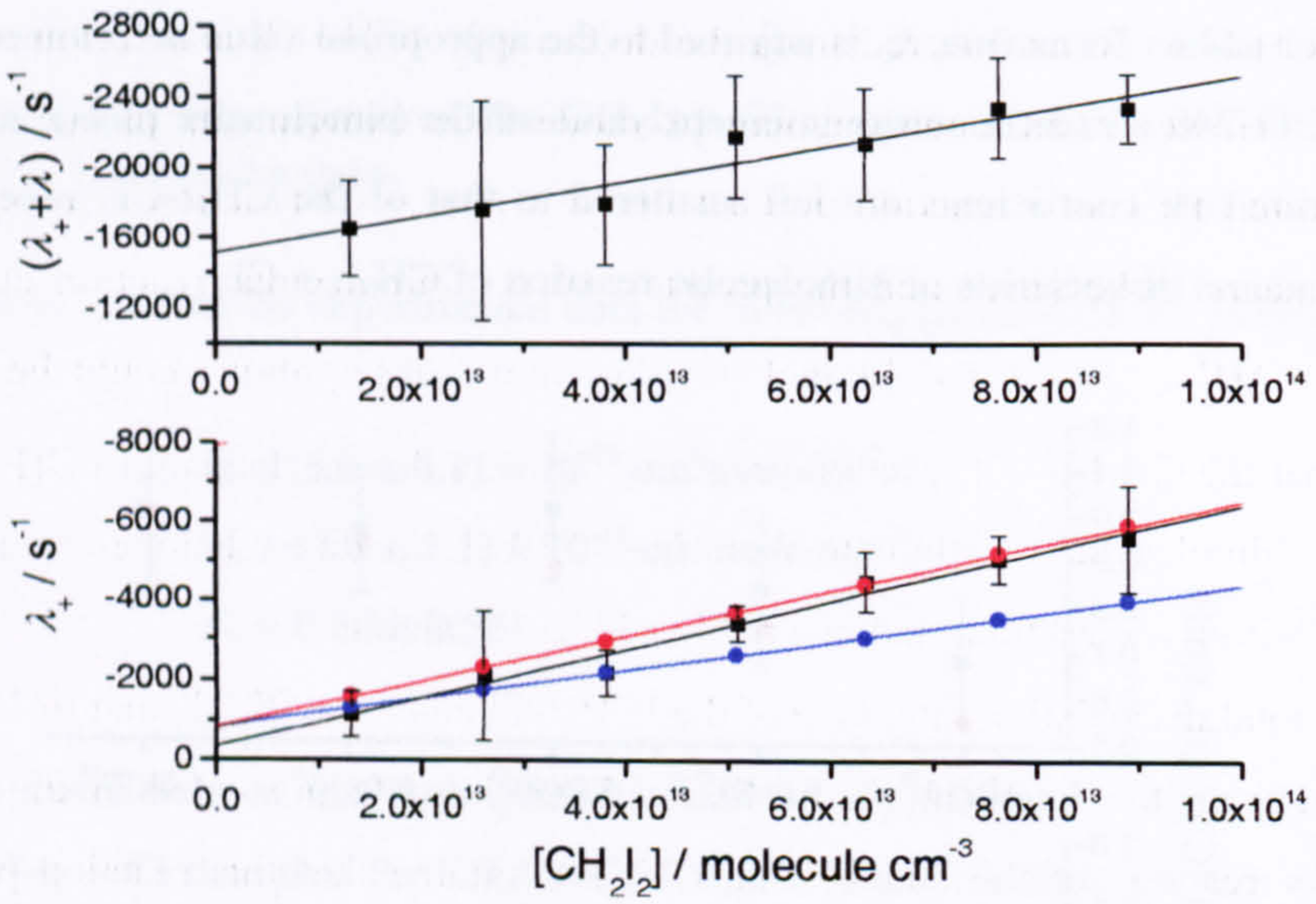

Fig. 5.5-5 – Plot of (λ_++λ_-) against diiodomethane concentration (top panel) for the reaction of CH_2I_2 + Cl at 296 K and 100 Torr. From the linear fit: $-m = (9.98 \pm 3.59) \times 10^{-11}$ $cm^3 molecule^{-1} s^{-1}$, $-c = (15090 \pm 2040)$ s^{-1}. Experimental conditions: $\Delta[CH_2I_2] = 7.59 \times 10^{13}$ molecule cm^{-3} ($\Delta[CH_2I/I] = 5.46 \times 10^{12}$ molecule cm^{-3}), $[Cl_2SO] = 1.05 \times 10^{13}$ molecule cm^{-3} ($[ClSO] = 3.03 \times 10^{12}$ molecule cm^{-3}), $[N_2]$ = balance, $F = 4.27 \times 10^{16}$ photons cm^{-2}, λ_{pr} = 365.57 nm. The bottom panel shows a plot of λ_+ as a function of [CH_2I_2] along with model predictions (explained below) assuming adduct dissociation to CH_2I_2 + Cl (blue) or ICl + CH_2I (red).

As no previous kinetic studies of the CH_2I_2 + Cl reaction are reported in the existing literature, the rate coefficients for the separate processes occurring within the chemical system cannot be deconvoltued, as no information can be obtained about the rate of the bimolecular reaction at 296 K, producing HCl + CHI_2 (or I + CH_2ICl – see below). However, assuming that

the ICH_2I-Cl adduct reacts with radicals at the same rate as the CH_3I-Cl adduct, we can conclude that the sum of the association and bimolecular reaction rate coefficients at 296 K is $(7.42 \pm 2.67) \times 10^{-11}$ $cm^3molecule^{-1}s^{-1}$ in 100 Torr of N_2. This result implies that the bimolecular rate coefficient is the predominant component and that HCl formation is the major reaction channel at room temperature. At ~ 206 K, where we assumed the bimolecular reaction to be of negligible importance, the rate coefficient for the association reaction at 100 Torr was found to be $(4.86 \pm 1.07) \times 10^{-11}$ $cm^3molecule^{-1}s^{-1}$. As the association reaction was found to be pressure dependent, the rate coefficient, k_a, is also expected to have a negative temperature dependence. Hence, the enhanced total rate coefficient for the reaction of CH_2I_2 + Cl at 296 K must be due to a greater extent of bimolecular reaction. If we assume that the ratio of k_a at 204 and 296 K in 100 Torr of N_2 for the CH_2I_2 + Cl reaction is the same as that for the CH_3I + Cl reaction (k_a(296 K)/k_a(204 K) = 0.44) then we can estimate the rate coefficient for the bimolecular reaction as 5.3×10^{-11} $cm^3molecule^{-1}s^{-1}$ at 296 K. Enami *et. al.*[20] predict that the ICH_2I-Cl adduct is not formed at temperatures beyond (315 ± 12) K due to enhanced bimolecular reaction of CH_2I_2 + Cl, as inferred from the decrease in ICH_2I-Cl absorption with increasing temperature. However, although ongoing IR diode laser experiments in our laboratory have directly detected HCl as a reaction product of the CH_2I_2 + Cl reaction at room temperature, the yield appears to be small and the products of the bimolecular reaction channel may be I + CH_2ICl ($\Delta H^0_{r,298}$ = - 125.4 kJ mol^{-1}). The above observations could be interpreted as indicating that the CH_2I_2 + Cl reaction proceeds *via* a similar mechanism to CH_3I + Cl at room temperature: bimolecular reaction (to form I + CH_2ICl *via* direct halogen atom substitution, rather than H-atom abstraction) and reversible adduct formation.

The total dissociation rate, k_{diss}, of the ICH_2I-Cl adduct at 296 K and in 100 Torr N_2 can be evaluated from the intercept of the linear fit to the data presented in Fig. 5.5-5. After correction for reaction of the adduct with ClSO (assuming that this reaction proceeds at the same rate determined in section 5.3.2.B), loss of Cl atoms in the absence of CH_2I_2, and diffusion of the adduct, we obtain, k_{diss} = (13200 ± 1800) s^{-1}. However, the mechanism and products of dissociation are initially unclear. It can be thought unlikely that the adduct decomposes to form HCl + CHI_2, as this dissociation route would not appear to be energetically accessible for dissociation of the CH_3I-Cl or CH_2ClI-Cl adducts – rather the bimolecular reaction channel to HCl formation is favoured. Therefore, by analogy with the CH_3I-Cl and CH_2ClI-Cl adducts, there would appear to be two potential dissociation channels: i) back to reactants, CH_2I_2 + Cl, or ii) onto products, ICl + CH_2I. The correct mechanism of adduct dissociation can be determined by a simple modeling exercise and individual examination of the parameters, λ_+ and λ_-, returned from the fitting procedure of the experimental data to E. 5.3-5. If dissociation of the adduct regenerates reactants, the formation and removal of ICH_2I-Cl are intrinsically coupled

and the experimental data must be analysed using the kinetic scheme represented by E. 5.3-5. However, if adduct dissociation generates products of ICl + CH_2I, then adduct formation and removal kinetics can be treated as independent processes – thus the experimental data can effectively be fitted to E. 5.3-2. In this case, $P2$ would be equal to the sum of the (pseudo-)first-order rate coefficients, k_a, k_{Cl} and k_{bi}, and $P3$ would be equal to the sum of the (pseudo-)first-order rate coefficients, k_{diss}, k_{ClSO}, k_{loss} and k_d. Therefore, plotting $P2$ against [CH_2I_2] would yield a straight line with slope, $k_a + k_{bi}$ and intercept, k_{Cl}. Plotting $P3$ against [CH_2I_2] would yield a straight line with intercept, $k_{diss} + k_{ClSO} + k_d$ and slope, k_{eff} (the effective rate coefficient for the reaction of the adduct with CH_2I_2, due to reaction with photolysis products). To investigate which mechanism should be employed to analyse the data (and hence determine the correct adduct dissociation mechanism), the FACSIMILE model described in section 5.3.3 was used to simulate kinetic traces for the ICH_2I-Cl adduct, under the exact experimental conditions of the 296 K investigation, for both scenarios. In the model, adduct formation, $k_{form} = k_a + k_{bi}$, is given a rate coefficient of 6.0×10^{-11} $cm^3molecule^{-1}s^{-1}$ (see below), $k_{Cl} = 740$ s^{-1}, $k_{eff} = 2.56 \times 10^{-11}$ $cm^3molecule^{-1}s^{-1}$, $k_{ClSO} = 3.66 \times 10^{-10}$ $cm^3molecule^{-1}s^{-1}$ and $k_d = 20$ s^{-1}. Note that k_{eff} and k_{ClSO} are evaluated using the room temperature rate coefficients determined for the CH_3I-Cl adduct-radical reactions determined in section 5.3.3. Adduct dissociation, k_{diss}, is given the value 13200 s^{-1} and kinetic traces are simulated for each dissociation channel, *i.e.* adduct → CH_2I_2 + Cl, or adduct → ICl + CH_2I. The returned model output kinetic traces are then fitted to E. 5.3-5 to return values for $\lambda+$ and $\lambda-$ for each set of experimental conditions. In the bottom panel of Fig. 5.5-5, the experimental values of $\lambda+$ are plotted against [CH_2I_2] along with the returned model values for the two different dissociation mechanisms (reactants = blue, products = red). Thus it can be seen that the experimental data fit the model output extremely well when adduct dissociation yields ICl + CH_2I at 100 %, providing conclusive evidence that the fate of the ICH_2I-Cl adduct at 296 K and 100 Torr N_2 is predominantly (if not exclusively) dissociation to ICl + CH_2I (or any products which are not CH_2I_2 + Cl). In light of the modeling implications, the experimental data were reanalysed using E. 5.3-2. The adduct growth, $P2$, and removal, $P3$, rates are plotted against [CH_2I_2] in Fig. 5.5-6. From the linear fit of $P2$ against [CH_2I_2], we obtain: k_{Cl} = (336 ± 597) s^{-1}, ($k_a + k_{bi}$) = (6.0 ± 1.1) × 10^{-11} $cm^3molecule^{-1}s^{-1}$. From the linear fit of $P3$ against [CH_2I_2]: k_{diss} = (13600 ± 1800) s^{-1} (once corrected for reaction of the adduct with ClSO) and k_{eff} = (4.0 ± 3.3) × 10^{-11} $cm^3molecule^{-1}s^{-1}$. If we convert k_{eff} into $k(CH_2I / I)$ by applying E. 5.3-8 we obtain a rate coefficient of (5.9 ± 4.8) × 10^{-10} $cm^3molecule^{-1}s^{-1}$. This value is in good agreement with that obtained at low temperature (4.9 ± 3.9) × 10^{-10} $cm^3molecule^{-1}s^{-1}$.

Fig. 5.5-7 displays a plot of the experimental ICH_2I-Cl peak LIF signal as a function of [CH_2I_2] (normalised to unity for the highest CH_2I_2 concentration), along with the normalised

peak adduct concentrations returned from the model outlined above. The significant increase in adduct yield with increasing diiodomethane concentration is indicative of the relatively large degree of adduct dissociation, and the reasonable agreement between experiment and model gives confidence that the chemistry occurring within the reaction system is well understood.

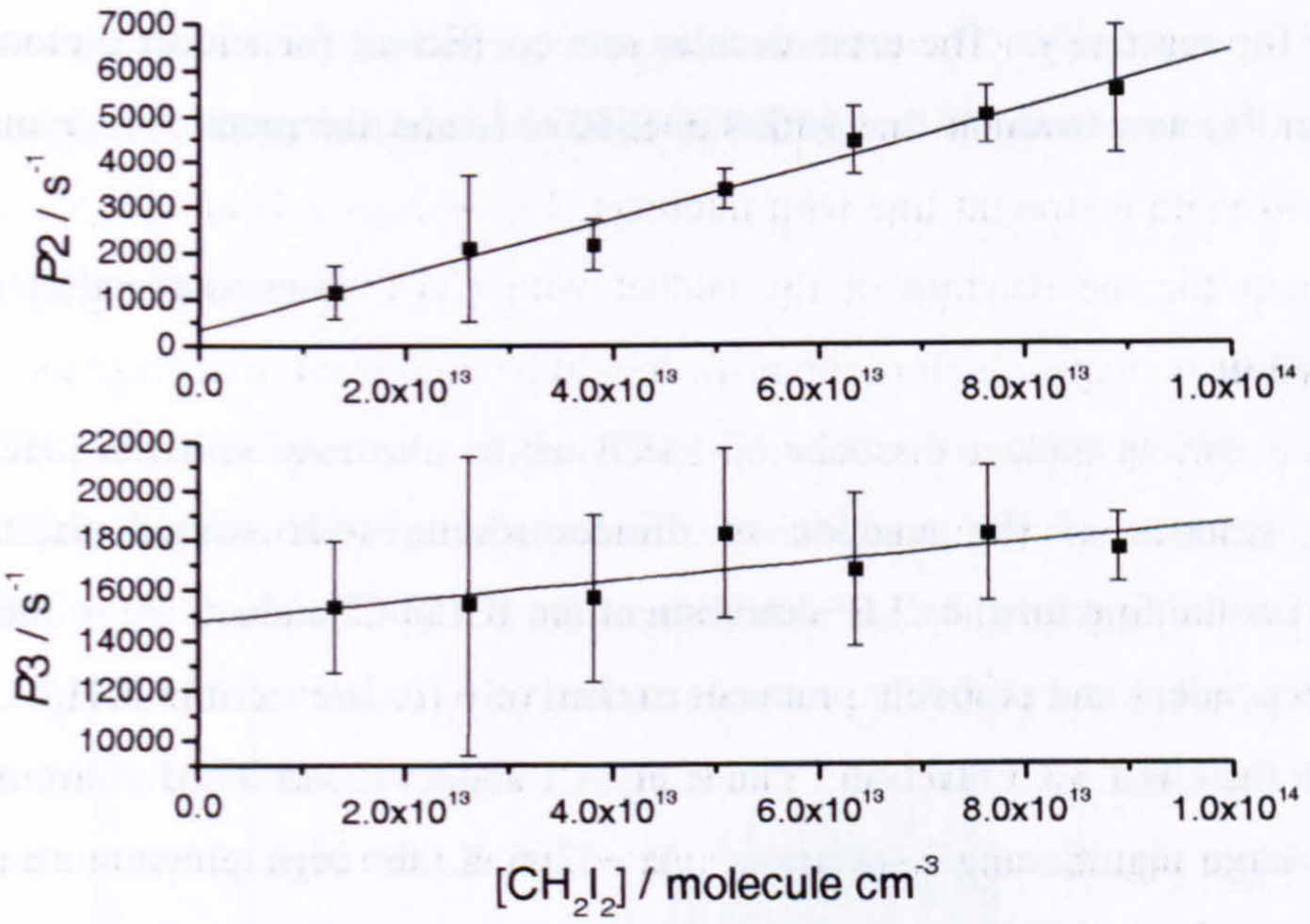

Fig. 5.5-6 – Bimolecular plots for ICH_2I-Cl adduct formation (top panel) and removal at 296 K and 100 Torr in the CH_2I_2 + Cl system. From the linear fits: m = (6.01 ± 1.1) (top panel) and (3.98 ± 3.25) × 10^{-11} $cm^3 molecule^{-1} s^{-1}$, c = (336 ± 597) (top panel) and (14760 ± 1850) s^{-1}.

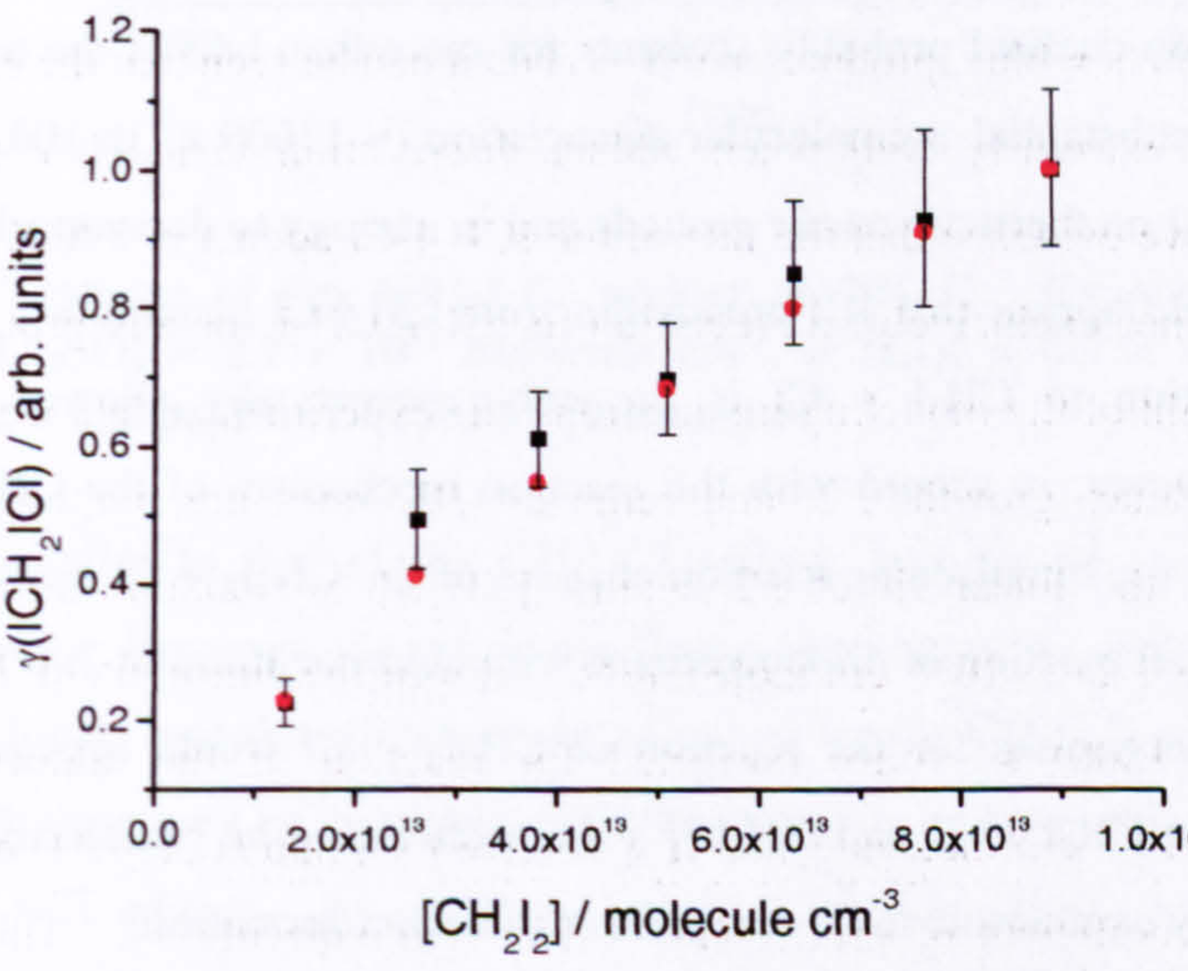

Fig. 5.5-7 – ICH_2I-Cl yield plot for the reaction of CH_2I_2 with Cl at 100 Torr and 296 K. The black squares represent the experimental data points (with 2σ uncertainty). The model calculations are represented by the red circles.

The 296 K study of the reaction of CH_2I_2 + Cl in 100 Torr of N_2 has enabled the mechanism of reaction to be qualitatively determined. The reaction proceeds *via* two independent reaction channels – i) bimolecular reaction (probably forming I + CH_2ICl), and ii) ICH_2I-Cl adduct formation. At 296 K and 100 Torr (N_2), the sum of the two processes is $(6.0 \pm 1.1) \times 10^{-11}$ $cm^3molecule^{-1}s^{-1}$, with the bimolecular channel expected to account for at least half of the reactivity. The unimolecular rate coefficient for adduct dissociation at 296 K and 100 Torr N_2 was found to be (13600 ± 1800) s^{-1}, and the products are most likely to be ICl + CH_2I.

5.5.3 Discussion

The kinetics of the reaction of diiodomethane with atomic chlorine have been investigated for the first time, by LIF detection of the ICH_2I-Cl adduct. At ~ 206 K, the reaction is pressure dependent and probably proceeds exclusively *via* irreversible ICH_2I-Cl formation, by analogy with the CH_3I + Cl reaction. The ICH_2I-Cl adduct is stabilised at low temperature and does not undergo significant dissociation. At ~ 206 K, the high pressure rate coefficient for ICH_2I-Cl adduct formation is approximately twice as large as that for the formation of CH_3I-Cl in the reaction of methyl iodide with atomic chlorine.

At room temperature, the CH_2I_2 + Cl reaction would appear to proceed *via* two competing reaction channels: i) bimolecular reaction (possibly forming I + CH_2ICl), and ii) association reaction to form ICH_2I-Cl. The combined rate coefficients of these processes at 296 K and in 100 Torr N_2 is found to be $(6.0 \pm 1.1) \times 10^{-11}$ $cm^3molecule^{-1}s^{-1}$, and the bimolecular reaction channel probably accounts for more than half of the total reactivity. The adduct undergoes substantial unimolecular dissociation (~ 13600 s^{-1} in 100 Torr N_2), probably yielding ICl + CH_2I on thermodynamic grounds and in analogy to decomposition of the CH_2ClI-Cl adduct. It would appear that ICl production from CH_3I-Cl dissociation is too endothermic and that dissociation to CH_3I + Cl is the only energetically allowed pathway at room temperature. However, in accord with the reaction mechanism of the CH_3I + Cl reaction at room temperature, the bimolecular reaction channel of the CH_2I_2 + Cl reaction is an important process in the overall reaction of diiodomethane with chlorine atoms at 296 K. In summary, the 296 K reaction mechanism for the reaction of CH_2I_2 + Cl would appear to lie somewhere between that of the CH_3I + Cl and CH_2ICl + Cl reactions – the bimolecular reaction channel must be sufficiently exothermic to be competitive to adduct formation.

Although the reaction of diiodomethane with Cl will be of no atmospheric significance, due to the very short photolysis lifetime of CH_2I_2, the information obtained in this study provides insight into the reaction mechanisms of the alkyl iodides with atomic chlorine. Ongoing infrared diode laser absorption experiments in our laboratory will determine the

Arrhenius parameters for the bimolecular reaction of $CH_2I_2 + Cl \rightarrow$ products and determine the HCl yield from the reaction as a function of temperature. The adduct dissociation mechanism could be verified *via* ICl detection in the reaction system. The detection of I atoms would also provide useful information.

5.6 Spectroscopic Investigation of the ICH_2I-Cl Adduct at 296 K

5.6.1 LIF Excitation Spectrum

The LIF excitation spectrum of the ICH_2I-Cl adduct, recorded at 296 K and 100 Torr total pressure N_2, is displayed in Fig. 5.6-1.

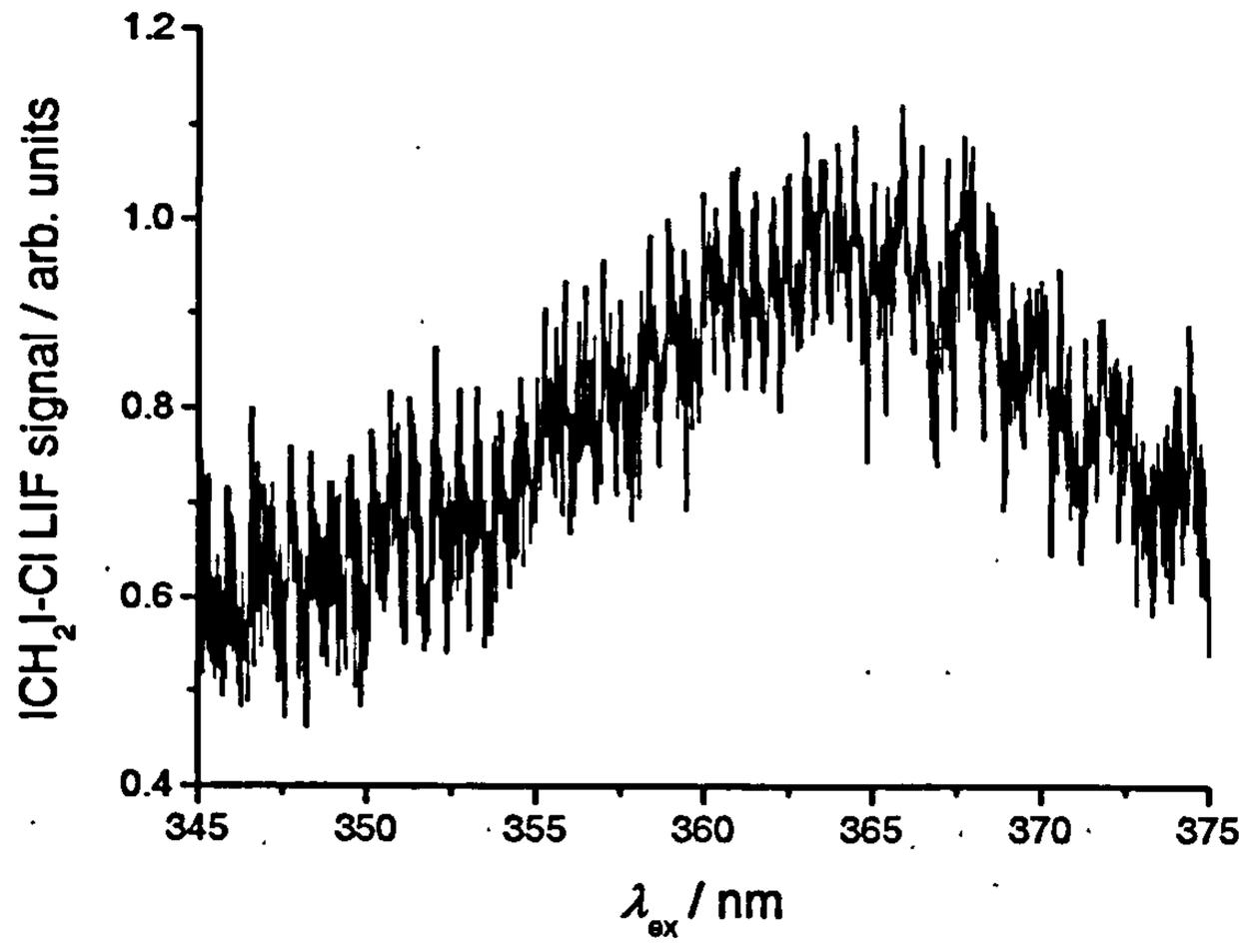

Fig. 5.6-1 – LIF spectra of the ICH_2I-Cl adduct at 296 K. Experimental conditions: P = 100 Torr, $[Cl_2SO] = 2.1 \times 10^{13}$ molecule cm^{-3}, $[CH_2I_2] = 4.2 \times 10^{13}$ molecule cm^{-3}, $[N_2]$ = balance, Δt = 150 μs, $F = 7.61 \times 10^{16}$ photons cm^{-2}.

The spectrum is similar to that of the CH_3I-Cl adduct, both in its continuous nature and structural components. However, the maximum fluorescence intensity of the ICH_2I-Cl adduct is shifted to slightly longer wavelengths than was observed for the CH_3I-Cl adduct (*cf.* Figs. 5.6-1 and 5.4-1). This feature may be consistent with the presence of a second, electron rich, iodine atom in the ICH_2I-Cl adduct. As observed for the CH_3I-Cl adduct, a second peak in the ICH_2I-Cl LIF spectrum was observed at an excitation wavelength of ~ 340 nm.

5.6.2 Dispersed Fluorescence of the ICH_2I-Cl Adduct

Fig. 5.6-2 displays the dispersed fluorescence spectrum of the ICH_2I-Cl adduct at 296 K and 100 Torr total pressure N_2. The spectrum is essentially identical to that of the CH_3I-Cl adduct. In agreement with the LIF spectra, the peak fluorescence intensity from ICH_2I-Cl may be slightly red-shifted (< 5 nm) relative to that of the CH_3I-Cl adduct (*cf.* fluorescence intensity at ~ 440 nm in Figs. 5.6-2 and 5.4-6), although this feature cannot be quantitatively assigned under the low resolution of the monochromator.

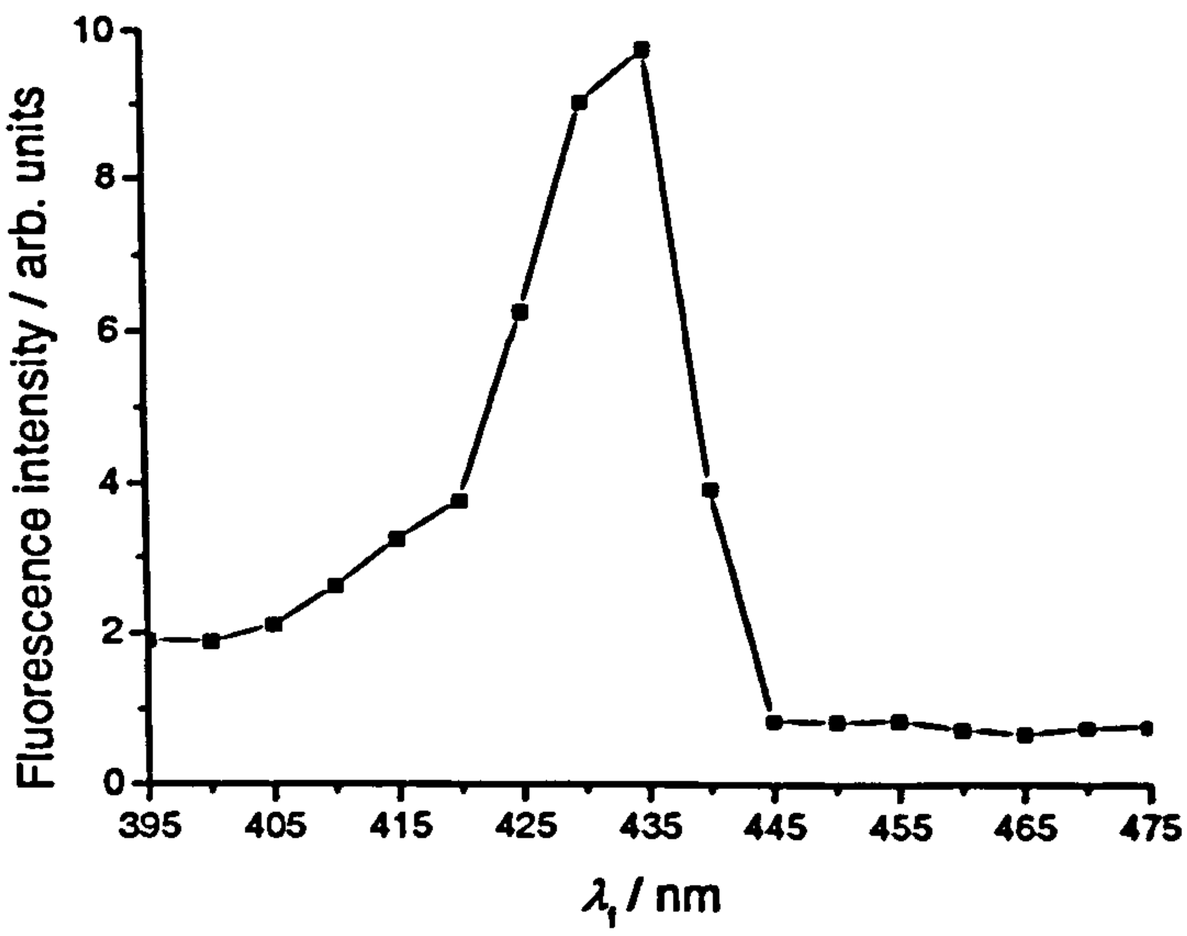

Fig. 5.6-2 – Dispersed fluorescence spectra of the ICH_2I-Cl adduct at 296 K and 100 Torr. Experimental conditions: $[Cl_2SO] = 3.2 \times 10^{13}$ molecule cm^{-3}, $[CH_2I_2] = 4.2 \times 10^{13}$ molecule cm^{-3}, $[N_2]$ = balance, $\Delta t = 100$ μs, $F = 7.6 \times 10^{16}$ photons cm^{-2}, $\lambda_{pr} = 365.57$ nm. The data are corrected for the probe laser background and are relative to an instrumental signal, in the absence of fluorescence, of zero.

The observed dispersed fluorescence could unambiguously be assigned to originate from the ICH_2I-Cl adduct by recording kinetic traces *via* the monochromator, and comparing the observed temporal profile of the fluorescing species with the reaction kinetics determined in section 5.5.2. No change in the frequency of the peak fluorescence intensity of the ICH_2I-Cl adduct was observed in altering the excitation wavelength from 365.57 to 350.57 nm. Presumably the structure of the CH_3I-Cl and ICH_2I-Cl adducts is very similar (in agreement with theoretical calculations of a number of chloro-alkyl iodide adducts[16,20,25]), as are the nature of their electronic states, and the energies of the transitions occurring between them.

5.6.3 Zero Pressure Lifetime and Quenching Measurements of the ICH_2I-Cl Adduct Excited State

The fluorescence lifetime of the ICH_2I-Cl adduct was measured as a function of N_2 pressure. The data were analysed in the same procedure described in section 5.4.3. Fig. 5.6-3 displays a plot of the ICH_2I-Cl fluorescence decay rate, k_f, as a function of $[N_2]$.

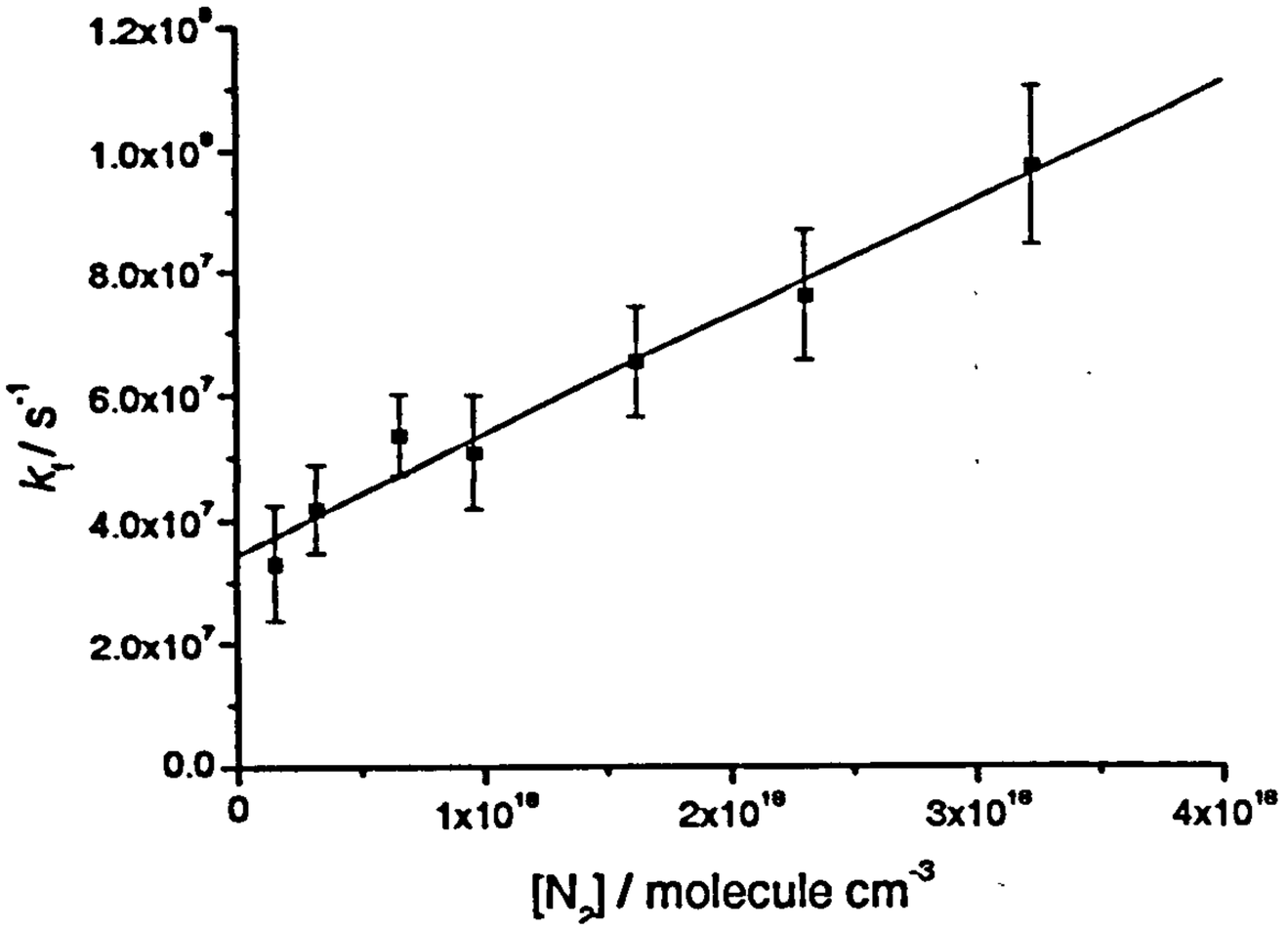

Fig. 5.6-3 – Plot of the inverse fluorescence lifetime of the ICH_2I-Cl adduct, k_f, against $[N_2]$ for an excitation wavelength of 375.57 nm. From the linear fit, $k(N_2, 296\ K) = (1.91 \pm 0.36) \times 10^{-11}$ cm^{3}molecule^{-1}s^{-1} and $(A_f + A_p) = (3.45 \pm 0.71) \times 10^7$ s^{-1}.

From the linear fit, the bimolecular quenching rate coefficient of the ICH_2I-Cl excited state by N_2 at 296 K is thus evaluated to be, $k = (1.91 \pm 0.36) \times 10^{-11}$ cm^{3}molecule^{-1}s^{-1} for an excitation wavelength of 375.57 nm. The zero pressure lifetime of the ICH_2I-Cl adduct excited state (*i.e.* $1/(A_f + A_p)$), at an energy of 375.57 nm above the ground state, is evaluated to be (29 ± 6) ns. Thus the rate of quenching of ICH_2I-Cl fluorescence would appear to be more rapid than for CH_3I-Cl. As the electronic structure, and hence excited states, of the two adducts are expected to be very similar, the reason for this observation could be due to the difference in excitation wavelength employed in the two experiments. In section 5.4.3 it was proposed that the mechanism for quenching may be VET to low lying vibrational states where predissociation is more predominant. Hence, at longer excitation wavelengths, the population of lower lying vibrational levels in the adduct excited state may result in the more efficient VET to predissociative states. However, the zero pressure lifetimes of the CH_3I-Cl and ICH_2I-Cl adducts were effectively found to be the same. A more thorough investigation of the excitation wavelength dependence (and temperature dependence) of the quenching rate of both adducts is required in order to fully determine the mechanism of excited state quenching by N_2.

5.6.4 Discussion

As for the CH_3I-Cl adduct, the LIF spectrum, dispersed fluorescence spectrum and measurements of the fluorescence lifetime of the ICH_2I-Cl adduct have been reported for the first time. The ICH_2I-Cl LIF spectrum over the 345 – 375 nm excitation range is generally very similar to that of the CH_3I-Cl adduct, with the exception of a slightly greater amount of fluorescence intensity towards the red-end of the spectrum. This observation is perhaps consistent with the presence of a second iodine atom in the ICH_2I-Cl adduct, lowering the energy of corresponding transitions.

The dispersed fluorescence spectrum of the ICH_2I-Cl adduct, following the 365.57 nm excitation of the adduct in 100 Torr of N_2 at 296 K was also found to be very similar in structure to that of the CH_3I-Cl adduct. Again, the ICH_2I-Cl dispersed fluorescence spectrum is perhaps slightly red-shifted (< 5 nm) to the CH_3I-Cl spectrum. The similar nature of the spectra of the CH_3I-Cl and ICH_2I-Cl adducts indicates that the same electronic transitions are occurring within the molecules after laser excitation in the 345 – 375 nm region, and that the electronic structure of the two molecules is very similar. High resolution (*i.e.* as greater resolution as the continuum of adduct states will allow) dispersed fluorescence spectra of both adducts should be recorded in order to locate the precise origins of transitions occurring within the molecules, and any differences between the two.

The fluorescence quenching rate of the ICH_2I-Cl excited state by N_2 was measured at 296 K. The quenching rate for the ICH_2I-Cl adduct after 375.57 nm laser excitation is ~ 50 % greater than that for the CH_3I-Cl adduct after 360.57 nm laser excitation. As the electronic structure of the two adducts is expected to be very similar, this may be indicative of quenching occurring *via* vibrational energy transfer to states which lie close to the location of a predissociative state as postulated in section 5.4.3. Further fluorescence lifetime measurements of both adducts are required to verify this hypothesis and to further probe the structure of the electronically excited states.

5.7 Conclusions

In this work, laser-induced fluorescence of the CH_3I-Cl and ICH_2I-Cl adducts has been reported for the first time. Fluorescence could be definitively assigned to the CH_3I-Cl adduct by the close agreement of the reaction kinetics of the reaction of methyl iodide with atomic chlorine, determined in this study, with that of the previous literature. At ~ 206 K, the reaction of CH_3I + Cl was found to proceed *via* irreversible adduct formation, in a pressure dependent association reaction mechanism. At room temperature, the CH_3I-Cl adduct is observed to undergo substantial dissociation, which can almost exclusively be assigned to reforming

reactants, CH_3I + Cl, by comparison of this work with the previous literature. The CH_3I-Cl adduct has been demonstrated to react gas kinetically (or faster) with radical species. Fluorescence could largely be assigned to the ICH_2I-Cl adduct from the different reaction kinetics determined for the reaction of CH_2I_2 + Cl (to that of CH_3I + Cl). No previous studies of the reaction of atomic chlorine with diiodomethane are reported in the literature. At ~ 206 K, the reaction of CH_2I_2 + Cl probably proceeds largely *via* the same mechanism of CH_3I + Cl – *i.e.* irreversible adduct formation in a pressure dependent association reaction. At room temperature, ICH_2I-Cl dissociation becomes important, and probably results in the formation of ICl + CH_2I (rather than CH_2I_2 + Cl) as inferred from the reaction kinetics and in analogy to dissociation of the CH_2ClI-Cl adduct. The larger total rate coefficient for the reaction of CH_2I_2 + Cl at room temperature (as compared to ~ 206 K) suggests that the bimolecular reaction of diiodomethane with Cl (probably forming I + CH_2ICl) is the major reaction channel at room temperature. The results of the kinetic investigation reported in this work show that the reaction of the alkyl iodides with atomic chlorine can progress *via* two independent mechanisms: i) bimolecular H-atom abstraction or halogen-atom substitution reactions, and ii) association reaction to form chloro-iodoalkane adducts. Neither reaction investigated in this work is expected to have any atmospheric relevance due to the relatively low concentrations of Cl in the MBL and rapid solar photolysis of the alkyl iodides.

The CH_3I-Cl and ICH_2I-Cl adducts exhibit continuous fluorescence over an excitation wavelength range of 345 – 375 nm. The LIF spectra display signs of vibrational structure and it is most likely that the electronic transitions occurring are originating in the thermal groundstate of the adducts. The LIF spectra reported in this work cannot be rationalised by recent theoretical calculations of the excited electronic states of CH_3I-Cl[20]. However, absorption of the CH_3I-Cl and ICH_2I-Cl adducts has not previously been reported below 405 nm and it has been shown in this work that the electronic transitions assigned to adduct absorption above 405 nm[20,21] are incorrect. The dispersed fluorescence spectra of the CH_3I-Cl and ICH_2I-Cl adducts show that fluorescence is considerably red shifted to the excitation wavelength. The observed pressure dependence of the dispersed fluorescence spectra indicates that high vibrational levels of the adduct excited states are initially populated, which can then be quenched to lower vibrational levels *via* VET. The relatively sharp cut-off wavelength of adduct fluorescence at ~ 445 nm probably corresponds to the difference in energy between the dissociation limit of the adduct groundstates and the ground vibrational level of the adduct excited states.

Measurement of the fluorescence lifetime of the electronically excited adduct states shows that fluorescence quenching is rapid, and is probably preceded by VET. The zero pressure lifetime of the adducts is relatively short (~ 30 ns) and may indicate the presence of predissociative states. The quenching rate coefficient may be dependent on the energy of the state initially populated by the laser excitation.

This work has provided a useful insight in to the reaction kinetics of the reaction of alkyl iodides with atomic chlorine and shown that halogen containing adducts can fluoresce with very high intensity. Important information has been obtained as to the electronic structure of the CH_3I-Cl and ICH_2I-Cl adducts, at least at a qualitative level, providing a basis for future research into these interesting molecules at both an experimental and theoretical level. The intense fluorescence of the adducts observed in this study may offer a new method by which to investigate the reaction of halogen atoms with a number of iodine containing molecules. Further, the low detection limit (particularly for the CH_3I-Cl adduct) achievable by this technique could potentially lead to the development of an *in situ* field instrument for the detection of alkyl iodides in the atmosphere with high temporal resolution.

References

1. B. J. Finlayson-Pitts, "Chlorine atoms as a potential tropospheric oxidant in the marine boundary layer", *Res. Chem. Intermed.*, **19**, 235-249, 1993.
2. A. Notario, G. Le Bras and A. Mellouki, "Absolute Rate Constants for the Reactions of Cl Atoms with a Series of Esters", *J. Phys. Chem. A.*, **102**, 3112 – 3117, 1998.
3. C. E. Canosa-Mas, E. S. N. Cotter, J. Duffy, K. C. Thompson and R. P. Wayne, "The reactions of atomic chlorine with acrolein, methacrolein and methyl vinyl ketone", *Phys. Chem. Chem. Phys.*, **3**, 3075 – 3084, 2001.
4. W. Wang, M. J. Ezell, A. A. Ezell, G. Soskin and B. J. Finlayson-Pitts, "Rate constants for the reactions of chlorine atoms with a series of unsaturated aldehydes and ketones at 298 K: structure and reactivity", *Phys. Chem. Chem. Phys.*, **4**, 1824 – 1831, 2002.
5. G. Thiault, A. Mellouki and G. Le Bras, "Kinetics of gas phase reactions of OH and Cl with aromatic aldehydes", *Phys. Chem. Chem. Phys.*, **4**, 2194 – 2199, 2002.
6. M. J. Ezell, W. Wang, A. A. Ezell, G. Soskin and B. J. Finlayson-Pitts, "Kinetics of reactions of chlorine atoms with a series of alkenes at 1 atm and 298 K: structure and reactivity", *Phys. Chem. Chem. Phys.*, **4**, 5813 – 5820, 2002.
7. J. Albaladejo, A. Notario, C. A. Cuevas, E. Jimenez, B. Cabanas and E. Martinez, "Gas-phase chemistry of atmospheric Cl atoms: a PLP-RF kinetic study with a series of ketones", *Atmos. Environ.*, **37**, 455 – 463, 2003.
8. C. A. Cuevas, A. Notario, E. Martinez and J. Albaladejo, "A kinetic study of the reaction of Cl with a series of linear and ramified ketones as a function of temperature", *Phys. Chem. Chem. Phys.*, **6**, 2230 – 2236, 2004.
9. C. A. Cuevas, A. Notario, E. Martinez and J. Albaladejo, "Influence of temperature in the kinetics of the gas-phase reactions of a series of acetates with Cl atoms", *Atmos. Environ.*, **39**, 5091 – 5099, 2005.
10. L. J. Carpenter, W. T. Sturges, S. A. Penkett, P. S. Liss, B. Alicke, K. Hebestreit and U. Platt, "Short-lived alkyl iodides and bromides at Mace Head, Ireland: links to biogenic sources and halogen oxide production", *J. Geophys. Res..-Atmos.*, **104**, 1679-1689, 1999.
11. H. B. Singh, "Low ozone in the marine boundary layer of the tropical Pacific Ocean: Photochemical loss, chlorine atoms, and entrainment", *J. Geophys. Res.*, **101**, 1907-1918, 1996.
12. H. B. Singh, A. N. Thakur, Y. E. Chen and M. Kanakidou, "Tetrachloroethylene as an indicator of low Cl atom concentrations in the troposphere", *Geophys. Res. Lett.*, **23**, 1529-1532, 1996.
13. C. W. Spicer, E. G. Chapman, B. J. Finlayson-Pitts, R. A. Plasteridge, J. M. Hubbe, J. D. Fast and C. M. Berkowitz, "Unexpectedly high concentrations of molecular chlorine in coastal air", *Nature*, **394**, 353 – 356, 1998.
14. E. S. N. Cotter, N. J. Booth, C. E. Canosa-Mas, D. J. Gray, D. E. Shallcross and R.P. Wayne, "Reactions of Cl atoms with CH_3I, C_2H_5I, 1-C_3H_7I, 2-C_3H_7I and CF_3I: kinetics and atmospheric relevance", *Phys. Chem. Chem. Phys.*, **3**, 402-408, 2001.
15. K. G. Kambanis, Y. G. Lazarou and P. Papagiannakopoulos, "Absolute reaction rate of chlorine atoms with iodomethane", *Chem. Phys. Lett.*, **268**, 498-504, 1997.
16. Y. G. Lazarou, K. G. Kambanis and P. Papagiannakopoulos, "Ab initio computational study of the interaction of Cl atoms with HI, CH_3I and CH_3OCH_2I", *Chem. Phys. Lett.*, **271**, 280-286, 1997.
17. Y. V. Ayhens, J. M. Nicovich, M. L. McKee and P.H. Wine, "Kinetic and Mechanistic Study of the Reaction of Atomic Chlorine with Methyl Iodide over the Temperature Range 218 – 694 K", *J. Phys. Chem. A.*, **101**, 9382-9390, 1997.
18. W. S. Goliff and F.S. Rowland, "Methyl chloride formation by gas phase thermal chlorine atom reaction with methyl iodide and methyl bromide", *Geophys. Res. Lett.*, **24**, 3029-3032, 1997.

19. M. Bilde and T.J. Wallington, "Atmospheric Chemistry of CH_3I: Reaction with Atomic Chlorine at 1 – 700 Torr Total Pressure and 295 K", *J. Phys. Chem. A.*, 102, 1550-1555, 1998.
20. S. Enami, S. Hashimoto, M. Kawasaki, Y. Nakano, T. Ishiwata, K. Tonokura and T.J. Wallington, "Observation of Adducts in the Reaction of Cl Atoms with XCH_2I (X = H, CH_3, Cl, Br, I) Using Cavity Ring-Down Spectroscopy", *J. Phys. Chem. A.*, 109, 1587-1593, 2005.
21. S. Enami, T. Yamanaka, S. Hashimoto, M. Kawasaki and K. Tonokura, "Direct Observation of Adduct Formation of Alkyl and Aromatic Iodides with Cl Atoms Using Cavity Ring-Down Spectroscopy", *J. Phys. Chem. A.*, 109, 6066-6070, 2005.
22. V. Dookwah-Roberts, J. M. Nicovich and P. H. Wine, "Spectroscopy and kinetics of weakly-bound adducts of Cl atoms with CH_3I and C_2H_5I", Abstracts of Papers, 231st ACS National Meeting, Atlanta, GA, United States, March 26 – 30, 2006.
23. M. Bilde, J. Sehested, O. J. Nielsen, T. J. Wallington, R. J. Meagher, M. E. McIntosh, C. A. Piety, J. M. Nicovich and P.H. Wine, "Kinetics and Mechanism of the Gas Phase Reaction of Atomic Chlorine with CH_2ICl at 206 – 432 K", *J. Phys. Chem. A.*, 101, 8035-8041, 1997.
24. J. Qi, G. Wang, K. Han Y. Sha, G. He and N. Lou, "Reactive scattering of crossed supersonic beams: $Cl + CH_2I_2 \rightarrow ICl + CH_2I$", *Mol. Phys.*, 92, 71 – 75, 1997.
25. K. G. Kambanis, D. Y. Argyris, Y. G. Lazarou and P. Papagiannakopoulos, "Absolute Reaction Rate of Chlorine Atoms with Chloroiodomethane", *J. Phys. Chem. A.*, 103, 3210-3215, 1999.
26. G. Baum, C. S. Effenhauser, P. Felder and J.R. Huber, "Photofragmentation of thionyl chloride: competition between radical, molecular, and three-body dissociations", *J. Phys. Chem.*, 96, 756, 1992.
27. H. Wang, X. Chen and B.R. Weiner, "Laser Photodissociation Dynamics of Thionyl Chloride: Concerted and Stepwise Cleavage of S-Cl Bonds", *J. Phys. Chem.*, 97, 12260-12268, 1993.
28. S. P. Sander, R. R. Friedl, A. R. Ravishankara, D. M. Golden, C. E. Kolb, M. J. Kurylo, R. E. Huie, V. L. Orkin, M. J. Molina, G. K. Moortgat and B.J. Finlayson-Pitts, *"Chemical Kinetics and Photochemical Data for Use in Atmospheric Studies: Evaluation Number 14"*, JPL Publication 02-25, February 1, 2003.
29. A. P. Uthman, P. J. Demiein, T. D. Allston, M. C. Withiam, McClements and G.A. Takacs, Photoabsorption Spectra of Gaseous Methyl Bromide, Ethylene Dibromide, Nitrosyl Bromide, Thinoyl Chloride, and Sulfuryl Chloride, *J. Phys. Chem.*, 82, 2252-2257, 1978.
30. Atkinson R., Baulch D.P., Cox R.A., Crowley J.N., Hampson R.F., Hynes R.G., Jenkin M.E., Rossi M.J. and J. Troe, Evaluated kinetic and photochemical data for atmospheric chemistry: Volume I – gas phase reactions of O_x, HO_x, NO_x and SO_x species, *Atmos. Chem. Phys.*, 4, 1461-1738, 2004.

"It is hard enough to remember my opinions, without also remembering my reasons for them!"

1. http://www.brainyquote.com/quotes/authors/f/friedrich-nietzsche.html

Appendix I: Kinetics study of the reaction of iodine monoxide radicals with dimethyl sulphide

RESEARCH PAPER

PCCP
www.rsc.org/pccp

Kinetics study of the reaction of iodine monoxide radicals with dimethyl sulfide

Tom Gravestock, Mark A. Blitz and Dwayne E. Heard*

School of Chemistry, University of Leeds, Leeds, UK LS2 9JT. E-mail: d.e.heard@leeds.ac.uk; Fax: 0113 343 6565; Tel: 0113 343 6471

Received 28th February 2005, Accepted 8th April 2005
First published as an Advance Article on the web 25th April 2005

The temperature and pressure dependence of the rate coefficient for the reaction of iodine monoxide radicals with dimethyl sulfide (DMS), IO + DMS → I + DMSO (1), was studied using laser induced fluorescence (LIF) to monitor the temporal profile of IO following 351 nm photolysis of RI/DMS/NO_2/He (RI = CH_3I/CF_3I) mixtures. The study was performed over the range T = 296–468 K yielding a positive activation energy and $k_1 = (9.6 \pm 8.8) \times 10^{-12} \exp\{-(1816 \pm 397)/T\}$. No dependence was observed on total pressure between 5–300 Torr. The rate coefficient at 296 K was determined as $(2.0 \pm {}^{0.4}_{0.6}) \times 10^{-14}$ cm^3 molecule^{-1} s^{-1}, more than an order of magnitude smaller than a recent study[34] but in reasonable agreement with the previous literature.

1. Introduction

Dimethyl sulfide (DMS, $(CH_3)_2S$) is the most abundant biogenic form of sulfur emitted into the atmosphere.[1] The atmospheric gas phase oxidation of sulfur compounds is thought to be an important process in the formation of aerosol particles and cloud condensation nuclei (CCN).[1 4] DMS therefore exerts a potential influence over the radiative balance in the marine boundary layer (MBL) and the Earth's climate in general. In order to fully understand the marine sulfur cycle the oxidation pathways of DMS are key and remain an area where the current knowledge is lacking.[5,6]

The main gas phase oxidisers of DMS in the MBL are OH[7 9] (day time) and NO_3[10 12] (night time). The recommended IUPAC values for the rate coefficients of these reactions at 298 K are $(6.5 \pm 0.3) \times 10^{-12}$ cm^3 molecule^{-1} s^{-1} and $(1.1 \pm 0.15) \times 10^{-12}$ cm^3 molecule^{-1} s^{-1}, respectively.[13] However, some studies[14,15] have shown that the removal rate of DMS in the marine atmosphere is too rapid to be explained simply by these sinks, indicating the presence of further gas phase oxidants. The possibility of halogen chemistry as a missing sink has received significant attention and a recent modelling study has shown the reaction of BrO with DMS to be of atmospheric significance and highlighted the reaction between IO and DMS (1) as requiring further study:[16]

$$IO + CH_3SCH_3 \rightarrow CH_3SOCH_3 + I \qquad (1)$$

Iodine monoxide is produced in the MBL by the reaction of ozone with I atoms, generated by the photolysis of biogenically emitted organic iodo-compounds[17] and I_2:[18]

$$I + O_3 \rightarrow IO + O_2 \qquad (2)$$

Once formed, IO can be photolysed reproducing I + O_3 (under atmospheric conditions), or undergo self-reaction or reaction with other trace species (HO_2, NO_2) propagating O_3 depleting cycles.[19] Iodine oxides can also undergo heterogeneous uptake to aerosol particles and may be important for particle formation in the MBL.[20 22] As well as affecting DMS oxidation, if sufficiently fast, reaction (1) could result in catalytic O_3 destruction *via* the formation of an I atom. The critical parameters required in order to assess the importance of IO upon DMS oxidation are the rate coefficient of reaction (1) under atmospheric conditions, and the concentration of IO in the MBL. Hitherto IO has exclusively been detected in the atmosphere by differential optical absorption spectroscopy (DOAS)[23,24] with measured concentrations of up to 10 pptv ($\sim 2.5 \times 10^8$ molecule cm^{-3}).[18,25] However, as the DOAS measurements are long path experiments, reported concentrations are typically averaged over km path lengths. Recent observations of high I_2 concentrations[18] correlated with tidal height suggest that the concentration of IO in the MBL may be much higher, and more localised in nature, than previously thought.

The reaction of IO with DMS has received significant experimental study. The earliest investigations[26,27] found k_1 to be of the order of 10^{-11} cm^3 molecule^{-1} s^{-1}, making IO an important sink for DMS. However, a subsequent study[28] found the reaction to be almost three orders of magnitude slower ($k_1 < 3.5 \times 10^{-14}$ cm^3 molecule^{-1} s^{-1}) than the previous determinations. A modelling study[29] found better agreement with field data when using the lower value for k_1. Several later experimental studies confirmed the lower value of k_1[6,30 33] and the current IUPAC room temperature value is $(1.3 \pm 0.2) \times 10^{-14}$ cm^3 molecule^{-1} s^{-1}.[13] The only one of these studies to investigate the pressure dependence of k_1 was that of Daykin and Wine[28] who found no change in the rate coefficient over a pressure range of 40–300 Torr (M = N_2/O_2/air). The earliest high measurements of k_1 did not involve direct detection of IO, and are considered erroneous due to secondary chemistry and heterogeneous reactions within the system.[13] It was generally accepted that IO and DMS did not react at a significant enough rate to couple the sulfur and iodine cycles in the MBL. However, a recent study of reaction (1) by cavity ring-down spectroscopy (CRDS)[34] measured a room temperature rate coefficient, $k_1 = (2.5 \pm 0.2) \times 10^{-13}$ cm^3 molecule^{-1} s^{-1}, of more than an order of magnitude greater than the recommended value, and found both a pressure dependence and a negative activation energy, suggesting an association complex reaction mechanism. A value for k_1 of this magnitude indicates IO as a predominant sink for DMS in the MBL (as important as OH). Furthermore, a recent computational study[35] of the reaction of the halogen oxides with DMS found reasonable agreement between calculated and experimental rate coefficients for ClO and BrO, but obtained a value for k_1 of 1.5×10^{-11} cm^3 molecule^{-1} s^{-1}, approximately three orders of

DOI: 10.1039/b502989a

magnitude greater than the preferred experimental determinations.

2. Experimental

2.1. Apparatus

The experimental arrangement consisted of a typical slow flow, pulsed-laser photolysis-laser-induced fluorescence system (PLP-LIF), similar to systems described elsewhere.[36,37] The reaction cell was a stainless steel vessel of ~200 cm^3 volume with a six port configuration; two on the vertical axis and four orthogonally arranged on the horizontal axis. All ports, other than that on the pumping axis, were covered with fused silica 50 mm diameter windows and sealed with O-rings. The experiment required two laser systems, a Nd:YAG-pumped dye laser (Spectron Laser Systems, SL803 Nd:YAG laser/Sirah, Cobra Stretch dye laser) acting as the probe laser, and an excimer laser (Lambda Physik, LPX 100) for photolysis of precursors. The two horizontal axes of the reaction cell were used as the principal laser axes. The excimer beam was unfocused and passed directly through the reaction cell to a beam dump. An iris of ~1 mm diameter aperture was placed over the probe beam entrance port, in order to improve the probe laser beam shape, and reduce the scatter of laser radiation inside the chamber. The reagent gas mixture was introduced into the upper vertical axis of the cell through stainless steel tubing (1/4″ outer diameter), which was connected to a gas handling line, consisting of four calibrated mass flow controllers (MFC), a mixing manifold, and a rotary/diffusion vacuum pump combination (Leybold Vakuum, D8B/Edwards High Vacuum, EO2). The gas handling line allowed preparation and purification of reagents. A second rotary/diffusion pump arrangement was attached at the lower vertical axis port of the reaction chamber and used to regulate cell pressure (in conjunction with the total gas flow rate) and remove reagent deposits on the cell walls between experiments. The base reaction cell pressure was $<10^{-5}$ Torr. The gas flow through the reaction cell was always such that the total chamber residence time is <1 s, and the photolysis region was replenished with fresh gas several times between laser shots.

Radiation from fluorescing species was detected at the upper port of the vertical reaction cell axis. The fluorescence was imaged onto a photomultiplier tube (PMT) (Hamamatsu, R928) by means of two plano-convex lenses (CVI Technical Optics Ltd., PLCX-50.8-38.6-2.00), arranged at their optimum distance from both the laser excitation region and PMT. An appropriate colour glass filter (CVI Ltd., CG-GG-495-2.00-2.0) was placed after the second lens, and prior to the PMT, to remove unwanted probe laser scattered light. The analogue signal from the PMT was sent to an oscilloscope (LeCroy, Waverunner LT262) and a gated integrator and boxcar averager (Stanford Research Systems Inc., SR250). A digital-to-analogue converter transferred the boxcar signal to a PC for data analysis. The oscilloscope, boxcar, excimer laser and Nd:YAG laser were triggered at appropriate time intervals by a delay generator (SRS Inc., DG535) operating under computer control. The dye laser wavelength was controlled by PC. The reaction chamber could be electrically heated by several cartridge heaters, embedded into the main body of the cell, and regulated by a feedback mechanism controlled by a thermocouple in the cell. The reaction chamber pressure was measured by a 0–1000 Torr capacitance manometer (MKS Instruments, 626A).

2.2. Generation and detection of IO

The title reaction (1) was studied by monitoring the temporal profile of IO using LIF from the R_1 (2,0) bandhead of the $A^2\Pi_{3/2} \leftarrow X^2\Pi_{3/2}$ electronic transition. Fig. 1 displays a typical scan of the (2,0) band of the $A^2\Pi_{3/2} \leftarrow X^2\Pi_{3/2}$ electronic

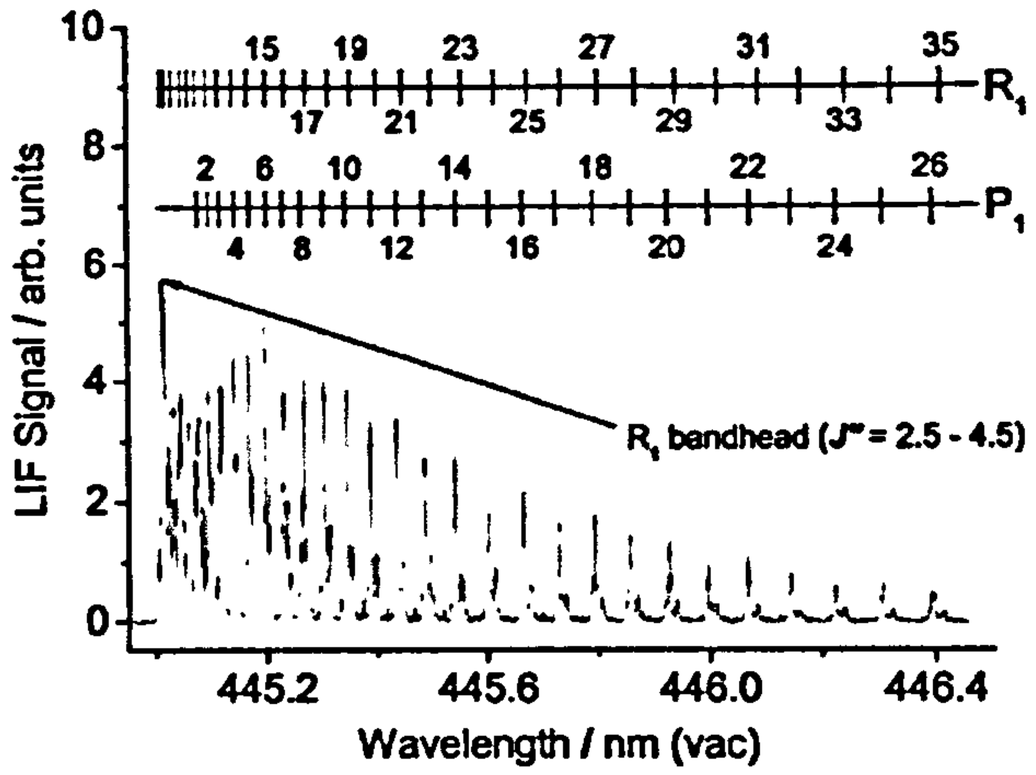

Fig. 1 Laser-excitation spectrum of the IO $A^2\Pi_{3/2} \leftarrow X^2\Pi_{3/2}$ (2,0) band, taken at 50 Torr total pressure and 296 K. The time delay between photolysis and probe lasers, Δt, was set at 50 μs. For clarity, only a limited assignment of the rotational transitions is given. The F_2 component of the electronic transition is missing, due to the large spin–orbit splitting of IO (>2000 cm^{-1}),[61] and the Q_1 manifold is of low intensity, typical of a $^2\Pi$–$^2\Pi$ transition. The R_1 bandhead, indicated by the arrow, was used for all kinetic measurements in this study. For the experimental resolution used, the $J'' = 2.5$, 3.5 and 4.5 rotational lines are all excited by the laser in the R_1 bandhead.

transition of IO. The excitation wavelength, *i.e.* at the (2,0) bandhead, was measured at 445.011 nm (vacuum wavelength, 22 471.35 cm^{-1}, Coherent WaveMaster) and the probe laser line width was estimated as 0.006 nm by comparison to a spectral simulation program.[38] The excitation wavelength (~5 mJ $pulse^{-1}$) was generated by pumping the dye laser (operating on Coumarin 2) with 355 nm radiation from the Nd:YAG laser. IO radicals were generated by reaction of O (^3P) atoms, produced by the 351 nm photolysis of NO_2, with either methyl iodide (CH_3I) or trifluoromethyl iodide (CF_3I) in a He buffer gas.

A simplified reaction sequence is given below

$$NO_2 + 351\ nm \rightarrow NO + O\ (^3P) \quad (3)$$

$$O\ (^3P) + RI \rightarrow IO + R \quad (4)$$

$$O\ (^3P) + CH_3SCH_3 \rightarrow CH_3SO + CH_3 \quad (5)$$

$$IO + CH_3SCH_3 \rightarrow CH_3SOCH_3 + I \quad (1)$$

Typical concentrations were $[NO_2] = (1–2) \times 10^{13}$ molecule cm^{-3}, $[RI] = (5–7) \times 10^{16}$ molecule cm^{-3} and [He] = balance. All concentrations are determined from the reaction chamber pressure, total gas flow rate and MFC settings. Based on laser fluence measurements (~3.5×10^{16} photons cm^{-2} $pulse^{-1}$ at 351 nm), and the concentration and absorption cross-section of NO_2 ($\sigma_{351} = 4.3 \times 10^{-19}$ cm^2 $molecule^{-1}$),[39] we estimate that $[IO]_{max} \leq [O]_{max} \leq 3.1 \times 10^{11}$ molecule cm^{-3} under our experimental conditions. From this we derive an IO detection limit for our apparatus, at the peak of the (2,0) bandhead, of ~1×10^9 molecule cm^{-3} with no averaging of the fluorescence signal (*i.e.* for one laser shot). The concentration of NO_2 was deliberately kept low so as to avoid reaction between IO and NO_2 (and impurities). As fluorescence from NO_2 is much longer lived than that from IO ($\tau < 1$ ns),[40] the NO_2 contribution to the fluorescence signal, following 445 nm excitation, could largely be distinguished from that of IO by manipulation of the boxcar gate width, which was set at 50 ns and overlapped the probe laser pulse width (*i.e.* where all IO fluorescence occurred).

With the exceptions of He (BOC Gases, 99.999 99%) and CF_3I (Aldrich, 99%) all reagents were purified. Nitric oxide impurities within the NO_2 (Aldrich, >99.5%) were removed

by distillation in a cardice/acetone slurry after initial freezing at 77 K. The purified NO_2 was diluted in He and stored in a 5 l glass bulb. Methyl iodide (Aldrich, 99%) was repeatedly purified by freeze pump thawing and kept in a glass finger. Throughout the experiments, the reaction chamber pressure was below the room temperature saturated vapour pressure of CH_3I, and the iodide could be transferred directly from the glass finger to the mixing manifold, through a MFC. Trifluoromethyl iodide was flowed from a gas cylinder to the mixing manifold *via* a MFC. Dimethyl sulfide (Aldrich, >99%) was purified and administered to the reaction vessel in the same manner as CH_3I. An advantage of this procedure was that a dilution of the DMS did not have to be performed, and, as [DMS] is crucial to the determination of k_1, and calculated from mass flow rates, it was therefore beneficial to avoid preparing a bulb where DMS (or CH_3I) could have condensed out of the vapour phase. All reactions were performed under pseudo-first-order conditions, such that the concentration of DMS was four-to-five orders of magnitude higher than that of IO, and the IO concentration was low enough so that the IO self-reaction did not interfere with the kinetics being determined (see section 3.2).

Upon addition of DMS to the system, O atoms are rapidly lost *via* reaction (5). As k_5 is *ca.* five times higher than that of O + CH_3I and ten times higher than O + CF_3I, the concentration of alkyl iodide was always kept in excess of DMS, to ensure a satisfactory IO production yield for subsequent LIF detection. The bimolecular rate coefficient for the title reaction was determined by measuring the pseudo-first-order rate coefficient, k', of IO decay as a function of [DMS], which was typically varied between (5–50) × 10^{15} molecule cm^{-3}. For each [DMS], the temporal decay profile of IO was monitored by varying the time delay (Δt) between excimer and probe lasers over a suitable temporal range. The temporal range was set to capture several $1/e$ lifetimes of IO decay, by which time the fluorescence signal had fallen to the pre-trigger excimer laser baseline. All experiments were performed at a laser pulsed-repetition-frequency (PRF) of 2 Hz, and the IO signal always returned close to the pre-trigger baseline (<5% of the peak IO fluorescence signal—see section 3.2). All IO decays were exponential in nature, confirming that the reaction was carried out under pseudo-first-order conditions.

3. Results and discussion

3.1. Determination of k_1

The pseudo-first-order rate coefficients (k') were determined by fitting the temporal IO decays to a single exponential function:

$$[IO]_t = [IO]_0 \exp^{(-k't)} + b \quad (6)$$

where,

$$k' = k_1[DMS] + k_d \quad (7)$$

k_d is the sum of the first-order losses of IO due to diffusion and reaction with impurities in the system (excluding those in the DMS), and b is an experimental offset allowing for slight deviations from the pre-trigger baseline (see section 3.2). It should be noted that as the experiment utilises fluorescence, $[IO]_t$ and $[IO]_0$ are not required, rather a fluorescence signal intensity that is proportional to the concentration of IO. Fig. 2 displays typical IO decays in the absence and presence of DMS.

A bimolecular plot of k' against [DMS] yields k_1 as the slope, as displayed in Fig. 3. For each determination of k' the reaction chamber was evacuated before refilling with the new reagent mixture, and the DMS concentrations were varied in both random and systematic fashions to obtain bimolecular plots under different conditions. We note that the IO decay rate in the absence of DMS (*i.e.* k_d, ~200 s^{-1}) appears too fast to simply be explained by diffusion. We attribute this IO loss to

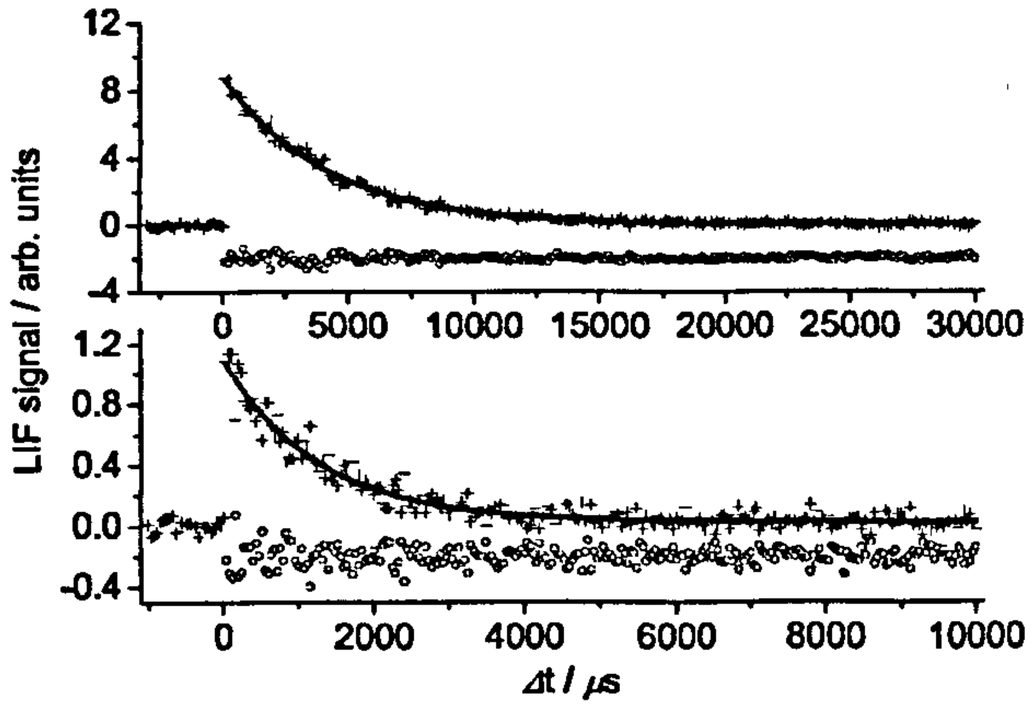

Fig. 2 IO decays in the absence of DMS (top panel) and presence (bottom panel) of 2.90 × 10^{16} molecule cm^{-3} DMS at 296 K and 300 Torr. Note the change in x axis scale. For both decays: $[NO_2]$ = 1.5 × 10^{13} molecule cm^{-3}; $[CF_3I]$ = 5.33 × 10^{16} molecule cm^{-3}; [He] = balance. The scattered data points (+++) are the experimental data and the ● are the exponential fits of eqn. (6) to the data. The residuals are also displayed (O) and offset by −2 (top panel) and −0.2 units (bottom panel) for clarity.

the combined effect of diffusion, and reaction of IO with NO_2, impurities (in NO_2 and RI), and photolysis products. A more detailed discussion of possible interferences in our system is given in section 3.2. All determinations of k_1 in this study are derived from individual experiments, where an average of ten pseudo-first-order IO decays (each yielding k') were recorded for nine different DMS concentrations and one decay trace in the absence of DMS. A minimum of five k' values were measured for any determination of k_1. Table 1 presents all rate coefficient data obtained in this study, along with selected rate data from various other investigations of XO + DMS reactions (X = I, Br, Cl). We observe no pressure dependence of k_1 between 5–300 Torr total pressure (M = He). Fig. 4 displays the results of the pressure dependence study, along with those of Nakano *et al.*[34] and Daykin and Wine.[28] From our data, we determine the room temperature (296 K) rate coefficient of reaction (1) as k_1 = (2.0 ± 0.3) cm^3 molecule^{-1} s^{-1}, where the error is 1σ standard deviation of all room temperature rate data acquired. Fig. 5 displays rate coefficients obtained between 296–468 K for the title reaction, showing a positive activation energy, with k_1 (T) = (9.6 ± 8.8) × 10^{-12} exp{−(1816 ± 397)/T} cm^3 molecule^{-1} s^{-1} obtained from a fit

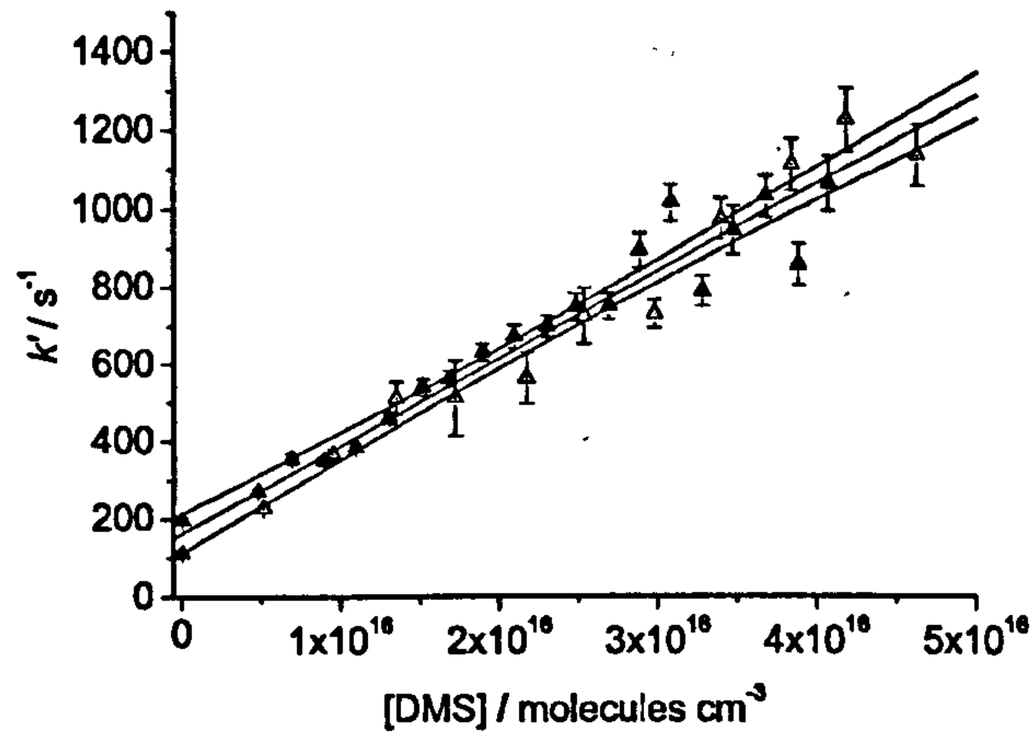

Fig. 3 Bimolecular plots for the reaction of IO + DMS at 296 K and 50 Torr total pressure, with IO generated from O + CH_3I (▲) and O + CF_3I (△). $[NO_2]$ = 1.5 × 10^{13} molecule cm^{-3} and [RI] = 7 × 10^{16} molecule cm^{-3}. The error bars represent 2σ uncertainty from individual fits of eqn. (6) to the experimental data. From the gradient, k_1 = (2.25 ± 0.10) × 10^{-14} cm^3 molecule^{-1} s^{-1}.

Table 1 Summary of rate coefficient data obtained in this work (bold font), and room temperature data from other selected studies of XO + DMS reactions. All errors are 2σ random errors returned from unweighted least squares fitting to the bimolecular plots of k' *versus* [DMS] (*e.g.*, as shown in Fig. 3)

XO	Method	Precursors, M	T/K	P/Torr	$10^{14}\ k_1$/cm^3 molecule^{-1} s^{-1}	Ref.
IO	**PLP-LIF**	**CF_3I/NO_2, He**[a]	**296**	**5**	**1.64 ± 0.20**	**This work**
		CH_3I	**296**	**5**	**1.71 ± 0.18**	
		CH_3I	**296**	**10**	**2.29 ± 0.40**	
		CH_3I	**296**	**15**	**1.84 ± 0.17**	
		CH_3I	**296**	**30**	**2.39 ± 0.24**	
		CH_3I	**296**	**50**	**2.11 ± 0.13**	
		CF_3I	**296**	**50**	**2.45 ± 0.23**	
		CH_3I, low NO_2[b]	**296**	**50**	**1.64 ± 0.16**	
		CH_3I, high NO_2[c]	**296**	**50**	**1.84 ± 0.16**	
		CH_3I	**296**	**75**	**2.08 ± 0.21**	
		CH_3I	**296**	**150**	**1.79 ± 0.16**	
		CF_3I	**296**	**300**	**2.08 ± 0.15**	
		CH_3I	**308**	**50**	**4.24 ± 0.31**	
		CH_3I	**343**	**50**	**4.20 ± 0.43**	
		CH_3I	**368**	**50**	**11.6 ± 1.2**	
		CH_3I	**393**	**50**	**6.11 ± 0.25**	
		CF_3I	**393**	**50**	**6.98 ± 0.33**	
		CH_3I	**418**	**50**	**12.8 ± 1.1**	
		CH_3I	**468**	**50**	**20.6 ± 3.3**	
IO	PLP-CRD	CF_3I/O_3, N_2	298	100	25 ± 2	34
IO	PLP-LPA	I_2/NO_2, O_2/N_2/air	298	40–300	< 3.5	28
IO	DF-MS	I_2/O_2, He	298	1.82–5.09	0.88 ± 0.21	30
IO	DF-MS	I_2/O_2, He	298	1.1–1.4	1.5 ± 0.2	31
IO	DF-MS	I_2/O_2, He	298	2.5–2.7	1.6 ± 0.3	32
IO	Computational		298	760	1500	35
BrO	DF-MS	Br_2/O_2, He	298	0.35–2.52	27 ± 5	30
BrO	DF-MS	$Br_2/O_3/O_2$, He	298	0.97–1.03	27 ± 2	41
BrO	PLP-UV	Br_2/O_3, N_2	295	60–200	44.0 ± 6.6	42
BrO	PLP-CRD	Br_2/O_3, N_2/SF_6	300	100–200	46 ± 6	43
BrO	Computational		298	760	87	35
ClO	DF-MS	Cl_2/O_3, He	298	0.84–4.76	0.95 ± 0.02	30
ClO	DF-MS	Cl_2/O_3, He	298	0.5–2.0	0.39 ± 0.12	44
ClO	Computational		298	760	0.3	35

PLP-LIF: pulsed-laser photolysis-laser-induced fluorescence; PLP-CRD: pulsed-laser photolysis-cavity ring down spectroscopy; PLP-LPA: pulsed-laser photolysis-long path absorption: DF-MS: discharge flow-mass spectrometry; PLP-UV: pulsed-laser photolysis ultra violet absorption spectroscopy.[a] In our study; [He] = balance. [RI] = (5–7) × 10^{16} molecule cm^{-3}; [DMS] = (5–50) × 10^{15} molecule cm^{-3}; [NO_2] = (1–2) × 10^{13} molecule cm^{-3}; [b] (with exceptions where [NO_2] = 1 × 10^{13} molecule cm^{-3}; [c] 6 × 10^{13} molecule cm^{-3}.

of the relevant data in Table 1 to the Arrhenius equation. Also included are the results of the temperature dependence study by Nakano *et al.*,[34] and various other room temperature determinations of k_1. Table 2 gives all Arrhenius parameters, obtained to date, for XO + DMS reactions. This study is the first reported investigation of the title reaction by laser flash-photolysis/LIF, and the rate coefficient determined at room temperature is towards the lower limit achievable by this technique, especially given an intercept, k_d, of *ca.* 200 s^{-1}.

The results of this study provide evidence that the title reaction (1) proceeds *via* a bimolecular mechanism, and a detailed discussion, together with a comparison of previous studies of XO + DMS reactions, is given in section 3.3.

3.2. Potential interferences from secondary chemistry

This section discusses in detail the potential of interferences in the determination of k_1. The reaction system in this study is "photolytically clean" with a minimum generation of unwanted photolysis products. The 351 nm absorption cross-sections of CF_3I,[46,47] CH_3I [46,47] and DMS [48] are $<2 \times 10^{-22}$, $<6 \times 10^{-23}$ and $\ll 10^{-22}$ cm^2 molecule^{-1}, respectively, at 298 K. Therefore, despite the high concentrations of RI and DMS used in this study, for a photolysis laser fluence of 20 mJ cm^{-2} pulse^{-1}, the concentration of any photolysis products (*e.g.* CH_3, CF_3, CH_3S, I) is negligible ($\approx[O]_0$) in our system. The loss of IO from reaction with these photolysis products is therefore small (even for 10^{-10} cm^3 molecule^{-1} s^{-1} rate coefficients), compared to reaction with DMS. As a check for secondary reactions, IO decay rates were measured in the absence of DMS with varying RI concentrations, for a constant concentration of NO_2. No significant difference in the decay rate (<10%) was observed and no systematic relationship was seen. However, the concentration of RI was maintained at a constant value across a bimolecular data set to minimise potential interference from RI photolysis. The production of IO from photolytically generated I atoms does not occur due to the small degree of RI photolysis and the composition of our reagent mixture. The only reactions capable of rapidly producing IO from I (in an iodine only system), are I + O_3 and I + NO_3.[49] The experiments are oxygen-free, hence no O_3 should be present in our system, and considering the high concentrations of RI and DMS (and the relatively low pressures studied), the production of NO_3 from O + NO_2 is not viable.

The absorption cross-sections of CH_3I and CF_3I increase with temperature, particularly at longer wavelengths, for example 351 nm[46,47] as used in this study. The IO decay rate in the absence of DMS generally increased with temperature, indicative of increased photolysis of precursors. However, [RI] was constant for the range of [DMS] used to measure k_1 for a given temperature, and so an increased concentration of photolysis products should not affect the determination of k_1, assuming pseudo-first-order kinetics. Determinations of k_1

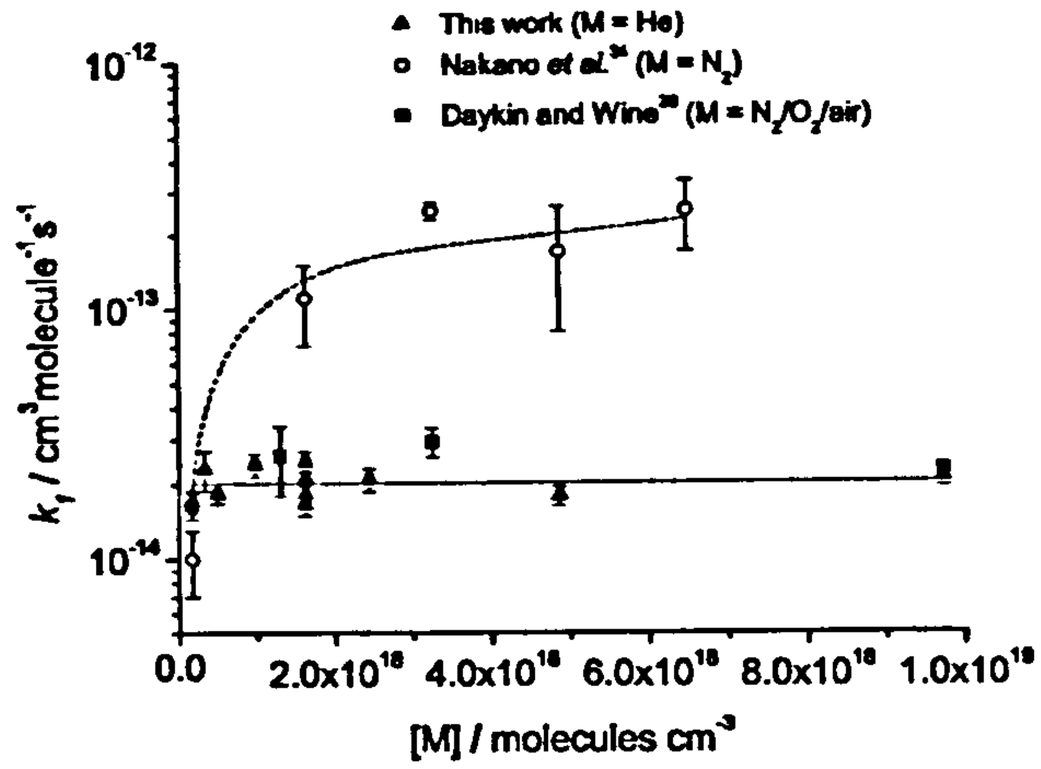

Fig. 4 Pressure dependence of k_1 obtained in this study, along with the results of Nakano *et al.*[34] and Daykin and Wine.[28] In the work of Daykin and Wine,[28] a pressure independent rate coefficient was determined with an upper limit of 3.5×10^{-14} cm^3 molecule^{-1} s^{-1}. Bimolecular plots of k' *versus* [DMS] were constructed from the results presented in their paper in order to obtain values of k_1. Error bars presented for this study, and also that of Daykin and Wine,[28] are the 2σ uncertainties of linear least squares fits to plots of k' *versus* [DMS], for example as shown in Fig. 3. The rate coefficient data obtained in this study are fitted to the form $k_1 = s[M] + k_1^0$, as shown by a -- line, yielding $s = 9.6 \times 10^{-37}$ cm^6 molecule^{-2} s^{-1} and $k_1^0 = 2.0 \times 10^{-14}$ cm^3 molecule^{-1} s^{-1}. The data of Nakano *et al.*[34] are fitted to a function given in ref. 34, and is shown by a dashed line.

were performed with both CF_3I and CH_3I at 296 K and 393 K (Table 1). Despite a factor of >2 difference in the absorption cross-sections of CH_3I and CF_3I, the measured rate coefficients are in good agreement and we conclude that any increased photolysis of RI did not interfere with the determination of k_1. The unimolecular thermal dissociation of DMS was negligible ($k_{uni} < 10^{-15}$ s^{-1}),[50] although we are unable to comment on the possibility of heterogeneously catalysed pyrolysis of DMS on the vessel walls.

For the entire study, the concentration of NO_2 was held constant in order to minimise any interference from the reaction of IO with NO_2 (and impurities within it), despite IO removal from this channel being small due to the low concentrations of NO_2. As the DMS concentration is increased, the fractional yield of IO (from O + RI) and hence the IO

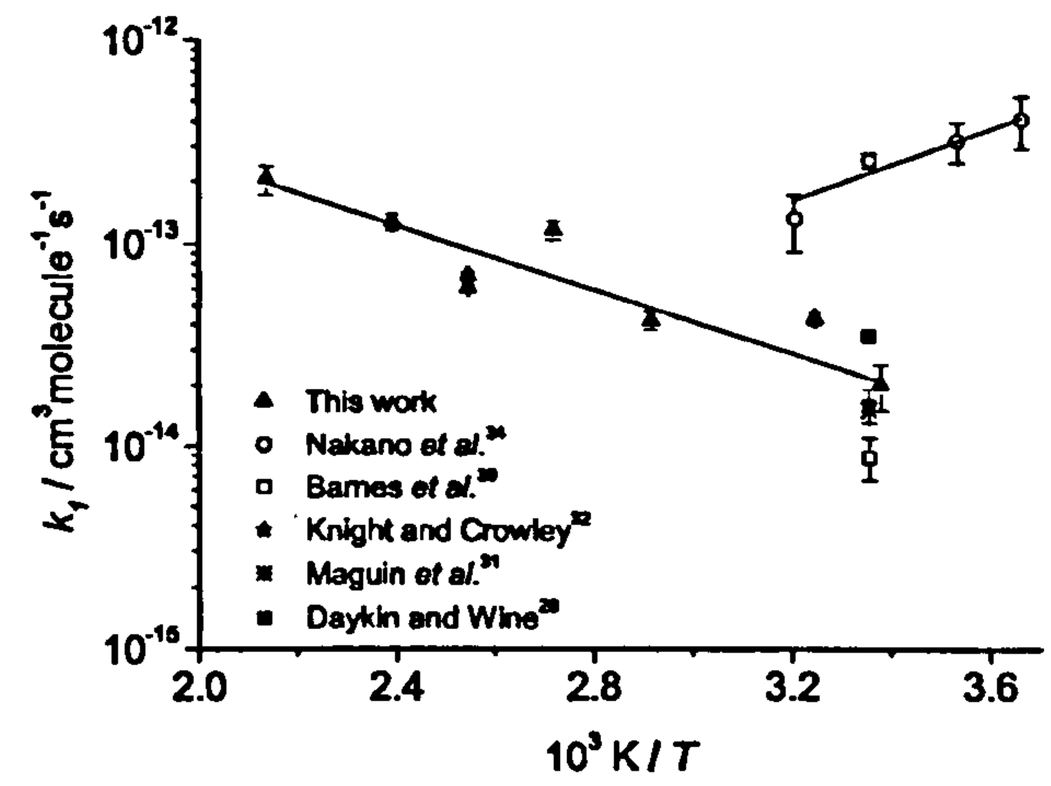

Fig. 5 The temperature dependence of the rate coefficient k_1 measured in this study compared with the results of Nakano *et al.*[34] and other room temperature determinations of k_1. Error bars for this work are the 2σ uncertainties returned from linear least squares fits to plots of k' *versus* [DMS], for example, as shown in Fig. 3. No error bars are given for the room temperature determination of k_1 from the study of Daykin and Wine[28] as an upper limit was reported.

Table 2 Summary of experimental Arrhenius parameters for XO + DMS reactions. The temperature dependence of k_1 is given by: $k_1(T) = A \exp(-E/RT)$. The errors given for this study are obtained directly from an unweighted fit of the Arrhenius equation to the experimental data

XO	Ref.	A/cm^3 molecule^{-1} s^{-1}	(E/R)/K	T range/K
IO	**This work**	$(9.6 \pm 8.8) \times 10^{-12}$	**1816 ± 397**	**296–468**
IO	34	$1.2^{+4.5}_{-1.0} \times 10^{-16}$	−2230 ± 460	273–312
BrO	45	9.17×10^{-14}	−343 ± 78	265–338
BrO	41	$(1.5 \pm 0.4) \times 10^{-14}$	−845 ± 175	233–320
BrO	43	$(1.3 \pm 0.1) \times 10^{-14}$	−1033 ± 265	278–333
ClO	44	$(1.2 \pm 0.7) \times 10^{-15}$	−354 ± 163	259–335

concentration, decreases because of competition from O + DMS. However, as the maximum IO concentration is $\leq 3.1 \times 10^{11}$ molecule cm^{-3}, IO loss from the self-reaction is very small compared to the pseudo-first-order loss for IO + DMS, and bimolecular plots of k' with [DMS] were always linear. To investigate further, a simple model in FACSIMILE was constructed to determine the contribution to k' from the IO self-reaction, as a function of [IO]. The model included three loss processes for IO, namely; (i) pseudo-first-order loss by reaction with DMS; (ii) first-order loss by diffusion, reaction with NO_2 and impurities; and (iii) the IO self-reaction. The rate coefficients, k_i, k_{ii} and k_{iii}, are given the values 2.0×10^{-14} cm^3 molecule^{-1} s^{-1} (our experimentally determined value), 200 s^{-1} (our typical IO decay rate in the absence of DMS) and 9.9×10^{-11} cm^3 molecule^{-1} s^{-1} (literature value),[51] respectively. IO decays were simulated for initial DMS and IO concentrations, and eqn. (6) was fitted to the model output to return a pseudo-first-order rate coefficient k' (*i.e.* k_i[DMS]). This process is repeated over the range of DMS concentrations used in our experiment (with the initial IO concentration adjusted to take into account partitioning between O + RI and O + DMS), to generate a bimolecular plot of k' *versus* [DMS]. For an initial IO concentration of 1×10^{12} molecule cm^{-3} (*i.e.* in the absence of DMS), the value of k_1 is reduced by ~10% due to the self-reaction, whereas for an initial IO concentration of 5×10^{11} molecule cm^{-3} (slightly higher than the calculated experimental maximum in the absence of DMS), k_1 is reduced by <5%. Therefore, we conclude that the self-reaction does not pose a serious interference to our experimental determination of k_1, particularly in light of the highly exponential nature of the IO decays (Fig. 2).

To experimentally verify the model results, we measured k_1 (296 K, 50 Torr) in back-to-back experiments with $[NO_2] = 1 \times 10^{13}$ molecule cm^{-3}, and 6×10^{13} molecule cm^{-3}, respectively. Although k_d was about twice as large in the latter case (increased IO removal with NO_2 and impurities therein), the slopes of the bimolecular plots are within the statistical uncertainties, yielding $k_1 = (1.65 \pm 0.16)$ and $(1.84 \pm 0.16) \times 10^{-14}$ cm^3 molecule^{-1} s^{-1}, for the low and high $[NO_2]$ experiments, respectively (Table 1).

As the room temperature rate coefficient, k_1, obtained in this study is lower than the most recent determination by Nakano *et al.*,[34] we were concerned by the possibility of IO recycling, despite the apparent lack of an IO regeneration mechanism in our system. LIF is a highly selective technique as any absorber must also fluoresce, and over a similar timescale to the molecule of interest, to pose an interference. Any baseline drift in the IO decays was therefore investigated carefully. The probe laser wavelength was tuned below the IO (2,0) bandhead by ~0.1 nm, a spectral region where no IO absorption occurs, and a kinetic trace was recorded under typical experimental conditions. A weak fluorescence signal was observed above the pre-trigger baseline, but no apparent temporal evolution (on the timescale of an IO decay trace) of this fluorescing species, X, could be determined outside the experimental noise. When

the laser PRF was increased to 7 Hz, this "offline" fluorescence signal became more pronounced and was seen to slowly increase over the time scale of the experiment (0–30 ms). This kinetic growth was fitted to eqn. (8)

$$[X]_t = [X]_0 (1-\exp^{-k''t}) \quad (8)$$

where $[X]_0$ is the signal due to species X at long times after the photolysis pulse and k'' is the pseudo-first-order rate constant for production of X, determined to be $k'' = 75 \pm 4\ s^{-1}$, being independent of [DMS]. A variety of bimolecular data sets for IO + DMS were then reanalysed by fitting to eqn. (9), which accounts for the slow growth of species X:

$$[IO]_t + [X]_t = [IO]_0 \exp^{(-k't)} + [X]_0(1 - \exp^{-k''t}) \quad (9)$$

where k'' is fixed to the previously determined value of 75 s^{-1}. The result of this analysis was to reduce the determined values of k', and hence k_1. The *worst* case deviation to the determination of k_1 was −15% for a 7 Hz laser PRF. It should be noted that at a 2 Hz PRF the baseline discrepancy was a minor interference (<5% of the peak IO signal) and exhibited no detectable temporal evolution on the time scale of IO decay. It must be stressed that the 7 Hz experiment was unrepresentative of our experimental conditions, but illustrates the potential interference more clearly, as gas replenishment of the photolysis region is not as efficient at the higher PRF, and renders the experiment more susceptible to the build-up of long-lived photolysis products (such as I_2). Furthermore, although the baseline deviation was most commonly positive, negative baseline discrepancies were also observed under all experimental conditions. Daykin and Wine[28] observed a negative baseline deviation in their experiment, which increased with [DMS]. They attributed this phenomenon to an increased removal of NO_2 by products of the O + DMS reaction. However, in their experiment, the concentration of NO_2 was typically two orders of magnitude greater than in this work, and we do not expect this chemistry to have been a significant interference in our study. Although unlikely to effect the kinetics of the title reaction, the small-scale photolysis of RI in our experimental system (as discussed previously) could lead to the formation of low concentrations of species such as I_2, INO, INO_2, CH_3NO_2, CH_3NO and I–DMS (by analogy to that of the Cl–DMS[55] and Br–DMS adducts—first reported by Wine *et al.* in the book cited in ref. 45). It is considered unlikely, however, that INO, INO_2 or I–DMS would exhibit fluorescence spectra due to the continuous nature of their absorption spectra and weak bond energies.[54] We feel that I_2 is the most likely candidate for species X. It should, again, be emphasised that the production of low concentrations of I_2 ($< 5 \times 10^{11}$ molecule cm^{-3}), or another such species, will not affect the determination of k_1 in this work.

The IO decays shown in Fig. 2 show the temporal decay of IO in the absence and presence of DMS. From the concentrations of RI (5.33×10^{16} molecule cm^{-3}) and DMS (2.90×10^{16} molecule cm^{-3}), and the room temperature values of k_4 ($(4.25 \pm 0.26) \times 10^{-12}$ cm^3 $molecule^{-1}$ s^{-1})[53] and k_5 ($(4.83 \pm 0.46) \times 10^{-11}$ cm^3 $molecule^{-1}$ s^{-1}),[52] the peak IO signal in the presence of DMS is calculated to be (13.9 ± 1.6)% of the peak IO signal in the absence of DMS. The observed value is (12.9 ± 0.4)% indicating that IO production is extremely well characterised in our system and that contribution to the fluorescence signal from other species is negligible. We therefore feel justified in analysing the data as described in section 3.1, but acknowledge that, ideally, it would have been desirable to have measured each IO decay "on" and "off" the IO (2,0) bandhead, thus obtaining differential fluorescence decay traces, but at the expense of considerably longer experiments. To account for a possible interference to our determination of k_1 from the baseline discrepancy outlined above, we introduce a −15% error to our room temperature rate coefficient (in line with the *worst case* scenario). A +5% error is also introduced, to account for any interference from the IO self-reaction discussed previously. The room temperature rate coefficient, k_1, obtained in this work, is thus $(2.0 \pm {}^{0.4}_{0.6}) \times 10^{-14}$ cm^3 $molecule^{-1}$ s^{-1}.

3.3. Comparison of k_1 with previous literature values

This study represents a comprehensive investigation of the IO + DMS reaction over a wide range of temperatures and pressures. The room temperature determination of k_1 in this study is in reasonable agreement with the previous investigations of Daykin and Wine,[28] Barnes *et al.*,[30] Maguin *et al.*[31] and Knight and Crowley,[32] but is in poor agreement with the recent study of Nakano *et al.*[34] (at pressures greater than 5 Torr—see below) and the computational study of Sayin and McKee[35] (Table 1). The study of Daykin and Wine[28] employed detection of IO by absorption, and although relatively high IO concentrations were present, the upper limit for k_1 given in their work is in accordance with the k_1 values obtained from the "cleaner" discharge–flow mass spectrometric (DF-MS) reaction systems. For the pressure dependence of k_1, our results are in agreement with those of Daykin and Wine,[28] who observed no pressure dependence, but again are in disagreement with Nakano *et al.*[34] (Fig. 4). Although our experiment was conducted in He, which is less efficient at collisional themalisation compared with N_2, it is highly unlikely that a pressure dependence as marked as that described by Nakano *et al.*[34] (reaching the high pressure limit by 100 Torr N_2) would not also be apparent in 300 Torr He (the highest pressure determination of k_1 in the current study). Further, in the study of Daykin and Wine,[28] which employed similar precursors to this study, the reaction was performed in N_2/O_2/air over a pressure range of 40–300 Torr. It is interesting that Nakano *et al.*[34] determined a value for k_1 at 5 Torr and 298 K ($(1.0 \pm 0.3) \times 10^{-14}$ cm^3 $molecule^{-1}$ s^{-1}) that is in good agreement with the rest of the literature. The most notable experimental differences in the work of Nakano *et al.*[34] are the photolysis wavelength of 266 nm, and the choice of O_3 as an O atom precursor. Although photolysis of DMS will be negligible in their system, due to the small absorption cross section ($\sigma_{266} = 1.2 \times 10^{-21}$ cm^2 $molecule^{-1}$),[48] this wavelength is near the UV absorption maximum of CF_3I ($\sigma_{266} = 6.3 \times 10^{-19}$ cm^2 $molecule^{-1}$),[39] and under their reaction conditions, a significant amount of the iodide precursor will be photolysed. We estimate that a concentration of up to 1×10^{13} molecule cm^{-3} of I atoms and CF_3 radicals are generated in the work of Nakano *et al.*[34] Under their experimental conditions, the CF_3 radicals are likely to react with O_2, forming CF_3O_2. We note that the IO decay rate in the absence of DMS, k_d, in the work of Nakano *et al.*[34] is fairly high (~700 s^{-1}) and we hypothesise that this may be due to reaction of IO with CF_3O_2:

$$IO + CF_3O_2 \rightarrow OIO + CF_3O \quad (10a)$$

$$\rightarrow I + O_2 + CF_3O \quad (10b)$$

The exothermicity of reactions (10a) and (10b) are −81 and −51 kJ mol^{-1}, respectively.[54] A study by Shah *et al.*[56] estimated the rate coefficient for $IO + CH_3O$ as $(4 \pm 2) \times 10^{-11}$ cm^3 $molecule^{-1}$ s^{-1}, and the same authors have recently indicated that the $IO + CH_3O_2$ and $IO + CF_3O_2$ (10) reactions proceed at similar rates.[57] Bale *et al.*[57] have measured the rate coefficient for reaction (10) and have found it to be $(3.7 \pm 0.9) \times 10^{-11}$ cm^3 $molecule^{-1}$ s^{-1}, and have found it to be pressure independent. A rate coefficient for reaction (10) of this magnitude may be able to account for the high, "zero DMS", IO decay in the study of Nakano *et al.*[34] However, the presence of reaction (10) would not interfere with the determination of k_1 in their study, providing $[CF_3I]$ is maintained at a constant value across a bimolecular data set of varying [DMS].

By modelling (using FACSIMILE) the reaction system employed in the study of Nakano *et al.*,[34] and using the information provided in their paper, we find that generation of IO from reaction (2) is not negligible in their experiment, particularly at long time delays between excimer and probe lasers. A more insightful conclusion can be drawn from the IO decays in the absence and presence of DMS, presented in the paper by Nakano *et al.*[34] We predict that the peak IO concentration in the presence of DMS should be substantially lower (<5%) than that in the absence of DMS. The observed ratio (>30%) is much greater than the experimental conditions should permit and is thus indicative of either; (i) an additional IO source in their system; (ii) an overestimation of [DMS]; (iii) an increased concentration of CF_3I at higher [DMS]; or (iv) the absorption of laser radiation by a species other than IO. The presence of a non-IO absorber, namely the I–DMS adduct, is the most likely explanation for this anomaly. In the kinetic traces presented in their paper the IO concentrations return to (or close to) zero at long time delays, contrary to our model predictions. We conclude that there must be a more predominant I atom sink than O_3 in their system, and we consider this species to be DMS. Bromine[42,43] and chlorine[55] atoms are known to react rapidly with DMS, forming Cl–DMS and Br–DMS adducts. We propose that this is also the case for I + DMS. Furthermore, if such an I–DMS adduct were to exist, and was analogous to its Br and Cl counterparts, it may well be expected to exhibit broad, structureless and strong absorption, in the same region of the electromagnetic spectrum as IO. The Br–DMS adduct has been found to react rapidly with Br atoms, forming molecular bromine and DMS.[42] Again, we see no reason why an iodine analogue to this reaction is unfeasible. The pressure-dependent formation of a possible I–DMS adduct in the work of Nakano *et al.*[34] provides an absorbing species whose concentration and temporal evolution may be dependent on the concentration of DMS, and could account for their experimental results. However, this hypothesis is highly speculative and we do not feel able to comment further on such a mechanism.

Considering the high precursor concentration in the study of Daykin and Wine,[28] it was considered prudent to investigate the potential formation of an I–DMS adduct in their experimental system. Although high I_2 concentrations were present, the amount of I atoms generated by the photolysis of I_2 was less than that in the work of Nakano *et al.*,[34] due to the small absorption cross-section of I_2 at 351 nm[58]. Furthermore, any I atoms produced are likely to have reacted with the high concentrations of NO_2, forming INO_2[54] (which can also react with I).[59] We have modelled both the production rate of IO and the maximum IO concentrations for their system, both in the presence and absence of DMS, and obtain consistent results within <25%. The formation of IO is thus well characterised in their reaction system, and does not suggest the presence of a non-IO absorber. Indeed, Daykin and Wine[28] performed a limited number of "off-band" decay traces and found that, after correction, the "on band" IO decay was altered by less than 1%. In the DF-MS[30 32] studies, O atoms were produced by the microwave discharge of O_2/He mixtures, with no photolysis necessary, and hence the formation of I–DMS is not applicable.

In summary, the work of Nakano *et al.*[34] has the most potential for interference from unwanted chemistry. Underestimating the value of k_1 in our study seems unlikely as there is no evidence for IO recycling and a reasoned mechanism for this process cannot be postulated given our reagent mixture. A potential explanation that could lead to an underestimation of k_1 is a large overestimation of [DMS]. The affinity of DMS for surfaces makes the overestimation of DMS using metered flows a possibility, but by an order of magnitude seems extremely unlikely. Using a similar reagent mix, no dark reactions were observed in the study of Daykin and Wine.[28] Furthermore, the ratio of the peak signals for our IO decay traces (Fig. 2) in the absence and presence of DMS is indicative of [RI] and [DMS] being well defined in our experiment.

3.4. Reactivity trends for XO + DMS, X = Cl, Br, I

The apparent reactivity trend between the halogen oxides and DMS is perhaps surprising. The current recommended IUPAC rate coefficients for the reactions of ClO, and BrO, with DMS at 298 K are $(9.0 \pm 0.5) \times 10^{-15}$ cm^3 molecule^{-1} s^{-1} and $(4.4 \pm 0.3) \times 10^{-13}$ cm^3 molecule^{-1} s^{-1}, respectively.[13] This gives a trend for XO + DMS of, ClO ≈ IO, <BrO, which is not confirmed by the computational study of Sayin and McKee,[35] who find k_1 (X = I) to be >1000 times higher than the recommended literature value. The poorer agreement between theoretical and experimental determinations of k_1, compared with ClO/BrO + DMS, is not surprising given the difficulty in calculating electronic basis sets for heavy atom systems. This experimental trend of reactivity is not observed for the bimolecular reaction XO + NO → X + NO_2,[54] which are all fast and consistent with no barrier to reaction. All XO + DMS reactions are assumed to predominantly proceed through an oxygen-atom transfer mechanism to yield DMSO + X.[30 32,42,44] The reaction enthalpies for XO + DMS at 298 K are −93.9, −121.4 and −122.7 kJ mol^{-1} for X = Cl, Br and I, respectively.[13] On the basis of thermodynamics, one might therefore expect the reactivity order to be IO ≈ BrO > ClO, where the primary difference in reaction rate is explained by the strength of the XO bond. It is noted that the results of Nakano *et al.*[34] are consistent with this argument. It is worth mentioning, however, that there is sufficient uncertainty in the values of $\Delta_f H$ (298 K) IO (116 ± 5 kJ mol^{-1})[54] and $\Delta_f H$ (298 K) BrO (120 ± 6 kJ mol^{-1})[54] to reverse the reaction exothermicities of BrO + DMS and IO + DMS by ~10 kJ mol^{-1}. This could help explain a lower rate of reaction for IO + DMS. Another consideration is the influence of steric factors, which are probably more severe for IO, resulting in a higher frequency of reactive collisions in the BrO + DMS reaction.

The pressure independence and positive temperature dependence for k_1, determined in this study, provide evidence of a bimolecular reaction mechanism. In contrast, an association complex mechanism has been suggested for the BrO + DMS reaction:

$$\mathrm{BrO + DMS \leftrightarrow [BrO\text{–}DMS] \rightarrow Br + DMS} \qquad (11)$$

The evidence for this mechanism is based on the negative temperature dependencies reported in the studies of Bedjanian *et al.*[41] and Nakano *et al.*,[43] and also the higher rate coefficients determined by Ingham *et al.*[42] and Nakano *et al.*[43] at higher pressures (>60 Torr N_2) than the rate coefficients reported in the low pressure flow tube studies. It is worth exploring the features of this mechanism further, as it is used by Nakano *et al.*[34] to explain the pressure dependence observed for k_1 in their IO + DMS system. Extension of the complex mechanism (11), *via* a Lindemann-type scheme, explicitly gives the pressure dependence of the system:

$$\mathrm{XO + DMS} \underset{k_{-A}}{\overset{k_A}{\rightleftharpoons}} \mathrm{[XO\text{-}DMS]^*} \xrightarrow{k_C} \mathrm{X + DMSO}$$
$$\mathrm{[XO\text{-}DMS]^*} \xrightarrow{k_M[M]} \mathrm{[XO\text{-}DMS]} \qquad (12)$$

The pressure dependence in the above scheme is due to stabilisation of the [XO–DMS]* adduct. In order for stabilisation to occur, the [XO–DMS] adduct is required to be sufficiently strongly bound. The calculated binding enthalpy of the

BrO–DMS adduct is <8 kJ mol^{-1},[35] being too small (even when allowing for calculation uncertainty) to allow collisional stabilisation of the excited adduct. A prediction of scheme (12) is that the yield of DMSO decreases with increasing pressure. However, this is not borne out in the work of Ingham *et al.*[43] where the yield of Br + DMSO is unity at all pressures up to 200 Torr. Scheme (12) is therefore inconsistent with the literature. The factor of *ca.* two difference in the room temperature rate coefficients for BrO + DMS measured at low pressure in a flow-tube and by pulsed-laser photolysis at high pressure is thus not due to pressure stabilisation of a complex intermediate. If a complex intermediate is formed, then it must be weakly bound, and could explain a pressure independent rate coefficient with a small negative activation energy. The temperature dependent studies of the BrO + DMS reaction were performed over a relatively narrow temperature range, and report a small, negative activation barrier (Table 2).

Nakano *et al.*[34] observed a pressure dependence for IO + DMS that reached a limit >10 times the room temperature observed here, but these results should be treated with caution, as they imply that the IO–DMS intermediate, in scheme (12), is strongly bound (>35 kJ mol^{-1}). It seems unlikely that an IO–DMS adduct would be more strongly bound than BrO–DMS. The *ab initio* study by Sayin and McKee[35] calculated a binding energy for IO–DMS of ~6 kJ mol^{-1}, comparable to that of the BrO analogue.

The ClO + DMS reaction has been studied over a limited pressure range (0.5–5 Torr), and the only temperature dependent study (three values in the narrow range 259–335 K) reported a very small, negative activation energy. The computational investigation[35] only considered the bimolecular reaction pathway for ClO + DMS, as the binding enthalpy of a ClO–DMS adduct could not compensate for the loss of entropy associated with its formation. The computational study[35] predicts a room temperature rate coefficient of 3×10^{-15} cm^3 molecule^{-1} s^{-1}, in excellent agreement with the experimental determination of $(3.9 \pm 1.2) \times 10^{-15}$ cm^3 molecule^{-1} s^{-1} by Diaz-de-Mera *et al.*,[44] but a positive activation barrier, in disagreement with the experimental findings.

Due to the wide temperature range of ~170 K, and the absence of interfering chemistry, the current study should yield accurate Arrhenius parameters for IO + DMS. The results presented in our study for IO + DMS suggest that the reaction proceeds *via* a bimolecular reaction mechanism, and that it is the barrier to products that is controlling the temperature dependence. While the reaction may proceed *via* a weakly bound intermediate, it is the barrier that controls the reaction. The rate coefficient for ClO + DMS is even smaller than for IO + DMS, and would also appear to be a bimolecular reaction controlled by a barrier. The rate constant for BrO + DMS is at least an order of magnitude higher than for the ClO and IO analogues, and appears to have a negative temperature dependence. This suggests that the reaction kinetics are controlled by the formation of a weakly bound intermediate, with no barrier to reaction.

4. Conclusions

Of all XO + DMS investigations to date, this study of the IO + DMS reaction covers the widest temperature range and is subject to negligible interference from undesirable secondary chemistry, and hence should give accurate and reliable Arrhenius parameters. The results obtained in this study are in poor agreement with recent experimental and computational studies[34,35] of the IO + DMS reaction, but are in good agreement with the previous literature.[28,30–32] The results are consistent with the IO + DMS reaction proceeding *via* a bimolecular reaction mechanism, although further work is required to probe the mechanisms of reactions between halogen oxides and DMS.

For typical IO concentrations measured in the marine boundary layer (MBL),[18,23–25] the room temperature rate coefficient determined in this study implies that the IO + DMS reaction is not an important atmospheric sink for DMS. However, localised IO concentrations in the MBL may be significantly higher than those measured from the shore and averaged across several km of ocean, as evidenced by recent observations of high I_2 concentrations correlated with tidal height.[18] An *in situ* detection method for the measurement of IO in the MBL is therefore highly desirable[60] in order to verify if the IO + DMS reaction is of atmospheric significance under localised conditions.

Acknowledgements

The authors would like to thank M. J. Pilling from the University of Leeds for valuable discussions concerning section 3.2, and also T. Ingham and W. J. Bloss from the University of Leeds, for helpful comments and interest in this work.

References

1 R. J. Charlson, J. E. Lovelock, M. O. Andreae and S. G. Warren, *Nature*, 1987, **326**, 655–661.
2 E. K. Bigg, J. L. Gras and C. Evans, *J. Atmos. Chem.*, 1984, **1**, 203–214.
3 S. N. Pandis, L. M. Russell and J. H. Seinfeld, *J. Geophys. Res.*, 1994, **99**, 16945–16957.
4 A. Gross and A. Baklanov, *Int. J. Environ. Pollut.*, 2004, **22**, 51–71.
5 J. Langer and H. Rodhe, *J. Atmos. Chem.*, 1991, **13**, 225–263.
6 A. R. Ravishankara, Y. Rudich, R. Talukdar and S. B. Barone, *Philos. Trans. R. Soc. London, Ser. B*, 1997, **352**, 171–182.
7 P. H. Wine, N. M. Kreutter, C. A. Gump and A. R. Ravishankara, *J. Phys. Chem.*, 1981, **85**, 2660–2665.
8 A. J. Hynes and P. H. Wine, *ACS Symp. Ser.*, 1987, **349**, 133–141.
9 S. B. Barone, A. A. Turnipseed and A. R. Ravishankara, *J. Phys. Chem.*, 1996, **100**, 14694–14702.
10 T. J. Wallington, R. Atkinson, A. M. Winer and J. N. Pitts, Jr., *J. Phys. Chem.*, 1986, **90**, 4640–4644.
11 E. J. Dlugokencky and C. J. Howard, *J. Phys. Chem.*, 1988, **92**, 1188–1193.
12 E. P. Daykin and P. H. Wine, *Int. J. Chem. Kinet.*, 1990, **22**, 1083–1094.
13 R. Atkinson, D. L. Baulch, R. A. Cox, J. N. Crowley, R. F. Hampson, R. G. Hynes, M. E. Jenkin, M. J. Rossi and J. Troe, *Atmos. Chem. Phys.*, 2004, **4**, 1461–1738.
14 B. C. Nguyen, B. Bonsang and A. Gaudry, *J. Geophys. Res.*, 1983, **88**, 10903–10914.
15 J. D. James, R. M. Harrison, N. H. Savage, A. G. Allen, J. L. Grenfell, B. J. Allan, J. M. C. Plane, C. N. Hewitt, B. Davison and L. Robertson, *J. Geophys. Res.*, 2000, **105**, 26379–26392.
16 R. Von Glasow and P. J. Crutzen, *Atmos. Chem. Phys.*, 2004, **4**, 589–608.
17 W. L. Chameides and D. D. Davis, *J. Geophys. Res.*, 1980, **85**, 7383–7398.
18 A. Saiz-Lopez and J. M. C. Plane, *Geophys. Res. Lett.*, 2004, **31**, L04112.
19 G. McFiggans, J. M. C. Plane, B. J. Allen, L. J. Carpenter, H. Coe and C. O'Dowd, *J. Geophys. Res.*, 2000, **105**, 14371–14385.
20 C. D. O'Dowd, J. L. Jimenez, R. C. Bahreini, J. H. Seinfeld, K. Hemeri, L. Pirjola, M. Kulmala, S. G. Jennings and T. Hoffman, *Nature*, 2002, **417**, 632–636.
21 J. L. Jimenez, R. Bahreini, D. R. III. Cocker, H. Zhuang, V. Varutbangkul, R. C. Flagan, J. H. Seinfeld, C. D. O'Dowd and T. Hoffmann, *J. Geophys. Res.*, 2003, **108**(D10), 4318, AAC5.
22 G. McFiggans, H. Coe, R. Burgess, J. Allan, M. Cubison, M. R. Alfarra, R. Saunders, A. Saiz-Lopez, J. M. C. Plane, D. J. Wevill, L. J. Carpenter, A. R. Rickard and P. S. Monks, *Atmos. Chem. Phys.*, 2004, **4**, 701–713.
23 B. Alicke, K. Hebestreit, J. Stutz and U. Platt, *Nature*, 1999, **397**, 572–573.
24 B. J. Allan, G. McFiggans, J. M. C. Plane and H. Coe, *J. Geophys. Res.*, 2000, **105**, 14363–14369.
25 U. Frieß, T. Wagner, I. Pundt, K. Pfeilsticker and U. Platt, *Geophys. Res. Lett.*, 2001, **28**, 1941–1944.
26 I. Barnes, K. H. Becker, P. Carlier and G. Mouvier, *Int. J. Chem. Kinet.*, 1987, **19**, 489–501.

27 D. Martin, J. L. Jourdain, G. Laverdet and G. Le Bras, *Int. J. Chem. Kinet.*, 1987, **19**, 503–512.
28 E. P. Daykin and P. H. Wine, *J. Geophys. Res.*, 1990, **95**, 18547–18553.
29 R. B. Chatfield and P. J. Crutzen, *J. Geophys. Res.*, 1990, **95**, 22319–22341.
30 I. Barnes, V. Bastian, K. H. Becker and R. D. Overath, *Int. J. Chem. Kinet.*, 1991, **23**, 579–591.
31 F. Maguin, A. Mellouki, G. Laverdet, G. Poulet and G. Le Bras, *Int. J. Chem. Kinet.*, 1991, **23**, 237–245.
32 G. P. Knight and J. N. Crowley, *Phys. Chem. Chem. Phys.*, 2001, **3**, 393–401.
33 I. K. Larin, N. A. Messineva, A. I. Spasskii, E. M. Trofimova and L. E. Turkin, *Kinet. Catal.*, 2000, **41**, 437–443.
34 Y. Nakano, S. Enami, S. Nakamichi, S. H. Aloisio, S. Hashimoto and M. Kawasaki, *J. Phys. Chem. A*, 2003, **107**, 6381–6387.
35 H. Sayin and M. L. McKee, *J. Phys. Chem. A*, 2004, **108**, 7613–7620.
36 M. A. Blitz, D. G. Johnson, M. Pesa, M. J. Pilling, S. H. Robertson and P. W. Seakins, *J. Chem. Soc., Faraday Trans.*, 1997, **93**, 1473–1479.
37 M. A. Blitz, M. Pesa, M. J. Pilling and P. W. Seakins, *J. Phys. Chem. A*, 1999, **103**, 5699–5704.
38 M. E. Green and C. M. Western, *J. Chem. Phys.*, 1996, **104**, 848–864, *PGOPHER* spectral simulation program written by C. M. Western. A description of the Hamiltonian used.
39 S. P. Sander, R. R. Friedl, D. M. Golden, M. J. Kurylo, R. E. Huie, V. L. Orkin, G. K. Moortgat, A. R. Ravishankara, C. E. Kolb, M. J. Molina and B. J. Finlayson-Pitts, in *Chemical Kinetics and Photochemical Data for Use in Atmospheric Studies Evaluation Number 14*, Jet Propulsion Laboratory, California Institute of Technology, Pasadena, CA, USA, 2003, Section 4: Photochemical Data.
40 S. M. Newman, W. H. Howie, I. C. Lane, M. R. Upson and A. J. Orr-Ewing, *J. Chem. Soc., Faraday Trans.*, 1998, **94**, 2681–2688.
41 Yu. Bedjanian, G. Poulet and G. Le Bras, *Int. J. Chem. Kinet.*, 1996, **28**, 383–389.
42 T. Ingham, D. Bauer, R. Sander, P. J. Crutzen and J. N. Crowley, *J. Phys. Chem. A*, 1999, **103**, 7199–7209.
43 Y. Nakano, M. Goto, S. Hashimoto, M. Kawasaki and T. J. Wallington, *J. Phys. Chem. A*, 2001, **105**, 11045–11050.
44 Y. Diaz-de-Mera, A. Aranda, D. Rodriguez, R. Lopez, B. Cabanas and E. Martinez, *J. Phys. Chem. A*, 2002, **106**, 8627–8633.
45 I. Barnes, K. H. Becker and R. D. Overath, in *The Tropospheric Chemistry of Ozone in the Polar Regions: NATO ASI Series I: Global Environmental Change*, ed. H. Niki and K. H. Becker, 1993, vol. 7, p. 371.
46 O. V. Rattigan, D. E. Shallcross and R. A. Cox, *J. Chem. Soc., Faraday Trans.*, 1997, **93**, 2839–2846.
47 C. M. Roehl, J. B. Burkholder, G. K. Moortgat, A. R. Ravishankara and P. J. Crutzen, *J. Geophys. Res.*, 1997, **102**, 12819–12829.
48 C. H. Hearn, E. Turcu and J. A. Joens, *Atmos. Environ.*, 1990, **24**, 1939–1944.
49 R. M. Chambers, A. C. Heard and R. P. Wayne, *J. Phys. Chem.*, 1992, **96**, 3321–3331.
50 S. H. Mousavipour, L. Emad and S. Fakhraee, *J. Phys. Chem. A*, 2002, **106**, 2489–2496.
51 M. H. Harwood, J. B. Burkholder, M. Hunter, R. W. Fox and A. R. Ravishankara, *J. Phys. Chem. A*, 1997, **101**, 853–863.
52 J. H. Lee, I. N. Tang and R. B. Klemm, *J. Chem. Phys.*, 1980, **72**, 1793–1796.
53 M. A. Teruel, T. J. Dillon, A. Horowitz and J. N. Crowley, *Phys. Chem. Chem. Phys.*, 2004, **6**, 2172–2178.
54 R. Atkinson, D. L. Baulch, R. A. Cox, R. F. Hampson, Jr., J. A. Kerr, M. J. Rossi and J. Troe, *J. Phys. Chem. Ref. Data*, 2000, **29**, 167–266.
55 S. P. Urbanski and P. H. Wine, *J. Phys. Chem. A*, 1999, **103**, 10935–10944.
56 D. Shah, C. E. Canosa-Mas, N. J. Hendy, M. J. Scott, A. Vipond and R. P. Wayne, *Phys. Chem. Chem. Phys.*, 2001, **3**, 4932–4938.
57 C. S. E. Bale, C. E. Canosa-Mas, D. E. Shallcross and R. P. Wayne, *PCCP*, 2005, DOI: 10.1039/b501903f.
58 A. Saiz-Lopez, R. W. Saunders, D. M. Joseph, S. H. Ashworth and J. M. C. Plane, *Atmos. Chem. Phys.*, 2004, **4**, 1443–1450.
59 H. Van Den Bergh and J. Troe, *J. Chem. Phys.*, 1976, **64**, 736–742.
60 W. J. Bloss, T. J. Gravestock, D. E. Heard, T. Ingham, G. P. Johnson and J. D. Lee, *J. Environ. Monit.*, 2003, **5**, 21–28.
61 S. Roszak, M. Krauss, A. B. Alekseyev, H. P. Liebermann and R. J. Buenker, *J. Phys. Chem. A*, 2000, **104**, 2999–3003.

Appendix II: Absorption cross-sections of the $A^2\Pi_{3/2} \leftarrow X^2\Pi_{3/2}$ electronic transition of IO at 296 K (Section 4.3.1)

λ / nm	σ / 10^{-20} cm^{2}molecule^{-1}	λ / nm	σ / 10^{-20} cm^{2}molecule^{-1}
414.6	265	428.4	1045
414.9	279	428.7	732
415.2	271	429	517
415.5	241	429.3	419
415.8	195	429.6	185
416.1	289	429.9	179
416.4	207	430.2	96
416.7	274	430.5	107
417	208	430.8	50
417.3	259	431.1	18
417.6	371	431.4	22
417.9	385	431.7	-15
418.2	615	432	88
418.5	798	432.3	-91
418.8	1092	432.6	-12
419.1	1606	432.9	18
419.4	1932	433.2	-44
419.7	1888	433.5	-15
420	1678	433.8	54
420.3	1354	434.1	-8
420.6	1084	434.4	-125
420.9	886	434.7	25
421.2	701	435	-42
421.5	519	435.3	-42
421.8	369	435.6	2637
422.1	306	435.9	2838
422.4	199	436.2	1938
422.7	157	436.5	1452
423	16	436.8	1041
423.3	95	437.1	746
423.6	60	437.4	512
423.9	24	437.7	300
424.2	16	438	242
424.5	25	438.3	159
424.8	-44	438.6	129
425.1	85	438.9	115
425.4	-5	439.2	33
425.7	-35	439.5	158
426	25	439.8	119
426.3	74	440.1	156
426.6	203	440.4	70
426.9	1489	440.7	35
427.2	3600	441	-52
427.5	2877	441.3	4
427.8	2002	441.6	-71
428.1	1509		

Note that all cross-sections are relative to that at 427.2 nm, which is assigned a value of $\sigma = 3.6 \times 10^{-17}$ cm^{2}molecule^{-1}, and are reported for a spectral resolution of 0.3 nm FWHM.

Appendix III: Estimated absorption cross-sections of species "X" at 296 K (Section 4.3.2.3)

λ / nm	σ / 10^{-20} cm^{2}molecule^{-1}
249.7	-8
259.7	30
269.7	12
279.7	55
289.7	66
299.7	86
307.2	132
317.2	152
327.2	170
337.2	146
347.2	157
357.2	121
367.2	103
377.2	78
387.2	57
397.2	51
407.2	31
417.2	14
427.2	27
437.2	9
447.2	0
457.2	5

Note that all cross-sections are relative to that at 327.2 nm, which is assigned a value of $\sigma = 1.7 \times 10^{-18}$ cm^{2}molecule^{-1}, and are reported for a spectral resolution of 0.3 nm FWHM.